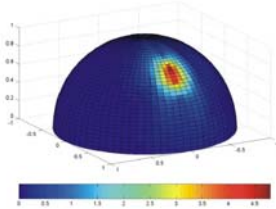


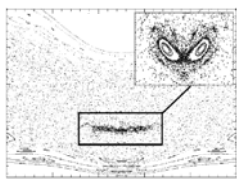
中国科学院物理研究所
光物理实验室 L05 组

研究工作报告

(2001 – 2003)



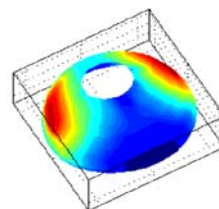
Directional emission of
hot electrons (2001)



Stochastic acceleration
of electrons (2002)



Long plasma channel
formation (2002)



Double peak emission of
hot electrons (2003)

Progress Report of Group L05
(2001 to 2003)

LABORATORY OF OPTICAL PHYSICS, INSTITUTE OF
PHYSICS, CHINESE ACADEMY OF SCIENCES

前 言

近年来随着超短脉冲激光啁啾放大 (CPA) 技术的重大突破，激光强度一下子提高了 5~6 个数量级。利用这种放大技术建立的激光装置的脉冲宽度可以短至几个光周期 (十几个飞秒)，输出功率达到 Petawatt (10^{15} 瓦)，聚焦光强超过 10^{20}W/cm^2 。这种激光不仅可以产生远大于原子内电场的超强电场，而且可以产生大于 10^{11} 巴的超高压 (相当于地球表面大气压的 1000 亿倍)，1 亿 (10^8) 高斯的超强磁场，高达 10 亿 (10^9) 度 (远高于太阳中心的温度) 的黑体辐射温度，比地球引力大 10^{23} (千万亿亿) 倍的加速度，接近光速的电子振荡速度等一系列无法用其他手段产生的极端条件，为人们提供了前所未有的机遇和挑战。同时也极大地拓展了天体物理、材料科学、等离子体物理、核聚变物理、原子核物理、相对论物理、凝聚态物理、激光物理、加速器物理、非线性光学、高能物理等学科的研究范围。

强场与超快物理研究组是中国科学院物理研究所光物理重点实验室的一个研究小组。它是 1999 年我从英国卢瑟福实验室回国后与我的同事魏志义、盛政明等人一起建立起来的。强场与超快物理研究组的主要研究方向包括发展新的超短超强激光技术，研究超短超强激光与物质相互作用，超短超强激光在大气中的传输过程，飞秒激光泵浦产生的 X 射线激光、新型等离子体粒子加速器、超短超强 X/ γ 射线、实验室天体物理学、快点火激光核聚变相关的物理过程等。

在过去三年时间里，我们在朝着建立世界一流的研究小组上取得了一系列重要进展 — 从建成输出功率达到聚焦功率密度高达 10^{19}W/cm^2 的极光二号激光装置到超短超强激光在大气中的传输过程的研究。小组的每个成员为这些工作都做出了他们独特的贡献。这份研究报告介绍了我们组在这三年里的科研活动，其中有小组的概况，成员介绍，科研成果的总结，发表文章目录等。部分发表文章的复印件附在后面。

我们组的这些研究成果得到了国家科技部、国家自然科学基金委、国家高技术 ICF 主题、中国科学院以及物理所的支持和资助。我们也非常感谢客座教授对我们小组做出的特别贡献。

张 杰
二〇〇三年十二月二十日，北京

FOREWORD

With the invention of the chirped pulse amplification (CPA) technology more than 10 years ago, a new generation of lasers appear. Based on this technology, people are now capable of dealing with lasers which can deliver laser pulses at a duration of a few laser cycles (several femtoseconds), at a petawatt level, and over the intensity 10^{20} W/cm². The studies of laser interaction with matter by use of ultra-short intense lasers have attracted great interest world wide, partially because this kind of lasers can be built within a small dimension and at a reasonable cost. Numerous of applications have been proposed based upon these studies.

The group on high field laser physics at the Institute of Physics, CAS, was established in 1999 when I returned China from the Rutherford Laboratory in England. Our research includes the development of new ultra-short intense laser systems, the technology of ultra-short lasers and its applications, the interactions of laser radiation with matter, and their various applications in X-ray lasers, table-top plasma-based particle accelerations, ultra-short X/ γ -ray sources, laboratory astrophysics, the Fast Ignition of fusion targets and related topics, etc.

In the past these years, we have made important progress toward establishing a high level research group, ranging from up-grading our laser systems to 20Terawatt to new findings in ultra-short intense laser-solid interactions. This report presents the activities of our group in the period of 2001-2003. Following a brief introduction of the research group and its members is a summary of research activities. A selection of publication in journals and conferences is included and reprints from selected publications are given at the end.

The scientific work of our group was made possible because of the support from the Ministry of Science and Technology, National Natural Science Foundation of China, the National High-Tech program 973, and the Chinese Academy of Sciences, and the Institute of Physics. We thank also many scientific visitors and guests for their special contribution.

Beijing, December 20, 2003

Jie Zhang
Group Leader for High Field Laser Physics

目 录

1. L05 组概况	4
2. 2001~2003 年工作总结	6
2.1. 研究课题	6
2.2. 获奖及专利	6
2.3. 人才培养	6
2.4. 国际合作	6
3. 研究工作简介	7
4. 代表性论文目录	27
5. 重要国际会议邀请报告	33
6. 论文选集	35

CONTENTS

1. General of our group	5
2. Summary of research activities	6
3. Brief description of research work	16
4. List of selected publications	27
5. Invited talks on international conferences	33
6. Selected papers	35

1. 中国科学院物理研究所光物理实验室L05组概况

1.1. 组成员

组长： 张杰 院士
固定研究人员： 魏志义 研究员
盛政明 研究员
鲁欣 副研究员
李玉同 副研究员

在站博士后（2名）： 孙敬华、郑家安

在读研究生（27名）： 博士生： 2000 级： 苍宇、王薇、张军
2001 级： 张秋菊、彭晓昱、李昆
王琛
2002 级： 金展、燕飞、于全芝
郑志远、令维军、田金荣
贾玉磊、王兆华、郑君
2003 级： 刘运全、郝作强、王鹏
韩海年、武慧春、徐慧
仲佳勇、远晓辉
硕士生： 2002 级： 陈民、徐妙华、李汉明

秘书： 高原
技术人员： 邱阳、陈亦飞

客座研究员： 余玮 研究员 赵刚 研究员
钱列加 教授 张志刚 教授
马锦秀 教授 李英骏 教授
张希成 教授 梁天骄 博士

联系地址：

中国科学院物理研究所光物理重点实验室
北京市中关村南三街 8 号，100080。

E-mail: jzhang@aphy.iphy.ac.cn <http://highfield.iphy.ac.cn/l05>

Tel. /Fax: +86-10-8264-9356

1.2. 研究方向

超短超强激光物理、超快相互作用物理、强激光实验室天体物理、X 射线激光，超短超强激光在大气中的传输过程、THz 辐射，固体激光技术、超短脉冲激光技术的研究和应用。

1. General of Group L05, Institute of Physics, CAS

1.1. Members of Group CL05

SCIENTIFIC STAFF: Jie ZHANG (Group leader, Academician)

Zhi-Yi WEI (Professor)

Zheng-Ming SHENG (Professor)

Xin LU (Associate Professor)

Yu-Tong LI (Associate Professor)

POSTDOCTORS: Jing-Hua SUN, Jia-An ZHENG

GRADUATE STUDENTS: Doctorate:2000: Yu CANG, Wei Wang, Jun ZHENG

2001: Qiu-Ju ZHANG, Xiao-Yu PENG

Kun LI, Chen WANG

2002: Zhan JIN, Fei YAN, Quan-Zhi YU,

Zhi-Yuan ZHENG, Wei-Jun LING,

Jin-Rong TIAN , Zhao-Hua WANG,

Yu-Lie JIA, Jun ZHENG

2003: Yun-Quan LIU, Zuo-Qiang HAO,

Peng WANG, Xiao-Hui YUAN,

Hai-Nian HAN, Hui XU,

Hui-Chun WU, Jia-Yong ZHONG,

Xiao-Hui YUAN

Masterate: 2002: Min CHEN, Miao-Hua XU, Han-Ming LI

SECRETARY: Yuan GAO

TECHNICIAN: Yang QIU, Yi-Fei CHEN

SCIENTIFIC GUESTS:

Prof. Wei YU (Shanghai Institute of Optics and Fine Mechanics, Shanghai)

Prof. Lie-Jia QIAN (Department of Physics, Fudan University, Shanghai)

Prof. Gang ZHAO (Beijing Astronomical Observatory, Beijing)

Prof. Zhi-Gang ZHANG (Tianjin University, Tianjin)

Prof. Jin-Xiu MA (University of Science and Technology of China, Hefei)

Prof. Ying-Jun LI (China University of Mining & Technology, Beijing)

Prof. Xi-Cheng ZHANG

Dr. Tian-Jiao LIANG

CONTACT ADDRESS:

Laboratory of Optical Physics, Institute of Physics

PO Box 603, Beijing 100080, PR China

Email: jzhang@aphy.iphy.ac.cn <http://highfield.iphy.ac.cn/l05>

Tel. (fax): +86-10-8264-9356

1.2. Main research interests:

Ultra-short intense laser pulse interaction with matter, relativistic laser plasma interactions, particle accelerations, fast Ignition and related topics, X-ray lasers, THz radiation, technology on ultra-short lasers and applications

2. 2001 ~ 2003 年工作总结

2.1. 研究课题

共承担研究课题 26 项，其中包括：

- 杰出青年基金 3 项(含海外)；百人计划 2 项；973 项目 2 项；院创新方向性项目 2 项；基金委重大项目 2 项；基金委面上基金 11 项；国家 863 项目 4 项。

2.2. 获奖及专利

获奖共 19 项

- 一人次获中国青年科学家奖 (张杰)
- 一人次获香港求是杰出青年学者奖 (张杰)
- 一人次获中科院青年科学家奖 (魏志义)
- 二人入选中科院百人计划 (张杰、盛政明)
- 三人次获国家杰出青年基金 (张杰、张希成、魏志义)
- 四人次获蔡诗东等离子体物理研究奖 (陈黎明, 董全力, 杨辉, 王薇)
- 四人次获蔡诗东基金会培养高水平等离子体博士荣誉奖 (张杰)
- 一人次获中国光学学会王大珩光学奖 (张杰)
- 一人次获中国物理学会饶毓泰物理奖 (张杰)
- 中科院科技进步二等奖 (魏志义、张杰等)

专利共 12 项

- 获实用新型专利 7 项：一种宽波段晶体谱仪、一种激光测量装置、一种具有高时间分辨的电子显微镜、一种飞秒激光多通预放大器、一种小型化固体飞秒激光振荡器、双功能小型超短激光脉冲自相关测量仪、超环面静调节装置。
- 获发明专利 1 项：一种激光天线。
- 申请实用新型专利 1 项：高精度飞秒激光同步技术及装置。
- 申请发明专利 3 项：一种监控激光聚焦的方法、一种激光引雷装置、强电磁能定向发射的激光武器。

2.3. 人才培养

- 已毕业硕士：吕铁铮，仲佳勇
- 已毕业博士：梁天骄，陈黎明，李玉同，董全力，陈正林，滕浩，杨辉
- 王薇，张军
- 已出站博士后：刘世炳，满宝元，林景全，夏江帆，李英骏，鲁欣，梁天骄，李玉同

2.4. 国际合作：

- 于 2000 年 ~ 2002 年与英国卢瑟福实验室进行合作研究。
合作项目名称：“高功率激光实验室天体物理研究”。
项目执行人：张杰、王薇、鲁欣、梁天骄
- 于 2002 年 ~ 2003 年与日本大阪大学激光工程研究所进行合作研究。
合作项目名称：“快点火相关物理实验及理论研究”
项目执行人：张杰、盛政明、鲁欣、李玉同、金展

3. 研究工作简介

在过去的 3 年里，我们主要围绕着“快点火”激光核聚变开展了一系列的研究工作。

“快点火”是指在聚变燃料被均匀压缩到最大密度时，将一束超短脉冲激光聚焦在靶丸表面，依靠激光和靶面相互作用产生的大量超热电子射入高密核使离子温度迅速上升至点火要求的温度。因此，与快点火激光核聚变密切相关的物理问题包括了超短超强激光脉冲与等离子体相互作用过程中的超热电子的产额、能谱、发射方向，以及在高密度等离子体中的输运；超短超强脉冲激光在低密度以及高密度等离子体中的传播和能量吸收等。针对这些物理问题我们进行了大量的实验和理论研究。同时，我们在 x 射线激光、飞秒激光在大气中的传输、实验室天体物理学方面也做了一些理论和实验研究。

● 激光系统方面

“极光一号”装置 (1.4TW)：“极光一号”是我们主要利用国产的元器件组装而成的基于啁啾脉冲放大技术的台面型 TW 激光装置。该激光装置建成于 1999 年，输出脉宽 25 飞秒，峰值功率大于 1.4 TW。在此装置上我们做过大量的超短超强脉冲与固体，气体和团簇相互作用的实验研究。在 2001 年，我们改善“极光一号”装置光束质量，并利用该装置做了许多实验比如：超热电子向高密度等离子体区域传输的实验、超短超强脉冲在大气中传输实验、超热电子时间分辨衍射实验等。

“极光二号”装置 (20TW)：为了进行相对论光强下的物理实验，使我们的科研工作上一个新的台阶，我们于 2001 年建成了脉宽 30 飞秒，输出能量大于 640 毫焦，峰值功率大于 20TW 的“极光二号”激光装置。该激光装置主要有以下 4 个特点：(1) 预放大器采用再生放大方案，主要是为了提高输出激光的光束质量。(2) 主放大器采用两台 1.5J 绿光泵浦，可将展宽后的啁啾脉冲能量放大到 900mJ。(3) 建立真空压缩室，将压缩器置于真空中。(4) 压缩光栅 (1500/mm) 和展宽器光栅 (1200/mm) 采用不同密度的光栅，可以充分抵消高色散和材料色散的影响，使压缩后的脉冲更接近种子脉冲。

自适应光学系统：为“极光 II”装置配备了一套自适应光学系统，用于激光脉冲波前的探测和校正。该系统主要包括 (1) Shack-Hartmann 波前传感器，其主要用途是测量输出光束的波前畸变量；(2) 波前校正系统，在上述装置中采用的是 Bimorph 型变形镜来校正波前传感器测量到的畸变量，使校正后的波前接近于理想的平面波波前；

(3) 相应的控制软件：主要包括两部分，一部分是根据传感器的探测来计算光束的波前畸变情况并提供相应的光束质量报告；另一部分则是对变形镜各电极电压的控制软件。调试的结果显示，该系统能够正确的进行工作，对“极光 II”装置输出激光波前进行了明显的校正，校正后的光束质量接近 1.5 倍的衍射极限。

腔倒空飞秒激光器的研制：对于物理、生物、化学等领域中的大量超快应用研究而言，通常振荡器直接输出的脉冲功率太低，不足以激发物质中超快过程的产生，其极高的重复频率引起的信号积累效应还会影响到结果的准确性。而放大器不仅技术复杂，成本昂贵，并且重复频率又过低，制约着超快测量中所能得到的精度。腔倒空激光器不

但具备振荡器的稳定输出，而且大大提高了单脉冲的输出能量并且可以调解脉冲的输出频率，是研究超快物理、化学、生物过程的理想光源。我们投入大量人力和物理，研制成了具有国际先进水平的腔倒空激光器，该激光器输出脉冲宽度最短可以到 17fs，对应的谱宽为 60nm 左右，单脉冲激光能量一般为 40–60nJ，最大可达 85nJ，脉冲重复频率从 20kHz – 2MHz 可调。该激光器设计紧凑，锁模启动快，一般锁模稳定时间超过 5 小时。

● 激光技术

高效率的啁啾脉冲多通预放大器：研制了带有两对球面镜的多通预放大器，其抽运效率达到 23%，增益系数高达 4×10^{-6} 。在我们所知的范围内，该多通预放大器的效率是同类装置中最高的。*Journal of the Korean Physical Society 39, 831–833 (2001)*.

被动同步飞秒激光技术：独立提出新型被动同步飞秒激光技术，不仅克服了传统被动同步技术增益竞争等不足，大大提高了同步系统的稳定性和同步精度，而且可以实现多台飞秒激光之间的高精度同步。采用该同步技术首次实现了掺钛蓝宝石和美橄榄石的同步输出，同步精度 < 2fs。这不仅是国际上同步精度最高的结果，而且是首次实现不同频谱区域的同步输出，对激光的频谱扩展及相干合成有重要意义。掺钛蓝宝石和美橄榄石及其高次谐波的相干合成，理论上可以产生阿秒激光脉冲，对超快动力学研究有重要意义。采用该技术建成了高稳定性，高同步精度的同步飞秒激光器，较采用主动同步方式的同步激光器同步精度高 1 至两个数量级。对许多应用研究领域，如泵浦探测、激光成像、激光光谱学、光频标、激光脉冲的相干合成、阿秒激光的产生（1 阿秒 = 10^{-18} 秒）、利用量子纠缠态的量子通讯等有重要的学术和应用价值。*Appl. Phys. B 74, S171–S176 (2002)*.

● 超短脉冲强激光与固体靶作用中高能粒子的产生及输运

强激光与固体靶相互作用过程中高能电子、离子以及韧致 χ/γ 射线辐射的角分布：研究了强激光与固体靶相互作用过程中高能电子、离子以及韧致 χ/γ 射线辐射的角分布。找到了高能电子和离子的发射角与粒子动能，电荷的库仑势和激光入射角之间的依赖关系。粒子模拟结果显示，粒子的加速机制与激光的偏振方向是相互独立的。韧致 χ/γ 射线辐射的角分布与高能电子的角分布之间有着清楚的对应关系。*Phys. Rev. Lett. 85, 5340–5343 (2000)*.

激光偏振状态对高能粒子产生的影响：当飞秒激光脉冲聚焦到固体靶上时，产生大量的高能电子。高能电子的产生及其角分布对快点火聚变方案，射线源，等方面的应用是至关重要的。近年来很多研究小组对此问题作了大量的研究。但是激光偏振状态对高能粒子产生的影响被忽略。研究激光偏振状态对高能粒子产生的影响对认识高能电子产生机制是非常有帮助的。我们发现 p 偏振与 s 偏振光产生的高能电子有不同的方向。我们的数值模拟也证实了这一点。其中的物理还有待进一步的解析。*Phys. Rev. Lett. 87, 225001 (2001)*.

飞秒激光脉冲真空加热产生超热电子：对脉宽 150fs，能量 5mJ，波长 800nm，P 偏振

的激光脉冲与固体靶相互作用过程中由于真空加热产生的超热电子进行了实验研究。测量结果显示真空加热过程是高能超热电子产生的主要机制，真空加热产生的超热电子的能量高于按照共振吸收理论预测的能量。粒子模拟结果也证明了在该实验条件下真空加热是超热电子的主要产生机制。*Phys. Plasmas 8, 2925–2929 (2001)*.

亚皮秒激光和金属、绝缘靶的相互作用：实验研究了脉宽 150fs, 波长 800nm, 能量 5mJ, P 偏振的激光脉冲与金属和绝缘体靶材料相互作用时激光能量的吸收，超热电子的发射及其能谱。激光脉冲在靶面上的聚焦强度为 $8 \times 10^{15} \text{ W/cm}^2$ 。由于绝缘体靶的电导率低，因此产生的电荷分离势比金属靶高，这就导致了绝缘体靶和金属靶相比具有较低的激光吸收效率，较低的超热电子产额和超热电子温度。*Phys. Rev. E 63, 036403 (2001)*.

中等激光强度下飞秒激光脉冲与薄膜靶相互作用产生的超热电子研究：高能电子的产生和在高密度等离子体中的传播是快点火概念中重要物理问题。在相对论激光强度下，已经有几个研究组观察到了准直的超热电子束发射，但这种现象并不是相对论激光等离子体所特有的。我们对中等激光强度下飞秒激光脉冲和薄膜靶相互作用产生的超热电子特性进行了研究，实验发现在靶面法线方向也产生了准直的超热电子束。此外还发现前向超热电子的高能分量透过薄膜靶后向激光传播方向发生了偏折，低能分量由于在等离子体和靶材料中的碰撞效应散射为连续背景。3D 蒙特卡洛模拟支持了这一看法。超热电子能谱测量和能量吸收测量表明共振吸收可能对超热电子产生起了重要作用。*Phys. Rev. E 64, 046407 (2001); Journal of the Korean Physics Society 39, 825–830 (2001)*.

飞秒激光脉冲和水等离子体相互作用产生的高能电子、爆轰波和前向动力学研究：研究了飞秒激光脉冲和液体等离子体相互作用的三个主要物理过程：超热电子产生、向空气中膨胀的爆轰波和向水下传播的等离子体前向动力学过程。比较单脉冲和多脉冲飞秒激光和水等离子体相互作用产生的高能电子特性，发现多脉冲激光构型可以大幅度增强超热电子的产生和提高其温度。实验观测到在激光偏振面内、沿与激光轴反向夹角 46° 的方向对称喷射出两束能量大于 25 keV 的高能电子。实验和理论都表明，这些超热电子是通过后续脉冲与前面脉冲形成的球形液滴相互作用产生的，具体机制为共振吸收。二维粒子模拟结果和实验符合很好。由水等离子体压力导致的爆轰波在向空气中膨胀时，遵从考虑了源质量的平面波模型，而不是球面波模型。在爆轰波波前顶部，观察到一个瘤状结构，该结构起因于激光脉冲在到达水面前的自聚焦效应。自聚焦效应引起的通道膨胀过程可以用柱面膨胀模型描述。此外在研究水等离子体在激光方向的前向动力学演化过程中发现，在早期等离子体密度波前以超声速运动，这和理论模拟一致。到了晚期，膨胀过程完全退化为纯流体力学过程，膨胀速度也趋向于声速。*Phys. Rev. Lett. 90, 165002 (2003); Phys. Plasmas 9, 4028–4031 (2002); Phys. Rev. E 67, 056403 (2003)*.

激光与液滴的相互作用：研究了激光液滴相互作用过程中的共振吸收效应。激光吸收的角分布可以用来理解液滴靶产生的对称双叶超热电子束。同时发现激光总的能量吸收强烈地依赖于液滴等离子体的标尺长度。*Appl. Phys. B 77, 687–689 (2003)*.

超热电子在固体靶中的输运：研究了超强激光与固体靶相互作用中产生的超热电子向高密度等离子体区域传输的空间和时间特性。超热电子向高密度等离子体区域传输特性是快点火聚变方案中的一个重要物理问题。我们采用探针光照射端面镀铝膜的透明靶，对超热电子在透明靶只能感的离化径迹成像，可获得超热电子在高密度等离子体区的 jet 结构、能量、温度、穿透深度等重要信息。*Phys. Rev. E 67, 026408 (2003)*.

超热电子在薄膜靶背面诱导形成等离子体：用探针光捕捉到了激光脉冲和薄膜靶相互作用时在靶背面产生的等离子体喷射图象。实验结果显示，靶背面的等离子体喷射与入射激光同向，大约在入射激光到达靶面后几皮秒的时间内形成。靶背面的等离子体喷射是在激光和靶作用时产生的超热电子穿过薄膜靶的过程中形成的，靶背面的等离子体喷射因收到自生磁场的约束而具有较好的方向性。*Appl. Phys. B 76, 687-690 (2003)*.

● 超短脉冲强激光与气体作用

超短激光脉冲在大气中的传播：我们在激光与大气的相互作用的研究方面，主要做了理论和实验两方面的研究。对超短激光脉冲在大气中传输的物理过程进行了理论分析，并且提出了理论模型。通过理论分析，发现由于介质的非线形自聚焦和等离子体的散焦相互作用，使激光脉冲在大气中能产生很长的等离子体通道。实验上，利用我组建造的极光II号超强超短脉冲激光装置，在80mJ的激光输出能量下，观测到了长于几百米的等离子体通道。同时对等离子体通道的特性进行了研究，利用干涉法测量到通道的电子的密度最大达到 $10^{18}/\text{cm}^3$ ，对应通道的电阻率小于 $1\Omega\cdot\text{m}$ 。另外，利用阴影法对细丝形成的动态过程进行了研究，观测到了细丝的精细结构，以及细丝分裂和融合的过程。我们研究了激光脉冲在大气中传播产生的其它非线形效应。例如，发现了激光脉冲在大气中可以产生超连续辐射、锥角辐射以及谐波辐射。在实验中观测到了大于0.12%的转换效率的三次谐波辐射。主要是因为超短脉冲在自导引的传播下刚好能满足谐波的相位匹配条件，因此可以大大地延长相互作用长度。*Phys. Rev. E 65, 016406 (2001)*；*Phys. Rev. E 66, 016406 (2002)*；*Phys. Rev. E 67, 015401(R) (2003)*.

超短脉冲强激光与气体作用产生高次谐波：进一步发展了激光脉冲和原子气体相互作用时产生高次谐波的经典理论模型。理论模型中考虑了激光脉冲有限的作用时间和激光的磁场对高次谐波的影响。得到了最佳的激光强度与激光脉冲宽度的关系以获得更强的高次谐波发射和更好的功率谱特征，原有的高次谐波截断定律在本理论模型中依然成立。*Physica Scripta 67, 122 -126 (2003)*.

● 超短脉冲强激光与团簇作用

飞秒激光与团簇作用产生高能电子：近几年来，超短激光脉冲与团簇作用的研究引起了人们的极大兴趣。这种作用被证明可以对光有很高的吸收效率，并产生能量高达MeV量级的高能离子和中子，以及非常强的X射线辐射。我们测量了高强度飞秒激光和氩或氪团簇作用时产生的能量在100kev附近的超热电子的能谱。脉冲宽度为28fs的激光和团簇靶的相互作用会因为激光的强度不同而呈现出很大的差别。当激光强度为 $1\times 10^{16}\text{W/cm}^2$ 时，氪团簇对激光的吸收效率约为25%；当激光强度提高到 $1\times 10^{17}\text{W/cm}^2$ 时，

吸收效率提升到 78%，并且产生能量高达 500kev 的高能电子。根据不同的原子和背压估算的超热电子温度大约在 30 至 90kev 的范围。*Phys. Plasmas 9, 3595–3599 (2002)*.

超短脉冲激光和团簇相互作用产生定向发射的超热电子：对超短脉冲激光和氩团簇相互作用时产生的超热电子进行了实验研究。当脉宽 28fs，强度为 $1 \times 10^{17} \text{W/cm}^2$ 的激光脉冲辐照氩团簇时，沿激光的入射方向观测到了能量超过 100keV 的定向喷射的超热电子。定向发射的超热电子只有用线偏振的激光和团簇作用时才能观测到，圆偏振的激光不能产生定向发射的超热电子。通道内电子回旋共振加速应该是定向超热电子喷射的主要产生机制。*Phys. Rev. E 66, 025402 (2002)*.

● 实验室天体物理学

激光等离子体X射线转换与辐射加热的数值模拟研究：九十年代以来，随着激光功率变得越来越强，采用强激光装置使得在实验室里模拟天体物理的某些过程成为可能。为了增加激光等离子体与天体等离子体的相关性，一般在实验室中采用激光等离子体产生的X射线辐射加热样品来获得类似于大多数天体等离子体状态即满足局域热力学平衡条件的、具有均匀电子温度和密度分布的等离子体，这对于实验室天体物理学的研究起着非常重要的作用。激光X射线转换是辐射加热靶的一个重要的关键技术。我们利用一维辐射流体力学程序MULTI，数值模拟研究了激光等离子体产生的X射线的能量输运过程。详细分析了功率为 10^{14}W/cm^2 ，脉冲宽度为 1ns，波长为 0.35μm 的激光辐照平面Au 靶时能量输运过程和X射线能谱分布以及辐射热波的性质；讨论了靶的厚度对X射线转换效率的影响；通过优化靶的厚度得到了作为近似黑体辐射的转换靶的最佳厚度范围；利用转换靶产生的x射线辐射加热样品Al靶，在样品靶中得到了密度和温度梯度很小的均匀等离子体。此外我们还利用研究非局域热力学平衡态下等离子体状态程序包NIMP与MULTI结合就近似Planck 分布的辐射场对等离子体中的激发和离化态的影响进行了数值模拟研究，所有这些研究对于未来研究天体物理中的辐射输运过程相关的实验的设计具有一定理论价值。*Phys. Plasmas 9, 3978–3983 (2002)*.

● X-射线激光

预-主脉冲的时间延迟对瞬态类镍 X 射线激光的影响：激光等离子体只有在电子温度，离子温度，离化度等参数符合一定条件时才能成为 X 射线激光的增益介质。尽管一些大型的激光与物质相互作用的模拟程序如 LASNEX, MED103 等软件能够较精确地预言激光等离子的状态，但需要耗费大量的计算时间。为了对激光等离子体的流体力学性质做出迅速而有效的判断，我们采用解析求解自相似流体力学方程的方法推导出了激光和平板靶相互作用时产生的等离子体的参数的解析表达式。我们采用该自相似解析理论系统地研究了瞬态类镍 X 射线激光的预脉冲和主脉冲之间的时间延迟对 X 射线激光增益介质的定标长度，能量吸收，以及电子温度，离化度等流体力学性质的影响。瞬态类镍 X 射线激光的实验方案一般采用纳秒脉宽的预脉冲产生含有大丰度类镍离子的预等离子体，然后用高强度的皮秒脉冲快速加热预等离子，产生瞬态的高增益系数。我们的研究结果表明，增大预-主脉冲之间的时间延迟能够减小等离子的密度梯度，但过长的延迟会使预脉冲的温度降得过低以至于离化度达不到类镍状态。在延迟时间较长的情况下可以通过提高预脉冲的强度或者增加预脉冲的宽度来维持预等离子体的离化

度。详细的计算表明增加预脉冲的宽度比提高预脉冲的强度更能有效地节约泵浦能量。
Phys. Rev. E 63, 036410 (2001); Phys. Rev. E 66, 046501 (2002)

瞬态类氖镥 X 射线激光的泵浦机理：深入研究了瞬态类氖镥 X 射线激光的泵浦机理，用数值模拟的方法详细比较了飞秒脉冲和皮秒脉冲与平板镥靶相互作用时产生的等离子体的流体力学状态，增益系数以及离化平衡态。参照瞬态 X 射线激光的标准定义，发现对于类氖镥离子，即使泵浦脉冲短到几百飞秒，产生的增益仍然属于准稳态泵浦的范畴，而理想的瞬态 X 射线激光需要用几十飞秒的泵浦脉冲产生。这一重要结论纠正了长期以来人们对瞬态 X 射线激光泵浦条件的错误认识。
Phys. Plasmas 9, 1412-1415 (2002).

台面型类氖钛X射线激光的理论模拟：采用一维激光与固体靶相互作用的流体模拟程序 MED103 结合原子反转动力学程序研究了掺钛蓝宝石 CPA 激光（波长 800nm）泵浦的类氖钛 32.6nm 波长 ($3p \rightarrow 3s$, $J=0 \rightarrow 1$ 跃迁) 的软 X 射线激光。自主开发了计算 X 射线激光在等离子体增益介质中的传播和放大过程的射线追踪程序。数值模拟采用高斯形预-主脉冲辐照 100 μm 厚平板钛靶的几何模型。尝试了不同的泵浦脉冲结构，包括单预脉冲，短间隔 (360ps) 和长间隔 (3ns) 的双预脉冲。预脉冲的宽度均为 300ps，主脉冲的宽度为 300fs，峰值强度为 10^{15}W/cm^2 。针对每一种泵浦脉冲结构分别进行了优化计算，找到了预脉冲的最佳峰值强度。计算结果显示，在 $50\mu\text{m} \times 5\text{mm}$ 的焦线上用 1 焦耳左右的激光能量即可产生高达 40cm^{-1} 的增益。采用射线追踪程序计算了三种泵浦脉冲结构产生的 X 射线激光的相对输出光强。通过输出光强的比较发现对于类氖钛这类电离度较低的离子的 X 射线激光，采用长间隔的双预脉冲并不能有效地提高泵浦效率。
Phys. Rev. A 67, 013810 (2003)

瞬态类镍铌X射线激光的数值模拟：我们采用 MED103 程序对超短脉冲泵浦的波长 20.3 纳米 ($4d \rightarrow 4p$, $J=0 \rightarrow 1$ 跃迁) 的类镍铌 X 射线激光进行了详细的模拟计算，优化了泵浦脉冲的结构。数值模拟采用波长 800 纳米的脉宽 1 纳秒的预脉冲和皮秒主脉冲辐照 100 μm 厚平板铌靶的几何模型。预-主脉冲随时间呈高斯形变化。首先模拟了不同强度的预脉冲产生的预等离子体的状态，通过比较预等离子体中类镍铌离子的丰度确定了最佳的预脉冲强度，约为 $2.2 \times 10^{11}\text{W/cm}^2$ 。然后模拟了不同的预-主脉冲延迟时间下等离子体介质中的增益随时间和空间的变化。在主脉冲宽度 1 ps，峰值强度为 10^{15}W/cm^2 ，延迟为 0.6ns 时，峰值增益高于 $150/\text{cm}$ 。用射线追踪的办法计算了各个时间延迟条件下 X 射线激光的相对输出强度随线聚焦长度的变化，确定了最佳的延迟时间（约为 0.6 ns）。我们还研究了主脉冲的状态对增益系数的影响，计算结果表明，当主脉冲的脉宽在几百飞秒到几个皮秒的范围内变化时，增益系数的时空特征主要取决于主脉冲的能量。
Phys. Plasmas 10, 2978-2982 (2003).

皮秒钕玻璃激光脉冲产生短波长相干辐射：用皮秒钕玻璃激光脉冲作为泵浦源研究了相干软 X 射线辐射的产生，实验中采用了纵向泵浦瞬态类镍钼的 X 射线激光和在固体-真空界面激发高次谐波两种方法来产生相干软 X 射线辐射。在纵向泵浦 X 射线激光的实验中，出乎意料地看到了钼等离子体的喷射，射流的伸展长度达到了几个毫米。有趣的是等离子体喷流只在纵向泵浦功率密度为 5×10^{14} and $7 \times 10^{14} \text{ W/cm}^2$ 的范围内时发生。研究了等离子体的标长和密度梯度对表面高次谐波的影响。通过使用预脉冲，能够使

接近固体密度的等离子体发射出的高次谐波的效率提高 2-3 倍。等离子体的标长用一维流体力学模拟程序进行了计算，高次谐波效率的提高和粒子模拟程序的计算结果一致。*Laser and Particle Beams, 20, 59-65 (2002)*

光泵浦X射线激光：模拟计算了类氢Cl激发类锂Se的光泵浦X射线激光的光子模密度和增益。模拟中采用大功率激光辐照Cl和Se靶产生等离子体，利用等离子体中类氢Cl的Ly- α 发射线将类锂Se离子由 $2p_{3/2}$ 激发到 $5d_{5/2}$ 。采用二维射线追踪方法计算了泵浦光子的模密度并且在计算过程中考虑了等离子体的密度梯度，进一步计算了类锂Se离子的光泵浦X射线激光在39.5埃波长的增益随时间和空间的分布。计算结果显示要获得高增益系数(200cm^{-1} 以上)必须使用预脉冲。泵浦射线在被激发的等离子体中的吸收会使增益降低20%。时间相关的计算得到的增益比稳态增益小30%。 $5d_{5/2} - 2p_{3/2}$ 跃迁的光谱形状和自发辐射会使类锂Se的增益减少2%左右。*JQSRT 83, 203 -213 (2004)*.

● 超短脉冲激光与等离子体相互作用的理论研究和数值模拟

激光能量的吸收数值模拟：利用粒子模拟程序研究了飞秒激光与固体靶相互作用过程中的物理机制，结合实验，比较系统地讨论了激光能量的吸收、高能电子的发射与等离子体密度梯度的关系。特别是发现了在 p 偏振光入射作用下，等离子体对光的吸收随等离子体密度梯度的标尺长度变化呈现多个吸收峰的现象。这与我们的实验结果吻合。

强激光在近临界密度的均匀等离子体中的自调制：理论研究了相对论强度的激光束在近临界密度 ($n_e > 1/4 n_c$) 的均匀等离子体中传播时发生的纵向强度调制。以描述激光的电磁场矢势的非线性薛定鄂方程为出发点，针对系统的作用量和拉格朗日量进行变分法处理，得到了描述激光强度包络的方程。纵向不变的或调制的脉冲结构相当于方程的不同的解。采用数值模拟的方法研究了两种不同的脉冲结构的稳定性，结果表明其稳定性受到激光脉冲的横向结构的影响。*Phys. Plasmas 8, 1707-1717 (2001)*.

对撞激光场中的随机电子加速：用超短脉冲强激光与等离子体作用产生高能电子是强激光等离子体物理的核心问题之一。由于在强激光与等离子体相互作用过程中存在大量复杂的波与粒子作用的过程，高能电子的产生往往包含较复杂的物理过程。迄今为止，人们提出了多种激光在等离子体中加速电子的机制，这些机制的有效性与等离子体的状态，包括等离子体密度及其标尺长度有极大关系。在激光等离子体中，我们可以把电子加速机制分成等离子体波加速(纵向场加速)、激光直接加速(横向场加速)、以及纵向场与横向场混合加速。通常激光直接加速包括激光有质动力加速、逆自由电子激光加速等。我们提出一种在真空及低密度等离子体中通过一对反向传播的(对撞)光脉冲形成的激光场作用产生的高效加速机制。它是一种激光场直接加速机制。对单电子的计算表明，当激光场的振幅超过电子在场中作随机运动的阈值时，这种加速机制开始起作用。粒子模拟计算也表明电子在对撞激光场中的加速要比在单脉冲场中有效得多。在等离子体中，电子与一对反向传播的电磁场相互作用的情况是普通存在的。在不均匀等离子体中，当入射光从高密度区域被部分反射，低密度区的电子即受到一对相对传播的电磁波场的作用。当强激光在低密度等离子体中传播时。一种叫受激拉曼背散射不稳定产生的电磁波很快地增长起来。因它的传播方向与入射光相对，这也

构成电子与相向传播的电磁场相互作用。因此即使只有一个光脉冲在等离子体中传播，电子也可被加速到远高于光脉冲相应的有质动力势。这种对撞激光场中的电子随机加速机制已经被最近的实验所证实。*Phys. Rev. Lett.* 88, 055004 (2002); *Phys. Rev. Lett.* 91, 225001 (2003).

互调制尾波场电子加速器：自从 1979 年 Tajima 和 Dawson 提出等离子体波电子加速器以来，这方面的研究一直吸引人们极大的兴趣。按照等离子体波产生的方法，等离子体波加速器可以分成（由高能电子束驱动的）等离子体尾波场加速器、激光拍频波加速器、激光尾波场加速器、激光自调制尾波场加速器等。近年来随着超短脉冲技术的发展，人们提出用超短脉冲激光激发的尾波场来加速电子的设想。为达到共振激发，其中所需的激光脉冲必须小于一个等离子体周期。同时光脉冲要达到足够的光强。为克服这些条件的限制，人们又提出了用相对较长脉冲通过自调制产生大振幅等离子体波的方案。但由此必须要先产生超过一个瑞利长度的均匀等离子体，并且激光脉冲能够形成自聚焦传播。此外，激光自调制尾波场加速器是通过自调制不稳定产生的，它存在不可控性。我们提出一种新的方案，叫互调制尾波场粒子加速。它采用两个同向传播的光强相对较低的激光脉冲，其中前一个短脉冲产生低振幅的尾波场，用此尾波场调制后一个长脉冲。被调制的长脉冲反过来放大此尾波场。我们用数值模拟证实了这种方案。*Phys. Plasmas* 9, 3147 (2002).

飞秒激光与固体靶相互作用过程中的粒子加速：采用粒子模拟程序对飞秒激光和固体靶的相互作用进行了数值模拟。得到了超热电子能谱的双温分布。其中较低的超热电子温度可认为是激光场的共振吸收产生的，较高的超热电子温度是靶面上的静电场和激光诱导产生的位于真空和靶面之间的等离子体薄层中的振荡电场协同加速产生的。研究了激光与固体靶相互作用过程中的激光的吸收，尤其详细地讨论了真空加热机制。解释了在飞秒激光和固体靶相互作用过程中的电子加速、离子加速；研究了激光与不同密度梯度的等离子体作用时产生的谐波光谱，比较详细地讨论了由入射到靶内的高能电子束诱导产生的等离子体自发射谱线。研究了超薄膜在超强、超短激光脉冲辐照下，靶厚对离子加速的优化。我们发现，当靶足够薄以至于激光可以穿透等离子体的时候，我们得到了离子的最大加速。具体的研究表明，由于激光可以穿透等离子体薄膜，因此，在薄膜前后两侧的静态电场都可以参与电子的加速，从而加大了激光的吸收率，得到的高能电子的温度和数量都比激光不能够穿过薄膜等离子体时要大和高。因此，我们得到了更高的离子能量。我们还根据 PIC 模拟的结果，归纳出获得最大的离子能量的靶厚随激光强度和激光脉冲宽度的经验公式。*Phys. Plasmas* 8, 1025–1028 (2001); *Phys. Rev. E* 64, 026411 (2001); *Phys. Rev. E* 68, 026408 (2003).

低密等离子体中并行传输的两束激光脉冲的相互作用：研究了低密等离子体中并行传输的两束激光脉冲的行为。在所用的方程中，显式地给出了激光有质动力对等离子体密度的扰动和排空对激光传输的影响。我们发现，两光束可以出现诸如融合、自导引，分叉等行为。激光有质动力对电子密度的排空和扰动在上述激光行为中具有决定性的作用。*Phys. Rev. E* 66, 027402 (2002).

相对论等离子体中的光学陷阱：利用脉宽 400fs，功率 1TW，强度小于 $2.4 \times 10^{18} \text{ W/cm}^2$ 的激光脉冲在时空域进行干涉的方法制造出了能够约束动能小于 350kev 的相对论电子的

光学陷阱。理论分析和数值模拟的结果均预言等离子体的密度被强烈地调制，其最高密度能够达到最低密度的 10 倍。电荷分离激发的静电场强度可达到 $2 \times 10^{11} \text{ eV/m}$ 。这个预言已被汤姆森和拉曼散射的实验所证实。两束交叉传播的激光束在等离子体中形成的密度栅能够象多层反射镜一样在交叉的激光束之间传输能量，使得其中较弱的一束激光的功率提高了约 50%。光学陷阱能够有效加热电子，使电子的温度提高两个数量级。实验结果显示，和单束激光辐照相比，被加速的高能电子的数量沿着两束激光中的一束激光的方向提高到大约 3 倍，电子温度大约提高 100keV。*Phys. Plasmas 10, 2093-2099 (2003)*.

高强度短脉冲激光和低密度等离子体相互作用引起的电子加速：用解析的方法研究了激光脉冲对电子的直接加速与激光尾波场加速之间的关系。有质动力引起的电荷分离场的强度和位置决定了两种加速机制的效率。激光尾波场加速机制存在着一个最佳条件。光脉冲内部的加速在脉冲足够短时占主导地位，电子可被光脉冲直接驱动甚至捕获。被加速的电子可以达到很高的能量，并且在激光与固体靶相遇时被提取出来。*Phys. Plasmas 10, 2468-2474 (2003)*.

BRIEF DESCRIPTION OF RESEARCH WORK

In the past 3 years, our research was mainly concentrated on the basic physical problems of “fast ignition” process. One of the major physical issues is the property of hot electron generated by interaction of ultra-intense laser pulse with plasmas. The effective temperatures, the generation and the propagation of energetic hot electrons in a high-density plasma, the laser energy conversion efficiency to hot electrons, the angular distributions of hot electrons are studied theoretically and experimentally. At the same time, we also studied some problems of the x-ray laser, the propagation of femtosecond laser pulse in air and the laboratory astrophysics.

● LASER SYSTEMS

JIGUANG I laser facility (1.4TW): This laser system capable of output 1.4 TW in 25 fs was built-up in 1999. We conducted numerous experimental researches on laser interactions with solid, gas, and clusters with this system. In 2001, we improved the beam quality of output pulses, and conducted a few new experiments such as the hot electron transport through overdense plasma region, propagation of ultra-short laser pulses in atmosphere, time-resolved diffraction of hot electrons, etc.

JIGUANG II laser facility (20TW): In the 2001 year, we completed JIGUANG II laser facility. The final output after the compressor is grater than 600mJ in 30fs pulse duration. This corresponds to a peak power as high as 20TW. This system includes: (1) The re-amplifiers are adopted for the pre-amplifiers to improve the beam quality. (2) The main amplifiers are pumped with two green pumbers, with maximum energy up to 900mJ. (3) Build-up of compressors in a vacuum chamber. (4) The compressing grating and expanding grating are taken to be at different densities, which enables to dismiss the higher order dispersion and dispersion from the materials, to make the compressed pulse more close to the seeding pulse. (5) An adaptive optics system is installed on the laser facility. By using this adaptive optic system, the beam quality of output laser pulse can be improved to 1.5 diffraction limits.

Adaptive optics system: An adaptive optics system is equipped to “JIGUANG II” laser facility for correction of wave front of output beam. This adaptive optic system includes: (1) Shack-Hartmann wave fornt sensor, which is used for measurement of spatial intensity and phase distributions of laser beam. (2) Wave front corrector based on deformable mirror. (3) Control software, which analyzes the wavefront and controls the applied voltages on electrodes in deformable mirror. By using this adaptive optic system, the beam quality of output laser pulse from “JIGUANG II” can be improved to 1.5 diffraction limits.

Cavity dumped femtosecond laser: A cavity-dumped Kerr-lens Mode Locked (KLM) Ti:S laser is demonstrated. Stable mode-locked laser pulses with a peak power of 4.5MW are obtained with 5.4W pump power. The pulse duration width is shorted than 18f and the repetition rates can be tuned as low as 20 kHz. To our knowledge, this is the lowest repetition rates and the most compact size from the

solid-state cavity-dumped femtosecond laser.

● DEVELOPMENT OF LASER TECHNIQUES

Effcient chirped-pulse multi-pass preamplifier: A multi-pass preamplifier with two pairs of spherical mirrors has been developed, and an extraction efficiency as high as 23% has been obtained. This corresponds to a gain of 4×10^6 . To our best knowledge, this is the highest efficiency achieved for multi-pass preamplifiers. *Journal of the Korean Physical Society 39, 831-833 (2001)*

Passive synchronization between femtosecond lasers: Two independent femtosecond Ti:sapphire and Cr:forsterite lasers were stably synchronized by crossing both lasers inside the Ti:sapphire crystal. We obtained two-color femtosecond pulse trains at the completely different wavelengths of around 820 nm and 1250 nm respectively. This new technique overcomes the gain competition and enables us to greatly broaden the tunable ranges. By optimizing the overlap of the beams, we realized a large tolerance of cavity-length mismatch of 5 μm and demonstrated long-term synchronization that continuously remained over several hours. The measured FWHM of the cross-correlation trace is 74 ± 2 fs based on the 43 ± 2 fs Ti:sapphire and 52 ± 1 fs Cr:forsterite lasers. The exact coincidence with the theoretical calculated value infers the two-color laser being synchronized with a timing jitter of only a few femtoseconds. *Appl. Phys. B 74, S171-S176 (2002)*.

● ULTRA-SHORT LASER PULSE INTERACTION WITH SOLID TARGETS

Angular distributions of fast electrons, ions, and bremsstrahlung x/ γ -rays in intense laser interaction with solid targets: We study the angular distributions of fast electrons, ions, and bremsstrahlung x/ γ -rays generated during the interaction of an ultrashort intense laser pulse with solid targets. A relation is found on the angular directions for fast electrons and ions as a function of the particle's kinetic energy, experienced Coulomb potential changes, and the incident angle of the laser pulse. It is valid independent of the acceleration mechanisms and the polarization of the laser pulse, as confirmed by particle-in-cell simulations. The angular distribution of bremsstrahlung x/ γ -rays is presented to show explicitly its correlation with the corresponding angular distributions of electrons. *Phys. Rev. Lett. 85, 5340-5343 (2000)*.

Effects of laser polarization on jet emission of fast electrons in femtosecond-laser plasmas: When intense fs-laser pulses are focused on solid targets, a large number of electrons are generated. Fast electrons and ions generated in the interaction of intense laser pulses with solid targets play a key role for various applications of intense lasers, such as the fast ignitor, ultra-short x/ γ -ray sources, and laser induced nuclear processes, etc. The angular distributions of fast electrons are one of the important issues for those proposed applications. Fast electron production and transport were extensively studied both experimentally and theoretically. However, there is still not enough understanding of physics mechanisms that control the emission direction of fast electrons. In our experimental

study, Jet emission of outgoing fast electrons collimated in the polarization direction was observed for the s-polarized laser irradiation, whereas for the p-polarized irradiation, very directional emission of outgoing fast electrons was found close to the normal direction of the target. 2D PIC simulations can reproduce the main characteristics of outgoing fast electrons generated by interaction of obliquely incident p-polarized laser pulses with prepulses. However, the simulations failed to reproduce the jet emission of outgoing fast electrons in the specular direction produced by moderate intensity p-polarized laser pulses obliquely incident on a steep profile plasma. *Phys. Rev. Lett.* **87**, 225001 (2001).

Hot electron generation via vacuum heating process in femtosecond laser-solid interactions: Hot electron generation by the vacuum heating process has been studied in the interaction of 150 fs, 5 mJ, 800 nm P-polarized laser pulses with solid targets. The measurements have suggested that the “vacuum heating” is the main heating process for the hot electrons with high energies. The energy of the vacuum-heated hot electrons has been found to be higher than the prediction from the scaling law of resonance absorption. Particle-in-cell simulations have confirmed that the hot electrons are mainly generated by the vacuum heating process under certain experimental conditions. *Phys. Plasmas* **8**, 2925-2929 (2001).

Experimental study of a subpicosecond pulse laser interacting with metallic and dielectric targets: We have studied laser absorption, hot electron emission, and the energy spectrum of hot electrons produced during the interaction of a 150 fs, 5 mJ, 800 nm p-polarized laser pulse at 8×10^{15} W/cm² with metallic and dielectric target materials. Because dielectric targets are much less conductive, the charge separation potential in dielectric targets is higher than that of metallic targets. This leads to a smaller laser absorption, fewer emitted electrons, and a lower hot electron temperature in dielectric than in metallic targets. *Phys. Rev. E* **63**, 036403 (2001).

Hot electrons produced in the interactions of femtosecond laser pulses with foil targets at a moderate laser intensity: One of the major physics issues to implement fast ignition is the generation and propagation of energetic hot electrons in high-density plasma. The laser energy conversion efficiency to hot electrons, the electron direction, and the effective temperature are main issues of studies. The collimated electron beams into vacuum and dense plasmas were observed by several research groups at relativistic laser intensity. This is not unique phenomena only at relativistic laser intensity. In this project, characteristics of hot electrons produced in the interaction of femtosecond laser pulses with foil targets is investigated at moderate laser intensity. A collimated jet of hot electrons is observed in the target normal direction. However, the forward energetic hot electron beam deflects to the laser propagation direction. The low energy electrons disperse into wider cone angle due to the collisional effect in the plasma and target material, which presents as a continuous background. This is supported by 3D Mento Carlo simulations. The hot temperature obtained from the electron spectrum and absorption experiments implies that resonance absorption is partly responsible for the generation of hot electrons. *Phys. Rev. E* **64**, 046407 (2001); *Journal of the Korean Physical Society* **39**, 825-830(2001).

High energy electrons, blast waves and forward dynamics of water-plasmas produced by femtosecond laser pulses: Three main physical processes of the interactions of femtosecond laser pulses with water plasma, hot electron emission, blast waves expanded into air and forward expansion dynamics into water, have been studied experimentally and theoretically. High energy electrons emitted by water plasmas produced by a single or a multiple laser pulse are investigated. The multipulse mode greatly enhances the generation and the temperature of hot electrons. Directional emission of high energy electrons over 25 keV is observed in two symmetric directions with respect to the laser axis and at 46° from the directions of the laser electric field. Two-dimensional particle-in-cell simulations reproduce well the experimental results and indicate the acceleration mechanism of the high energy electrons is mainly due to the resonance absorption at the edge of the spherical droplets formed by the leading pulse. The behaviors of the blast waves produced by femtosecond laser-water interactions, and the blast waves induced by laser self-focusing in air, also have been investigated using optical shadowgraphy. The temporal evolution of the blast wave launched by the water plasma can be described by a planar blast wave model including source mass. An aneurism-like structure, due to the quick propagation inside a hollow channel formed by laser self-focusing, is observed. The expansion of the channel in air is found to agree with a cylindrical self-similar blast wave solution. For the evolution of the forward density front of water-plasmas, it is found that the density front moves with supersonic speed at the beginning, as predicted by a hydrodynamics simulation. This plasma-expansion process is followed by a fluid mechanical process. The expansion rate gradually reduces to the acoustic speed in water. *Phys. Rev. Lett.* **90**, 165002 (2003); *Phys. Plasmas* **9**, 4028-4031 (2002); *Phys. Rev. E* **67**, 056403 (2003).

Resonance absorption of femtosecond laser pulses by liquid droplets: The resonance absorption of femtosecond pulses by liquid droplets is studied. Angular dependence of the laser absorption may be used to understand the symmetric double lobe emission of hot electrons generated from liquid droplets. The total laser absorption fraction is found to be strongly related with the scale length of the microplasmas. *Appl. Phys. B* **77**, 687-689 (2003).

Transport of hot electrons in solid targets: The temporal and spatial structures of hot electrons were studied experimentally. It is one of the key issue concerning the fast ignitor of fusion targets. In our experiments, an Aluminium foil is plated at one end of a transparent target. By use of another diagnostic light, we obtain pictures of hot electrons which transport through the Aluminium foil and ionize inside the solid target. In this way, we obtain information on hot electron jet structure, energy level, temperature, and the tunneling depth. *Phys. Rev. E* **67**, 026408 (2003).

Hot-electron-induced plasma formation on the rear surface of a foil: The plasma jet formed on the rear surface of a foil in laser-solid interaction is investigated by laser probing. The rear plasma jet, which is in line with the laser, formed a few picoseconds after the incidence of the focused laser, is due to a beam of fast electrons propagating through the target and is collimated by a strong

magnetic field in the plasma. *Appl. Phys. B* **76**, 687-690 (2003).

● INTERACTION OF ULTRA-SHORT LASER PULSE WITH GASES

Propagation of ultra-short laser pulses in atmosphere: We found that intense ultra-short infrared laser pulses can propagate over very long distances with the self-guiding scheme. This is due to the dynamical balance between the two effects. One is self-focusing due to the nonlinear Kerr effect of air; the other is the defocusing effect caused by plasmas generated by With ultra-short laser pulses (30 fs) and low energy ($E=80$ mJ) in our home-made laser system JIGUANG II, we observe laser plasma channels with a length over hundreds of meter in air. The maximum electron density in the channel is inferred to be about 10^{18} with an interferometric method. The resistivity in the plasma channel is measured to be less than $1 \text{ Om}^*\text{cm}$. Shadow-graphy technique allows us to directly observe the fine structure, which consists of a number of fine filaments to develop and split out from the initial filament. The propagation of intense laser pulses in transparent matter also causes other strong nonlinear effects such as supercontinuum generation, conical radiation and harmonics radiation. Strong third harmonic (TH) emission is observed with a conversional efficiency higher than 10^{-3} from a plasma channel formed by self-guided femtosecond laser pulses propagating in air. The intensity of the phase-matching condition is just equal to the laser intensity of the self-guiding propagation in air. So the interaction length is largely prolonged due to the self-guiding propagation of an ultra-short laser pulse in air. *Phys.Rev.E* **65**, 016406 (2001); *Phys. Rev. E* **66**, 016406 (2002); *Phys. Rev. E* **67**, 015401(R) (2003).

Classical model for high-Harmonic generation by a laser pulse in atomic gas: A classical model for high-harmonic generation from the interaction of a laser pulse and an atomic gas is introduced. The effects of finite pulse width and laser agneticfield are included. The optimum intensity-pulse width relation for high-harmonic emission and the corresponding power spectrum are presented. The existing high-harmonicc utoff law is found to remain valid. *Physica Scripta* **67**, 122-126 (2003).

● ULTRA-SHORT LASER INTERACTION WITH CLUSTERS

Energetic electrons from atomic clusters irradiated by intense femtosecond laser pulses: In recent years, there have been a lot of studies on laser interaction with clusters. It is proved to give high absorption efficiency of laser energy and produce high energy ions up to MeV level as well as strong X-ray radiations. We have studied laser absorption by Xe, Ar. and He clusters. It is found that the working pressure has strong effect on the clusters' size and their absorption of laser energy. The spectra of energetic electrons in the 100 keV range were measured from the interaction of intense femtosecond laser pulses with clusters of xenon or argon. The interaction of 28 fs pulses with cluster targets revealed quite different results with respect to applied laser intensity. At the laser intensity of $1\times 10^{16} \text{ W/cm}^2$, the absorption by xenon clusters was about 25%; however, at the laser intensity of $1\times 10^{17} \text{ W/cm}^2$, the laser energy absorption drastically increased to 78%, and the efficient coupling between the laser pulse and cluster target produced electrons with energy as high as 500 keV. The estimated hot electron temperatures ranged from

about 30 to 90 keV depending on atoms and backing pressures. *Phys. Plasmas* **9**, 3595-3599 (2002).

Emission of a hot electron jet from intense femtosecond-laser-cluster interactions: A directional hot electron jet with energy higher than 100 keV was generated along the laser propagation direction from Ar clusters irradiated with a laser pulse of duration 28 fs and intensity 1×10^{17} W/cm². The hot electron jet was detected only with linearly polarized laser pulses, not with circularly polarized pulses. Channel betatron resonance is believed to be the main accelerating mechanism for this directional hot electron jet. *Phys. Rev. E* **66**, 025402 (2002).

● SOME PROBLEMS OF LABORATORY ASTROPHYSICS

Numerical simulation of the conversion of thermal x-ray radiation from laser-produced plasmas and radiation heating: With the rapid increase of laser intensities, it has become possible to simulate some astrophysical processes by controlling the conditions of laser-produced plasmas in the laboratory. To attain the plasmas similar to the most of astrophysical plasmas which are in the local thermodynamic equilibrium (LTE) conditions with uniform temperature and density, it is now impossible to use the intense, approximately Planck's x-ray sources produced from laser-irradiated targets. This has been achieved experimentally by use of directly heating a sample foil with soft X-rays produced from laser-irradiated targets. In our researches, the conversion of intense laser light into thermal x-ray radiation in laser plasmas is investigated using one dimensional radiation hydrodynamic code MULTI. The conversion efficiency and spectral distribution of the x-ray radiation are optimized. By optimizing the thickness of targets, one unique plasma environment can be obtained. In addition, the effects of an ambient radiation field on the processes of excitation and ionization in a plasma using a non-LTE ionised material package NIMP was also researched. All the results are very important in the future for the experimental design to the study the effects of the radiation field on the physical processes in the astrophysical research. *Phys. Plasmas* **9**, 3978-3983 (2002).

● X-RAY LASERS

Effects of delay time on transient Ni-like x-ray lasers: In transient collisional excitation scheme, a long (nanosecond) prepulse is used to perform and ionize plasmas. After a delay time, a short (sub- or picosecond) intense laser pulse is used to rapidly heat the plasma. This results in transient x-ray lasers with high gain. Effects of delay time on transient collisional excitation *nickel-like* x-ray lasers are investigated analytically using a simple model. The calculations show that the longer delay time can greatly relax the density gradient. This is very critical for the propagation of x-ray lasers. However, a too long delay will reduce the electron temperature of the plasma before the arrival of the short pulse. Increasing the intensity of the long pulse or extending the pulse duration can keep the temperature required to maintain a high percentage of Ni-like ions while the delay time is longer. Similarly, increasing the intensity of the short pulse or extending the duration can also raise the electron temperature, resulting in higher gain coefficient. Our results

indicate that extending the pulse duration is more efficient than that of increasing the intensity. *Phys. Rev. E* 63, 036410 (2001); *Phys. Rev. E* 66, 046501 (2002).

The transient nature of Ne-like Ge x-ray laser: The transient nature of Ne-like Ge x-ray laser at 19.6 nm has been investigated numerically for a 100 μm thick Ge planar target irradiated by a nano-second prepulse followed by a short drive pulse with different durations but a fixed energy. The comparison of ionization balance created by different drive pulse shows that in the dynamic range from 500fs to 50ps, the transient collisional excitation does not exist. The real transient x-ray laser of Ne-like GE at 19.6 nm wavelength can only be generated by a short laser pulse with tens of femtoseconds duration. *Phys. Plasmas* 9, 1412-1415 (2002).

Simulation study of a Ne-like Ti x-ray laser at 32.6 nm driven by femtosecond laser pulses: A femtosecond laser driven collisional Ne-like Ti x-ray laser at 32.6 nm is numerically investigated using a hydrodynamic code coupled with an atomic data package for a 100-mm-thick Ti planar target irradiated by a single or double prepulse followed by an intense femtosecond laser pulse. By using an optimized drive pulse configuration, a gain of 40 cm^{-1} can be generated from a $5 \text{ mm} \times 50 \mu\text{m}$ line focus using only about 1 J pump energy. *Phys. Rev. A* 67, 013810 (2003).

Numerical optimization of a picosecond pulse driven Ni-like Nb x-ray laser at 20.3 nm: Detailed simulations of a Ni-like Nb x-ray laser pumped by a nanosecond prepulse followed by a picosecond main pulse are presented. The atomic physics data are obtained using the Cowan code. The optimization calculations are performed in terms of the intensity of prepulse and the time delay between the prepulse and the main pulse. A high gain over 150 cm^{-1} is obtained for the optimized drive pulse configuration. The ray-tracing calculations suggest that the total pump energy for a saturated x-ray laser can be reduced to less than 1 J. *Phys. Plasmas* 10, 2978-2982 (2003)

Simulations of a photopumped X-ray laser: Calculations of the modal photon densities and gain in a photopumped Cl XVII-Se XXXII X-ray laser are presented. In this paper we undertake a realistic simulation of the generation of both Cl and Se plasmas, using a high-power optical laser, which includes radiation from both Ly- α fine-structure components of H-like Cl pumping the $2p_{3/2} - 5d_{5/2}$ transition in Li-like Se. The calculations are performed in two dimensions in a realistic geometry taking into account plasma gradients. This gives information about the spatial extent and time evolution of X-ray lasing gain on the 5 - 4 transitions (39.5 Å) in Li-like Se. We find that gain (about 200 cm^{-1}) is expected only when the optical laser includes a pre-pulse. Calculations show that the absorption of pumping radiation in the pumped plasma can reduce the gain by 20%. Time-dependent calculations have shown that the gain is reduced by 30% in comparison to the steady-state calculations. The effect of the spectral profile and self-radiation of $5d_{5/2} - 2p_{3/2}$ transition in Li-like Se reduces the gain by about 2%. *JQSRT* 83, 203 – 213 (2004).

Coherent short wavelength radiation via picosecond Nd:glass lasers: The generation of coherent soft X rays is studied using a terawatt picosecond Nd:glass laser system. Two different methods are investigated as candidates for efficient

generation of such radiation, namely, longitudinally pumped transient collisional excitation nickel-like molybdenum X-ray laser, and high-harmonic generation from solid-vacuum interfaces. In the course of experiments on longitudinally pumped X-ray lasers, unexpected jetlike structures are observed in the visible emission of the molybdenum plasma, extending over a length of several millimeters. An interesting characteristic of this phenomena is that clear jets are observed only for longitudinal pump intensities between 5×10^{14} and $7 \times 10^{14} \text{ W/cm}^2$. The effects of a finite scale length density gradient on surface harmonics is also investigated. The efficiency of harmonic generation from near-solid density plasma is found to increase by a factor of 2 to 3 when using prepulses. The scale length of the preplasma is simulated using a one-dimensional hydrodynamic code, and the increase in efficiency is verified to be in accordance with particle-in-cell simulation results. *Laser and Particle Beams*, 20, 59-65 (2002).

● THEORY AND SIMULATIONS ON ULTRA-SHORT INTENSE LASER INTERACTION WITH PLASMAS

Simulations of laser absorption by solid targets: By use of particle-in-cell simulation code, we have simulated the laser absorption by solid targets. Together with experimental results, we have studied the laser absorption, high energy electron generation in relation with the plasma density scale-lengths. In particular, we find that, with the increase of plasma density scale-lengths, there exist several absorption peaks for p-polarized incidence of laser pulses. In the case of s-polarized incidence, there is only one absorption peak. This is in agreement with our experiments.

Self-modulation of an intense laser beam in near-critical homogeneous plasma: An investigation of longitudinal intensity modulation of a relativistic laser beam in near-critical homogeneous plasma ($n_e > 1/4n_c$) is performed in this paper. On the basis of a nonlinear Schrodinger equation of electromagnetic vector potential, a model equation of the intensity profile is derived via the variational approach from Action and Lagrangian. Longitudinally uniform and longitudinally modulated pulse structures are viewed as different solutions of this model equation. For these two different types of pulse structure, their relative stability under different structure parameters is numerically studied. Numerical results indicate that this relative stability depends closely on the transverse structures of the laser pulse. *Phys. Plasmas* 8, 1707-1717 (2001).

Stochastic heating and acceleration of electrons in colliding laser fields: The mechanisms leading to significant acceleration of electrons in laser-plasma interactions have been the topic of many theoretical and experimental studies over the past two decades. A few mechanisms of laser-driven electron acceleration have been proposed, including plasma wave acceleration, direct laser acceleration with the assistance of additional fields or by the laser ponderomotive force, and mixed acceleration from both the transverse and longitudinal fields. We propose that efficient acceleration of electrons in vacuum and underdense plasmas by an intense laser pulse can be triggered in the presence of another counter-propagating or intersecting laser pulse. This mechanism works when the laser fields exceed some threshold amplitudes for stochastic motion of electrons, as found in single-electron

dynamics. Particle-in-cell simulations confirm that electron heating and acceleration in the case with two counter-propagating laser pulses can be much more efficient than with one laser pulse only. Two different diagnoses show that the increased heating and acceleration are caused mainly by direct laser acceleration rather than by plasma waves. In plasma at moderate densities such as a few percent of the critical density and when the underdense plasma region is large enough, the Raman backscattered and side-scattered waves can grow to a sufficiently high level to serve as the second counter-propagating/intersecting pulse and trigger the electron stochastic motion. As a result, even with a single intense laser pulse only in plasma, electrons can be accelerated to an energy level much higher than the corresponding laser ponderomotive potential. This acceleration mechanism is verified by recent experiments. *Phys. Rev. Lett.* **88**, 055004 (2002); *Phys. Rev. Lett.* **91**, 225001 (2003).

Cross-phase-modulated laser wake-field accelerator: Since the plasma-based particle accelerators were suggested two decades ago, some innovations have been proposed, which allow the plasma-based accelerators to work in different parameter regimes and different geometry configurations. In the proposed self-modulated laser wake-field accelerator (SM-LWFA), the plasma wave is generated through a resonant self-modulation process of a relatively long pulse of a few plasma oscillation periods, which is usually coupled with forward Raman scattering. For the plasma wave to grow up to a high level for efficient acceleration, a time scale of tens times that for forward Raman scattering growth is necessary. In this case, the corresponding spatial extension is usually larger than the Rayleigh length in tenuous plasma. Therefore a guiding channel for the laser pulse is necessary. We introduce a new scheme to generate a high amplitude wake-field up to the wave-breaking amplitude by use of two laser pulses only at modest intensities. The first pulse is an ultrashort laser pulse shorter than a plasma oscillation period, which produces a seed wake-field. The second pulse is relatively long pulse, such as a few plasma oscillation periods. During the propagation process, the second pulse is cross-phase-modulated (XPM) by the density gradient of the seed wake-field, and is split up into a multi-pulse train, where each sub-pulse has duration around a plasma oscillation period. This pulse train then in turn amplifies the seed wake-field up to high level. This process develops in a time scale shorter than that for the SM-LWFA, and there is no necessary for particular timing between the two pulses. This scheme is verified by particle-in-cell simulations. *Phys. Plasmas* **9**, 3147 (2002).

Particle acceleration by ultra-intense laser: We have studied the effects of the plasma density scale length on the absorption mechanism of the femtosecond laser pulses interacting with solid targets. Experiments and particle-in-cell (PIC) simulations demonstrate that the vacuum heating is the main absorption in the plasma in the interaction of fs laser pulses with solid targets when no pre-pulses are applied. The energy spectra of hot electrons ejected out of or injected into the plasma show a bi-temperature distribution. While the first temperature of the two groups of hot electrons can be attributed to the resonant absorption of the laser field, the second temperature refers to the electrons accelerated by the static part in the front of the target and the oscillating part in the plasma layer of the laser-induced electric field, respectively. PIC simulations also show that with an appropriate

density scale length, the femtosecond laser energy can be absorbed locally through different mechanisms. The ion emission from plasmas produced by femtosecond (fs) laser pulses was also investigated using PIC simulations and laboratory experiments. PIC simulation results indicated that it is the laser induced and sustained electrostatic field in front of the target that accelerates ions to high energies and determines the main features of the ion emission. The density scale length on the ion acceleration behavior is also presented. Ion emission is investigated using particle-in-cell simulations where a femtosecond laser pulse incidence obliquely onto ultrathin solid foils. The relation of the optimal target thickness with parameters of the incident laser pulse and foil targets is also discussed. *Phys. Plasmas* 8, 1025-1028 (2001); *Phys. Rev. E* 64, 026411 (2001); *Phys. Rev. E* 68, 026408 (2003).

Propagation of collimating laser beams in underdense plasma: The propagation of two laser beams copropagating in underdense plasma has been studied numerically by solving their coupled envelope equations. It shows that two beams can merge each other, or split into three beams, or propagate with unstable trajectories, depending upon their power and initial beam separation. During the merging process, strong emission of radiation is observed. It also shows that the density cavitation channels due to the transverse ponderomotive force of the beams tend to trap them inside and prevent them from merging each other. *Phys. Rev. E* 66, 027402 (2002).

Electron acceleration by static and oscillating electric fields produced in the interaction between femtosecond laser pulses and solid targets: The interaction of modest, femtosecond laser pulses with solid targets is studied with particle-in-cell (PIC) simulations. A bi-temperature distribution of hot electrons is found. The first hot electron temperature can be attributed to the resonance absorption of the laser field, whereas the second hot electron temperature is identified to be due to the combined acceleration by the static electric field in front of the target and by the laser induced oscillating electric field in the thin plasma layer between the vacuum and the target. *Phys. Plasmas* 8, 1025-1028(2001).

An optical trap for relativistic plasma: The first optical trap capable of confining relativistic electrons, with kinetic energy <350 keV was created by the interference of spatially and temporally overlapping terawatt power, 400 fs duration laser pulses ($<2.4 \times 10^{18} \text{ W/cm}^2$) in plasma. Analysis and computer simulation predicted that the plasma density was greatly modulated, reaching a peak density up to 10 times the background density ($n_e/n_0 \sim 10$) at the interference minima. Associated with this charge displacement, a direct-current electrostatic field of strength of $\sim 2 \times 10^{11} \text{ eV/m}$ was excited. These predictions were confirmed experimentally by Thomson and Raman scattering diagnostics. Also confirmed were predictions that the electron density grating acted as a multi-layer mirror to transfer energy between the crossed laser beams, resulting in the power of the weaker laser beam being nearly 50% increased. Furthermore, it was predicted that the optical trap acted to heat electrons, increasing their temperature by two orders of magnitude. The experimental results showed that the number of high energy electrons accelerated along the direction of one of the laser beams was enhanced by a factor of 3 and electron temperature was increased ~ 100 keV as compared with single-beam illumination. *Phys.*

Plasmas 10, 2093-2099 (2003).

Electron acceleration by an intense short-pulse laser in underdense plasmas: Electron acceleration from the interaction of an intense short-pulse laser with low density plasma is considered. The relation between direct electron acceleration within the laser pulse and that in the wake is investigated analytically. The magnitude and location of the ponderomotive-force-caused charge separation field with respect to that of the pulse determine the relative effectiveness of the two acceleration mechanisms. It is shown that there is an optimum condition for acceleration in the wake. Electron acceleration within the pulse dominates as the pulse becomes sufficiently short, and the latter directly drives and even traps the electrons. The latter can reach ultrahigh energies and can be extracted by impinging the pulse on a solid target. *Phys. Plasmas 10, 2468-2474 (2003).*

4. 代表性论文目录

List of selected publications

1. YT Li, J Zhang, H Teng, TJ Liang, XY Peng, X Lu, YJ Li, XW Tang, "High-energy electrons and x-ray photons emitted by water plasmas produced by femtosecond laser pulses", **Phys. Rev. Lett.**, **90**, 1650021-4 (2003).
2. P Zhang, N Saleh, S. Chen, Z.M. Sheng and D Umstadter, "Laser-Energy transfer and enhancement of plasma waves and electron beams by interfering high-intensity laser pulses", **Phys. Rev. Lett.**, **91**, 225001-4 (2003).
3. ZM Sheng, K Mima, Y Sentoku, MS Jovanovic, T Taguchi, J Zhang, J Meyer-ter-Vehn, "Stochastic heating and acceleration of electrons in colliding laser fields in plasmas", **Phys. Rev. Lett.**, **88**, 0550041-4 (2002).
4. LM Chen, J Zhang, YT Li, H Teng, TJ Liang, ZM Sheng, LZ Zhao, ZY Wei, XW Tang, "Effects of laser polarization on jet emission of fast electrons in ultrashort pulse laser-plasmas", **Phys. Rev. Lett.**, **87**, 225001-4 (2001).
5. ZM Sheng, Y Sentoku, K Mima, J Zhang, W Yu and J Meyer-ter-Vehn, "Angular distribution of fast electrons, ions and Bremsstrahlung X/gamma rays in intense laser interaction with solid targets", **Phys. Rev. Lett.**, **85**, 5340-5343 (2000).
6. HC Wu, W Yu, TJ Liang, Z Jin, YT Li, ZM Sheng, XW Tang, and J Zhang, "A simple estimate of resonance absorption of femtosecond laser pulses by liquid droplets", **Appl. Phys.** **B77**, 687-689 (2003).
7. ZM Sheng, J Zhang, D. Umstater, "Plasma density gratings induced by intersecting laser pulses in underdense plasmas", **Appl. Phys.** **B77**, 673-680 (2003).
8. H Teng, J Zhang, ZL Chen, YT Li, K Li, XY Peng, JX Ma, "Propagation of hot electrons through high-density plasmas", **Phys. Rev. E** **67**, 0264081-6 (2003).
9. H Yang, J Zhang, LZ Zhao, YJ Li, H Teng, YT Li, ZH Wang, ZL Chen and ZY Wei, "Third-order generation by self-guided femtosecond pulses in air", **Phys. Rev. E** **67**, 0154011-4 (2003).
10. H Teng, J Zhang, ZL Chen, YT Li, K Li, XY Peng, "Hot-electron-induced plasma formation on the rear surface of a foil", **Appl. Phys.** **B76**, 687-690 (2003).
11. W Yu, ZY Chen, MY Yu, J Zhang, RX Li, JX Ma, ZZ Xu, "Classical model for high harmonic generation by a laser pulse in atomic gas", **Physica Scripta**, **67**, 122-126 (2003).
12. QL Dong, ZM Sheng, MY Yu, J Zhang, "Optimization of ion acceleration in the interaction of intense femtosecond laser pulses with ultrathin foils", **Phys. Rev.**, **E68**, 0264081-6 (2003).
13. ZM Sheng, J Zhang, "A new mechanism of electron acceleration with relativistic-intense laser pulses in plasmas", **Physics**, **32**, 16-18 (2003).
14. IR Al'Miev, X Lu, SJ Rose, J Zhang and JS Wark, "Simulations of a photopumped X-ray laser using the H-like Cl-Li-like Se scheme", **J. Quant. Spectr. & Radiative Transfer**, **83**, 203-213 (2003).
15. K Li, J Zhang, W Yu, "High-order harmonic generation by laser interaction with solid target using moving mirror model", **Acta Physica Sinica**, **52**, 1412-1417 (2003).

16. QL Dong, J Zhang, "Vacuum heating of solid target irradiated by femtosecond laser pulses", **Science in China**, **46**, 71-77 (2003).
17. X Lu, YJ Li, Y Cang, K Li, J Zhang, "Simulation study of Ne-like Ti x-ray lasers at 32.6 nm driven by femtosecond laser pulses", **Phys. Rev. A****67**, 0138101-5 (2003).
18. YT Li, J Zhang, ZM Sheng, H Teng, TJ Liang, XY Peng, YJ Li, XW Tang, "High energy electron emission from water plasmas produced by femtosecond laser pulses", **Physics**, **32**, 572-576 (2003).
19. ZH Wang, ZY Wei, H Teng, J Zhang, "Measurement of femtosecond laser pulses using SHG frequency-resolved optical gating techniques", **Acta Physica Sinica**, **52**, 363-366 (2003).
20. QZ Yu, YT Li, J Zhang, "Interaction of ultrashort high intensity laser pulses with liquids", **Physics**, **32**, 585-589 (2003).
21. X. Lu, J.Y. Zhong, Y.J. Li, J. Zhang, "Numerical optimization of a picosecond pulse driven Ni-like Nb x-ray laser at 20.3nm", **Phys. Plasmas**, **10**, 2978-82 (2003).
22. K. Li, J Zhang, W Yu, "high-order harmonic generation by laser interaction with solid target using moving mirror medel", **Acta Physica Sinica**, **52**, 1412-1417 (2003).
23. ZY Zheng, X Lu, J Zhang, "Overview and future prospects of laser plasma propulsion technology", **Physics**, **32**, 533-538 (2003).
24. Jun Zhang, J Zhang, ZM Sheng, Y Qiu, YT Li, Z Jin, H Teng, "Effects of laser intensity on the directional emission of hot electrons ", **Science in China**, **33**, 317-322 (2003)
25. ZM Sheng, J Zhang, W Yu, "Generation of low frequency electromagnetic solitons in plasmas near the critical density with ultrashort intense laser pulses", **Acta Physica Sinica**, **52**, 125-133 (2003).
26. J Zhang, LM Chen, YT Li, H Teng, TJ Liang, ZM Sheng, QL Dong, LZ Zhao, ZY Wei, XW Tang, "Dependence on hot electron emission on laser polarization in femtosecond laser-plasmas", **Progress in Natural Science**, **13**, 533-536 (2003).
27. Jun Zhang, WZ Yi, ZH Wang, LH Zhao, Y Qiu, J Zhang, "Supercontinuum generation in photonic crystal fiber by femtosecond laser pulses", **Acta Optica Sinica**, **23**, 511-512 (2003).
28. ZL Chen, J Zhang, LM Chen, H Teng, QL Dong, LZ Zhao, ZY Wei, "Absorption of femtosecond laser pulses in metallic and dielectric slabs", **Acta Physica Sinica**, **52**, 1672-1675 (2003).
29. W Wang, J Zhang and VK Senecha, "Numerical simulation of the conversion of thermal x-ray radiation from laser-induced plasmas and radiation heating", **Acta Physica Sinica**, **51**, 590-595 (2002).
30. H Yang, J Zhang, YJ Li, J Zhang, YT Li, ZL Chen, H Teng, ZY Wei, ZM Sheng, "Characteristics of self-guided laser plasma channels generated by femtosecond laser pulses in air", **Phys. Rev. E****66**, 0164061-4 (2002).
31. H Yang, J Zhang, W Yu, YJ Li, ZY Wei, "Long plasma channels for laser triggered lighting", **Phys. Rev. E****65**, 0164061-5 (2002).
32. YT Li, J Zhang, "Physical phenomena related to sonoluminescence of bubbles in liquids", **Physics**, **31**, 293-297 (2002).

33. LM Chen, JJ Park, KH Hong, JL Kim, J Zhang, CH Nam, "Emission of hot electron jet from intense femtosecond-laser-cluster interaction", **Phys. Rev.** E66, 0254021-4(R) (2002).
34. FL Wang, G Zhao, J Zhang, "Laboratory studies of astrophysical opacity", **Physics**, 31, 298-301 (2002).
35. ZM Sheng, K Mima, Y Sentoku, K Nishihara, J Zhang, "Generation of high-amplitude plasma waves for particle acceleration by cross-modulated laser wave fields", **Phys. Plasmas**, 9, 3147-53 (2002).
36. LM Chen, JJ Park, KH Hong, IW Choi, JL Kim, J Zhang, and CH Nam, "Measurement of energetic electrons from atomic clusters irradiated by intense femtosecond laser pulses", **Phys. Plasmas**, 9, 3595-99 (2002).
37. LH Zhao, ZY Wei, J Zhang, "Development of a high-pleas-power femtosecond laser oscillator", **Physics**, 31, 729-732 (2002).
38. TZ Lu, T Wang, LJ Qian, X Lu, ZY Wei, J Zhang, "Calculation of frequency doubling efficiency of femtosecond pulses in BBO crystals", **Acta Physica Sinica**, 51, 1268-71 (2002).
39. X Lu, YJ Li, J Zhang, "Transient characteristics of a neon-like x-ray laser at 19.6 nm", **Phys. Plasmas**, 9, 1412-7 (2002).
40. H Teng, LF Cao, JX Cheng, JB Chen, XD Yang, ZL Liu, ZJ Zhen, "Spatial distribution of thermonuclear-burn-region for D-T-filled microshell", **Acta Physica Sinica**, 51, 834-838 (2002).
41. YT Li, J Zhang, X Lu, H Teng, YJ Li, XY Peng, Z Jin, LZ Zhao, "Forward dynamics of water plasmas generated by femtosecond laser pulses", **Phys. Plasmas**, 9, 4028-31 (2002).
42. Y Cang, J Zhang, Y Qiu, J Zhang, LM Peng, "Study of the moving track of hot electrons in an inhomogeneous magnetic field", **Acta Physica Sinica**, 51, 842-846 (2002).
43. QL Dong, ZM Sheng, J Zhang, "Self-focusing and emerging of two copropagating laser beams in underdense plasma", **Phys. Rev.** E66, 0274021-4 (2002).
44. F Yan, J Zhang, "Optimization of drive pulse configuration for transient Ne-like Fe x-ray laser", **Acta Physica Sinica**, 51, 2524-2527 (2002).
45. ZL Chen, J Zhang, H Teng, J Zhang, QL Dong, "Experimental study on isotop separation with femtosecond laser pulses", **Acta Physica Sinica**, 51, 1081-6 (2002).
46. W Wang, QL Dong, J Zhang, "Simulation study of conversion of laser energy into x-rays in laser plasmas", **Phys. Plasmas**, 9, 3978-83 (2002).
47. X Lu, J Zhang, YJ Li, "Prospective application of laser plasmas propulsion in rocket technology", **Physics**, 31, 796-99 (2002).
48. J Zhang, J Zhang, Q Chen, LM Peng, Y Cang, HB Wang, JY Zhong, "Feasibility study on temporal-resolved diffraction of high-energy electrons produced in femtosecond laser-plasmas", **Acta Physica Sinica**, 51, 1764-1767 (2002).
49. H Kuroda, T Ozaki, A Ishizawa, T Kanai, K Yamanoto, RX Li, J Zhang, "Coherent short wavelength radiation via picosecond Nd:glass Lasers", **Lasers and Particle Beams**, 20, 59-65 (2002).
50. ZH Wang, ZZ Wei, J Zhang, "Measurements of femtosecond laser pulses", **Physics**,

- 31, 659-666 (2002).
51. LM Chen, J Zhang, H Teng, QL Dong, ZL Chen, TJ Liang, LZ Zhao, ZY Wei, "Experimental study of subpicosecond pulse laser interacting with metallic and dielectric targets", **Phys. Rev. E****63**, 036403-4 (2001).
 52. YJ Li and J Zhang, "Hydrodynamic Characteristics of transient Ni-like x-ray lasers", **Phys. Rev. E****63**, 036410-6 (2001).
 53. QL Dong, J Zhang and H. Teng, "Absorption of fs laser pulses in interaction with solid targets", **Phys. Rev. E****64**, 026411-6 (2001).
 54. QL Dong and J Zhang, "Electron acceleration by static and oscillating electric fields produced in interaction between femtosecond laser pulses and solid targets", **Phys. Plasmas** **8**, 1025-8 (2001).
 55. LM Chen, J Zhang, Q L Dong, H Teng, TJ Liang, LZ Zhao, ZY Wei, "Studies on the vacuum heated hot electrons generated by femtosecond laser-solid interactions", **Phys. Plasmas** **8**, 2925-9 (2001).
 56. H Lin, LM Chen, J Zhang, P Zhang, WB Fan, "Self-modulation of an intense laser beam in near-critical homogeneous plasmas", **Physics of Plasmas**, **8**, 1707-17 (2001).
 57. YT Li, J Zhang, LM Chen, YF Mu, TJ Liang, ZY Wei, QL Dong, ZL Chen, H Teng, ST Chunyu, WM Jiang, ZJ Zheng, "Hot electrons in the interaction of femtosecond laser pulses with foil targets at a moderate laser intensity", **Phys. Rev. E****64**, 046407-6 (2001).
 58. Z Jin, J Zhang, "Study of aluminum emission spectra in astrophysical plasmas", **Acta Physica Sinica**, **50**, 365-368 (2001).
 59. YT Li, J Zhang, LM Chen, JF Xia, H Teng, YJ Li, LZ Zhao, JQ Lin, ZY Wei, WM Jiang, "Optical diagnostics of femtosecond laser-plasmas", **Science in China A****44**, 98-102 (2001).
 60. YT Li, J Zhang, LM Chen, JF Xia, H Teng, YJ Li, L Z Zhao, JQ Lin, ZY Wei, WM Jiang, L Wang, "Shadowgraphs of femtosecond laser-plasmas", **Science in China A****31**, 85-89 (2001).
 61. YJ Li, J Zhang, "Analytical study of transient Ni-like x-ray lasers", **Journal de Physique IV**, **11**, Pr2-83-86 (2001).
 62. J Zhang, LZ Zhao, LM Chen, P Zhang, TJ Liang, L Wang, ZM Sheng, "Studies on fast electrons in ultrashort pulse laser plasmas", **Journal de Physique IV**, **11**, Pr2-211-216 (2001).
 63. JF Xia, J Zhang, J Zhang, "Modeling the astrophysical dynamical process with laser-plasmas", **Acta Physica Sinica**, **50**, 994-1000 (2001).
 64. JQ Lin, J Zhang, YJ Li, LM Chen, TZ Lu, H Teng, BY Man, LZ Zhao, "Measurement of laser absorption and ion energy in femtosecond laser-cluster interaction", **Chinese Phys. Lett.**, **18**, 211 (2001).
 65. H Teng, J Zhang, "Mass spectrometry and its applications in laser plasma studies". **Physics**, **9**, 556-559 (2001).
 66. P Zhang, TJ Liang, LM Chen, YT Li, DB Chen, ZH Li, JT He, ZY Wei, L Wang, XW Yang, J Zhang, "Effects of polarization on super hot electron generation in femtosecond laser-plasma interaction", **Chinese Phy. Lett.**, **18**, 1374-1376 (2001).

67. JF Xia, ZY Wei, Y Qiu, TZ Lu, H Teng, ZH Wang, J Zhang, "Temporal characterization of laser pulses from Jiguang-I laser facility with a compact dual function autocorrelator", **Chinese Physics**, **10**, 946-950 (2001).
68. LM Chen, J Zhang, YT Li, TJ Liang, L Wang, ZY Wei, WM Jiang, "Behaviors of hot electrons in the interaction between ultrashort laser pulses and solid targets", **Science in China**, **A31**, 178-184 (2001).
69. H Yang, Y Qiu, H Teng, J Zhang, Y Cang, TZ Lu, ZH Wang, FF Wang, ZY Wei, J Zhang, "Generation of 4.5MW femtosecond pulse with a compact all solid-state cavity-dumped Ti:Sapphire laser", **Acta Physica Sinica**, **50**, 1930-1934 (2001).
70. QL Dong, J Zhang, TJ Liang, P Zhang, LM Chen, "Ion acceleration by an electrostatic field in the interaction between femtosecond laser pulses and solid targets", **Chinese Phys. Lett.**, **18**, 796-798 (2001).
71. Y Cang, W Wang, J Zhang, "Dynamics of interaction of ultrashort laser pulses with solid targets", **Acta Physica Sinica**, **50**, 1742-1746 (2001).
72. J Zhang, YT Li, LM Chen, H Teng, QL Dong, ZY Wei, "Studies on interaction of femtosecond laser pulses with solid targets", **J. Korean Phys. Society**, **39**, 825-830 (2001).
73. W Wang, J Zhang, SJ Rose, "Effects of the radiation field on the physical process of laser-produced plasmas", **Acta Physica Sinica**, **50**, 1517-1520 (2001).
74. X Lu, YJ Li, J Zhang, "Optimization of drive pulse configuration for a high gain transient x-ray laser at 19.6 nm", **Chinese Physics Lett.**, **18**, 1353-1355 (2001).
75. H Yang, ZW Zhao, J Zhang, PZ Deng, J Xu, ZY Wei, J Zhang, "Continuous-wave laser oscillation of Yb:FAP crystals at a wavelength of 1043 nm", **Chinese Physics**, **10**, 1136-1138 (2001).
76. JF Xia, J Zhang, "Scaling law in laboratory astrophysics", **Physics**, **30**, 545-548 (2001)
77. YT Li, J Zhang, LM Chen, LZ Zhao, JF Xia, H Teng, YJ Li, CY Zhu, WM Jiang, "Study on filamentation in femtosecond laser plasmas", **Acta Physica Sinica**, **50**, 204-208 (2001).
78. SB Liu, QF Tu, W Yu, ZH Chen, J Zhang, "Simulation for interaction of linearly polarized relativistic laser pulses with foil targets", **Chinese Phys. Lett.**, **18**, 646-649 (2001).
79. H Teng, J Xia, Z Wei, J Zhang, "An efficient chirped-pulse multi-pass preamplifier", **J. Korean Phys. Society**, **39**, 831-833 (2001).
80. LM Chen, J Zhang, H Lin, YT Li, LZ Zhao, L Wang, WM Jiang, "Disappearance of Two-Plasmon Decay Instability in Plasmas Produced by Ultrashort Laser Pulses", **Chinese Physics**, **10**, 40-43 (2001).
81. H Yang and J Zhang, "Application of ultra-short pulse lasers in induced lighting", **Physics**, **30**, 18-21 (2001).
82. JQ Lin, J Zhang, YJ Li, LM Chen, TZ lu, H Teng, "Absorption of femtosecond laser pulses by atomic clusters", **Acata Physica Sinica**, **50**, 457-461 (2001).
83. YJ Li, J Zhang, AP Teng, "An analytic model for transient collisional x-ray lasers", **Chinese Physics**, **10**, 516-522 (2001).

84. ZL Chen, J Zhang, “Configuration of magnetic fields induced by superthermal electrons”, **Acta Physica Sinica**, **50**, 735-740 (2001).
85. Y Cang, ZY Wei, J Zhang, “New frontier of ultrafast lasers, attosecond science”, **Physics**, **30**, 681-4 (2001).
86. W Wang, J Zhang, VK Senecha, “Numerical simulation study of laser-driven shock wave propagation in planar Al foil targets”, **Acta Physica Sinica**, **50**, 741-747 (2001).
87. JF Xia, J Zhang, “Intense laser astrophysics (I)”, **Physics**, **30**, 210-216 (2001).
88. JF Xia, J Zhang, “Intense laser astrophysics (II)”, **Physics**, **30**, 340-348 (2001).

5. 重要国际会议邀请报告 Invited talks on international conferences

1. J Zhang, *et al.*, "Conceptual design of the Chinese Neutron Spallation Source", **Invited Lecture** on the 16th Meeting of the International Collaboration on Advanced Neutron Sources, May 11 -15, 2003 Juelich, Germany.
2. J Zhang, "Interaction between intense laser pulses and matter", **Tutorial Talk** on The 2nd International Workshop on Nonlinear Plasma Science, July 31- August 1, 2003, Hangzhou, China.
3. J Zhang, YJ Li, X Lu, F Yan, JY Zhong, Z Jin, ZY Wei., "Investigation on femtosecond laser pumped x-ray lasers", **Invited Talk** on SPIE Soft X-ray and Applications V Conference, August 3-8, 2003, San Diego, USA.
4. J Zhang, ZY Wei, ZM Sheng, X Lu, YT Li, TJ Liang, Z Jin, XY Peng, "Research on High Field Physics at IoP, CAS", **Invited Talk** on International Photonics Technology Conference (IPTC) 2003, September 2-5, 2003, Seoul, Korea.
5. J Zhang, ZY Wei, ZM Sheng, X Lu, YT Li, TJ Liang, Z Jin, XY Peng, "Generation and Propagation of hot electrons", **Plenary Talk** on Third International Conference on Inertial Fusion Sciences and Applications (IFSA2003), September 7-12, 2003, Monterey, USA.
6. J Zhang, QL Dong, YT Li, TJ Liang, ZL Chen, ZM Sheng, H Teng, ZY Wei, "A 20 TW high power femtosecond laser facility at the Institute of Physics, CAS", **Invited talk** on the Third Asian pacific Laser Symposium (APLS 2002), August 22-25, 2002, Osaka, Japan.
7. J Zhang, H Yang, YJ Li, ZM Sheng, HC Wu, "Propagation of intense fs laser pulses in air", **Invited talk** on International Conference on Laser Propagation in Air, October 13-16, 2002, Bad Honnef, Germany.
8. J Zhang, YT Li, H Yang, Z Jin, XY Peng, "Interaction between femtosecond laser pulses with clusters", **Invited talk** on The Fifth Asian Interaction Seminar on Atomic and Molecular Physics (AISAMP5), October 1-5, 2002, Nara, Japan.
9. J Zhang, YJ Li, X Lu, F Yan, Z Jin, XY Peng, "Research on new schemes of ultrashort x-ray lasers ", **Invited talk** on The 8th International Conference on X-Ray Lasers, May 27-31, 2002, Aspen, USA.
10. J Zhang, QL Dong, YT Li, TJ Liang, ZL Chen, ZM Sheng, H Teng, ZY Wei, "Interaction between intense ultrashort lasers with tailored plasmas", **Invited talk** on The International Conference on the Frontiers of Plasma Physics and Technology, December 9-14, 2002, Bangalore, India.
11. J Zhang, QL Dong, ZL Chen, H Teng, Z Jin, XY Peng, ZY Wei, ZM Sheng, XW Tang, "Ultrashort laser-plasma interaction", **Invited Talk** on The 27th European Conference on Laser Interaction with Matter ECLIM 2002, October 7-11, 2002, Moscow, Russia.
12. J Zhang, ZL Chen, H Teng, QL Dong, XY Peng, Z Jin, ZY Wei, ZM Sheng, "Hot electron generation and propagation related to fast ignition", **Invited talk** on The 6th

Workshop on fast ignition of fusion targets, November 16-19, 2002, Florida, USA.

13. J Zhang, H Teng, YT Li, TJ Liang, LM Chen, ZM Sheng, QL Dong, LZ Zhao, ZY Wei, “Generation and propagation of hot electrons in laser-plasmas”, **Invited talk** on The Second International Conference on Inertial Fusion Sciences and Applications (IFSA2001), September 9-14, 2001, Kyoto, Japan.
14. J Zhang, YJ Li, X Lu, “Possible ways to generate hard x-ray lasers”, **Invited talk** on SPIE Conference on Soft X-ray Lasers and Applications IV, August 1-3, 2001, San Diego, USA.
15. J Zhang, ZL Chen, H Teng, LM Chen, YT Li, LZ Zhao, ZY Wei, “Observation of jet emission of hot electrons in laser-plasmas”, **Invited talk** on CLEO/Pacific Rim Conference on Lasers and Electro-optics (CLEO/Pacific Rim 2001), July 15-19, 2001, Chiba, Japan.
16. J Zhang, H Yang, “Research on laser induced lightning at IoP, CAS”, **Invited talk** on International Symposium on Ultrafast Intense Laser Science, October 4-6, 2001, Quebec City, Canada.
17. ZL Chen, J Zhang, H Teng, LM Chen, YT Li, “Effects of charge separation potential on emission of hot electrons”, **Invited talk** on CLEO/Pacific Rim Conference on Lasers and Electro-optics (CLEO/Pacific Rim 2001), July 15-19, 2001, Chiba, Japan.
18. J Zhang, LM Chen, YT Li, TJ Liang, “Recent progress of high field physics at the Institute of Physics”, **Invited talk** on Optical Society of Korea, February 13-18, 2001, Seoul, Korea.

**6. 论文选集（见附页）
Selected papers (see appendix)**

Spatial Distribution of High-Energy Electron Emission from Water Plasmas Produced by Femtosecond Laser Pulses

Y.T. Li,¹ J. Zhang,^{1,*} Z.M. Sheng,¹ H. Teng,¹ T.J. Liang,² X.Y. Peng,¹ X. Lu,¹ Y.J. Li,¹ and X.W. Tang²

¹Laboratory of Optical Physics, Institute of Physics, Chinese Academy of Sciences, Beijing 100080, People's Republic of China

²Institute of High Energy Physics, Chinese Academy of Sciences, Beijing 100039, People's Republic of China

(Received 24 January 2002; published 25 April 2003)

High energy electrons emitted by water plasmas produced by a single or a multiple laser pulse are investigated. The multipulse mode greatly enhances the generation and the temperature of hot electrons. Directional emission of high energy electrons over 25 keV is observed in two symmetric directions with respect to the laser axis and at 46° from the directions of the laser electric field. Two-dimensional particle-in-cell simulations reproduce well the experimental results and indicate that the acceleration mechanism of the high energy electrons is due mainly to the resonance absorption at the edge of the spherical droplets formed by the leading pulse.

DOI: 10.1103/PhysRevLett.90.165002

PACS numbers: 52.38.-r, 52.38.Kd, 52.50.Jm

Research during the past decades on laser-produced liquid plasmas has mainly concentrated on x-ray emission from liquid jet [1], laser-induced breakdowns resulting from focusing a long laser (nanosecond or subnanosecond) pulse inside a liquid [2,3]. More recently, there has also been research on single cavitation bubble luminescence in liquids [4,5]. However, many practical applications such as laser surgery, etc. [6] involve the interaction of a laser beam with an air-liquid interface instead of inside a liquid. In this Letter, we study the high energy electron emission from water plasmas produced by focusing femtosecond laser pulses on the water surface. We find that the spatial distribution of the hot electrons is very different from the behavior of hot electrons emitted from the interactions of ultrashort laser pulses with solids, gases, and clusters.

The experiments are carried out on an ultrashort-pulse laser facility (5 mJ, 150 fs, 800 nm, and 10 Hz). Figure 1 shows the experimental setup. The laser beam is focused by an f/4 spherical lens onto the air-liquid surface of distilled water, forming a focal spot with a diameter of $\sim 10 \mu\text{m}$. One can produce a single pulse or a multiple pulse train by adjusting the Pockels cell in the laser chain. The inset in Fig. 1 shows the shape of the multipulse measured by a Tektronix TDS 520A digital oscilloscope. The separation time between two pulses in the multipulse is 10 ns. The peak intensity on the target surface is about $1 \times 10^{16} \text{ W/cm}^2$ for the single pulse case.

The hot electrons are recorded by LiF (Mg, Cu, P) thermoluminescence dosimeters (TLDs) with a 6- μm -thick aluminum filter. The dimension of the LiF detector is 4.5 mm diam \times 0.8 mm. The space over the laser focus is covered by more than 100 TLDs mounted on a 2π spherical shell. A hole is left on the top of the hemispheric bracket for the incident laser beam. A rotatable reflection mirror, M2, converts the horizontal laser beam to vertical or obliquely incident on the water surface. The angular resolution of this system is about 6°.

LiF is sensitive to ions, x-ray photons, and electrons. However, the long distance in air and aluminum filter are the natural filters for the ions generated in the experiment. Comparison of the dosages at the TLDs with and without a 1500 G magnetic field shows that the contribution of x rays is 20 times lower than that of electrons. Thus, the dosage recorded by the TLDs is contributed mainly by the hot electrons.

A γ -ray spectrometer is used to measure the x-ray bremsstrahlung [7]. The plasma expansion is probed by splitting a small portion of the laser beam from the main beam and passing it parallel across the plasma after frequency doubling to 400 nm.

Figure 2 shows the x-ray spectra for the single and multiple laser pulse cases, respectively. The spectra are obtained by the γ -ray spectrometer, viewing the plasma at 80° with respect to the target normal. The laser pulses

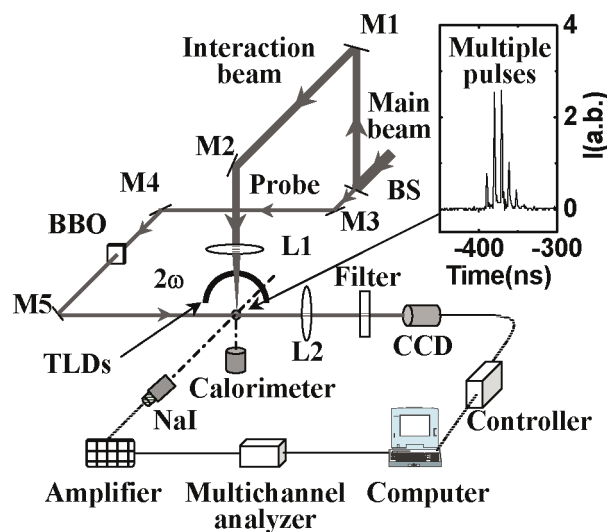


FIG. 1 (color online). The experimental layout. M1–M5 are reflection mirrors and BS represents the beam splitter.

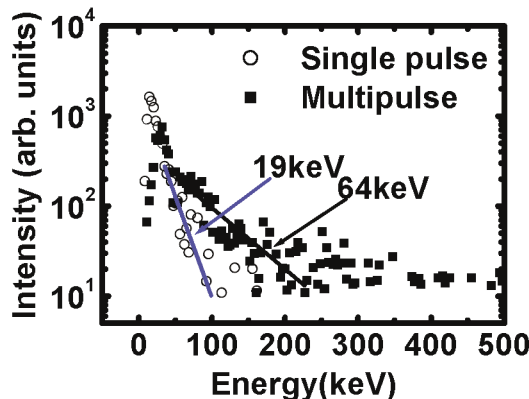


FIG. 2 (color online). Comparison of the hard x-ray spectra emitted from laser-water plasmas produced by a single pulse and a multipulse train.

are incident on the water surface normally. Compared with the case of the single pulse, the multiple pulse train greatly enhances the emission of x rays. The maximum photon energy exceeds 300 keV, and the effective temperature of the hot electrons is up to 64 keV by fitting an $\exp(-E/kT)$ to the tail of the photon distribution. This temperature is comparable to the values in the laser-solid interaction under similar experimental conditions [8].

Figure 3(a) displays the spatial distribution of electrons with energies higher than 25 keV produced by multiple pulses at the normal incidence. The dose is accumulated over 10 000 shots. A striking aspect is the presence of two distinct peaks, symmetric with respect to the laser incident direction, in the plane formed by the electric vector and the propagation vector. The direction of the two peaks is at 46° backward from the electric vector with a full width at half-maximum (FWHM) (Gaussian profile) of 34° . When the plane of the laser polarization is rotated by 90° using a $\lambda/2$ wave plate, the direction of the electron emission is found to rotate by 90° correspondingly, as shown in Fig. 3(b). The solid line and the square points in Fig. 3(c) show the angular distribution of electrons on the chord through the electron jets obtained from Fig. 3(a), where 0° corresponds to the laser propagation axis and 90° and 270° correspond to the direction of the electric vector. Assuming the electrons are subjected to a Maxwellian distribution with an effective temperature of 64 keV (deduced from the hard x-ray spectrum), we estimate the total number of electrons is $2 \times 10^5/\text{sr}$ per shot in the jets using the ITS 3.0 code (Integrated TIGER Series of Coupled Electron/Photon) [9].

When the p -polarized laser pulses are incident at 20° with respect to the target normal, two peaks of hot electron emission are again found. The latter retains the axial symmetry with respect to the laser propagation vector in the plane of polarization. When s -polarized laser beams are used at an incident angle of 20° , the two peaks of hot electrons also rotate by 90° . Note that the results here are quite different from those observed in corresponding laser-solid plasma interactions [8].

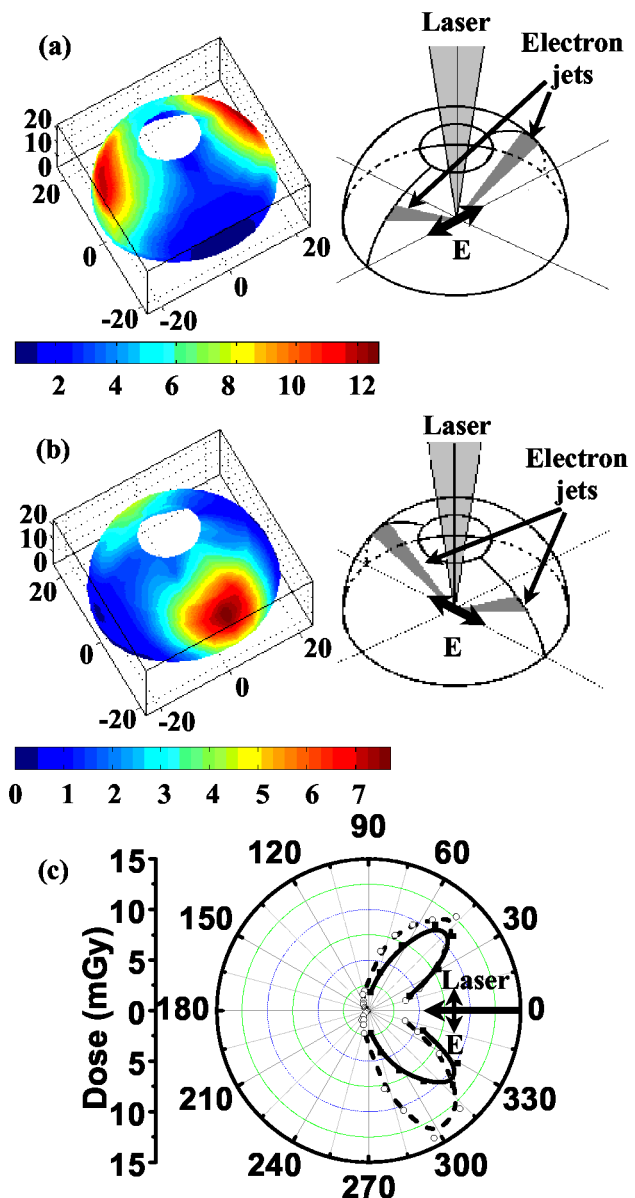


FIG. 3 (color online). (a) Spatial distribution of hot electrons with energies > 25 keV at the normal incidence. (b) The plane of the polarization rotated by 90° , the two electron peaks are rotated correspondingly. Angular distribution on the chord through the electron jets obtained from (a) (solid line and squares) and angular distribution of the hot electrons emitted from the direct laser-water droplets interaction (dashed line and circles) are shown in (c).

We have also investigated hot electrons generated by a single pulse, but the dosage recorded by the TLDs is only slightly higher than that of the background. This is expected because the average temperature of the hot electrons is only 19 keV (see Fig. 2), and most of them cannot penetrate the $6\text{-}\mu\text{m}$ -thick aluminum filter in front of the TLDs. For comparison, a prepulse with a very short separation time of 50 ps is introduced in some shots. We find that the effect of such a short separation time is

negligible. It is of interest to compare the case of interaction with solid targets, where such a prepulse would dramatically enhance the production of hot electrons [7].

To understand the characteristics of the plasma produced by the leading pulse in the multipulse mode, we model the interaction using a 1D hydrodynamic simulation code (MED103) [10]. We find that a very cool preplasma with temperature <0.1 eV and low-density gradient is formed at 10 ns. Thus, more energy of the following laser pulses can be deposited in the interaction region [11]. The energy of the forward scattered light for both single and multiple pulses is measured in our experiment by an energy calorimeter and we find that energy absorption is more efficient in the multipulse mode. However, this higher energy deposition cannot fully explain the behavior of the hot electrons observed.

To clarify the effects of the leading pulse on the interaction, the plasma is diagnosed by the optical shadowgraphy. Typical shadowgrams of the backward expansion into air and the forward expansion into water of the water plasma produced by a single laser pulse are shown in Fig. 4. The shadowgrams are recorded at a delay time of 10 ns, the same time as the separation time in the multipulse mode. The filaments in water are caused by the leakage of the laser beam. A shock wave into air and a density cavity (or crater) into water are simultaneously produced by the plasma pressure. When the second pulse arrives after 10 ns, both the shock wave front in air and the bottom of the water crater have moved away, ~ 150 and $\sim 110 \mu\text{m}$ from the focus, respectively. Most of the preplasma produced by the first pulse will recombine after 10 ns. Therefore, the possible candidates to be interacted with by the following pulses are (a) the spherical critical density surface at the bottom of the water crater; (b) the compressed ambient air and the water vapor

wrapped between the shock wave and the concave water surface (these gases may be partially ionized); and (c) the water droplets from the condensation of water vapor or from the direct explosive emission from the focus. A simple interaction model is illustrated in Fig. 4(c). Next we find out which one is responsible for the experimental results and how the hot electrons are produced.

One might think that the generation of hot electrons is related to the resonance absorption on the spherical critical surface of the water crater or on a backward propagating critical density ionization front produced by the first pulse. The following laser beam effectively defocused by the air breakdown would meet two parts of the surface that are at the correct angle for the resonance absorption, which would lead to the two electron beams as a result of the spherical symmetry of the surface. To check this speculation, we carried out a test experiment in which only the air breakdown was imaged. Figure 4(d) shows a shadowgram of the air breakdown taken at 1 ns produced by a single 2 mJ laser pulse when the water vessel is removed. We can see that most of the laser energy still remains within a $20 \mu\text{m}$ diam region at a $\sim 110 \mu\text{m}$ distance away from the focus. The area of the defocusing beam is only $\sim 1\%$ of the area of the half spherical density cavity. Therefore, the defocusing light actually irradiates a near-planar critical density surface. This cannot produce the two electron beams symmetrical with the incident laser axis. From Fig. 4(d) we also note that the self-focusing, which may enhance the local laser intensity and the yield of hot electrons, takes place. However, this cannot explain the two peaks of electron emission.

When the following pulses interact with the compressed air and water vapor partially ionized behind the shock wave into air produced by the leading pulse, instabilities may occur in such conditions. However, from the viewpoint of hot electron generation, in principle, the instabilities cannot fully explain the emission direction of hot electrons and their dependence on the incident angle and laser polarization [12].

The generation of nanometer-size and micrometer-size particles by pulsed laser ablation on solid in air have been widely studied [13]. In our experiments, the separation time between pulses is 10 ns. The water droplets can be produced by the first pulse through condensation of water vapor in the ablation plume and direct explosive emission from the focus. Figure 4(e) shows an image of the droplets near the initial water surface taken at 15 ns with a magnification factor of 165. A single pulse with an energy of 2 mJ was used to produce the droplets. We can see the size of the droplets is within $1\text{--}6 \mu\text{m}$. The average size is about $3 \mu\text{m}$. The submicro droplets cannot be observed due to the optical resolution.

To check the electron generation mechanism, we have run 2D particle-in-cell (PIC) simulations. A p -polarized laser pulse with a normalized amplitude $a_0 = 0.1$ and a duration of 50 laser cycles is incident from left normally onto a spherical droplet microplasma with a diameter

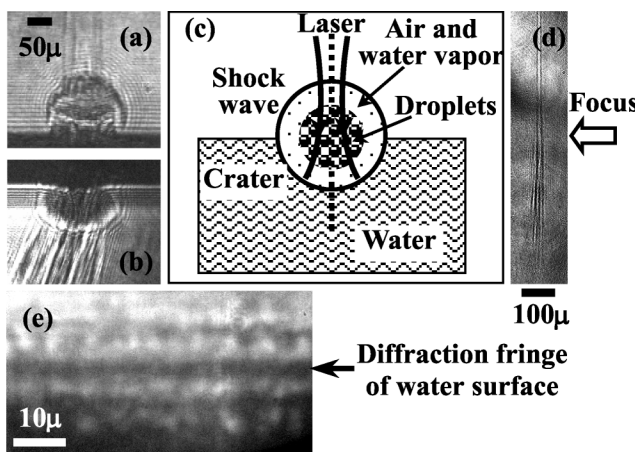


FIG. 4. (a) Shadowgrams of the backward expansion in air at the normal incidence; (b) the forward density cavitation in the water at the oblique incidence; (c) schematic showing the interaction model; (d) self-focusing and defocusing of a single pulse taken at 1 ns; and (e) a typical image showing the droplets above the water surface.

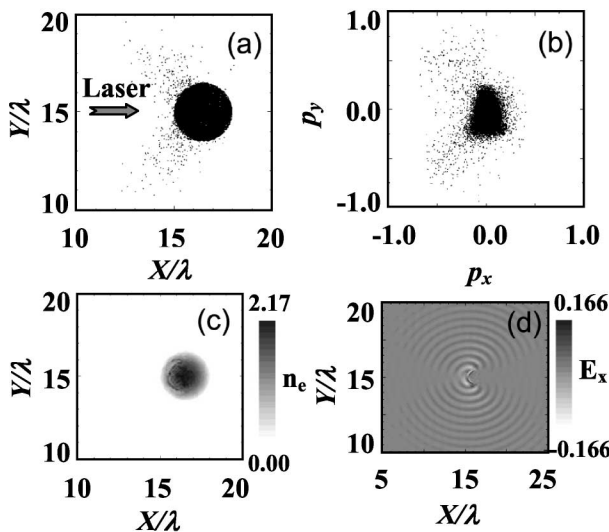


FIG. 5. 2D PIC simulation results for a p -polarized laser pulse at the 40 laser cycle. (a) X - Y plot of electron positions; (b) the distribution of electron momentum in the phase space (p_x, p_y); (c) electron density; and (d) the resonantly excited longitudinal component of the electric field.

of 3λ and a radial density rising parabolically from $0.2n_c$ at the surface to $2n_c$ at the center, where n_c is the critical density. To simplify the problem and save computing time, only one droplet is taken here. However, this does not affect the main interaction physics. Figure 5 shows the distributions of electron positions, momentum, density, and the longitudinal component of the electric field at the 40 laser cycle, respectively. Figures 5(a) and 5(b) show clearly that some of the electrons are accelerated to high energies symmetrically with respect to the laser axis. The ejection angles of most hot electrons are around 40° relative to the laser electric vector. This agrees quite well with the angular distribution measured in experiments. The acceleration mechanism is the resonance absorption occurring at the edge of the microplasma, as judged by the local density increase near the resonant critical surface in Fig. 5(c) and the enhancement of the electrostatic field E_x in Fig. 5(d) (the maximum field of 0.166 is greater than the initial field of $a_0 = 0.1$). On the other hand, no jets of hot electron emission are observed when an s -polarized laser pulse is used. This further proves that resonance absorption is the main mechanism. The fact that there are no jets for an s -polarized laser in the 2D simulations does not contradict our experimental results when the polarization plane is rotated by 90° . In practice, the interaction geometry is three dimensional, where the p -polarized light and s -polarized light is identical for a spherical microplasma.

In the simulations, we find that the ejection angle depends very weakly on the diameter of the droplet microplasma between 2λ and 8λ . This feature remains

valid when one adopts different density profiles for the droplet. It shows that the laser field diffraction around the droplet also plays a role, which, combining with the linear mode conversion around the critical surface, is responsible for the two electron jets. No distinct electron jets are observed for droplets with diameter less than λ .

To further confirm the analysis above, an experiment of femtosecond laser direct interaction with water droplets has been performed [14]. The droplets are generated by a gas nozzle with a backed pressure. The droplet size is measured to be $\sim 4 \mu\text{m}$ on average. The diagnostics are the same as the laser-water experiments in air. When a single 2 mJ laser pulse irradiates the droplets in vacuum, we find that the angular distribution of the hot electrons is very similar for both experiments. The results are also shown as the dashed line and circle points in Fig. 3(c) for comparison.

The intrinsically spherical symmetry of the droplets results in the fact that the geometry of the interaction is determined only by the state of the incident laser pulses, even for the case of oblique incidence relative to the water surface. Therefore, the directions of hot electron jets follow the incident laser axis and the electric vector closely whether the laser is obliquely or normally incident and also whether the laser is p polarized or s polarized.

The authors gratefully thank M. Y. Yu and J. X. Ma for useful discussions. This work is supported by the NSFC (Grants No. 10204023, No. 10075075, No. 10105014, and No. 10176034), the K. C. Wang Education Foundation (Hong Kong), the National High-Tech ICF program, and the NKBRSF (Grant No. G199990-75200).

*Author to whom correspondence should be addressed.

Email address: jzhang@aphy.iphy.ac.cn

- [1] M. Berglund *et al.*, Rev. Sci. Instrum. **69**, 2361 (1998).
- [2] J. Noack *et al.*, Appl. Opt. **37**, 4092 (1998).
- [3] A. G. Doukas *et al.*, Appl. Phys. B **53**, 237 (1991).
- [4] C. D. Ohl *et al.*, Phys. Rev. Lett. **80**, 393 (1998).
- [5] O. Baghdassarian *et al.*, Phys. Rev. Lett. **86**, 4934 (2001).
- [6] A. Vogel *et al.*, J. Acoust. Soc. Am. **100**, 148 (1996).
- [7] P. Zhang *et al.*, Phys. Rev. E **57**, R3746 (1998).
- [8] Y.T. Li *et al.*, Phys. Rev. E **64**, 046407 (2001).
- [9] J. A. Halbleib *et al.*, ITS 3.0: Integrated TIGER Series of Coupled Electron/Photon Monte Carlo Transport Codes, SAND91-1634, March 1992.
- [10] J. P. Christiansen *et al.*, Comput. Phys. Commun. **7**, 271 (1974).
- [11] J. Zhang *et al.*, Science **276**, 1097 (1997).
- [12] W. L. Kruer, *The Physics of Laser Plasma Interactions* (Addison-Wesley, Redwood City, California, 1988).
- [13] C.-B. Juang *et al.*, Appl. Phys. Lett. **65**, 40 (1994); Ching Bo Juang *et al.*, Appl. Phys. Lett. **65**, 40 (1994); H. Schittenhelm *et al.*, J. Phys. D **29**, 1564 (1996).
- [14] T.J. Liang *et al.* (private communication).

Laser-Energy Transfer and Enhancement of Plasma Waves and Electron Beams by Interfering High-Intensity Laser Pulses

P. Zhang,¹ N. Saleh,¹ S. Chen,¹ Z. M. Sheng,² and D. Umstadter¹

¹*FOCUS Center, University of Michigan, Ann Arbor, Michigan 48109, USA*

²*Laboratory of Optical Physics, Institute of Physics, P.O. Box 603, Beijing 100080, People's Republic of China*
(Received 14 February 2003; published 25 November 2003)

The effects of interference due to crossed laser beams were studied experimentally in the high-intensity regime. Two ultrashort (400 fs), high-intensity (4×10^{17} and $1.6 \times 10^{18} \text{ W/cm}^2$) and $1 \mu\text{m}$ wavelength laser pulses were crossed in a plasma of density $4 \times 10^{19} \text{ cm}^{-3}$. Energy was observed to be transferred from the higher-power to the lower-power pulse, increasing the amplitude of the plasma wave propagating in the direction of the latter. This results in increased electron self-trapping and plasma-wave acceleration gradient, which led to an increased number of hot electrons (by 300%) and hot-electron temperature (by 70%) and a decreased electron-beam divergence angle (by 45%), as compared with single-pulse illumination. Simulations reveal that increased stochastic heating of electrons may have also contributed to the electron-beam enhancement.

DOI: 10.1103/PhysRevLett.91.225001

PACS numbers: 52.38.Kd, 41.75.Jv, 52.57.-z

The interactions of high-intensity laser pulses in plasma are of much current interest because of their relevance to advanced radiation sources, inertial fusion concepts, and accelerators [1]. These interactions often take the form of intersecting beams, in which case several novel physical phenomena are expected to occur. For instance, when an intense laser pulse interacts with a solid-density target, it is partially reflected, and the beating between the incident and reflected light in the underdense plasma region will create interference, which can modify the optical properties of the plasma [2], excite plasma waves [3], and heat electrons [4]. It has been suggested theoretically [5] that this stochastic heating of electrons is ultimately responsible for the acceleration of multi-MeV energy beams of ions from laser-irradiated thin foils [6–8]. In inertial fusion research, the electron heating and modification of the laser reflectivity that results from crossed laser beams [9–12] must be controlled in order to efficiently couple energy to the fusion target. High-intensity crossed beams are relevant to fast-ignition fusion research [13]. The overlapping of intense laser pulses in plasmas has also been suggested theoretically [14–16] as one of several means [14–19] to optically inject electrons into laser-driven plasma waves.

Reported here are experimental results on crossed-beam interference in the high-intensity (relativistic-electron) regime and its effects on the dielectric and thermal properties of a plasma. Energy transfer between the two laser beams as well as plasma-wave and electron-beam enhancement are observed. The mechanism responsible for the energy transfer in this case differs from that studied in previous long-pulse and low-power crossed-beam experiments [9–12]. In our study, the mechanism was scattering from a stationary electron-density grating that was driven directly by optical interference, while in these previous experiments it was scattering from ion

waves. The physics of overlapping short-duration pulses in plasmas were previously studied theoretically [2–4]. For instance, plasma-wave excitation [3] and energy transfer by superradiant amplification of a short pulse by a counterpropagating pulse [2] are predicted to occur when the difference in frequency between the two pulses is equal to the plasma frequency. We studied the degenerate case, where the frequency difference is zero, which closely approximates the interference that occurs when light is reflected at its critical density.

The experiments were performed with a hybrid Ti:sapphire and Nd:glass laser system, delivering short pulses (400 fs, $1.053 \mu\text{m}$) in a single shot, with power up to 10 TW. The laser beam was split into two beams, one of which contained 80% of the laser energy (injection) and the other one 20% (pump). These two beams were focused with two $f/3$ parabolic mirrors to near-Gaussian vacuum spot sizes of $12 \mu\text{m}$ FWHM (full width at half maximum), which contained 60% of the total energy. This corresponds to focal intensities ranging from (3×10^{17}) – $(5 \times 10^{17}) \text{ W/cm}^2$ for pump beam and (1.2×10^{18}) – $(2 \times 10^{18}) \text{ W/cm}^2$ for injection. The two beams of the parallel polarization were perpendicularly overlapped onto the edge of a supersonic helium gas jet. The pressure of the helium gas was 800 psi and the gas was fully photoionized, creating a plasma with density that was $4 \times 10^{19}/\text{cm}^3$, corresponding to $n_0/n_c = 0.04$, where n_c is the critical density.

The laser powers for both pump and injection pulses were above 1 TW, higher than the critical power for relativistic self-focusing, given by $P = 17(\omega_0/\omega_p)^2 \text{ GW}$, where ω_0 and ω_p are the laser and plasma frequencies, respectively. The pulse durations ($\tau = 400 \text{ fs}$) were many plasma periods long $\tau > 50(2\pi/\omega_p)$. In previous experiments performed with similar parameters [20], plasma waves were observed to be driven by the self-modulated

wakefield mechanism [21–23]. Images of crossed plasma channels were observed with top and side imaging of Thomson scattering and recorded by a CCD camera. Spatial profiles of pump electron beam were recorded with a scintillating screen (LANEX) coupled to a CCD camera. The LANEX screen was blocked by two layers of Al foils each of the thickness of 40 μm , which blocked electrons whose kinetic energies were below 170 keV. Pump electron spectra were obtained with an electron spectrometer (260 keV–5 MeV), composed of a dipole permanent magnet with a LANEX screen imaged by a CCD camera. In this case, a single aluminum foil of 40 μm thickness in front of the screen blocked the laser light. A 1-mm wide slit was placed in front of the magnet in order to select a narrow range of angles for electrons entering the magnet. The distance between the slit and the gas jet was 30 mm. Spatial and temporal overlap was achieved by adjusting the positions and delay between the beams until a bright spot in the intersection of the two plasma channels was observed. The bright spot was due to enhanced Thomson scattering [24] by the density bunched in the interference valleys.

Figure 1 shows the spatial profiles of the pump-accelerated electrons of the kinetic energy above 170 keV at laser power of 1.5 TW. It can be seen that with injection a more collimated and intensified electron jet was found (right inset), with a beam divergence angle of about 7° (the angle corresponding to the FWHM of the electron-beam profile), while without injection (left inset) it was nearly 12°. Integration of the intensity distributions

showed that, with injection, the charge of electron-beam was increased ~ 3 times.

In the conditions of best laser pulse temporal overlap, when the time delay between pump and injection was ± 30 fs, and with a pump laser power of 1.05 TW, the electron spectra in the direction of the pump, with and without injection, are as shown in Fig. 2. With injection, it can be seen that the portion of the electrons with kinetic energies greater than 400 keV is enhanced. As in previous experiments [20], the electron spectra approximated a Maxwellian-like distribution, i.e., $\exp(-\epsilon_k/T_e)$ with a high-energy tail, where ϵ_k is the electron kinetic energy and T_e is the electron temperature. The corresponding electron temperatures were fitted and shown in Fig. 2, and an increase of electron temperature with injection was observed to be more than 60%. Figure 3 shows the temperatures fitted from the electron spectra, with or without injection, at different laser powers. When injection was on, the increase of electron temperature was between 30% and 70% and corresponds roughly to the depth of the ponderomotive potential well due to the interference between the two pulses. In the high-energy tails, the temperature difference was only about 10%, even though the relative electron number was higher with injection.

Figure 4 shows the spectra of light exiting the plasma in the pump direction, with and without injection. With dual-beam illumination, the light signals in a broad spectrum range were obviously increased indicating that energy was transferred from the high-power to the low-power beam. It can also be seen from Fig. 3 that a 20% increase in pump power results in an electron temperature and number to levels that are nearly the same as

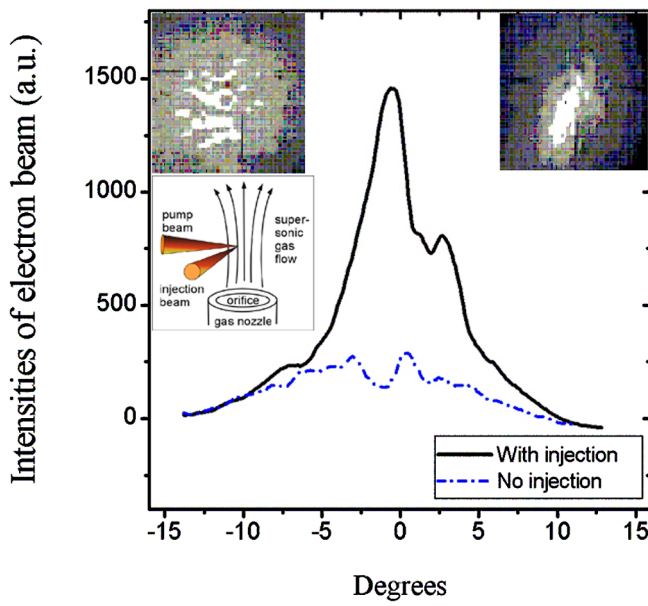


FIG. 1 (color online). Profiles of the spatial distributions of the electron beams (kinetic energies above 170 keV) in the direction of the pump at pump laser power of 1.5 TW, with (right inset) and without injection (left inset). Schematic diagram of the laser beams intersecting in the gas flow (middle left inset).

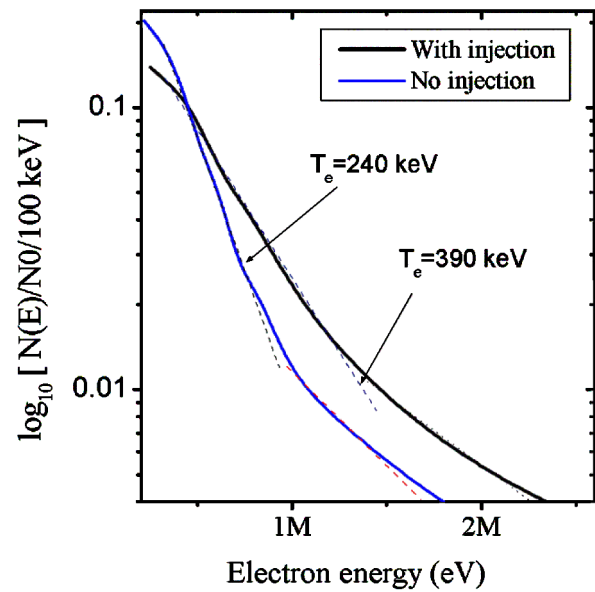


FIG. 2 (color online). The energy spectra of pump electron beam at pump laser power 1.05 TW, with (top curve) and without (bottom curve) injection. Dotted lines are exponential fits. The higher energy tails are 600 keV without injection and 660 keV with injection.

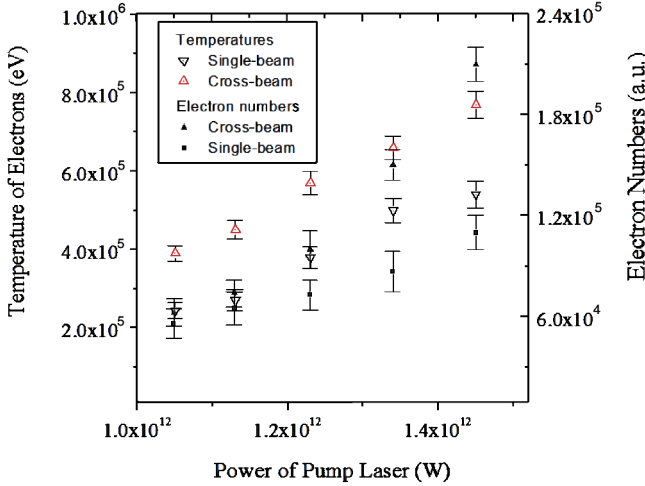


FIG. 3 (color online). The dependence of the electron temperature and number on the power of the pump laser, with and without injection.

those achieved by the addition of the injection pulse without increasing the pump.

A two-dimensional particle-in-cell (PIC) code computer simulation was also run with parameters similar to those of the experiment. A rectangular simulation box of $160\lambda \times 60\lambda$ was used, which was split into many cells, each with a size of $1/10\lambda \times 1/10\lambda$ for the integration of Maxwell's equations. A homogeneous plasma volume with an initial density of $0.04n_c$ occupied part of the simulation box. The pump pulse along the x direction and the injection pulse along the y direction initially were $a_{10} = 0.5$ and $a_{20} = 1.0$, respectively. Nine particles per cell were used for electrons and ions. Absorption boundaries for the fields and reflection boundaries for particles were used both in the x and the y directions.

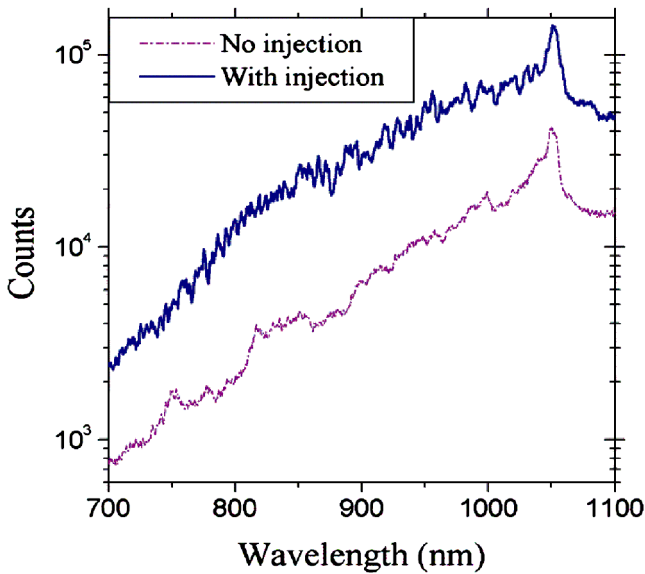


FIG. 4 (color online). The light spectra in the pump direction, with and without injection.

The results show that, in the region of laser intersection, electrons were trapped in the potential valleys by the ponderomotive force of the laser interference, resulting in the formation of a density grating with peak density modulation $n > 10n_0$, where n_0 was the background density. This same density bunching was predicted by balancing the ponderomotive force with the electrostatic force and electron thermal pressure. It was this density modulation that enhanced the scattering [24] observed in the experiments. The potential of ponderomotive force $\phi_p = (\gamma - 1)m_0c^2$, where $\gamma = \sqrt{1 + a_0^2/2}$ was the relativistic factor, $a_0 = 8.5 \times 10^{-10}\lambda[\mu\text{m}]I^{1/2}[\text{W/cm}^2]$ was the normalized vector potential, and λ and I were the laser wavelength and focal intensity, respectively. At the peak intensity of laser interference, $I = 4 \times 10^{18} \text{ W/cm}^2$, the potential depth of the ponderomotive force valleys was estimated to be about 300 keV.

Figure 5(a) shows snapshots of the pump laser field, the electric field of the pump plasma wave, and the momentum of electrons at $t = 100$ laser cycles. The two laser pulses fully overlapped at $t = 80$ laser cycles. It can be seen that, during the time when the beams crossed, the velocities of electrons were increased to close to the speed of light in both positive and negative directions, indicating that the electrons were heated isotropically. Calculations indicate that the ponderomotive force of the injection pulse could increase the electron kinetic energy in the direction of the pump by 200 keV. But this might also be explained by stochastic motion of electrons in the region of laser intersection [4]. The calculated Liapunov exponent of the electron trajectory indicates that the amplitudes of pump and injection laser were sufficient to trigger stochastic motion. In addition, the plasma disturbance of the high density gradient (scale length of $\sim 0.7\lambda$ and $n_e/n_0 \sim 10$) excited by laser interference does create ideal conditions for stochastic heating of electrons. With these preheated electrons injected in the plasma wave in a broad range of phases, the number increase of high-energy electrons is to be expected.

In order to investigate the mechanism for electron heating and distinguish between the effects of laser power increase due to energy transfer and the role of stochastic heating, we did additional simulations under conditions of both dual-beam and single pump beam illumination, but in the latter case with a 20% power increase [Fig. 5(b)]. With injection, electrons of the kinetic energies less than 1 MeV are obviously increased. With 400-fs injection laser pulses, electrons are injected into the self-modulated plasma wave at all phases. In the relatively short acceleration distance in the simulation ($\sim 100 \mu\text{m}$), these initial velocity changes are obvious in the spectrum, while the maximum electron kinetic energy depends on the strength of the plasma wakefield, which was proportional to the laser power. The reason why the injection effects were not obvious in the results (Fig. 3) is that the optical injection happens only in the laser beam intersection over

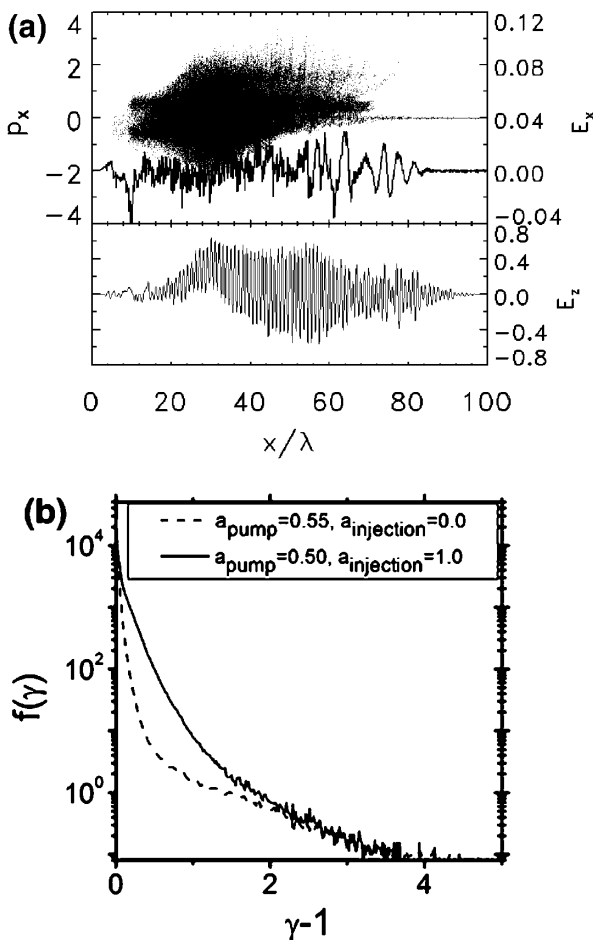


FIG. 5. (a) Simulation result showing snapshots of the pump laser field, the electric field of the pump plasma wave, and the momentum of electrons at $t = 100$ laser cycles. (b) Simulated electron spectrum under conditions of both dual-beam and single pump beam illumination, but in the latter case with a 20% power increase of the weaker beam.

a scale length of $\sim 10 \mu\text{m}$, while the distance of plasma-wave propagation is nearly 1 mm, about 100 times longer. Along the path of propagation, the self-modulated plasma wave continues to self-trap electrons over a large range of phases and accelerates them.

In summary, the first controlled experimental study of crossed-beam interference in the weakly relativistic regime was discussed. When the two high-intensity laser pulses were overlapped with each other in an underdense and uniform plasma, significant energy exchange from the higher-power to the lower-power laser beam was observed. The charge, temperature, and divergence angle of the electron beam that was accelerated in the direction of the lower-power laser beam were found to dramatically change with dual-laser-pulse illumination. These effects are unavoidable in current experiments on ion acceleration and fast-ignition fusion and in future experiments on laser-plasma accelerators. In the latter case, simulations [14–19] indicate that, through the ponderomotive force,

one laser pulse can inject electrons into the plasma wave driven by the other laser pulse. When the pulse durations are equal to a plasma period, rather than many plasma periods, as in our experiment, and the plasma-wave amplitude is kept below the self-trapping threshold, this injection mechanism can reduce the electron-beam energy spread to just a few percent (as compared with 100% currently), rendering laser-wakefield accelerators more practical for applications in nuclear physics research, x-ray free-electron lasers, and medicine. This study suggests that the effects of energy transfer must be considered and the mechanism of stochastic heating might also be used for optical injection. However, laser-plasma parameters that differ from those used in our experiment must be carefully chosen in order to inject electrons over a narrow range of phases, as required to produce monoenergetic electron beams.

The authors acknowledge the support of Division of High-Energy Physics, Office of Science, U.S. Department of Energy, Award No. DE-FG02-98ER41071, with lasers supported by the National Science Foundation FOCUS Center, Grant No. 0114336. We also thank G. Shvets, Y. Sentoku, and K. Mima for many useful discussions, and A. Maksimchuk for valuable assistance with the laser.

-
- [1] D. Umstadter, Phys. Plasmas **8**, 1774 (2001).
 - [2] G. Shvets, N. J. Fisch, and J.-M. Rax, Phys. Rev. Lett. **80**, 2598 (1998).
 - [3] G. Shvets, N. J. Fisch, and A. Pukhov, Phys. Plasmas **9**, 2383 (2002).
 - [4] Z.-M. Sheng *et al.*, Phys. Plasmas **9**, 3147 (2002).
 - [5] Y. Sentoku *et al.*, Appl. Phys. B **74**, 207 (2002).
 - [6] E. L. Clark *et al.*, Phys. Rev. Lett. **84**, 670 (2000).
 - [7] A. Maksimchuk *et al.*, Phys. Rev. Lett. **84**, 4108 (2000).
 - [8] R. A. Snavely *et al.*, Phys. Rev. Lett. **85**, 2945 (2000).
 - [9] R. K. Kirkwood *et al.*, Phys. Rev. Lett. **76**, 2065 (1996).
 - [10] K. B. Wharton *et al.*, Phys. Rev. Lett. **81**, 2248 (1998).
 - [11] C. Labaune *et al.*, Phys. Rev. Lett. **85**, 1658 (2000).
 - [12] R. K. Kirkwood *et al.*, Phys. Rev. Lett. **89**, 215003 (2002).
 - [13] M. Tabak *et al.*, Phys. Plasmas **1**, 1626 (1994).
 - [14] D. Umstadter, J. K. Kim, and E. Dodd, Phys. Rev. Lett. **76**, 2073 (1996).
 - [15] E. Esarey *et al.*, Phys. Rev. Lett. **79**, 2682 (1997).
 - [16] R. G. Hemker *et al.*, Phys. Rev. E **57**, 5920 (1998).
 - [17] B. Rau, T. Tajima, and H. Hojo, Phys. Rev. Lett. **78**, 3310 (1997).
 - [18] S. V. Bulanov *et al.*, Plasma Phys. Rep. **25**, 701 (1999).
 - [19] C. Moore *et al.*, Phys. Rev. Lett. **82**, 1688 (1999).
 - [20] D. Umstadter *et al.*, Science **273**, 472 (1996).
 - [21] P. Sprangle, A. Ting, E. Esarey, and A. Fisher, J. Appl. Phys. **72**, 5032 (1992).
 - [22] T. M. Antonsen, Jr. and P. Mora, Phys. Rev. Lett. **69**, 2204 (1992).
 - [23] N. E. Andreev *et al.*, JETP Lett. **55**, 571 (1992).
 - [24] R. E. Slusher and C. M. Surko, Phys. Fluids **23**, 472 (1980).

Stochastic Heating and Acceleration of Electrons in Colliding Laser Fields in Plasma

Z.-M. Sheng,^{1,2} K. Mima,¹ Y. Sentoku,¹ M. S. Jovanović,¹ T. Taguchi,³ J. Zhang,² and J. Meyer-ter-Vehn⁴

¹Institute of Laser Engineering, Osaka University, 2-6 Yamada-oka, Suita, Osaka 565-0871, Japan

²Laboratory of Optical Physics, Institute of Physics, Chinese Academy of Science, Beijing 100080, China

³Department of Electrical Engineering, Setsunan University, Neyagawa, Osaka, Japan

⁴Max-Planck-Institut für Quantenoptik, D-85748 Garching, Germany

(Received 27 May 2001; revised manuscript received 16 October 2001; published 18 January 2002)

We propose a mechanism that leads to efficient acceleration of electrons in plasma by two counterpropagating laser pulses. It is triggered by stochastic motion of electrons when the laser fields exceed some threshold amplitudes, as found in single-electron dynamics. It is further confirmed in particle-in-cell simulations. In vacuum or tenuous plasma, electron acceleration in the case with two colliding laser pulses can be much more efficient than with one laser pulse only. In plasma at moderate densities, such as a few percent of the critical density, the amplitude of the Raman-backscattered wave is high enough to serve as the second counterpropagating pulse to trigger the electron stochastic motion. As a result, even with one intense laser pulse only, electrons can be heated up to a temperature much higher than the corresponding laser ponderomotive potential.

DOI: 10.1103/PhysRevLett.88.055004

PACS numbers: 52.38.Kd, 52.35.Mw

Electron acceleration by intense laser fields in plasmas has been the subject attracting a great deal of attention recently due to the advent of high power laser pulses and their potential applications. Various acceleration mechanisms have been proposed, including the plasma wave acceleration [1,2], the direct laser acceleration [3–5], and the mixed acceleration from both the transverse and the longitudinal fields [6,7].

In this Letter, we discuss a new kind of direct laser acceleration of electrons in two counterpropagating laser fields. Recently, there is a proposal, so called the superradiant amplification of ultrashort laser pulses by use of a counterpropagating laser pulse in plasma [8]; generation of periodic accelerating structures in a similar configuration has also been suggested [9]. Both of these phenomena are associated with the *coherent motion of electrons* driving by the two colliding laser pulses slightly detuned by the electron plasma frequency. Here, in contrast, our mechanism of electron acceleration results from the *stochastic motion of electrons*, which occurs when the amplitudes of two laser pulses exceed some thresholds, now easily accessible with chirped pulse amplification lasers. Moreover, the present mechanism is insensitive to their frequency differences; also it can work without a self-focusing channel, essential for the betatron resonance mechanism [5]. In plasma at a few percent of the critical density, the Raman backscattering wave of a driving pulse can serve as the second counterpropagating laser pulse, which could be intense enough to trigger stochastic acceleration if the first pulse has an intensity over $I\lambda^2 \sim 10^{18} \text{ W cm}^{-2} \mu\text{m}^2$. Therefore the present mechanism could be dominant in certain cases in laser interaction with underdense plasma. It may help to explain how the maximum electron energy can exceed the dephasing limit for particle acceleration from wave breaking observed in some particle-in-cell (PIC) simulations [10].

There have been considerable studies on electron motion in multiwave systems [11–14]. It is well-known that the Hamiltonian in multiwaves is usually not integrable. In this case, electron motion becomes stochastic when certain thresholds of the wave amplitudes are exceeded. It has been proposed by Mendonça that the formation of suprathermal electron tails observed in laser plasma interaction may be explained by the occurrence of stochastic motion of electrons in two electromagnetic waves [13,15]. However, this and other earlier studies on electron motion in a standing longitudinal plasma wave or two electromagnetic wave have been limited to the problem of the stochastic instability near the separatrices, and mostly in nonrelativistic electron motion. The potential of this stochastic instability with particle acceleration in plasma with powerful lasers focused up to relativistic intensities has not been fully explored. Here, with single particle calculations and particle-in-cell simulations, we demonstrate how electrons can be accelerated much more efficiently with the presence of a second counterpropagating pulse even at a very small amplitude than without it.

We start by considering the electron motion in two colliding planar laser fields in vacuum. The laser pulses can be described by their vector potential $\mathbf{A}_i = a_i(\xi_i) \cos(\xi_i + \psi_i)\hat{\mathbf{y}} \equiv A_i\hat{\mathbf{y}}$, where $i = 1, 2$, $\xi_1 = x - t$, and $\xi_2 = k_2(x + t)$; the frequencies of the two laser pulses are ω_1 and ω_2 , respectively; x and t are normalized to c/ω_1 and ω_1^{-1} , respectively; k_2 and $\omega_2 (= k_2 c)$ are normalized to ω_1/c and ω_1 , respectively; and ψ_i are constants. The first pulse propagates in the positive x direction and the second one propagates in the negative x direction. The Hamiltonian for electrons is given by $H = [1 + (\mathbf{P} + \mathbf{A})^2]^{1/2}$, where the canonical momentum $\mathbf{P} = \mathbf{p} - \mathbf{A}$ is normalized by mc and vector potential \mathbf{A} by mc^2/e . Since \mathbf{A} is independent of y , one finds that $P_y = \text{const} = p_{y0}$. For simplicity, we assume $p_z = 0$ in the following. Therefore

the longitudinal motion can be described by Hamiltonian $H = [1 + p_x^2 + (p_{y0} + A_1 + A_2)^2]^{1/2}$. This Hamiltonian is still more complicated than that for electron motion in counterpropagating plasma waves [11]. Even in the nonrelativistic limit, making the canonical transform with $\eta = x - t$, $F_2 = \eta p_\eta$, and $p_\eta = p_x$, assuming $p_{y0} = 0$ and $\epsilon = a_2/a_1 \ll 1$, the resulting Hamiltonian contains two perturbation terms oscillating at different frequencies.

The instability regime for stochastic motion can be examined conveniently in geometry by the use of the surface of section plots at $\phi_2 = \xi_2 + \psi_2 \bmod 2\pi = \text{const}$. Figure 1 shows the surface of section plots for two lasers at the same frequency. When the amplitudes of the two pulses are the same, the electron trajectories in longitudinal momentum space are symmetric about zero as shown in Fig. 1(a). Electron trapping is found around $(p_x, \eta) =$

$[0, -(2N + 1)\pi/2]$ by the ponderomotive potential resulting from the beating of the two laser pulses. Stochastic motion first appears around the separatrices. According to the Kolmogorov-Arnol'd-Moser (KAM) theorem [12], there exist many KAM tori around a separatrix. Local stochastic motion sets in when nearby KAM tori overlap. Thresholds for local stochastic motion have been estimated to be about $a_1 a_2 = 1/16$ by Mendonca [13]. When the amplitude of the forward-moving pulse a_1 is larger than a_2 for the backward-moving pulse, the electron trajectories becomes nonsymmetric about zero; stochastic motion of electrons spreads widely in positive momentum space. The larger the amplitude a_1 , the wider the region for stochastic motion in positive momentum space, as shown in Fig. 1(b). For a given a_2 , the width for stochastic motion scales roughly proportional to a_1^2 . One notes that there remains regular motion for electrons trapped around $(p_x, \eta) = (0, 0)$, where acceleration cannot occur. However, with the increase of a_1 or a_2 further, this trapping island is gradually suppressed. Before it is fully suppressed, bifurcation occurs at certain amplitudes when the trapping island splits into two parts as shown in Fig. 1(c). This shows a transition of the stochastic motion from a local to a global one, where, in the later case, electrons initially at rest or small energy will be driven into stochastic motion and gain energy from laser fields. Until now, we have taken the frequencies of the two pulses to be the same. If the frequency of the second pulse is changed, the basic features are qualitatively similar, indicating that the stochastic motion is not sensitive to the frequency difference of the two pulses. One notes that there is no stochastic motion if the two pulses copropagate.

The Liapunov exponents can provide a quantitative measure of the degree of stochasticity for a given Hamiltonian system [12]. Let the test electron initially at rest and the amplitudes of the infinite planar pulse increase from zero in a function $\tan(t/t_L)$ with $t_L = 50$ laser cycles. The Liapunov exponents are calculated when the laser fields reach the maximum amplitudes or $t > 2t_L$. As either the amplitude a_1 or a_2 increases, the Liapunov exponents increase suddenly as the laser amplitudes exceed some threshold amplitudes. Since we start with electrons at rest initially, the obtained threshold corresponds to that for the global stochasticity around the fundamental trapping island in the surface of the section plot. This is shown in Fig. 2 by the solid line marked with $v_{x0} = 0$. It is approximately $a_1 a_2 \sim 1/2$, which is larger than that estimated by Mendonca for local stochastic motion [13], but close to that for the bifurcation of the fundamental trapping island, as expected. It is worthwhile to point out that the so-called global stochastic motion is relative and limited only to the region between some upper and lower boundaries in longitudinal momentum, beyond which, the electron motion becomes regular again. Therefore one can understand that it also depends on its initial velocity whether the trajectory of a test electron is stochastic or regular. If electrons

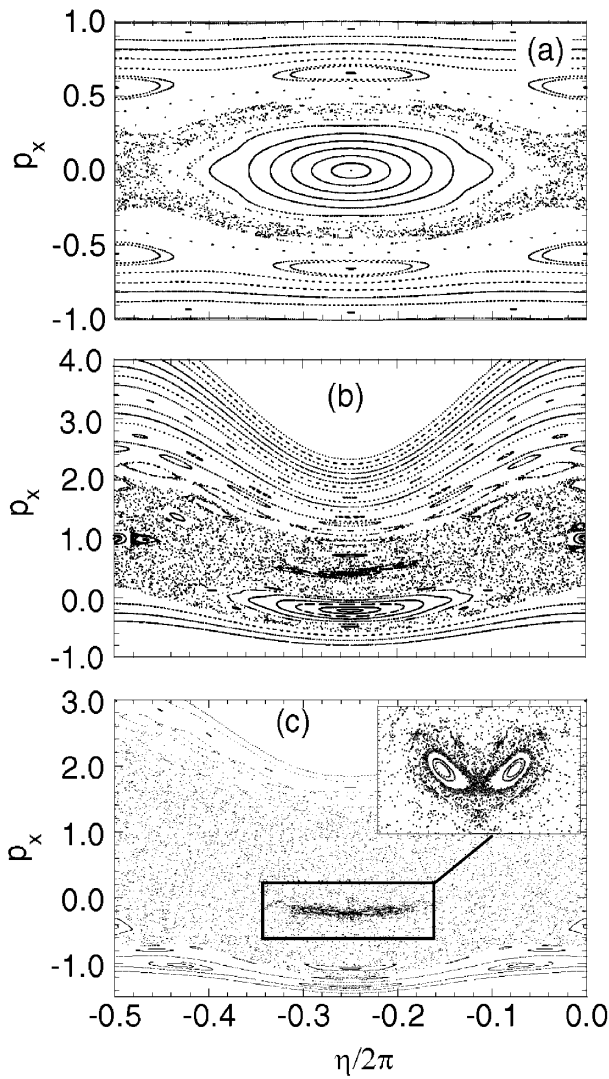


FIG. 1. Surface of section plots at $\xi_2 + \psi_2 = 2N\pi$ for electron motion in counterpropagating laser fields. (a) $a_1 = a_2 = 0.3$; (b) $a_1 = 1.0$ and $a_2 = 0.1$; (c) $a_1 = 1.0$ and $a_2 = 0.42$. Here $\eta = (\xi_1 + \psi_1) \bmod 2\pi$ and $\omega_{01} = \omega_{02}$. Note that η is in the period of π when the two pulse frequencies are the same.

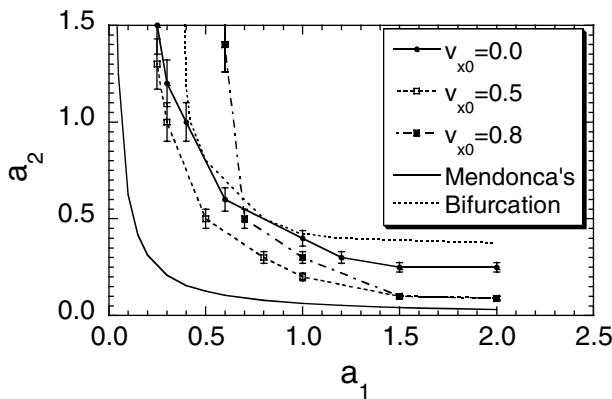


FIG. 2. Threshold amplitudes for stochastic motion for different initial electron velocities obtained numerically. Also shown are the thresholds for local stochastic motion by Mendonca and for the occurrence of bifurcation for trajectories trapped in the fundamental island around $(p_x, \eta) = (0, 0)$.

have some initial longitudinal velocity, such as that driven by the ponderomotive force at the front of the forward-propagating pulse, the threshold amplitudes can either reduce or increase as shown in Fig. 2. For $v_{x0} \geq 0.5$, the threshold amplitude of the counterpropagating a_2 reduces to only about 0.1 when $a_1 > 1.5$.

To confirm this acceleration mechanism, we have performed numerical simulations with PIC codes. We first try to simulate it with a 1D PIC code since it is essentially a one-dimensional effect. In simulations, the plasma is homogeneous, which occupies a region of $L = 50 \sim 100\lambda$, where λ is the incident laser wavelength. The laser pulses, which are semi-infinite and at the same frequency, increase to the maximum amplitudes in ten laser cycles. The electron energy distributions shown in Fig. 3(a) have been obtained in plasma with $n = 0.01n_c$ (n_c is the critical density). Both the electron temperatures and the maximum electron energy are much higher with a counterpropagating pulse than without it. The temperature increases up to about 3 MeV at 350 laser cycles after interaction with the counterpropagating pulse, which is 5 times larger than without it, even though its amplitude is only at $a_2 = 0.1$. We find that the temperature tends to be saturated after interaction for a certain time. This can be explained by the surface of the section plot, which shows that stochastic motion is found only in limited phase space around the separatrices. For very energetic electrons, their trajectories remain regular, and therefore net energy gain from the laser fields does not occur. Notice that the peaks near $\gamma = 3$ in the distributions are due to ponderomotive push with semi-infinite pulses, which would be absent for pulses with finite duration. This simple example demonstrates obviously that the presence of the second counterpropagating pulse is very important to trigger the stochastic motion, which can lead to effective energy transfer from laser fields to electrons. Figure 3(b) has been obtained with a 2D PIC code, where the *s*-polarized laser pulses focused at a diameter

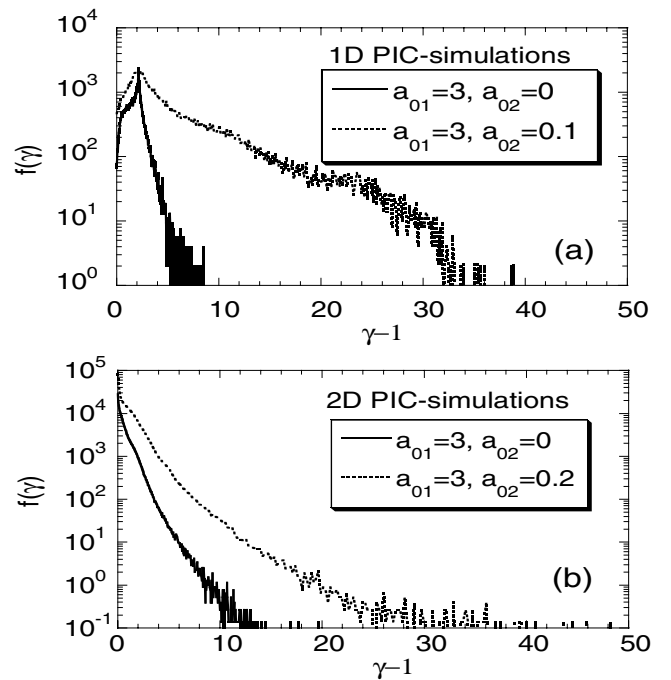


FIG. 3. Snapshots of electron energy distributions from PIC simulations of laser interaction with plasma slab $L = 50\lambda$. (a) With 1D PIC code in plasma at $n/n_c = 0.01$ at $t = 350$ laser cycles; (b) with 2D PIC codes in plasma at $n/n_c = 0.01$ and the laser beam diameter is 12 laser wavelengths at $t = 300$. The laser pulses are semi-infinite.

of 12 laser wavelengths are incident into the underdense plasma slab with the same parameters as for 1D simulation. The *s* polarization rules out possible electron acceleration through the Betatron resonance mechanism [5]. In this simulation, when with the second counterpropagating pulse $a_2 = 0.2$, the hot electron temperature is about twice that without it. Meanwhile, the quasistatic current and the corresponding quasistatic magnetic field with $a_2 = 0.2$ are found to be more than doubled than without it. However, the acceleration in the 2D simulation appears to be not as efficient as in the 1D case. This comes because high energy particles, usually having larger transverse momenta, tend to escape from the pulse center in the 2D geometry and therefore experience shorter acceleration time than in the 1D case. In passing, we mention that, if we change the initial phases of the incident laser pulses, the electron energy distributions can be changed. This is particularly evident for the relatively low energy part in the distribution function. However, the high energy tail appears not very sensitive to the initial phase difference of the laser pulses.

To verify that electrons gain energy mainly from the transverse laser fields rather than from the longitudinal fields, one can make use of the relation $\gamma = 1 + \Gamma_{||} + \Gamma_{\perp}$ following the equation of motion for electrons [5], where $\Gamma_{||} = - \int_0^t dt' E_x v_x$ and $\Gamma_{\perp} = - \int_0^t dt' E_{\perp} v_{\perp}$; E_x and E_{\perp} are the normalized longitudinal and transverse electric fields, respectively. Here $\Gamma_{||}$ stands for the energy gain due to the longitudinal electric field, while Γ_{\perp}

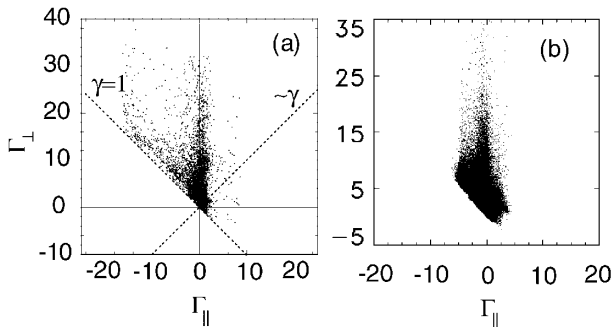


FIG. 4. Electron energy gain from longitudinal fields versus that from transverse laser fields in plasma with density $n = 0.01$. (a) $a_1 = 3.0$ and $a_2 = 0.1$ in 1D simulation at $t = 350$ laser cycles; (b) $a_1 = 3.0$ and $a_2 = 0.2$ in 2D simulation at $t = 300$.

represents the direct laser acceleration by the transverse field. The energy gain from the laser field is eventually directed in the longitudinal direction through the Lorentz force. Figure 4 shows electrons distributed in $\Gamma_{\parallel} \sim \Gamma_{\perp}$ space found in 1D and 2D simulations. It demonstrates that electrons are accelerated mainly by the transverse laser fields in both cases.

When increasing the plasma density up to $n = 0.04n_c$ or beyond, we find that electrons can be accelerated to a similar level with or without the injection of the second pulse at $a_2 = 0.1$ in 1D simulations. This can be explained by the presence of Raman-backscattered waves, which have an amplitude even higher than 0.1 as seen in the simulation, large enough to trigger the stochastic motion of electrons. In the case with $n = 0.01n_c$ and $L = 50\lambda$, however, the Raman-backscattered wave has an amplitude smaller than 0.1. Therefore a second counterpropagating wave is necessary to trigger the stochastic motion of electrons.

To see the dependence of electron temperatures on the pulse amplitudes, we take plasma at low density $n = 0.01n_c$ to avoid the high Raman-backscattered wave and change either a_1 or a_2 . For the interested forward acceleration rather than the isotropic heating, we usually take $a_1 \gg a_2$. As found in 1D PIC simulations, the hot electron temperature scales similar to $T \sim a_1^{\delta_1} a_2^{\delta_2} t^{\delta_3}$, where t is the interaction duration. For the case with semi-infinite laser pulses, we find $\delta_1 \sim 2$ and $\delta_2 \sim 0.5$; while for pulses with finite pulse duration, we find $\delta_1 \sim 1$ and $\delta_2 \sim 0.5$ after the laser pulses pass through the plasma region. These different scaling laws with the intensity of the first pulse are related to the different ponderomotive push of the two cases. Scaling to the interaction duration is normally similar to $\delta_3 \approx 0.5 \sim 1.0$ before the high electron temperature becomes saturated. One notes that, although the final energy is relevant to the pulse shapes and duration, the present acceleration mechanism itself is irrelevant to these pulse parameters.

In summary, we propose a scheme that can efficiently accelerate electrons by the use of two counterpropagat-

ing laser pulses. The acceleration is triggered by stochastic motion of electrons. The threshold amplitudes for stochastic motion have been found numerically. Particle-in-cell simulations show that this mechanism can be dominant in laser interaction with underdense plasma, where the counterpropagating wave can either be the Raman-backscattered wave or the reflected wave of an incident pulse from overdense plasma. Energetic electrons generated through this scheme move predominantly in the direction of the pulse with higher intensity.

This work was supported in part by the Japan Society for Promotion of Science, the Bairen Jihua (Oversea Talents) Program of the Chinese Academy of Science, the National Natural Science Foundation of China (Grant No. 10105014), and the Bundesministerium für Bildung und Forschung (Bonn).

- [1] M. N. Rosenbluth and C. S. Liu, Phys. Rev. Lett. **29**, 701 (1972); T. Tajima and J. M. Dawson, Phys. Rev. Lett. **43**, 267 (1979); for a review, see E. Esarey *et al.*, IEEE Trans. Plasma Sci. **24**, 252 (1996).
- [2] D. Umstadter *et al.*, Phys. Rev. Lett. **76**, 2073 (1996); E. Esarey *et al.*, Phys. Rev. Lett. **79**, 2682 (1997).
- [3] G. Schmidt and T. Wilcox, Phys. Rev. Lett. **31**, 1380 (1973); C. I. Moore *et al.*, Phys. Rev. Lett. **74**, 2439 (1995); F. V. Hartmann *et al.*, Phys. Rev. E **51**, 4833 (1995); B. Rau *et al.*, Phys. Rev. Lett. **78**, 3310 (1997); E. Esarey *et al.*, Phys. Rev. E **52**, 5443 (1995); C. J. McKinstry and E. A. Startsev, Phys. Rev. E **56**, 2130 (1997); B. Quesnel and P. Mora, Phys. Rev. E **58**, 3719 (1998).
- [4] G. R. Smith and A. N. Kaufman, Phys. Rev. Lett. **34**, 1613 (1975); Phys. Fluids **21**, 2230 (1978); C. R. Menyuk *et al.*, Phys. Rev. Lett. **58**, 2071 (1987); S. Kawata, *ibid.* **66**, 2072 (1991); M. S. Hussein and M. P. Pato, *ibid.* **68**, 1136 (1992); J. Meyer-ter-Vehn and Z. M. Sheng, Phys. Plasmas **6**, 641 (1999).
- [5] A. Pukhov *et al.*, Phys. Plasmas **6**, 2847 (1999); C. Gahn *et al.*, Phys. Rev. Lett. **83**, 4772 (1999).
- [6] F. Brunel, Phys. Rev. Lett. **59**, 52 (1987).
- [7] W. L. Kruer and K. Estabrook, Phys. Fluids **28**, 430 (1985).
- [8] G. Shvets *et al.*, Phys. Rev. Lett. **81**, 4879 (1998).
- [9] G. Shvets *et al.*, Phys. Rev. E **60**, 2218 (1999).
- [10] K.-C. Tzeng, W. B. Mori, and T. Katsouleas, Phys. Rev. Lett. **79**, 5258 (1997).
- [11] G. M. Zaslavskii and N. N. Filonenko, Sov. Phys. JETP **25**, 851 (1968); G. Schmidt, Comments Plasma Phys. Control. Fusion **7**, 87 (1982).
- [12] A. J. Lichtenberg and M. A. Lieberman, *Regular and Stochastic Motion* (Springer-Verlag, New York, 1981), and references therein.
- [13] J. T. Mendonca and F. Doveil, J. Plasma Phys. **28**, 485 (1982); Phys. Rev. A **28**, 3592 (1983).
- [14] Z.-M. Sheng *et al.*, Phys. Rev. Lett. **85**, 5340 (2000); Z.-M. Sheng and J. Meyer-ter-Vehn, in *Superstrong Fields in Plasmas*, edited by M. Lontano *et al.*, AIP Conf. Proc. No. 426 (AIP, Woodbury, NY, 1998), p. 153.
- [15] D. W. Forslund *et al.*, Phys. Rev. Lett. **54**, 558 (1985).

Effects of Laser Polarization on Jet Emission of Fast Electrons in Femtosecond-Laser Plasmas

L. M. Chen,¹ J. Zhang,^{1,*} Y. T. Li,¹ H. Teng,¹ T. J. Liang,² Z. M. Sheng,^{1,3} Q. L. Dong,¹ L. Z. Zhao,¹ Z. Y. Wei,¹ and X. W. Tang²

¹*Laboratory of Optical Physics, Institute of Physics, Chinese Academy of Sciences, Beijing 100080, China*

²*Institute of High Energy Physics, Chinese Academy of Sciences, Beijing 100039, China*

³*Institute of Laser Engineering, Osaka University, 2-6 Yamada-oka, Suita, Osaka 565-0871, Japan*
(Received 28 March 2000; revised manuscript received 30 May 2001; published 7 November 2001)

Effects of laser polarization on fast electron emission are studied from an aluminum target irradiated by ultrashort laser pulses at $2 \times 10^{16} \text{ W/cm}^2$. Jet emission of outgoing fast electrons collimated in the polarization direction is observed for *s*-polarized laser irradiation, whereas for *p*-polarized irradiation highly directional emission of outgoing fast electrons is found in the direction close to the normal of the target. The behavior of ingoing fast electrons into the target for *s*- and *p*-polarized irradiation is also investigated by observing x-ray bremsstrahlung radiation at the backside of the target.

DOI: 10.1103/PhysRevLett.87.225001

PACS numbers: 52.50.Jm, 52.25.Os, 52.38.Kd

Fast electron production and transport have been studied extensively [1–11]. However, there is still not enough understanding of physics mechanisms that control the emission direction of fast electrons. Especially, the experimental observations made by different groups on the emission direction of fast electrons generated by ultrashort pulse laser-solid interactions are not very consistent [2,5–8,10]. Some experiments have observed highly peaked MeV electrons in the laser axial direction [6], whereas the others have found collimated emission of fast electrons in the specular direction [7] or in the normal direction of targets [8].

Collimated fast electron emission can be accelerated by different acceleration mechanisms, such as resonance absorption, vacuum heating, $\mathbf{j} \times \mathbf{B}$ heating, or different sorts of skin effects [11]. Most of these mechanisms are present only for *p*-polarized obliquely incident irradiation. It is very important to study the effects of laser polarization on the electron emission because many basic plasma behaviors are controlled by strong laser fields rather than by plasma density and temperature [7].

The main aim of this paper is to investigate the effects of the laser polarization on acceleration mechanisms by observing outgoing fast electrons and ingoing fast electrons generated by *p*- and *s*-polarized ultrashort laser pulses that are obliquely incident on an overdense plasma with or without a corona preplasma. Our measurements raised some important disagreements with simulations. These disagreements may shine new insights on acceleration mechanisms and are certainly worth further investigation.

The experiments were carried out with a Ti:sapphire laser operating at 800 nm at a repetition rate of 10 Hz. The laser delivered 5 mJ energy in 150 fs pulses into a focal spot with a diameter of $< 15 \mu\text{m}$ (due to the limitation of the pinhole size of $15 \mu\text{m}$) and produced a peak intensity at the laser focus $> 2 \times 10^{16} \text{ W/cm}^2$. The contrast ratio of the laser pulse was measured to be better than 10^{-5} (at 1 ps before the main pulse). The laser beam was focused on a $70\text{-}\mu\text{m}$ -thick Al target with a 10-cm focal length off-axis

parabola. The Al target with a size of $4 \text{ cm} \times 2 \text{ cm}$ was placed on a 3 mm thick backing glass mount. For some shots, 8% energy was split off from the main laser beam to form a low intensity prepulse, which was 50 ps in advance of the main pulse in order to provide a corona preplasma for interaction [12]. Plane polarized (*p* or *s* polarized) laser pulses were incident at 45° from the target normal.

The main diagnostic of fast electrons was a magnetic spectrometer [12]. The energy range of this instrument covered from 7 to 500 keV. The angular distribution of the fast electron emission was measured by placing an Al foil covered direct-exposure film (DEF) in an 8-cm-diameter cylinder around the laser focus [13]. Two calibrated γ -ray spectrometers were used to study the x-ray Bremsstrahlung radiation from the laser plasma [14]. The absorption of the laser beam was determined by a 4π calorimeter. Absolute measurements of fast electrons with high energies were made by measuring charge separation potential at the laser focus. As some fast electrons with high energies outwards are ejected out of the plasma, a charge separation potential is simultaneously established by the background ions at the target surface [15]. By converting the instantaneous charging current into a slow varying discharging process with an *LCR* circuit, the number of outgoing fast electrons can be counted accurately.

Figure 1 shows the cutaway view of the angular distribution of fast electrons generated by *s*-polarized irradiation without prepulses. The sharp boundary of the exposure on the DEF films and the geometry of the target ensured that the electrons recorded by the film came from the front side of the Al target. The outgoing fast electrons were found to be collimated along the laser polarization direction in a plane perpendicular to the incident plane. In the incident plane, no fast electrons were measured. It was also found that the fast electrons with higher energies have narrower angular divergence. When there was a corona preplasma in front of the target, a very small percentage of outgoing fast electrons could be found in the incident plane. This suggests that the outgoing fast electrons were mainly

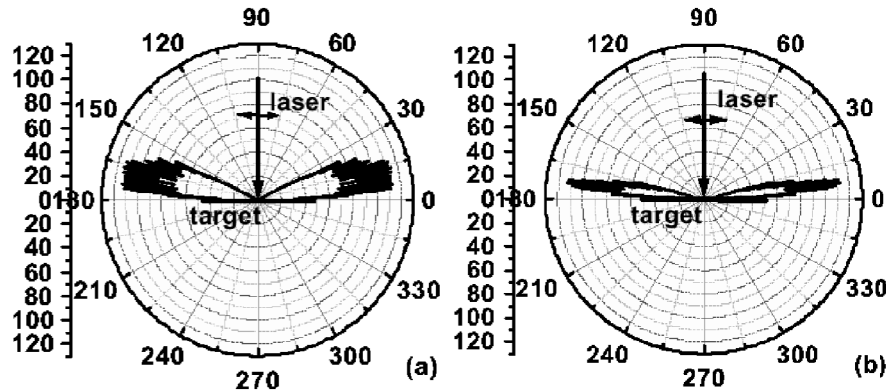


FIG. 1. The cutaway view of the angular distribution of outgoing fast electrons with energies over (a) 50 keV and (b) 250 keV in the plane perpendicular to the incident plane.

accelerated by the electric field of the *s*-polarized laser pulses. When there is a corona preplasma in front of the overdense plasma, the possible modulation of the critical surface of the preplasma will steer a very small percentage of the fast electrons out of the polarization direction. This phenomenon seems to be similar to the results of laser-accelerator injector based on laser ionization and the ponderomotive acceleration of electrons in gas, where electrons are accelerated in the polarization direction [13,16], but the heating mechanisms are obviously different.

When the target was irradiated by a *p*-polarized laser pulse with a prepulse 50 ps in advance of the main pulse, the behaviors of fast electrons were much different from those generated by *s*-polarized laser pulses. As Fig. 2 shows, almost all of the outgoing fast electrons were emitted in the normal direction. The emission direction of the fast electrons obeys the momentum conservation [8,17].

The emission angle of fast electrons over 250 keV ($\gamma > 1.4$) in the incident plane was found to be 16° from the target normal direction (Fig. 2b), where γ is the relativistic factor of the fast electrons. Further measurements, with thicker filters, of emission angle of small fraction of fast electrons over 1 MeV ($\gamma > 2.95$) gave a value of 30°. It is apparent that the emission direction of the fast electrons

with higher energies moved towards the specular direction (45°). The full width at half maximum of the emission of fast electrons with energies over 20, 50, and 250 keV was measured to be 32°, 28°, and 15°, respectively.

In the interaction between ultrashort laser pulses and plasmas, the bulk of thermal electrons are generated by collisional absorption. A small fraction of fast electrons can be generated by different heating processes. It is interesting to know the fraction of fast electrons with high energies versus bulk of thermal electrons with modest energies. The lower limit of the fraction of the fast electrons with energies over 50 keV, which is the measured charge separation potential, was measured to be 2.6% of the total laser energy, assuming that the number of ingoing fast electrons is equal to that of outgoing electrons. Because the total laser absorption by the plasmas was measured to be about 74%, the fraction of energy of fast electrons was, at least, 3.5% of the total energy of thermal electrons. By measuring the fraction of fast electrons with energies over 250 keV and 1 MeV, respectively, relative to those with energies over 50 keV, the fraction of fast electrons over 250 keV and 1 MeV was estimated to be 0.35% and 0.1%, respectively, of the total energy of thermal electrons.

Unlike the observation with a prepulse, a jet emission of fast electrons was observed in the specular direction,

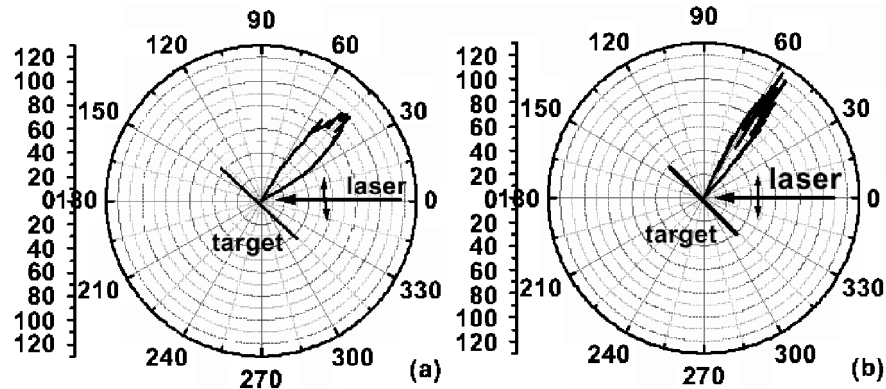


FIG. 2. The angular distribution of outgoing fast electrons with energies over (a) 50 keV and (b) 250 keV in the incident plane, respectively. The fast electrons were generated by *p*-polarized obliquely incident laser pulses with a prepulse 50 ps in advance. The FWHM is about 28° and 15°, respectively.

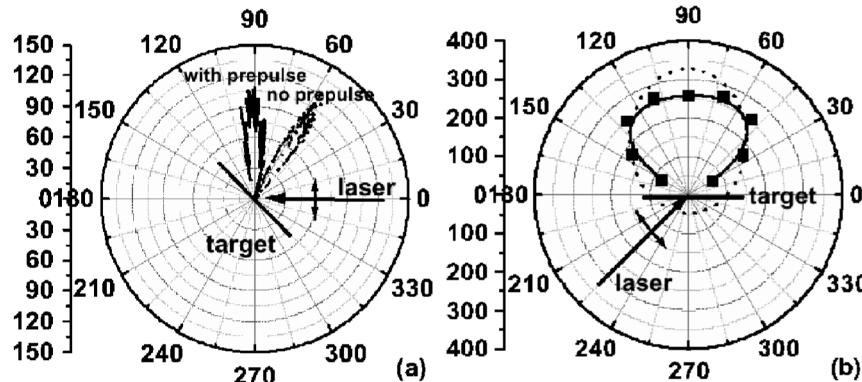


FIG. 3. (a) Angular distribution of fast electrons generated by a *p*-polarized laser without prepulse (solid line) and with a prepulse 50 ps in advance (dashed line) in the incident plane. (b) The x-ray distribution at the backward of the target with energies >50 keV in the incident plane, irradiated by *p*-polarized obliquely incident laser pulses with a prepulse 50 ps in advance. The dotted line is the theoretical calculation for the target interaction with a 50 keV electron beam.

when the target was irradiated by a *p*-polarized irradiation without prepulses. This agreed with Bastiani's experimental results [7]. Figure 3a shows this change. This is very different from the behaviors of fast electrons generated by *p*-polarized irradiation with prepulses. This suggests that a corona preplasma does play a very critical role in determining the emission direction of fast electrons.

It is important to know the propagation process of the ingoing fast electrons into targets because these fast electrons are critical to the concept of fast ignition [1]. Fast ignition is of importance to the inertial confinement fusion research through its potential to give higher inertially confined fusion gain than the conventional indirect or direct drive schemes and thereby to reduce the driver energy required for inertial confinement fusion. Fast electrons injected into targets will undergo multiple Coulomb scattering with nuclei and produce x-ray Bremsstrahlung radiation. Therefore, the x-ray energy spectrum at the backside of the target could provide rich information on ingoing fast electrons in targets. Figure 3b shows the angular distribution of x rays. The angular distribution shows a symmetrical structure around the target normal. The FWHM of x-ray angular distribution was about 100° . It is clear that the main characteristics of the angular distribution of x-ray Bremsstrahlung radiation is very similar to those produced by a collimated fast electron beam with 50 keV energy in the normal direction injected into the target [16]. By comparison, a rather random distribution of x rays was observed at the backside of targets irradiated by *s*-polarized laser pulses with a prepulse 50 ps in advance. The x-ray flux was about 10 times weaker than that driven by *p*-polarized irradiation. This indicated that there was no jet forming of ingoing electrons for *s*-polarized irradiation, and this is against the simulation prediction [8].

To explain the experiments, we have run two-dimensional particle-in-cell (PIC) simulations. The simulation box size is $24\lambda \times 40\lambda$. Particles are filled only in a limited region, typically with 25 cells per laser wavelength and 16 particles per cell. We find that the simulation can

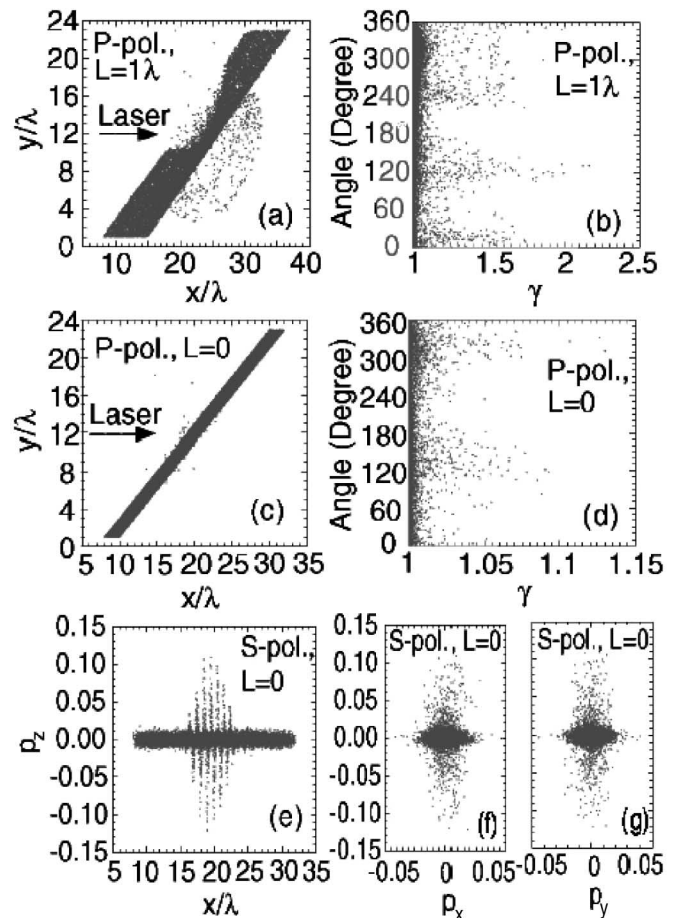


FIG. 4. Electron distributions in geometry and momentum space found from two-dimensional PIC simulations. A laser pulse with normalized amplitude $a_0 = 0.2$ and a duration of 50 laser cycles is incident obliquely at 45° . (a) plots (x, y) electron positions and (b) angular distribution at $t = 60$ laser cycles for *p*-polarized incidence onto plasma with scale length $L = 1\lambda$; (c) plots (x, y) positions and (d) angular distribution at $t = 50$ for *p*-polarized incidence onto plasma with a steep density profile; (e) plots (p_z, x) positions, (f) plots (p_z, p_x), and (g) plots (p_z, p_y) all at $t = 50$ for *s*-polarized incidence onto plasma with a steep density profile.

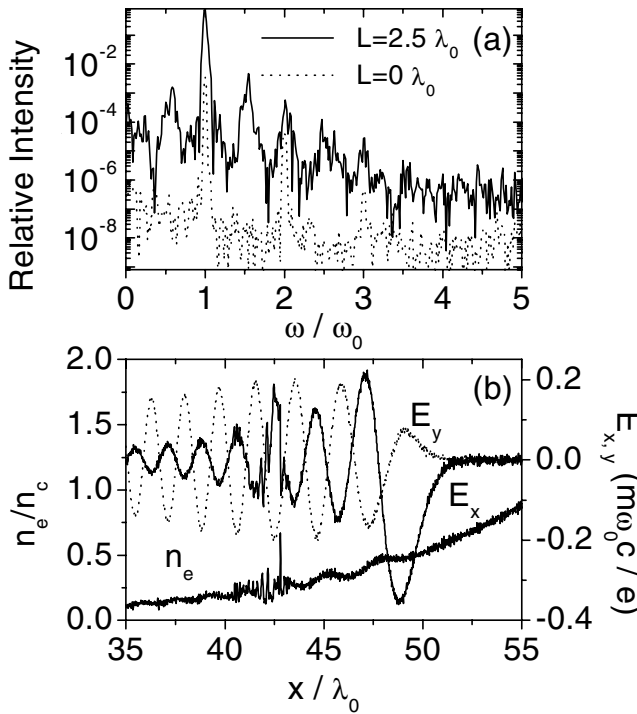


FIG. 5. The time integrated frequency spectra of the reflected *p*-polarized light obliquely irradiating on plasmas with different density scale lengths (a). (b) shows the density and electric field disturbance around the quarter critical density where the Raman instability has the highest growth rate under our conditions.

best reproduce our main experimental results, if we take $a_0 = 0.2$. This implies that the laser intensity at focus might be larger than $2 \times 10^{16} \text{ W/cm}^2$ due to the possible self-focusing effects occurring in the laser plasma, resulting in higher intensity in the interaction. Figures 4a and 4b show the (x, y) positions of electrons and their angular directions, respectively, at $t = 60$ laser cycles, obtained for *p*-polarized incidence onto plasma. Initially, the electron density increases from $0.01n_c$ exponentially with a scale length of 1λ until about $2.5n_c$. They show evidently that electrons are pushed out around the normal to the target direction (i.e., 135° and 315° , since it assumes that the incident laser propagates in 0°). This agrees with the experiments for the case with prepulses and the theory in [17].

Figures 4c and 4d show the case with a steep density profile. Unlike the experimental observation, outgoing electrons are observed in wide angular distributions, including in a reflected direction (90°). Figures 4e, 4f, and 4g are obtained for *s*-polarized incidence. Note that during the laser interaction, the momentum in the polarization direction is much larger than that in the *x* and *y* directions.

Thus if electrons are pulled out from the target, they must be directed in a small angle against the target surface. This is exactly what was observed in the experiments.

It appears that parametric instabilities excited around the quarter critical density are responsible for the acceleration for $L > \lambda$. This is obvious from the frequency spectra of the reflected light (Fig. 5). For $L > \lambda$, emission near half of the laser frequency as well as at one half and one half the laser frequency appear.

In summary, we found that both *s*- and *p*-polarized lasers can generate jet emission of fast electrons at moderate laser intensities. This provides new insights into acceleration of fast electrons in laser-plasma interaction. Our experimental results have indicated that the 2D PIC simulations can reproduce the main characteristics of outgoing fast electrons generated by *p*-polarized laser pulses with prepulses. However, the simulations failed to reproduce the jet emission of outgoing fast electrons in the specular direction produced by *p*-polarized laser pulses without prepulses. In this case, our experimental results have settled down the disagreement between two groups on the emission direction of fast electrons generated by *p*-polarized laser pulses on a steep profile plasma [7,8].

This work was jointly supported by the National Natural Science Foundation of China (under Grants No. 19825110, No. 10005014, and No. 10075075), the National Hi-tech ICF Program, and the National Key Basic Research Special Foundation under Grant No. G1999075200.

*Author to whom coorespondence should be addressed.

Email address: jzhang@aphy.iphy.ac.cn

- [1] M. Tabak *et al.*, Phys. Plasmas **1**, 1626 (1994).
- [2] M. H. Key *et al.*, Phys. Plasmas **5**, 1966 (1998).
- [3] J. R. Davies *et al.*, Phys. Rev. E **59**, 6032 (1999).
- [4] S. C. Wilks *et al.*, Phys. Rev. Lett. **69**, 1383 (1992).
- [5] C. Rousseau *et al.*, Phys. Fluids B **4**, 2589 (1992).
- [6] G. Malka *et al.*, Phys. Rev. Lett. **79**, 2053 (1997).
- [7] S. Bastiani *et al.*, Phys. Rev. E **56**, 7179 (1997).
- [8] Y. Sentoku *et al.*, Phys. Plasmas **6**, 2855 (1999).
- [9] L. Gremillet *et al.*, Phys. Rev. Lett. **83**, 5015 (1999).
- [10] P. A. Norreys *et al.*, Phys. Plasmas **6**, 2150 (1999).
- [11] F. Brunel, Phys. Rev. Lett. **73**, 664 (1994).
- [12] L. M. Chen *et al.*, Phys. Plasmas **8**, 2925 (2001); Q. L. Dong and J. Zhang, Phys. Plasmas **8**, 1025 (2001).
- [13] C. I. Moore *et al.*, Phys. Rev. Lett. **82**, 1688 (1999).
- [14] P. Zhang *et al.*, Phys. Rev. E **57**, R3746 (1998).
- [15] V. V. Ivanov *et al.*, JETP **82**, 677 (1996).
- [16] D. Pesme *et al.*, Phys. Rev. Lett. **84**, 278 (2000).
- [17] Z. M. Sheng and Y. Sentoku *et al.*, Phys. Rev. Lett. **85**, 5340 (2000).

Angular Distributions of Fast Electrons, Ions, and Bremsstrahlung x/γ -Rays in Intense Laser Interaction with Solid Targets

Z.-M. Sheng,¹ Y. Sentoku,¹ K. Mima,¹ J. Zhang,² W. Yu,³ and J. Meyer-ter-Vehn⁴

¹*Institute of Laser Engineering, Osaka University, 2-6 Yamada-oka, Suita, Osaka 565-0871, Japan*

²*Laboratory of Optical Physics, Institute of Physics, Chinese Academy of Science, Beijing 100080, China*

³*Shanghai Institute of Optics and Fine Mechanics, Shanghai 201800, China*

⁴*Max-Planck-Institut für Quantenoptik, D-85748 Garching, Germany*

(Received 3 April 2000)

We study the angular distributions of fast electrons, ions, and bremsstrahlung x/γ -rays generated during the interaction of an ultrashort intense laser pulse with solid targets. A relation is found on the angular directions for fast electrons and ions as a function of the particle's kinetic energy, experienced Coulomb potential changes, and the incident angle of the laser pulse. It is valid independent of the acceleration mechanisms and the polarization of the laser pulse, as confirmed by particle-in-cell simulations. The angular distribution of bremsstrahlung x/γ -rays is presented to show explicitly its correlation with the corresponding angular distributions of electrons.

PACS numbers: 52.40.Nk, 52.25.Nr, 52.25.Tx, 52.65.Rr

Fast electrons and ions generated in the interaction of ultrashort intense laser pulses with solid and gas targets play a key role for the various applications of intense lasers, such as the fast ignitor of fusion targets, ultrashort x/γ -ray sources, and laser induced nuclear processes, etc. Depending upon the target types (solid or gas), plasma parameters (scale length, density, etc.) and the laser intensities, fast electrons can be produced through vacuum heating [1], plasma wave excitation, and breaking through resonance absorption and electron parametric instabilities [2–5], ponderomotive force acceleration [6,7], and recently proposed direct laser acceleration for electrons inside self-focusing channels [8]. Ions are mainly accelerated by the induced electrostatic fields in recent experiments [6,9,10]. Currently, the angular distributions of fast electrons, ions, and x/γ -ray emissions have been the subject of experimental and theoretical studies in several groups [11–18]. As is obvious, it is one of the important issues for these proposed applications. In this Letter, we present a theory on the angular directions of fast electrons and ions generated in laser-solid interactions, supported by numerical simulation using a 1D3V particle-in-cell (PIC) code. The angular distributions of bremsstrahlung x/γ -rays, obtained by the Monte Carlo method using PIC simulation results, show explicitly the correlation with the angular distributions of electrons.

We consider a geometry shown in Fig. 1 where a planar laser pulse is incident at angle α onto a solid target. The target is modeled with an electrostatic field around the target surface. As a result, the Hamiltonian of electrons normalized by mc^2 is $H = [1 + (\mathbf{P} + \mathbf{A})^2]^{1/2} - \Phi$, where $\mathbf{P} = \mathbf{p} - \mathbf{A}$ is the canonical momentum normalized by mc , $\mathbf{A}(x, y, t)$ and $\Phi(x, t)$ are the vector potential of the laser field and scalar potential associated with the electrostatic field, respectively, both normalized by mc^2/e , and m the rest mass of electrons. For convenience, we

normalize x and y by c/ω_0 and t by ω_0^{-1} with ω_0 the laser frequency. Assuming the laser is reflected specularly from the target, the vector potential on the left region of the targets can be written as $\mathbf{A}(x, y, t) = \mathbf{A}(x, \eta)$, which includes both the incident and reflected laser fields; here $\eta = (ck_0/\omega_0)y \sin(\alpha) - t$ with $ck_0/\omega_0 = 1$ by ignoring the dispersion of laser pulse in preplasma. Using the canonical transform, $F_2 = \eta P_\eta$, one finds $P_y = P_\eta \sin(\alpha)$ and the new Hamiltonian: $\tilde{H} = \gamma - P_\eta - \Phi$. If electron energy changes in a time scale much shorter than the scalar potential [19], \tilde{H} is an adiabatic constant of motion. If particles are at rest before the interaction and $\Phi = \Phi_0$, one has $\tilde{H} = 1 - \Phi_0$. When the laser pulse leaves the target region, one obtains $\mathbf{P} = \mathbf{p}$. Assuming $p_z = 0$, generally true both for P and S polarization, defining $\tan(\theta) = p_y/p_x$, and making use of the adiabatic \tilde{H} and the definition $\gamma = (1 + p_x^2 + p_y^2)^{1/2}$, we obtain

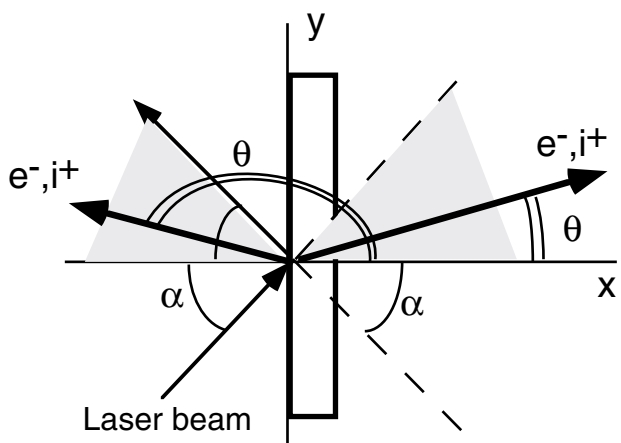


FIG. 1. Schematic drawing of the laser-target interaction geometry shows the equivalence of target interaction with two intersecting laser pulses.

$$\tan(\theta) = \pm \left[\frac{2(\gamma - 1)(1 + \delta\Phi) - \delta\Phi^2}{(\gamma - 1 - \delta\Phi)^2} \sin^{-2}(\alpha) + \tan^{-2}(\alpha) \right]^{-1/2}, \quad (1)$$

where $\delta\Phi = \Phi(x, t) - \Phi_0$. It shows that the angular directions of individual electrons are simply related with their kinetic energy and the experienced Coulomb potential changes. Equation (1) is valid only for electrons. For ions, one needs to replace $\delta\Phi$ with $-(Zm/M)\delta\Phi$ in Eq. (1), where Z and M are the charge and rest mass of ions, respectively. Since electrons are relatively easy to escape from the target during and after the interaction with laser pulses, the target is usually positively charged. Thus we have $\delta\Phi > 0$ for all particles. Figures 2(a) and 2(b) show the angular directions of forward moving electrons and ions as a function of their kinetic energy under some given Coulomb potential changes, respectively. It shows that electrons/ions at the same kinetic energy can be found in different angular directions if they experience different Coulomb potential changes. The Coulomb fields tend to *reduce* the ejecting angles of electrons and to *enhance* the angles of ions. Electrons with $\gamma < 1 + \delta\Phi$ are trapped by the Coulomb potential; when $\gamma > 1 + \delta\Phi$, electrons can escape at angles between 0° and α in the forward direction, or between 180° and $180^\circ - \alpha$ in the backward direction. Angular directions between α and $180^\circ - \alpha$ are forbidden. Energetic electrons with $\gamma \gg 1 + \delta\Phi$ are found at angles close to the laser direction of incidence and reflection; since the value of γ for ions is usually close to 1, the corresponding angle θ is small, about a few degrees for $\gamma < 1.1$. In normal incidence $\alpha = 0^\circ$, one obtains $\tan(\theta) = 0$ no matter what values γ and $\delta\Phi$ take. It means that particles at any energy are directed either in 0° or 180° . When $\delta\Phi = 0$, Eq. (1) reduces to

$$\tan(\theta) = \pm \left[\frac{2}{\gamma - 1} + \frac{\gamma + 1}{\gamma - 1} \tan^{-2}(\alpha) \right]^{-1/2}. \quad (2)$$

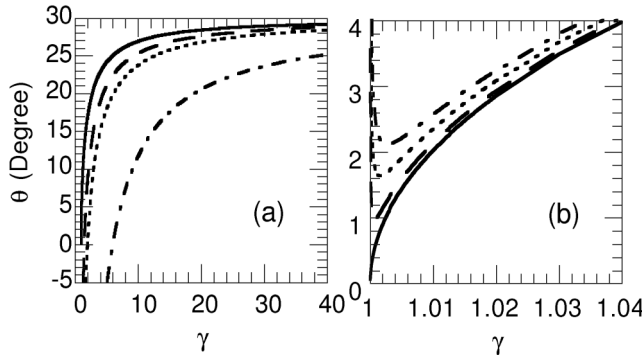


FIG. 2. Angular directions of electrons (a) and ions (b) as a function of particle energy at various electrostatic potential levels when $\alpha = 30^\circ$. In (a) $\delta\Phi = 0$ for —, 0.5 for - - -, 1.0 for · · ·, and 5.0 for - · -; in (b) $\delta\Phi = 0$ for —, 1.0 for - - -, 3.0 for · · ·, and 5.0 for - · -.

This is equivalent to a relation proposed for single electrons scattered in two intersecting laser beams in vacuum [20]. It also extends the scattering formula for electrons by single laser beams in vacuum or tenuous plasma (which is recovered when $\alpha = 90^\circ$) [7,12]. Alternatively, Eq. (2) can be rewritten as $\sin(\theta) = [(\gamma - 1)/(\gamma + 1)]^{1/2} \sin(\alpha)$, a relation derived earlier by assuming that the momentum is conserved along the target surface between the absorbed photons and accelerated electrons [18].

To confirm the validity of Eq. (1), we performed numerical simulations for laser interaction with a solid target using a 1D3V PIC code accommodated in the Lorenz-boosted frame for oblique incidence of laser pulses [21]. We use targets composed of a high density region at $5n_c$ with width $d = (3 \sim 8)\lambda$ and preformed plasma which decreases exponentially with scale length $L = 0 \sim 3\lambda$ from the high density platform, where n_c and λ are the critical density and laser wavelength in vacuum, respectively. The ions are protons with a mass ratio $M/m = 1836$ and $Z = 1$. The temporal profile of the laser pulse is $f(t) = \sin^2(\pi t/t_0)$ for $0 \leq t \leq t_0$. Usually, we take $t_0 = 50\tau$ with τ the oscillating period of the pulse.

Initially before the laser interaction, the angular distributions of electrons are homogeneous in all directions between 0° and 360° . During the interaction, the angular distributions evolve into anisotropic ones with time owing to the quiver motion and acceleration of electrons in the laser fields. After the reflection of the laser pulse, electrons move only in the induced electrostatic fields. Figure 3(a) is a typical phase-space plot in angle-energy space (called angular distribution in the following) for all electrons after the laser pulse is fully reflected and leaves the target region. As shown, fast electrons move in the angular direction between 0° and $\theta(\gamma)$ in the forward direction and between

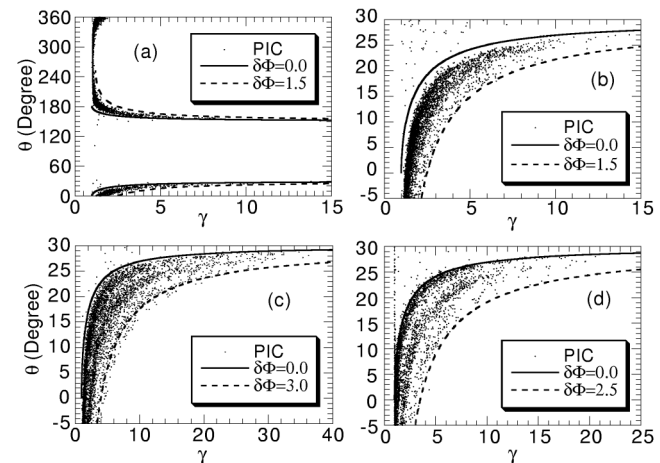


FIG. 3. Angular distributions of electrons after the interaction of a laser pulse (with peak amplitude $a_0 = 3$, $t_0 = 50\tau$, and $\alpha = 30^\circ$) with a solid target. The density scale length is (a) $L = 0$, (b) $L = 0.2\lambda$, (c) $L = 3\lambda$ for p -polarized incidence, and (d) $L = 3\lambda$ for s -polarized incidence of the laser pulse. The solid and dashed lines are obtained from Eq. (1).

180° and $180^\circ - \theta(\gamma)$ in the backward direction, where $\theta(\gamma)$ is given by Eq. (2). Since we use a relatively thin target with $d = 3\lambda$, all electrons are pushed in the laser fields and induced electrostatic fields. As a result, few electrons are found in the angular direction between 30° and 150°, which are forbidden according to Eqs. (1) and (2). In Figs. 3(b)–3(d), we show the angular distributions of forward moving electrons for different density scale lengths and laser polarizations. For $L = 0$, the main acceleration mechanism is vacuum heating [1]; for $L = 0.2\lambda$, plasma wave excitation and wave breaking through resonance are dominant for the observed fast electrons [2,3], while for $L = 3\lambda$, parametric excitation of plasma wave and wave breaking around the quarter critical density play a dominant role both for P and S -polarized light. In spite of these different mechanisms and laser polarization, electrons are found in angular directions $\theta(\gamma, \delta\Phi)$ given by Eq. (1), where $0 \leq \delta\Phi \leq \delta\Phi_{\max}$. Equation (1) gives the high boundary when $\delta\Phi = 0$ and the low boundary when $\delta\Phi = \delta\Phi_{\max}$. Electrons with the same energy may move in different directions when they have experienced different Coulomb potentials during acceleration. In simulations changing various parameters, $\delta\Phi_{\max}$ is found to be closely related with the laser absorption in the target. We find that

$$\delta\Phi_{\max} \approx C(\eta_{\text{abs}} a_0^2 t_0)^{1/2}, \quad (3)$$

where η_{abs} is the total absorption rate (which is also a function of laser intensities, polarizations, and plasma scale lengths), t_0 is the pulse duration, and C is a constant around unity when t_0 is in units of 50 laser cycles. Moreover, we find that the temperature of hot electrons T_h scales linearly with $\delta\Phi_{\max}$. Since the hot electron energy $n_h T_h \sim \eta_{\text{abs}} a_0^2 t_0$, one expects that the number of hot electrons n_h also scales like $\delta\Phi_{\max}$. This proves to be true in our simulations. With the scaling of $\delta\Phi_{\max}$, one can predict angular distributions of electrons by measuring the absorption rate. In Fig. 3(b), for example, we find that $\delta\Phi_{\max} \approx 1.5$ when fitting the simulation result with Eq. (1), which is just close to the value $\eta_{\text{abs}} a_0^{1/2}$ found in the simulation. One notes that $\delta\Phi_{\max}$, though proportional to, is not equivalent to the maximum Coulomb potential found in the simulation box.

Angular distributions of ions shown in Fig. 4 are obtained for similar parameters as for Fig. 3 at a time when the laser pulse is reflected and leaves the target region. They can be well described by Eq. (1) modified for ions as stated before with $0 < \delta\Phi < \delta\Phi_{\max}^i$. Usually $\delta\Phi_{\max}^i > \delta\Phi_{\max}$ ($\delta\Phi_{\max}^i \approx 1.7\delta\Phi_{\max}$ in this simulation, for example) because ions move at lower velocities and remain relatively localized as compared to electrons. With the increase of laser power, both the kinetic energy of ions and their ejecting angles increase as shown in Fig. 4(d). The nonzero ejecting angle or momentum component along the target surface indicates explicitly that there is a momentum transfer from laser to ions via the ponderomotive force in

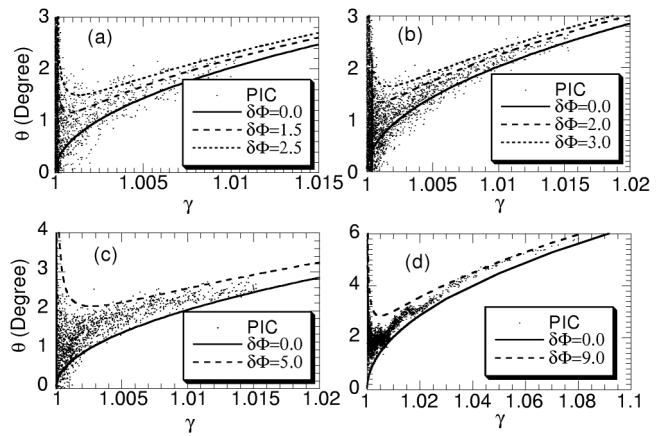


FIG. 4. Angular distributions of forward moving ions after the interaction of a laser pulse (with $t_0 = 50\tau$ and p polarization with $\alpha = 30^\circ$). The density scale lengths are (a) $L = 0$, (b) $L = 0.2\lambda$, (c) $L = 3\lambda$ with pulse amplitude $a_0 = 3$, and (d) $L = 3\lambda$ with $a_0 = 10$. The solid and dashed lines are obtained from Eq. (1) with $\delta\Phi$ replaced by $-(Zm/M)\delta\Phi$.

addition to the acceleration by electrostatic fields along the normal to the target surface.

Now let us compare Eqs. (1) and (2) with some related experiment and 2D PIC simulation results. For example, in an experiment [14], one observed fast electron jets with energy around 170 KeV ($\gamma = 1.33$) in an angular direction about $\theta = 11^\circ$ when the incident angle $\alpha = 45^\circ$. At the same energy, Eq. (2) gives $\theta = 15.4^\circ$ when the electrostatic field is not considered, which slightly overestimates the angle direction. Taking into account this field, the experimental result is reproduced by Eq. (1) with $\delta\Phi = 0.1$. In recent 2D PIC simulations [18], electron jets with $\gamma \approx 3.0$ are found in $\theta = 16.7^\circ$ when the incident angle of the laser pulse $\alpha = 28.9^\circ$. We find that Eq. (2) gives $\theta = 20^\circ$ and Eq. (1) gives the 2D simulation result with $\delta\Phi = 0.32$.

We notice that, although Eqs. (1) and (2) are obtained for plane laser pulses, primary numerical study on single electrons interacting with two intersecting Gaussian beams in vacuum shows that Eq. (2) is essentially valid for focused beams. Other 2D/3D effects which may modify the angular distributions include the quasistatic magnetic field generation, laser self-focusing, and hole boring. While it is difficult to delineate clearly how the magnetic field would affect the angular distributions of fast electron flows, generally one expects that it tends to reduce the width of angular distributions due to magnetic field pinching. On the other hand, the generation of return currents may lead to the development of Weibel and filamentation instabilities, which could ultimately result in multipeaked emissions as pointed out in [16]. This may happen in cases with high laser intensities such as 10^{19} W/cm^2 or higher and long plasma scale lengths ensuring efficient absorption of laser energy and large $n_h T_h$ values. This effect is, however, not expected to be significant in laser interaction with thin targets. The hole-boring effect could break our assumption

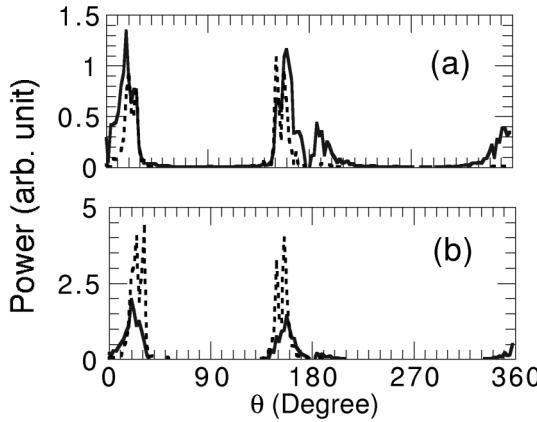


FIG. 5. Angular distributions of x-ray bremsstrahlung for a laser pulse with the same parameters as in Fig. 3 and with plasma scale lengths (a) $L = 0$ and (b) $L = 3\lambda$ for p -polarized incidence. The solid and dashed lines are for bremsstrahlung between 0.01–0.5 MeV and 0.5–30 MeV, respectively.

of specular reflection and introduce a self-focusing effect [8] when $UT > R$, where U is the hole-boring velocity given in [6] with modification taking into account the incident angle, T the pulse duration, and R the beam radius. Thus, this effect will not be significant for subpicosecond pulses with intensity less than 10^{19} W/cm^2 and radius sizes around $R \gtrsim 5 \mu\text{m}$.

The angular distributions of electrons are closely related to the angular distribution of the bremsstrahlung x/γ -rays. We calculate the bremsstrahlung by use of the Monte Carlo method by postprocessing the distributions of electron momenta obtained from PIC simulations [22]. Example results are given in Fig. 5. It shows that, when $L = 0$, there are two forward-radiation peaks around $\theta = 0^\circ$ (or 360°) and 30° , respectively, for radiation between 10 keV and 0.5 MeV. Radiation with higher energy between 0.5 and 30 MeV is only found around 30° near which high energy electrons are directed. The angular distribution for the backward radiation is just similar. When $L = 3\lambda$, the radiation near 0° is relatively much weaker than around 30° , indicating that electrons are more efficiently accelerated in this case as is evident in Fig. 3. This scale length effect is similar to that found in a recent experiment [16].

In conclusion, a relation on angular directions of electrons and ions is found analytically as a function of the

incident angle of laser pulses, particle kinetic energy, and experienced Coulomb potential changes. It is verified by PIC simulations for a variety of laser pulse and target parameters and is in reasonable agreement with some recent experiments and other simulations. The angular distribution of bremsstrahlung is shown to depend on the energy range of x/γ -rays and the angular distribution of electron energy.

Z. M. S. acknowledges the support of the Japan Society for the Promotion of Science.

- [1] F. Brunel, Phys. Rev. Lett. **59**, 52 (1987).
- [2] W. L. Kruer, *The Physics of Laser Plasma Interaction* (Addison-Wesley, New York, 1988).
- [3] P. Gibbon and A. R. Bell, Phys. Rev. Lett. **68**, 1535 (1992); Th. Schlegel *et al.*, Phys. Rev. E **60**, 2209 (1999).
- [4] E. Esarey *et al.*, Phys. Rev. Lett. **72**, 2887 (1994).
- [5] K. C. Tzeng *et al.*, Phys. Plasmas **6**, 2105 (1999).
- [6] S. C. Wilks *et al.*, Phys. Rev. Lett. **69**, 1383 (1992).
- [7] F. V. Hartemann *et al.*, Phys. Rev. E **51**, 4833 (1995); B. Quesnel and P. Mora, *ibid.* **58**, 3719 (1998).
- [8] A. Pukhov *et al.*, Phys. Plasmas **6**, 2847 (1999); C. Gahn *et al.*, Phys. Rev. Lett. **83**, 4772 (1999); J. Meyer-ter-Vehn and Z. M. Sheng, Phys. Plasmas **6**, 641 (1999).
- [9] J. Denavit, Phys. Rev. Lett. **69**, 3052 (1992).
- [10] G. S. Sarkisov *et al.*, Phys. Rev. E **59**, 7042 (1999).
- [11] S. Bastiani *et al.*, Phys. Rev. E **56**, 7179 (1997).
- [12] C. I. Moore *et al.*, Phys. Rev. Lett. **74**, 2439 (1995); G. Malk *et al.*, *ibid.* **78**, 3314 (1997).
- [13] M. H. Key *et al.*, Phys. Plasmas **5**, 1966 (1998).
- [14] J. Zhang *et al.*, Proc. SPIE Int. Soc. Opt. Eng. **3886**, 332 (1999); P. Zhang *et al.*, Phys. Rev. E **57**, R3746 (1998).
- [15] R. Kodama *et al.*, Phys. Rev. Lett. **84**, 674 (2000).
- [16] M. I. K. Santala *et al.*, Phys. Rev. Lett. **84**, 1459 (2000).
- [17] P. Norreys *et al.*, Phys. Plasmas **6**, 2150 (1999).
- [18] Y. Sentoku *et al.*, Phys. Plasmas **6**, 2855 (1999); H. Ruhl *et al.*, Phys. Rev. Lett. **82**, 743 (1999).
- [19] PIC simulation shows that the spectra of the electron density fluctuation and electrostatic field has the highest peak near $\omega = 0$; see also Ref. [18].
- [20] Z. M. Sheng and J. Meyer-ter-Vehn, in *Superstrong Fields in Plasmas*, edited by M. Lontano *et al.*, AIP Conf. Proc. No. 426 (AIP, Woodbury, 1998), p. 153.
- [21] R. Lichters *et al.*, Phys. Plasmas **3**, 3425 (1996); P. Gibbon *et al.*, Phys. Plasmas **6**, 947 (1999).
- [22] Y. Sentoku *et al.*, Phys. Plasmas **5**, 4366 (1998).



PERGAMON

Journal of Quantitative Spectroscopy &
Radiative Transfer 83 (2004) 203–213

Journal of
Quantitative
Spectroscopy &
Radiative
Transfer

www.elsevier.com/locate/jqsrt

Simulations of a photopumped X-ray laser using the H-like Cl – Li-like Se scheme

Il'dar R. Al'Miev^{a,*}, Xin Lu^b, Steven J. Rose^a, Jie Zhang^b, Justin S. Wark^a

^aClarendon Laboratory, Department of Physics, University of Oxford, Parks Road, Oxford, OX1 3PU, UK

^bLaboratory of Optical Physics, Institute of Physics, Chinese Academy of Sciences, Beijing 100080,
People's Republic of China

Received 29 July 2002; received in revised form 1 November 2002; accepted 4 November 2002

Abstract

Calculations of the modal photon densities and gain in a photopumped Cl XVII-Se XXXII X-ray laser are presented. In this paper we undertake a realistic simulation of the generation of both Cl and Se plasmas, using a high-power optical laser, which includes radiation from both Ly- α fine-structure components of H-like Cl pumping the $2p_{3/2}$ – $5d_{5/2}$ transition in Li-like Se. The calculations are performed in two dimensions in a realistic geometry taking into account plasma gradients. This gives information about the spatial extent and time evolution of X-ray lasing gain on the 5–4 transitions (39.5 Å) in Li-like Se. We find that gain (about 200 cm^{-1}) is expected only when the optical laser includes a pre-pulse. Calculations show that the absorption of pumping radiation in the pumped plasma can reduce the gain by 20%. Time-dependent calculations have shown that the gain is reduced by 30% in comparison to the steady-state calculations. The effect of the spectral profile and self-radiation of $5d_{5/2}$ – $2p_{3/2}$ transition in Li-like Se reduces the gain by about 2%.

© 2003 Elsevier Ltd. All rights reserved.

Keywords: Laser plasma interactions; X-ray lasers; Hydrodynamic simulation; Radiative transfer; Population kinetics; Spectral profile

1. Introduction

In the last decade electron-collision and recombination pumped X-ray lasers have undergone considerable development [1–8]. In addition effort has been put into the development of OFI and free-electron X-ray lasers [9,10]. A demonstration of X-ray lasing based on the line coincidence photopumping has been attempted for many years [11–13], but to date there has been no experimental evidence that the scheme operates in the XUV and X-ray range.

* Corresponding author. Tel.: +44-1865-272301; fax: +44-1865-272400.

E-mail addresses: i.almiev1@physics.ox.ac.uk (I.R. Al'Miev), luxin@aphy.iphy.ac.cn (X. Lu).

In three previous papers [14–16] we simulated two line coincidence schemes. In the first scheme, H- and He-like K pumps H-like Cl and we predicted gain on the H-like Cl 4–3 transitions (65 Å) of about 8 cm⁻¹. In the second scheme we simulated H-like Al pumping Li-like Fe; we predicted gain on the Li-like Fe 5–4 transitions (70 Å) of about 20 cm⁻¹. In [17,18] Nilsen has undertaken a systematic search for line-coincidence pairs involving other Li-like ions. One of the possible schemes involves Ly- $\alpha_{1,2}$ radiation from H-like Cl ions pumping the 2p_{3/2}–5d_{5/2} line in Li-like Se, where gain is expected on the 5–4 transitions. It is this scheme that is studied in this paper.

This work differs from previous simulations [14–16] by including effects that we did not previously consider. The calculation of the modal photon density and gain takes into account absorption of the pumping radiation in the pumped Se plasma, the effect of time dependence of the rate equations. We also consider the effect of the spectral profile of 5d_{5/2}–2p_{3/2} transition in Li-like Se on the gain. The spatial variation in velocity, density and temperature in both the pumping and the pumped plasmas were also considered. Incorporation of variation of the relative spatial position of the two plasmas allowed us to explore realistic experimental geometries.

2. Methodology

To calculate the pumping radiation we investigated two geometries in which the surface normals of the Cl and Se targets were parallel (PS, parallel-stream), shown in Fig. 1, and anti-parallel (OS, opposite-stream) (Fig. 1 in Ref. [15]). The OS geometry was considered because the Cl Ly- α_2 line lies at longer wavelength than the 2p_{3/2}–5d_{5/2} line of Li-like Se and the counter-propagating plasmas provide the Doppler shift necessary for resonance. The PS geometry is also of interest as it is more easily studied experimentally and the 2p_{3/2}–5d_{5/2} transition can also be pumped by H-like Cl Ly- α_1 line that lies at shorter wavelength.

The position between the two plasmas can be adjusted to alter the modal photon density in the local fluid frame of the Se plasma. The wavelengths of H-like Cl Ly- α_1 and Ly- α_2 transitions (4.1840 and 4.1894 Å, respectively) and of the Li-like Se 5d_{5/2}–2p_{3/2} transition (4.1882 Å) were calculated using the codes HITR [31] and GRASP [19], respectively.

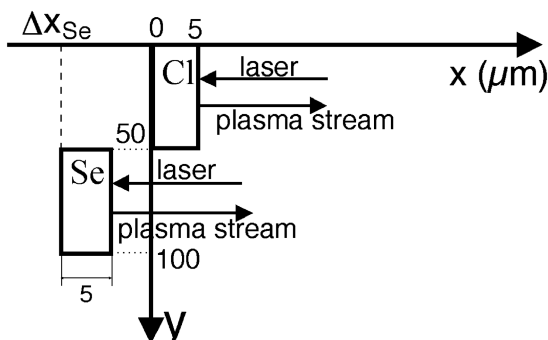


Fig. 1. Schematic diagram of the experimental set-up used in the simulations. The initial thickness of both Cl and Se targets is 5 μm. They are irradiated with trapezoidal pulses, of 0.53 μm wavelength, using the pre-pulse technique. The peak intensity of the main pulse was chosen to be 1×10^{14} , 3×10^{14} , 5×10^{14} and 10^{15} W cm⁻² for both the Cl and Se targets.

The methodology behind these simulations is similar to that explained in previous papers [14–16], so only a brief account will be given here. To calculate the hydrodynamic evolution of both Cl and Se plasmas we used the hydrocode MED103 [20,21]. To calculate the photopumping radiation we adapted the postprocessor described in [14] to the particular experimental geometries. Knowing the pump spectrum in the local fluid frame of the Se plasma, we use the 0-D time-independent non-LTE code GALAXY [22] to compute the local gain. A new time-dependent version of GALAXY, called ORION, was written using an algorithm described in [23]. The effect of line-coincidence photopumping is included in the rate equations. Because there is a velocity gradient in the pumped plasma, the average distance that photons travel to escape is taken to be the Doppler de-coupling distance. This is used in the calculation of the effect of optical depth on the resonance lines that are not photo-pumped using an escape factor.

In all the simulations that follow we assume that both Cl and Se targets are irradiated with an optical 0.53 μm (green) laser pulse with a peak intensity of less than or equal to $10^{15} \text{ W cm}^{-2}$. We considered 1 ns optical pulses of trapezoidal temporal shape. A planar expansion of both Cl and Se plasmas is assumed. The simulation also assumed that the plasmas were 50 μm wide and 2 cm in length.

The pumping of the Se plasma depends in a complex manner on the density, temperature and velocity of the Cl plasma. Optimization therefore, requires enhancing the pumping radiation and optimising the Se plasma conditions.

3. Conditions for the Se plasma and gain

To achieve maximum gain on the 5–4 transitions in Li-like Se the population of the $n = 4$ levels needs to be as small as possible compared to the $n = 5$ level populations. This is possible because the $n = 4$ level is mainly populated by cascading transitions from the upper levels and by collisional excitation from lower states, particularly, the ground state. The latter contribution can be decreased in plasmas with relatively low temperatures that still produce an appreciable Li-like ion population. To estimate electron temperatures and ion densities that might be optimal to produce Li-like Se ions, we used the code GALAXY. Fig. 2 shows the fractional population of different ionization stages calculated by the code. For electron densities usually realized in laser-produced plasmas (about 10^{21} cm^{-3}) the population of Li-like ions has a maximum abundance between 1500 and 3500 eV. For electron and ion densities of $N_e = 3 \times 10^{21}$ the fraction of Li-like Se ions achieved is about 50% at $T_e = 2500 \text{ eV}$. We found similar results for $N_e = 10^{21}$ and $5 \times 10^{21} \text{ cm}^{-3}$. Thus, electron temperatures of between 1500 and 3500 eV and electron densities of between 1×10^{21} and $5 \times 10^{21} \text{ cm}^{-3}$, generate a high fraction of Li-like Se ions (assuming a steady state).

To estimate the gain dependence on material density and pump radiation, we again used GALAXY. Taking an electron temperature of 2000 eV the gain as a function of modal photon density for the $5g_{9/2}-4f_{7/2}$ transition is shown for different densities in Fig. 3. A gain of about 180 cm^{-1} is achieved with a modal photon density of 0.025.

The problem of optimizing the Cl-Se X-ray laser scheme is divided into two distinct parts: the need to create an Cl plasma with an abundance of H-like ions so as to produce radiation of sufficiently high modal photon density, and the need to create a Se plasma with the conditions ($T_e = 1500\text{--}3500 \text{ eV}$ and $N_e \approx 10^{21} \text{ cm}^{-3}$) to produce high population of Li-like ions.

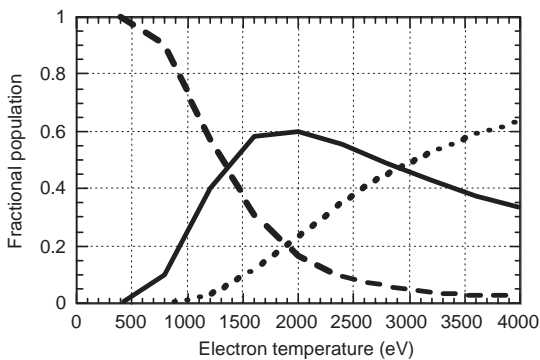


Fig. 2. Fractional populations of the Se ions as a function of electron temperature taking an electron density of $3 \times 10^{21} \text{ cm}^{-3}$: He-like (dots), Li-like (solid), and Be-like (dashed).

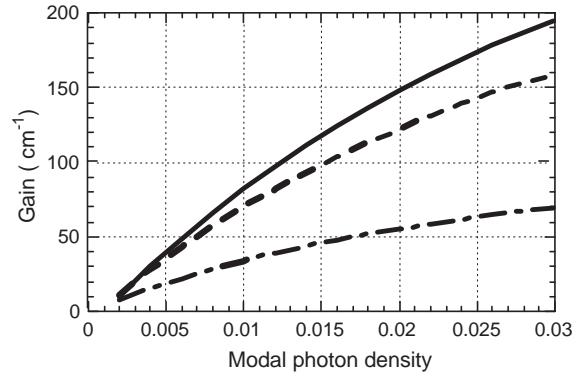


Fig. 3. Gain as a function of modal photon density for $5\text{g}_{9/2}-4\text{f}_{7/2}$ sub-transition in Li-like Se taking an ion densities of 1.0×10^{20} (dot dashed), 2.0×10^{20} (dashed), and 2.7×10^{20} (solid) cm^{-3} .

4. Optical laser parameters

Simulations over a wide range of parameters indicate that single pulse irradiation of a Se-target does not produce enough Li-like ions to obtain gain. To overcome this we investigated the use of a pre-pulse technique [24–30]. The target is first irradiated by an optical pulse of low intensity so that the material can expand but remain in a low-ionization stage (a pre-plasma). The thermal energy transferred to electrons and ions is then transformed into the macroscopic motion of an expanding pre-plasma, leading to plasma cooling and a decreasing electron number density. Because the absorption coefficient is proportional to $T_e^{-3/2}$, the energy of the main pulse can efficiently heat the pre-plasma and ionize the expanding material. The energy of the second pulse is chosen so as to produce a plasma of the desired degree of ionization. The shape of both pre- and main pulses was taken to be trapezoidal with a rise time of 0.1 ns followed by a 0.9 ns plateau with a 0.1 ns fall time. The time interval between the end of the pre- and the beginning of the main pulses denoted by Δt could be varied.

To compare the two experimental geometries (PS and OS) we first calculated the modal photon density at the middle of the main pulse using an intensity of $5 \times 10^{14} \text{ W cm}^{-2}$ a 10% pre-pulse and with $\Delta t = 1 \text{ ns}$.

5. H-like Cl XVII pumping radiation

The modal photon density was calculated as a function of the x -coordinate and as a function of the velocity v , at which an observer is moving in the local Se plasma frame. We found that the maximum of the modal photon density both in PS and OS geometries is realized at $v = 5.5 \times 10^7 \text{ cm s}^{-1}$. The results from the calculations assuming $v = 5.5 \times 10^7 \text{ cm s}^{-1}$ are shown in Fig. 4, which demonstrates that in the case of the PS geometry the pumping radiation is considerably greater than in the case of OS geometry.

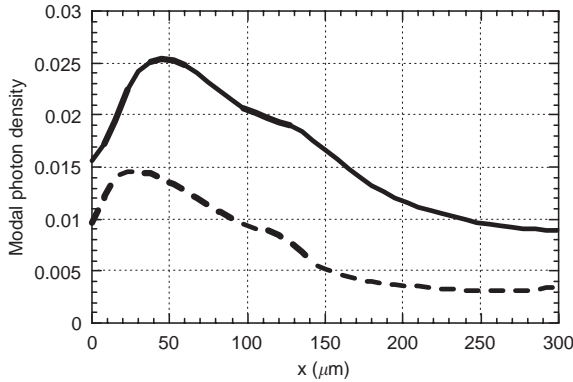


Fig. 4. The modal photon density as a function of x -coordinate, at $y = 70 \mu\text{m}$, $t = 2.7 \text{ ns}$, and $v = 5.5 \times 10^7 \text{ cm s}^{-1}$ in the frame of the observer at a wavelength of 4.1882 \AA , calculated for the PS (solid) and OS (dashed) geometries. The chlorine target is irradiated by a trapezoidal pulse of $0.53 \mu\text{m}$ wavelength, 1 ns duration, $5 \times 10^{14} \text{ W cm}^{-2}$ peak intensity, with 10% pre-pulse, and time delay of $\Delta t = 1 \text{ ns}$.

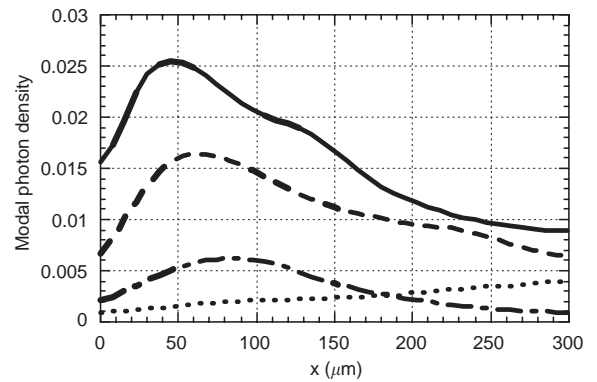


Fig. 5. The modal photon density as a function of x -coordinate, at $y = 70 \mu\text{m}$, $t = 2.7 \text{ ns}$, and $v = 5.5 \times 10^7 \text{ cm s}^{-1}$ in the frame of the observer at a wavelength of 4.1882 \AA , assuming different peak intensities of the main pulse: 10^{14} (dot dashed), 3×10^{14} (dashed), 5×10^{14} (solid), and $10^{15} \text{ W cm}^{-2}$ (dots), and 10% pre-pulse.

As it is likely that the PS geometry can be more easily realized in an experiment and because the pumping radiation calculated to be high enough to produce gain (cf. Fig. 3), we explored the PS geometry in our subsequent calculations. To estimate how the modal photon density depends on the peak intensity of the main pulse, calculations were performed using different peak intensities. We assumed 10% pre-pulse. The results of these calculations are shown in Fig. 5. As the intensity increases from $1-5 \times 10^{14} \text{ W cm}^{-2}$ the modal photon density increases, because more energy transfers into the ionization of the material. The maximum modal photon density is achieved at $5 \times 10^{14} \text{ W cm}^{-2}$. At higher intensities, for example $10^{15} \text{ W cm}^{-2}$, the plasma is so hot that the population of H-like Cl ions decreases, and, therefore, the modal photon density decreases. Hence, we take intensities near $5 \times 10^{14} \text{ W cm}^{-2}$ as optimal in the sense of achieving the maximum photo-pumping radiation. This intensity was used in all further calculations.

To address the scaling of the pre-pulse we performed a series of calculations using 1%, 10%, 30%, 50%, and 100% pre-pulses. Fig. 6 shows the pumping radiation profiles calculated using these parameters. As the pre-pulse level increases from 1–10% the modal photon density increases. Between 10% and 30% the magnitude of the pumping radiation is similar. Further increase of the pre-pulse (not on graph), leads to the decrease of the pumping radiation, because a high pre-pulse causes an expansion of the material, resulting in the decrease of the density. From our calculations we have chosen a 10% pre-pulse as optimal. However, we note that this is true only for $5 \times 10^{14} \text{ W cm}^{-2}$ intensity, because at intensities of, for example, 1×10^{14} and $3 \times 10^{14} \text{ W cm}^{-2}$, we found that 50–100% pre-pulses leads to the increase of the photopumping radiation.

It is also interesting to address how the modal photon density depends on the time delay, Δt , between the pre- and main pulse. As time delay increases modal photon density increases. This is shown in Fig. 7. An increase of the time delay leads to that plasma is cooled

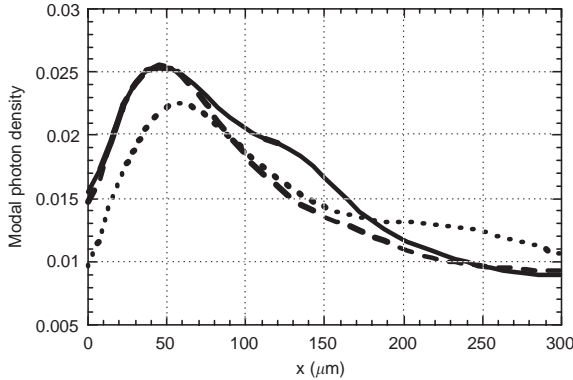


Fig. 6. The modal photon density as a function of x -coordinate, at $y = 70 \mu\text{m}$, $t = 2.7 \text{ ns}$, and $v = 5.5 \times 10^7 \text{ cm s}^{-1}$ in the frame of the observer at a wavelength of 4.1882 \AA , assuming different levels of the pre-pulse: 1% (dots), 10% (dashed), and 30% (solid). The peak intensity of the main pulse was taken to be $5 \times 10^{14} \text{ W cm}^{-2}$ and $\Delta t = 1 \text{ ns}$.

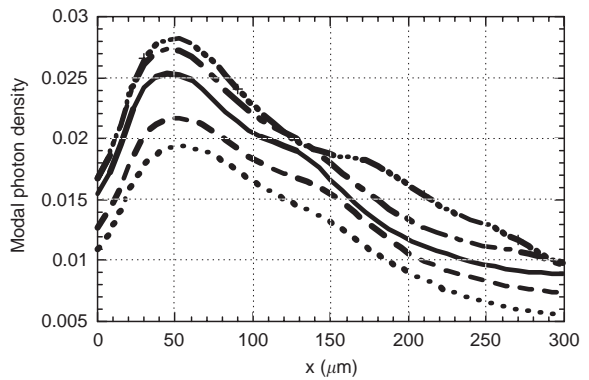


Fig. 7. The modal photon density as a function of x -coordinate, at $y = 70 \mu\text{m}$, $t = 2.7 \text{ ns}$, and $v = 5.5 \times 10^7 \text{ cm s}^{-1}$ in the frame of the observer at a wavelength of 4.1882 \AA , assuming different delays between the pre- and main pulses: 0 (dots), 0.5 (dashed), 1.0 (solid), 1.5 (dot dashed), and 2.0 (triple dot dashed) ns. The peak intensity of the main pulse was taken to be $5 \times 10^{14} \text{ W cm}^{-2}$ with a 10% pre-pulse.

effectively, and, because energy absorption coefficient is proportional to $T_e^{-3/2}$, more H-like Cl ions are produced.

At this point we conclude that among all cases of the optical laser parameters considered in our simulations the highest modal photon density is found at an intensity of $5 \times 10^{14} \text{ W cm}^{-2}$ with a 10% pre-pulse and a 1 ns interval between the pre- and main pulses. These parameters were used to calculate detailed (x, v)-distributions of the modal photon density at different times and y -coordinates. The resultant plot calculated at $t=2.7 \text{ ns}$ and $y=70 \mu\text{m}$ is shown in Fig. 8. The overall distribution of the modal photon density is not symmetric and exhibits two local maxima resulting from a complex interplay between plasma gradients and opacities.

6. Gain calculations

Taking the values of the modal photon density plotted in Fig. 8 we calculate the gain in the Se plasma using the code GALAXY. By performing a number of hydrodynamic simulations we found that an optical laser with the main pulse intensity of $(3-5) \times 10^{14} \text{ W cm}^{-2}$ and 1–30% pre-pulse with $\Delta t = 0.1-2 \text{ ns}$ focused onto a Se target will give an optimal electron temperature and electron density of $1500-3500 \text{ eV}$ and $5 \times 10^{21} \text{ cm}^{-3}$, respectively. The peak value of the gain was found at an intensity $5 \times 10^{14} \text{ W cm}^{-2}$ with 1% pre-pulse and time interval $\Delta t = 1 \text{ ns}$.

Gain as a function of x -coordinate at $y = 70 \mu\text{m}$ is shown in Fig. 10. We use Fig. 10 as a rough guide as to where to place the Se plasma relative to the Cl plasma. Knowing the velocity, electron temperature and density profiles within the Se plasma, we can identify where to place the Se target so as to ensure that the Li-like Se ions experience the maximum modal photon density from the H-like Cl Ly- $\alpha_{1,2}$ radiation.

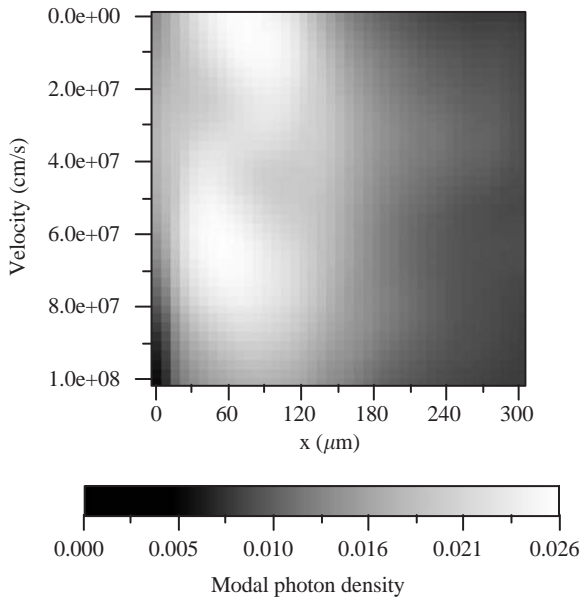


Fig. 8. The modal photon density as a function of position x and velocity v in the frame of the observer at a wavelength of 4.1882 Å. Peak intensity is $5 \times 10^{14} \text{ W cm}^{-2}$, pre-pulse level is 10%, and the time delay is $\Delta t = 1 \text{ ns}$.

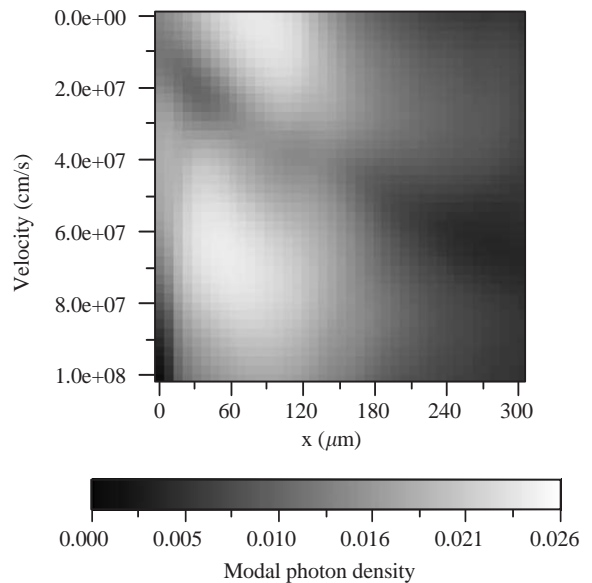


Fig. 9. The modal photon density as a function of position x and velocity v in the frame of the observer at a wavelength of 4.1882 Å. Absorption in the pumped Se plasma was taken into account. The peak intensity is $5 \times 10^{14} \text{ W cm}^{-2}$, the pre-pulse level is 10%, and the time delay, $\Delta t = 1 \text{ ns}$.

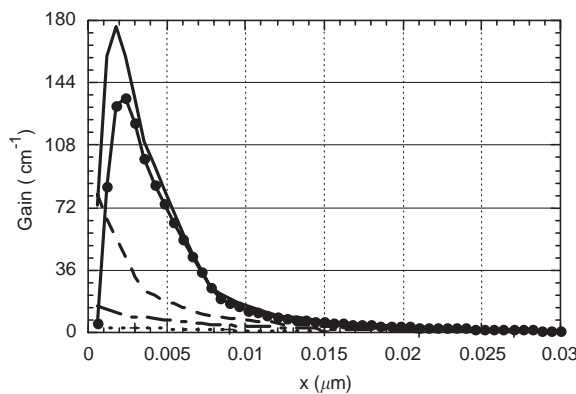


Fig. 10. Gain as a function of x -coordinate at $y = 70 \mu\text{m}$ and at the centre of the main pulse, $t = 2.7 \text{ ns}$, for different separations, Δx , between Cl and Se targets: 0 μm (solid), 50 μm (dashed), 100 μm (dot dashed), and 200 μm (dots). The gain curve with solid dots was calculated assuming an absorption in Se plasma and $\Delta x = 0 \mu\text{m}$. The gain is calculated for the $5g_{9/2}-4f_{7/2}$ transition at 39.5 Å.

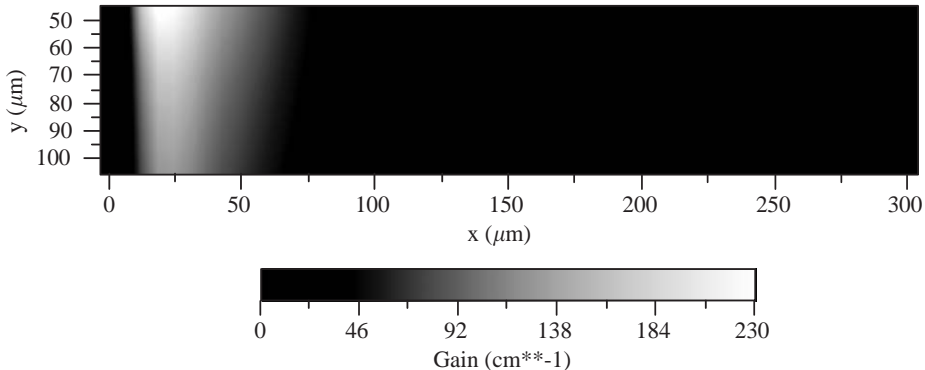


Fig. 11. XY-distribution of the gain at the 39.5 Å, 5f_{9/2}–4f_{7/2}, lasing transition; Se plasma conditions were taken at $t = 2.7$ ns assuming 1% pre-pulse and $\Delta t = 1$ ns. Cl Ly- α radiation was calculated at $t = 2.7$ ns with 10% pre-pulse and $\Delta t = 1$ ns irradiance of the Cl target.

From our calculations the peak value of gain is about 170 and 80 cm⁻¹ when the Se target is positioned at $\Delta x_{\text{Se}} = 0$ and -50 μm, respectively. As the Se target moves further in the $-x$ -direction the gain profile is also shifted in the x -direction and the peak value decreases because of the decrease in modal photon density. In the PS geometry only small separation of Cl and Se targets, $\Delta x_{\text{Se}} \approx 10$ μm, is expected to result in gain bigger than 5 cm⁻¹.

Fig. 11 shows the spatial XY-distribution of gain for the 5g_{9/2}–4f_{7/2} transition at $t = 2.7$ ns. High gain of 230 cm⁻¹ is calculated near the Cl plasma slab boundary ($y = 50$ μm) in a wide x -interval of about 250 μm. As the y -distance from Cl plasma increases, the gain and its spatial extent decreases because of the decrease of modal photon density. From this one can see that the experimentally useful area is 250×50 μm² next to the Cl target in the y -direction.

Absorption of the H-like Cl Ly- $\alpha_{1,2}$ pumping radiation in the pumped Li-like Se plasma can have an effect on the gain. We found that in both PS and OS geometries, an absorption of the pumping radiation in the Li-like Se plasma reduces the modal photon density and the gain by about 20% at $t = 2.7$ ns (cf. Figs. 8–10). Self-emission of the Li-like Se 5d_{5/2}–2p_{3/2} transition was found to increase the modal photon density and the gain by about 2%. However, it remains high, the maximum value is found to be 120 cm⁻¹, and the spatial interval in x -direction, where gain is > 1 cm⁻¹, is extended in ≈ 150 μm.

The time history of the peak value of the gain at $y = 70$ μm is shown in Fig. 12. A maximum gain of 180 cm⁻¹ is found near the center of the main pulse, $t \approx 2.65$ ns. Although the modal photon density increases during the main pulse, the population of Li-like ions decreases. Because of this, the gain profiles decrease and are extended in the x -direction.

The calculations of the gain given above were made using the steady-state approximation for the excitation and ionization in the Se plasma. We generalized GALAXY so that rate equations can be solved time-dependently (calling the new code ORION). The time history of the Se plasma, including the modal photon density, is used as input into the ORION calculations. Given this, we calculated the gain at different x -coordinates, 30, 60, 90, 120, and 150 μm, and at $y = 70$ μm, finding that the time-dependent calculations lead to the decrease of gain by approximately 25% in the region where the gain is expected to be high, for example $x = 30$ μm (cf. Fig. 12).

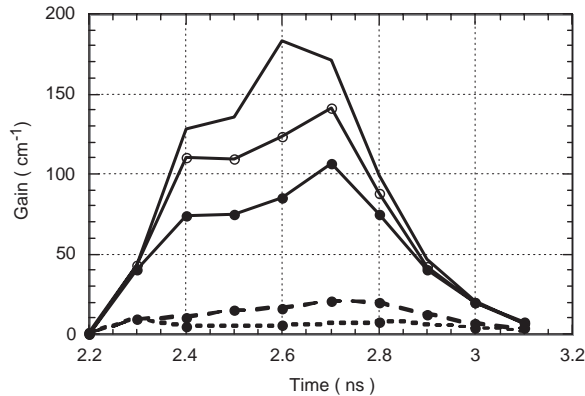


Fig. 12. Peak value of gain as a function of time at $y = 70 \mu\text{m}$ (solid line), and gain as a function of time calculated at different x -coordinates, assuming steady-state (ss) and time-dependent (td) regimes: 30 μm with ss (solid with open circles) and with td (solid with solid circles), 90 μm with ss (dashed with open circles) and with td (solid with solid circles), 150 μm with ss (dots with open circles) and with td (dots with solid circles). The gain was calculated for the $5g_{9/2}-4f_{7/2}$ transition in Li-like Se. The position of the Se-target was taken to be $x_{\text{Se}} = 0 \mu\text{m}$.

GALAXY calculates gain using the modal photon density at the center of the pumped line, effectively ignoring the line width of the pumped transition. To take into account the effect of the spectral profile on gain [31–33] we calculated a correction factor to the pumping rate, denoted Q

$$Q = \frac{\int n_{\text{ph}}(\nu)\varphi(\nu) d\nu}{n_{\text{ph}}(\nu_{ij})}, \quad (1)$$

where $n_{\text{ph}}(\nu)$ is the frequency-dependent modal photon density of the pumping radiation seen in the local frame of Se plasma, and $\varphi(\nu)$ is the spectral profile of $5d_{5/2}-2p_{3/2}$ transition in SeXXXII. Comparing the Doppler width and the natural width of the $5d_{5/2}-2p_{3/2}$ spectral line in Li-like Se at $t = 2.7 \text{ ns}$ at $x = 30, 60, 90, 120$, and $150 \mu\text{m}$, shows that the Doppler width is dominant (10^{14} versus 10^{13} Hz , respectively), and $\varphi^{\text{Doppler}}(\nu)$ was used for the line shape in Eq. (1). Calculations of the Q -factor have shown that it is 0.98–1.00 for all x -coordinates, indicating that the approximation of not accounting for the line width of the pumped line is acceptable in this case. Using a new value of the modal photon density, $n_{\text{ph}}^{\text{(new)}} = n_{\text{ph}}Q$, in GALAXY, we found that gain decreases by less than 2%.

7. Conclusions

We have investigated the H-like Cl – Li-like Se X-ray laser photopumping scheme in a laser-produced plasma. The peak value of the modal photon density, about 0.026, was found for a Cl target irradiance of $5 \times 10^{14} \text{ W cm}^{-2}$ with a 10% pre-pulse and 1 ns delay between the pre- and main pulse. The optimal conditions in the selenium plasma were obtained by applying the pre-pulse technique.

High gain, about 220 cm^{-1} , is calculated at the boundary of the Cl plasma slab ($y = 50 \mu\text{m}$) assuming parallel stream geometry of Cl and Se plasmas and no separation between the targets. From

our calculations it is expected that gain can be observed in a plasma of extending to $250 \times 50 \mu\text{m}^2$. Including the absorption of Cl Ly- $\alpha_{1,2}$ radiation in Li-like Se plasma in our calculations showed that the gain decreases by about 20%. Including time dependence in the calculation shows a further decrease of 30%. The effect of the Se line profile and self-emission of $5d_{5/2}-2p_{3/2}$ transition in Li-like Se onto the modal photon density and gain is less than 2%.

These results are encouraging for X-ray laser investigations and can be relevant for the future experiments, although to provide irradiation conditions over a length and a width of, for example 2 cm and 50 μm , respectively, which our calculations suggest, would require a total energy of about 10 kJ. Future work will concentrate on the effects of two-dimensional expansion of the plasma in realistic experimental geometries.

Acknowledgements

This work was supported by EPSRC under Grant No. GR/N38091, by the Royal Society under Grant No. Q787, by the National Nature Science Foundation of China under Grant Nos. 19974074, 19825110, and 60108007, and National Hi-tech ICF Program of China.

References

- [1] Matthews DL, Hagelstein PL, Rosen MD, Eckart MJ, Ceglio NM, Hazi AU, Medecki HM, MacGowan BJ, Trebes JE, Whitten BL, Campbell EM, Hatcher CW, Hawryluk AM, Kauffman RL, Pleasance LD, Rambach G, Scofield JH, Stone G, Weaver TA. Demonstration of a soft X-ray amplifier. *Phys Rev Lett* 1985;54:110.
- [2] Lee TN, Mcleau EA, Elton RC. Soft X-ray lasing in neonlike germanium and copper plasmas. *Phys Rev Lett* 1987;59:1185.
- [3] Jaegle P, Jamelot G, Carillon A, Klisinick A, Sureau A, Guennou H. Soft-X-ray amplification by lithiumlike ions in recombining hot plasmas. *J Opt Soc Am B* 1987;64:563.
- [4] Skobelev IY, Dyakin VM, Faenov AY, Bartnik A, Fiedorowicz H, Jarocki R, Kostecki J, Szczurek M, Biemont E, Quinet P, Nilsen J, Behar E, Doron R, Mandelbaum P, Schwob JL. The X-ray emission spectra of multicharged xenon ions in a gas puff laser-produced plasma. *J Phys B: Atom Mol Opt Phys* 1999;32:113.
- [5] Lin JY, Tallents GJ, Zhang J, MacPhee AG, Lewis CL, Neely D, Nilsen J, Pert GJ, Orourke RMN, Smith R, Wolfrum E. Gain saturation of the Ni-like X-ray lasers. *Opt Commun* 1998;158:55.
- [6] Kalachnikov MP, Nickles PV, Schnurer M, Sandner W, Shlyaptsev VN, Danson C, Neely D, Wolfrum E, Zhang J, Behjat A, Demir A, Tallents GJ, Warwick PJ, Lewis CLS. Saturated operation of a transient collisional X-ray laser. *Phys Rev A* 1998;57:4778.
- [7] Zhang J, MacPhee AG, Lin J, Wolfrum E, Smith R, Danson C, Key MH, Lewis CLS, Neely D, Nilsen J, Pert GJ, Tallents GJ, Wark JS. A saturated X-ray laser beam at 7 nanometers. *Science* 1997;276:1097.
- [8] MacGowan BJ, Maxon S, Hagelstein PL, Keane CJ, London RA, Matthews DL, Rosen MD, Scofield JH, Whelan DA. Demonstration of soft X-ray amplification in nickel-like ions. *Phys Rev Lett* 1987;59:2157.
- [9] Rocca JJ, Clark DP, Chilla JLA, Shlyaptsev VN. Energy extraction and achievement of the saturation limit in a discharge-pumped table-top soft X-ray amplifier. *Phys Rev Lett* 1996;77:1476.
- [10] Lemoff BE, Yin GY, Gordon CL, Barty CPJ, Harris SE. Demonstration of a 10-Hz femtosecond-pulse-driven XUV laser at 41.8 nm in Xe IX. *Phys Rev Lett* 1995;74:1574.
- [11] Vinogradov AV, Sobel'man II, Yukov EA. Possibility of constructing a far-ultraviolet laser utilizing transitions in multiply charged ions in an inhomogeneous plasma. *Sov Phys Quant Electron* 1975;5:59.
- [12] Norton BA, Peacock NJ. Population inversion in laser-produced plasmas by pumping with opacity-broadened lines. *J Phys B* 1975;8:989.
- [13] Lee YT, Howard WM, Nash JK. Soft X-ray lasing in Li-like iron by resonant photo-pumping. *JQSRT* 1990;43:335.

- [14] Al'Miev IR, Rose SJ, Wark JS. Simulations of Al XIII-Fe XXIV X-ray laser photopumping scheme. JQSRT 2001;71:129.
- [15] Al'Miev IR, Rose SJ, Wark JS. Further simulations of the gain in a K XIX/CIXVII resonantly photopumped X-ray laser. JQSRT 2001;70:11.
- [16] Beer ME, Patel PK, Rose SJ, Wark JS. Calculations of the modal photon densities and gain in a K/Cl resonantly photopumped X-ray laser. JQSRT 2000;65:71.
- [17] Nilsen J. Resonantly photo-pumped Li-like X-ray lasers. Appl Opt 1992;31:4957.
- [18] Nilsen J, Scofield JH, Chandler EA. Reinvestigating the early resonantly photopumped X-ray laser schemes. Appl Opt 1992;31:4950.
- [19] Dyall KG, Grant IP, Johnson CT, Parpia FA, Plummer EP. GRASP: a general-purpose relativistic atomic structure program. Comput Phys Commun 1988;55:425.
- [20] Christiansen JP, Ashby DETF, Roberts KV. MEDUSA—a one-dimensional laser fusion code. Comput Phys Commun 1974;7:271.
- [21] Djaoui A. A user guide for the laser-plasma simulation code: MED103. Technical report RAL-TR-96-099, Rutherford Appleton Laboratory, 1996.
- [22] Rose SJ. The non-LTE excitation/ionization code GALAXY. J Phys B 1998;31:2129.
- [23] Rose SJ. The effect of relativity on the oscillator strengths of hydrogen-like ions. Technical report RAL-TR-97-020, Rutherford Appleton Laboratory, 1997.
- [24] Boehly T, Russotto M, Craxton RS, Epstein R, Yakobi B, Da Silva LB, Nilsen J, Chandler EA, Fields DJ, MacGowan BJ, Matthews DL, Scofield JH, Shimkaveg G. Demonstration of a narrow-divergence X-ray laser in neonlike titanium. Phys Rev A 1990;42:6962.
- [25] Nilsen J, MacGowan BJ, Da Silva LB, Moreno JC. Prepulse technique for producing low-Z Ne-like X-ray lasers. Phys Rev A 1993;48:4682.
- [26] Lunney JG. Waveguiding in soft X-ray laser experiments. Appl Phys Lett 1986;48:891.
- [27] Kodama R, Neely D, Diado H, Murai K, Yuan G, MacPhee A, Lewis CLS. Generation of small-divergence soft X-ray laser by plasma waveguiding with a curved target. Phys Rev Lett 1994;73:3215.
- [28] Healy SB, Cairns GF, Lewis CLS, Pert GJ, Plowes JA. A computational investigation of the neon-like germanium collisionally-pumped laser considering the effect of prepulses. IEEE J Sel Top Quant Electron 1995;1:949.
- [29] Nantel M, Klisnick A, Jamelot G, Holden PB, Rus B, Carillon A, Jagle P, Zetoun Ph, Tallents G, MacPhee AG, Lewis CLS, Jacquemot S, Bonnet L. Spectroscopic characterization of prepulsed X-ray laser plasmas. Phys Rev E 1996;54:2852.
- [30] Li Y, Pretzler G, Fill EE. Spatial position of prepulse induced $J = 0$ to 1, 3p–3s lasing in low-Z neonlike ions. Phys Rev A 1995;51:R4341.
- [31] Al'Miev IR. Simulations of photopumped X-ray lasers. D. Phil. thesis, University of Oxford, Oxford, 2000.
- [32] Sondhauss P, Lee RW, Rose SJ, Al'Miev IR, Wark JS. Extension of the code suite FLY to a multi-cell postprocessor for hydrodynamic plasma simulation codes. JQSRT 2001;71:721.
- [33] Loboda PA, Popova VV, Shinkarev MK. Line profile and spectral gain calculations for high-Z ions in X-ray laser plasmas. JQSRT 1997;58:757.

H. TENG
J. ZHANG✉
Z.L. CHEN
Y.T. LI
X. LU
K. LI
X.Y. PENG

Hot-electron-induced plasma formation on the rear surface of a foil

Laboratory of Optical Physics, Institute of Physics, Chinese Academy of Sciences, Beijing 100080, P.R. China

Received: 14 January 2003 / Revised version: 2 April 2003
Published online: 2 June 2003 • © Springer-Verlag 2003

ABSTRACT The plasma jet formed on the rear surface of a foil in laser-solid interaction is investigated by laser probing. The rear plasma jet, which is in line with the laser, formed a few picoseconds after the incidence of the focused laser, is due to a beam of fast electrons propagating through the target and is collimated by a strong magnetic field in the plasma.

PACS 52.50.Jm; 52.38.Fz; 52.38.Kd

1 Introduction

Experimental investigation of the interaction of an ultra-intense ultra-short laser with a plasma has recently become possible with the advent of multiterawatt, short-pulse lasers [1, 2]. Such an interaction has many applications [3], such as the ‘fast ignitor’ scheme [4], in which an intense short laser pulse is focused onto high-density pre-compressed thermonuclear fuel to generate fast electrons and create an ignition spark that initiates a propagating thermonuclear burn. In this paper we present laser-probing results on the plasma on the rear surface of a foil target arising from laser-generated hot-electron beams propagating through the solid-density target.

Several mechanisms can be responsible for transferring laser energy to the plasma electrons [5]. One mechanism for electron acceleration is the ponderomotive-force acceleration, in which the laser pulse terminates at the critical-density surface; the $v \times B$ force can ponderomotively accelerate electrons in the direction of laser propagation [6, 7]. Other collisionless electron-acceleration mechanisms at the critical-density surface include vacuum heating [8, 9], resonance absorption [10], and parametric instabilities [11]. We shall attribute our experimental results to the ponderomotive acceleration.

2 Experimental setup

The experiment was performed using the ‘JG-I’ Ti:sapphire laser system [1] based on chirped pulse amplification. As shown in Fig. 1, a 25 fs, 800 nm laser pulse

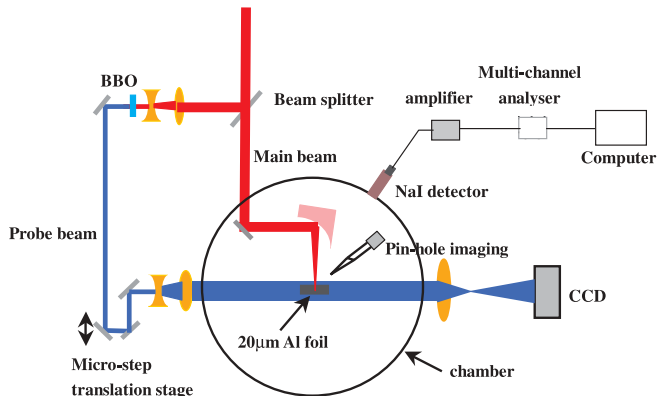


FIGURE 1 Schematic of the experimental setup. The 2D transverse image of the foil was obtained by a CCD with a 400 nm probe beam. Pinhole imaging was used to monitor the focal spot. A NaI system was used to monitor the intensity of hard X-ray emission

with an energy up to 36 mJ was focused onto an aluminum foil with a thickness of 20 μm at 10° to the target normal. The roughness of the Al foil surface is less than 1 μm . The mount is controlled by three-dimensional microstep motors to ensure that the laser pulse interacted with a fresh target surface at each shot. Low-energy equivalent-plane measurements showed a 10–20 μm full width at half maximum focal spot, giving a maximum intensity of $1 \times 10^{17} \text{ W/cm}^{-2}$. Pinhole imaging of X-ray emission monitored the focal spot size for each full-energy shot. A small fraction of the main beam, frequency doubled to 400 nm in a BBO crystal, is used as a temporally independent probe beam. The probe beam passed transversely across the foil target, both the front and the rear surfaces being in the field of view. A 2D transverse image of the back-lit target was recorded on a charge-coupled device (CCD) with a 400 nm band transmission filter, with spatial and temporal resolutions of the order of 2 μm and 1 ps, respectively. The region that has been ionized up to a fraction of the critical density of 400 nm light becomes opaque to the probe. Refraction of the probe in the strong density gradient region limited observations to regions with electron density less than $6.9 \times 10^{21} \text{ cm}^{-3}$. By varying the time delay between the probe beam and the main beam, we can analyze the plasma formation on the front and rear surfaces. The probe beam was timed by decreasing the relative delay to a value such that no

plasma was seen by the diagnostics. This was taken to be the time zero. A calibrated γ -ray spectrometer is used to monitor the X-ray Bremsstrahlung from the plasma. The γ -ray spectrometer consists of a NaI detector, an electronic gated shutter, a photomultiplier, an amplifier, and a multichannel energy analyzer. A 20 mm diameter hole in a 50 mm thick Pb block is used to collimate the X-ray radiation and to shield the detector. The detector response is calibrated using a 511 keV and 1.274 MeV γ -ray ^{22}Na source and a 665 keV ^{137}Cs source.

3 Experimental results and discussion

The hard X-ray Bremsstrahlung spectrum has the same Maxwellian distribution as the colliding electrons. The hard X-ray spectrum is generally dominated by the Bremsstrahlung produced by high-energy hot electrons colliding with atomic nuclei. The shape and intensity of the Bremsstrahlung is the principal diagnostic for the outgoing hot-electron flux and temperature. The hard X-ray spectrum shows a bi-Maxwellian distribution and the hot-electron temperature is 73 keV, as shown in Fig. 2. However, the space-charge field stops hot electrons with energies below ~ 20 keV, so that the out-going hot-electron temperature is about 90 keV.

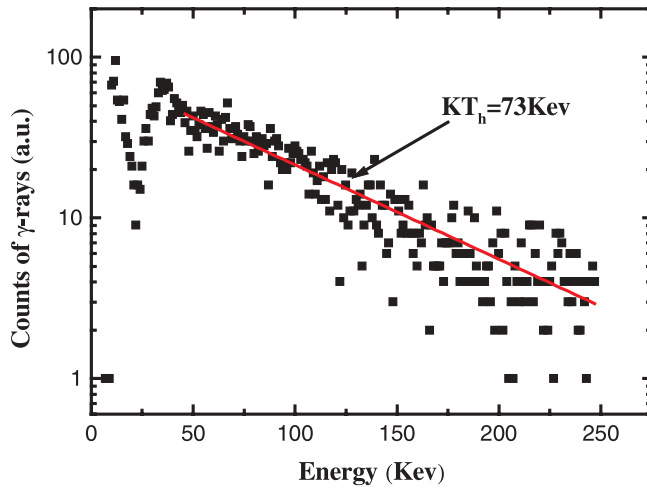


FIGURE 2 The X-ray Bremsstrahlung from the Al target. The solid line is the Maxwellian distribution fit for the temperature

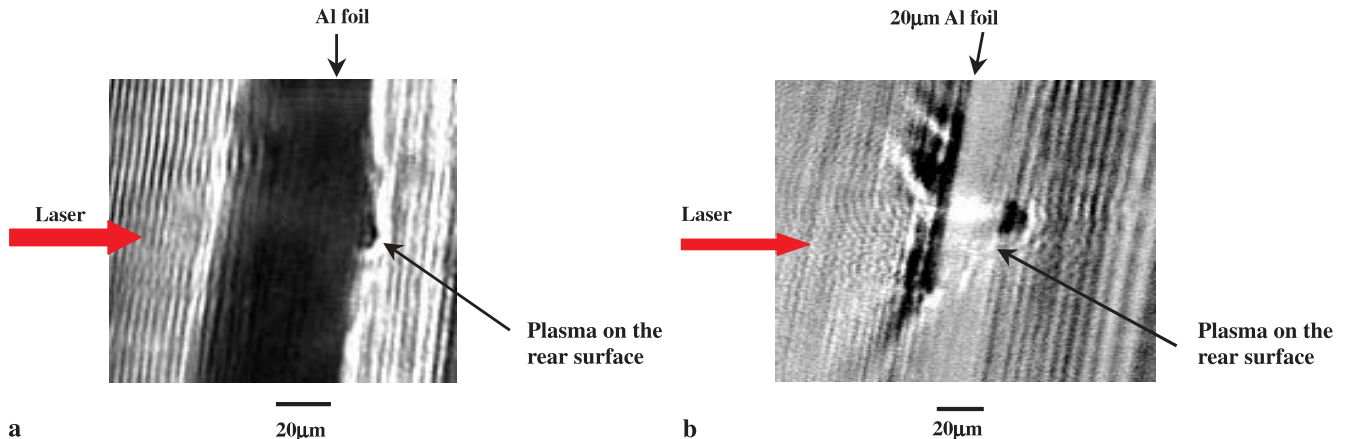


FIGURE 3 Shadowgrams taken at **a** 11 ps and **b** 44 ps for the interaction of the 36 mJ, 25 fs laser pulse with a 20 μm Al foil, showing a plasma on the rear surface. In **b**, the plasma on the front surface is not seen because of blocking of the probe beam by the curled side of the Al foil. The front plasma did exist

The energy spectra of the out-going and the in-coming (to the foil) hot electrons are the same; hence the in-coming hot-electron temperature is also 90 keV. There is a dip in the hard X-ray spectrum at about 25 keV in Fig. 2; the dip may be a demarcation point between the high-temperature electron group and the low-temperature electron group, which is not under consideration due to the low-energy electrons. The propagation of the hot electrons through the Al foil is investigated.

Shadowgrams of the target were recorded at different times. Figure 3a and b show the typical shadowgrams of the interaction at 11 ps and 44 ps, respectively. The main laser beam is from left to right. In order to enhance the contrast in Fig. 3b, we have subtracted from it the image of the unperturbed target in the presence of the probe beam alone. This results in quite different gray-scaling for the two figures. In Fig. 3a, the front plasma is not seen because of blocking of the probe beam by the curled side of the Al foil; for the same reason the target looks thicker than it actually is. In fact, the front plasma was already formed at this time. In Fig. 3b, at the left-hand edge of the Al foil, we clearly see that a plasma is formed. The very dark regions represent plasma densities larger than $6.9 \times 10^{21} \text{ cm}^{-3}$, the critical density of 400 nm light. We also see that the jet-like plasma expansion into the back vacuum is not cone shaped but laser aligned, as it should be if the electrons are accelerated forward by the laser ponderomotive force [7], and the resulting space charge pulls out the ions to form the plasma. The mushroom-like jets on the rear surface of the foil can be observed in both Figs. 3a and 3b. They have diameters (at the surface) of 4 μm and 10 μm , respectively. The jets were always in line with the laser and expanded with time. The small jets in both figures disappeared when there is only the main beam (without the probe beam), so they are not from self-emission but are indeed plasmas formed at the rear surface. The latter may be due to three mechanisms. The first is from the transmission of the laser pulse through the foil. But this mechanism is impossible because the 20 μm Al foil blocks the laser pulse completely. The second possibility is that the leading edge of the pre-pulse is transmitted and the main part of the pulse is then focused on the rear surface of the foil. To rule out this possibility, we monitor the focal spot

on the front surface with a pinhole imaging camera. We did not find any significant change of the focal spot size. From the formation time, we can rule out the possibility of shock breakout, which is also inconsistent with the small diameter. The third possibility is the transmission of fast ions from the interaction, but this can be ruled out because of the thickness of the target. The contrast ratio of the heating pulse is 10^5 at 1 ps, which was measured by a high-dynamic third autocorrelator. We made a hydrodynamical simulation on the ablation depth of the pre-pulse (Figs. 4 and 5), which shows that it did not ablate a 1-micron Al foil and a shock wave caused by the pre-pulse propagated through the 1-micron Al foil after 100 ps. However, during that time, the hot electrons produced by the main pulse had already propagated through the Al foil. So the contribution of the pre-pulse can be ruled out.

Thus, we propose that the rear plasma is formed by a beam of collimated fast electrons. The fast-electron temperature can be obtained by several means: K_{α} spectra, γ -ray spectra, or fast-electron spectra. Here we obtain the fast-electron temperature (kT_e) from Beg et al. [12], obtained with $K\alpha$ emission measurements for laser–solid experiments:

$$kT_e \simeq 100 \left(\frac{I\lambda^2}{10^{17} \text{ W/cm}^{-2}} \right)^{1/3} \text{ keV}, \quad (1)$$

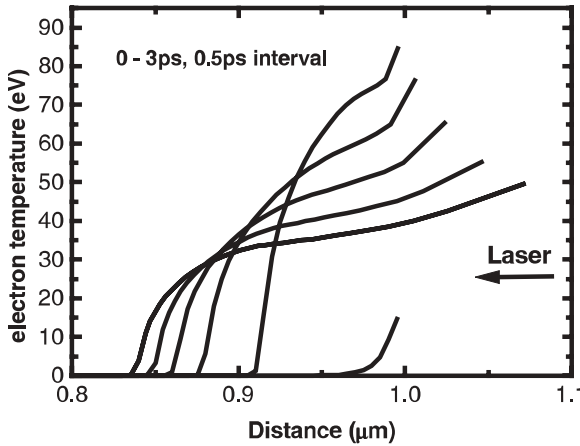


FIGURE 4 Spatial distribution of electron temperature and density for 1 ps pre-pulse

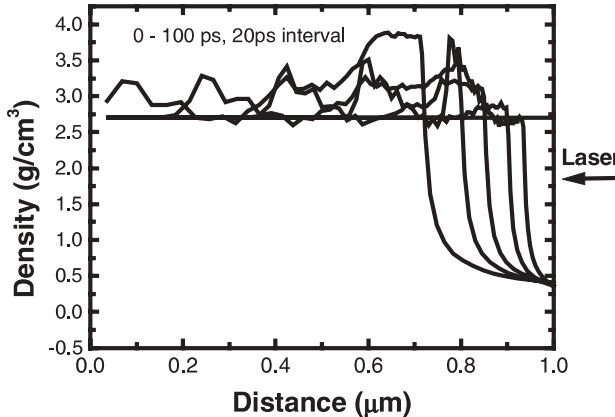


FIGURE 5 Spatial distribution of electron temperature and density for 100 ps pre-pulse

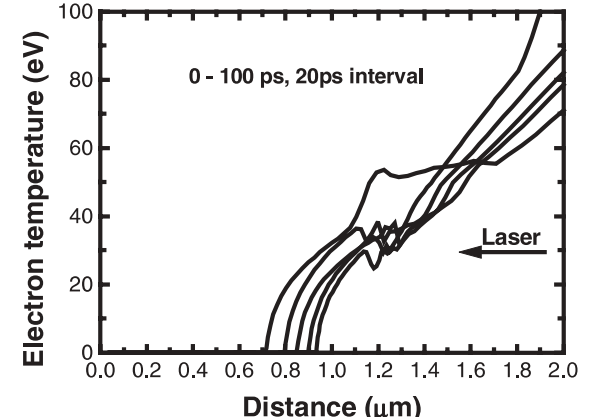
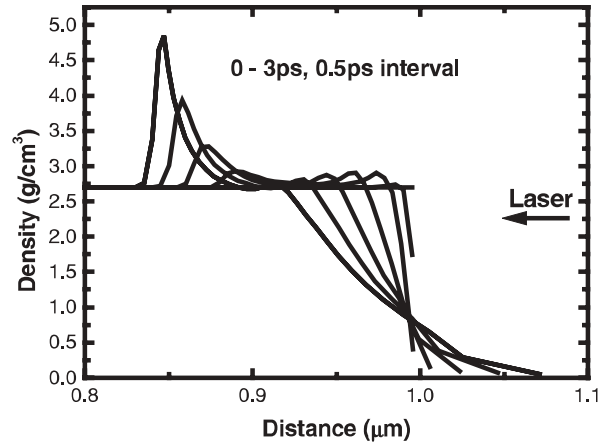
where I and λ are the intensity and the wavelength of the laser, respectively. The laser intensity we used is $\sim 8 \times 10^{16} \text{ W/cm}^{-2}$, corresponding to a fast-electron temperature of $\sim 80 \text{ keV}$. The range of these electrons can be obtained from the model of Harrach and Kidder [13]. We find

$$kT_e \sim 18.1(R_0)^{0.58}, \quad (2)$$

where kT_e is in keV and R_0 is in mgcm^{-2} . This gives a range of $47 \mu\text{m}$, which is much larger than the thickness of the Al foil in our case. Thus, the fast electrons, originating from the interaction area, can propagate through the solid target. As they leave the rear surface, a space-charge potential is quickly built up, forming an electron sheath at the surface with a scale length given by the Debye length [14]. If the electric field in this sheath is much higher than that for field ionization of aluminum, a plasma is formed at the rear surface of the foil. The electric field in the sheath can be estimated [15] to be

$$E \sim \frac{kT_e}{e\lambda_D^2} \sim 1.3 \times 10^{-1}(n_e T_e)^{1/2} \text{ V/m}^{-1}, \quad (3)$$

where n_e and T_e are the number density (cm^{-3}) and temperature (eV) of the electrons on the surface and λ_D is the Debye length. If we assume that the absorption into the hot electrons is about 20% with a mean energy of 90 keV, and the hot electrons fill the $20 \mu\text{m}$ thick foil target with a 45° cone



angle, we have $E \sim 7.6 \times 10^{11} \text{ V/m}^{-1}$. Such an electric field can easily ionize the rear target surface and accelerate the ions outwards.

To account for the limited diameter of the plasma on the rear surface, we propose that the electron flow is pinched inwards towards the rear surface of the foil by a strong magnetic field. Electric and magnetic fields, variable resistivity, as well as collisions, can all play a part in fast-electron transport through the solid target. The electric field lowers the energy of the electrons as they enter the target. The transport of the electrons inside the target is determined by the collisions and the magnetic field. The ratio of the force on the fast electrons from the magnetic field to that from the electric field is [15]

$$\frac{vB}{cE} \sim 12 \left(\frac{2\tau}{1 \text{ ps}} \right) \left(\frac{10 \mu\text{m}}{R} \right) \left(\frac{v}{c} \right), \quad (4)$$

where R is the focal spot size, τ is the duration of the laser pulse, and v is the hot-electron speed. From Davies' simulation [15], the electric field is not a major effect at an intensity of $10^{16} \text{ W/cm}^{-2}$, and the magnetic field is significant at this or higher intensity. Thus, in our case the fast electrons are pinched inwards towards the rear of the foil by a strong magnetic field. The diameter of the plasma at the rear surface is about $10 \mu\text{m}$, corresponding to a spread angle of 10° over a distance of $20 \mu\text{m}$, which is comparable to the radius of the observed plasma. If the fast electrons had propagated freely, the spread angle would be greater than 40° in the $20 \mu\text{m}$ foil target. The observed restricted cross section of the rear plasma jet also suggests the existence of strongly collimated fast electrons, giving indirect evidence for the presence of a magnetic field in the target.

4 Conclusion

The transport of fast electrons is of critical importance in the fast ignitor concept in fusion research. In our ex-

periment a localized plasma jet on the rear surface of the target is observed through laser probing. The plasma jet is attributed to ponderomotively generated fast electrons that are collimated by the self-generated magnetic field. The fast-electron beam propagates through the target and creates a strong space-charge electric field which ionizes the back surface of the aluminum target and pulls out the ions, forming the observed plasma.

ACKNOWLEDGEMENTS This work was jointly supported by the NSFC (under Grant Nos. 10075075, 10005014, and 10176034) and the National Hi-tech ICF programme and NKBRSF (under Grant No. G19990752000)

REFERENCES

- 1 Z.Y. Wei, J. Zhang, J.F. Xia, B.H. Feng, X.L. Zhang, Y. Qiu: *Sci. China A* **43**, 1083 (2000)
- 2 P. Maine, D. Strickland, P. Bado, M. Pessot, G. Mourou: *IEEE J. Quantum Electron.* **QE-24**, 398 (1998)
- 3 M.D. Perry, G. Mourou: *Science* **264**, 917 (1994)
- 4 M. Tabak, J. Hammer, M.E. Glinsky, W.L. Kruer, S.C. Wilks, J. Woodworth, E.M. Campbell, M.D. Perry: *Phys. Plasmas* **1**, 1626 (1994)
- 5 S.C. Wilks, W.L. Kruer: *IEEE. J. Quantum Electron.* **QE-33**, 1954 (1997)
- 6 W. Yu, M.Y. Yu, J.X. Ma, Z.M. Sheng, J. Zhang, H. Daido, S.B. Liu, Z.Z. Xu, R.X. Li: *Phys. Rev. E* **61**, 2220 (2000)
- 7 S.C. Wilks, W.L. Kruer, M. Tabak, A.B. Langdon: *Phys. Rev. Lett.* **69**, 1383 (1992)
- 8 F. Brunnel: *Phys. Rev. Lett.* **59**, 52 (1987)
- 9 L.M. Chen, J. Zhang, Q.L. Dong, H. Teng, T.J. Liang, L.Z. Zhao, Z.Y. Wei: *Phys. Plasmas* **8**, 2925 (2001)
- 10 N.H. Ebrahim, H.A. Baldis, C. Joshi, R. Benesch: *Phys. Rev. Lett.* **45**, 1179 (1980)
- 11 K. Estabrook, W.L. Kruer: *Phys. Fluids* **26**, 7 (1983)
- 12 F.N. Beg, A.R. Bell, A.E. Dangor, C.N. Danson, A.P. Fews, M.E. Glinsky, B.A. Hammel, P. Lee, P.A. Norreys, M. Tatarakis: *Phys. Plasmas* **4**, 447 (1996)
- 13 R.J. Harrach, R.E. Kidder: *Phys. Rev. A* **23**, 887 (1981)
- 14 H. Hora: *Physics of Laser Driven Plasmas* (Wiley, New York, Chichester 1981)
- 15 J.R. Davies, A.R. Bell, M.G. Haines, S.M. Guérin: *Phys. Rev. E* **56**, 7193 (1997)

H.C. WU¹
W. YU²
T.J. LIANG¹
X.Y. PENG¹
Z. JIN¹
Y.J. LI^{1,3}
Z.M. SHENG¹
X.W. TANG⁴
J. ZHANG^{1,✉}

A simple estimate of resonance absorption of femtosecond laser pulses by liquid droplets

¹ Laboratory of Optical Physics, Institute of Physics, Chinese Academy of Sciences,
Beijing 100080, P.R. China

² Shanghai Institute of Optics and Fine Mechanics, Chinese Academy of Sciences,
Shanghai 201800, P.R. China

³ Department of Science and Arts, China University of Mining and Technology, Beijing 100083, P.R. China

⁴ Department of Physics, Zhejiang University, Hangzhou 310027, P.R. China

Received: 3 April 2003 / Revised version: 30 June 2003

Published online: 8 October 2003 • © Springer-Verlag 2003

ABSTRACT The resonance absorption of femtosecond pulses by liquid droplets is studied. The angular dependence of the laser absorption may be used to understand the symmetric double-lobe emission of hot electrons generated from liquid droplets. The total laser absorption fraction is found to be strongly related to the scale length of the microplasmas.

PACS 52.50.Jm

1 Introduction

The development of ultrashort, high-intensity lasers based on chirped-pulse amplification (CPA) has enabled a broad range of studies of laser-plasma interactions to be carried out by irradiating both solids and atomic clusters. Generally, the average diameter of atomic clusters is much shorter than the laser wavelength. Under irradiation from an ultrashort, high-intensity laser, the clusters expand quickly and become underdense plasmas. Recently, motivated by possible applications, such as table-top X-ray sources, some experiments were conducted on the interaction between ultrashort laser pulses and droplets. This is an intermediate interaction regime between that of a continuous solid and a nm-size atomic cluster. Because the sizes of these liquid droplets are comparable with the laser wavelength, a number of new phenomena were reported in these experiments [1–4]. The phenomena indicated that collisional heating is not important in the interaction of laser pulses and microplasmas generated from the liquid droplets. The resonance absorption becomes the most important process in the interaction.

The angular dependence of the resonance absorption has been investigated for plane plasmas under irradiation from obliquely incident *p*-polarized laser pulses [5]. It is found that there is an optimum incident angle for maximum absorption. Hot electrons are generated due to the resonance absorption [6] and the hot electrons have collimated emission in the normal direction of the plane targets [7]. Cylindrical plasmas [8] also have been studied, under irradiation from *p*-polarized laser pulses whose polarization direction is orthogonal to the fiber target axis. There are two optimum angles

for maximum resonance absorption in the surface of the fiber. In this paper, the resonance absorption of femtosecond laser pulses by spherical plasmas generated from liquid droplets is investigated. From our simple model, it is found that the angular dependence of the laser absorption can be used to explain the double-lobe emission of hot electrons observed in our experiment [4, 9]. The total laser absorption fraction is found to be strongly related to the scale length of the microplasmas.

2 The model

A simple expression for resonance absorption was proposed by Krueer [8, 10] for plane plasmas under irradiation from an obliquely incident *p*-polarized light wave, where the incidence angle β is defined as the angle between the propagation direction of the light wave and the direction of the density gradient:

$$I_{\text{abs}} = \frac{1}{2} \Phi^2(\tau) I_{\text{lp}}, \quad (1a)$$

$$\Phi(\tau) = \varepsilon \tau \exp(-2\tau^3/3), \quad (1b)$$

where $\varepsilon = 1.76$ [8], $\tau = (k_0 L)^{1/3} \sin(\beta)$, $I_{\text{lp}} = I_l \sin^2(\gamma)$ is the intensity for the *p*-polarized component of the incident laser, $I_l = (c/8\pi)E_l^2$ is the intensity of the incident laser in free space, γ is the angle between the laser polarization direction and the normal (*s*-polarized) direction of the incident plane, $k_0 = 2\pi/\lambda$ is the wave number in vacuum and L is the plasma scale length, which is defined as the distance from the interface between the plasma and the vacuum to the critical density surface for the light wave.

The scale length L is given by [10]:

$$L = C_s t_l \approx 0.31 t_l \sqrt{T_e} (\mu\text{m}), \quad (2)$$

where t_l is the laser pulse duration in ps, T_e is the plasma temperature in keV, and $C_s = \sqrt{Z T_e / m_i}$ is the ion sound speed.

Because of the different angle of incidence in the curving surface of the target, there is a different absorption fraction of the laser energy in different places on the target. The places with higher resonance absorption are expected to generate more hot electrons which have a collimated emission in the normal direction of plane, so the angular dependence of the resonance absorption can be used to understand the angular

dependence of the collected hot electrons. Below, we will calculate the angular dependence of the resonance absorption by liquid droplets.

3 Absorption by liquid droplets

An experiment was carried out where liquid droplets (ethanol) with an average radius of $R = 5 \mu\text{m}$ were irradiated by 150-fs, 798-nm linearly polarized laser pulses focused at an irradiance of $1 \times 10^{16} \text{ W/cm}^2$ from a Ti : sapphire laser. In Fig. 1 we draw a schematic diagram to illustrate the experimental configuration. The focal spot size was $20 \mu\text{m}$. In this case, the microplasma radius was much less than the focal spot size, so that the laser wave could be regarded as a plane wave. The laser pulses propagated along the opposite direction of the x -axis. The polarization direction was along the y -axis. θ and φ are the polar angle and azimuth angle in the spherical coordinates, respectively.

We used the analytic geometry to obtain the β and γ functions. The unit vector of the laser propagation direction is $-\hat{x} = [-1, 0, 0]$, the unit vector of the laser polarization direction is $\hat{y} = [0, 1, 0]$, and the unit vector of the normal direction in the differential surface element of the sphere is $\hat{n} = [\sin \theta \cos \varphi, \sin \theta \sin \varphi, \cos \theta]$. We find that $\cos \beta = \hat{x} \cdot \hat{y}$, $\cos \gamma = \frac{(\hat{n} \times \hat{x}) \cdot \hat{y}}{|\hat{n} \times \hat{x}|}$, so we obtain:

$$\sin(\beta) = \sqrt{1 - \sin^2(\theta) \cos^2(\varphi)}, \quad (3a)$$

and

$$\sin(\gamma) = \frac{\sin(\theta) \sin(\varphi)}{\sqrt{1 - \sin^2(\theta) \cos^2(\varphi)}}. \quad (3b)$$

Now we can calculate the relative absorption distribution of the laser energy in the spherical surface:

$$\alpha(\theta, \varphi) d\Omega = (I_{\text{abs}}/I_l) d\Omega_{\text{eff}}, \quad (4)$$

where $d\Omega_{\text{eff}} = \sin(\theta) \cos(\varphi) d\Omega$ means the effective absorption surface element, $d\Omega = R^2 \sin(\theta) d\theta d\varphi$, and R is the spherical radius. In our experiment [9], we measured the hot electron emission in the laser polarization plane (xy plane). So, letting $\theta = \pi/2$ in (4) and substituting (1) and (3) into (4), we obtain:

$$\alpha(\varphi) = \left(\frac{L}{\lambda} \right)^{2/3} \sin^2(\varphi) \cos(\varphi) \exp \left[-\frac{8\pi L}{3\lambda} |\sin(\varphi)|^3 \right], \quad (5)$$

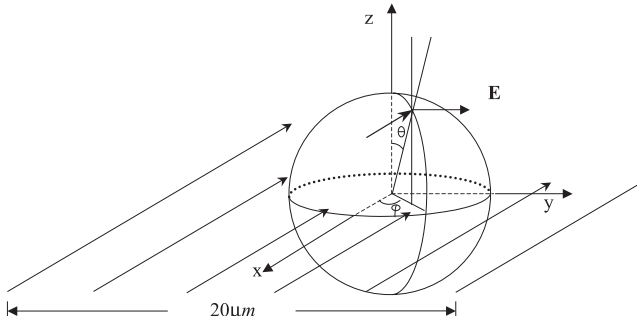


FIGURE 1 A schematic diagram of the interaction between laser pulses and a liquid droplet

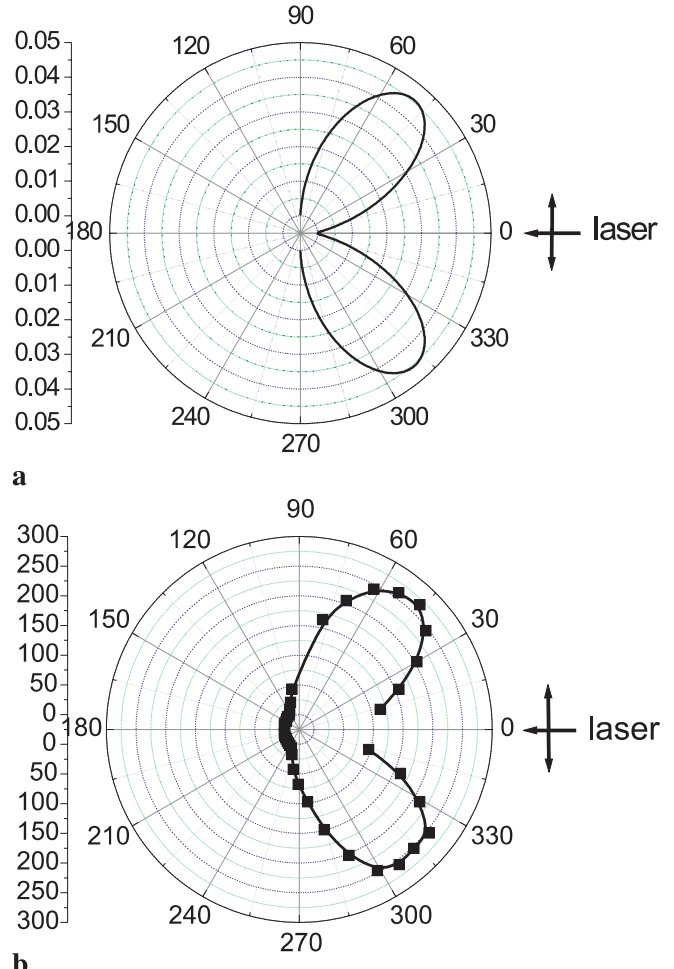


FIGURE 2 **a** Calculated angular dependence of the resonance absorption on the liquid droplets. **b** Measured angular distribution of hot electrons generated from liquid droplets under irradiation of 150-fs, $1 \times 10^{16} \text{ W/cm}^2$ laser pulses at 798 nm

where the constant coefficient is omitted. Assuming that the plasma temperature is 1 keV, we can obtain $L/\lambda = 0.058$ from (2). Substituting this into (5), as Fig. 2a shows, we find that the maximum absorption is at $\varphi = 49.4^\circ$ and $\varphi = 310.6^\circ$. Figure 2b shows our experimental measurements, and most hot electrons are emitted at $\varphi = 50^\circ$ and $\varphi = 310^\circ$. It is shown that the angular dependence of resonance absorption is very similar to that of the emitted hot electrons. In our experiment, the sizes of the liquid droplets always have a distribution, and the laser pulses will interact with differently sized droplets. However, one finds that this maximum emission angle is independent of the droplet radius because R is not involved in (5), i.e. differently sized droplets will have the same maximum absorption angle.

Furthermore, from $\partial\alpha/\partial\varphi = 0$, we obtain the maximum absorption angle φ_{max} :

$$-\frac{8\pi L}{\lambda} |\sin(\varphi_{\text{max}})|^3 + \tan^2(\varphi_{\text{max}}) - 2 = 0. \quad (6)$$

As Fig. 3 shows, φ_{max} decreases as the scale length increases.

The total absorption fraction A is defined as the ratio of the absorbed energy and the irradiated energy on a single liquid

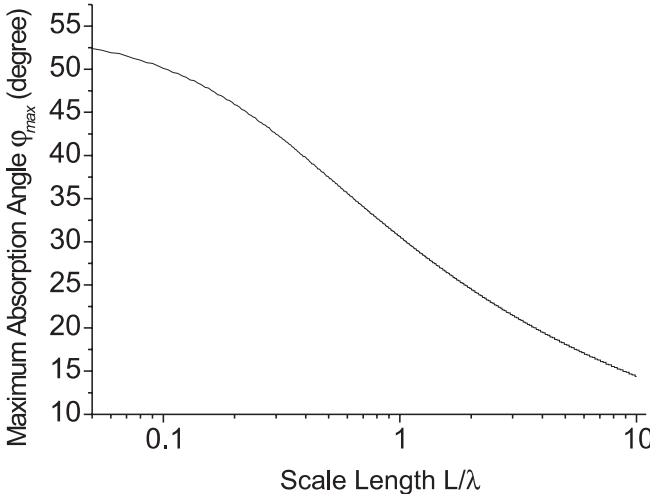


FIGURE 3 The maximum absorption angle as a function of the scale length droplet surface. It can be calculated by integrating (1):

$$\begin{aligned}
 A &= \frac{\int I_{\text{abs}} ds_{\text{eff}}}{\pi R^2 I_l} \\
 &= \frac{\varepsilon^2}{(2\pi)^{1/3} R^2} \left(\frac{L}{\lambda}\right)^{2/3} \int \sin^2 \theta \sin^2 \varphi \\
 &\quad \times \exp \left\{ -\frac{8\pi L}{3\lambda} [\cos^2 \theta + \sin^2 \theta \sin^2 \varphi]^{3/2} \right\} ds_{\text{eff}} \\
 &= \frac{\varepsilon^2}{(2\pi)^{1/3} R^4} \left(\frac{L}{\lambda}\right)^{2/3} \\
 &\quad \times \int y^2 \exp \left[-\frac{8\pi L}{3\lambda R^3} (y^2 + x^2)^{3/2} \right] dy dz \\
 &= \frac{\pi \varepsilon^2}{(2\pi)^{1/3} R^4} \left(\frac{L}{\lambda}\right)^{2/3} \int_0^R r^3 \exp \left[-\frac{8\pi L}{3\lambda} \frac{r^3}{R^3} \right] dr \\
 &= \frac{\varepsilon^2}{8} \left(\frac{2\pi L}{\lambda}\right)^{-1/3} \left[\int_0^1 \exp \left(\frac{8\pi L}{3\lambda} \zeta^3 \right) d\zeta - \exp \left(\frac{8\pi L}{3\lambda} \right) \right], \tag{7}
 \end{aligned}$$

where $\zeta = r/R$. As Fig. 4 shows, $L/\lambda = 0.17$ is the optimum value for the maximum absorption. From (2), we can show that a laser pulse with a duration of 438 fs has the strongest absorption as the irradiation on the liquid droplets remains the same.

We can also learn that this model is applicable for droplets with a diameter from 0.1 μm to 20 μm. For smaller droplets or atomic clusters under irradiation from ultrafast, high-intensity laser pulses, they quickly become underdense plasmas and cannot support enough plasma scale length for the resonance absorption. For droplets much larger than the laser focal size, we assume the result will be similar to that we observed for the case of interaction with planar targets [7].

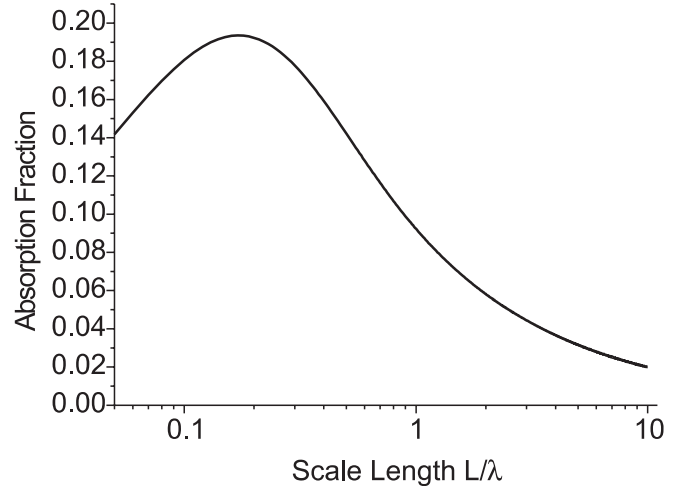


FIGURE 4 The total absorption fraction as a function of the scale length in the interaction between liquid droplets with an average radius of 5 μm and laser pulses at 798 nm

4 Conclusions

It may be concluded that resonance absorption of femtosecond laser pulses by liquid droplets can be simply estimated using an analytical model as a function of geometry and the scale length of the microplasmas generated from the liquid droplets. The angular distribution of the hot electron emission from the liquid droplets can be well understood from our model calculation. Finally, the calculation suggests that the maximum absorption occurs when the laser pulse has a duration of 438 fs at 798 nm.

ACKNOWLEDGEMENTS We are thankful for helpful discussions with Y.T. Li. This work was supported by the NSFC, Grant Nos. 60078008, 10176034, 10105014, and 10005014, the National High-Tech ICF program and the NKBRSF, under Grant No. G1999075200.

REFERENCES

- 1 E. Parra, I. Alexeev, J. Fan, K.Y. Kim, S.J. McNaught, H.M. Milchberg: Phys. Rev. E **62**, R5931 (2000)
- 2 T.D. Donnelly, M. Rust, I. Weiner, M. Allen, R.A. Smith, C.A. Steinke, S. Wilks, J. Zweiback, T.E. Cowan, T. Ditmire: J. Phys. B **34**, L313 (2001)
- 3 E.T. Gumbrell, A.J. Comley, M.H.R. Hutchinson, R.A. Smith: Phys. Plasmas **8**, 1329 (2001)
- 4 Y.T. Li, J. Zhang, Z.M. Sheng, H. Teng, T.J. Liang, X.Y. Peng, X. Lu, Y.J. Li, X.W. Tang: Phys. Rev. Lett. **90**, 165 002 (2003)
- 5 K.R. Manes, V.C. Rupert, J.M. Auerbach, P. Lee, J.E. Swain: Phys. Rev. Lett. **39**, 281 (1977); R.P. Godwin, R. Sachsenmaier, R. Sigel: Phys. Rev. Lett. **39**, 1198 (1977); J.E. Balmer, T.P. Donaldson: Phys. Rev. Lett. **39**, 1084 (1977)
- 6 D.W. Forslund, J.M. Kindel, K. Lee: Phys. Rev. Lett. **39**, 284 (1977)
- 7 L.M. Chen, J. Zhang, Y.T. Li, H. Teng, T.J. Liang, Z.M. Sheng, Q.L. Dong, L.Z. Zhao, Z.Y. Wei, X.W. Tang: Phys. Rev. Lett. **87**, 225 001 (2001)
- 8 W. Yu, J. Zhang: Opt. Commun. **134**, 91 (1997)
- 9 X.Y. Peng, Z. Jin, J. Zhang: submitted to Phys. Rev. E
- 10 W.L. Kruer: *The Physics of Laser Plasma Interactions* (Addison-Wesley Publishing Company, California 1987)

Z.-M. SHENG^{1,✉}
J. ZHANG¹
D. UMSTADTER²

Plasma density gratings induced by intersecting laser pulses in underdense plasmas

¹ Laboratory of Optical Physics, Institute of Physics, Chinese Academy of Sciences,
Beijing 100080, P.R. China

² Center for Ultrafast Optical Science, University of Michigan, Ann Arbor, MI 48109, USA

Received: 25 February 2003 / Revised version: 30 July 2003
Published online: 29 October 2003 • © Springer-Verlag 2003

ABSTRACT Electron and ion density gratings induced by two intersecting ultrashort laser pulses at intensities of 10^{16} W/cm^2 or lower are investigated. The ponderomotive force generated by the inhomogeneous intensity distribution in the intersecting region of the interfering pulses produces deep electron and ion density modulations at a wavelength less than a laser wavelength in vacuum. Dependence of the density modulation on the plasma densities, temperatures, and the ion mass, as well as the laser pulse parameters are studied analytically and by particle-in-cell simulations. It is found that the density peaks of such gratings can be a few times that of the initial plasma density and last as long as a few picoseconds. It is also demonstrated that the scattering of signal pulses by such a bulk density grating results in high-harmonic generation. The density gratings may be incorporated into ion-ripple lasers [K.R. Chen and J.M. Dawson, Phys. Rev. Lett. **68**, 29 (1992)] to generate ultrashort X-ray pulses of a few angstroms by using electron beams at only a few tens of MeV only.

PACS 52.35.Mw; 42.65.Ky; 52.25.Os

1 Introduction

Nonlinear effects in plasmas involving multiple laser beams has been a subject attracting increasing attention in recent years. A few novel features have been found in various interaction configurations. These include the degenerate four wave mixing and phase-conjugating reflection [1], the superradiant amplification of an ultrashort laser pulse by a counter-propagating long pulse [3, 4], and electromagnetically induced guiding of counter-propagating laser pulses in a plasma [5], energy exchange of two intersecting laser beams in a streaming plasma [6, 7], braiding and hosing of two co-propagating beams [8, 9], etc. The interactions of two laser pulses in plasmas also finds applications in particle acceleration through the plasma beat-wave excitation [10], wake-field excitation of pulse trains [11], laser injection of electrons [12], colliding beam acceleration [13], crossed-modulated laser wake-fields [14], and stochastic heating and acceleration [15], etc.

Recently, it has been shown that when two laser beams intersect at an overdense plasma surface, a grating-like electron density modulation is induced [16]. In the case of a single laser pulse interacting with a solid target, it has been shown that the incident and specularly reflected electromagnetic waves can also drive such a density modulation [17]. The oscillating component of the density modulation can serve as a moving mirror, which can efficiently convert the incident pulse into its high-harmonics, as shown theoretically and by simulations [18–20], and demonstrated experimentally [21–25]. Moreover, the slowly varying density modulation can act as a diffraction grating back-reflecting the incident pulse [17]. It should be noted that laser-induced gratings in various optical media have been studied extensively before [26]. Recently, laser-induced gratings have found new applications, such as the fabrication of periodic lateral nanostructures on semiconductor surfaces, laser surface modification, ultrafast optical switching, and laser-induced grating spectroscopy, etc. [27–30]. In underdense plasma, the bulk density modulations may find applications in the phase-matched relativistic harmonic generation [31], backward-wave oscillators [32], and the ion-ripple lasers [33, 34], where the latter may be used to generate X/ γ -ray radiation. By use of refractive index gratings induced by counter-propagating intense laser pulses in a gas jet, quasi-phase-matched high-harmonic generation has been suggested [35, 36]. Obviously, an investigation of the electron and ion density gratings induced by two laser pulses in underdense plasma is necessary for some applications mentioned above.

This paper studies the formation of deep electron and ion density gratings in underdense plasma ($n_0/n_c \sim 0.01 - 0.5$) by use of two short counter-propagating/intersecting laser pulses at moderate intensities. In this case, one obtains bulk density gratings rather than surface gratings as in laser interaction with overdense plasma [16, 17]. Bulk plasma density gratings induced by infinite plane electromagnetic waves have been analyzed even earlier by M. Botton and A. Ron [32], where a stationary solution of the density modulation is given by assuming quasi-charge-neutrality in the interaction. The ion dynamics has been neglected, as well as in surface density grating formation [16, 17], where the electron density modulation is determined by assuming that the electrostatic force on the electrons is compensated by the ponderomotive force. Here, without these assumptions, the electron and ion dynam-

ics during the buildup of the density gratings are studied analytically and by particle-in-cell simulations. It was found that ion motion has important effects in the formation of the density gratings after the laser pulse interaction, even though the intensities of the ultrashort pump laser pulses are just around $10^{16} \text{ W cm}^{-2}$. Significant ion motion occurs in a time scale of $(M/m)^{1/2}(I_{18}\lambda^2)^{-1/2}\omega_0^{-1}$, which is around a few tens of laser cycles, $2\pi/\omega_0$, for the ion-electron mass ratio $M/m = 1800$ and laser intensity of $10^{16} \text{ W cm}^{-2}$. Here the laser intensity multiplied by the wavelength squared is normalized by $10^{18} \text{ W cm}^{-2} \mu\text{m}^2$.

In Sect. 2, the problem is studied analytically. Solutions of electron and ion density gratings at the linear stage will be given. A stationary solution is derived under the quasi-charge-neutrality condition, which is used to compare with the particle-in-cell (PIC) simulations. Section 3 presents the PIC simulations of the density grating formation for different parameters of the laser pulses and plasma. In Sect. 4 examples of the scattering of signal pulses by the preformed density gratings are shown. Emission of high-frequency radiation is observed. A summary is given in Sect. 5 with a discussion on the potential application of such density gratings to the ion-ripple laser.

2 Formulations of the problem

For simplicity, assume that two plane laser pulses counter-propagate along the x -axis. Since the focus of interest is in the induced plasma density modulation, the evolution of the laser pulses can be neglected for simplicity. As a result, the density modulation is governed by the following set of equations:

$$\partial p_{e,x}/\partial t = c\partial(\varphi - \bar{\gamma})/\partial x, \quad (1)$$

$$\partial n_e/\partial t + c\partial(n_e v_{e,x})/\partial x = 0, \quad (2)$$

$$\partial p_{i,x}/\partial t = -c(m/M)\partial\varphi/\partial x, \quad (3)$$

$$\partial n_i/\partial t + c\partial(n_i v_{i,x})/\partial x = 0, \quad (4)$$

$$\partial^2\varphi/\partial x^2 = (\omega_p^2/c^2)(n_e - n_i), \quad (5)$$

where n_e and n_i are the electron and ion densities normalized by the unperturbed density n_0 , respectively, φ is the scalar potential normalized by mc^2/e , $v_{e,x}$ and $v_{i,x}$ are the x -components of the electron and ion velocities normalized to the vacuum speed of light c , $p_{e,x}$ and $p_{i,x}$ are the x -components of the electron and ion momenta normalized by mc and Mc , respectively. Here m and M are the rest masses of electron and ion, respectively. Also, $\omega_p^2 = 4\pi n_0 e^2/m$ is the electron plasma frequency. The simplified equations of motion (1) and (3) have been used following the derivation given in [37, 38]. For laser pulses at intensities well below the relativistic threshold of about 10^{18} W/cm^2 , the relativistic factor can be written approximately as $\bar{\gamma} = 1 + \frac{1}{4}[a_1^2 + a_2^2 + 2a_1a_2 \cos(2kx)]$, where $k = k_0(1 - n_0/n_c)^{1/2}$ is the laser wave vector in plasma, with $k_0 = \omega_0/c$ is the laser wave vector in vacuum. As a result, the normalized ponderomotive force is $F/(mc^2k_0) = -(c/\omega_0)(\partial\bar{\gamma}/\partial x) = (kc/\omega_0)a_1a_2 \sin(2kx)$, if ignoring the finite pulse profile. Note that the ponderomotive force on ions in (3) is also neglected, which is smaller than the electrostatic field by the order of $O(m/M)$.

At the very beginning of the interaction of an ultrashort laser pulse with plasma, one can ignore the ion motion and assume a weak density perturbation of electrons. Letting $\delta n_e = n_e - 1$, obtains

$$\frac{\partial^2\delta n_e}{\partial t^2} + \omega_p^2\delta n_e = c^2\frac{\partial^2}{\partial x^2}\bar{\gamma}. \quad (6)$$

Assuming that there is no density perturbation at the beginning: $\delta n_e|_{t=0} = 0$ and $\partial\delta n_e/\partial t|_{t=0} = 0$, obtains

$$\delta n_e = -(2k^2c^2/\omega_p^2)a_1a_2 \cos(2kx)[1 - \cos(\omega_p t)], \quad (7)$$

and $\varphi = -(\omega_p^2/4k^2c^2)\delta n_e$. This approximation breaks down when $\delta n_e \sim 1$ or $t > (2k^2c^2a_1a_2)^{-1/2}$. For $a_1 = a_2 = 0.1$, the time scale is about 1 laser cycles. Within this limitation, substituting φ and $\bar{\gamma}$ into (1), one obtains $p_{e,x} = (kc/\omega_p)a_1a_2 \sin(\omega_p t) \sin(2kx)$. In the generated electrostatic field, one finds that the ions move with $p_{i,x} = (kc/\omega_p)(m/M) \times a_1a_2 \sin(2kx)[\omega_p t - \sin(\omega_p t)]$ and the ion density perturbation changes like

$$\delta n_i = -(k^2c^2/\omega_p^2)(m/M)a_1a_2 \cos(2kx) \times \left\{ \omega_p^2 t^2 - 2[1 - \cos(\omega_p t)] \right\}. \quad (8)$$

Comparing (7) and (8), it is clear that the modulation of the ion density is in phase with that of the electron density. They form a bulk grating-like structure with a wavelength of π/k . The time for building up significant ion density perturbations is $t \sim (M/m)^{1/2}(k^2c^2a_1a_2)^{-1/2}$, which scales like $(M/m)^{1/2}$. For $a_1 = a_2 = 0.1$ and $M/m = 1836$, it is within a time less than 100 laser cycles. Thus, the evolution of both the electron and ion density perturbations enters the nonlinear stage very quickly, and one has to resort to numerical simulations to obtain a complete picture about the grating-like density modulation.

For infinite plane waves, the stationary solution can be found. For this, one needs to add a thermal pressure term on the right-hand-sides of (1) and (3) with $-\partial P_{eT}/\partial x/(n_e mc)$ and $-\partial P_{iT}/\partial x/(n_i Mc)$, respectively. For a stationary solution, one has $\partial p_{e,x}/\partial t = 0$ and $\partial p_{i,x}/\partial t = 0$ on the left-hand-sides of (1) and (3), respectively. Meanwhile, there should be quasi-charge-neutrality for a long time, i.e., $Zn_i \approx n_e$. Assuming it is an isothermal process [39], one finds $\varphi = (\bar{\gamma} - 1)\varepsilon/(1 + \varepsilon)$ and $Zn_i = n_e = n_s \exp[-\mu \cos(2kx)]$ with $\mu = a_1a_2/[2\varepsilon_e(1 + \varepsilon)]$, $\varepsilon = T_i/ZT_e$, $\varepsilon_e = k_B T_e/mc^2$, Z is the ion charge number, T_e and T_i are the electron and ion thermal temperatures, respectively, and n_s a constant needing determination. This density profile is quite similar to that obtained by Botton and Ron [32]. Now, from the Poisson's equation (5), one can find that the quasi-charge-neutrality is satisfied if $(k^2c^2/\omega_p^2)a_1a_2\varepsilon \ll 1$. After normalization with the help of particle number conservation, one finds $n_s = 1/I_0(\mu)$ with I_0 the modified zero-order Bessel function. Using $I_0(\mu) \approx (2\pi\mu)^{-1/2} \exp(\mu)$ for $\mu \gg 1$, one obtains

$$Zn_i \approx n_e \approx (2\pi\mu)^{1/2} \exp\{-\mu[1 + \cos(2kx)]\} = (2\pi\mu)^{1/2} \exp[-2\mu \cos^2(kx)], \quad (9)$$

which are normalized by the unperturbed density, n_0 . This relation shows that the maximum plasma density is $n_{\max} =$

$\sqrt{2\pi\mu}$ and the width of the density peak around $2kx = (2N + 1)\pi$ is $k\Delta x = 1/\sqrt{2\mu}$. Note that they are associated only with the combined variable μ , a quantity depending upon the laser amplitudes and the electron and ion temperatures. For example, if $a_1 = a_2 = 0.1$, $T_e = 10$ eV, and $T_i = 1$ eV, one obtains $n_{\max} = 38.2n_0$. If taking $T_e = 100$ eV accounting for electron heating by the induced electrostatic field, one obtains $n_{\max} = 12.6$. However, these maximum densities prove to be overestimated when compared with the simulation results given below.

3 Particle-in-Cell simulations

Since the interaction of crossing laser pulses with plasma involves deep plasma density modulations even if the intensities of the laser pulses are very low, such as 10^{15} W/cm², PIC simulations are used to study the buildup process of the plasma density gratings. For simplicity, simulations with a one-dimensional code are conducted. The simulation box has a dimension of 100λ with λ the laser wavelength in vacuum. A homogeneous plasma is located in the central region of the simulation box as shown in Fig. 1a. Two laser pulses with the same frequency ω_0 are launched from the two boundaries of the simulation box. They have the profiles $a_1 = a_{10} \sin^2(\pi t/t_L)$ and $a_2 = a_{20} \sin^2(\pi t/t_L)$ with $0 \leq t \leq t_L$ for the vector potential. Figure 1b shows the interaction geometry of two counter-propagating pulses in the simulation box, where $a_{10} = a_{20} = 0.1$ and $t_L = 60\tau$ for the laser pulses, and $n_0/n_c = 0.3$ for the plasma density. Here $\tau = 2\pi/\omega_0$ is the period of a laser cycle. The initial electron and ion temperatures are $T_e = 10$ eV and $T_i = 1$ eV, respectively. The mass ratio of ions to electrons is taken to be $M/m = 1836$ and the ion charge number to be $Z = 1$ in the simulations.

Figure 2 illustrates the buildup process of electron and ion density gratings for the laser and plasma parameters given in Fig. 1. Note that density peaks up to 4.6 times of the initial plasma density are produced both for electrons (Fig. 2a) and ions (Fig. 2b) at $t = 250\tau$, even though it is still much less than

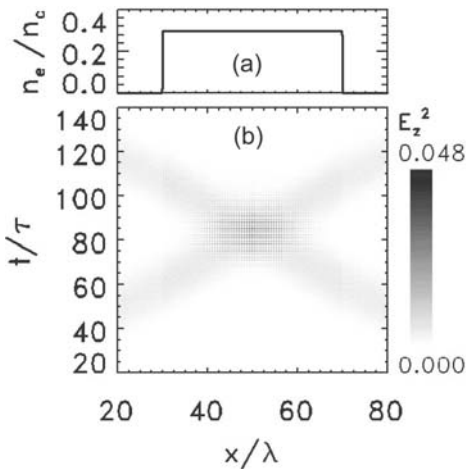


FIGURE 1 (a) This shows the initial plasma density distribution used in the simulations, where the peak density is $n_0/n_c = 0.3$; (b) shows the propagation of two counter-propagating pulses (called pump pulses) in the simulation box, where the two pulses are identical with a peak amplitude $a_{10} = a_{20} = 0.1$ and a duration $t_L = 60\tau$, where τ is the laser period of the pump pulses

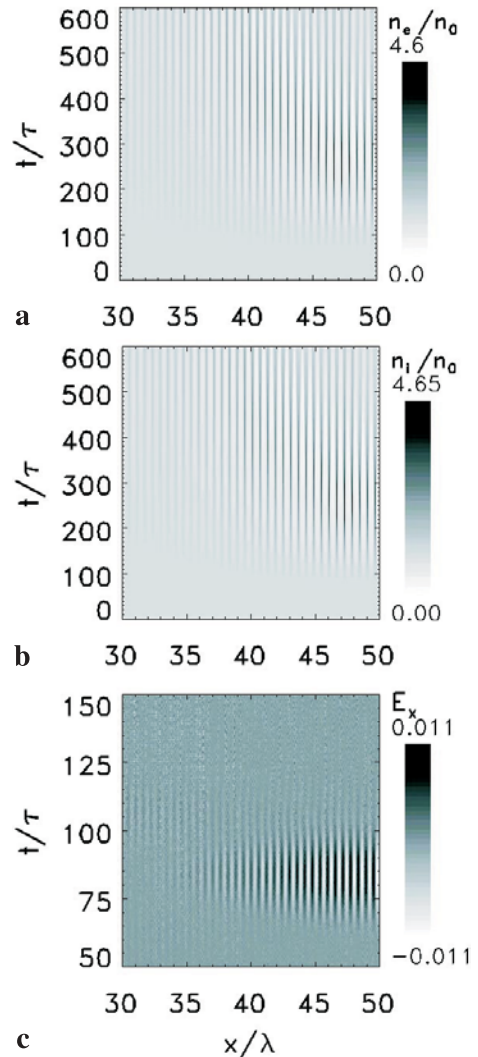


FIGURE 2 Evolution of the electron density, n_e/n_0 (a), the ion density, n_i/n_0 (b), and the induced electrostatic field, E_x (c) for plasma and laser pulse parameters as those given in Fig. 1. Note that there is symmetry around $x/\lambda = 50$ within $30 \leq x/\lambda \leq 70$

that estimated from the stationary solution given by (9). Electrostatic fields are found only during the intersecting stage of the two pulses as shown Fig. 2c. The maximum electrostatic field is found to be $E_{x,\max}/(m\omega_0 c/e) = 0.01$ when the peaks of the two pulses are crossing each other at $t = 80\tau$. Its value is weakly dependent on the plasma density and is comparable to the ponderomotive force, i.e.,

$$\begin{aligned} \frac{E_{x,\max}}{m\omega_0 c/e} &\approx \frac{c}{\omega_0} \frac{\partial \bar{\gamma}}{\partial x} \Big|_{\max} = \left(\frac{kc}{\omega_0} \right) a_{1m} a_{2m} \\ &= \frac{kc}{\omega_0} \frac{4}{(1+k/k_0)^2} a_{10} a_{20} \sim a_{10} a_{20}. \end{aligned} \quad (10)$$

Here a_{1m} and a_{2m} are the peak amplitudes of the incident pulses in the plasma, which are related to their corresponding values in vacuum by $a_{1m} = [2/(1+k/k_0)]a_{10}$ and $a_{2m} = [2/(1+k/k_0)]a_{20}$, assuming $k/k_0 = (1 - n_0/n_c)^{1/2} \sim 1$ still holds for underdense plasma, and $a_{10} \ll 1$ and $a_{20} \ll 1$ for low laser intensities. Quasi-charge-neutrality is realized quickly after the laser pulses propagate away, even though the grat-

ings are further deepened afterwards. This deepening process has been caused by the ion motion. During the laser crossing stage, electrons are pushed first by the ponderomotive force of the laser interference. As a result, electrostatic fields are induced. Ions are then pushed by the electrostatic fields before the quasi-charge-neutrality is realized. It is obvious that the formed density grating only occupies a region where the two pulses overlap. Figure 3 shows snapshots of the distributions of electron and ion momenta and the electron density. Around $t = 130\tau$, one finds full plasma neutralization, i.e., $n_e \approx n_i$ and $E_x \sim 0$. Therefore, ions already reach the maximum acceleration, even though the density grating is not very deep. The maximum velocity is about $0.00086c$, i.e.,

$$v_{i,\max} \sim kct_L(m/M)a_{10}a_{20}, \quad (11)$$

which basically corresponds to the calculation given in the last section. Later on, the electron density follows the ion density to maintain the quasi-charge-neutrality while the maximum ion density becomes higher and higher due to the ion motion, as shown in Fig. 3b. At later times, intercrossing of the neighboring ions set in around the density peaks, and the structures of ion density gratings begin to break. As a result, the density gratings of both electrons and ions decay with time afterwards.

A series of simulations were conducted to see the dependence of the grating formation on the initial plasma density, plasma temperature, laser pulse intensities, and their durations. First, when one changes the initial plasma density from

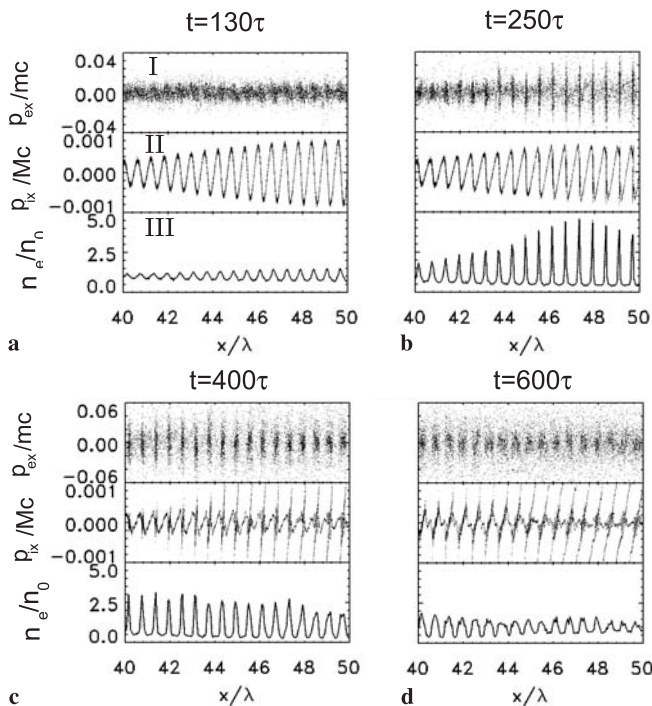


FIGURE 3 Snapshots of the longitudinal components of electron (frame I) and ion (frame II) momenta as well as the electron (in solid lines) and ion (in dotted lines) densities (frame III) at different times. The parameters for the plasma and laser pulses are the same as in Fig. 2. Note that one cannot distinguish the distribution of the ion density from that of the electron density plotted in this scale, indicating that a quasi-charge-neutrality state is achieved at these times

$n_0/n_c = 0.01$ to 0.5 , there is not much change in the formation of the density gratings. This agrees with the analysis given in the last section. For example, if the initial plasma density is set to be $n_0/n_c = 0.04$, this produced very similar results as for $n_0/n_c = 0.3$: the maximum electrostatic field is found to be about 0.01 at $t = 80\tau$ when the two pulse peaks cross each other, which follows (10); the peak ion velocity is found to be about $0.00085c$, around $t = 130\tau$, when the electrostatic field begins to disappear, which follows (11); the maximum density of the grating is about $4.2n_0$ around $t = 250\tau$.

In another case, the initial electron and ion temperatures were increased to $T_e = 100$ eV and $T_i = 10$ eV. In this case, it was found that the maximum density of the grating reduces to $2.7n_0$ around $t = 240\tau$. It is apparent that thermal pressure plays the role of reducing the density peaks, qualitatively in agreement with the theory in Sect. 2. Other results are similar to those given before. When increasing the ion mass to $M/m = 3672$ while keeping other parameters fixed, it is found that the maximum electrostatic field is found to be still 0.01

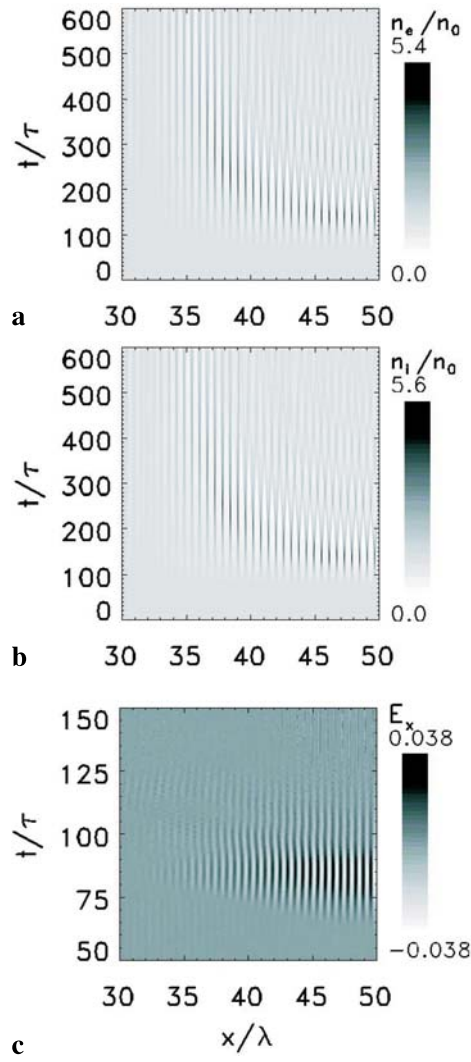


FIGURE 4 Evolution of the electron density, n_e/n_0 , (a) the ion density, n_i/n_0 , and (b) the induced electrostatic field, E_x (c) for plasma and laser pulse parameters as those given in Fig. 1, except for the pulse amplitudes $a_{10} = a_{20} = 0.2$. Note that there is symmetry around $x/\lambda = 50$ within $30 \leq x/\lambda \leq 70$

around $t = 80\tau$. The maximum ion velocity is about $0.00043c$ at $t = 120\tau$, in consistency with (11). As a result, it takes longer time to reach the maximum density. The maximum density of the grating reduces to $3.7n_0$ at $t = 400\tau$.

When increasing the pulse durations to $t_L = 90\tau$ while keeping the other parameters the same as in Fig. 2, it is found the maximum density of the grating increases to $5.3n_0$ at $t = 220\tau$. The maximum electrostatic field is found to be still 0.01 around $t = 100\tau$ when the peaks of the two pulses overlap each other. The maximum ion velocity is about $0.0013c$ at $t = 180\tau$, which is consistent with the fact that it is proportional to the pulse durations as shown by (11).

When increasing the pulse peak amplitudes to $a_{10} = a_{20} = 0.2$ while keeping other parameters fixed, the induced maximum electrostatic field is found to be about 0.038 around $t = 80\tau$. The maximum ion velocity is about $0.0032c$ at $t = 120\tau$. Again these are consistent with (10) and (11). The maximum density of the grating increases to $5.5n_0$ at $t = 130\tau$. Figure 4 shows the electron and ion densities, as well as the electrostatic field as a function of time and space. It demonstrates that the density grating decays with time more quickly than those obtained with lower light intensities. This is because of the high ion velocity so that the intercrossing of neighboring ions around the density peaks occurs more quickly. Figure 5 shows snapshots of the electron and ion momenta and the electron density. They are qualitatively similar to those given in Fig. 3. Note that when further increasing the pulse amplitudes, the peak amplitudes of the density gratings decrease. They also decay more quickly owing to the higher electron and ion velocities obtained during the interactions.

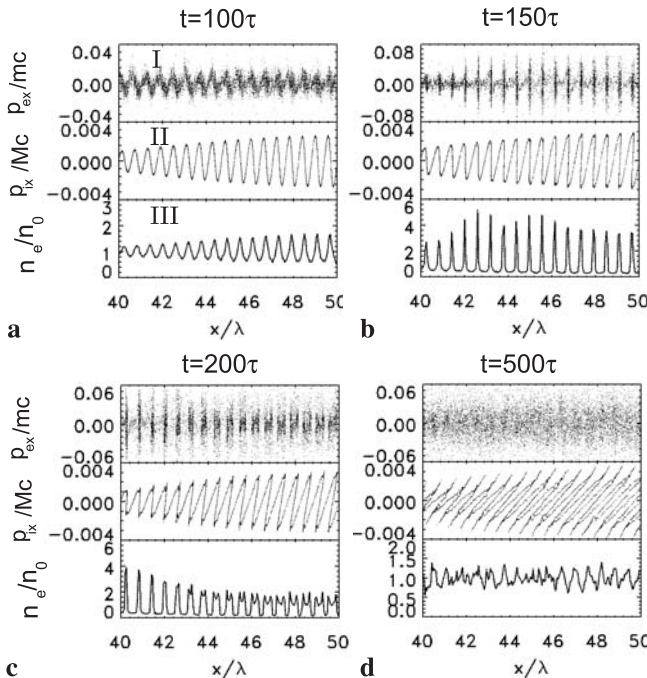


FIGURE 5 Snapshots of the longitudinal components of electron (frame I) and ion (frame II) momenta as well as the electron (in solid lines) and ion (in dotted lines) densities (frame III) at different times. The parameters for the plasma and laser pulses are the same as those in Fig. 4. Note that one cannot distinguish the distribution of the ion density from that of the electron density plotted in this scale, indicating that a quasi-charge-neutrality state is established at these times

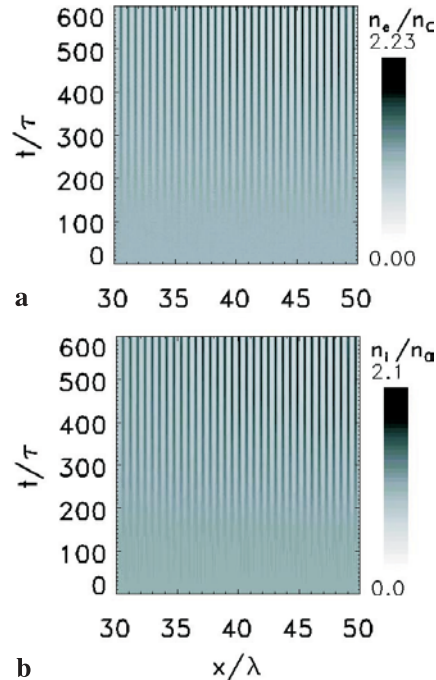


FIGURE 6 The evolution of the electron density, n_e/n_0 (a), and the ion density, n_i/n_0 (b) for similar plasma and laser pulse parameters as those given in Fig. 1, except for the pulse amplitude $a_{10} = a_{20} = 0.03$. Note that there is symmetry around $x/\lambda = 50$ within $30 \leq x/\lambda \leq 70$

Finally when reducing the pulse peak amplitudes to $a_{10} = a_{20} = 0.03$ while keeping other parameters unchanged from Fig. 2, it is found that a homogeneous density grating can be formed which subsists as long as a few picoseconds. The maximum density of the grating is about $2.2n_0$ at $t = 450\tau$ as shown in Fig. 6. The maximum ion velocity is about $0.0002c$ at $t = 400\tau$. Therefore, one can use laser pulses at intensities of 10^{15} W/cm^2 to generate long lasting density gratings for potential applications.

4 Examples of laser pulse scattering with density gratings and high-frequency radiation generation

Naturally it could be assumed that the bulk plasma density gratings as a kind of stratified index layers can scatter light as acoustic waves do in acousto-optic modulators [40]. To check this, first a density grating was produced such as given in Fig. 2, except for an initial plasma density of $n_0 = 0.5n_c$. The resulting density grating is similar to that given in Fig. 2; however, its maximum density exceeds the critical density associated with the pump pulses. Then a signal pulse with a duration of a few laser cycles and a peak amplitude of $a_{s0} = 0.01$ is launched into the density gratings from the left boundary. This signal pulse is incident with a polarization different from that of the pump pulses and with a central frequency $\omega_{s0} = 0.8\omega_0$. Figure 7a shows the backscattered light wave. Obviously it is composed of three parts. The first part is due to the left vacuum-plasma boundary, the second part is due to the electron density grating formed inside the plasma, and the third part is due to the right plasma-vacuum boundary. By taking Fourier transforms of these three parts, their frequency spectra are obtained, as shown in Fig. 7b. It was

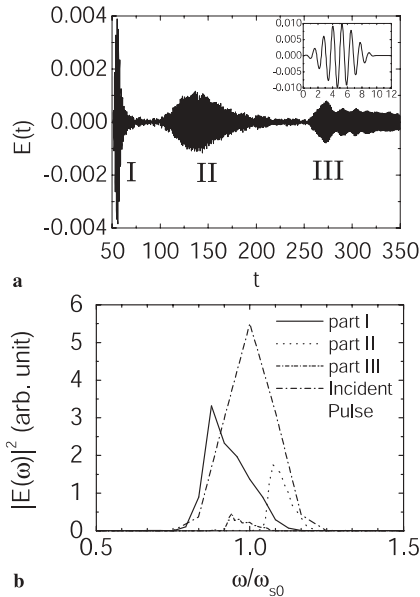


FIGURE 7 **a** Backscattered light of a short signal laser pulse (see *inserted frame*) from the density grating formed by the two pump laser pulses with the same parameters as those given in Fig. 1 and an initial electron density $n_0 = 0.5n_c$; The signal pulse is incident with a peak amplitude $a_{s0} = 0.01$ at the central frequency $\omega_{s0} = 0.8\omega_0$ and with a polarization different from the pump pulses. **b** Spectra of the different parts of the backscattered light

found that the frequency spectra of the parts I and III of the reflected wave are all slightly red-shifted, and the spectrum of part II appears slightly blue-shifted. These shifts may be attributed to the wide spectrum of the incident signal pulse of a few cycles, which extends down to the unperturbed electron plasma frequency $\omega_p = 0.707\omega_0$. Qualitatively, since the low frequency component of the signal pulse has a high reflectivity at the vacuum-plasma boundary, one observes the red-shifted parts I and III. Inside the density grating, the peak density is higher than the unperturbed density and the criti-

cal density associated with the central frequency of the signal pulse. Thus the high frequency component of the signal pulse can be reflected, leading to the blue-shifted part II. In addition, part III has a slightly higher frequency than part I. This is due to the presence of the density grating in the center, which tends to block the lower frequency component. Note that most of the signal pulse is still transmitted through the plasma slab with its central frequency unshifted.

If the amplitude of the signal pulse is increased, nonlinear scattering occurs, resulting in high-frequency radiation emission and breakdown of the bulk density grating. Figure 8 shows the spectra of the backscattered (a, and c) and transmitted (b, and d) light for $a_{s0} = 0.3$, $\omega_{s0} = 0.8\omega_0$, and $t_L = 60\tau$. When the unperturbed plasma density is relatively low such as $n_0 = 0.1n_c$, one observes emissions close to the harmonics of the pump pulse (at frequency ω_0) in the backscattered light. The spectrum of the transmitted light is still mainly peaked at the frequency of the incident signal pulse (see Fig. 8b). With the increase of the initial unperturbed plasma density, high-frequency components are observed both in the backscattered and transmitted light. Their frequencies are, however, shifted from the harmonic order of both the pump pulse and signal pulse (see Figs. 8c and d). Note that, at the same light intensity, the efficiency of high-frequency radiation generation is larger than that of relativistic laser harmonics in homogeneous underdense plasma [41], and is comparable to that of laser harmonics from solid surfaces [18–20].

In the next example, a plasma density grating with two pulses intersecting under 90 degrees was generated. In the two-dimensional(2D) PIC simulations, the two pump pulses are *s*-polarized (with electric component in *z* direction) and propagate along *x* and *y* directions, respectively. The pump pulses all have a peak amplitude of 0.2, a duration of 80τ , and are focused to 30λ in diameter. The initial plasma density is $n_0 = 0.5n_c$. Figure 9a shows the induced ion density grating at $t = 200\tau$. The electron density is almost the same as

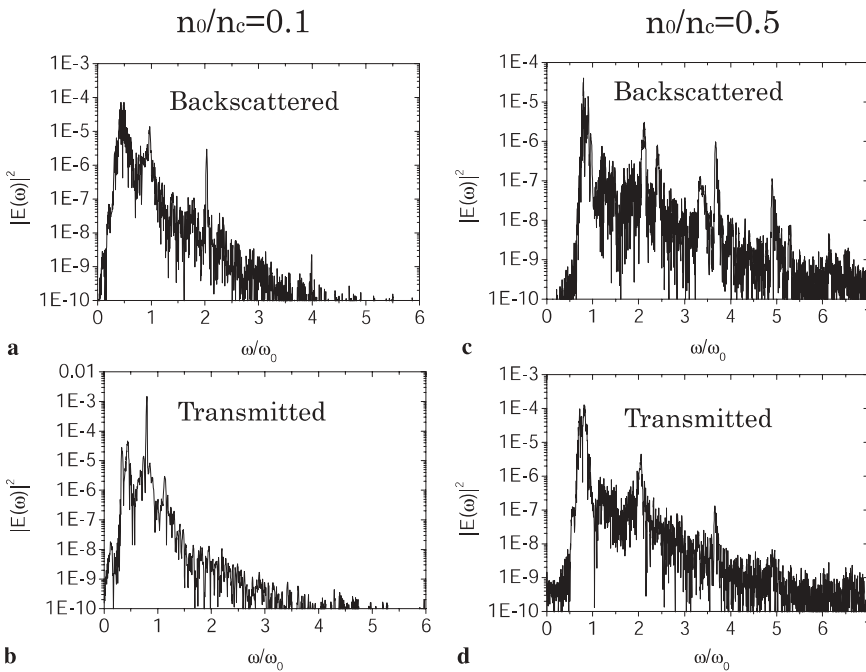


FIGURE 8 Spectra of backscattered and transmitted pulses in a density grating formed by two laser pulses with the same parameters as those given in Fig. 1. The signal pulse has $a_{s0} = 0.3$, $\omega_{s0} = 0.8\omega_0$, and $t_L = 60\tau$. Frames **a** and **b** show the backscattered and transmitted spectra, respectively, for the case with $n_0 = 0.1n_c$; frames **c** and **d** show the backscattered and transmitted spectra, respectively, for the case with $n_0 = 0.5n_c$

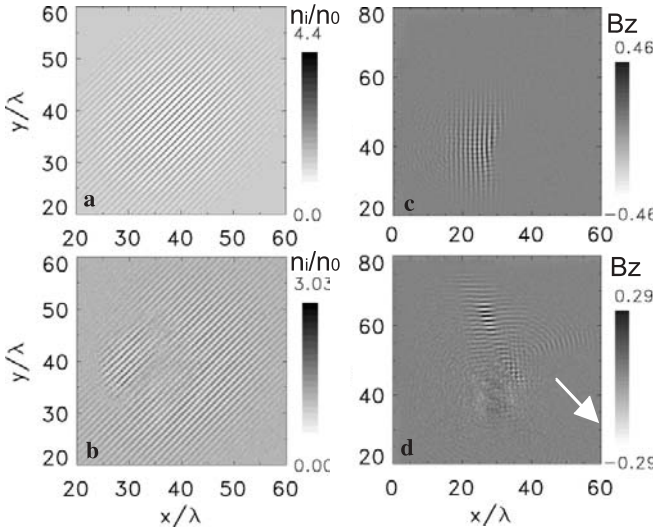


FIGURE 9 2D PIC simulations of the density grating induced by two s-polarized pump pulses, one along the x -direction and another along the y -direction. Both the pump pulses have a peak amplitude $a_{10} = a_{20} = 0.2$ and a duration of 80τ , and are focused to 30λ in diameter. The initial plasma density is $n_0 = 0.5n_c$. The signal pulse is incident with p -polarization along the x -axis, with a delay of 150τ relative to the pump pulses, and with a peak amplitude $a_{s0} = 0.3$, and is focused diameter of 20λ . **a** Ion density at 200τ ; **b** Ion density at 300τ ; **c** Signal pulse at 200τ ; **d** Signal pulse at 240τ . The arrow in frame (d) shows the propagation direction of the emission near the second harmonic

the ion density at this time. A signal pulse is launched along the x -direction, which has a time delay of 150τ relative to the pump pulses. The signal pulse is p -polarized with the same central frequency as the pump pulses $\omega_{s0} = \omega_0$ and has a duration of about 30τ , a peak amplitude of 0.3, and a focused diameter of 20λ . Figure 9b shows the ion density after interaction, which is found to be deformed after the interaction. Figure 9c displays a snapshot of the magnetic field, B_z , of the incident signal pulse interacting with the density grating at $t = 200\tau$. This B_z field allows us to distinguish the signal pulse from the pump pulses. Figure 9d shows the distribution of the magnetic field component, B_z , of the signal pulse after interaction with the density gratings at $t = 240\tau$. It is found that a significant part of the signal pulse is scattered along the y -direction. A small amount of energy is still transmitted through the density grating even if the density peak in the grating is twice the critical density. From the Fourier transforms of the scattered and transmitted parts of the pulse, their frequency spectra are obtain as shown in Fig. 10. Here Fig. 10a shows the spectrum of the scattered wave through the top y -boundary in the simulation box and Fig. 10b the spectrum of the transmitted wave through the right x -boundary. It appears that after the interaction, there is a new frequency around $1.7\omega_0$ both in the scattered and transmitted light. Moreover, there is one emission near the second harmonic through the low right x -boundary, which has the same polarization as the signal pulse. This can be seen also in Fig. 9d. Qualitatively, similar features of the spectra for the scattered and transmitted light are observed as in 1D PIC case.

Up to now, however, the physical origins of the high-frequency emissions are still not clear. They are possibly related to the electron oscillation inside the bulk gratings driven by the signal pulse. There may also be some instability of the

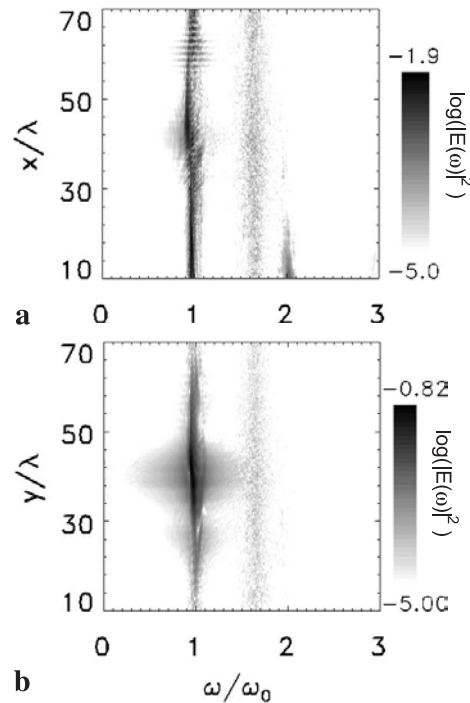


FIGURE 10 Spectra ($|E(\omega)|^2$ in logarithmic scale) of the transmitted light through the right x -boundary (**a**) and scattered light through the top y -boundary (**b**) as obtained in a 2D PIC simulation for laser and plasma parameters as those given in Fig. 9

density grating under the signal pulse interaction. In a few other simulations, it is found that the spectra are related with the duration and intensity of the signal pulse. An identification of the physical mechanism of the emission is still quested.

5 Summary and discussions

The generation of deep plasma density gratings caused by two intersecting laser pulses at moderate intensities has been studied. It is produced through the interference of the two pulses which results in an intensity interference pattern. Since the distance between the intensity peaks can be less than a laser wavelength, a huge ponderomotive force is produced which drives electrons out of the high-intensity regions. As a result, electrostatic fields are induced. The maximum electrostatic field is found when the pump pulse peaks overlap, which depends mainly on the peak amplitudes of the pulses and more weakly on the initial plasma density. The ions build up velocities in the induced electrostatic field before the quasi-charge-neutrality is established in a time proportional to the pulse duration. Later on, electrons move and follow ions in a way so as to maintain the quasi-charge-neutrality. The maximum densities of electrons and ions in the formed grating are reached just before the on-set of the intercrossing of neighboring ions near the density peaks. Afterwards, with the intercrossing of neighboring ions, the density gratings decay with time. It was found that the maximum densities of electrons and ions depend on the pulse amplitudes and plasma temperatures. The analytic solutions agree qualitatively with the particle-in-cell simulations, even though the quasi-stationary solution (9) usually overestimates the maximum densities of

the induced gratings. If one uses pulses at a low intensity, such as a few 10^{15} W/cm^2 , and a few hundred femtoseconds, the produced density gratings can last as long as a few tens of picoseconds.

When a signal pulse propagates in such a density gratings, it is found that the pulse can still be partially transmitted even if the peak density of the density grating exceeds the critical density. The pulse is also strongly scattered by the density grating. In addition to the radiation at the frequency of the original signal pulse, radiations also exist at higher frequencies both in the scattered and transmitted waves. Their physical origin is not clear. They are possibly related to electron oscillations driven by the signal pulse in the density gratings.

A possible application of the produced density gratings is in the ion-ripple laser as proposed by Chen and Dawson [34]. It is supposed to be able to generate radiation at the resonant frequency $\sim 2\gamma_b^2 K_g c \cos \theta$, where γ_b is the relativistic factor of the incident electron beam, K_g is the wave number of the density grating, θ is the incident angle of the electron beam against the grating vector. It is obvious that very high-frequency radiation in the hard X-ray regime at a few angstroms in wavelength can be generated with electron beams at a few tens of MeV if such density gratings discussed above are employed. Since the density modulation is nearly 100% in our case, it is expected that the growth rate and the efficiency can increase significantly as compared with the primary scheme of ion-ripple lasers by use of an acoustic grating. Moreover, harmonics of the above mentioned resonant frequency can be generated owing to the deep modulation in the density gratings, where the latter also contains harmonics at wave numbers NK_g . However, a theoretical analysis of this problem is still required, with plasma density gratings produced in such a way as discussed in this paper.

ACKNOWLEDGEMENTS We wish to thank Dr. X. Lu, Dr. J.A. Zheng, and many colleagues in the laboratory for some useful discussions on this work. This work has been supported in part by the National Natural Science Foundation of China (Grant Nos. 10105014, 19825110, 10075075), the Bairen Jihua Program of the Chinese Academy of Sciences, the National High-Tech ICF Committee in China, National Key Basic Research Special Foundation (NKBRSF) under Grant No. G1999075200, and the U.S. National Science Foundation.

NOTE ADDED IN PROOF Related works on the interaction of intersecting laser pulse in underdense plasma in the high-intensity regime can be found in recent publications: P. Zhang et al., Phys. Plasmas **10**, 2093 (2003) and Phys. Rev. Lett. (to be published).

REFERENCES

- 1 I. Nebenzahl, A. Ron, N. Rostoker: Phys. Rev. Lett. **60**, 1030 (1988)
- 2 J.X. Ma, R. Chen, Z. Xu, J. Op. Soc. Am. B **8**, 1442 (1991)
- 3 G. Shvets, N.J. Fisch, A. Pukhov, J. Meyer-ter-Vehn: Phys. Rev. Lett. **81**, 4879 (1998); Y. Ping, I. Geltner, N.J. Fisch, G. Shvets, S. Suckewer: Phys. Rev. E **62**, R4532 (2000)
- 4 V.M. Malkin, G. Shvets, N.J. Fisch: Phys. Plasmas **7**, 2232 (2000)
- 5 G. Shvets, A. Pukhov: Phys. Rev. E **59**, 1033 (1999)
- 6 C.J. McKinstrie, J.S. Li, R.E. Giaccone, H.X. Vu: Phys. Plasmas **3** 2686 (1996); ibid. **5**, 1142 (1998)
- 7 W.L. Kruer, S.C. Wilks, B.B. Afeyan, R.K. Kirkwood: Phys. Plasmas **3**, 382 (1996); V.V. Eliseev, W. Rozmus, V.T. Tikhonchuk, C.E. Capjack: ibid. **3**, 2215 (1996); H.A. Rose, S. Ghosal, ibid. **5**, 1461 (1998); C. Labaune, H.A. Baldis, B. Cohen, W. Rozmus, S. Depierreux, E. Schi-fano, B.S. Bauer, A. Michard: ibid. **6**, 2048 (1999); K.B. Wharton, R.K. Kirkwood, S.H. Glenzer, K.G. Estabrook, B.B. Afeyan, B.I. Cohen, J.D. Moody, B.J. MacGowan, C. Joshi: ibid. **6**, 2144 (1999)
- 8 C. Ren, R.G. Hemker, R.A. Fonseca, B.J. Duda, W.B. Mori: Phys. Rev. Lett. **85**, 2124 (2000); Phys. Rev. E **64**, 067401 (2001); Phys. Plasmas **9**, 2354 (2002)
- 9 Q.L. Dong, Z.-M. Sheng, J. Zhang: Phys. Rev. E **66**, 027402 (2002)
- 10 M.N. Rosenbluth, C.S. Liu: Phys. Rev. Lett. **29**, 701 (1972); T. Tajima, J.M. Dawson: Phys. Rev. Lett. **43**, 267 (1979); R.J. Noble: Phys. Rev. A **32**, 460 (1985)
- 11 D. Umstadter, E. Esarey, J. Kim: Phys. Rev. Lett. **72**, 1224 (1994); V.I. Berezhiani, I.G. Murusidze, Physica Scripta **45**, 87 (1992); S. Dalla, M. Lontano: Phys. Rev. E **49**, R1819 (1994); G. Bonnau, D. Teychenne, J.L. Bobin: Phys. Rev. E **50**, R36 (1994)
- 12 D. Umstadter, J.K. Kim, E. Dodd: Phys. Rev. Lett. **76**, 2073 (1996); E. Esarey, R.F. Hubbard, W.P. Leemans, A. Ting, P. Sprangle: Phys. Rev. Lett. **79**, 2682 (1997)
- 13 G. Shvets, N.J. Fisch, A. Pukhov, J. Meyer-ter-Vehn: Phys. Rev. E **60**, 2218 (1999)
- 14 Z.-M. Sheng, K. Mima, Y. Sentoku, K. Nishihara, J. Zhang: Phys. Plasmas **9**, 3147 (2002)
- 15 Z.-M. Sheng, K. Mima, Y. Sentoku, M.S. Jovanovic, T. Taguchi, J. Zhang, J. Meyer-ter-Vehn: Phys. Rev. Lett. **88**, 055004 (2002)
- 16 L. Plaja, L. Roso: Phys. Rev. E **56**, 7142 (1997)
- 17 A.A. Andreev, K.Yu. Platonov, R.R.E. Salomaa: Phys. Plasmas **9**, 581 (2002)
- 18 R. Lichters, J. Meyer-ter-Vehn, A. Pukhov: Phys. Plasmas **3**, 3425 (1996)
- 19 P. Gibbon: Phys. Rev. Lett. **76**, 50 (1996)
- 20 D. von der Linde, K. Rzàzewski: Appl. Phys. B **63**, 499 (1996)
- 21 S. Kohlweyer, G.D. Tsakiris, C.G. Wahlström, C. Tillman, I. Mercer: Opt. Commun. **177**, 431 (1995)
- 22 P.A. Norreys, M. Zepf, S. Moustazis, A.P. Fews, J. Zhang, P. Lee, M. Bakarezos, C.N. Danson, A. Dyson, P. Gibbon, P. Loukakos, D. Neely, F.N. Walsh, J.S. Wark, A.E. Dangor: Phys. Rev. Lett. **76**, 1832 (1996)
- 23 M. Zepf, G.D. Tsakiris, G. Pretzler, I. Watts, D.M. Chambers, P.A. Norreys, U. Andiel, A.E. Dangor, K. Eidmann, C. Gahn, A. Machacek, J.S. Wark, K. Witte: Phys. Rev. E **58**, R5253 (1998)
- 24 D. von der Linde: Appl. Phys. B **68**, 315 (1999); A. Tarasevitch, A. Orisch, D. von der Linde, P. Balcou, G. Rey, J.-P. Chambaret, U. Teubner, D. Klöpfel, W. Theobald: Phys. Rev. A **62**, 023816 (2000)
- 25 U. Teubner, G. Pretzler, T. Schlegel, K. Eidmann, E. Förster, K. Witte: Phys. Rev. A **67**, 013816 (2003)
- 26 H. Kalt, V.G. Lyssenko, R. Renner, C. Klingshirn: J. Opt. Soc. Am. B **7**, 1188 (1985), and refs. therein
- 27 T.H. Metzger, K. Haj-Yahya, J. Peisi, M. Wendel, H. Lorenz, J.P. Kott-haus: J. Appl. Phys. **81**, 1212 (1997)
- 28 D. Walgraef, N.M. Ghoniem: J. Comp.-Aided Mat. Des. **6**, 323 (1999)
- 29 T. Schneider, D. Wolfframm, R. Mitzner, J. Reif: Appl. Phys. B **68**, 749 (1999)
- 30 D.E. Govoni, J.A. Booze, A. Sinha, F.F. Crim: Chem. Phys. Lett. **216**, 525 (1993); J.A. Booze, D.E. Govoni, F.F. Crim: J. Chem. Phys. **103**, 10484 (1995); A.G. Gorshunov, V.N. Grigor'ev, V.I. Grinev, K.L. Litvinenko, V.G. Lysenko, JETP **82**, 356 (1996); D.N. Kozlov, R. Bombach, B. Hemmrling, W. Hubschmid: Opt. Lett. **22**, 46 (1997)
- 31 J.M. Rax, N.J. Fisch: Phys. Rev. Lett. **69**, 772 (1992); IEEE Trans. Plasma Sci. **21**, 105 (1993)
- 32 M. Bottin, A. Ron: Phys. Rev. Lett. **66**, 2468 (1991)
- 33 H. Kupershmidt, A. Ron: Appl. Phys. Lett. **63**, 1733 (1993)
- 34 K.R. Chen, J.M. Dawson: Phys. Rev. Lett. **68**, 29 (1992), K.R. Chen, J.M. Dawson: Phys. Rev. A **65**, 4077 (1992)
- 35 S.L. Voronov, I. Kohl, J.B. Madsen, J. Simmons, N. Terry, J. Titensor, Q. Wang, J. Peatross: Phys. Rev. Lett. **87**, 133902 (2001)
- 36 K. Mima: private communications (2003)
- 37 P. Sprangle, E. Esarey, J. Krall, G. Joyce: Phys. Rev. Lett. **69**, 2200 (1992)
- 38 Z.-M. Sheng, J. Meyer-ter-Vehn, A. Pukhov: Phys. Plasmas **5**, 3764 (1998)
- 39 If assuming that it is an adiabatic process, then one obtains $n_e \approx Zn_i \approx (2\mu/3)^{1/2} n_0 [C - \cos(2kx)]^{1/2}$ in the quasi-neutrality approximation. Thus there is $C \geq 1$. In this case, one finds that the particle number conservation cannot be satisfied
- 40 H.A. Haus: *Waves and Fields in Optoelectronics* (Prentice-Hall, Inc., Englewood Cliffs, New Jersey 1984) Chapt. 9
- 41 E. Esarey, A. Ting, P. Sprangle, D. Umstadter, X. Liu: IEEE Trans. Plasma Sci. **21**, 95 (1993); W.B. Mori, C.D. Decker, W.P. Leemann: ibid. **21**, 110 (1993); B. Shen, W. Yu, G. Zeng, Z. Xu: Phys. Plasmas **2**, 4631 (1995)

Physica Scripta

An International Journal for Experimental and Theoretical Physics

Dear

Please find attached a PDF of your article that has appeared in issue _____ of Physica Scripta. This file has been optimised for viewing on screen, but can be printed off. If you would like a version of this file, optimised for printing, or would like to purchase a number of printed copies of your paper, please contact me.

Best Wishes,

Emma Dowdeswell

Journal Controller

Physica Scripta Production

The Royal Swedish Academy of Sciences

PO BOX 168

Didcot D. O.

OX11 7WD

email: dowdeswelle@physica.org

voice: +44 1235 518700

fax: +44 1235 515777

web: <http://www.physica.org>

Editorial office

Physica Scripta
The Royal Swedish Academy of Sciences
Box 50005
S-104 05 Stockholm, Sweden

Telephone

+46-(0)8-673 95 00

Telefax

+46-(0)8-673 95 90

Electronic Mail

physica@kva.se

Home Page

<http://www.physica.org>

Classical Model for High-Harmonic Generation by a Laser Pulse in Atomic Gas

Wei Yu^{1,2}, Z. Y. Chen^{1,2}, M. Y. Yu¹, J. Zhang³, R. X. Li², J. X. Ma⁴, and Z. Z. Xu²

¹ Institut für Theoretische Physik I, Ruhr-Universität Bochum, D-44780 Bochum, Germany

² Shanghai Institute of Optics and Fine Mechanics, Shanghai 201800, P.R. China

³ Institute of Physics, Beijing 100081, P.R. China

⁴ University of Science and Technology of China, Hefei, Anhui 230027, P.R. China

Received September 17, 2002; accepted October 2, 2002

PACS Ref: 52.25.Os, 52.25.Jm, 42.65.Ky, 52.38.Ph

Abstract

A classical model for high-harmonic generation from the interaction of a laser pulse and an atomic gas is introduced. The effects of finite pulse width and laser magnetic field are included. The optimum intensity-pulse width relation for high-harmonic emission and the corresponding power spectrum are presented. The existing high-harmonic cutoff law is found to remain valid.

1. Introduction

In a typical plasma or gas, an electron has a very low probability of colliding and thus recombining with an ion [1]. For example, in a plasma with charge number $Z = 2$, density $n_0 = 10^{17} \text{ cm}^{-3}$, and temperature $T_e = 100 \text{ eV}$, the electron-ion collision rate is only $\nu_{ei} \sim 2 \times 10^{-6} \text{ s}^{-1}$. However, the situation is very different for an atomic electron induced to tunnel from an atom, being ionized by a laser electric field. The motion of such an electron is mainly determined by the electric field of the laser. Although its trajectory can take it very far from the parent atom, the projection of the trajectory along the wave vector remains very small. That is, although the electric field of the parent atom is negligible for most of the electron's long trajectory, the electron has nevertheless a very high probability of returning to its parent atom at the first half cycle after its ionization if the laser is linearly polarized. As the highly energized electron returns to its parent ion, recombination occurs and radiation is emitted. The ionization/recombination process is repeated every half optical cycle. Such repeating emissions lead to the appearance in the frequency spectrum odd harmonics of the laser frequency. Clearly, since the trajectory of an electron ionized by a *circularly* polarized light never intersects its parent ion, in this case there will be no harmonic generation.

It has been found that the interaction of a laser with an atomic gas can lead to the emission of very high harmonics of the laser [2–4]. In the past decade such a high harmonic generation (HHG) process has been of much interest [2–15]. HHG depends strongly on the return of the ionized electron to its parent atom and how much energy it can gain from the laser before the recombination occurs. Thus, the details of the electron trajectory and energization by the laser field play a crucial role. Corkum [5,7] proposed a model to study the classical, or plasma physics, aspects of the HHG process. The model considers the effect of an oscillating electric field on the classical electron's trajectory until its return and leads to the well

known harmonic cutoff law. To obtain a more detailed picture of the laser-ionized electrons and how they contribute to HHG when a laser pulse enters an atomic gas, in this paper we extend Corkum's model to include the effects of finite pulse width in a plasma and the wave magnetic field. The atomic processes of ionization and recombination are modeled classically by invoking an ionization threshold and a recombination impact parameter. Emission of radiation is assumed to be instantaneous when the returning electron enters the impact region. That is, the quantum processes involved in the problem are modeled in terms of their classical limits. On the other hand, the effects of depletion of the atoms available for ionization and the deviation of the electron trajectory by the wave magnetic field are included. The power and spectrum of the harmonics generated by electrons excited and guided by a laser with optimized (for HHG) intensity-pulsewidth relation are presented. It is shown that the upper harmonic cutoff law [5,6] remains valid as expected. The bulk of the higher harmonic emission spectrum is also given accurately by the classical theory. On the other hand, the structural detail of the very-high-harmonic regime, which is determined by the few very highly energized electrons and thus depends on the details of the ionization and recombination processes such as finite interaction time and momentum spread, are not predicted by the classical model.

2. Classical dynamics of the ionized electrons

The motion of an electron in a planar laser pulse with vector potential $A(\eta)$, where $\eta = z - ct$, is given by

$$\frac{d}{dt} \left(m\gamma u_{x,y} - \frac{e}{c} A_{x,y} \right) = 0, \quad (1)$$

$$\frac{d}{dt} (m\gamma u_z) = \frac{d}{dt} (m\gamma c) = -\frac{e}{c} \mathbf{u} \cdot \frac{\partial}{\partial \eta} \mathbf{A}, \quad (2)$$

where \mathbf{u} is the electron velocity and γ is the relativistic factor. Note that $A(\eta)$ is the general solution of the wave equation and is valid for all planar pulses.

For an electron ionized at $\eta = \eta_i$ with zero initial velocity, its velocity \mathbf{u} and displacement δ in a linearly

polarized non-relativistic laser pulse is given by

$$\gamma u_x = a - a_i, \quad \gamma u_z = \gamma - 1 = (a - a_i)^2/2, \quad (3)$$

$$\delta_x = - \int (a - a_i) d\eta, \quad (4)$$

$$\delta_z = -\frac{1}{2} \int (a - a_i)^2 d\eta, \quad (5)$$

where $a = eA/mc^2$ is the laser strength and $a_i = a(\eta_i)$ its value at ionization, \mathbf{u} has been normalized by c , t by ω^{-1} , and the space parameters such as δ and η by c/ω . The corresponding kinetic energy of the ionized electron is

$$W = \gamma - 1 = \frac{1}{2}(a - a_i)^2, \quad (6)$$

which has been normalized by mc^2 . From Eqs. (3)–(6), one can numerically determine which electrons will return to their parent ions, the time interval between the ionization and recombination, and the kinetic energy of the returning electron.

3. The harmonic cutoff

We first briefly discuss the harmonic cutoff based on Corkum's model [5], which tracks the electron trajectory in an oscillating electric field whose vector potential can be written as $a = a_0 \sin t$. In this one-dimensional case, an electron is first pulled away from its parent ion at x_i and then driven back when the laser electric field changes direction. The actual electron trajectory and energization is determined by the phase of the laser electric field as the electron becomes free. When the electron intersects x_i (or $\delta_x = 0$) on its return path, it is assumed to recombine with its parent ion with a photon of energy $\hbar\omega = W_f + I_a$ emitted, where $W_f = u_f^2/2$, and u_f is the speed of the returning electron at recombination, and I_a the ionization potential. The corresponding scaling law for the high-harmonic cutoff frequency is [5,6]

$$\hbar\omega_c = I_a + 3.17U_p, \quad (7)$$

where $3.17U_p$ is the maximum kinetic energy of the returning electron. Here $U_p = a_0^2/4$ is the ponderomotive potential, $a_0 = 0.85 \times 10^{-9}\lambda\sqrt{I}$ is the laser strength parameter, I is the laser intensity in W/cm^2 , and λ is the wavelength in μm .

One can also derive the cutoff law analytically in a physically more transparent manner. The condition (for the return of the electron to its parent atom) $\delta_x = 0$ at $t = t_f$ leads to the expression [16]

$$\cos t_i = \cos(t_i + 2\alpha) + 2\alpha \sin t_i, \quad (8)$$

where $\alpha = (t_f - t_i)/2$. The kinetic energy of the returning electron is then

$$W_f = \frac{1}{2}(a_f - a_i)^2 = \frac{8U_p \sin^2 \alpha (\sin \alpha - \alpha \cos \alpha)^2}{\alpha^2 + \sin^2 \alpha + \alpha \sin 2\alpha}, \quad (9)$$

where Eq. (8) has been used to eliminate t_f in favor of α . It is easy to verify that the kinetic energy W_f has a maximum at $\alpha = 2.06$, which corresponds to the fact that an electron ionized at $a_i = 0.29a_0$ will have maximum energy, the well-known value $W_f = 3.17U_p$, upon return. This derivation

shows that the harmonic cutoff is a classical effect, and that it is valid for all laser strengths.

4. Effect of laser magnetic field

As the laser magnetic field is expected to modify the electron trajectory only in a minor way, it is convenient to first discuss its effect. Although the wave magnetic field contributes very little to the electron's kinetic energy, it does displace the electron in the direction of wave propagation and thereby the chance of intersecting the parent atom. Here we take into account the laser magnetic field and reconsider the trajectory of the returning electron. Accordingly, we set

$$a(\eta) = a_0 \sin \eta \quad (10)$$

for a planar laser of infinite duration. In the now two-dimensional situation a proper "return" suitable for recombination would be given by $|\delta_x| < r_B$ and $|\delta_z| < r_B$, i.e., the returning electron should reach an area (around the parent ion) bounded by the Bohr radius r_B . However, because of the geometry the condition $|\delta_x| < r_B$ is not different from $\delta_x = 0$, since an electron reaching $|\delta_x| < r_B$ will intersect x_i . As a result, the conclusions of the last section are also valid in the 2D situation.

We solve Eqs. (1) and (2) numerically for a linearly polarized $1.06\mu\text{m}$ laser of strength $a_0 = 0.02$. Figure 1 shows the trajectories (curves from bottom to top) of electrons ionized at $t_i = -\pi/18, \pi/9$, and $\pi/3$, respectively. As expected, the motion in the z direction is considerably less than that in the x direction, as is emphasized in the figure by the different scalings for the x and z axes. The dotted lines enclose an area bounded by the normalized Bohr radius r_B . We see that some electrons, such as that ionized at $t_i = \pi/9$, can enter the Bohr region within half a laser period, while others, such as that with $t_i = -\pi/18$ and $\pi/3$, cannot. Electrons that fail to return within the first laser cycle after ionization will have little chance in reaching the Bohr region at a later time. It should be emphasized that in the ionization-recombination process

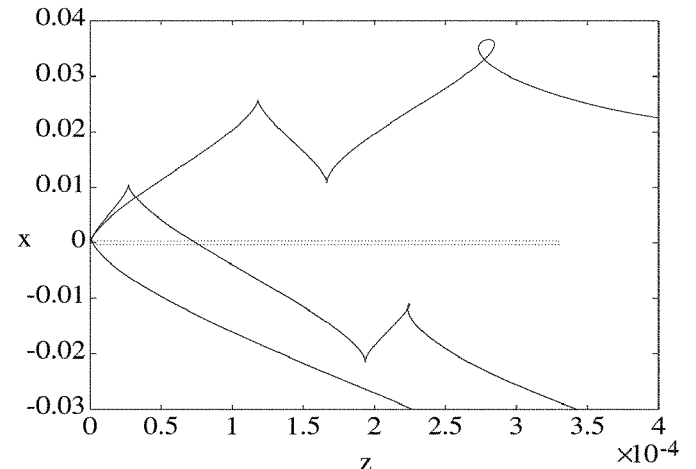


Fig. 1. Trajectories of electrons ionized at $t_i = -\pi/18, \pi/9$, and $\pi/3$ (bottom to top) for $a_0 = 0.02$. The space variables are in units of c/ω and the dotted line shows the region (highly deformed because an amplified scale is used for the z axis) bounded by the Bohr radius. Electrons entering this region are recombinant.

for HHG, a recombined electron is ionized again as a new electron.

Figure 2 shows the kinetic energy W_f and longitudinal displacement δ_{zf} of a returning electron as a function of t_i for $a_0 = 0.01$. The maximum energy is again $W_f \sim 3.17U_p$. That is, the wave magnetic field does not affect the high-harmonic cutoff. This is expected since it hardly affects the energization of the electron. Our calculation shows that electrons ionized at lower a_i will have larger longitudinal displacement δ_{zf} upon return. We found that about one third of the ionized electrons can reach the Bohr neighborhood of their parent ions if the ionization probability is equal at all ionization phases η_i .

In reality the ionization probability has a very strong dependence on the laser strength. In fact, no electron will be ionized at very low a_i even if the ionization phase allows the ionized electrons to return. Most free electrons are produced when $a_i \sim a_0$ (if the ground states of atoms are not totally depleted). When these electrons return to their parent ions, with comparatively low kinetic energy and small longitudinal displacement, they contribute with the major part of the radiation and determine the main features of the HHG spectrum.

As in all existing theories on HHG, it is difficult to describe accurately the high-frequency regime of the HHG spectrum. This regime is attributed to electrons ionized at $a_i \sim 0.29a_0$. These electrons, expected to have higher kinetic energy and larger longitudinal displacement upon return, are very few in number. As a result, the generation of highest order harmonics is sensitive not only to the dynamics of this small group of electrons in the wave fields, but also to the (quantum) details of the ionization and recombination processes. The ionization and recombination models used here are not sufficient to describe such details. The tunnel ionization model may become less applicable at lower a_i , and the recombination of high velocity electrons are not accurately reflected by the Bohr radius as impact parameter.

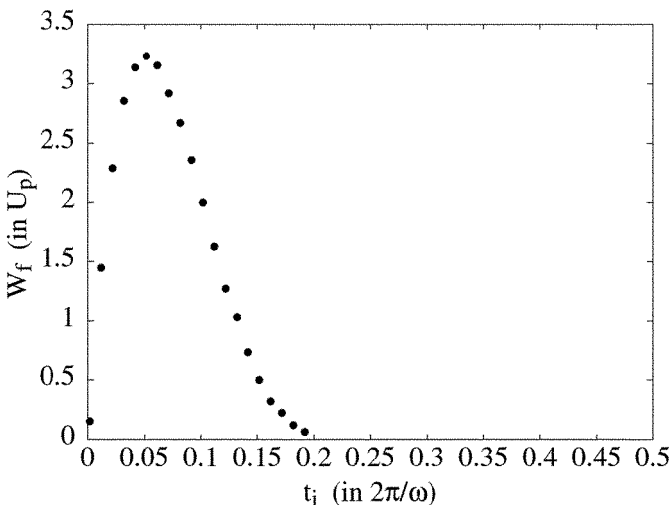


Fig. 2. The kinetic energy W_f of returned electrons as a function of the time t_i of ionization, for $a_0 = 0.01$.

5. Effect of finite pulse width

It is well known that the laser pulse duration is of importance in the HHG experiments since the front part of the pulse can completely ionize the atomic gas before the maximum of the pulse arrives. Based on the above results, we propose here a model for HHG from the interaction of a *finite* laser pulse with an atomic gas. Since Eqs. (3)–(5) are valid for any planar pulse, a Gaussian pulse can be represented by

$$a(\eta) = a_0 \exp[-(\eta - \tau/2)^2/\tau^2] \sin \eta, \quad (11)$$

where τ is the pulse width normalized by ω^{-1} .

The HHG mechanism under consideration depends on the availability of neutral atoms and the acceleration of the ionized electrons by the laser electric field. With a typical finite pulse shape such as Gaussian, there is the possibility that most or all of the gas atoms are ionized by the leading (low-field) part of the pulse before the energetic part arrives. In this case the corresponding harmonic generation would be of very low efficiency. It is thus desirable to obtain a suitable intensity-pulse width relation which optimizes the HHG. For this purpose it is first necessary to discuss some details of the ionization process.

For convenience we shall consider a simple ionization mechanism. When the Keldysh parameter $\gamma_K = \sqrt{I_a/U_p}$ is less than unity, the tunnel ionization models [17] accurately describe laser-induced ionization in atomic gases. The corresponding ionization rate normalized by ω is given by

$$p = 4 \frac{\omega_a \varepsilon_i^{5/2}}{\omega |\varepsilon_L|} \exp\left(-\frac{2\varepsilon_i^{3/2}}{3|\varepsilon_L|}\right), \quad (12)$$

where $\omega_a = 4 \times 10^{16} \text{ s}^{-1}$ is the atomic frequency unit, $\varepsilon_i = I_a/I_H$, I_H is the ionization potential of hydrogen, $\varepsilon_L(z, t) = E(\eta)/E_a = 1.16 \times 10^5 (r_B/\lambda) a(\eta)$, E_a is the atomic unit of the field, and λ is the laser wavelength.

Twice in a laser period, when the laser electric field temporarily dominates over the static (atomic core) Coulomb field, electrons are released from the atoms. The density n of the ionized electrons is given by

$$dN/dt = (1 - N)p = p \exp\left(-\int pdt\right), \quad (13)$$

or

$$N = 1 - \exp\left(-\int pdt\right), \quad (14)$$

where $N = n/n_0$, and n_0 is the density of gas atoms before the arrival of the laser.

6. Optimum laser intensity and the harmonic spectrum

For given pulse shape and width, one can define an optimum laser intensity by requiring that the density of the laser-ionized electrons at $t = \tau$ is $n = n_0(1 - e^{-1})$, or $\int pdt = 1$. Figure 3 shows the optimum intensity as a function of the pulse width for a Gaussian pulse with $I_a = 24.6 \text{ eV}$. Thus, for long pulses, one has to choose lower intensities in order to ensure that the ground states of the atoms are not totally depleted when the laser intensity

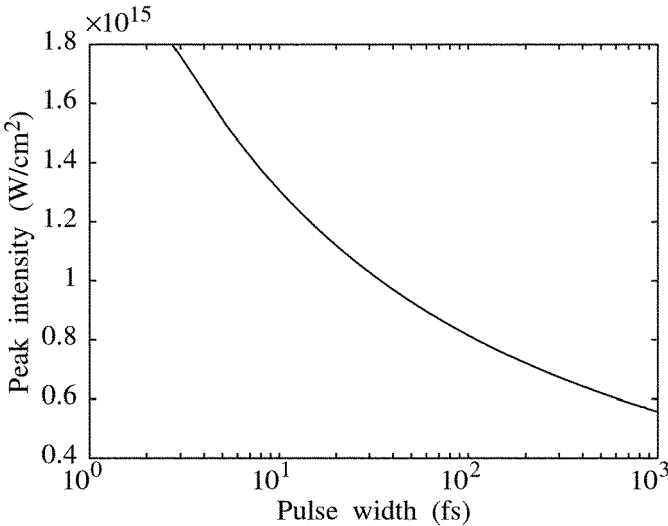


Fig. 3. The optimum intensity as a function of the laser duration, for $I_a = 24.6 \text{ eV}$.

peaks. As the pulse width decreases, one can increase the laser intensity for efficient HHG. That is, for shorter laser pulses more intense lasers can be used and higher radiation power can be achieved.

The motion of the ionized electron in the presence of a Gaussian laser pulse is fully determined by Eqs. (3)–(6). The power P radiated at the recombination of the returned electron can be written as

$$P = [W_f(t_f) + I_a] dN(t_i)/dt, \quad (15)$$

where the time delay between ionization and recombination is accounted for. That is, W_f is evaluated at the time of recombination and dN/dt is evaluated at the time of ionization.

Using the Larmor formula we can obtain the power radiated per unit solid angle $dP/d\Omega = (3P/8\pi) \sin^2 \theta$, where θ is measured from the direction of polarization. We have then

$$\frac{dP}{d\Omega} = \frac{3P}{8\pi} \equiv |G(\omega)|^2, \quad (16)$$

for $\theta = \pi/2$. Figure 4 shows the time evolution of the radiative power at $\theta = \pi/2$ for a 10 fs Gaussian pulse of intensity $1.3 \times 10^{15} \text{ W/cm}^2$ irradiated on a gas with $I_a = 24.6 \text{ eV}$. That is, the intensity is close to the optimum (from Fig. 3) for the given pulse duration. One can see that radiation peaks appear twice in each laser period (here about 3.15 fs).

The frequency spectrum corresponding to Eq. (16) is $|G(\omega)|^2$, where $G(\omega)$ is the Fourier transform of $G(t)$. Figure 5 shows the frequency spectrum of the radiation shown in Fig. 4. Only odd harmonics appear in the spectrum since the peaking interval in the time evolution is at about half a laser period. The highest harmonic (173rd) agrees well with that of the cutoff law. We have also considered longer and weaker pulses. Figure 6 shows the frequency spectrum from the irradiation of a 100 fs $8 \times 10^{14} \text{ W/cm}^2$ laser pulse on the same gas. The intensity chosen is again optimized. In this case, the cutoff (at the 113th harmonic) is again close to that predicted by the cutoff law.

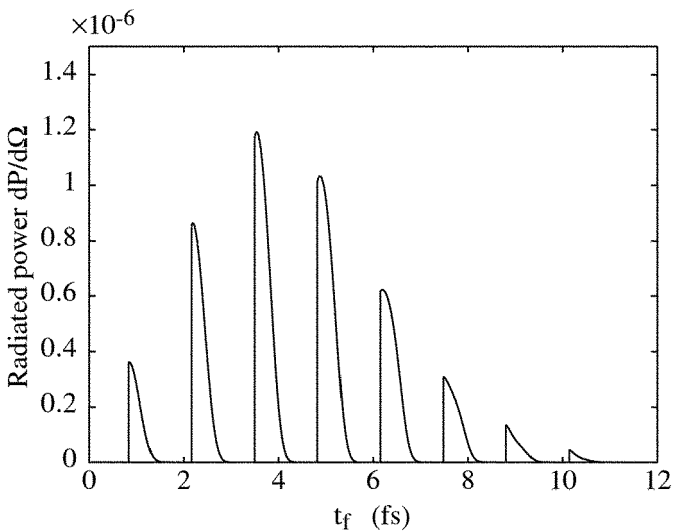


Fig. 4. The time evolution of the normalized radiation power $dP/d\Omega$ emitted at $\theta = \pi/2$ for a 10 fs, $1.06 \mu\text{m}$, $1.3 \times 10^{15} \text{ W/cm}^2$ Gaussian laser pulse irradiating a gas with $I_a = 24.6 \text{ eV}$. The intensity chosen is close to the optimum one.

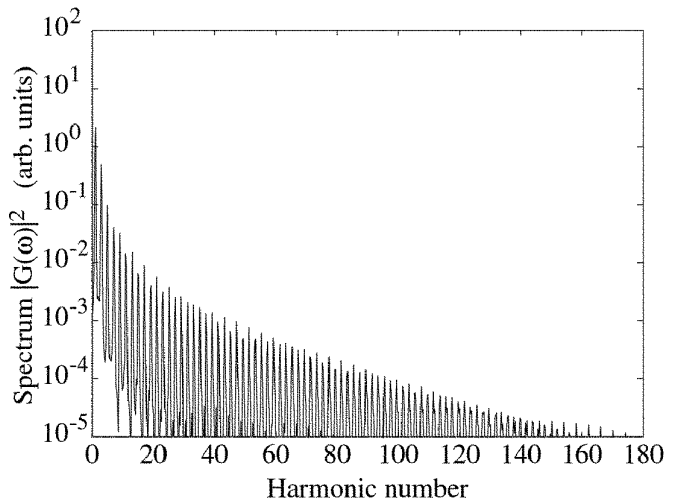


Fig. 5. The harmonic spectrum corresponding to Fig. 4.

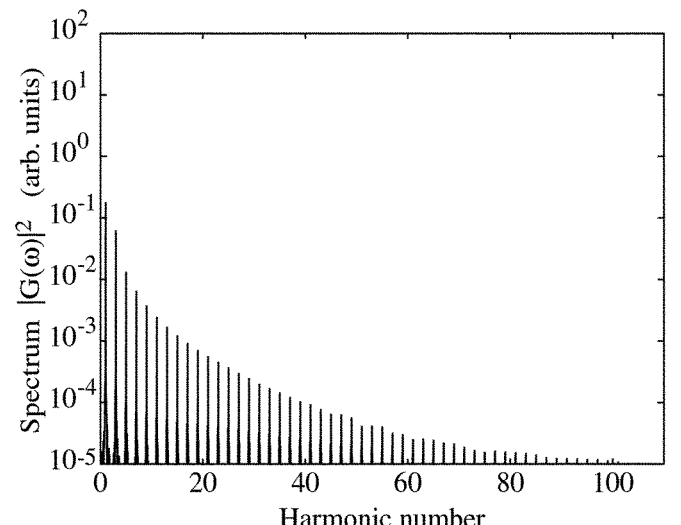


Fig. 6. The harmonic spectrum of the radiation emitted from irradiating a 100 fs, $1.06 \mu\text{m}$, $8 \times 10^{14} \text{ W/cm}^2$ laser pulse on a gas with $I_a = 24.6 \text{ eV}$. The intensity chosen is again close to the optimum one.

7. Discussion

In this paper we have presented a classical model for HHG including the effects of finite pulse width and laser magnetic field. Although the wave magnetic field hardly affects the energy of a laser-ionized electron, its effect on the latter's return to the parent atom can be remarkable. Since the electron trajectory gets a small component along the wave-vector direction, it is thus more difficult for a returning electron to reach the Bohr neighborhood of its parent atom. We have also obtained a relation between the laser intensity and pulse width that optimizes HHG. The power and spectrum of the radiation emitted at recombination of the returning electrons with their parent atoms are then obtained.

Our classical model for HHG shows that the existing harmonic cutoff law remains applicable even when the finite pulse width and magnetic field of the laser are taken into account. For longer pulses the laser intensity must be kept low such that the ground states of the gas atoms are not depleted before the laser peak arrives. Higher intensities can be used for shorter-pulse lasers, and one can realize higher radiation power. It should be pointed out that some features often associated with HHG, such as the plateau and sharp cutoff in the harmonic spectrum, are not distinctive in our results. Generation of the highest order harmonics is attributed to a small group of electrons which are ionized at the optimum phase, and is sensitive to the exact ionization and recombination probabilities as well as the finite interaction time of these electrons. The latter quantum processes are beyond the scope of our simple classical model.

Acknowledgements

This work was supported by a Chinese Academy of Sciences-Max-Planck Gesellschaft Exchange Program, the National High-Technology Program of China (Contract 863-416-1) and the National Natural Science Foundation of China (Grants 19974058 and 69789801).

References

1. Chen, F. F., "Introduction to Plasma Physics," (Plenum, New York, 1974), Chap. 1.
2. Akiyama, Y. *et al.*, Phys. Rev. Lett. **69**, 2176 (1992).
3. Macklin, J. J., Kmetec, J. D. and Gordon, C. L., Phys. Rev. Lett. **70**, 766 (1993).
4. L'Huillier, A. and Balcou, Ph., Phys. Rev. Lett. **70**, 774 (1993).
5. Corkum, P. B., Phys. Rev. Lett. **71**, 1994 (1993).
6. Krause, J. L., Schafer, K. J., and Kulander, K. C., Phys. Rev. Lett. **68**, 3535 (1992).
7. Corkum, P. B., Optics and Photonics News/May, 18 (1995).
8. Richards, D., J. Phys. B **29**, 2925 (1996).
9. Christov, I. P., Murnane, M. M., and Kapteyn, H. C., Phys. Rev. Lett. **78**, 1251 (1997).
10. Spielmann, Ch. *et al.*, Science **278**, 661 (1997).
11. Chang, Z. *et al.*, Phys. Rev. Lett. **79**, 2967 (1997).
12. de Bohan, A., Antoine, P., Milosevic, D. B., and Piraux, B., Phys. Rev. Lett. **81**, 1873 (1998).
13. Krausz, F., Brabec, T., Schurer, M., and Spielmann, C., Optics & Photonics News /July, 46 (1998).
14. Schnurer, M. *et al.*, Phys. Rev. Lett. **80**, 3236 (1998).
15. Corkum, P. B., Burnett, N. H. and Brunel, F., Phys. Rev. Lett. **62**, 1259 (1989).
16. Recall that $\delta_z \ll \delta_x$ in general, and $\delta_z = 0$ if the effect of the wave magnetic field is excluded.
17. Landau, L. D. and Lifshitz, E. M., "Quantum Mechanics," (Pergamon, New York, 1965), p.276.

Numerical optimization of a picosecond pulse driven Ni-like Nb x-ray laser at 20.3 nm

X. Lu

Laboratory of Optical Physics, Institute of Physics, Chinese Academy of Sciences, Beijing 100080, People's Republic of China

J. Y. Zhong

Laboratory of Optical Physics, Institute of Physics, Chinese Academy of Sciences, Beijing 100080, People's Republic of China
and National Astronomical Observatories, Chinese Academy of Sciences, Beijing 100012, People's Republic of China

Y. J. Li

Department of Physics, China University of Mining & Technology, Beijing 100083, People's Republic of China

J. Zhang^{a)}

Laboratory of Optical Physics, Institute of Physics, Chinese Academy of Sciences, Beijing 100080, People's Republic of China

(Received 27 February 2003; accepted 10 April 2003)

Detailed simulations of a Ni-like Nb x-ray laser pumped by a nanosecond prepulse followed by a picosecond main pulse are presented. The atomic physics data are obtained using the Cowan code [R. D. Cowan, *The Theory of Atomic Structure and Spectra* (University of California Press, Berkeley, CA, 1981)]. The optimization calculations are performed in terms of the intensity of prepulse and the time delay between the prepulse and the main pulse. A high gain over 150 cm⁻¹ is obtained for the optimized drive pulse configuration. The ray-tracing calculations suggest that the total pump energy for a saturated x-ray laser can be reduced to less than 1 J. © 2003 American Institute of Physics. [DOI: 10.1063/1.1579693]

I. INTRODUCTION

The electron collisional excitation Ni-like x-ray laser scheme was first proposed by Maxon *et al.*¹ in 1985 when the first collisional excitation soft x-ray laser amplification was demonstrated for Ne-like Se ions.² Similar to the Ne-like scheme, the Ni-like x ray is also based on transitions of ions with a closed shell. In the Ni-like scheme, the upper laser level $3d^94d\ ^1S_0$ is populated due to the monopole collisional excitation from the ground state $3d^{10}\ ^1S_0$, a population inversion can be built on the $3d^94d\ ^1S_0 \rightarrow 3d^94p\ ^1P_1$ and $3d^94d\ ^1S_0 \rightarrow 3d^94p\ ^3D_1$ transitions. Principally, to obtain an x-ray lasing at similar wavelength, Ni-like scheme requires much lower pump energy than Ne-like scheme due to the higher quantum efficiency. This makes the Ni-like scheme more promising to scale down to a shorter wavelength than the Ne-like scheme. Using the prepulse technique and multi-target design, saturated output has been demonstrated for Ni-like Ag (14 nm),³ Ni-like Sm (7 nm),⁴ and Ni-like Dy (5.8 nm) x-ray lasers.⁵ The amplification at wavelengths toward the “water window” has also been observed.⁶ In recent years, the use of ultra-short pulse pumping has been shown to be able to save significantly the drive energy of collisional x-ray lasers.^{7–9} Gain saturation has been reached for various Ne-like or Ni-like x-ray lasers at wavelengths >10 nm using only a few joules total pump energy.^{10–14} On the theoretical

side, Daido *et al.* reported atomic physics calculations for Ni-like ions with atomic number from 47 (Ag) to 66 (Dy).¹⁵ A self-similarity model for hydrodynamic characteristics of Ni-like transient collisional excitation x-ray lasers was also developed.^{16,17}

In recent years, the high power compact Ti:sapphire chirped pulse amplification (CPA) lasers at 800 nm have become available for university laboratories. Such laser systems have great potential to be used as the pump source of Ne-like or Ni-like table-top x-ray lasers with high repetition rate. The Ni-like x-ray laser has numerous advantages in pump efficiency by comparison to Ne-like x-ray laser. However, the population inversion of Ni-like ions is much more sensitive to the plasma conditions than that of Ne-like ions. In this paper we simulate the Ni-like Nb x-ray laser of $4p \rightarrow 4d$, $J=0 \rightarrow 1$ transition at 20.3 nm driven by a Ti:sapphire CPA laser. The pump geometry was set to be the standard line focus on a slab target. The Ni-like Nb ion state is modeled for the ground state $3d^{10}\ ^1S_0$, and the four most important excited levels, i.e., $3d^94p\ ^3D_1$, $3d^94p\ ^1P_1$, $3d^94d\ ^1S_0$, $3d^94f\ ^1P_1$, and the ground state of next ionization stage (Co-like state). The modified version of the one-dimensional Lagrangian hydrodynamic code MED103¹⁸ coupled with an atomic physics code was used to predict the time evolution of laser-plasma interactions and gain coefficient. The rate equations of level populations are solved for the spontaneous emission, collisional excitation and de-excitation, collisional ionization and recombination processes. The energy levels,

^{a)}Author to whom correspondence should be addressed. Electronic mail: jzhang@aphy.iphy.ac.cn

TABLE I. Energy levels of Ni-like Nb XIV.

Index	State configuration	RCN/RCG (eV)	Experimental (eV)
1	$3d^{10} 1S_0$	0	
2	$3d^9 4p ^1P_1$	218.8	219.4
3	$3d^9 4p ^3D_1$	221.0	221.6
4	$3d^9 4d ^1S_0$	280.1	
5	$3d^9 4f ^1P_1$	315.3	316.2

radiative transition probability (Einstein coefficient A) and the electron collisional excitation rates are calculated using the code RCN/RCG developed by Cowan,¹⁹ because the published data about Nb XIV ions are not sufficient for x-ray laser calculation.^{15,20,21} The drive pulse configuration used in the simulation is a nanosecond prepulse followed by an ultra-short main pulse. The optimization calculations are performed in terms of peak intensity of the prepulse and the delay between the prepulse and the main pulse. A ray-tracing postprocessor is used to calculate the output and also the spatially averaged gain-length product.

II. ATOMIC PHYSICS CALCULATION

The energy levels used in the x-ray laser simulations are calculated using the Cowan code in orbital-spin (LS) coupling and presented in Table I. Some energy levels are compared with other reported values. Here we can see a good agreement of theoretical calculations with the experimental results from Ref. 21. Table II lists the wavelengths and the radiative rates of dipole transitions between levels. The calculated wavelength of the strongest lasing transition of $3d^9 4d ^1S_0 \rightarrow 3d^9 4p ^1P_1$ is in good agreement with the experimental measurement of 20.3 nm.²² The collisional excitation rates between levels as a function of electron temperature are shown in Figs. 1(a) and 1(b). Figure 1(a) presents the excitation rates from ground state to excited states, and the collisional mixing rates between excited states are shown in Fig. 1(b). The monopole excitation rate [transition $1 \rightarrow 4$ in Fig. 1(a)] has high value when the electron temperature is higher than the excitation energy of 280 eV. The collisional mixing rates of transition $3d^9 4p ^1P_1 \rightarrow 3d^9 4p ^3D_1$ and $3d^9 4p ^3D_1 \rightarrow 3d^9 4f ^1P_1$ are negligibly small and are not plotted in the figure. We also compare our calculation for monopole excitation rates from the ground state $3d^{10} 1S_0$ to the upper laser level $3d^9 4d ^1S_0$ with the published results of the relativistic distorted wave code YODA [see the dashed curve in Fig. 1(a)].¹⁵ Here we can see about 20% deviation from the YODA calculation, because the Cowan code uses

TABLE II. Wavelength and radiative transition rates in Ni-like Nb XIV.

Transition ($J \rightarrow i$)	Wavelength (nm)	A_{ji} (10^{10} s^{-1})
2 → 1	5.67	36.47
3 → 1	5.61	6.92
5 → 1	3.93	576.67
4 → 2	20.23	9.08
4 → 3	20.98	1.50
5 → 4	35.23	1.03

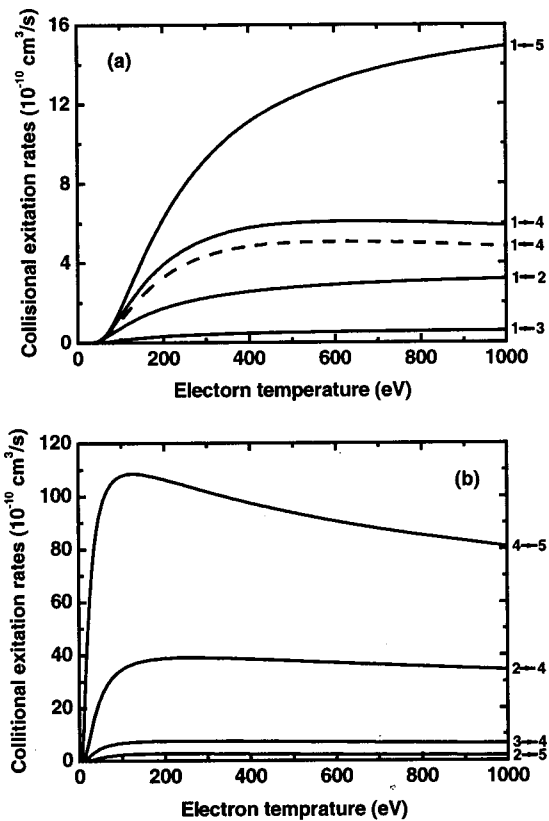


FIG. 1. Collisional excitation rates as a function of electron temperature for transitions from the ground state to the excited levels (a), and between the excited levels (b). The solid curves are calculated by the Cowan code. The dashed curve corresponds to the monopole collisional excitation rates from the YODA code.

plain wave approximation to calculate the electron-atom scattering process. The strong collisional mixing between the levels of $3d^9 4p ^1S_0$ and $3d^9 4f ^1P_1$ [see Fig. 1(b)] can have significant effects on the population of the upper laser level. This is the reason why the $3d^9 4f ^1P_1$ level must be included in the calculations.

III. OPTIMIZATION OF THE CONDITIONS OF A PREPLASMA

Simulations are performed for 100-μm-thick niobium planar targets irradiated by a 1 ns prepulse. The prepulse is assumed to be the chirped pulse before the final compression. If the uncompressed chirped pulse has only several hundreds of picosecond duration, then the best way is to use two connected chirped pulses to simulate a nanosecond pulse. This is because the preplasma produced by the prepulse with few hundreds of picosecond duration usually has short scale length and high density gradient.

It is well known that for an ultrashort pulse driven x-ray laser, where prepulses should produce a properly ionized preplasma with large scale length, the main pulse is used to rapidly heat the preplasma and make a sudden jump of electron temperature. The functions of the prepulse and the main pulse can be independent of each other, so they can be optimized separately. In order to obtain an optimum intensity of prepulses, simulations have been performed for 1 ns full

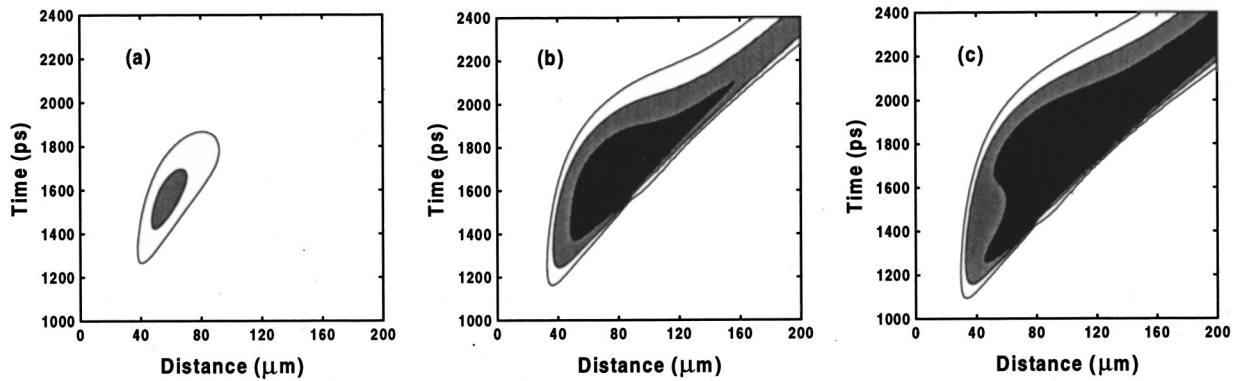


FIG. 2. The Ni-like Nb ion fraction vs space and time in the plasma generated by 1 ns prepulse with peak intensities of $2.0 \times 10^{11} \text{ W/cm}^2$ (a), $2.2 \times 10^{11} \text{ W/cm}^2$ (b), and $2.4 \times 10^{11} \text{ W/cm}^2$ (c). The fraction in plot is from 60% (blackest) to 20% (white) by a step of 20%.

width at half maximum Gaussian prepulses with various peak intensities. Figure 2 shows the spatio-temporal profile of the ground state population of Ni-like Nb ions fraction in plasmas produced by 1 ns prepulses with peak intensities of $2.0 \times 10^{11} \text{ W/cm}^2$ (a), $2.2 \times 10^{11} \text{ W/cm}^2$ (b), and $2.4 \times 10^{11} \text{ W/cm}^2$ (c). The horizontal axis presents the spatial distance from the target surface. The prepulses reach their peak at 1.2 ns in the time scale used in Fig. 2. From Fig. 2 we can see that the ionization state of preplasmas is very sensitive to the intensity of prepulses. It is apparent that a prepulse at $2.0 \times 10^{11} \text{ W/cm}^2$ is not powerful enough to ionize the preplasma to the Ni-like ionization state. The prepulse with a peak intensity of $2.2 \times 10^{11} \text{ W/cm}^2$, and $2.4 \times 10^{11} \text{ W/cm}^2$ can produce a high fraction of Ni-like ions in preplasmas. But in Fig. 2(c) we can see an over-ionized region near 50 μm distance at 1400–1600 ps, and later the over-ionized ions recombine to Ni-like state again. The prepulse at $2.2 \times 10^{11} \text{ W/cm}^2$ can produce a high fraction of Ni-like ions without over-ionization. In experiments the intensity of prepulse is usually set to be higher than the threshold value to make preplasma slightly over-ionized. The optimized condition of preplasmas can be achieved by optimizing the delay time between prepulse and main pulse, because changing of the delay time is much easier than changing of the intensity.

IV. X-RAY LASER SIMULATION

In our simulations the x-ray laser gain is generated by a 1 ps, $1 \times 10^{15} \text{ W/cm}^2$ peak intensity main pulse after a 1 ns, $2.2 \times 10^{11} \text{ W/cm}^2$ intensity prepulse. Before the main pulse, the preplasma should have a rich population of Ni-like ions and large scale length, so the suitable delay time can be determined from Fig. 2(b). The time region at 1.6–1.8 ns seems to be a good starting time for the main pulse. To investigate the effect of the delay time, we modeled the x-ray laser for different delay times of 0.4, 0.6, and 0.8 ns. Figures 3(a), 3(b) and 3(c) show the x-ray laser gain at 20.3 nm versus space and time for 0.4, 0.6, and 0.8 ns delays, respectively. The detailed spatial profiles of the local gain coefficient and electron density at the moment when the gain reaches its peak are presented in Figs. 4(a), 4(b), and 4(c) for the delay time of 0.4, 0.6, and 0.8 ns, respectively. From Fig. 4 we can see that all gain regions are located far from the critical density surface and have a low density gradient. The gain higher than 150 cm^{-1} can be generated with delay times of 0.4 and 0.6 ns. The gain area is enlarged with the delay time, but the peak gain coefficients are decreased. This situation can be easily understood because the scale length of the plasma increases with the delay time. Lower population of Ni-like ions causes the decrease of gain. If we compare Fig.

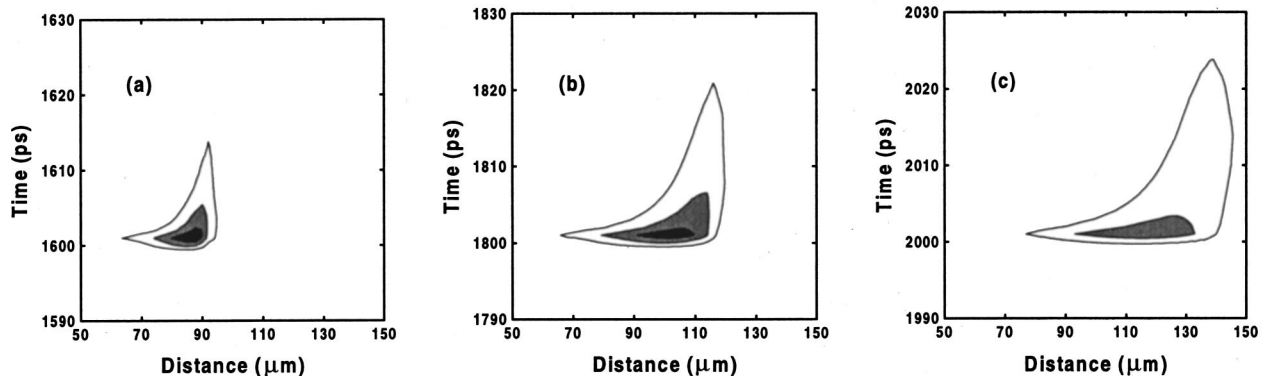


FIG. 3. Contours of Ni-like Nb x-ray laser gain at 20.3 nm generated by a 1 ps, $1 \times 10^{15} \text{ W/cm}^2$ drive pulse with delay time of 0.2 ns (a), 0.4 ns (b), and 0.6 ns (c). The gain in the plot is from 150 cm^{-1} (blackest) to 50 cm^{-1} (white) by a step of 50 cm^{-1} .

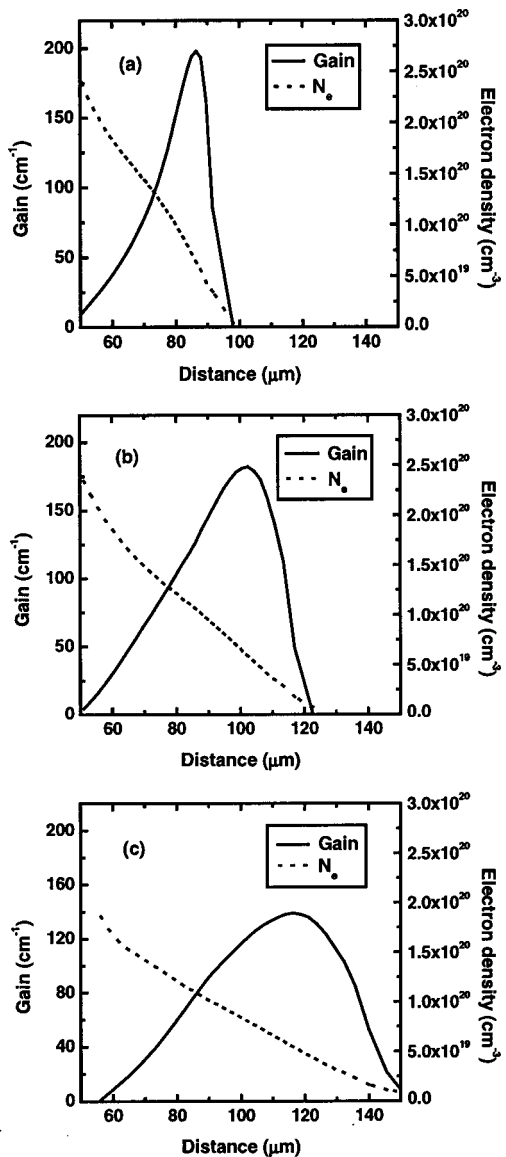


FIG. 4. The spatial profiles of the local gain coefficient and electron density at the peak gain time for delay times of 0.4 (a), 0.6 (b), and 0.8 ns (c).

3 with Fig. 2(b), then we can see that the position of the peak gain and the position of high fraction of Ni-like ions just before the main pulse are consistent.

V. RAY-TRACING CALCULATIONS

The optimum delay between the long prepulse and the short main pulse should be determined by the output intensity of x-ray laser. The refraction of x-ray laser in the plasma can strongly affect the laser output. In order to model the propagation and amplification of the x-ray laser in the plasma medium, we developed a two-dimensional ray tracing postprocessor to calculate the relative output intensity of x-ray laser for delay times of 0.4, 0.6, and 0.8 ns. We assumed that the traveling wave excitation is used, so the spatial profiles of gain and electron density can keep their form unchanged along the line focus. For simplification, the time evolution of the x-ray laser output and gain saturation effect were not included. In our ray-tracing calculation the spatial

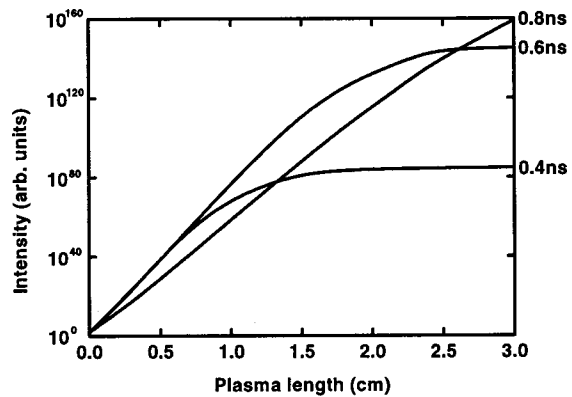


FIG. 5. Spatially integrated laser output intensity vs the target length at the peak gain time for the time delays between prepulse and main pulse of 0.4, 0.6, and 0.8 ns.

profiles of gain and electron density are in the moment of peak temporal and spatial gain, taken from Figs. 4(a)–4(c). The intensity of each ray is weighted by the upper-level population of the laser transition at the beginning of the ray. Figure 5 shows the dependence of the spatially integrated laser output intensity on the plasma length for illustration of the role of refraction. From Fig. 5 we can see that the effect of refraction decreases with the delay time. For short plasma length, 0.4 and 0.6 ns delays give a similar laser output, and the output intensity of 0.8 ns delay is much lower than that of 0.4 and 0.6 ns delays for short plasma lengths due to lower gain. The refraction effect breaks the exponential growth of output intensity near 0.7, 1.0, and 2.0 cm propagation distances for 0.4, 0.6, and 0.8 ns delays, respectively. Theoretically, for more than 2.6 cm target length, the output intensity of 0.8 ns delay can exceed the output intensity of 0.6 ns delay, but actually x-ray lasers cannot be amplified on such long distance for two reasons. First, it is too difficult to make a 2.6-cm-long uniform plasma column in experiment. Second, the propagation time of an x-ray laser through a 2.6-cm-long plasma column is about 90 ps, and during this time the condition of the preplasma can be significantly changed. So the ray tracing on a centimeter long plasma column can be used only for illustration of the role of refraction. In ideal conditions, the effective gain length production reaches 14 at 1.2 mm target length for 0.4 and 0.6 ns delays. That means if the line focus is 50 μ m wide, then the total pump energy for saturated x-ray laser output can be less than 1 J. The time delay of 0.6 ns has a little advantage in amplification distance by comparison with 0.4 ns delay.

Simulations are also performed for different main pulses with the optimum delay time of 0.6 ns. Table III lists several examples of peak gain and the width of gain region (where $g > 50 \text{ cm}^{-1}$ at peak gain time) produced by some main pulses with different intensity and duration. From Table III we can see that the gain characteristics are mainly dependent of the energy of the short pulse. For main pulses with the same energy but different durations from hundreds of femtoseconds to few picoseconds, the gain region keeps its width and the shorter main pulse generates higher gain.

TABLE III. Gain characteristics produced by different main pulses.

Peak intensity of main pulse (10^{15} W/cm 2)	Duration of main pulse (ps)	Peak gain (cm $^{-1}$)	Width of gain region (μm)
1.0	0.5	86	26
1.0	1.0	182	50
1.0	2.0	222	53
0.5	1.0	85	25
2.0	1.0	254	60
0.5	2.0	158	45
2.0	0.5	186	52

VI. CONCLUSIONS

In conclusion, we have investigated the Ni-like Nb x-ray laser at 20.3 nm numerically using a one-dimensional hydrodynamic code MED103 coupled with an atomic data package for Nb planar target irradiated by a 1 ns prepulse followed by a 1 ps, 10^{15} W/cm 2 drive pulse from a Ti:sapphire laser. The energy levels, radiative transition rates, and collisional excitation rates are calculated using the Cowan code. The optimization calculations are performed in terms of the intensity of the prepulse and the delay time between the prepulse and the main pulse. High gains greater than 150 cm^{-1} are predicted by using optimized drive pulse configuration. The relative output intensity of x-ray laser is predicted using the ray-tracing method. We predicted that a saturated Ni-like Nb soft x-ray laser at 20.2 nm could possibly be generated using less than 1 J pump energy from a table-top Ti:sapphire laser system.

ACKNOWLEDGMENTS

This work is supported by the National Nature Science Foundation of China under Grant Nos. 60108007, 60078008, NKBRSF under Grant No. G1999075200, and National Hi-tech Program.

¹S. Maxon, P. Hagelstein, K. Reed, and J. Scofield, *J. Appl. Phys.* **57**, 971 (1985).

²D. L. Matthews, P. L. Hagelstein, M. D. Rosen, M. J. Eckart, N. M. Ceglio, A. U. Hazi, H. Medecki, B. J. MacGowan, J. E. Trebes, B. L. Whitten, E. M. Campbell, C. W. Hatcher, A. M. Hawryluk, R. L. Kauff-

man, L. D. Pleasance, G. Rambach, J. H. Scofield, G. Stone, and T. A. Weaver, *Phys. Rev. Lett.* **54**, 110 (1985).

³J. Zhang, A. G. MacPhee, J. Nilsen, J. Lin, T. W. Barbee, Jr., C. Danson, M. H. Key, C. L. S. Lewis, D. Neely, R. M. N. O'Rourke, G. J. Pert, R. Smith, G. J. Tallents, J. S. Wark, and E. Wolfrum, *Phys. Rev. Lett.* **78**, 3856 (1997).

⁴J. Zhang, A. G. MacPhee, J. Lin, E. Wolfrum, R. Smith, C. Danson, M. H. Key, C. L. S. Lewis, D. Neely, J. Nilsen, G. J. Pert, G. J. Tallents, and J. S. Wark, *Science* **276**, 1097 (1997).

⁵R. Smith, G. J. Tallents, J. Zhang, G. Eker, S. McCabe, G. J. Pert, and E. Wolfrum, *Phys. Rev. A* **59**, R47 (1999).

⁶H. Daido, S. Sebba, N. Sakaya, Y. Tohyama, T. Norimatsu, K. Mima, Y. Kato, S. Wang, Y. Gu, G. Huang, H. Tang, K. Murai, R. Butzbach, I. Uschmann, M. Vollbrecht, and E. Forster, *J. Opt. Soc. Am. B* **16**, 2295 (1999).

⁷Yu. V. Afanasiev and V. N. Shlyaptsev, *Sov. J. Quantum Electron.* **19**, 1606 (1989).

⁸P. V. Nickles, V. N. Shlyaptsev, M. Kalachnikov, M. Schnürer, I. Will, and W. Sandner, *Phys. Rev. Lett.* **78**, 2748 (1997).

⁹J. Dunn, A. L. Osterheld, R. Shepherd, W. E. White, V. N. Shlyaptsev, and R. E. Stewart, *Phys. Rev. Lett.* **80**, 2825 (1998); J. Dunn, J. Nilsen, A. L. Osterheld, Y. Li, and V. N. Shlyaptsev, *Opt. Lett.* **24**, 101 (1999).

¹⁰P. J. Warwick, C. L. S. Lewis, M. P. Kalachnikov, P. V. Nickles, M. Schnürer, A. Behjat, A. Demir, G. J. Tallents, D. Neely, E. Wolfrum, J. Zhang, and G. J. Pert, *J. Opt. Soc. Am. B* **15**, 1808 (1998).

¹¹M. P. Kalachnikov, P. V. Nickles, M. Schnürer, W. Sandner, V. N. Shlyaptsev, C. Danson, D. Neely, E. Wolfrum, J. Zhang, A. Behjat, A. Demir, G. J. Tallents, P. J. Warwick, and C. L. S. Lewis, *Phys. Rev. A* **57**, 4778 (1998).

¹²J. Y. Lin, G. J. Tallents, A. G. MacPhee, A. Demir, C. L. S. Lewis, R. M. N. O'Rourke, G. J. Pert, D. Ros, and P. Zeitoun, *Opt. Commun.* **166**, 211 (1999).

¹³Y. L. Li, J. Dunn, J. Nilsen, T. W. Barbee, Jr., A. L. Osterheld, and V. N. Shlyaptsev, *J. Opt. Soc. Am. B* **17**, 1098 (2000).

¹⁴J. Dunn, Y. Li, A. L. Osterheld, J. Nilsen, J. R. Hunter, and V. N. Shlyaptsev, *Phys. Rev. Lett.* **84**, 4834 (2000).

¹⁵H. Daido, S. Ninomiya, T. Imani, Y. Okaichi, M. Takagi, R. Kodama, H. Takabe, Y. Kato, F. Koike, J. Nilsen, and K. Murai, *Int. J. Mod. Phys. B* **11**, 945 (1997).

¹⁶Y. J. Li and J. Zhang, *Phys. Rev. E* **63**, 036410 (2001).

¹⁷Y. J. Li, X. Lu, and J. Zhang, *Phys. Rev. E* **66**, 046501 (2002).

¹⁸J. P. Christiansen, D. E. T. F. Ashby, and K. V. Roberts, *Comput. Phys. Commun.* **7**, 271 (1974).

¹⁹R. D. Cowan, *The Theory of Atomic Structure and Spectra* (University of California Press, Berkeley, CA, 1981).

²⁰E. Alexander, M. Even-Zohar, B. S. Fraenkel, and S. Goldsmith, *J. Opt. Soc. Am.* **61**, 508 (1971).

²¹P. G. Burkhalter, L. Cohen, R. D. Cowan, and B. V. Sweeney, *J. Opt. Soc. Am.* **72**, 95 (1982).

²²Y. L. Li, J. Nilsen, J. Dunn, and A. L. Osterheld, *Phys. Rev. A* **58**, R2668 (1998).

An optical trap for relativistic plasma^{a)}

Ping Zhang,^{b)} Ned Saleh, Shouyuan Chen, Zhengming Sheng,^{c)} and Donald Umstadter
FOCUS Center, University of Michigan, Ann Arbor, Michigan 48109-2099

(Received 13 November 2002; accepted 14 February 2003)

The first optical trap capable of confining relativistic electrons, with kinetic energy ≤ 350 keV was created by the interference of spatially and temporally overlapping terawatt power, 400 fs duration laser pulses ($\leq 2.4 \times 10^{18}$ W/cm²) in plasma. Analysis and computer simulation predicted that the plasma density was greatly modulated, reaching a peak density up to 10 times the background density ($n_e/n_0 \sim 10$) at the interference minima. Associated with this charge displacement, a direct-current electrostatic field of strength of $\sim 2 \times 10^{11}$ eV/m was excited. These predictions were confirmed experimentally by Thomson and Raman scattering diagnostics. Also confirmed were predictions that the electron density grating acted as a multi-layer mirror to transfer energy between the crossed laser beams, resulting in the power of the weaker laser beam being nearly 50% increased. Furthermore, it was predicted that the optical trap acted to heat electrons, increasing their temperature by two orders of magnitude. The experimental results showed that the number of high energy electrons accelerated along the direction of one of the laser beams was enhanced by a factor of 3 and electron temperature was increased ~ 100 keV as compared with single-beam illumination.

© 2003 American Institute of Physics. [DOI: 10.1063/1.1566033]

I. INTRODUCTION

Trapping has often been used with great success to confine ultracold matter, leading to many important applications, such as Bose–Einstein condensation and matter-wave lasers. Traps capable of confining ultrahot matter, or plasma, have also been built for applications in the basic plasma research and thermonuclear fusion. For instance, low-density, $n_e \sim 10^7$ cm⁻³, non-neutral plasmas with temperature $T_e \leq 1$ keV have been confined with static magnetic fields in Malmberg–Penning traps.¹ Low-density, $n_e \sim 10^{14}$ cm⁻³, $T_e \sim 10$ –100 keV plasmas are confined in magnetic mirrors and tokamaks. Since the discovery of the ponderomotive force over 40 years ago, it has been well known that charged particles interacting with an oscillating electromagnetic field will seek regions of the minimum light intensity (dark-seeking behavior).² The idea of trapping charged particles by the ponderomotive force with the appropriate electromagnetic field distribution was then proposed.³ Two-dimensional electron confinement with a specially shaped laser beam has been discussed.^{4–6} By modulating laser pulse intensities via wave-plates, a strong three-dimensional optical trap capable of confining electrons of kinetic energies up to 10 keV was built.^{7,8}

In this paper, we discuss an optical trap capable of confining extremely high density (close to critical density) and hot (relativistic) plasmas, of kinetic energy up to 350 keV, by means of the interference of two terawatt-class (TW) femtosecond laser pulses. In the intersection region of laser beams, the modulated total laser intensity formed ponderomotive po-

tential troughs of subwavelength width (0.7 μm), and very high ponderomotive potential gradients, up to 10¹² eV/m. The Thomson scattering, stimulated Raman scattering, analysis, and computer simulation all indicate that the electrons were bunched by the strong ponderomotive force into sheets of thickness two orders of magnitude less than the laser wavelength, and an electron density up to 10 times higher than that of the background n_0 . Correspondingly, the stimulated Raman side scattering indicates strong electron density depletion (0.4% of n_0) between the density-bunched regions. An electrostatic field of 10¹¹ eV/m was produced by the bunched electrons. Unlike the electric field of an electron plasma wave,^{9–12} the electrostatic field in this optical trap was a localized direct-current field, with zero phase velocity and a fixed field direction during the laser beam interference.

II. ANALYSIS AND COMPUTER SIMULATION

The physical picture of this optical trap is simple. A ponderomotive force $\vec{F}_p \propto \nabla I$, where I is the intensity of laser, is produced when light intensity has a spatial gradient. Two intense laser beams of the intensities I_1 and I_2 , with same frequency and parallel polarization, perpendicularly crossing each other, interfere, causing spatial modulation of the light intensity given by $I = I_1 + I_2 + 2\sqrt{I_1 I_2} \cos \delta$, where δ is the phase difference of these two laser pulses. In the experiment described in the following, $I_1 = 0.25 I_2$ and the peak interference intensity is nine times higher than that of the valley, and the distance of the intensity peak-to-valley is $0.35\lambda_L$, where λ_L is the wavelength of the laser. These intensity peaks and valleys lie along x , which is the spatial dimension perpendicular to the bisector of the two laser propagation directions. By means of the interference of two high-power laser pulses, a very high intensity gradient cre-

^{a)}Paper GI2 2, Bull. Am. Phys. Soc. **47**, 137 (2002).

^{b)}Invited speaker.

^{c)}Also at Laboratory of Optical Physics, Chinese Academy of Sciences, Beijing 100080, People's Republic of China.

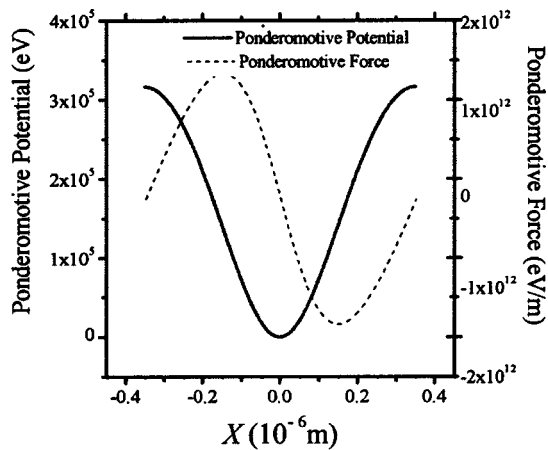


FIG. 1. Ponderomotive force and potential distribution. The potential valley forms the optical trap.

ated. If free electrons are present, they will oscillate in the high frequency laser field and Thomson-scatter light. On a time scale of several laser cycles, they experience a ponderomotive force that pushes them to the intensity valleys. The ponderomotive force is

$$\vec{F}_p = -m_e c^2 \frac{\partial \gamma}{\partial x}, \quad (1)$$

where $\gamma = \sqrt{1 + a^2/2}$ is the relativistic factor and $a = 8.5 \times 10^{-10} \lambda_L (\mu\text{m}) \sqrt{I (\text{W/cm}^2)}$ is the normalized vector potential of the laser field, λ_L is the laser wavelength, I is the total intensity, and $m_e c^2$ is the rest-energy of the electron. The interference laser intensity expressed by the normalized vector potential is $a^2 = 8a_1^2 \sin^2(\pi x/D)$, where D is the distance between the two laser intensity peaks and $|x| \leq D/2$. The ponderomotive force can be calculated using Eq. (1), which gives

$$\vec{F}_p = -\frac{2\pi m_e c^2 a_1^2}{\gamma D} \sin\left(\frac{2\pi x}{D}\right) \frac{\vec{x}}{x}. \quad (2)$$

Using the laser parameters in the experiment described in the following, in the interference region, the peak laser intensity is $4 \times 10^{18} \text{ W/cm}^2$. The corresponding ponderomotive force is up to 10^{12} eV/m , and the ponderomotive potential ϕ_p , defined by $\vec{F}_p = -\nabla \phi_p$, is about 300 keV (Fig. 1).

Initially, because the plasma is uniform, the electrons experience only the ponderomotive force, which pushes them toward the interference troughs, where they are trapped and bunched. Because the much heavier ions do not have time to move significantly during the interference of subpicosecond duration pulses, but electrons do, a large direct-current electrostatic field \vec{E}_{es} is created, which exerts an electrostatic force on the electrons in the direction opposite to the ponderomotive force.

The value of electrostatic force $e\vec{E}_{es}$ increases with bunching, based on Gauss' law

$$\int_S \vec{E}_{es} \cdot d\vec{S} = \frac{e}{\epsilon_0} \int_V (n_e - n_0) dV,$$

where S and V are the boundary surface and volume of the

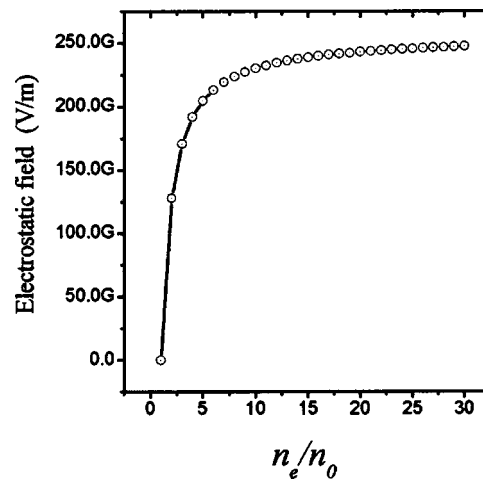


FIG. 2. Electrostatic field vs electron density ratio n_e/n_0 .

bunched electrons, respectively, and n_e and n_0 are the bunched and background electron (or positive charge) densities, respectively. This charge distribution is localized in the optical trap, but all these charged particles (inside the Gaussian pillbox) will contribute to the field no matter if these charges are in motion or not. When the bunched electron density n_e is higher than n_0 in the pillbox during the laser beam interference, the direction of the electrostatic field is fixed and thus the field is a direct-current one. Assuming that the bunching process is in one dimension, the electrostatic force created by the electron bunch is given by

$$\vec{E} = \frac{n_0 |e|}{\epsilon_0} \left(\frac{n_e}{n_0} - 1 \right) \vec{X}, \quad (3)$$

where X is 1/2 the thickness of the bunched electron sheet. The maximum intensity of the electrostatic field is reached at the boundaries of the pillbox. Using Eq. (3), the dependence of electrostatic field on the electron density ratio n_e/n_0 is shown in Fig. 2. In the experiment described in the following, the background electron density n_0 is $4 \times 10^{25} \text{ m}^{-3}$. With $n_e/n_0 = 2$, the field strength jumps to $E_{es} = 1.28 \times 10^{11} \text{ eV/m}$, and when $n_e/n_0 = 6$, E_{es} reaches $2.1 \times 10^{11} \text{ eV/m}$, and then it increases gradually with n_e/n_0 to the saturation value of $\sim 2.5 \times 10^{11} \text{ eV/m}$.

A similar grating-like electron distribution at the surface of a plasma was previously predicted and observed by means of a one-dimensional particle-in-cell code,²³ but this model neglected the influence of electron thermal pressure.

In the bunch process, the force of electron thermal pressure \vec{F}_T prevents the electron accumulation. Assuming that the bunch process is adiabatic, \vec{F}_T and the electron thermal pressure P_e are given by

$$\vec{F}_T = \frac{\nabla P_e}{n_e},$$

$$P_e = n_0 T_{e0} (\text{eV}) \left(\frac{n_e}{n_0} \right)^3, \quad (4)$$

$$n_e(x) = \alpha n_0 \exp \left[\left(\frac{x}{X} \right)^2 \right],$$

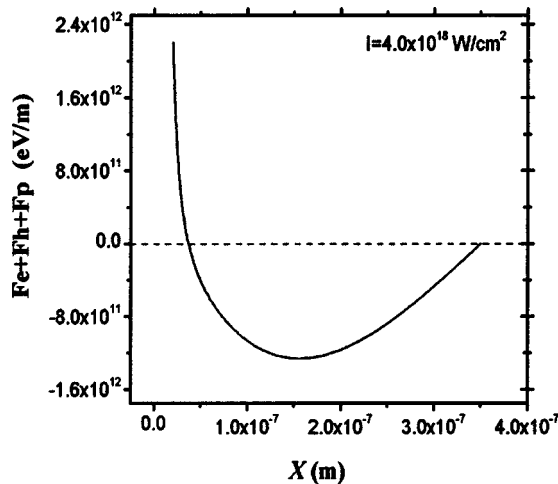


FIG. 3. Combination of the ponderomotive force, electrostatic force, and force of thermal pressure.

where $T_e(eV)=100$ eV is the initial electron temperature and α is a parameter determined by the restriction of electron number conservation

$$\frac{\alpha}{D} \int_{-D/2}^{D/2} \exp\left[-\left(\frac{x}{X}\right)^2\right] dx = 1. \quad (5)$$

Then the force of thermal pressure on the boundary of the bunched electron sheet is

$$\vec{F}_T = 6\alpha^2 T_{e0}(eV) \frac{\vec{X}}{X^2}. \quad (6)$$

Assuming the bunched electron sheet boundary locates at the force balance points where

$$\vec{F}_P(X) + \vec{F}_{es}(X) + \vec{F}_T(X) = 0, \quad (7)$$

the thickness ($2X$) of the electron sheets and the corresponding electron densities at different interference intensities can be calculated. Figure 3 shows the dependence of the combination of the three forces on the thickness of the bunched-electron sheets at peak laser intensity of 4×10^{18} W/cm². The total force looks like van der Walls force, where at points beyond the balance point closer to the interference fringe, the force is a bunching force, while points closer to the bunched electron distribution, the force is thermal-pressure dominated, resist the further accumulation. The electron density ratio $n_e/n_0 \sim D/2X = 9.2$ is then calculated. At peak laser intensity of 4.8×10^{18} W/cm², the highest intensity observed in the experiment, the width of each bunched density region was then reduced to $0.68 \mu\text{m}$ or about $D/10.2$, which implies $n_e/n_0 = 10.2$ and $E_{es} \sim 2.3 \times 10^{11}$ eV/m.

The bunched electron in the laser beam intersection has the structure of a density grating or multi-layer mirror. It will diffract or reflect incident laser light resulting in laser energy transfer between the two crossed laser beams. Based on the density-grating model, the density grating satisfies

$$D(\sin \theta_m - \sin \theta_t) = m\lambda, \\ m = 0, \pm 1, \pm 2, \dots, \quad (8)$$

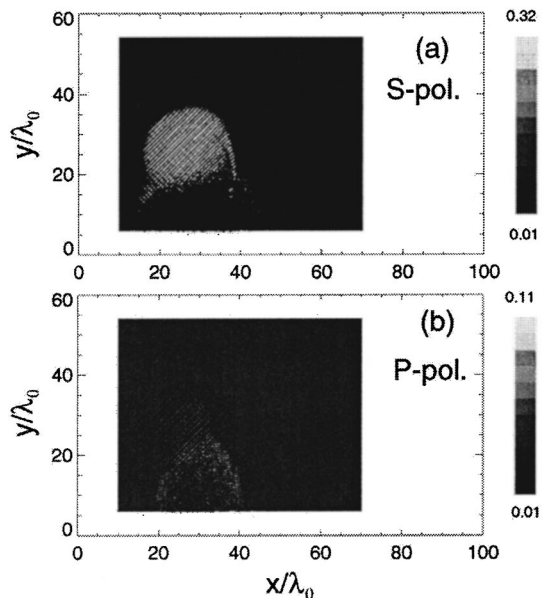


FIG. 4. Simulation shows that, with the interference of two *s*-polarized laser pulses, there is an electron-density bunching and grating structure at the laser intersection (upper picture), while, with two *p*-polarized laser pulses, no such density bunching (lower picture).

where θ_i is the incident angle and θ_m is the diffraction angle of m order. In our experiment, the weaker laser beam I_1 was named pump and the stronger one I_2 was injection. If the injection beam is the incident laser, the only possible diffraction direction is in the pump direction with ($m = -1$), and vice versa. The weaker pump beam will get more energy from injection during the dual beam interference. By using the multi-layer mirror mode, the same results of energy transfer are obtained.

The above-given calculation is consistent with a two-dimensional particle-in-cell code computer simulation, which solves Maxwell's equations and the equation of motion for the particles in plasma. In this simulation, a rectangular simulation box of $100\lambda \times 60\lambda$ is used, which is split into 1000×600 cells for the integration of the Maxwell's equations. A homogeneous plasma volume with an initial density of $0.04n_c$ occupies part of the simulation box. The pump laser of the normalized vector potential $a_1 = 0.5$, and it is along the x direction. The injection pulse of $a_2 = 1.0$, which is four-times stronger in intensity than pump, is along the y direction. Nine particles per cell are used for electrons and ions. Absorption boundaries for the fields and reflection boundaries for particles are used in both the x and y directions. The simulation results are depicted in Fig. 4, where the bunched charge regions exhibit a peak density ratio of $n_e/n_0 \sim 10$ and width $\sim 1/10$ of the distance between interference peaks, at the time of maximum overlap. The simulation also predicts that the bunched electrons Thomson scatter the laser so that there is significant energy transfer from injection to pump, making the pump laser increase about 50% (Fig. 5). This energy transfer was also predicted by previous theory.¹³

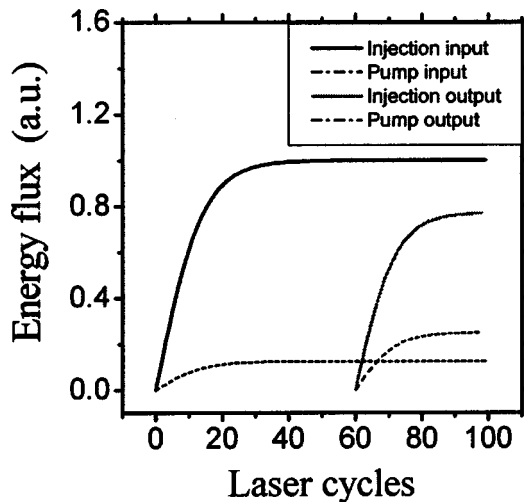


FIG. 5. Energy transfer from stronger injection laser to the weaker pump laser shown by simulation.

III. EXPERIMENTAL RESULTS

In a proof-of-principle experiment, two $1.053 \mu\text{m}$ wavelength laser pulses, each ultra-short in duration (400 fs) and high peak power (1.5 and 6.0 TW), were focused perpendicularly to each other, with $f/3$ parabolic (vacuum spot-size of $12 \mu\text{m}$ full width at half maximum), reaching peak intensities of 6×10^{17} and $2.4 \times 10^{18} \text{ W/cm}^2$, respectively. The beams were predominantly upward polarized, but had a small component of horizontal polarization due to the tight focusing geometry. Using a delay line, the pulses were overlapped temporally to within 30 fs inside a supersonic helium gas jet (at $5.5 \times 10^6 \text{ Pa}$).

Plasma with density $n_0 = 4 \times 10^{25} \text{ m}^{-3}$ was created by photoionization of the gas. Light propagation through the plasma was observed from top-view Thomson scattering pictures. The bright spot in Fig. 6 showed that the Thomson scattered light was significantly enhanced along the bisector of the laser beam intersection region. A line out of the bright spot indicated that the spatially averaged Thomson scattered power $\langle P_s \rangle$ from the region of the beam's intersection was more than ten times $\langle P_0 \rangle$. The latter was from the background electrons outside the intersection region with density in the channel created by the more powerful of the two laser beams. This enhancement, $\langle P_s / P_0 \rangle = 10$, implied that the scattering was coherent, i.e., the Bragg scattering formula,¹⁴ $P_s / P_0 \propto (n_e / n_0)^2$ applied, and indicated that $n_e / n_0 > 10$, which was 100 times higher than the largest reported amplitude for a plasma wave, which—unlike a trap modulation—was limited in amplitude by wave-breaking.^{15,16}

The top-view spectra of the scattering lights are shown in Fig. 7. With only the pump laser, the signals of spectrum were in the level of background. When the two laser pulses were crossed, the spectrum clearly shows peaks of the stimulated Raman scattering (SRS) of the frequency shift $\Delta\omega \sim \omega_p = 1.9 \times 10^{13} \text{ arc/sec}$ corresponding to plasma density $n_e \sim 4 \times 10^{-3} n_0$ determined using $\omega_p = \sqrt{e^2 n_e / \gamma \epsilon_0 m_e}$, where γ was the relativistic factor and $\epsilon_0 = 8.85 \times 10^{-12} \text{ F/m}$ was the permittivity of free space. The result

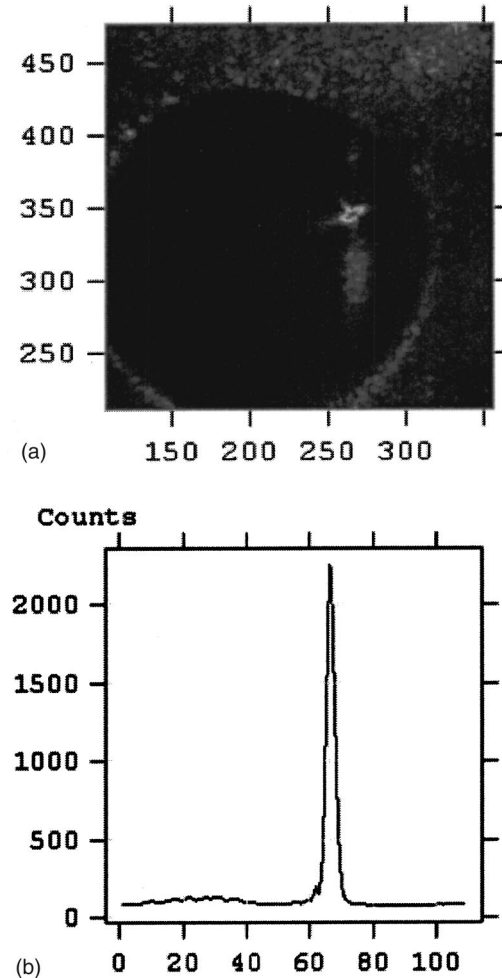


FIG. 6. (a) Image of the Thomson scattered light viewed from top downward to the throat of the nozzle. The weaker pump beam propagated from right to left while the stronger injection beam from top to bottom. (b) Intensity distribution of Thomson scattering light along the injection plasma channel showed the light enhancement at the beam intersection. From this result, an accumulated plasma density with amplitude $n_e \sim 10 n_0$ was inferred.

indicates relatively large density accumulation, about ten times of the background. Plasma cavities were dug to nearly 99.6% electron density depletion. Figure 7 also showed that the unshifted light, originating from Thomson scattering, was about five times stronger with crossed laser pulses than from only injection pulse. When the effects of spatial integration were accounted for, the ratio $\langle P_s / P_0 \rangle \sim 10$ is again obtained.

With crossed laser pulses, two strong satellite lines were observed in the spectrum in Fig. 7, with the wavelength shifts $\sim \pm 3.8 \text{ nm}$ away from the fundamental light. These two satellite lines may have originated from stimulated Brillouin scattering (SBS). The associated ion acoustic wave was excited by the beating or optical mixing of the crossed laser pulses, which had the frequency bandwidths that exceeded the ion acoustic frequency shift. The ion acoustic wave and SBS signals will be discussed in detail in a forthcoming publication.

The spectra of light scattered in the direction of pump beam were also measured (Fig. 8), and the results indicate

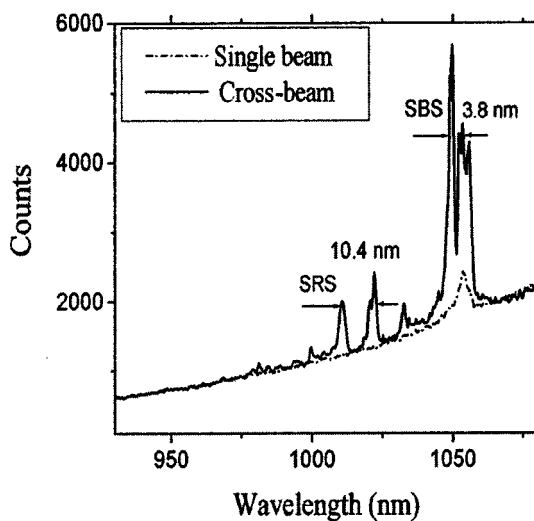


FIG. 7. Top view spectra of the scattered light, with/without the pump beam.

that the pump laser beam was enhanced by energy transfer. This result confirmed the prediction of the analysis, simulation, and theory. The bunched electrons not only reflected the fundamental laser but also all the scattering light signals from injection to pump or vice versa. The reflection of forward stimulated Raman scattering light from injection to pump may especially bring about optical mixing between the fundamental light and the reflected scattering, resulting in the pump plasma wave being resonantly driven. It was observed in some spectra that with dual pulse illumination, the scattered lights in the pump direction were obviously enhanced while the fundamental laser signal was barely increased. A possible reason is that resonant excitation of the plasma waves effectively absorbed the driving laser energy.

In order to test the calculation model prediction for the dependence of the n_e/n_0 on the laser interference intensities, the values of $\langle P_s/P_0 \rangle$ were measured at peak laser intensities ranging from 8×10^{17} to $4.8 \times 10^{18} \text{ W/cm}^2$. Discounting

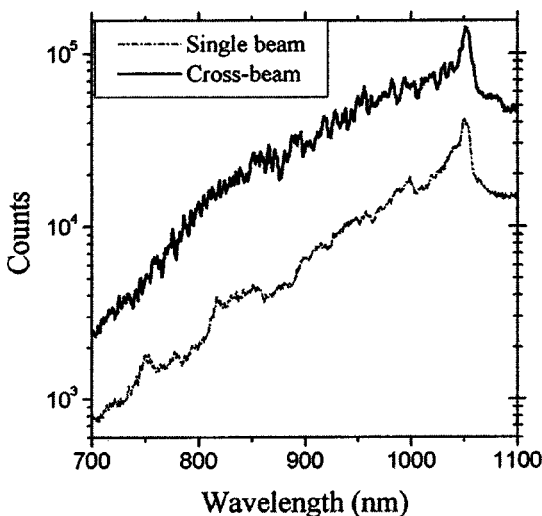


FIG. 8. Spectra of the laser and scattered light in the pump beam direction, with/without injection beam.

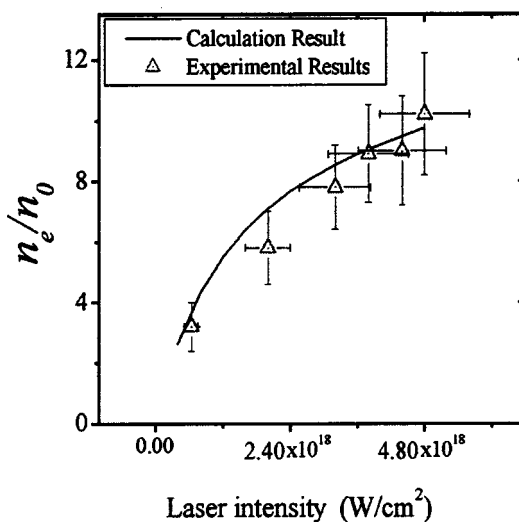


FIG. 9. Comparison of the analytical and experimental results of the inferred electron-density-ratio vs laser intensities.

the background and the contribution of SBS, the result was shown in Fig. 9, and the inferred values of n_e/n_0 coincided relatively well with the theoretical prediction.

IV. ELECTRON HEATING AND INJECTION

We have previously discussed that the optical trap can bunch the electrons and produce high electron densities, up to $10n_0$, resulting in the excitation of a strong electrostatic field, on the order of 10^{11} eV/m . The resistance of the electrostatic force against the bunching ponderomotive force increases the electric potential energy of the bunched electrons. $P\text{-}V$ work will increase the electron temperature. Assuming that the bunching process is adiabatic, the temperature of the bunched electrons is

$$T_e(\text{eV}) = \left(\frac{n_e}{n_0} \right)^{\Gamma-1} T_{e0}(\text{eV}). \quad (9)$$

If the process is in one dimension, $\Gamma=3$, with a ten-time electron density increase, the corresponding electron temperature $T_e(\text{eV})$ will be increased by two orders.

It has to be pointed out that the above-mentioned adiabatic model works well in a quasi-static process in which Maxwell distribution applies. Actually in the short time period of the interference of 400 fs, the bunched electron system approaches, but never reaches, such an equilibrium state. The boundary of the accumulated electron bulk vibrates around the force balance points. If the vibration is assumed harmonic, the frequency of the vibration can be simply estimated from Fig. 3. Near the force balance point, the slope $\Delta F/\Delta X$ is about -2.7 N/m , and thus a frequency $1.6 \times 10^{15} \text{ s}^{-1}$ can be calculated. The resistance of the electron thermal pressure against the bunching increases the electron kinetic energies of random motion, which is related to the electron temperature, and the work of electrostatic force increases the electron potential energies. With increases of the electron temperature and potential energy, the laser energy

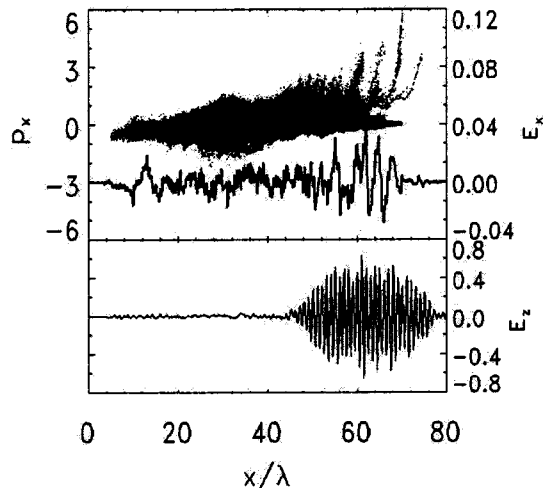


FIG. 10. Snapshot of simulation taken at 80 laser cycles shows that with dual laser illumination, the electric field in pump laser direction x was obviously enhanced and electrons were heated and accelerated primarily in the pump-laser direction. The results were consistent with the electrons being heated during the period of beam overlap and then injected into the acceleration phase of the enhanced plasma waves in the pump direction.

is gradually absorbed by the bunched electrons and the vibration amplitude gradually decreases until the end of the laser pulse interference.

Computer simulation shows that the electrons are heated in the beam intersection and then these preheated electrons are injected into the enhanced pump plasma wave. Acceleration by the resulting plasma wave produces a beam of high energy electrons in the direction of pump (Fig. 10). The measurement of the electron spectra and beam profiles in pump direction with/without injection shows that with crossed laser pulses, the number of high energy electrons is increased three times and the corresponding temperature increase is more than 100 keV (Fig. 11). Possible mechanisms for the stronger electron beam are the enhancement of pump plasma wave by the laser energy transfer, the beating of the reflected forward SRS light from injection with the pump laser light, and the injection of the preheated electrons into pump plasma wave, which made more electrons phase-matched with the wave. Simulations also indicated that by using this technique with shorter pulse lasers, the energy spread of these accelerators might be significantly reduced.¹⁷ Details of the effects of the two crossed laser pulses on electron acceleration in the laser driven plasma wave will be discussed in a separate publication.

V. DIFFERENCES BETWEEN THE OPTICAL TRAP AND PLASMA WAVES

The electrostatic field of our optical trap is different from that in a plasma wave (the field strength of a plasma wave can be on the order of 10^{11} eV/m). First, the optical trap and the electrostatic field of the optical trap are localized and have zero phase velocity. A plasma wave, on the other hand, moves with velocity of $v_p \sim c \sqrt{1 - \omega_p^2/\omega^2}$. Second, the distance (wavelength) between the two bunched electron density peaks is only $0.7\lambda_L$, while in a plasma wave, the wavelength, based on the parameters of laser and back-

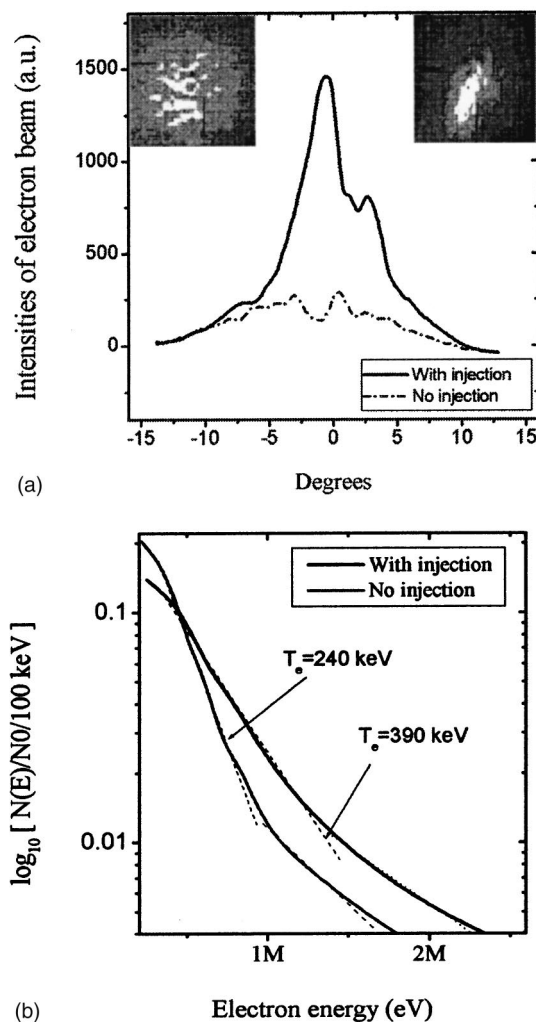


FIG. 11. (a) Enhancement of electron number with injection on upper left picture: the electron beam profile without injection. Upper right picture: the profile with injection. (b) Increase in electron temperature in pump beam direction with injection on.

ground plasma in our experiment, is much longer (by greater than ten times) than the laser wavelength. Third, the bunched electrons have density modulation $\delta n_e/n_e = (n_e - n_0)/n_0$ up to 10, while in a plasma wave the corresponding density modulation is less than 1. Fourth, the function of the optical trap is to hold electrons and increase their electrostatic potentials and the kinetic energies of random motion. A plasma wave, on the other hand, acts to increase the electron kinetic energies of directional motion along the propagation direction. These differences make this optical trap unique in laser plasma physics.

There are several important applications of the optical trap besides electron acceleration. For instance, it might be used as a test bed for the study of relativistic nonlinear Thomson scattering.⁸ The ponderomotive force can be expressed in another form

$$\vec{F}_p = -\nabla(T + m_0c^2) = -\nabla \left[m_0c^2 \left(1 + \frac{I_{18}\lambda_L^2}{1.37} \right)^{1/2} \right], \quad (10)$$

where T is the kinetic energy of the electrons and I_{18} is the interference laser intensity in units of 10^{18} W/cm². If the

interference intensity is $I_{18} \sim 10$, then $T_{\max} = 1$ MeV, or about $2m_e c^2$. When the electrons oscillating with this energy collide with the stationary nuclei of plasma ions, they will produce positrons,¹⁸ which can either be accelerated in laser driven wakefield or allowed to annihilate with the electrons to generate bright gamma ray bursts with 511 keV energy. This research is also relevant to fast ignition fusion¹⁹ or ion acceleration experiments,²⁰ in which a laser pulse may potentially beat with a reflected weaker pulse, with intensities comparable to those used in our experiment. Last, an electron beam that enters the trap with kinetic energy exceeding the trapping threshold will be “wiggled” by the periodically spaced electrostatic field, causing emission of coherent short-wavelength radiation, as discussed previously in the context of plasma-wave wiggler.²¹ Remarkably, the strength of the optical-trap field is almost one million times higher, and the wavelength is almost a million times shorter, than a conventional magnetic wiggler. Calculations indicate that 100-times shorter wavelength light can be generated in the former case, with electrons of the same given energy.

VI. CONCLUSIONS

By interfering two TW femtosecond laser pulses in plasma, an optical trap of potential depth ~ 350 keV was experimentally created. An unprecedented electron bunching of $n_e/n_0 \sim 10$ was inferred from scattering diagnostics. A localized electrostatic field of strength $\sim 2 \times 10^{11}$ eV/m was excited by the electron accumulation inside the optical trap. Transfer of light energy from one beam to another was also observed. Optical mixing by two crossed laser pulses resonantly excited electron plasma waves and ion acoustic waves. As predicted by analysis and simulation, electrons were heated in the optical trap and these preheated electrons were then injected into the enhanced pump plasma wave, resulting in enhancements of the electron beam both in in-

tensity and temperature. The latter is the first step toward the experimental realization of the laser injected laser acceleration concept (LILAC).²²

ACKNOWLEDGMENTS

We thank A. Maksimchuk for help with the laser and useful comments from W. Theobald, G. Shvets, N. Fisch, and D. D. Meyerhofer.

We acknowledge support from the Department of Energy, Award No. DE-FG02-98ER41071 and the National Science Foundation Grants Nos. 0078581 and 0114336.

- ¹F. M. Penning, *Physica (Utrecht)* **3**, 873 (1936); J. H. Malmberg and J. S. de Grassie, *Phys. Rev. Lett.* **35**, 517 (1975).
- ²H. A. H. Boot and R. B. R.-S. Harvie, *Nature (London)* **180**, 1187 (1957).
- ³V. Gapanov and M. A. Miller, *J. Exp. Theor. Phys.* **34**, 242 (1958).
- ⁴N. J. Phillips and J. J. Sanderson, *Phys. Lett.* **21**, 533 (1966).
- ⁵U. Mohideen, H. W. K. Tom, R. R. Freeman *et al.*, *J. Opt. Soc. Am. B* **9**, 2190 (1992).
- ⁶C. I. Moore, *J. Mod. Opt.* **39**, 2171 (1992).
- ⁷J. L. Chaloupka, Y. Fisher, T. J. Kessler *et al.*, *Opt. Lett.* **22**, 1021 (1997).
- ⁸J. L. Chaloupka and D. D. Meyerhofer, *Phys. Rev. Lett.* **83**, 4538 (1999).
- ⁹C. S. Liu and V. K. Tripathi, *Interaction of Electromagnetic Waves With Electron Beams and Plasmas* (World Scientific, Singapore, 1994).
- ¹⁰E. Esarey and P. Sprangle, *IEEE Trans. Plasma Sci.* **24**, 252 (1996).
- ¹¹D. Umstadter, S-Y. Chen, A. Maksimchuk *et al.*, *Science* **273**, 472 (1996).
- ¹²R. Wagner, S-Y. Chen, A. Maksimchuk, and D. Umstadter, *Phys. Rev. Lett.* **78**, 3125 (1997).
- ¹³G. Shvets, N. J. Fisch, A. Pukhov *et al.*, *Phys. Rev. E* **60**, 2218 (1999).
- ¹⁴R. E. Slusher and C. M. Surko, *Phys. Fluids* **23**, 472 (1980).
- ¹⁵J. M. Dawson, *Phys. Rev.* **133**, 383 (1959).
- ¹⁶T. Tajima and J. M. Dawson, *Phys. Rev. Lett.* **43**, 267 (1979).
- ¹⁷D. Umstadter, *Phys. Plasmas* **8**, 1774 (2001), and references therein.
- ¹⁸E. P. Liang, S. C. Wilks, and M. Tabak, *Phys. Rev. Lett.* **81**, 4887 (1998).
- ¹⁹M. Roth, T. E. Cowan, M. H. Key *et al.*, *Phys. Rev. Lett.* **86**, 436 (2001).
- ²⁰Y. Sentoku, V. Y. Bychenkov, K. Flippo *et al.*, *Appl. Phys. B: Lasers Opt.* **74**, 207 (2002).
- ²¹R. L. Williams, C. E. Clayton, C. Joshi *et al.*, *IEEE Trans. Plasma Sci.* **21**, 156 (1993).
- ²²D. Umstadter, J. K. Kim, and E. Dodd, *Phys. Rev. Lett.* **76**, 2073 (1996).
- ²³L. Plaja and L. Roso, *Phys. Rev. E* **56**, 7142 (1997).

Electron acceleration by an intense short-pulse laser in underdense plasma

M. Y. Yu

Institut für Theoretische Physik I, Ruhr-Universität Bochum, D-44780 Bochum, Germany

Wei Yu

Shanghai Institute of Optics and Fine Mechanics, Shanghai 201800, People's Republic of China

Z. Y. Chen

Institut für Theoretische Physik I, Ruhr-Universität Bochum, D-44780 Bochum, Germany

and Department of Chemistry, University of Antwerp, B-2610 Wilrijk-Antwerp, Belgium

J. Zhang

Institute of Physics, Chinese Academy of Sciences, Beijing 100080, People's Republic of China

Y. Yin and L. H. Cao

National University of Defense Technology, Changsha 410073, People's Republic of China

P. X. Lu and Z. Z. Xu

Shanghai Institute of Optics and Fine Mechanics, Shanghai 201800, People's Republic of China

(Received 23 October 2002; accepted 10 March 2003)

Electron acceleration from the interaction of an intense short-pulse laser with low density plasma is considered. The relation between direct electron acceleration within the laser pulse and that in the wake is investigated analytically. The magnitude and location of the ponderomotive-force-caused charge separation field with respect to that of the pulse determine the relative effectiveness of the two acceleration mechanisms. It is shown that there is an optimum condition for acceleration in the wake. Electron acceleration within the pulse dominates as the pulse becomes sufficiently short, and the latter directly drives and even traps the electrons. The latter can reach ultrahigh energies and can be extracted by impinging the pulse on a solid target. © 2003 American Institute of Physics. [DOI: 10.1063/1.1572158]

I. INTRODUCTION

Rapid advances in short-pulse high-intensity lasers have given rise to many new applications. There is thus much interest in the physics of the interaction of intense short-pulse lasers with plasmas and solids. Simulations and experiments have shown that very energetic electrons are produced when an intense short-pulse laser interacts with a low-density plasma or impinges on a solid target. High-energy electrons have many applications, such as in fast ignition of fusion reaction,^{1,2} hard x-ray source,^{3–5} fast ion production,^{6–8} etc. Several theories for high-energy electron generation by laser light have been proposed. These include resonance absorption,⁹ $v \times B$ heating,¹⁰ vacuum heating,¹¹ nonadiabatic heating at the plasma-light interface,¹² and stochastic heating,¹³ etc. In most of these theories the laser light interacts with the electrons at or near the target surface as a standing wave.

When an intense short laser pulse propagates in an underdense plasma, the electrons are accelerated and decelerated by the ponderomotive force at its leading and trailing halves, respectively. The spatial displacement of the electrons can give rise to a large space charge field, whose relaxation after the pulse moves away can lead to strong electrostatic wake oscillations.^{14,15} A small number of electrons in the wake field can reach very high energies and they are released when wave breaking occurs. On the other hand, the ponderomotively accelerated electrons inside a sufficiently

short laser pulse can also reach very high energies. These energetic electrons can be extracted (before they are decelerated) by letting the laser pulse hit a solid target.^{16,17} Physically, electron acceleration inside a laser pulse and inside the laser-excited wake oscillation are separate but closely related processes. The latter are in fact governed by the same equations and can compete with each other. An understanding of the details of the relation between these processes would be helpful in the design of advanced schemes of wake and direct acceleration of electrons. However, they have traditionally been investigated separately. In this paper we investigate the interaction of a very short laser pulse with a plasma, such that the pulse width is less than the plasma-wave length, a situation that occurs in the very rarefied preplasma region of the interaction. In order to clarify the relationship between the two and their relative effectiveness under different conditions, we consider in a unified and transparent manner the electron dynamics in the wake and within the laser pulse. It is found and expressed quantitatively that the relative efficiencies of the two acceleration processes depend on the laser intensity and pulse width, as well as the background plasma density. The results are compared with that from a two-dimensional (2D) particle-in-cell (PIC) simulation.

II. GOVERNING EQUATIONS

When a short planar light pulse propagates in a uniform low-density plasma, the response of the plasma electrons can be described by^{15,18}

$$\mathbf{v}_\perp = \mathbf{a}/\gamma, \quad (1)$$

$$\partial_t(\gamma v_z) = \partial_z(\phi - \gamma), \quad (2)$$

$$\partial_t n = -\partial_z(nv_z), \quad (3)$$

$$\partial_z^2 \phi = n - Zn_i, \quad (4)$$

where \mathbf{v} is the electron velocity normalized by c , \mathbf{A} and ϕ are the vector and scalar potentials normalized by mc^2/e , t is the time normalized by ω^{-1} , the space coordinates are normalized by k^{-1} , where ω and k are the laser frequency and wave number, respectively. Furthermore, $\gamma = (1 - v^2)^{-1/2}$ is the relativistic factor or the normalized (by mc^2) electron energy, n and n_i are the electron and ion densities normalized by the critical density, and Z is the ion charge number. On the time scale of the light pulse and electron motion, the heavy ions are not much affected, so that n_i can be taken as a constant.

We assume that the plasma density is low, the laser intensity high, and the pulse width short, so that the normalized envelope $a = |\mathbf{A}|$ of the vector potential of the laser pulse can be taken to be nonevolving and that it propagates at a constant speed near that of light in the plasma.^{15,19} Thus a is a function of $\xi = z - v_g t$, where $v_g = \sqrt{1 - Zn_i}$ is the constant group velocity of the light waves in the plasma. Integrating Eqs. (2) and (3) and using the boundary condition that the plasma is undisturbed and homogeneous before the laser pulse arrives, or $v_z = 0$, $\phi = 0$, and $n = Zn_i$ at $z = \infty$, one easily obtains the governing equations¹⁵

$$\phi - \gamma + \gamma v_z v_g = -1, \quad (5)$$

$$n(v_z - v_g) = -Zn_i v_g. \quad (6)$$

Eliminating n , v_z , and γ , one obtains from Eq. (4),

$$d_\xi^2 \phi = v_g(1 + \phi)/\sqrt{(1 + \phi)^2 - Zn_i(1 + a^2)} - 1, \quad (7)$$

for ϕ . Equation (7) together with (5) and (6) govern the quasistationary dynamics of the electrons inside as well as behind the laser pulse. Weak transient behavior and damping of the light wave and wake oscillations are neglected. Equation (7) is highly nonlinear and inhomogeneous, but it can be easily integrated numerically.

III. HEURISTIC DESCRIPTION

It is instructive to first review and discuss qualitatively the interaction of a laser pulse with the plasma electrons under nonrelativistic conditions. As the pulse propagates in the plasma, the ponderomotive force at its rising front accelerates the electrons forward, creating a local charge separation, which tends to counteract the motion of the accelerating electrons. The electrons are also decelerated by the ponderomotive force exerted by the trailing part of the pulse. The strength and distribution of the charge separation field thus depend on the intensity, speed, and the width of the pulse, as well as the unperturbed electron density.

In general, the uncompensated electrostatic space charge field remains after the laser pulse passes. The relaxation of this field from electron redistribution then gives rise to the electron wake oscillations having a phase speed near the

speed of the light pulse and a frequency near the plasma frequency. The normalized wavelength λ_p of the wake oscillations is approximately v_g/ω_p , or $2\pi/\sqrt{Zn_i}$, which is a function only of the plasma density. One expects that the efficiency of wake field generation is highest¹⁴ if the separation between the ponderomotive acceleration and deceleration of the electrons by the laser pulse is half λ_p , so that the plasma wave and the ponderomotive force are locally phase matched or “resonant” in a region of about half a plasma wavelength.

On the other hand, if the laser pulse width is much smaller than the optimum value, the dynamics of the electrons therein can be so dominated by the ponderomotive force that the they bunch inside the pulse, at the expense of the downstream (in the pulse frame) electrons. In this case the electrons are trapped by the pulse. Wake oscillations can still be excited by the space charge field behind it. However, they will be much weaker than that of the optimum case.

IV. RESULTS

For the purpose of tracking the electron energy gain within the laser pulse, it is convenient to introduce the parameter

$$\eta = \left(\int a^2 d\xi \right)^{-1} \int 2n(\gamma - 1) d\xi, \quad (8)$$

where the integral is over the laser pulse. Thus, η is the ratio of the energy of the electrons inside the pulse to that of the laser. For a Gaussian pulse, a^2 is given by

$$a^2 = \frac{1}{2} a_0^2 \exp(-\xi^2/L^2)[1 + \cos(2\xi)], \quad (9)$$

for linearly polarized light, and

$$a^2 = a_0^2 \exp(-\xi^2/L^2), \quad (10)$$

for circularly polarized light, respectively. Here, $L = d/2$, and d is the pulse width. This difference in a^2 leads to a strong dependence of the results on the polarization, as will be discussed below. The response of the electrons to the laser pulse can be calculated numerically from Eqs. (5)–(7).

In the numerical evaluation, the electrostatic field and electron density are calculated in the presence of the given $a(\xi)$. The integration is initiated at a large positive ξ in front of the pulse where a is negligibly small. Both the electrostatic field and its derivative start from zero there. The integration is then carried out backwards, so that an overall picture of the electron dynamics and electric field behavior in the pulse and wake is obtained. We shall investigate both regions under the same laser and plasma conditions in order to determine the efficiencies of the two electron acceleration mechanisms.

A. Effectiveness of acceleration in the wake and in the pulse

In Fig. 1, the plasma response to a circularly polarized laser pulse is presented for $Zn_i = 10^{-4}$, and (a) $a_0 = 0.05$ and (b) $a_0 = 2$ and 5. The solid lines show the maximum wake field amplitude ϕ_{\max}/a_0 (here renormalized for the convenience of comparing with the laser field) as a function of

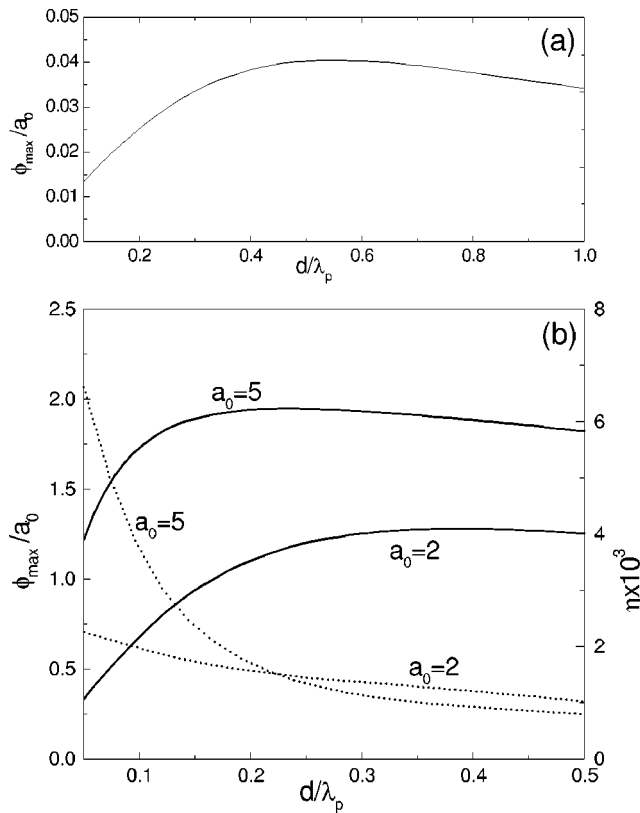


FIG. 1. Maximum wake amplitude (solid lines, renormalized by a_0) ϕ_{\max}/a_0 as a function of d/λ_p for $Zn_i=10^{-4}$, with (a) $a_0=0.05$ and (b) $a_0=2$ and 5. The dependence of the energy ratio η on d/λ_p is given by the dotted lines in (b). For the parameters chosen η is rather small (it is even smaller for the $a_0=0.05$ case in (a) and is therefore not shown), which is consistent with our assumption of constant laser intensity and negligible ion motion.

d/λ_p . Figure 1(a) shows that in the nonrelativistic regime the optimum pulse width for wake generation is about half a plasma wavelength as expected.¹⁴ In this case of relatively weak laser intensity, the laser pulse generates a charge separation field, which induces sinusoidal wake oscillations¹⁴ typical of linear waves. Even for this case one can achieve a wake field amplitude of $\phi_{\max}/a_0 \sim 0.8$. The charge separation field and wake potential can be increased by increasing the laser intensity. However, to optimize the process it is necessary to shorten the laser pulse since the intensity of the ponderomotive force affects the charge separation field. Figure 1 also shows that ϕ_{\max}/a_0 decreases rapidly (slowly) with d/λ_p if the laser pulse width goes below (above) its optimum value.

The dependence of the normalized electron energy η inside the pulse on the pulse width is given by the dotted lines in Fig. 1(b). It is too small to be shown clearly in Fig. 1(a), which is for small $a_0 (= 0.05)$. One can see that in general η increases with decreasing pulse width and increasing intensity of the laser. That is, for the same background plasma density, direct acceleration by the laser pulse is dominant for short and intense pulses.

B. Large amplitude wake oscillations

As the laser intensity increases, the optimum pulse width becomes smaller. Although the interaction scenario inside the

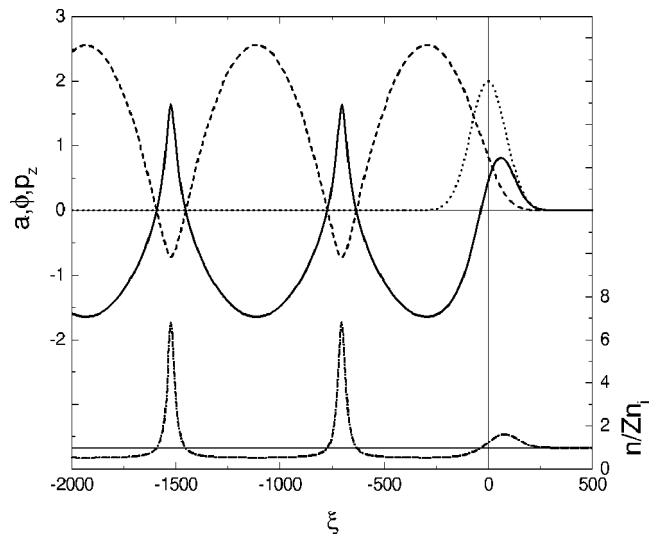


FIG. 2. Evolution of the normalized vector (a , dotted line) and scalar (ϕ , dashed line) potentials, longitudinal electron momentum (p_z , solid line), and electron density (n/Zn_i , dotted-dashed line), for $a_0=2$ and $Zn_i=10^{-4}$. Here, $d=0.35\lambda_p$, corresponding to the optimum width for wake generation.

laser pulse is physically similar to that of weaker pulses, a much stronger charge separation field is created. In fact, the wake oscillations can be of higher amplitude than that of the laser, or $\phi > a_0$, and they can become highly nonlinear. In Fig. 2, the laser–plasma interaction scenario and wake field generation process for a circularly polarized intense laser pulse is presented. Here, $a_0=2$ and $d=0.35\lambda_p$, corresponding to the optimum width for wake generation (see Fig. 1). The background electron density is again $Zn_i=10^{-4}$. The spatial behavior of the normalized vector and scalar potentials a and ϕ , the normalized longitudinal electron momentum $p_z=\gamma v_z$, and the renormalized electron density n/Zn_i are given by the dotted, dashed, solid, and dotted-dashed lines, respectively.

Inside the laser pulse, the electrons are accelerated and decelerated by the ponderomotive forces arising from the high gradients at the front and back of the laser envelope. Their displacement leads to a strong charge separation field, which in turn tends to restrict the motion of the displaced electrons as well as to induce motion by the neighboring electrons. After the pulse passes a large space charge field remains and its relaxation leads to highly nonlinear wake plasma oscillations. The electron density profile in the latter is characterized by localized peaks separated by shallow and flat depressions, characteristic of nonlinear plasma oscillations^{21,22} even in the absence of relativistic effects. It is of interest to point out that, except for the larger amplitudes of the physical quantities involved and the highly nonlinear wake oscillation, the scenario of the laser–plasma interaction in this case is still very similar to the low intensity case.

C. Direct electron acceleration in the laser pulse

Figure 3 is also for a circularly polarized laser with $a_0=2$, but much narrower pulse width ($d=0.05\lambda_p$). The latter

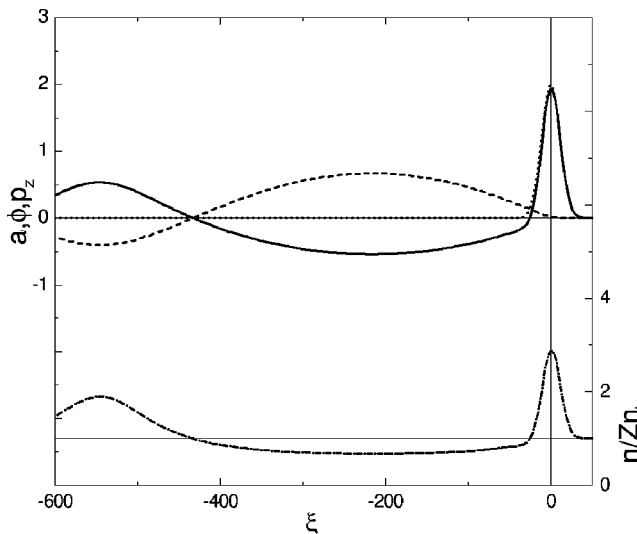


FIG. 3. Same as Fig. 2, but for a much shorter pulse width ($d=0.05\lambda_p$) than that of optimum for wake generation.

is much less than the width $\sim 0.35\lambda_p$ [see Fig. 1(b)] for optimum wake excitation. This case differs considerably from that of Fig. 2, and corresponds to direct electron acceleration by the laser pulse. Here a significant change (with respect to that of Fig. 2) in the behavior of the electron dynamics within the laser pulse occurs: the electron momentum and density profiles become nearly synchronized with that of the laser pulse. The electrons are strongly accelerated and decelerated by the predominating ponderomotive force at the leading and trailing fronts of the pulse, respectively.

In this case, the laser pulse traps the electrons and carries them with it as a soliton-like system, such as that found by Kaw *et al.*²³ The space charge field created by the electron bunching within the pulse is entirely downstream. Furthermore, this space charge field is weaker, and the number density and energy involved in the wake oscillations less, than that inside the laser pulse. They are also less than that for longer pulses (such as that in Fig. 2). It is of interest to note that this wake field reduction also occurs for weak laser intensities if the pulse is sufficiently short, since besides the lack of the local phase-matching between the ponderomotive force induced space charge field and the wake oscillations, the number of ponderomotively displaced electrons, and thus also the space charge field, is much less. The intermediate cases (not shown) shows that the transition from wake to direct acceleration when the pulse width becomes less than that of the optimum is rapid but continuous, as is also indicated in Fig. 1(b). In the latter figure one can also see that for the high intensity ($a_0=5$) case η increases rapidly as the pulse width is decreased, despite the fact that the number of electrons that can be accelerated in a short pulse is small.

D. Effect of background density

Besides the intensity a_0 and width d of the laser pulse, another important factor governing the behavior of the laser-plasma interaction is the density of the background electrons available for acceleration. In Figs. 4(a) and 4(b), the maxi-

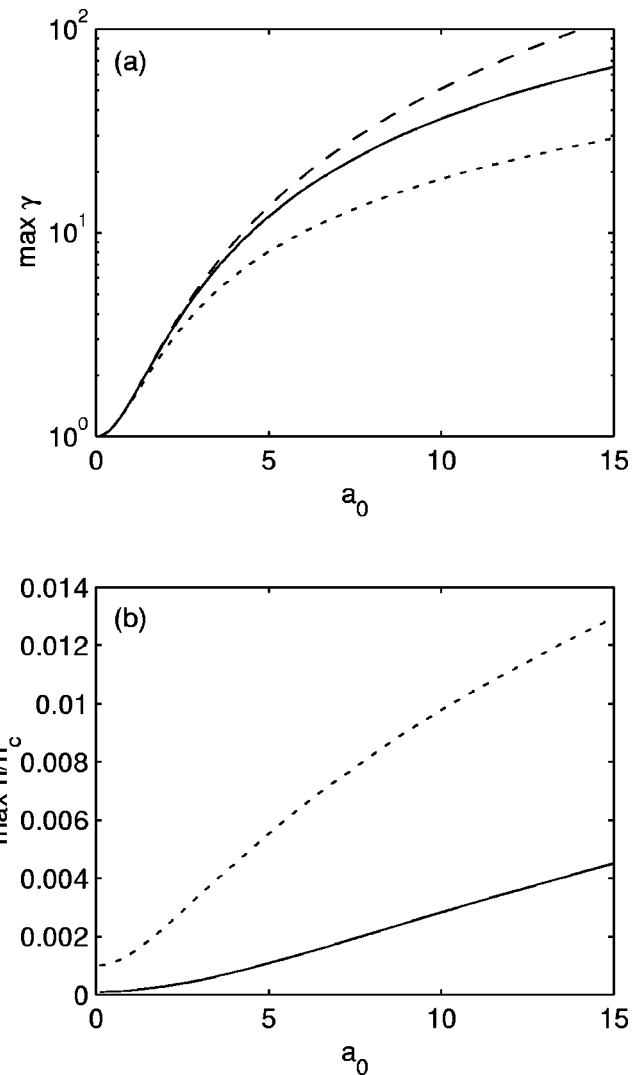


FIG. 4. Maximum electron energy γ (a) and density n/n_c (b) of the ponderomotively bunched electrons in the laser pulse vs the laser strength a_0 , for $d=5\lambda$, and $Zn_i=10^{-4}$ (solid curve) and $Zn_i=10^{-3}$ (dotted curve), respectively. The dashed curve in (a) is for $Zn_i=0$ or $v_g=1$.

mum electron energy and density of the ponderomotively bunched electrons are shown as functions of the laser strength a_0 for $d=5$, and $Zn_i=10^{-4}$ (solid curve, corresponding to $d/\lambda_p=0.05$). Recall that $\lambda_p=2\pi/\sqrt{Zn_i}$ and all lengths are normalized by the laser wavelength, and $Zn_i=10^{-3}$ (dotted curve, corresponding to $d/\lambda_p=0.16$), respectively. One can see that in both cases the maximum energy and density increase with the laser strength, as was already discussed. Figure 4 also shows that in plasmas of lower density the electrons bunched and accelerated by the laser pulse will have higher energy but lower density.

For completeness, the dashed curve in Fig. 4(a) shows the maximum electron energy for the case $Zn_i=0$ (no background ions). Here $v_g=1$ and $\phi=0$, and the problem reduces to the ponderomotive acceleration of an electron by a laser pulse propagating in vacuum. We then get from Eq. (1) and the definition of γ the well-known scaling,

$$\gamma_{\max} - 1 = a_0^2/2, \quad (11)$$

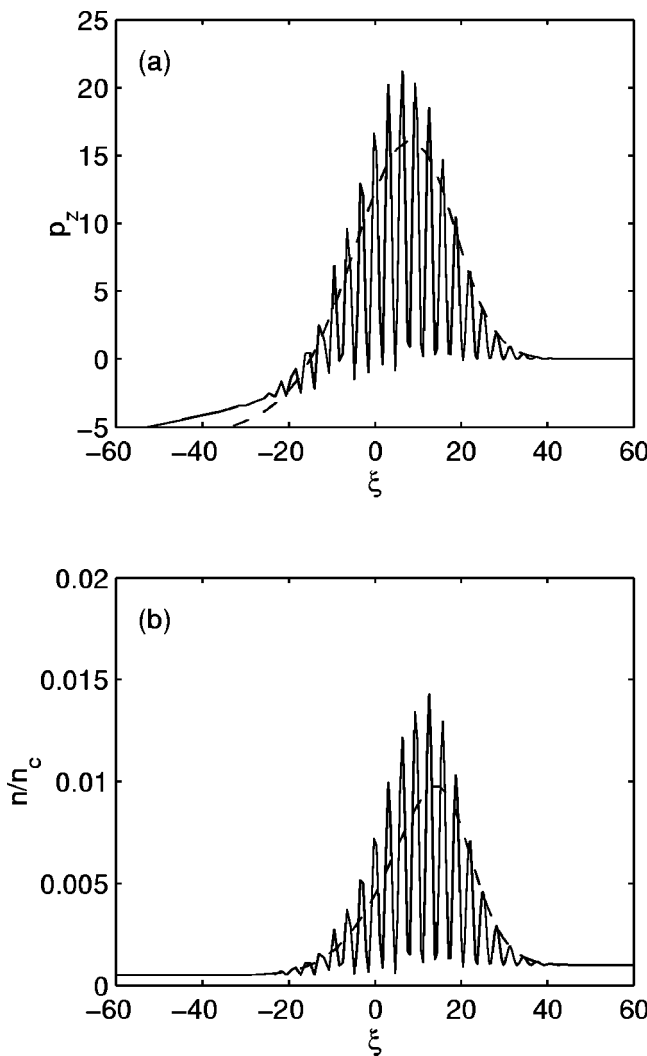


FIG. 5. Longitudinal electron momentum (a) and density (b) for linear (solid curve) and circular (dashed curve) polarizations, for $Zn_i=10^{-3}$, $a_0=10$, and $d=5\lambda$. The pulse width is again much smaller than that of optimum.

which shows that the electron acceleration and bunching processes discussed here are simply the relativistic ponderomotive acceleration of electrons *in a plasma*. In this case a self-consistent charge separation field appears when the electrons are displaced from the stationary ions.

E. Effect of polarization

Up to now we have concentrated on circularly polarized laser light. Figure 5 shows the effect of polarization. For both linear (solid curve) and circular (dashed curve) polarizations, the profiles of the longitudinal electron momentum and density are shown for $Zn_i=10^{-3}$, $a_0=10$, and $d=5\lambda$. The pulse width is again much smaller than half a plasma wavelength ($\sim 16\lambda$). The density and momentum profiles for the linear polarization case exhibit oscillatory behavior, which is due to the $\cos(2\xi)$ term in Eq. (9). Such a longitudinal modulation at twice the laser frequency appears only for linearly polarized light. It is from the oscillating component (which

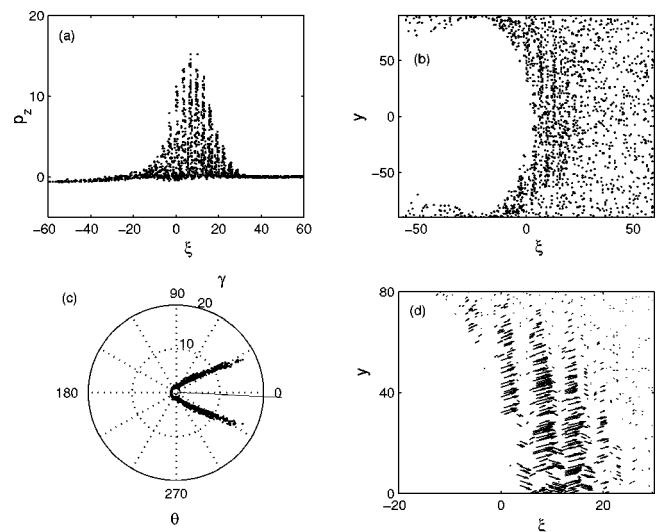


FIG. 6. Results from 2D PIC simulations of a tightly focused linearly polarized pulse in a rarefied plasma. The parameters are the same as in Fig. 5. (a) Longitudinal electron momentum vs the axial coordinate. (b) 2D spatial distribution of the electron density. (c) Angular distribution of the electron energy. The concentric circles from the center represent $\gamma=1, 10$, and 20, respectively. (d) Distribution of the electron momentum vectors.

does not appear for circularly polarized light) of the ponderomotive force, similar to that appearing in the well-known $\mathbf{u} \times \mathbf{B}$ heating effect.¹⁰

F. Higher dimensional effects

So far we have investigated electron acceleration in the propagation direction of an intense short-pulse laser using a one-dimensional (1D) analysis. Although it can be expected that the 1D approach is sufficient for the highly directional processes considered,¹⁴ in order to verify our results we have also carried out a 2D PIC simulation of a narrowly focused laser pulse in a low density plasma. In the simulation the laser pulse is assumed to have a narrow Gaussian profile in the transverse direction. The results are given in Fig. 6. In order to show the distributions more clearly, only 1/5 of the simulated electrons is represented in the figures. Figure 6(a) and (b) show the axial momentum and density distributions of the electrons in a linearly polarized laser pulse. The parameter values are the same as in Fig. 5. We see that the longitudinal electron momentum Fig. 6(a) is in good agreement with that of Fig. 5(a) obtained from the 1D analytical theory. Figure 6(b) shows that electrons are accelerated forward and a vacuum region or hole is formed in the tail of the laser pulse since now there is also a transverse ponderomotive force. As a result, the wake oscillation (not shown) appears as a series of electron holes. In the enhanced density region at the center, one can also see the local compression patterns formed by the *periodic* ponderomotive force of the linearly polarized light pulse. The angular dependence of the electron energy γ is shown in Fig. 6(c). The transverse spread is due to the ponderomotive force arising from the transverse profile of the laser pulse. If the laser were not so tightly focused, the transverse electron motion would be governed mainly by the laser field, as given by Eq. (1). In this

case the electrons would be (net) accelerated only in the axial direction. Figure 6(d) gives (in an enlarged region) the spatial distribution of the electron momentum vectors. One can again see the oscillatory nature of the longitudinal ponderomotive force. Electron acceleration is mainly in the forward direction and it occurs at the center of the pulse. Thus, together with the results from existing experiments¹⁷ and 2D numerical calculations,²⁵ as well as other simulations,¹⁶ our simulation shows that for *longitudinal electron acceleration* in the pulse and the wake, despite the significant difference in the actual configurations, 1D analyses yield quite accurate conclusions.

V. DISCUSSION

Using a simple one-dimensional analytical model, we have in this paper considered the relation between direct acceleration of electrons in a short intense laser pulse and acceleration in the laser-excited wake field. The two processes can compete with each other. Their relative importance depends on the response of the electrons to the pulse and is governed by the laser intensity and pulse width, as well as the background plasma density. For longer pulse lasers, especially when local phase matching in the laser pulse between the ponderomotive force and the wake plasma oscillation occurs, there is strong electron acceleration in the laser-excited wake field and little acceleration or trapping inside the laser pulse. For sufficiently short and intense pulses, there is strong acceleration of the electrons inside the pulse, and the corresponding wake field acceleration becomes much weaker. Direct acceleration of electrons inside the laser pulse is no other than the ponderomotively accelerated electrons in a plasma by the laser pulse. Its effectiveness depends on the number of background electrons available and therefore the unperturbed plasma density. In low density plasmas the ponderomotively accelerated electrons will have higher energy but lower density. Furthermore, for linearly polarized lasers the ponderomotively bunched electrons inside the pulse exhibit longitudinal oscillation at twice the laser frequency because of the oscillating component of the ponderomotive force.

Depletion of the laser energy has not been included in our theory. For higher background plasma densities, the reaction of the electron motion on the propagation of the laser pulse should be considered.^{18,23,25} For long ($\gg 1$ ps) pulses, higher dimensional and ion effects can also enter. However, investigations of related problems^{19,23,24} including self-consistent laser intensities and/or ion effects seem to indicate that these effects do not significantly change the one-dimensional electron energization behavior in the laser-plasma interaction process under consideration here.

It is of interest to mention that in their study of short-pulse laser propagation in high-density ($N_e \sim 10^{20} \text{ cm}^{-3}$, corresponding to $Zn_i \sim 0.1$ under the conditions of the present work) plasmas, Feit *et al.*² found that the laser-plasma interaction is unstable for short-wavelength longitudinal perturbations. However in that regime, $(N_e/N_c)^{1/2}$ is not small, and $L_p > k_p^{-1}$ (or $d > \lambda_p$) always holds. On the other hand, in the regime considered here the opposite condition $L_p < k_p^{-1}$ (or

$d < \lambda_p$) holds. That is, we confine ourselves to low-density plasmas with $Zn_i = 10^{-4} - 10^{-3}$, corresponding to the very low-density preplasma region that is normally produced by a much weaker prepulse or the low-intensity leading front of a high-intense laser pulse in laser-matter interactions. It should be emphasized that only at such low plasma densities the laser pulse width can be smaller than the plasma wavelength.

In practical applications, the highest-energy electrons in the large amplitude wake oscillation will be released when wave breaking occurs at the wave peaks.^{14,20} They can also be enhanced and extracted by elaborate methods. On the other hand, the ponderomotively accelerated ultrahigh energy electrons in the rising front of the pulse can be easily extracted by impinging the laser pulse onto a solid target.^{16,17} The pulse will then be reflected and the high energy electrons released into the target without suffering the ponderomotive deceleration in the trailing part of the pulse. The parameter η may then be considered as a coefficient of laser light absorption by the trapped (and released) electrons. Furthermore, the reflected pulse can also interact with the wake and significantly modifying the wake oscillation, leading to additional acceleration and the option of producing backward propagating ultrahigh energy electrons.^{5,16}

ACKNOWLEDGMENTS

This work was supported by the Max Planck Society-Chinese Academy of Sciences Exchange Program, the National High-Technology Program of China (Contract No. 863-416-1), and the National Natural Sciences Foundation of China (Contract No. 19974058).

- ¹M. Tabak, J. Hammer, M. E. Glinsky, W. L. Kruer, S. C. Wilks, J. Woodworth, E. M. Campbell, M. D. Perry, and R. J. Mason, Phys. Plasmas **1**, 1626 (1994).
- ²M. D. Feit, J. C. Garrison, and A. M. Rubenchik, Phys. Rev. E **53**, 1068 (1996).
- ³P. A. Norreys, M. Santala, E. Clark *et al.*, Phys. Plasmas **6**, 2150 (1999).
- ⁴Y. Sentoku, K. Mima, T. Taguchi, S. Miyamoto, and Y. Kishimoto, Phys. Plasmas **5**, 4366 (1998).
- ⁵R. Kodama, K. A. Tanaka, Y. Sentoku, T. Matsushita, K. Takahashi, H. Fujita, Y. Kitagawa, Y. Kato, T. Yamanaka, and K. Mima, Phys. Rev. Lett. **84**, 674 (2000).
- ⁶T. Zh. Esirkepov, Y. Sentoku, K. Mima *et al.*, JETP Lett. **70**, 82 (1999).
- ⁷G. S. Sarkisov, V. Yu. Bychenkov, V. N. Novikov, V. T. Tikhonchuk, A. Maksimchuk, S.-Y. Chen, R. Wagner, G. Mourou, and D. Umstadter, Phys. Rev. E **59**, 7042 (1999).
- ⁸M. Hegelich, S. Karsch, G. Pretzler *et al.*, Phys. Rev. Lett. **89**, 085002 (2002).
- ⁹N. A. Ebrahim, H. A. Baldis, C. Joshi, and R. Benesch, Phys. Rev. Lett. **45**, 1179 (1980).
- ¹⁰W. L. Kruer and K. Estabrook, Phys. Fluids **28**, 430 (1985).
- ¹¹F. Brunel, Phys. Rev. Lett. **59**, 52 (1987).
- ¹²S. C. Wilks, W. L. Kruer, M. Tabak, and A. B. Langdon, Phys. Rev. Lett. **69**, 1383 (1992).
- ¹³J. M. Rax, Phys. Fluids B **4**, 3962 (1992).
- ¹⁴T. Tajima and J. M. Dawson, Phys. Rev. Lett. **43**, 267 (1979).
- ¹⁵E. Esarey, P. Sprangle, J. Krall, and A. Ting, IEEE Trans. Plasma Sci. **24**, 252 (1996).
- ¹⁶W. Yu, V. Bychenkov, Y. Sentoku, M. Y. Yu, Z. M. Sheng, and K. Mima, Phys. Rev. Lett. **85**, 570 (2000).
- ¹⁷R. A. Snavely, M. H. Key, S. P. Hatchett *et al.*, Phys. Rev. Lett. **85**, 2945 (2000).

- ¹⁸M. Y. Yu, P. K. Shukla, and K. H. Spatschek, Phys. Rev. A **18**, 1591 (1978).
- ¹⁹P. Sprangle, E. Esarey, and A. Ting, Phys. Rev. Lett. **64**, 2011 (1990).
- ²⁰J. F. Drake, Y. C. Lee, K. Nishikawa, and N. L. Tsintsadze, Phys. Rev. Lett. **36**, 196 (1976).
- ²¹J. M. Dawson, Phys. Rev. **113**, 383 (1959).
- ²²R. C. Davidson, *Methods in Nonlinear Plasma Theory* (Academic, New York, 1972), Chap. 3.
- ²³P. K. Kaw, A. Sen, and T. Katsouleas, Phys. Rev. Lett. **68**, 3172 (1992).
- ²⁴F. Amiranoff, S. Baton, D. Bernard *et al.*, Phys. Rev. Lett. **81**, 995 (1998).
- ²⁵S. V. Bulanov, V. A. Vshivkov, G. I. Dudnikova, T. Zh. Esirkepov, F. Califano, F. F. Kamenets, T. V. Liseikina, N. M. Naumova, and F. Pegoraro, Plasma Phys. Rep. **25**, 701 (1999).

Simulation study of a Ne-like Ti x-ray laser at 32.6 nm driven by femtosecond laser pulses

X. Lu,¹ Y. J. Li,² Y. Cang,¹ K. Li,¹ and J. Zhang^{1,*}

¹Laboratory of Optical Physics, Institute of Physics, Chinese Academy of Sciences, Beijing 100080, People's Republic of China

²Department of Physics, China University of Mining & Technology, Beijing 100083, People's Republic of China

(Received 17 May 2002; revised manuscript received 27 August 2002; published 28 January 2003)

A femtosecond laser driven collisional Ne-like Ti x-ray laser at 32.6 nm is numerically investigated using a hydrodynamic code coupled with an atomic data package for a 100- μm -thick Ti planar target irradiated by a single or double prepulse followed by an intense femtosecond laser pulse. By using an optimized drive pulse configuration, a gain of 40 cm^{-1} can be generated from a 5 mm \times 50 μm line focus using only about 1 J pump energy.

DOI: 10.1103/PhysRevA.67.013810

PACS number(s): 42.55.Vc, 52.50.Jm, 52.59.Ye

I. INTRODUCTION

One of the main objectives in enhancing the efficiency of x-ray lasers is to develop “table-top” x-ray lasers for applications in university laboratories. In the “traditional” quasi-steady-state scheme, the prepulse is used only to create a preplasma. Delay is used to make a longer scale length. The main pulse then serves not only for heating the plasma to reach the electron temperature required by population inversion, but also for ionizing the plasma to the correct ionization state of Ne-like (Ni-like) ions [1,2]. By comparison, the prepulse and main pulse serve different functions in the transient collisional excitation (TCE) scheme. The prepulse is needed to prepare an optimized preplasma with a rich Ne-like (Ni-like) population. Then the main pulse heats the plasma rapidly to reach the required conditions with high electron temperature while keeping the ion temperature low. This is beneficial for forming a high gain in transient population inversion [3–10].

In this paper we numerically investigate the possibility of generating a Ne-like Ti x-ray laser from the $3p \rightarrow 3s$, $J=0 \rightarrow 1$ transition at 32.6 nm driven by femtosecond Ti:sapphire lasers, which are widely available at university laboratories. The pump geometry was set to be the standard line focus on a 100- μm -thick slab target. The one-dimensional (1D) Lagrangian hydrodynamic code MED103 [11] coupled with an atomic physics code and an atomic data package was used to predict the time evolution of laser-plasma interactions and to calculate the gain coefficient. The Ne-like Ti ion state was modeled for the ground state $2p^6$, all 26 excited levels of $2p^53s^1$, $2p^53p^1$, and $2p^53d^1$ states, and the next ionization stage (F -like states). The atomic physics code includes all possible radiative and collisional transitions between any two energy levels. Three different drive pulse configurations were studied: single prepulse, and double prepulse with short intervals (hundreds of picoseconds) and long intervals (nanoseconds). Detailed simulations were performed to optimize the drive pulse configurations.

II. SIMULATIONS FOR SINGLE PREPULSE CONFIGURATION

The plasma modeling aims to find the optimum intensity and temporal delay between drive pulses. The prepulse was assumed to be from the chirped pulse before final compression. Such chirped pulses usually have durations of a few hundreds of picoseconds. The main pulse duration can be regulated from tens of femtosecond to a few picoseconds by changing the distance between the gratings in the compressor. In our simulations the durations of prepulse and main pulse were set to be 300 ps and 300 fs full width at half maximum, respectively. The main drive pulse of tens of femtoseconds duration is not suitable for collisional x-ray laser excitation because of its low energy absorption [12]. Both the prepulse and the main pulse have Gaussian profiles. The peak intensity of the main pulse at the line focus was fixed at 10^{15} W/cm^2 .

It is well known that for ultrashort pulse driven collisional Ne-like x-ray lasers, the prepulse(s) should make the fraction of Ne-like ions in the preplasma as high as possible. We modeled the preplasma conditions produced by a single prepulse with different intensities. The optimum peak intensity of a 300 ps prepulse was found to be $3 \times 10^{11} \text{ W/cm}^2$. Figure 1(a) shows the spatiotemporal profile of the ground state Ne-like ion fraction in the plasma produced by an optimized prepulse. The horizontal axis presents the spatial distance in the direction of plasma expansion. The initial position of the target surface is located at 100 μm . The prepulse reaches its peak at 720 ps on the time scale used in Fig. 1(a). The maximum fraction of the ground state Ne-like ions can be higher than 80%, but the high fraction region has a narrow spatial extent. From Fig. 1(a) we can also get the best starting time of the main pulse. Obviously, the main pulse should turn on in the time interval from 850 ps to 1 ns. The contours of the electron temperature and gain at 32.6 nm versus space and time for a 130 ps delay between prepulse and main pulse are shown in Fig. 1(b) and Fig. 1(c), respectively. We can see that the gain region has a small space-time extent, because after prepulse irradiation the preplasma is not well expanded. Figure 1(d) shows the spatial profile of the

*Author to whom correspondence should be addressed. Electronic address: jzhang@aphy.iphy.ac.cn

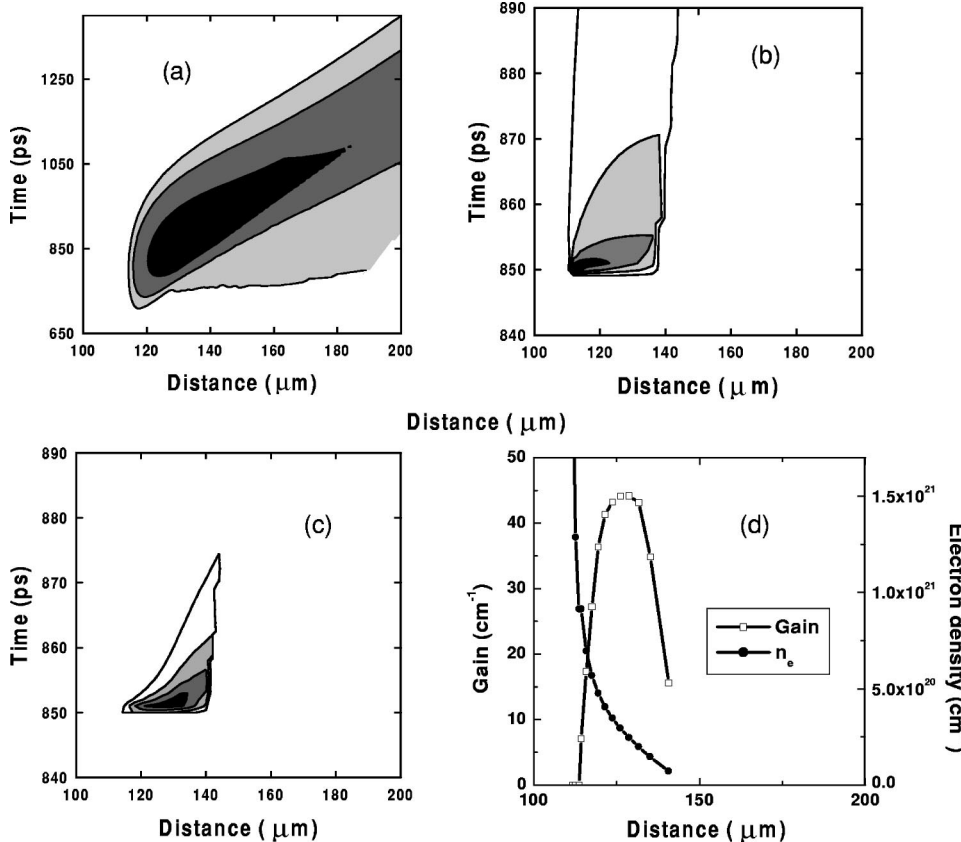


FIG. 1. (a) The ground state Ne-like Ti ion fraction versus space and time in the plasma generated by a 300 ps prepulse with a peak intensity of $3 \times 10^{11} \text{ W/cm}^2$. The fraction in the plot is from 80% (black) to 40% (white) by steps of 20%. (b) Contours of electron temperature in the plasma after the main pulse irradiation. The temperature in the plot is from 400 eV (black) to 100 eV (white) by steps of 100 eV. (c) Contours of Ne-like Ti laser gain at 32.6 nm generated by a 300 fs main pulse. The gain in the plot is from 40 cm^{-1} (black) to 10 cm^{-1} (white) by steps of 10 cm^{-1} . (d) The spatial profiles of the local gain coefficient and electron density at the peak gain time.

local gain coefficient and electron density at the moment when the highest gain exists. The maximum local gain is 44 cm^{-1} . The critical density surface is located at $112 \mu\text{m}$, where the electron density curve crosses the top frame of the figure. We can see that the gain region is located close to the critical density surface and has a high gradient of electron density. So this case is disadvantageous for the amplification of x-ray lasers.

III. DOUBLE PREPULSE WITH A SHORT INTERVAL

In order to improve the characteristics of the preplasma, a double prepulse configuration was considered. Earlier experiments showed that the double prepulse technique is an effective method to make a long scale and low density gradient preplasma [13]. In our simulations we used two 300 ps prepulses with 360 ps time delay. The first prepulse with $3 \times 10^{11} \text{ W/cm}^2$ peak intensity can generate a Ne-like preplasma. The second prepulse is used to hold the ionization stage of the preplasma and give it more time to expand. This pulse configuration is equivalent to using a nanosecond prepulse followed by an ultrashort main pulse. The optimized peak intensity of the second prepulse was found to be $2 \times 10^{11} \text{ W/cm}^2$. Figure 2(a) shows the much improved distribution of the ground state Ne-like ion fraction in the preplasma generated by such a double prepulse. Figures 2(b) and 2(c) show the electron temperature and gain generated

by a 300 fs, 10^{15} W/cm^2 main pulse, which reaches its peak intensity 120 ps later than the second prepulse. The spatial profiles of the local gain coefficients and electron density at the time for the highest gain are given in Fig. 2(d). The maximum local gain was 40 cm^{-1} . From Fig. 2(d) we can see that the gain extent is about twice as wide as in the case of single prepulse pumping, and the density gradient in the gain region becomes much lower.

IV. DOUBLE PREPULSE WITH A LONG INTERVAL

A different drive configuration was also investigated with a double prepulse with a long delay. The time interval between two prepulses was increased up to 3 ns. A similar pump scheme was successfully used in some earlier x-ray laser experiments [14,15]. After 3 ns expansion, the ionization degree of the preplasma will fall due to the long cooling interval. The second prepulse with $5.3 \times 10^{11} \text{ W/cm}^2$ peak intensity is used to ionize the preplasma to the Ne-like state again. The fraction of the ground state Ne-like ions in the plasma produced by this double prepulse is shown in Fig. 3(a). By irradiating the plasma with the 300 fs, 10^{15} W/cm^2 main pulse 300 ps later than the second prepulse, we obtained the electron temperature and gain contours shown in Figs. 3(b) and 3(c). The spatial profiles of the gain and the electron density at the peak gain time are shown in Fig. 3(d). For a longer interval between prepulses, the maximum gain

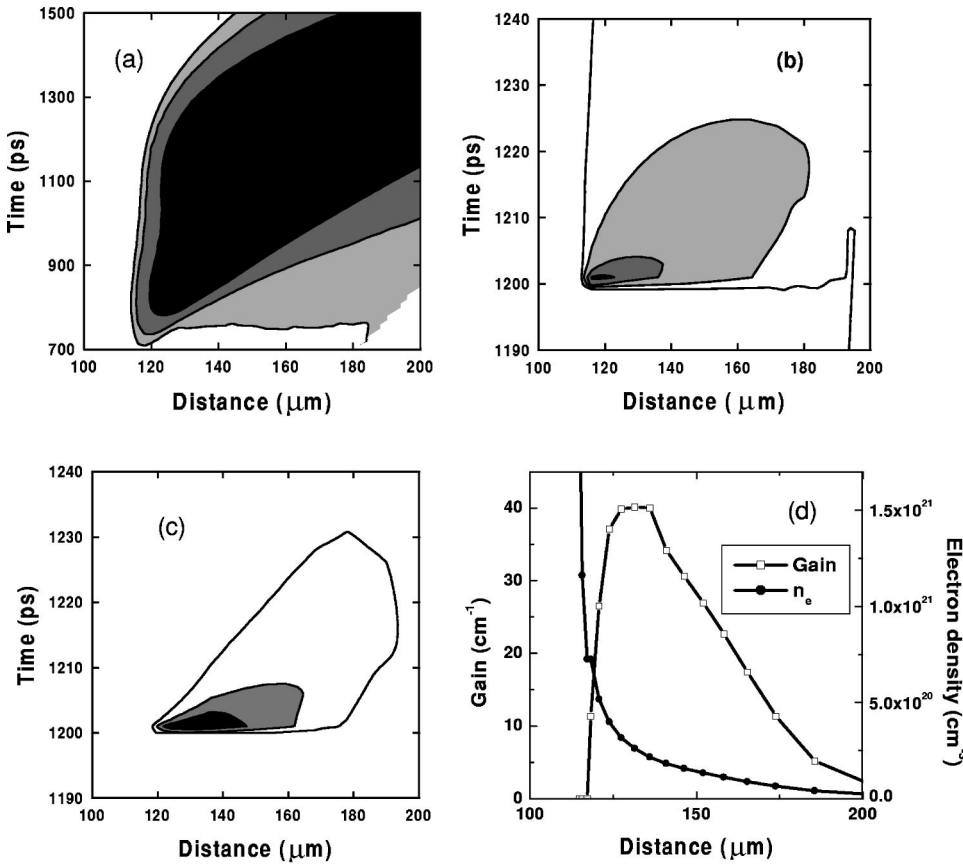


FIG. 2. (a) The ground state Ne-like Ti ion fraction versus space and time in the plasma generated by a double 300 ps prepulse with an interval of 360 ps. The fraction in the plot is from 80% (black) to 40% (white) by steps of 20%. (b) Contours of electron temperature in plasma after main pulse irradiation. The temperature in the plot is from 400 eV (black) to 100 eV (white) by steps of 100 eV. (c) Contours of Ne-like Ti laser gain at 32.6 nm generated by main pulse. The gain in the plot is from 30 cm^{-1} (black) to 10 cm^{-1} (white) by steps of 10 cm^{-1} . (d) The spatial profiles of the local gain coefficient and electron density at the peak gain time.

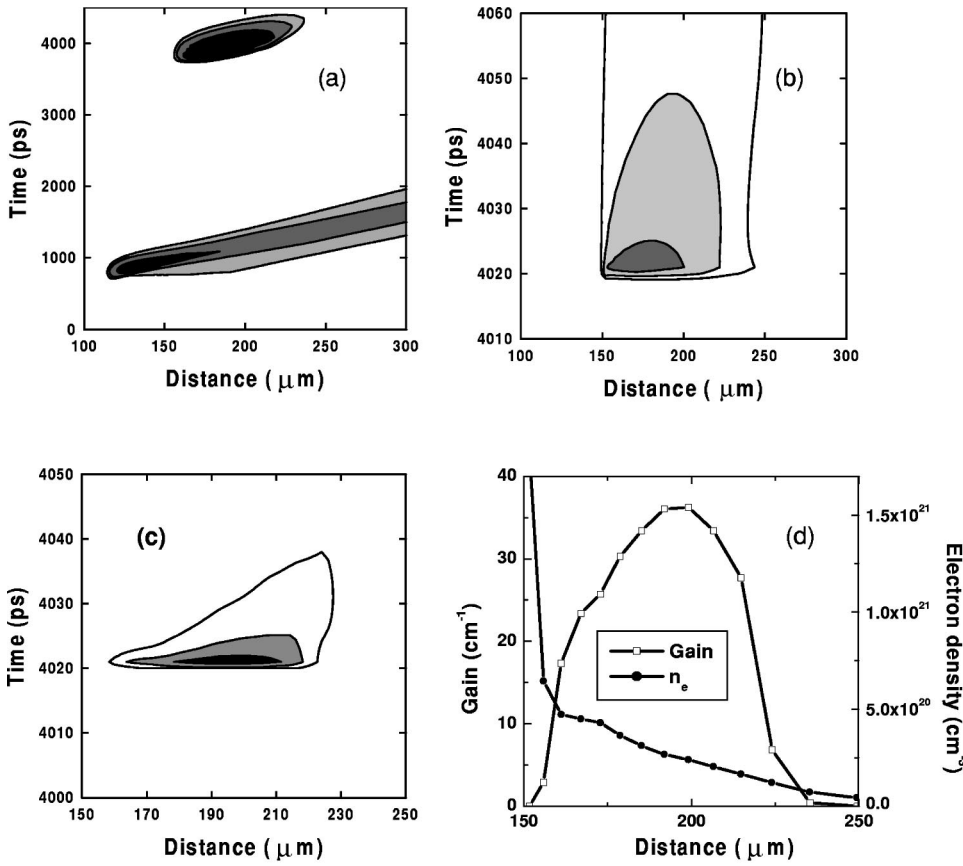


FIG. 3. (a) The ground state Ne-like Ti ion fraction versus space and time in the plasma generated by a double 300 ps prepulse with an interval of 3 ns. The fraction in the plot is from 80% (black) to 40% (white) by steps of 20%. (b) Contours of electron temperature in plasma after main pulse irradiation. The temperature in the plot is from 300 eV (black) to 100 eV (white) by steps of 100 eV. (c) Contours of Ne-like Ti laser gain at 32.6 nm generated by main pulse. The gain in the plot is from 30 cm^{-1} (black) to 10 cm^{-1} (white) by steps of 10 cm^{-1} . (d) The spatial profiles of the local gain coefficient and electron density at the peak gain time.

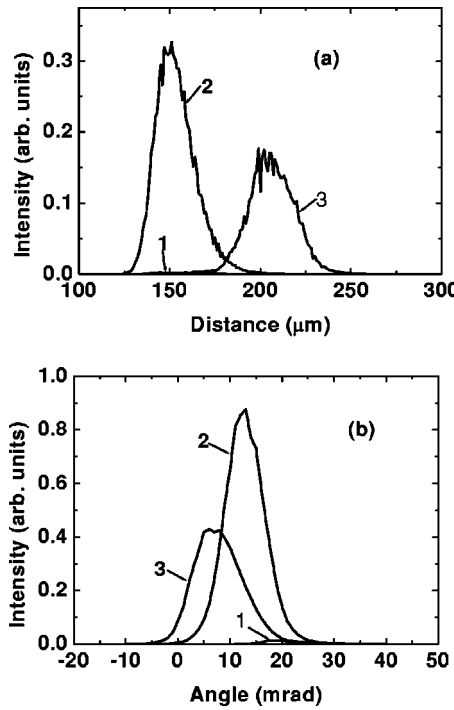


FIG. 4. The 32.6 nm x-ray laser output versus the source position (a) and the distribution angle (b) for single prepulse pumping (1), and double prepulse with short interval (2) and long interval (3).

falls to 36cm^{-1} , but the gain region has a broader spatial extent and lower density gradient.

In experiments, if we use a $5\text{ mm} \times 50\text{ }\mu\text{m}$ line focus, the total pump energy for the three pump schemes described above will be 1 J, 1.2 J, and 1.4 J, respectively. We have also performed optimization for the Nd:glass laser wavelength using the same pump schemes; the gain coefficient is about twice as high. This situation is caused by the relatively long wavelength of the pump laser pulses, because the efficiency of the inverse bremsstrahlung absorption is inversely proportional to the square of the laser wavelength.

V. RAY TRACING CALCULATIONS

It is difficult to compare the efficiency of the pump schemes using a double prepulse with short and long delays only by looking at Fig. 2 and Fig. 3. In order to illustrate the role of refraction, we developed a 2D ray tracing postprocessor to calculate the relative output intensity of the x-ray laser for each pump scheme. The line focus was set to be 5 mm long. The plasma expansion during the short pulse pumping can be ignored. We assumed that traveling wave excitation is used, so the spatial profiles of gain and electron density can keep their form unchanged along the line focus. For simplification, the time evolution of the x-ray laser output was not included. In our ray tracing calculations the spatial profiles of gain and electron density are taken from Figs. 1(d), 2(d), and 3(d). Figure 4 shows the ray integrated output intensity of the 32.6 nm laser line in the near (a) and far (b) fields. The intensity of each ray is weighted by the upper-level popula-

tion of the laser transition at the beginning of the ray. The result shows that the output intensity of single prepulse pumping is very small, and strong x-ray laser output can be obtained by using double prepulse schemes. When using a double prepulse with a short delay, the laser starts at $50\text{ }\mu\text{m}$ from the target surface and has $\sim 13\text{ mrad}$ tilt angle. When using a double prepulse with a long delay, the laser starts at $110\text{ }\mu\text{m}$ from the target surface and has $\sim 7\text{ mrad}$ tilt angle. Here we can see that using a double prepulse with long separation can really reduce the refraction, but the double prepulse with short delay produces the highest output intensity due to the relatively high gain coefficient. Altogether, the drive configuration of a double prepulse with a long delay does not have advantages in comparison with the case of a short delay between the prepulses. However, in some experiments with Ne-like Ge, the double prepulse with a long delay time was found to be a substantial improvement over a single nanosecond prepulse [14,15]. We believe that for ultrashort pulse pumping x-ray lasers, to use a double prepulse with a long delay is more effective for highly ionized ions like Ne-like Ge, Ni-like Sn, etc. But, for relatively low-ionized ions like Ne-like Ti or Ni-like Mo, the single nanosecond prepulse works best. The reason is that, in x-ray laser generation of highly ionized ions, most of the pump energy is spent on preparation of a properly ionized preplasma with a large scale length, using a double prepulse with a long delay can increase the efficiency of energy absorption of the prepulse, and finally save some total pump energy. X-ray lasers with low-ionized ions do not need much energy in the prepulse, so using a single nanosecond prepulse and a picosecond main pulse is a better choice.

VI. CONCLUSIONS

In conclusion, we have investigated a Ne-like Ti x-ray laser at 32.6 nm numerically using the one-dimensional hydrodynamic code MED103 coupled with an atomic data package for a $100\text{-}\mu\text{m}$ -thick Ti planar target irradiated by a single or double 300 ps prepulse followed by a 300 fs, 10^{15} W/cm^2 drive pulse from a Ti:sapphire laser. The optimization calculations were performed for various drive pulse combinations: single prepulse, and double prepulse with short (360 ps) and long (3 ns) intervals. The optimum intensity of the prepulse for each pump scheme was found. By using an optimized drive pulse configuration, an x-ray laser gain of about 40 cm^{-1} can be generated over a $5\text{ mm} \times 50\text{ }\mu\text{m}$ line focus using a pump energy of only $\sim 1\text{ J}$. We demonstrated the possibility of generating a Ne-like Ti soft x-ray laser at 32.6 nm using a table-top Ti:sapphire laser system. We also showed that the use of a double prepulse with a long delay time does not have any advantage for ultrashort pulse pumping of a Ne-like Ti x-ray laser.

ACKNOWLEDGMENTS

This work was supported by the National Nature Science Foundation of China under Grant Nos. 19974074, 19825110, and 60108007, and the National Hi-tech Program.

- [1] J. Zhang, A. G. MacPhee, J. Nilsen, J. Lin, T. W. Barbee, Jr., C. Danson, M. H. Key, C. L. S. Lewis, D. Neely, R. M. N. O'Rourke, G. J. Pert, R. Smith, G. J. Tallents, J. S. Wark, and E. Wolfrum, Phys. Rev. Lett. **78**, 3856 (1997).
- [2] J. Zhang, A. G. MacPhee, J. Lin, E. Wolfrum, R. Smith, C. Danson, M. H. Key, C. L. S. Lewis, D. Neely, J. Nilsen, G. J. Pert, G. J. Tallents, and J. S. Wark, Science **276**, 1097 (1997).
- [3] P. V. Nickles, V. N. Shlyaptsev, M. Kalachnikov, M. Schnürer, I. Will, and W. Sandner, Phys. Rev. Lett. **78**, 2748 (1997).
- [4] J. Dunn, A. L. Osterheld, R. Shepherd, W. E. White, V. N. Shlyaptsev, and R. E. Stewart, Phys. Rev. Lett. **80**, 2825 (1998); J. Dunn, J. Nilsen, A. L. Osterheld, Y. Li, and V. N. Shlyaptsev, Opt. Lett. **24**, 101 (1999).
- [5] M. P. Kalachnikov, P. V. Nickles, M. Schnürer, W. Sandner, V. N. Shlyaptsev, C. Danson, D. Neely, E. Wolfrum, J. Zhang, A. Behjat, A. Demir, G. J. Tallents, P. J. Warwick, and C. L. S. Lewis, Phys. Rev. A **57**, 4778 (1998).
- [6] J. Nilsen, Y. L. Li, and J. Dunn, J. Opt. Soc. Am. B **17**, 1084 (2000).
- [7] Y. J. Li and J. Zhang, Phys. Rev. E **63**, 036410 (2001); Y. J. Li, X. Lu, and J. Zhang, *ibid.* **66**, 046501 (2002).
- [8] J. Nilsen, B. J. MacGowan, L. B. Da Silva, and J. C. Moreno, Phys. Rev. A **48**, 4682 (1993).
- [9] Y. L. Li, J. Dunn, J. Nilsen, T. W. Barbee, Jr., A. L. Osterheld, and V. N. Shlyaptsev, J. Opt. Soc. Am. B **17**, 1098 (2000).
- [10] J. Dunn, Y. Li, A. L. Osterheld, J. Nilsen, J. R. Hunter, and V. N. Shlyaptsev, Phys. Rev. Lett. **84**, 4834 (2000).
- [11] J. P. Christiansen, D. E. T. F. Ashby, and K. V. Roberts, Comput. Phys. Commun. **7**, 271 (1974).
- [12] X. Lu, Y. J. Li, and J. Zhang, Phys. Plasmas **9**, 1412 (2002).
- [13] F. Löwenthal, R. Tommasini, and J. E. Balmer, Opt. Commun. **154**, 325 (1998); J. E. Balmer, R. Tommasini, and F. Löwenthal, IEEE J. Sel. Top. Quantum Electron. **5**, 1435 (1999).
- [14] J. Y. Lin, G. J. Tallents, A. G. MacPhee, A. Demir, C. L. S. Lewis, R. M. N. O'Rourke, G. J. Pert, D. Ros, and P. Zeitoun, Opt. Commun. **166**, 211 (1999).
- [15] R. E. King, G. J. Pert, S. P. McCabe, P. A. Simms, A. G. MacPhee, C. L. S. Lewis, R. Keenan, R. M. N. O'Rourke, G. J. Tallents, S. J. Pestehe, F. Strati, D. Neely, and R. Allott, Phys. Rev. A **64**, 053810 (2001).

Optimization of ion acceleration in the interaction of intense femtosecond laser pulses with ultrathin foils

Q. L. Dong,¹ Z.-M. Sheng,¹ M. Y. Yu,² and J. Zhang^{1,*}

¹Laboratory of Optical Physics, Institute of Physics, Chinese Academy of Sciences, Beijing 100080, People's Republic of China

²Institut für Theoretische Physik I, Ruhr Universität Bochum, D-44780 Bochum, Germany

(Received 22 August 2002; revised manuscript received 27 February 2003; published 19 August 2003)

Ion emission is investigated using particle-in-cell simulations where a Gaussian laser pulse with duration 50 fs and intensity $1.37 \times 10^{19} \text{ W/cm}^2$ is incident obliquely onto ultrathin solid foils. When the foil is thicker than $0.1 \mu\text{m}$, it is opaque to the laser light and the highest ion energy drops exponentially with target thickness. Optimization of ion acceleration occurs for a target with a thickness of $0.04 \mu\text{m}$ when it becomes transparent to the laser light. The behaviors of the high-energy electrons oscillating in the charge separation potential at the front and the rear of the target, as well as the enhanced electron acceleration in the laser pulse, play dominant roles for the observed features of ion emission. The relation of the optimal target thickness with parameters of the incident laser pulse and foil targets is also discussed.

DOI: 10.1103/PhysRevE.68.026408

PACS number(s): 52.38.Kd, 52.25.Tx, 52.50.Jm, 52.65.Rr

I. INTRODUCTION

Energetic electrons and ions generated in the interaction of ultrashort intense laser pulses with plasmas is of much interest because of their many potential applications. The interaction depends greatly on the parameters of the laser pulse, such as the intensity, wavelength, light polarization, pulse duration, etc. [1]. The initial plasma state, for example, the density profile, can also significantly affect the laser-plasma interaction process. Suitable plasmas can be produced by introducing a prepulse with a proper time delay to the main pulse [2] or by using targets with specific features [3–7]. Attempts to realize compact electron/proton accelerators and neutron sources are based on the interaction of ultrashort laser pulses with targets such as clusters, thin foils, etc. [4]. By using clusters, Ditmire *et al.* [5] observed enhanced laser absorption and x-ray emission. The electron acceleration was found to be related to the laser polarization, and the ion emission was almost isotropic [6]. The latter is different from the results by Kumarappan *et al.*, who found that the emission of ions with higher ionization states is preferable in the laser polarization direction [7]. Although one can obtain MeV ions from the cluster target, collimated ion beams would be preferable for most applications. Such ion beams can be obtained by using a planar solid target [3]. Many existing works considered the effects of target thickness on proton acceleration, which is related to the number, the effective temperature, and the spatial distribution of the hot electrons produced during the interaction. Maksimchuk *et al.* [3] found that thin foils with a thickness of $10 \mu\text{m}$ is optimal for proton acceleration. This was attributed to the enhanced electrostatic field arising from increased deposition of the most energetic electrons in the solid target. On the other hand, Mackinnon *et al.* [3] observed no optimal thickness, but the highest proton energy drops linearly as the tar-

get thickness is increased from 3 to $10 \mu\text{m}$, and then a plateau region appears. Differences between the two experiments mentioned above are believed to be due to the greatly different contrast ratio, the duration, and the intensity of the laser pulses applied. The common character between them is that the short laser pulse interacts only with the material in the front of the target, which is less than the laser wavelength. Energy transport from the laser-produced plasma to the rest of the solid target [8] significantly reduces the plasma temperature and can therefore prevent the ions from achieving higher energies. This effect can be eliminated by using ultrathin solid foils of sub-micrometer thickness.

In this paper, we use particle-in-cell (PIC) simulations to investigate the optimal conditions for the ion acceleration in the laser interactions with thin foils. We demonstrate that, by using an ultrathin foil, ions with energies up to tens of MeV can be produced within a very narrow spread angle around the normal direction of the target. Different from Maksimchuk *et al.* and Mackinnon *et al.* [3], we found that the optimal foil thickness for the ion acceleration is about several times of the effective skin depth when the foil is transparent to the laser pulse. The increased hot electron number and increased effective temperature due to the foil transparency are found to be responsible for the optimization behavior of the ion emission. When the target thickness increases and becomes opaque to the laser, the highest energy of the emitted ions decreases exponentially.

II. PIC SIMULATION RESULTS

Our PIC code is a 1D3V one, which can include the binary collisions between electrons and ions with a scheme given in Ref. [9]. Typically in simulations to be shown in the following, the simulation box has a dimension of 20 laser wavelengths, with the aluminum plasma foil located in the middle. The simulation box is divided into 100 000 cells, with maximally 200 electrons and ions in each cell in plasma initially. The thickness of foils varies from $0.01 \mu\text{m}$ to $15 \mu\text{m}$. The initial plasma profile is assumed to be a homogeneous slab with the electron density of $n_{e0} = 100n_c$, where

*Author to whom correspondence should be addressed.

Email address: jzhang@aphy.iphy.ac.cn

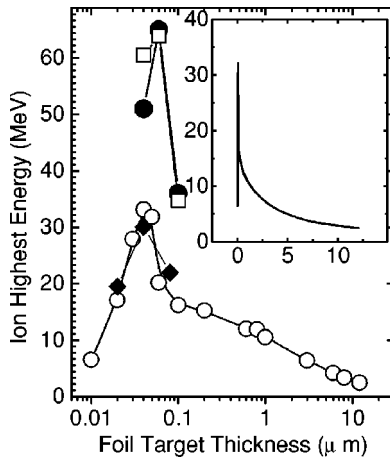


FIG. 1. Highest ion energy versus the foil thickness for three different p -polarized laser pulses incident at 45° to the target normal: (i) the open-circle line for $1.37 \times 10^{19} \text{ W/cm}^2$, 50-fs laser; (ii) the solid-circle line for $3.5 \times 10^{19} \text{ W/cm}^2$, 50-fs laser; (iii) the square line for $1.37 \times 10^{19} \text{ W/cm}^2$, 100-fs laser. The diamond-line is obtained for case (i) taking into account the binary-collision effect in the PIC code. The inset is also the dependence of the highest ion energy on target thickness for case (i), except for linear abscissa.

n_c is the critical electron density, which is about $1.1 \times 10^{21} \text{ cm}^{-3}$ for the laser wavelength of $1 \mu\text{m}$. The initial temperatures of electrons and ions were both set to zero, since the numerical self-heating is very limited during a short time duration such as a few hundred femtoseconds. Meanwhile, the level of the self-heating is much lower than the electron temperature gained from the relativistic laser-plasma interactions according to our PIC simulations. A Gaussian laser pulse either p or s polarized is incident on aluminum foil targets normally or at 45° , assuming $m_i/Zm_e = 1836 \times 27/3$ with $m_e = 1$ the normalized mass of electrons and Z , the charge number of ions, conservatively assumed to be 3 [10] because of the lack of the experimental data for the simulation conditions at present. Three types of p -polarized laser pulses were applied. The amplitude of the leading front of the Gaussian pulse increases from 0.2% of the peak value. Figure 1 shows the dependence of the highest ion energy on the target thickness with laser pulses incident at 45° to the target normal. The open-circle line represents the results for a laser pulse with a focused peak intensity of $1.37 \times 10^{19} \text{ W/cm}^2$ and full width at half maximum (FWHM) duration of 50 fs (i). The solid-circle line is for a $3.5 \times 10^{19} \text{ W/cm}^2$, 50 fs pulse (ii), and the square line is for a $1.37 \times 10^{19} \text{ W/cm}^2$, 100 fs pulse (iii). In case (i), the highest ion energy increases linearly from $0.01 \mu\text{m}$ to $0.04 \mu\text{m}$. After the optimal point the curve first drops rapidly and then slowly, following two distinct scaling laws. For targets with a thickness between $0.04 \mu\text{m}$ and $0.1 \mu\text{m}$, the highest ion energy drops linearly. After $0.1 \mu\text{m}$, however, the highest energy decreases exponentially. For cases (ii) and (iii), only the results for the optimal range of thickness is shown in Fig. 1, which is around $0.06 \mu\text{m}$. The diamond line in Fig. 1 represents the results of PIC simulations with laser pulses (i), where the effects of binary collisions between electrons and

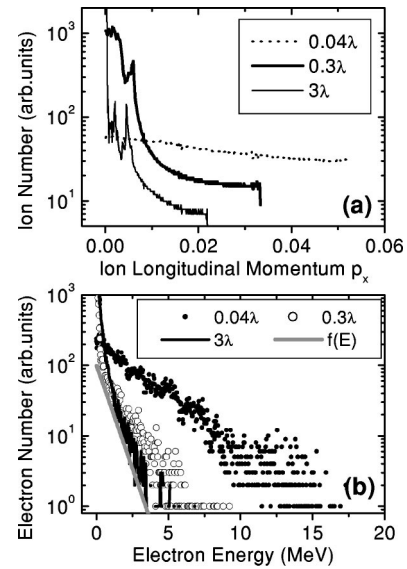


FIG. 2. (a) Ion momentum distribution for the laser pulse (i) and three target thicknesses: $0.04 \mu\text{m}$, $0.3 \mu\text{m}$, and $3 \mu\text{m}$. (b) Electron energy distribution. The simulation parameters are the same as in (a). The gray line shows the Maxwellian distribution $f(E) = 100 \exp[-E/0.74 (\text{MeV})]$.

ions are considered. We do not find much difference of the ion acceleration between that with and that without considering the binary collisions. We attribute this to the large mean free path of high-energy electrons in the solid target, which is about $100 \mu\text{m}$ for 100 keV as calculated [11]. Simulations for s -polarized laser pulses incident obliquely or normally on solid foils give much lower ion energies than that for p polarization. In the following context, only the results for p polarization are shown and discussed.

III. ELECTRON AND ION ACCELERATION

To explain the dependence of the highest ion energy on various target thicknesses, it is necessary to understand the mechanism of the ion acceleration and the electron heating. Figure 2(a) shows the ion momentum spectra for various target thicknesses. The most interesting common feature in the ion momentum spectra is the existence of a high-energy plateau, which ends up with a sharp cutoff typical of the electrostatic ion acceleration mechanism [12]. Another common feature, more obvious for thicker targets, is the presence of peaks in the spectra. The ion momentum spectra in Fig. 2(a) shows that as the target thicknesses increases, the cutoff energy and the effective temperature of the energetic ions decreases. Such a tendency is consistent with the features of the energetic electrons, which produces the electrostatic field locating at the front and the rear of the target, where ions are accelerated, as shown by Dong *et al.* and Wilks *et al.* [13]. The electron energy spectra are shown in Fig. 2(b) for different target thicknesses. It is interesting to point out that for the $0.04 \mu\text{m}$ target thickness, which is of the optimal thickness for the ion acceleration by applying laser pulses (i), one obtains not only a greater number of energetic electrons but also a higher electron effective temperature than other cases.

As the target becomes thicker, the energetic electron number as well as the effective temperature are dramatically reduced, as for the 0.3- μm and 3- μm targets. For comparison, the bold gray line shows the Maxwellian electron distribution with an effective temperature of 0.74 MeV, corresponding to the ponderomotive potential of the laser $0.511 \times (\sqrt{1 + \mathbf{a}^2/2} - 1)$ MeV, where \mathbf{a} is the dimensionless vector potential, which is defined as $a^2 = I\lambda^2(\text{W/cm}^2 \mu\text{m}^2)/(1.37 \times 10^{18})$. Here $a \sim 3.16$ in the simulation with $I\lambda^2 = 1.37 \times 10^{19} \text{ W/cm}^2 \mu\text{m}^2$.

The presence of the two different scaling laws in the decreasing part of the ion highest energy curves in Fig. 1 suggests that there are two different target-thickness regimes. One is the transparent regime (TR), with target thickness less than 0.1 μm . Indeed, with an initial plasma density $n_{e0} = 100n_c$, the effective skin depth $\gamma^{1/2}c/\omega_p$ of the target is about 0.025 μm , which increases as the density of the plasma decreases during the interaction. Here, we used $\gamma \sim \sqrt{1 + a^2/2} \sim 2.54$ and $\omega_p \sim 10\omega_0$ with $\omega_p^2 = (4\pi e^2 n_{e0})/(m)$ and ω_0 the frequency of the plasma and the laser, respectively. The other regime, with target thickness above 0.1 μm , is recognized as the opaque regime (OR). The normalized Hamiltonian of an electron (similar for an ion) is $H = [1 + (\mathbf{P} + \mathbf{a})^2]^{1/2} - \phi$, where $\mathbf{P} = \mathbf{p} - \mathbf{a}$ is the canonical momentum of the electron normalized by mc , and ϕ is the charge separation potential normalized here by mc^2/e . m and c are the rest mass of electron and the light velocity in the vacuum, respectively. Physically, the maximum value of ϕ is determined by the total number N_h and the effective temperature T_e of the produced hot electrons, $\phi_{max} \sim f(T_e, N_h)$ [14]. In TR, ϕ includes both the laser-induced electrostatic fields at the front and the rear of the target, whereas in OR ϕ includes only the front part. Such a difference significantly affects the electron acceleration and their angular distribution, as is discussed in the following.

A. Electron stochastic acceleration in TR

For transparent plasmas, laser absorption and electron heating are very strong [15], increasing the electrostatic field that causes ion acceleration [see Figs. 1 and 2(a)]. Figure 3(a) shows the phase space electron distribution when the target is at the optimal thickness of 0.04 μm . The maximum energy of the electrons is above 10 MeV. This energy is much larger than the ponderomotive potential of the laser pulse, which is only ~ 0.74 MeV. On the other hand, in such a thin target plasma waves cannot develop, so that the model of the electron acceleration by plasma waves cannot account for such a high energy gain. The irregularity of the electron phase distribution in Fig. 3(a) obviously excludes the possibility of the electron acceleration by plasma waves. It turns out that the charge separation field in the laser pulse plays a key role in the electron acceleration. The corresponding electrostatic potential bounds the electrons, preventing them from being pushed out of the focusing area before the arrival of the laser pulse peak as shown by Hu and Starace [16]. Figure 3(b) shows the temporal evolution of the longitudinal momentum of a selected typical electron, the laser field and the quasistatic electric field experienced by that electron. The

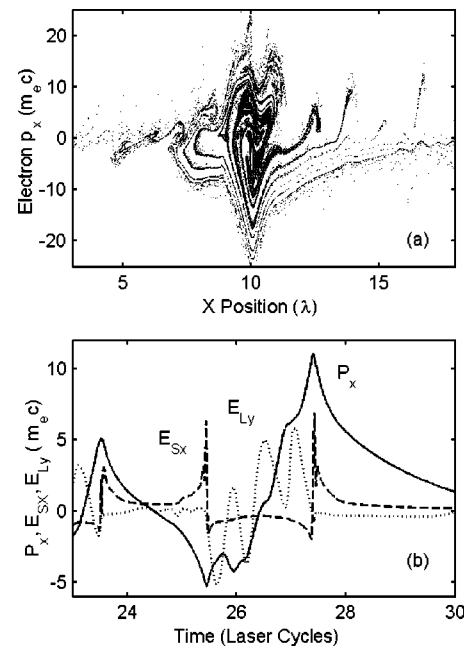


FIG. 3. (a) Phase space of electrons for a 0.04- μm target. (b) Temporal evolution of the longitudinal momentum p_x of a selected electron, the laser electric field E_{ly} , and the laser induced quasi-static electric field E_{sx} experienced by that electron, which show how the electron is accelerated.

latter provides instructive information about the acceleration process of that electron. At first, the electron gains energy at the front part of the laser pulse. Meanwhile, it oscillates irregularly, not with laser frequency as expected in a plane electromagnetic wave in the vacuum. At some time, it is stochastically in phase with the laser pulse and then is accelerated to much high energies [17], just as shown during the period between 26.5 and 27.5. After that, the highly energetic electron can either escape from the static electric potential, or continue to oscillate but with a larger phase-space amplitude. It can keep its energy until the end of the laser pulse. We have traced a set of 96 electrons which have $p_x > 15$ at the end of the laser pulse and found that 100% of them are accelerated in such a process. Another set of 96 electrons randomly selected were also traced. Among these only four are found to be highly energetic and have experienced the same acceleration process as the first set of 96 electrons. One cannot analyze all the electrons individually in the simulation box in detail, however, it is already obvious that the electron acceleration is due to the existence of the quasistatic electric field at the front and the rear of the target, which destroys the symmetry of the electromagnetic field experienced by the electron as expected in the vacuum, and makes it possible for electrons to be accelerated in the two consecutive half laser cycles. Such acceleration mechanism is also implied in previous works, for instance, in Refs. [16,18].

When the target thickness $d < 0.04 \mu\text{m}$, the laser pulse can pass through the plasma with 30% absorption and very little reflection. Electrons in such a foil plasma will have the same acceleration conditions, which results in a similar effective temperature in this regime. The thicker the target is, the more energetic electrons can be produced, i.e., $N_h(d)$

$\propto dn_{e0}$. The electrostatic potential increases linearly with the target thickness, $\phi(d)_{max} \propto d$, so does the highest ion energy as shown in Fig. 1. When the target is thicker than $0.04 \mu\text{m}$ but still thinner than $0.1 \mu\text{m}$, the laser pulse can still propagate through the target, but its energy will be increasingly reflected as the target thickness increases. This dramatically reduces the opportunity for those electrons originally located at or accelerated to the rear of the target to obtain higher energies. The effective temperature of the hot electrons is thus lowered, and in turn also the charge separation potential and the highest energy of ions are reduced, although there are more low-energy electrons due to the larger total number of electrons in thicker targets.

As the intensity and the duration of the incident laser pulse are increased, the optimal thickness increases as shown in Fig. 1. In case (ii) with the laser pulse at a higher intensity but with the same duration, the effective skin depth for the unperturbed target with $n_{e0} = 100n_c$ is $\gamma^{1/2}c/\omega_p \approx 0.031 \mu\text{m}$. During the laser-pulse interaction, however, the thin target expands with time owing to the laser heating and acceleration of target electrons, the average target density is reduced. Therefore, the real effective skin depth should be larger than $0.031 \mu\text{m}$. At these simulation conditions, the optimal target thickness for the ion acceleration is found to be about $0.06 \mu\text{m}$, almost two times of the skin depth calculated for the unperturbed target density. In case (iii) with a longer laser pulse duration, n_e decreases to a much lower value during the laser-pulse interaction than that in case (i). Moreover, electrons bounded in the electrostatic potential have more chance to encounter the right phase of the laser pulse to gain higher energy in a longer pulse duration. Both of them help to increase the penetration depth when the laser duration increases, which also results in an increased optimal thickness for the ion acceleration. Therefore, the optimal thickness also depends on the pulse duration. Through PIC simulations, we find the optimal target thickness for the ion acceleration is

$$d_{optm} \approx (c/\omega_p) \sqrt{1 + a^2 \tau/2}, \quad (1)$$

where τ is the laser pulse duration in units of 50 laser cycles. This means that the optimal thickness is proportional to the pulse energy $a^2 \tau$. The difference between increasing the laser intensity and increasing the pulse duration can be seen from the ion acceleration behavior at foil thicknesses below the optimal one. It should be pointed out that Eq. (1) is only valid for experimental conditions with ultrashort intense laser pulses. Once hydrodynamic behavior or parametric instability sets in as with picosecond laser pulses, Eq. (1) becomes invalid.

B. Electron's stochastic acceleration and $J \times B$ acceleration in OR

However, as the target becomes opaque ($>0.1 \mu\text{m}$) in case (i), a large part of the laser energy, for instance, with a target of $3 \mu\text{m}$, almost 98%, is reflected. Such low absorption is in contrast with that when $0.04\text{-}\mu\text{m}$ foil is applied. This is also different from PIC simulations by Wilks *et al.*

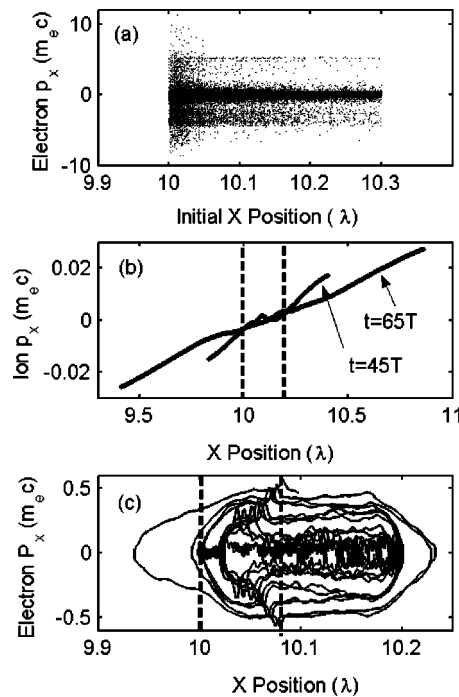


FIG. 4. PIC simulations for 0.3- and $0.2\text{-}\mu\text{m}$ targets. (a) Longitudinal momentum of energetic electrons versus their initial positions at 40 laser cycles. (b) The instantaneous phase space of ions at 45 and 65 laser cycles, respectively. (c) Typical trajectory of an electron, with the area between two dashed lines showing the $0.08 \mu\text{m}$ penetration depth of the laser pulse.

[19]. Wilks *et al.* used a much lower electron density, which makes the intense laser pulse penetrate easily into the plasma, causing great absorption [15].

It is interesting to study the dynamics of electrons. In OR case, we found that the electrostatic field around the rear side of the target now can no longer play roles in accelerating the electrons in the forward direction since the laser light cannot reach there. Figure 4(a) shows the acceleration of electrons at different *initial* positions for the $0.3\text{-}\mu\text{m}$ -thick target at $t = 40$ laser periods after the peak of the laser pulse arrives at the surface of the foil. The laser pulse penetrates about $0.08 \mu\text{m}$ into the target at the end of the laser pulse. Only electrons originally located within the laser penetrating depth can be accelerated to higher energies. Electrons in the remaining part of the target were accelerated to energies up to a cutoff, indicating that the acceleration of this part of electrons at that time may be attributed to the charge separation field located at the front and the rear of the target, where the ions are accelerated as shown by Fig. 4(b). But even in OR, for thin enough targets, hot electrons will be returned to the laser field from the rear of the target and probably accelerated for the second time, enhancing the electron heating to a higher effective temperature than that due to the laser ponderomotive potential alone. The trajectory of one typical electron in the phase space is shown in Fig. 4(c) for a $0.2\text{-}\mu\text{m}$ target. The multiple acceleration behavior of the oscillating electron is obvious. The area between the two dashed lines shows the penetration depth of the laser pulse into the plasma, which is about $0.08 \mu\text{m}$. However, for

thicker targets, the accelerated electrons will spend more time in the target. This means that there is little time for them to be accelerated again in the laser pulse. The more time an electron stays in the target, the lower is its energy, and the less its contribution to the electrostatic potential. Comparison [see Fig. 2(b)] between the electron spectra for the 0.3- μm and 3- μm targets shows the effect of the period of electron oscillation on the electron acceleration. In fact, if the target is thick enough, most of electrons will be accelerated only once during the laser pulse.

With thicker targets, the laser-induced electrostatic field is much weaker. The main mechanism of the electron acceleration transforms from the stochastic acceleration to the $\mathbf{J} \times \mathbf{B}$ force acceleration [19]. Therefore, electrons will have a Maxwellian distribution with an effective temperature that is similar to the ponderomotive potential of the laser pulse [19], say 0.74 MeV, as shown in Fig. 2(b) by the thick gray line. One sees that the electron spectrum for the 3- μm target agrees well with the expected distribution for acceleration by the $\mathbf{J} \times \mathbf{B}$ force of the laser pulse. For such a case, with the same or smaller number and the same effective temperature $T_e \approx 0.74$ MeV of the hot electrons, the effect of the target thickness on the density of electrons leaving the foil determines the variation of the highest ion energy as shown by Mackinon *et al.* [3].

IV. ANGULAR DISTRIBUTION OF ELECTRONS AND IONS

Now we consider the angular distribution of energetic electron and ion emission. Two of us [20] have shown that the angular direction of an accelerated electron is related to its kinetic energy and the local Coulomb potential variation by

$$\tan \theta = \left[\frac{2(\gamma - 1)(1 + \delta\phi) - \delta\phi^2}{(\gamma - 1 - \delta\phi)^2} \sin^{-2} \alpha + \tan^{-2} \alpha \right]^{-1/2}, \quad (2)$$

where θ is defined by $\tan \theta = p_y/p_x$, and $\alpha = 45^\circ$ is the incident angle. To derive Eq. (2), one assumes $p_y(t=0) = p_x(t=0) = 0$ and $p_z(t)=0$, which is generally true both for p and s polarizations. $\delta\phi = \phi(x, t) - \phi_0$ and normalized by mc^2/e , where ϕ_0 is the initial static electric potential and $\phi_0=0$ in our case. For ions, $\delta\phi$ should be replaced by $-Zm_e/m_i\delta\phi$. The angular distributions of the forward electrons and ions are shown in Fig. 5 for 0.04- μm and 3- μm targets. One sees that the most energetic electrons are distributed in a narrow cone along the direction (45°) of laser propagation. The Coulomb potential variation experienced by the hot electrons tends to limit their ejecting angles, as shown in Figs. 5(a) and 5(c) for 0.04- μm and 3- μm targets, respectively. For the 0.04- μm target, the hot electrons experience larger Coulomb potential changes, and thus have a wider angular spread for any given energy. In the transparent regime, because the Coulomb field includes the laser-induced electrostatic charge separation fields both at the front and the rear of the target, most of the hot electrons are located in an area limited by $\delta\phi=1.7$ and 3.4. However, in the opaque

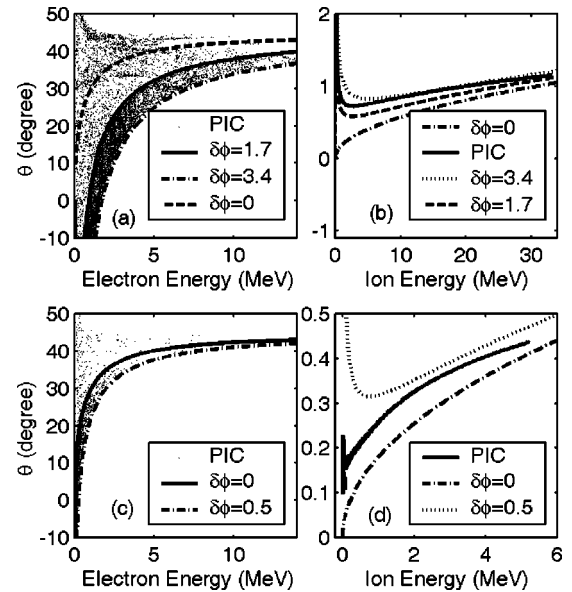


FIG. 5. Angular distribution of energetic electrons and ions for target thickness 0.04 μm [in (a) and (b)] and 3 μm [in (c) and (d)], respectively. $\delta\phi$ is the local Coulomb potential variation experienced by electrons, which is normalized by mc^2/e .

regime with 3- μm targets, the electrons locate within the area limited by $\delta\phi=0$ and 0.4, since here the potential includes only the target-front electrostatic field.

Figures 5(b) and 5(d) show the angular distribution of the ion emission. The ion emission for the 0.04- μm foil is mainly along $\sim 1^\circ$ from the target normal with a FWHM of 2° . As energy increases, the angle increases slightly. The properties of the ion emission indicate that planar electrostatic potentials in the front and the rear of the target are formed. The angular distribution of the energetic electrons and ions appears to show that the electric field is constructed mostly by those not so energetic electrons whose angular distribution spreads to the opposite side to the laser pulse with respect to the target normal and show the characteristic isotropic behavior. However, as shown above by Figs. 1 and 2 in Sec. III, the highest ion energy has the same trend with the energetic electrons and should be related to the number and effective temperature of all the energetic electrons. This apparent discrepancy is removed by taking into account of the electron oscillations in the electrostatic potential. Such behavior is shown clearly in Fig. 3(b). The oscillating energetic electrons stay around the foil target, contributing to the electrostatic field, and therefore play key roles in accelerating ions as shown above.

V. DISCUSSION AND CONCLUSION

One may note that our results of the target optimization for the ion acceleration are obtained with one-dimensional (1D) PIC code, and 2D/3D effects are excluded obviously. One of the 2D/3D effects is the self-generated quasistatic magnetic field that tends to pinch the angular distribution of energetic electrons and expand that of ions [21]. The existence of the strong self-generated magnetic field can also

play important roles in stochastically accelerating electrons [17]. Other 2D/3D effects such as breakup of the laser focus point caused by the fluctuation of the intensity distribution and/or the inhomogeneity of the plasma, can also have effects on the angular distribution of electrons and ions.

We also want to point out that our result is based upon a clean laser-pulse interaction with thin foil targets. To test our predicted optimization, laser pulses with a very high contrast ratio should be applied to avoid the breakup of the thin foil by the prepulses. Such kind of clean laser pulses may be obtained with the optical parametric chirped-pulse amplification technology [22].

In summary, the ion emission in the interactions of intense laser pulses with solid thin foils of sub-micrometer has been investigated using PIC simulations. The narrow angular spread of the energetic ion beam and the optimal ion acceleration curve indicate that such ultrathin foil target can be applied to generate collimated energetic ion beams. The optimal target thickness for the highest ion energy is found to be related to the intensity and the duration of the laser pulse. The enhanced number and effective temperature of hot electrons for a transparent target is responsible for the optimization characteristics of the sub-micrometer foil target.

ACKNOWLEDGMENTS

This work was supported in part by the National Natural Science Foundation of China (Grant Nos. 10105014, 19825110, 10075075), the National Key Basic Research Special Foundation (NKBRSF) under Grant No. G1999075200, and the National High-Tech ICF program.

-
- [1] E. Parra *et al.*, Phys. Rev. E **62**, R5931 (2000); L.M. Chen *et al.*, Phys. Rev. Lett. **87**, 225001 (2001); S. Ter-Avetisyan *et al.*, Phys. Rev. E **64**, 036404 (2001).
 - [2] J. Zhang *et al.*, Science **276**, 1097 (1997); S. Bastiani *et al.*, Phys. Rev. E **56**, 7179 (1997); P. Zhang *et al.*, *ibid.* **57**, R3746 (1998).
 - [3] A.J. Mackinnon *et al.*, Phys. Rev. Lett. **88**, 215006 (2002); J. Badziak *et al.*, *ibid.* **87**, 215001 (2001); A. Maksimchuk *et al.*, *ibid.* **84**, 4108 (2000); G. Kulcsár *et al.*, *ibid.* **84**, 5149 (2000); K. Krushelnick *et al.*, *ibid.* **83**, 737 (1999); A. Forsman *et al.*, Phys. Rev. E **58**, R1248 (1998); M. Lezius *et al.*, Phys. Rev. Lett. **80**, 261 (1998).
 - [4] T. Ditmire *et al.*, Nature (London) **398**, 489 (1999); J. Zweibak *et al.*, Phys. Rev. Lett. **84**, 2634 (2000).
 - [5] T. Ditmire *et al.*, Phys. Rev. Lett. **78**, 3121 (1997); T. Ditmire, T. Donnelly, R.W. Falcone, and M.D. Perry, *ibid.* **75**, 3122 (1995).
 - [6] Y.L. Shao *et al.*, Phys. Rev. Lett. **77**, 3343 (1996); T. Ditmire *et al.*, Nature (London) **386**, 54 (1997).
 - [7] V. Kumarappan, M. Krishnamurthy, and D. Mathur, Phys. Rev. Lett. **87**, 085005 (2001).
 - [8] B.-T.V. Vu, A. Szoke, and O.L. Landen, Phys. Rev. Lett. **72**, 3823 (1994); V.J.L. White *et al.*, Phys. Rev. E **49**, R4803 (1994); T. Ditmire *et al.*, Phys. Rev. Lett. **77**, 498 (1996).
 - [9] M.G. Cadjan and M.F. Ivanov, Phys. Lett. A **236**, 227 (1997).
 - [10] A. Zhidkov, A. Sasaki, and T. Tajima, Phys. Rev. E **61**, R2224 (2000).
 - [11] R.J. Harrach and R.E. Kidder, Phys. Rev. A **23**, 887 (1981); H. Teng *et al.*, Phys. Rev. E **67**, 026408 (2003).
 - [12] V.Y. Bychenkov, V.T. Tikhonchuk, and S.V. Tolokonnikov, JETP **88**, 1137 (1999).
 - [13] Dong Quan-Li *et al.*, Chin. Phys. Lett. **18**, 796 (2001); S.C. Wilks *et al.*, Phys. Plasmas **8**, 542 (2000).
 - [14] E.G. Gamaly, Phys. Fluids B **5**, 944 (1993).
 - [15] E. Lefebvre and G. Bonnaud, Phys. Rev. Lett. **74**, 2002 (1995); J. Fuchs *et al.*, *ibid.* **80**, 2326 (1998).
 - [16] S.X. Hu and A.F. Starace, Phys. Rev. Lett. **88**, 245003 (2002).
 - [17] Z.-M. Sheng *et al.*, Phys. Rev. Lett. **88**, 055004 (2002); M.S. Hussein and M.P. Pato, *ibid.* **68**, 1136 (1992); S. Kawata, T. Maruyama, H. Watanabe, and I. Takahashi, *ibid.* **66**, 2072 (1991); S. Kawata *et al.*, Jpn. J. Appl. Phys., Part 2 **29**, L179 (1990).
 - [18] J. Meyer-ter-Vehn and Z.-M. Sheng, Phys. Plasmas **6**, 641 (1998); A. Pukhov, Z.-M. Sheng, and J. Meyer-ter-Vehn, *ibid.* **6**, 2847 (1999).
 - [19] S.C. Wilks, W.L. Kruer, M. Tabak, and A.B. Langdon, Phys. Rev. Lett. **69**, 1383 (1992).
 - [20] Z.M. Sheng *et al.*, Phys. Rev. Lett. **85**, 5340 (2000).
 - [21] E.L. Clark *et al.*, Phys. Rev. Lett. **84**, 670 (2000), and references therein.
 - [22] I.N. Ross *et al.*, Opt. Commun. **144**, 125 (1997).

Blast waves produced by interactions of femtosecond laser pulses with water

Y. T. Li, J. Zhang,* H. Teng, K. Li, X. Y. Peng, Z. Jin, X. Lu, Z. Y. Zheng, and Q. Z. Yu

Laboratory of Optical Physics, Institute of Physics, Chinese Academy of Sciences, Beijing 100080, People's Republic of China

(Received 19 March 2002; revised manuscript received 21 January 2003; published 12 May 2003)

The behaviors of the blast waves produced by femtosecond laser-water interactions, and the blast waves induced by laser self-focusing in air, have been investigated using optical shadowgraphy at a maximum intensity of $1 \times 10^{16} \text{ W/cm}^2$. The temporal evolution of the blast wave launched by the water plasma can be described by a planar blast wave model including source mass. An aneurismlike structure, due to the quick propagation inside a hollow channel formed by laser self-focusing, is observed. The expansion of the channel in air is found to agree with a cylindrical self-similar blast wave solution.

DOI: 10.1103/PhysRevE.67.056403

PACS number(s): 52.35.Tc, 52.38.Hb

I. INTRODUCTION

When a high-intensity laser beam is focused on matter, the transient and localized energy deposition leads to a high-temperature plasma and a successive blast wave moving outward into the surrounding medium. A self-similar blast wave model proposed by Sedov [1] and Zel'dovich [2], which is valid for an intensively instant point explosion and zero initial source mass, is widely used to interpret the behaviors of the blast wave generated by laser-solid [3–6] and laser-cluster interactions [7,8]. Freiwald modified the model to include the explosive mass [9,10]. Long laser pulses were applied widely in previous studies on laser-produced blast wave. The recent developments of laser technology to produce ultrashort pulse make it possible to compare the femtosecond laser-induced blast wave with the Sedov theory.

In addition, some groups have investigated the behaviors of the blast waves generated by laser-induced breakdown inside liquid [11–14]. However, there is very little knowledge about the behaviors of blast waves generated on a liquid-air interface irradiated by laser pulses. In this paper, we investigate the evolution of the blast waves produced by femtosecond laser-water interaction on the water surface, and the evolution of a low-density channel in air due to laser self-focusing using optical shadowgraphy at a high laser intensity. The results show that the waves follow higher power laws than a self-similar spherical blast wave model. An aneurismlike structure on the top of the blast wave is also observed and its generation mechanism is analyzed.

II. EXPERIMENT

The experimental setup is illustrated schematically in Fig. 1. A chirped pulse amplification Ti:sapphire laser that delivers up to 5 mJ, 150 fs pulses at a wavelength of 800 nm was used. The linearly polarized laser pulses were focused with an $f = 40 \text{ mm}$ lens onto a distilled water surface in air, yielding a maximum peak intensity of about $1 \times 10^{16} \text{ W/cm}^2$.

A small portion of the laser beam split from the main beam, after being frequency doubled to 400 nm, was used as

a probe. The expansion of the plasma and the resultant blast wave was imaged on a 16 bit, 512×512 pixels CCD camera with a $14 \times$ magnification. An assembly of neutral filters and interference filters with a narrow bandwidth singled out the 400-nm probe beam from the background emission. In some shots, a $100\text{-}\mu\text{m}$ -diameter thread was placed at the back focus of the imaging lens to improve the contrast by blocking most of the undeflected probe light. Varying the delay of the probe beam with respect to the interaction beam on successive shots permitted mapping of the evolution of the blast waves. The time resolution was determined by the duration of the probe beam of about 150 fs.

The transmission energy was measured using a calorimeter in the laser propagation direction with a collective angle of 60° . Other diagnostics included hot electron measurements with an array of LiF thermoluminescence dosimeters

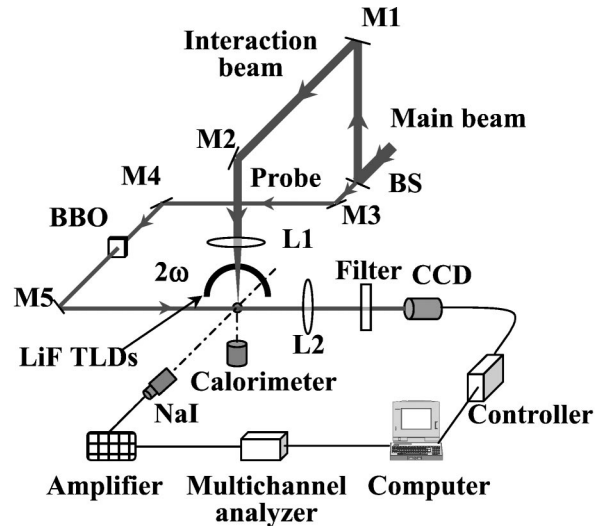


FIG. 1. The experimental layout. A small portion of the laser beam split from the main beam was frequency doubled and used to probe the blast wave. $M1-M5$ are reflective mirrors and BS represents the beam splitter. $L1$ and $L2$ are two lenses, which were used to focus the interaction beam on the water surface and image the plasma on CCD, respectively. The angular distribution of hot electrons emitted from the plasma was detected by an array of LiF detectors surrounding the plasma. The NaI system was used to measure the spectra of hard x rays.

*Author to whom correspondence should be addressed. Electronic address: jzhang@aphy.iphy.ac.cn

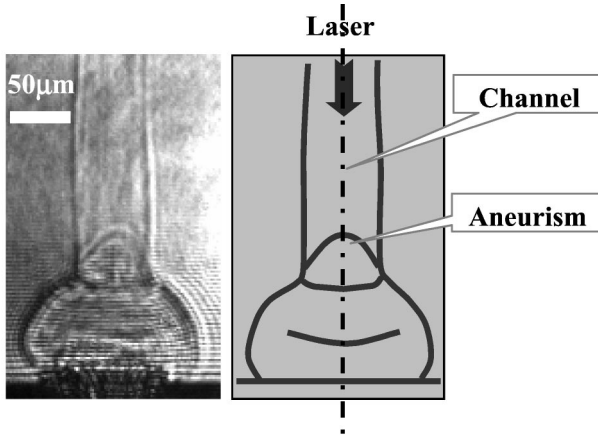


FIG. 2. A typical shadowgram of the blast wave taken at a delay time of 10 ns. The right one is an artificial sketch to guide the sightline.

[15], and hard x-ray measurements with a γ -ray spectrometer, which consisted of an NaI detector, a photomultiplier, an amplifier, and a multichannel energy analyzer [16]. Intense hard x-ray photon and electron emissions were also observed in the water plasma when multiple pulses with long separation time were used. These results will be presented elsewhere [17].

III. RESULTS AND DISCUSSION

A. Characteristics of the blast waves produced by femtosecond laser-water plasmas

Figure 2 shows a typical shadowgram of the blast wave taken at a delay time of 10 ns. An artificial sketch is also drawn on the right to lead the sightline. The femtosecond laser pulse with an energy of 3 mJ enters the image from the top. Note the main features in Fig. 2: generation of a hemispherical blast wave launched from the focal spot, an aneurismlike structure on the top of the wave, and a cylindrical blast wave trajectory generated before the laser pulse strikes on the water surface.

At first, we will discuss the evolution of the blast waves emitted from the water plasma. Figure 3 shows the images of the blast waves above the water surface at (a) 3 ns, (b) 4.7 ns, (c) 11.3 ns, (d) 16.9 ns, and (e) 30 ns produced by a laser beam with an energy of 3 mJ. The laser beam is incident from the top. The fringes near water surface are due to the diffractions of water surface. A half-circle dashed line whose center locates at the focal spot is overlaid on the shadowgram

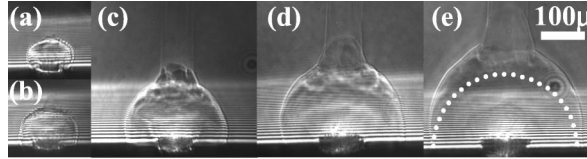


FIG. 3. Images of the blast waves above the water surface at 3 ns (a), 4.7 ns (b), 11.3 ns (c), 16.9 ns (d), and 30 ns (e). The laser beam is incident from the top.

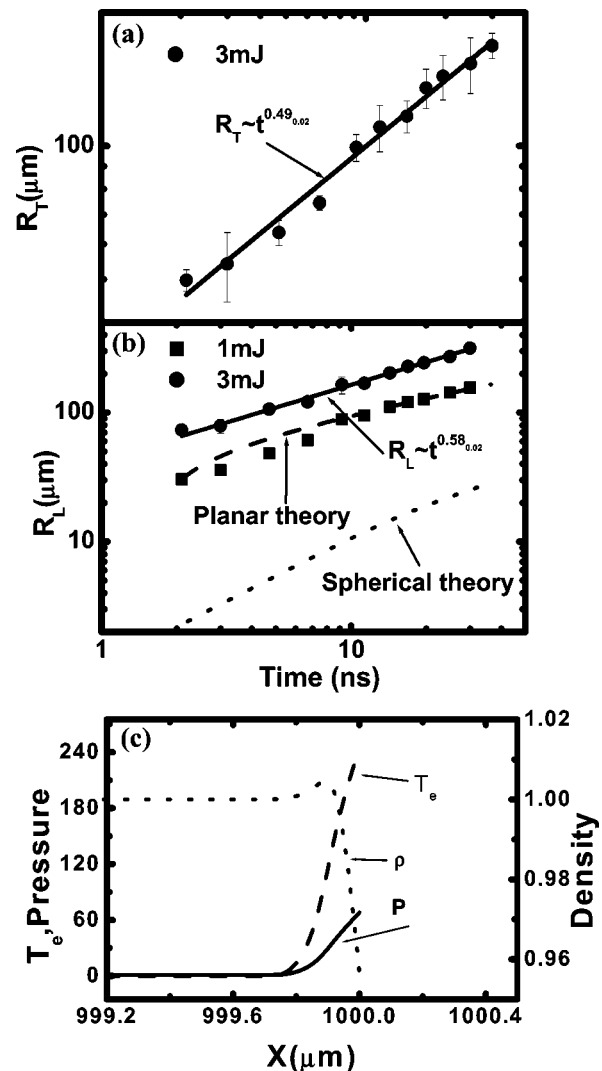


FIG. 4. Evolution of the blast waves produced by the femtosecond laser ablation of water as a function of time: transverse expansion for a 3-mJ laser energy (a), and longitudinal expansion for two laser energies, 3 mJ (circle) and 1 mJ (square) (b). The dashed line and the dotted line are theory curves for planar blast wave and spherical blast wave considering the initial source mass, respectively. (c) The hydrodynamical simulation results of the spatial profiles of the mass density ρ , pressure p , and electron temperature T_e are shown at the end of the laser pulse.

in Fig. 3(e). It is obvious that the blast wave propagates faster than an ideal spherical wave. The transverse expansion of the blast wave front for a 3-mJ laser energy, and the longitudinal expansion for 3-mJ (circle) and 1-mJ (square) laser energies are plotted as a function of time in Figs. 4(a) and 4(b), respectively. In the figures, R_T is denoted as the transverse expansion radius of the blast wave front parallel to the water surface, and R_L is the longitudinal expansion radius in the normal direction of water surface. The data from five measurements were averaged. The error bars correspond to the shot-shot fluctuations. For the transverse evolution, an allometric fit of the experimental data shows a dependence of $R_T \sim t^{0.49 \pm 0.02}$. For the longitudinal evolution, the data are

fitted by $R_L \sim t^{0.58 \pm 0.02}$ for 3 mJ and $R_L \sim t^{0.59 \pm 0.03}$ for 1 mJ (not shown).

It is well known that the evolution of the radius of a blast wave with time proposed by Sedov can be written as [1]

$$R^{n+2} = \alpha(\gamma) \frac{E_0}{\rho_1} t^2, \quad (1)$$

where E_0 is the original energy deposited per unit length in the cylinder, ρ_1 is the undisturbed mass density, α is a coefficient dependent on the adiabatic constant of the gas, γ , n is 1, 2, and 3 for plane, cylindrical, and spherical wave propagations. Sedov's theory indicates that the blast wave produced in our experiments is in agreement with a cylindrical blast wave for the transverse expansion, and is very close to a planar blast wave for the longitudinal expansion. Both the expansion directions deviate from a spherical blast wave predicted from Eq. (1). Similar results were also observed earlier [18,19].

Sedov's theory is valid only when the initial explosive mass is much less than the mass of the background gas swept over by the blast wave. We estimate the explosive mass of water to be 2.82×10^{-10} g by the hydrodynamic simulation of the femtosecond laser-water interaction (see next). This mass is equivalent to an air mass encompassed by a half-spherical blast wave with a radius of $\sim 50 \mu\text{m}$. Therefore, Sedov's theory cannot well describe our results of the blast wave, whose radius is less than $300 \mu\text{m}$ within the time observed.

Freiwald proposed an approximate theory including source mass for both spherical blast [9] and planar blast [10]. The spherical blast expansion in the near-target regime where the source mass is not negligible can be expressed analytically as

$$t = E_0^{-1/2} C_1^{1/2} \left(\frac{C_1}{C_2} \right)^{1/2} \left[\frac{3}{5} \frac{1}{3^{1/4}} F(\phi, 75^\circ) + \frac{2}{5} \beta (1 + \beta^3)^{1/2} - 0.842 \right], \quad (2)$$

where

$$C_1 = \frac{2m_s}{(\gamma+1)^2},$$

$$C_2 = \frac{8\pi}{3} \rho_1 \left(\frac{2}{(\gamma+1)^2} + \frac{1}{\gamma^2-1} \right),$$

$$\beta = R \left(\frac{C_2}{C_1} \right)^{1/3},$$

$$\phi = \cos^{-1} \left(\frac{\sqrt{3}-1-\beta}{\sqrt{3}+1+\beta} \right),$$

m_s is the initial mass, F is the incomplete elliptic integral of the first kind. The expansion of the planar blast wave with source mass is governed by

$$\frac{dR}{dt} = \left(\frac{E_0}{C_4 + C_5 R^3} \right), \quad (3)$$

where

$$C_4 = \frac{m_s}{2} \left(\frac{1}{\gamma+1} \right)^2,$$

$$C_5 = 2\pi\rho_1 \left(\frac{1}{\gamma^2-1} + \frac{4}{(\gamma+1)^2} \right).$$

We modify C_5 by rewriting the expression of the background gas mass to suit our experimental blast wave. The theoretical expansion of the planar blast is obtained by solving Eq. (3) with initial value problem. The comparison of Freiwald's theory with experimental results for 1-mJ laser pulse is also shown in Fig. 4(b). There exists a considerable amount of discrepancy between Freiwald's spherical blast model (dotted line) and experimental data even that the source mass is included. However, we find that Freiwald's planar blast wave theory agrees well with the experimental points when E_0 is set to be 0.15 mJ (see the dashed line). This indicates that the blast wave observed propagates closer to a plane blast wave instead of a spherical one, and that $\sim 15\%$ of the incident laser energy converts into the blast energy. It can be expected that the blast wave will decay to a spherical wave with the increasing propagation distance as the ambient gas accretion and the energy dissipation.

The higher power laws observed in our experiments may be due to the high intensity used and the nature of the femtosecond laser-matter interactions. To understand the initial explosive conditions of the blast wave, we use a one-dimensional two-temperature hydrodynamics code (MED103) [20] to simulate the behavior of the water plasma generated by 150-fs laser pulses at an intensity of $5 \times 10^{15} \text{ W/cm}^2$. Figure 4(c) shows snapshots of the spatial profiles of the mass density ρ , pressure p , and electron temperature T_e at the end of the laser pulse. The water surface was located at $1000 \mu\text{m}$; the laser pulse was incident from the right. When the laser pulse ends, a 68-Mbar peak pressure is produced. The maximum electron temperature is 244 eV. This high-temperature and high-pressure plasma will push the surrounding gas to generate intense shock wave in the air. We also simulate the case for nanosecond laser pulse that was used to produce blast wave in previous experiments widely. We find that the pressure and the temperature of the femtosecond laser-produced plasma are much higher than that of the nanosecond laser case at the same energy (the electron temperature is ~ 100 eV and the pressure is ~ 1 Mb for 1-ns laser). That is to say the femtosecond laser plasma will lead to a more intense explosion and will result in a

higher velocity blast wave expansion than that formed by long laser pulse at the same energy. The high-pressure and the high Mach number measured (~ 20) will make the blast wave to be strongly forward peaked. On the other hand, for an ultrashort laser-produced plasma, the plasma expansion during the pulse can be expressed as $c_s \tau$, where c_s is the ion velocity ($\sim 10^7$ cm/s) and τ is the pulse width. One can see that the scale of plasma during the interaction is several tens of nanometers, which is much less than the laser focal spot. This intrinsically planar interaction geometry may also be related with the behavior of the planar blast wave at early times.

Other reasons for the high power law is partial ionization and dynamic source effect [21]. The partial ionization induced by the blast wave front can accelerate the propagation in all directions. The nonadiabatic dynamic effect may increase the expansion velocity especially in the normal direction of the target surface. This may result in the higher velocity in the longitudinal direction than that in the transverse direction.

Second, we discuss the formation of the aneurism structure. The hollow channel in air plays a key role in the formation of the aneurism. From the blast wave theory, we know that the velocity of a blast wave dR/dt increases with the decrease of the ambient density. Therefore, the blast wave originating from the water plasma inside the low-density channel propagates more quickly than the outside part. This leads to the aneurism structure observed in our experiments. Stamper *et al.* also observed an aneurism production using 4 ns, ~ 100 J Nd-glass laser beams to irradiate foil targets at $\sim 10^{13}$ W/cm² in a low-pressure ambient gas, where a channel was formed by laser heating of the ambient gas through the inverse bremsstrahlung [22]. In our experiments, we believe that the initial ionization processes are different from theirs for our high-intensity and short-duration laser pulse because the laser field is comparable to the column potential.

B. Cylindrical blast waves produced by laser self-focusing in air

Now, we examine more closely the behavior of the blast wave produced by femtosecond laser pulses in air. When a femtosecond laser pulse is focused in air, a hot, elongated filament is formed due to the Kerr effect because the laser power is much higher than the self-focusing threshold (the critical power for self-focusing is $P_{cr} = \lambda^2/2\pi n_2 = 2$ GW, where λ is laser wavelength and n_2 is nonlinear refractive index). At atmospheric pressure, for air $n_2 = 3.2 \times 10^{-19}$ cm²/W), a blast wave is induced as a result of the high pressure exerted by the high-temperature filamentlike plasma. Figure 5 shows the shadowgrams of the blast waves produced by laser breakdown at 3 ns, 11.3 ns, 16.9 ns, and 24.9 ns. The geometry of the laser beam waist ($1/e^2$ contours) in the same scale as the shadowgrams is also shown for comparison. Laser is incident from the top. The abrupt jumps of the brightness in the shadowgrams indicate the shells of the waves.

Figure 6 shows the radial evolution of the blast wave

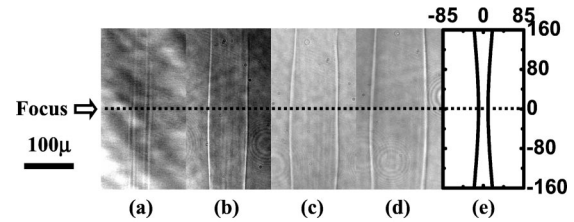


FIG. 5. Shadowgrams showing the evolution of the blast waves in air produced by a 3-mJ laser energy as a function of time: 3 ns (a), 11.3 ns (b), 16.9 ns (c), and 24.9 ns (d). The geometry of the laser beam waist ($1/e^2$ contours) in the same scale as the shadowgrams is also shown for comparison (e).

trajectory at the focal spot as a function of time for a 3-mJ laser energy. The data from five measurements were averaged. The error bars correspond to the shot-shot fluctuations. The experimental data are best fitted by an allometric function $R(t) \sim t^{0.49 \pm 0.01}$. This indicates that the blast wave expansion in air follows a cylindrical blast wave solution. From Eq. (1), the conversion efficiency of total laser energy to the blast wave is estimated to be less than 1%. This value is lower than the total absorption by air plasma, which is measured to be 6% by an energy calorimeter. This indicates that most of the energy absorbed by plasmas is transformed to other energy forms such as ionization energy, instead of the kinetic energy of blast wave. Compared with the previous laser-ablation experiments using long pulses, the conversion efficiency of laser pulse into blast waves is much lower for femtosecond laser-air interactions. In the nanosecond scale laser-air interactions, the plasma still absorbs energy from the succeeding part of the laser pulse through inverse bremsstrahlung after the air is ionized by the leading part of the pulse. Therefore, more laser energy can be deposited and transferred to the blast wave energy. However, for the case of femtosecond pulse, less energy can be absorbed from the tail of the femtosecond pulse.

IV. CONCLUSION

In summary, blast waves produced by femtosecond laser-water interaction have been investigated using an optical shadowgraphy technique. The temporal evolution of the blast

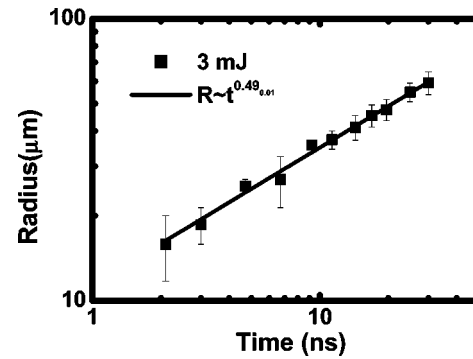


FIG. 6. Radial evolution of the blast waves in air as a function of time for a 3-mJ laser energy. The line is an allometric fit of the experimental data.

wave formed by the water plasma follows a planar blast wave model including the source mass. An aneurismlike structure, due to the quick propagation inside the air channel that is formed by laser filamentation, is observed. The blast wave in air is found to agree with a cylindrical self-similar blast wave solution.

ACKNOWLEDGMENTS

This work was supported by the NSFC (Project Nos. 10204023, 10075075, and 10176034), the K. C. Wang Education Foundation (Hong Kong), the National High-Tech ICF program, and the NKBRSF (Grant No. G1999075206).

-
- [1] L.I. Sedov, *Similarity and Dimensional Methods in Mechanics* (Infosearch LTD, London, 1959).
 - [2] Ya.B. Zel'dovich and Yu.P. Raizer, *Physics of Shock Waves and High-Temperature Hydrodynamic Phenomena* (Academic, New York, 1966).
 - [3] S.J. Lee, K. Imen, and S.D. Allen, *J. Appl. Phys.* **74**, 7044 (1993).
 - [4] G. Callies, P. Berger, and H. Hugel, *J. Phys. D* **28**, 794 (1995).
 - [5] T. Zyung, H. Kim, J.C. Postlewaite, and D.D. Dlott, *J. Appl. Phys.* **65**, 4548 (1989).
 - [6] K.S. Budil, D.M. Gold, K.G. Estabrook, B.A. Remington, J. Kane, P.M. Bell, D. Pennington, C. Brown, S. Hatchett, J.A. Koch, M.H. Key, and M.D. Perry, *Rev. Sci. Instrum.* **70**, 806 (1999).
 - [7] J. Zweiback and T. Ditmire, *Phys. Plasmas* **8**, 4545 (2001).
 - [8] M.J. Edwards, A.J. MacKinnon, J. Zweiback, K. Shigemori, D. Ryutov, A.M. Rubenchik, K.A. Keilty, E. Liang, B.A. Remington, and T. Ditmire, *Phys. Rev. Lett.* **87**, 085004 (2001).
 - [9] D.A. Freiwald and R.A. Axford, *J. Appl. Phys.* **46**, 1171 (1975).
 - [10] D.A. Freiwald, *J. Appl. Phys.* **43**, 2224 (1972).
 - [11] C.E. Bell, and J.A. Landt, *Appl. Phys. Lett.* **10**, 46 (1967).
 - [12] F. Docchio, P. Regondi, M.R.C. Capon, and J. Mellerio, *Appl. Opt.* **27**, 3661 (1988).
 - [13] A.G. Doukas, A.D. Zwieig, J.K. Frisoli, R. Birngruber, and T.F. Deutsch, *Appl. Phys. B: Photophys. Laser Chem.* **53**, 237 (1991).
 - [14] A. Vogel, S. Busch, and U. Parlitz, *J. Acoust. Soc. Am.* **100**, 148 (1996).
 - [15] L.M. Chen, J. Zhang, H. Teng, Q.L. Dong, Z.L. Chen, T.J. Liang, L.Z. Zhao, and Z.Y. Wei, *Phys. Rev. E* **63**, 046403 (2001).
 - [16] P. Zhang, J.T. He, D.B. Chen, Z.H. Li, Y. Zhang, J.G. Bian, L. Wang, Z.L. Li, B.H. Feng, X.L. Zhang, D.X. Zhang, X.W. Tang, and J. Zhang, *Phys. Rev. E* **57**, R3746 (1998).
 - [17] Y. T. Li, J. Zhang, H. Teng, T. J. Liang, X. Y. Peng, X. Lu, Y. J. Li, and X. W. Tang, *Phys. Rev. Lett.* **90**, 165002 (2003).
 - [18] A. Gupta, B. Braren, K.G. Casey, B.W. Hussey, and R. Kelly, *Appl. Phys. Lett.* **59**, 1302 (1991).
 - [19] S.H. Jeong, R. Grief, and R.E. Russo, *Appl. Surf. Sci.* **127**, 1029 (1998).
 - [20] J.P. Christiansen, D.E.T.F. Ashby, and K.V. Roberts, *Comput. Phys. Commun.* **7**, 271 (1974).
 - [21] K.R. Chen, J.N. Leboeuf, R.F. Wood, D.B. Geohegan, J.M. Donato, C.L. Liu, and A.A. Puretzky, *Phys. Rev. Lett.* **75**, 4706 (1995).
 - [22] J.A. Stamper and B.H. Ripin, *Phys. Fluids* **31**, 3353 (1988).

Propagation of hot electrons through high-density plasmas

H. Teng,¹ J. Zhang,^{1,*} Z. L. Chen,¹ Y. T. Li,¹ K. Li,¹ X. Y. Peng,¹ and J. X. Ma²

¹Laboratory of Optical Physics, Institute of Physics, Chinese Academy of Sciences, Beijing 100080, People's Republic of China

²Department of Modern Physics, University of Science and Technology, Anhui, People's Republic of China

(Received 11 March 2002; revised manuscript received 3 December 2002; published 10 February 2003)

Propagation of hot electrons through high-density plasmas generated by femtosecond laser pulses is investigated using three types of target configurations: Al-coated glass, Al and glass separated by a vacuum gap, and Al foil alone. Collimated ionization tracks lasting for 60 ps and extending 150–300 μm in length and 8 μm in cross section are observed via optical probing. For the Al-foil-alone target, a narrow plasma jet is formed at the rear surface in line with the laser. The collimation of the hot electrons may be attributed to a strong self-generated magnetic field in the target.

DOI: 10.1103/PhysRevE.67.026408

PACS number(s): 52.50.Jm, 52.40.-w, 52.25.Os, 52.38.-r

I. INTRODUCTION

With the advent of multiterawatt short pulse lasers [1], the “fast ignition” scheme [2] was proposed, by which an intense short laser pulse is focused onto a high-density pre-compressed thermonuclear fuel to generate hot electrons and create an ignition spark that initiates a propagating thermonuclear burn. This separation of compression and ignition greatly reduces the driver energy and relaxes the symmetry requirements for the compression. There are still several technical challenges to the fast ignition scheme, e.g., “hole boring” of short pulse laser in the low-density plasma region [3], efficient penetration of the laser into the high-density region though self-channeling [4], and interaction of the laser with the high-density fuel core to generate copious relativistic electrons [5]. Ideally, the electrons should propagate as a stable beam into the compressed fuel and deposit their energy in a small volume and heat the fuel to fusion temperature locally. Thus, in fast ignition, one of the critical issues is the propagation of hot electrons through high-density plasmas.

Several mechanisms that can transfer laser energy to the plasma electrons have been proposed [6]. One is the ponderomotive acceleration, in which the $\mathbf{v} \times \mathbf{B}$ force ponderomotively accelerates the electrons in the direction of laser propagation [7,8]. Other mechanisms include collisionless electron acceleration at the critical density, such as vacuum heating [9,10], resonant absorption [11], and parametric instabilities [12]. In addition, magnetic and electric fields, variable resistivity, as well as collisions can all play important roles on the propagation of hot electrons in a dense plasma. The latter have been studied by many measurements, such as $K\alpha$ emission diagnostics [13], γ -ray spectra, two-dimensional (2D) transverse imaging of solid target with a probe beam [14–17], and direct imaging of the emission from the hot electrons [18].

In this paper, we present an experimental investigation on the propagation of hot electrons through high-density plasmas. A bundle of ionization tracks was observed via optical probing inside two types of Al-coated glass targets. In order

to understand the behavior of the hot electrons right after their generation, the plasma jet at the rear surface of a 20 μm Al foil was also analyzed via optical probing. The acceleration and propagation of the electrons may be attributed to the ponderomotive force and their collimation to the self-generated magnetic field inside the target.

II. EXPERIMENTAL SETUP

The experiment is performed on the Ti:sapphire terawatt laser system “JIGUANG-I” [19] operating at 800 nm at a repetition rate of 10 Hz based on chirped pulse amplification. The system delivers up to 36 mJ energy in 25 fs, corresponding to a peak power of 1.4 TW. Low-energy equivalent-plane measurements show a 10–20 μm full width at half maximum focal spot, giving a maximum intensity of $1 \times 10^{17} \text{ Wcm}^{-2}$. The targets used are 1- μm -aluminum-coated fused glass slide, 5- μm aluminum on fused glass slide with a vacuum gap, and 20- μm -thick aluminum foil only. The roughness of the surfaces is less than 1 μm . The mount is controlled by three-dimensional microstep motor, in order to ensure that the laser pulse interacts with a fresh target surface at each shot.

The experimental setup is shown in Fig. 1. The laser pulse

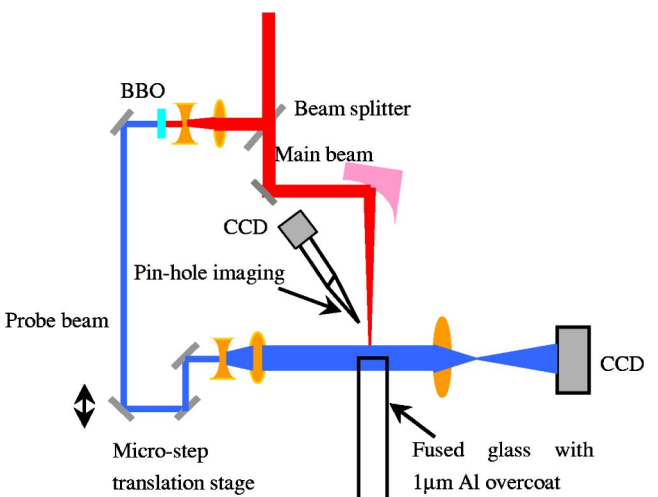


FIG. 1. Schematic of the experimental setup.

*Corresponding author. Email address: jzhang@aphy.iphy.ac.cn

is focused onto the target at 10° to the normal. A pinhole imaging of x-ray emission monitors the focal spot size for each full energy shot. A small fraction of the main beam, after frequency doubling to 400 nm in a BBO crystal, is used as a temporally independent probe beam. The latter passes transversely across the target. The front surface and target interior are in the field of view. A charge coupled device with a 400-nm band transmission filter is used to obtain a side view of the target at spatial and temporal resolutions of the order of $1 \mu\text{m}$ and 1 ps, respectively. A region that has been ionized up to a fraction of the critical density (of 400-nm light) becomes opaque to the probe. Refraction of the probe light in strong density gradients limits our observation to regions with electron density less than $6.9 \times 10^{21} \text{ cm}^{-3}$. By varying the time delay between the probe and the main beam, we can analyze the ionized channels in the fused glass and the plasma at the rear surface of Al foil. The probe beam is timed by decreasing the relative delay to a value such that no plasma is seen. This value is taken to be the zero point of time.

A calibrated γ -ray spectrometer was also used to monitor the x-ray bremsstrahlung from the laser plasma. The γ -ray spectrometer consists of a NaI detector, an electronic gated shutter, a photomultiplier, an amplifier, and a multichannel energy analyzer. A 20-mm-diameter hole in a 50-mm-thick Pb block is used to collimate the x-ray radiation and to shield the detector. The detector response is calibrated using a 511-keV and 1.274-MeV γ -ray ^{22}Na source and a 665-keV ^{137}Cs source.

III. RESULTS AND DISCUSSION

The bremsstrahlung hard x-ray spectrum has the same Maxwellian distribution as the colliding electrons. The hard x-ray spectrum is generally dominated by the bremsstrahlung produced by the high-energy hot electrons colliding with atom nuclei. The shape and intensity of the bremsstrahlung is the principal diagnostic for the outgoing hot electron flux and temperature. The hard x-ray spectrum shows a bi-Maxwellian distribution and the hot electron temperature is 73 keV, as shown in Fig. 2. However, the space-charge field stops hot electrons with energies below ~ 20 keV, so that the outgoing hot electron temperature is about 90 keV. The energy spectra of the outgoing and the incoming (to the glass) hot electrons are the same, hence the incoming hot electron temperature is also 90 keV. Propagation of these hot electrons through the high-density material is investigated below.

Shadowgrams of the target are recorded at different times. Figure 3 shows a typical shadowgram for the $1\text{-}\mu\text{m}$ -aluminum-coated fused glass slide at different times after the interaction. In order to enhance the contrast of this particular image, we have subtracted from it the image of the unperturbed target in the presence of the probe beam. Before the interaction, the fused glass slide is transparent to the probe beam. At the interaction, plasma formation can clearly be seen at the left edge of the Al-coated fused glass target. The dark region corresponds to a plasma density greater than $6.9 \times 10^{21} \text{ cm}^{-3}$ (the critical density of 400-nm light). It is also seen that the plasma expansion into the vacuum is not exactly cone shaped. This shows that the evolution from

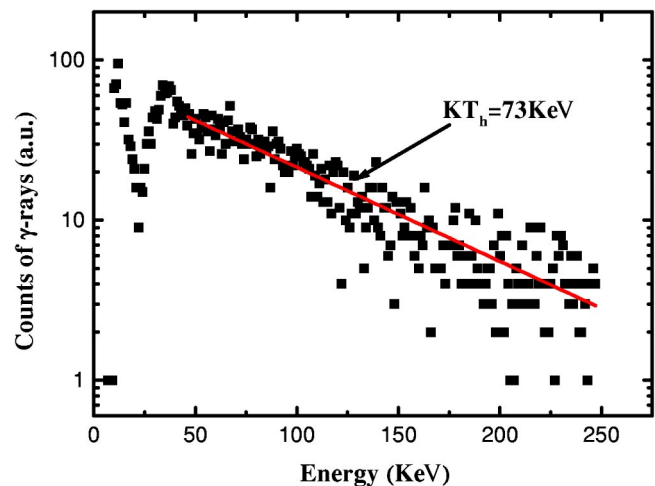


FIG. 2. The bremsstrahlung x-ray radiation from the Al target. The solid line in the figure is the Maxwellian distribution fit for the temperature.

compression to expansion of the plasma is due to the laser ponderomotive force. Opposite to the direction of the plasma expansion, a nearly isotropic dark region can clearly be seen. In view of the velocity ($\sim 2 \times 10^8 \text{ cm/s}$) of the expansion, the almost isotropic dark region may be attributed to radiation driven thermal transport ionization waves [20]. Furthermore, a few narrow jets above the ionization wave, originating from the interaction region, can be seen. In some images, there are many narrow jets, parallel to each other, with similar size ($8\text{-}\mu\text{m}$ cross section, $150\text{--}300 \mu\text{m}$ long) and separation distance ($13 \mu\text{m}$). These jets in the transparent glass slide are opaque to the probe beam, suggesting that they are dense plasma tracks corresponding to local ionization in the glass.

Three mechanisms can induce the ionization tracks in the glass: laser light, hard x rays, and hot electrons. During the interaction, the laser itself may penetrate into and form filaments within the target. However, the $1\text{-}\mu\text{m}$ -thick Al coating on the glass should block the incident laser. The contrast ratio of the laser pulse is 10^5 at 1 ps (measured by a high-dynamic third autocorrelator). A particle-in-cell simulation (Figs. 4 and 5) shows that the prepulse at 1 ps does not ablate the $1\text{-}\mu\text{m}$ Al, and only after 100 ps a shock wave propagates through the $1\text{-}\mu\text{m}$ Al. On the other hand, prior to that hot electrons produced in the interaction propagate through and out of the Al foil. Therefore, we can rule out the presence of laser light filaments in the glass. Furthermore, the cross section of the target surface was 1 mm, so that there is no possibility that light from the outer part of the laser pulse could wrap around the side of the target and initiate ionization.

Besides the hot electron beams, strong x-ray bremsstrahlung and thermal emission generated by the interaction may also propagate into the target and cause ionization tracks. In order to rule out the latter possibilities, a series of shots on a composite target were performed. The composite target consists of a vacuum gap between a $5\text{-}\mu\text{m}$ Al foil and fused glass. For comparison, some shots are also performed on $20\text{-}\mu\text{m}$ aluminum-foil-only targets.

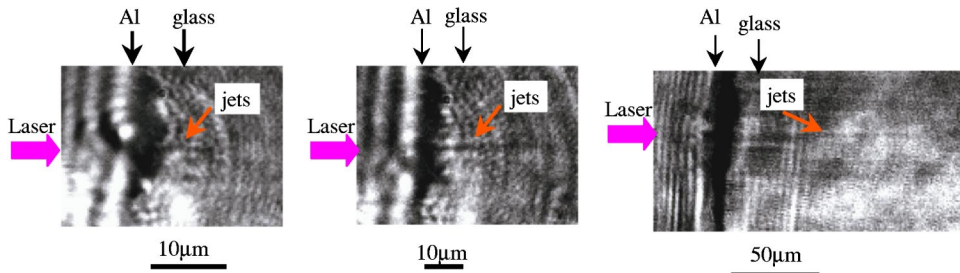


FIG. 3. Shadowgrams taken during the interaction of a 36-mJ, 25-fs laser with the 1- μm -Al-coated fused silica targets at three times: (a) 1 ps, (b) 3 ps, (c) 11 ps after the interaction. Note in pictures that the fringes at left of targets are diffraction patterns at the edge of targets.

When the laser pulse hits the Al-glass target with a vacuum gap, it first interacts with the Al foil. The regions of hot electron generation in the foil and transport through the glass are thus separated by a vacuum. A space-charge separation field builds up in the vacuum gap when the hot electrons move across it. Figure 6 shows a shadowgram taken at 13 ps after the interaction. Formation of the space-charge induced plasma in the vacuum gap at the rear surface of Al foil can be observed together with the jets in the glass slide. However, the length of the jets in Fig. 6 is significantly shorter than that in Fig. 3. When the hot electrons exit the Al foil, the space charge separation field is about 10^{11} V m^{-1} [13,21], which will stop electrons with energies below 23 keV (assuming that sheath width is of the order of the Debye length). Hot electrons above 23 keV can still go through the space-charge plasma but with somewhat reduced energy, enter the glass, and induce ionization. Thus, the length of the jets is shorter, as can be seen in Fig. 6. This supports the assertion that the ionization tracks in the glass are caused by the high-energy electrons, since the length of jets would be the same if the ionization were caused by hard x rays. We can thus exclude the possibility of hard x-ray induced ionization in the glass.

We have also performed a series of shots on 20- μm Al foils without the glass backing. Figure 7 shows the shadowgram taken at the same time (13 ps) as in Fig. 6. We can clearly see a dark mushroomlike structure with a diameter of 10 μm at the rear surface of the Al foil. It is always in line with the laser focal spot and expands with time. The dark cone does not appear when there is only the main beam (no

probe beam). Hence, the cone does not show self-emission, but emission from the plasma at the rear surface. The plasma formation at the rear surface could not be due to the laser light or hard x rays, since the laser is blocked by the 20- μm Al foil and hard x rays (that can penetrate the Al foil) do not form plasmas in vacuum. Moreover, from the formation time, we can also rule out shock breakout, which would induce a plasma cloud with much larger diameter. In addition, fast ions can also be ruled out because they cannot pass through thick targets. Therefore, hot electrons are the only source to produce the rear plasma. In our case, the average temperature of the hot electrons is about 93 keV, and their spatial range in aluminum is 62 μm . This is much longer than the thickness of the Al foil. Thus, the fast electrons, originated from the interaction area, can penetrate through the solid target. As they leave the rear surface, a space-charge field is set up, forming an electron sheath with a thickness of the order of the Debye length. If assuming the absorption into the hot electron is about 20% with a mean energy of 93 keV, and the hot electrons fill the 20- μm -thick target with a 45° cone angle, we find that the Debye length is $1.23 \times 10^{-7} \text{ m}$. The electric field (from the expression $eE\lambda_D \approx kT$ [21]) in the sheath is about $7.6 \times 10^{11} \text{ V/m}$, which is much higher than the field needed to cause ionization in aluminum. Hence, these fast electrons can heat the target and form a plasma on the rear surface of the foil. This feature demonstrates that the formation of plasma on the rear surface can only be due to the hot electrons. We have also varied the delay time of the probe beam. The time from generation of the plasma on the rear Al surface to its disap-

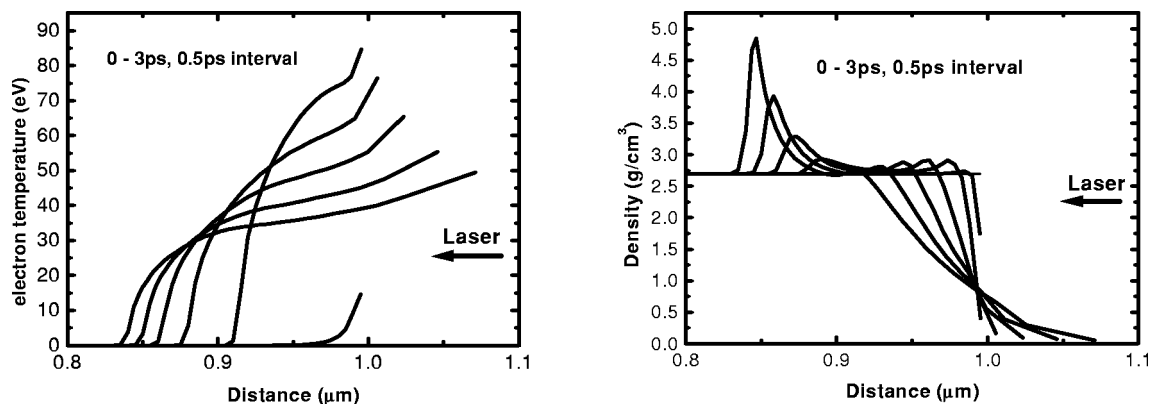


FIG. 4. Distribution of electron temperature and density for the 1-ps prepulse.

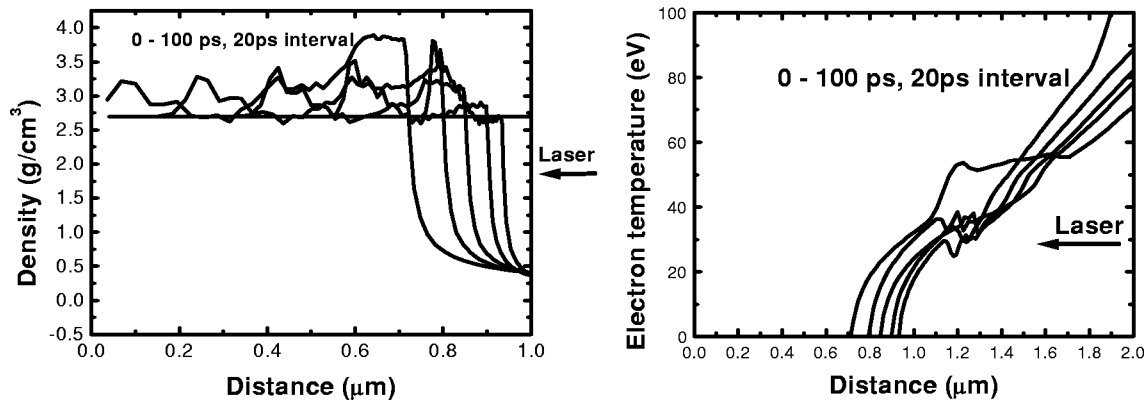


FIG. 5. Spatial distribution of electron temperature and density for the 100-ps prepulse.

pearance is about 60 ps, which is the same as the lifetime of the jets in the glass targets.

We propose that the jets in the transparent region are localized ionization region of hot electrons propagating through the glass. These hot electrons are generated in the interaction region, collimated by a strong magnetic field inside the target. The average hot electron energy can be obtained by many means, such as $K\alpha$ spectra, γ spectra, and fast electron spectra, etc. Using the results of Ref. [22] obtained from $K\alpha$ emission measurements of laser solid experiments, the fast electron temperature is

$$kT_e \approx 100 \left(\frac{I\lambda^2}{10^{17} \text{ Wcm}^{-2}} \right)^{1/3} \text{ keV}, \quad (1)$$

where I and λ are the intensity and wavelength of the laser, respectively. The laser intensity is about $8 \times 10^{16} \text{ W/cm}^2$, corresponding to an average hot electron energy of about 93 keV. From the table of energy losses and ranges of electrons and positrons [23], we find that the range is $110 \mu\text{m}$ for the 93-keV hot electrons in the glass. This is shorter than the length of jets observed. The discrepancy may be due to the existence of strong magnetic fields, which enhances the penetration of the hot electrons and reduces their angular spread

[14]. Magnetic fields, electric fields, and plasma resistivity can all play important roles on hot electron transport. The ratio of the magnetic to electric force on the hot electrons is [24]

$$\frac{vB}{E} \approx 12 \left(\frac{2\tau}{1 \text{ ps}} \right) \left(\frac{10 \mu\text{m}}{R} \right) \left(\frac{v}{c} \right), \quad (2)$$

where R is the focal spot size, τ is the duration of the laser pulse, and v is the hot electron speed. Thus, the effect of the magnetic field is significant. Simulation [21,24] has also shown that the electric field is not a major effect at an intensity of 10^{16} Wcm^{-2} . In the present case, the fast electrons are pinched inside the target by a strong magnetic field. Figure 6 shows that the diameter of the plasma at the rear surface of the Al foil is small, corresponding to a spreading angle of 10° over $20 \mu\text{m}$. This is comparable to the radius of the observed plasma. If the fast electrons had propagated freely, the spread angle would be greater than 32° in the $20-\mu\text{m}$ foil target due to collisional scattering of electrons with atom nuclei. Strong magnetic fields [25] that are ubiquitous to the interaction of intense lasers with high-density plasmas can suppress the radial spread of the hot electron.

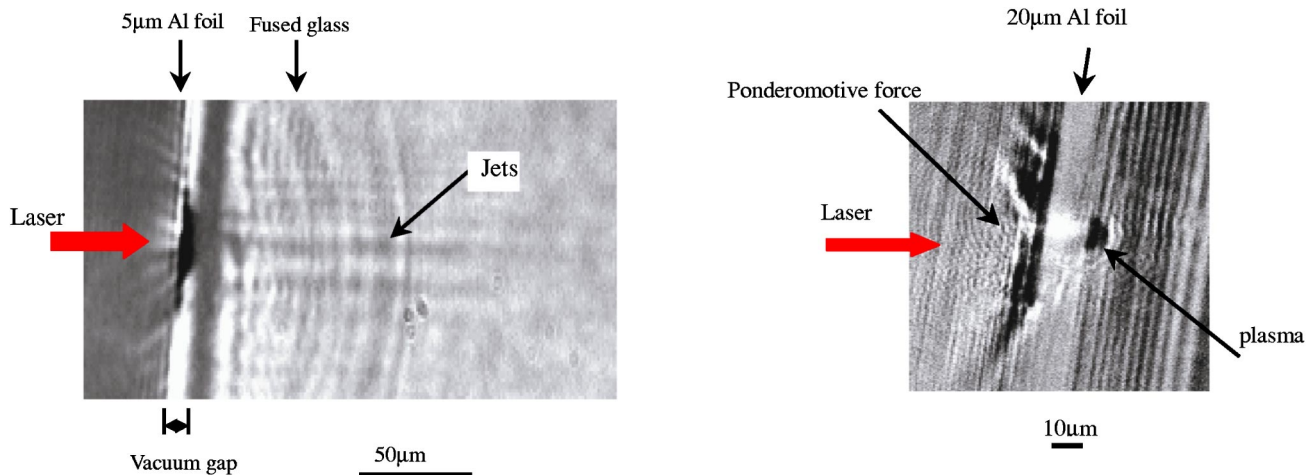


FIG. 6. Shadowgraphic image of the target during interaction of the main pulse with a composite target comprising a vacuum gap.

FIG. 7. Shadowgram taken during the interaction of 36-mJ, 25-fs laser with a 20-μm Al foil, showing a plasma on the rear surface.

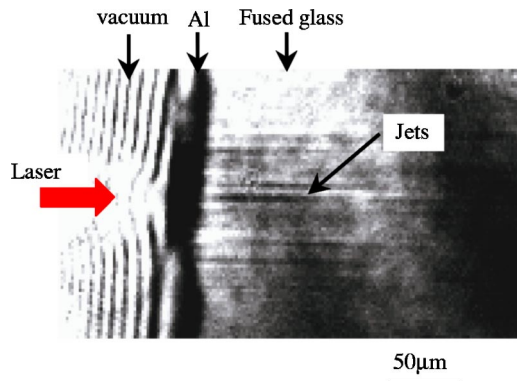


FIG. 8. Shadowgram taken during the interaction of the 36-mJ, 25-fs laser with a 1- μm -Al-coated fused glass. There are many more jets that are parallel to each other and their extension is wider than the focal spot.

The well collimated fast electrons give indirect evidence for the presence of such a magnetic field in the target.

It is of interest to note that in Fig. 8 there are two jets at the center of the focal spot, and several jets parallel but away from the axis of laser. This phenomenon is due to two reasons. The first is the fact that the focal spot was determined by low-energy equivalent-plane measurements, which showed a full width at half maximum of 10–20 μm . When energy is increased, the laser beam quality is strongly modulated by thermal effects and inhomogeneity of the dope concentration in the Ti:sapphire crystal. Thus there exist hot spots in the laser beam. When the laser is focused, there are many small local high intensity spots around the focus. Thus the effective size of the focal spot is much larger than that measured by low-energy equivalent-plane measurements. The intensity of each hot spot in the laser beam is sufficiently high to produce hot electrons to induce ionization in the fused silica. Thus the jets induced by the hot electrons can extend far from the axis of laser. This also explains why the length of jets was also almost the same, since the energy of each hot spot is almost the same. The second reason is due to Weibel instability [26], the measured beam size is full width at half maximum, because the hot electron beam is a Gaussian distribution, in fact, there are still some electrons near the bottom of the Gaussian distribution. When filaments were produced due to the splitting of the hot electrons, some hot electrons are diffused to two sides and the size of distribution becomes larger. Thus the jets induced by the hot electrons can extend far from the axis of the laser due to Weibel instability too.

Inside the target, the hot electron jets are parallel to the laser axis and they ionize the medium to form a bundle of parallel ionized filaments of dense plasma. The structure of the jets in the transparent targets is consistent with the results of the 2D simulation [27,28]. The filaments are the result of the splitting of the hot electron beam due to the Weibel instability [26,29], which generates strong magnetic fields transverse to the propagation direction of the hot electron beam, and the magnetic field in turn causes the beam to break up. The duration of the jets inside the target is 60 ps, which is longer than that from other observations [17]. The

ionization and recombination time is very short in the dense plasma of the filaments, so that an accurate measure of the duration is difficult. Furthermore, the resistive and dielectric properties of the plasma, as well as the electric and magnetic fields, play important roles in determining the duration of the jets. As a rough estimate, the duration can be calculated from the characteristic time of collisions between the electrons and ions [30],

$$\tau_{ei} \approx 3.5 \times 10^8 A T_e^{1.5} / N_0 Z_{av}^2, \quad (3)$$

where $A = 20$ is the atomic mass number of the ions, T_e is the electron temperature in the unit of eV, N_0 is the plasma density, Z_{av} is the average charge number of the ions. For the parameters of our experiment we obtain $\tau_{ei} \approx 22$ ps. Since the collision frequency of charge particles in the presence of magnetic field is smaller than that without the latter [31–33], the characteristic time of the jets will be longer when a strong magnetic field is present. Thus the duration of the jets in the experiment is in reasonable agreement with the estimate.

The conversion efficiency of laser energy into that of the hot electrons can be estimated from the structure of the closely packed bundle of ionized filaments in the glass. From the total ionized filament volume and the ionization energy of fused silica, the number of hot electrons can be estimated to be about 10^{11} . Thus, the conversion efficiency of laser energy into hot electrons is about 8%. This can also be obtained from the energy balance equation $n_e \varepsilon_e v_e = \eta I$, where n_e is electron density, ε_e is electron kinetic energy, η is the efficiency of laser energy conversion into hot electrons, and v_e is the velocity of hot electrons. For the intensity in our case, it is estimated that η is in the range of a few to ten percent. This is in accordance with the above estimate as well as with some other measurements [34].

IV. CONCLUSION

In conclusion, the propagation of hot electrons through high-density plasmas has been studied using optical probing techniques. A number of ionization tracks produced by hot electrons have been observed inside Al-coated glass targets. The plasma on the rear surface of a 20- μm Al foil has also been analyzed via optical probing. The jetlike tracks in the Al-coated fused glass originate from the focal spot, with about 150–300 μm in length and 8 μm in width. These tracks are parallel to each other and separated by a distance of 13 μm . The jets have a transverse structure and form bundles of ionized filaments. The structure is consistent with 2D PIC simulation, which shows that the propagation of a beam of hot electrons generated in the interaction region and propagates through the target is highly collimated by a strong self-generated magnetic field in the target.

ACKNOWLEDGMENTS

This work was jointly supported by the NNSFC (under Grant Nos. 10075075, 10005014, and 19825110), the National Hi-tech ICF program, and the NKBRSP (under Grant No. G19999075200).

- [1] P. Maine *et al.*, IEEE J. Quantum Electron. **24**, 398 (1998).
- [2] M. Tabak *et al.*, Phys. Plasmas **1**, 1626 (1994).
- [3] R. Krushelnick *et al.*, Phys. Rev. Lett. **78**, 4047 (1997).
- [4] M. Borghesi *et al.*, Phys. Rev. E **57**, 4899 (1998).
- [5] C. Deutsch *et al.*, Phys. Rev. Lett. **70**, 3075 (1993).
- [6] S.C. Wilks and W.L. Kruer, IEEE J. Quantum Electron. **33**, 1954 (1997).
- [7] W. Yu *et al.*, Phys. Rev. E **61**, 2220 (2000); Y.T. Li *et al.*, *ibid.* **64**, 046407 (2001).
- [8] S.C. Wilks *et al.*, Phys. Rev. Lett. **45**, 1383 (1992).
- [9] F. Brunel, Phys. Rev. Lett. **59**, 52 (1987).
- [10] L.M. Chen, J. Zhang *et al.*, Phys. Plasmas **8**, 2925 (2001); Q.L. Dong and J. Zhang, *ibid.* **8**, 1025 (2001).
- [11] N.H. Ebrahim *et al.*, Phys. Rev. Lett. **45**, 1179 (1980).
- [12] K. Estabrook and W.L. Kruer, Phys. Fluids **26**, 7 (1983).
- [13] M. H. Key *et al.*, Phys. Plasmas **5**, 1966 (1998).
- [14] M. Tatarakis *et al.*, Phys. Rev. Lett. **81**, 999 (1998).
- [15] T.A. Hall *et al.*, Phys. Rev. Lett. **81**, 1003 (1998).
- [16] D. Batani *et al.*, Phys. Rev. E **61**, 5725 (2000).
- [17] M. Borghesi *et al.*, Phys. Rev. Lett. **83**, 4309 (1999); L. Gremillet *et al.*, *ibid.* **83**, 5015 (1999).
- [18] R. Kodama *et al.*, Nature (London) **412**, 798 (2001).
- [19] Z.Y. Wei *et al.*, Sci. China, Ser. A: Math., Phys., Astron. **43**, 1083 (2000).
- [20] T. Ditmire *et al.*, Phys. Rev. Lett. **77**, 498 (1996).
- [21] J.R. Davies *et al.*, Phys. Rev. E **59**, 6032 (1999).
- [22] F.N. Beg *et al.*, Phys. Plasmas **4**, 447 (1996).
- [23] M. J. Berger and S. M. Seltzer, *Studies in Penetration of Charged Particles in Matter* (National Academy of Sciences, Washington, D.C., 1964).
- [24] J.R. Davies *et al.*, Phys. Rev. E **56**, 7193 (1997).
- [25] J. Stamper, Science **281**, 1469 (1998).
- [26] T. Taguchi *et al.*, Phys. Rev. Lett. **86**, 5055 (2001).
- [27] A. Pukhov and J. Meyer-ter-Vehn, Phys. Rev. Lett. **79**, 2686 (1997).
- [28] A. Pukhov, Phys. Rev. Lett. **86**, 3562 (2001).
- [29] R.L. Morse and C.W. Nielson, Phys. Fluids **14**, 830 (1971); T. Yabe and K. Mima *et al.*, Phys. Rev. Lett. **48**, 242 (1982); T. Taguchi *et al.*, *ibid.* **86**, 5055 (2001).
- [30] L. Spitzer, *Physics of Fully Ionized Gases* (Wiley, New York, 1962).
- [31] S. Imazu, Plasma Phys. Controlled Fusion **28**, 857 (1986).
- [32] S. Imazu, Phys. Rev. A **23**, 2644 (1981).
- [33] D. Montgomery, Phys. Fluids **17**, 2201 (1974).
- [34] J. Yu *et al.*, Phys. Plasmas **6**, 1318 (1999).

Third-order harmonic generation by self-guided femtosecond pulses in air

H. Yang,¹ J. Zhang,^{1,*} J. Zhang,¹ L. Z. Zhao,¹ Y. J. Li,^{1,2} H. Teng,¹ Y. T. Li,¹ Z. H. Wang¹ Z. L. Chen,¹ Z. Y. Wei,¹ J. X. Ma,³ W. Yu,⁴ and Z. M. Sheng¹

¹Laboratory of Optical Physics, Institute of Physics, Chinese Academy of Sciences, Beijing 100080, China

²Department of Physics, University of Mining and Technology of China, Beijing 100083, China

³Department of Modern Physics, University of Science and Technology of China, Hefei 230026, China

⁴Shanghai Institute of Optics and Fine Mechanics, Chinese Academy of Sciences, Shanghai 201800, China

(Received 12 June 2002; published 16 January 2003)

Strong third-order harmonic (TH) emission is observed with a conversion efficiency higher than 10^{-3} from a plasma channel formed by self-guided femtosecond laser pulses propagating in air. The main characteristics of TH emission in various conditions and the phase-matching condition between the fundamental and the TH wave are investigated. An optimized condition is found, under which the TH conversion efficiency is maximized. Our experimental results show that radiation of the emission in ultraviolet wavelength range makes a major attribution to TH emission, whereas the effects of self-phase modulation are not important when intense laser pulses interact with gaseous media.

DOI: 10.1103/PhysRevE.67.015401

PACS number(s): 52.35.Mw, 52.40.Db

I. INTRODUCTION

The propagation of intense laser pulses in transparent matter causes strong nonlinear effects such as self-focusing [1,2], self-phase modulation (SPM) [3–5], four-wave mixing [6–9], and stimulated Raman processes. Propagation of an intense laser pulse in air will lead to self-focusing due to the Kerr effect. The mechanism for femtosecond laser pulses propagating over long distance in air is the balance between the Kerr self-focusing due to the nonlinear effects in air and defocusing due to the tunneling ionization and the diffraction of the laser beam [10–12]. Recently, much attention has been paid to harmonic generation by the self-guided femtosecond pulses in gaseous media. The dynamic equilibrium between the self-focusing due to nonlinear intensity-dependent refractive index and defocusing due to plasmas in the channel can support a long plasma channel in the interaction of the intense laser pulses and gaseous media. This is beneficial to get high harmonic conversion efficiency in the interaction, because the conversion efficiency between the fundamental wave and harmonic wave does not only depend on laser intensity, but also on interaction length. Usually, tight focusing is used to gain higher laser intensity in the interaction region, but it also leads to very short interaction length. Moreover, the ionization of gas always prevents high laser intensity due to defocusing. Therefore extending the interaction length is a promising way to get high conversion efficiency. We can get very long interaction length because of self-guiding when intense laser pulses interact with gaseous media. Theoretical and experimental results [16–21] have demonstrated that a femtosecond laser pulse can propagate many Rayleigh lengths due to self-guiding. The third-order harmonic (TH) generation in gaseous media has been studied for many years. Fedotov *et al.* [22] have studied the effects of the temporal and spatial self-action of light in atmospheric air. Mar-

cus *et al.* [23] and Zhu *et al.* [24] tightly focused a femtosecond laser beam in atmospheric pressure methane and studied the TH generation process. In the process of ultrashort laser pulse propagation in air, the radiation of UV waves is considered as a result of the self-phase modulation, which leads to supercontinuum spectra expanding to UV waves when the ultrashort laser pulse propagates very long distance in air. However, the physics mechanism of TH generation in air is still not well understood.

In this paper, we will exploit the relationship between the TH generation and self-guiding propagation of intense laser pulses in air. It is demonstrated that the energy conversion efficiency of the fundamental wave to TH wave is very high, with a maximum efficiency up to 1.2×10^{-3} , because the interaction length is largely prolonged due to the self-guiding propagation of an ultrashort laser pulse in air. Our experimental results show that the emission of UV waves should be mainly responsible for the TH emission generation rather than self-phase modulation, when ultraintense laser pulses interact with air.

In this paper, we will exploit the relationship between the TH generation and the self-guiding propagation of ultraintense laser pulses in air. It is demonstrated that the energy conversion efficiency of the fundamental wave to TH wave is very high, with maximum efficiency reaching 1.2×10^{-3} , because the interaction length is largely prolonged due to the self-guiding propagation of ultrashort laser pulse in air. In earlier publications, in the process of ultrashort laser pulse propagation in air, the radiation of UV wave is considered as a result of the self-phase modulation, which leads to supercontinuum spectra expanding to UV waves when the ultrashort laser pulse propagates very long distance in air. Our experimental results show that the emission of UV waves should be attributed to TH rather than self-phase modulation, when the ultraintense laser pulse interacts with air.

II. EXPERIMENTAL SETUP

Figure 1 is a schematic diagram of the experimental setup. The laser system is a Ti:sapphire chirped-pulse amplification

*Author to whom correspondence should be addressed. Email address: jzhang@aphy.iphy.ac.cn

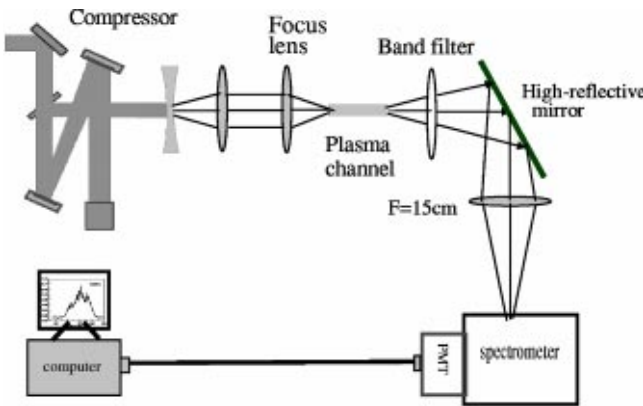


FIG. 1. A schematic representation of the experimental setup.

system (JG-II), which can provide up to 640 mJ energy, in 30 fs pulses, at a central wavelength of 800 nm. To prevent defocusing effects due to high intensity, in our experiment the maximum pulse energy used is about 28 mJ. In order to reduce the necessary distance before the formation of laser plasma channel, femtosecond laser pulses are slightly focused with different positive lens ($f=25,40,60,80,100$ cm) in air. The optical breakdown can be clearly observed in air with the appearance of the spark at the focus of the lens. In experiment, we observe that ultrashort laser pulses propagate many Rayleigh lengths, forming a long plasma channel. Generally, the length of the channel varies with the focal length of the focusing lens. A band filter is used to suppress the fundamental signal, which propagates in the same direction. The TH wave is collected into a photomultiplier tube with a $f=25$ cm quartz lens, and the TH spectra are detected with a spectrometer and processed by a computer. In the experiment, the characteristics of the spectra of the TH wave are studied in various conditions. We find that there exists an optimum condition, under which maximum conversion efficiency from the fundamental wave into the TH emission can be obtained.

III. RESULTS AND DISCUSSION

In order to study the characteristics of the TH emission in various conditions, we measure the spectrum of the fundamental wave emission in air from the position where filaments are formed by focusing the laser beam. The broadened spectrum of the fundamental wave due to SPM is observed as shown in Fig. 2. The solid and dotted curves represent the spectral profile with and without an $f=25$ cm lens, respectively. It can be seen that the fundamental spectra are greatly broadened because of the formation of the plasma filament channel in the air. This phenomenon can be attributed to self-phase modulation, which can greatly broaden the spectral component. The profile of the broadened spectrum is asymmetric and exhibits a blue shift. The broadening at short wavelength is more obvious than that at long wavelength. This is very consistent with theory and experiments [5].

After the filaments, very strong TH emission can be observed by applying a band filter, which can filter out fundamental waves. The TH spectrum is shown in Fig. 3. The peak

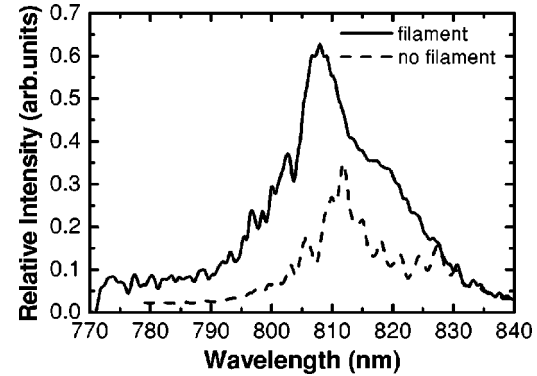


FIG. 2. The spectrum of the fundamental wave with and without lens.

of the TH spectrum occurs at 274 nm, which is red-shifted relative to the three fold (270 nm) of the fundamental wavelength (810 nm). Moreover, the spectral profile of the TH is clearly oscillatory. This spectral modulation may simultaneously be caused by two mechanisms. One is that the TH emission is generated with the modulated fundamental light as in Fig. 2. The other one is that the TH itself may experience self-phase modulation [14].

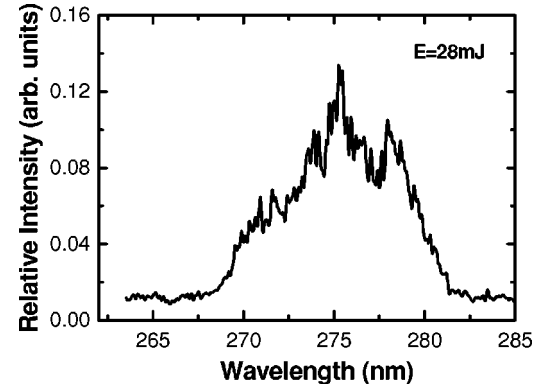
As is well known, the phase matching is necessary for an efficient conversion of the fundamental wave to the TH emission. The phase matching condition requires [13]

$$n(\omega) = n(3\omega). \quad (1)$$

Usually, air is a homogeneous medium and has normal dispersion. So it is very difficult to satisfy this condition. But when intense laser pulses form plasma channel in the air, this condition is easily satisfied. Since the fundamental wave intensity is much stronger than that of the TH emission, the intensity-dependent refractive index due to the Kerr effect in fundamental waves is much larger than that in the TH emission. Hence, Eq. (1) can be written as

$$n_0(\omega) + n_2 I(\omega) - n_e/2n_c(\omega) = n_0(3\omega) - n_e/2n_c(3\omega), \quad (2)$$

where n_0 is the refractive index of the air, and n_2 is the Kerr nonlinear coefficient, n_e is the electron density. Here we

FIG. 3. The spectra of the TH with a fundamental wave laser energy of $E=28$ mJ and a lens with a focal length of $f=40$ cm.

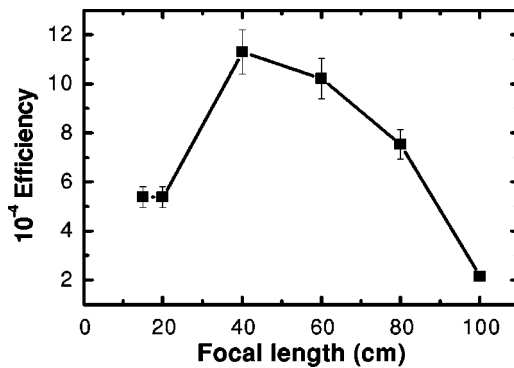


FIG. 4. The conversion efficiency between the fundamental wave and the TH versus focal length of the lens.

have neglected the intensity-dependent refractive index arising from the TH emission, because the intensity of the TH emission is very small. Considering the electron density in plasma channel is about $10^{16}\text{--}10^{17}/\text{cm}^{-3}$ as measured in Ref. [11], we can get phase-matching laser intensity of about $10^{13}\text{--}10^{14} \text{ W/cm}^2$, which is consistent with the laser intensity required for self-guiding in air [11,21]. Generally, the output intensity of the TH emission is about [15]

$$I_{3\omega}(Z) = \frac{(3\omega)^2}{n_{3\omega} n_\omega^3 \epsilon_0 c^4} I_\omega^3 l_{eff}^2, \quad (3)$$

where $l_{eff} = \chi_{eff} Z (\chi_{eff} = \hat{e}_{3\omega} \hat{\chi}^{(3)} : \hat{e}_\omega \hat{e}_\omega \hat{e}_\omega)$ is the effective interaction length, which represents the interaction length in which the phase-matching condition is maintained. From Eq. (3), the conversion efficiency is proportional to the product of the fundamental wave intensity and the effective length.

In our experiment, the output energy of the TH emission versus focal length of the lens is shown in Fig. 4. The highest conversion efficiency is larger than 1.2×10^{-3} . It is interesting to note that the conversion efficiency to the TH emission is maximized when the focal length of the lens is about 40–60 cm. From Eq. (3), we can explain the existence of this optimum focal length corresponding to the maximum conversion efficiency, because the output power of the TH emission is proportional to the laser intensity and the effective interaction length l_{eff} . So for a shorter (long) focal length, the laser intensity is higher (lower) in the channel, but l_{eff} will be shorter (longer). Thus, there exists an optimum focal length, with which the product of the laser intensity with effective interaction length will be maximized. On the other hand, for a shorter focal length, the conversion efficiency will be reduced due to ionization, which consumes a lot of fundamental wave energy.

With a fixed focal length of the lens ($f=40 \text{ cm}$), the TH spectral profile is plotted versus various pulse energies in Fig. 5. For higher energy, the spectral width of the TH is almost constant and the spectral profile of the TH is similar to that of the fundamental wave as shown in Fig. 5 (curves a and b). For lower energy, the TH spectrum becomes narrower as shown in Fig. 5 (curves c and d). With increasing energy, the oscillation of the TH spectra becomes more serious. This can be explained as follows. For higher energy

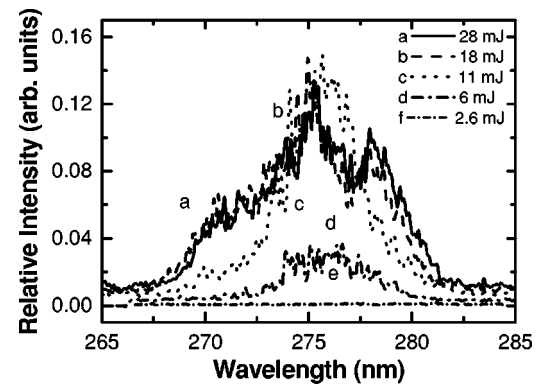


FIG. 5. The spectrum of the TH versus focal length of the lens.

of the fundamental wave, the self-phase modulation covers more spectral components and causes more serious oscillations in the fundamental wave. Thus, the higher fundamental wave energy results in stronger modulation and wider spectra in the TH emission. When the laser energy at the fundamental wave is less than 2.6 mJ in our experiment, the TH emission is not observable. At this energy, the corresponding laser intensity can be estimated to be $2.5 \times 10^{13} \text{ W/cm}^2$ from the focus spot size. This fundamental laser intensity may be considered as threshold for generating TH emission in air. We can evaluate the approximate threshold of the laser intensity required for generation of the TH in theory. The ionization term in Eq. (2) can be omitted at threshold laser intensity, so the laser threshold intensity is

$$I(\omega) = [n_0(3\omega) - n_0(\omega)/n_2] \approx 2 \times 10^{13} \text{ W/cm}^2. \quad (4)$$

This is almost the same as the direct estimate of the experimental value.

For a fixed energy ($E=28 \text{ mJ}$) of laser pulse, the measured TH spectral profile versus various focal lengths of the lens is shown in Fig. 6. With increasing focal length, the TH spectra are red shifted, which is largest at $f=60 \text{ cm}$ as shown by curve C in Fig. 6. When the focal length is longer than this focal length, the TH spectra become blue shifted. The reason for this phenomenon may be self-phase modulation. That is to say, relative red shift or blue shift may be decided by product of the laser intensity and effective interaction length, because the product of laser pulse intensity

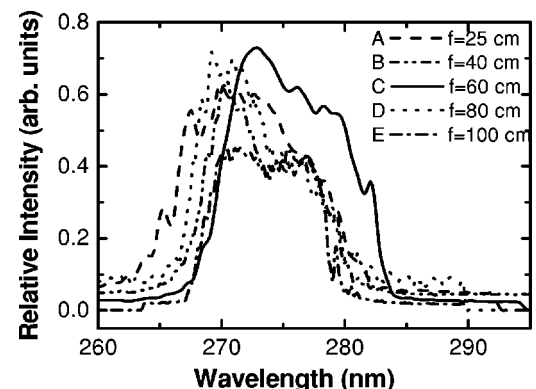


FIG. 6. The spectrum of the TH versus laser energy.

with effective interaction length is maximum at around $f = 60$ cm, which corresponds to the maximum conversion efficiency 1.2×10^{-3} [25–27].

IV. CONCLUSION

Because of the self-guiding of the ultrashort laser pulses in air, the interaction length between the ultrashort laser pulse and air is greatly elongated. During the interaction of the ultrashort laser with air, very strong TH emission is observed, with a maximum conversion efficiency higher than 10^{-3} . At the same time, the characteristics of the TH spectra are investigated, for different focal lengths and different energies of the laser pulse. We find that there exists an optimum focal length of the lens for the conversion efficiency to the TH emission for a constant input fundamental energy. This means that there is an optimum product of the laser intensity

with interaction length. Experimental results show that the radiation of UV waves in supercontinuum should attribute to harmonic generation instead of self-phase modulation when the intense laser pulses interact with gaseous media. Moreover, our experimental results not only show that the supercontinuum, which is observed during the propagation of the ultrashort laser pulse in air, originated from SPM or stimulated Raman processes, but also demonstrate that the third-order harmonic contributes to the supercontinuum generation.

ACKNOWLEDGMENTS

This work was supported by the NSFC (Grant Nos. 19825110, 10004015, and 19974074), National Hi-tech ICF program, and NKBRSPF (Grant No. G1999075200).

-
- [1] J.H. Glownia, G. Arjavalingam, P.P. Sorokin, and J.E. Rothenberg, Opt. Lett. **11**, 79 (1986).
 - [2] P.B. Corkum and C. Rolland, Int. J. Quantum Chem. **25**, 2634 (1989).
 - [3] A. Penzkofer, A. Laubereau, and W. Kaiser, Phys. Rev. Lett. **31**, 863 (1973).
 - [4] N. Bloembergen, Opt. Commun. **8**, 285 (1973).
 - [5] W.L. Smith, P. Liu, and N. Bloembergen, Phys. Rev. A **15**, 2396 (1977).
 - [6] R.L. Fork *et al.*, Opt. Lett. **8**, 1 (1983).
 - [7] P.B. Corkum, C. Rolland, and T. Srinivasan-Rao, Phys. Rev. Lett. **57**, 2268 (1986).
 - [8] G.Y. Yang and Y.R. Shen, Opt. Lett. **9**, 510 (1984).
 - [9] V. Francois, F.A. Ilkov, and S.L. Chin, Opt. Commun. **99**, 241 (1993).
 - [10] E.T.J. Nibbering *et al.*, Opt. Lett. **21**, 62 (1996).
 - [11] A. Braun *et al.*, Opt. Lett. **20**, 73 (1995).
 - [12] B. La. Fontaine *et al.*, Phys. Plasmas **6**, 1615 (1999).
 - [13] Y. R. Shen, *The Principles of Nonlinear Optics* (Wiley, New York, 1984).
 - [14] Y.-D. Qin *et al.*, Appl. Phys. B: Lasers Opt. **B71**, 581 (2000).
 - [15] P.S. Banks, M.D. Feit, and M.D. Perry, J. Opt. Soc. Am. B **19**, 102 (2002).
 - [16] S. Tzortzakis *et al.*, Phys. Rev. Lett. **86**, 5470 (2001).
 - [17] E.T.J. Nibbering *et al.*, Opt. Lett. **21**, 62 (1996).
 - [18] L. Woste *et al.*, Laser Optoelektron. **29**, 51 (1997).
 - [19] A. Couairon and L. Berge, Phys. Plasmas **7**, 193 (2000).
 - [20] L. Berge and A. Couairon, Phys. Plasmas **7**, 210 (2000).
 - [21] H. Yang *et al.*, Phys. Rev. E **65**, 016406 (2002).
 - [22] A.B. Fedotov *et al.*, Opt. Commun. **133**, 587 (1997).
 - [23] G. Marcus *et al.*, J. Opt. Soc. Am. B **16**, 792 (1999).
 - [24] C.J. Zhu *et al.*, Chin. Phys. Lett. **18**, 57 (2001).
 - [25] *The Supercontinuum Laser Source* edited by R. R. Alfano (Springer-Verlag, New York, 1989).
 - [26] P.B. Corkum and C. Rolland, IEEE J. Quantum Electron. **25**, 2634 (1989).
 - [27] F.A. Ilkov, L. Sh. Ilkov, and S.L. Chin, Opt. Lett. **18**, 681 (1993).

Z. WEI^{1,2,✉}
Y. KABOYASHI³
K. TORIZUKA³

Passive synchronization between femtosecond Ti:sapphire and Cr:forsterite lasers

¹ New Energy and Industrial Technology Development Organization, 3-1-1 Higashi-Ikebukuro, Tokyo 170-6027, Japan

² Laboratory of Optical Physics, Institute of Physics and Center of Condensed Matter Physics, Chinese Academy of Sciences, Beijing 100080, P.R. China

³ Institute of Photonics, National Institute of Advanced Industrial Science and Technology, 1-1-4 Umezono, Tsukuba, Ibaraki 305-8568, Japan

Received: 15 September 2001/

Revised version: 1 November 2001

Published online: 27 June 2002 • © Springer-Verlag 2002

ABSTRACT Two independent femtosecond Ti:sapphire and Cr:forsterite lasers were stably synchronized by crossing both lasers inside the Ti:sapphire crystal. We obtained two-color femtosecond pulse trains at the completely different wavelengths of around 820 nm and 1250 nm respectively. This new technique overcomes the gain competition and enables us to greatly broaden the tunable ranges. By optimizing the overlap of the beams, we realized a large tolerance of cavity-length mismatch of 5 μm and demonstrated long-term synchronization that continuously remained over several hours. The measured FWHM of the cross-correlation trace is 74 ± 2 fs based on the 43 ± 2 -fs Ti:sapphire and 52 ± 1 -fs Cr:forsterite lasers. The exact coincidence with the theoretical calculated value infers the two-color laser being synchronized with a timing jitter of only a few femtoseconds.

PACS 42.60.Fc; 42.60.By; 42.65.Re

In this paper, we present a novel passive technique of synchronizing two different femtosecond lasers based on the nonlinear coupling mechanism between Ti:sapphire and Cr:forsterite lasers. By crossing both lasers inside the Ti:sapphire crystal, we obtained two-color femtosecond pulse trains at the completely different wavelengths of around 820 nm and 1250 nm. This design overcomes the gain competition and gives us a potential of broadening the bandwidths and tunability. Compared to the active synchronization with electrical feedback scheme, the passive technique was stimulated by cross-phase modulation (XPM) and should be capable of operating at lower fluctuation, which will result in a very small timing jitter.

The mechanism of passive synchronization can be attributed to the XPM effect between two coupled femtosecond KLM lasers. Considering the lasers to operate at the repetition rates of f_1 and f_2 respectively, before the synchronization occurs, they cross in the Kerr medium at a repetition rate of $f_1 - f_2$ and suffer the instantaneous frequencies of ω_1 and ω_2 :

$$\omega_1 = \omega_{01} - n_2(\omega_{01}, \omega_{01}) \frac{\partial I_1}{\partial t} - n_2(\omega_{01}, \omega_{02}) \frac{\delta}{v_2} \frac{\partial I_2}{\partial t} \quad (1)$$

$$\omega_2 = \omega_{02} - n_2(\omega_{02}, \omega_{02}) \frac{\partial I_2}{\partial t} - n_2(\omega_{02}, \omega_{01}) \frac{\delta}{v_1} \frac{\partial I_1}{\partial t} \quad (2)$$

1 Introduction

The technology of Kerr-lens mode locking (KLM) in solid-state lasers has greatly pushed the development of femtosecond science. Up to now, the Ti:sapphire and Cr:forsterite lasers have been demonstrated as the two successful examples among the available KLM lasers. By inducing the intra-cavity self-phase-modulation (SPM) effect, recently C. Chudoba et al. [1] and R. Ell et al. [2] directly generated few-cycle pulses from both lasers with ultra-broadband spectra. Obviously, synchronizing the above lasers will give us a potential to produce two-color femtosecond pulses in unprecedented bandwidths and pulse durations. Such a laser will be an ideal tool as the frequency comb for the measurement of absolute optical frequency in metrology [3].

Previous two-color femtosecond solid-state lasers, using either active synchronization with an electrical feedback device [3–5] or passive synchronization by the nonlinear coupling effect, used only a Ti:sapphire crystal as the gain medium [6–11]. Because of the single gain medium, the latter laser suffered from limited bandwidths, poor tunability and close optical frequencies.

Here I_i ($i = 1, 2$) is the intra-cavity laser intensity, ω_{0i} is the central frequency, $n_2(\omega_{01}, \omega_{01})$ and $n_2(\omega_{02}, \omega_{02})$ are the SPM nonlinear indexes for laser 1 and laser 2 respectively, $n_2(\omega_{01}, \omega_{02})$ is the XPM nonlinear index, v_i is the mode volume and δ is the overlap volume between the two lasers. Considering the instant of time when both laser pulses start to cross, for the case of laser 1 behind laser 2, the leading part of laser 1 crosses with the trailing part of laser 2. From (1) and (2), we easily deduce that the spectrum of laser 1 is shifted into the blue because of the negative slope of intensity I_2 in the trailing pulse, and laser 2 is shifted into the red because of the positive slope of intensity I_1 in the leading pulse. In the laser cavities with negative group dispersions, the round-trip time of laser 1 will decrease but that of laser 2 will increase. If both cavity lengths have been adjusted to be nearly equal, the time interval of both laser pulses inside the Kerr medium will be shortened after one round trip and the next crossing will be further enhanced in the time domain. Therefore, the time in-

terval will become shorter and shorter, until both laser pulses maximally overlap in the time domain. Vice versa, if the laser 1 is ahead of the laser 2, the crossing will happen at the trailing part of laser 1 and the leading part of laser 2; which leads laser 1 and laser 2 in red and blue shifts respectively. So, we once again deduce that laser 2 will speed up and laser 1 will slow down corresponding to the times of the round trip in the cavities with negative group dispersions, resulting in both laser pulses also being maximally overlapped.

Once both laser pulses are maximally overlapped, the shifts of carrier frequency vanish because of the symmetrical spectral broadening and both pulses operate at the same round-trip time. For any minor jitter between the two pulses arising from noise and environmental perturbations, due to the above dynamics process the pulses can automatically maximally overlap again after enough round trips. This behavior corresponds to a pulling effect of two laser pulses on each other; in this case both pulses are locked together and the laser performs a synchronized operation.

2 Experimental setup

We synchronized the femtosecond KLM Ti:sapphire and Cr:forsterite lasers by coupling both laser pulses in the Ti:sapphire crystal. This design is based on two reasons: (i) the Ti:sapphire crystal is transparent for the Cr:forsterite laser and (ii) the high nonlinear index n_2 is expected in the Ti:sapphire crystal. A schematic of the novel two-color femtosecond laser is shown in Fig. 1. It consists of a prism dispersion controlled KLM Ti:sapphire laser and a self-starting KLM Cr:forsterite laser. The gain media are Ti:sapphire and Cr:forsterite crystals with the lengths of 4 mm and 7 mm respectively. Both of them were set at Brewster angles and maintained at the temperatures of 11 °C and 1 °C respectively. The Cr:forsterite crystal was also covered in a small plastic box and purged by flowing nitrogen to keep the surface dry. In order to induce a stronger XPM effect for synchronization by beam crossing with a narrower angle, we used two pairs of D-shaped concave mirrors around the Ti:sapphire crystal and set the mirrors at the gaps of less than 1 mm by

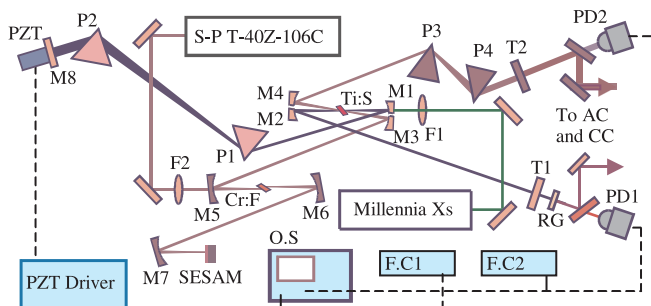


FIGURE 1 Experimental setup. Both Ti:sapphire and Cr:forsterite lasers are coupled inside the Ti:sapphire crystal by half-cut mirrors M1 to M4. M1–M6: CVI TLM2 mirrors with ROC of 10 cm and diameter of 0.5 in; M7: HR with ROC of 20 cm and diameter of 1 in; M8: mini-plate HR with 10-mm diameter \times 1-mm thickness; T1 and T2: output couplers with transmissivities of 5% and 3%; P1 and P2: fused-silica prisms; P3 and P4: SF6 prisms; PD1 and PD2: fast photodiodes; PZT: piezo-transducer; RG: orange glass filter; AC: auto correlator; CC: cross correlator. F.C1. and F.C2.: frequency counters; O.S.: oscilloscope; M3–M7 and T2 were coated at 1300 nm, others were coated at 850 nm

using independent mirror mounts. Where M1 and M2 were the focus mirrors for the Ti:sapphire laser, M3 and M4 were inserted into the Cr:forsterite laser cavity for introducing an additional focal point inside the Ti:sapphire crystal. This design greatly enhances the coupling between two laser beams with the standard commercial mirrors. For reliable KLM of the Cr:forsterite laser [12], a broadband SESAM (semiconductor saturable-absorber mirror) was used as the end mirror. A pair of fused-silica prisms (P1 and P2) and a pair of SF6 prisms (P3 and P4) were used to compensate the dispersion inside the respective cavities. Considering the basic condition of synchronizing lasers, we set both cavities at the same length. A piezo-transducer (PZT) was also used to drive the end mirror M8 in the Ti:sapphire laser to fine tune the match of cavity lengths between the two lasers. To measure the cross correlation easily in the latter, the lengths of the two arms from the Ti:sapphire crystal to output couplers of T1 and T2 were aligned as close as possible. An orange glass filter was placed behind the coupler T1 to block the remaining pump laser. After reflection by two pairs of mirrors, both Ti:sapphire and Cr:forsterite lasers were input to the auto correlators and cross correlator for the measurement of pulse durations and the cross-correlation trace.

We pumped the Ti:sapphire and Cr:forsterite lasers with the all-solid-state 532-nm (S-P Inc., Millennia Xs) and 1.06- μ m lasers (S-P Inc., T-40Z-106C) respectively. Both pump sources are diode-pumped Nd : YVO₄ lasers. Under the pump powers of 5 W at the 532-nm laser and 9 W at the 1.06- μ m laser, we obtained the stable KLM powers of about 600 mW and 110 mW from the Ti:sapphire and Cr:forsterite lasers respectively. The distance between the beam spots on two close D-shaped mirrors (M2 and M4) was about 3 mm. No obvious power reduction was observed in the Cr:forsterite laser compared to the standard configuration with five mirrors. By changing the inserted material of the prisms, we obtained the shortest pulses as 11 fs and 40 fs from each laser.

3 Results and discussion

3.1 Observation of synchronization

To observe the synchronization between the Ti:sapphire and Cr:forsterite lasers, we first used two frequency counters (HP 53132A) to measure the repetition rates of both KLM lasers. By fine tuning the cavity length of the Ti:sapphire laser, the repetition rates can be set at the same values; covering the lasers with a closed box to prevent air turbulence enables repetition rates with an accuracy of 1 ± 1 Hz and no obvious drift within one minute. Then, an oscilloscope (HP 54616B) was used to monitor the pulse trains of both lasers; triggering using one pulse train allows the other pulse train to be viewed. Before successful synchronization, the other pulse train could not be clearly displayed on the oscilloscope. Although the repetition rates were tuned to exactly the same values with the aid of frequency counters, slips of the trace were always observed due to the existing environmental perturbations (Fig. 2a). We considered this as failed synchronization due to weak coupling between the two pulses.

By aligning the overlap between two laser beams inside the Ti:sapphire crystal and re-driving the PZT again to fit the match of the cavity lengths, we found that the pulse trains

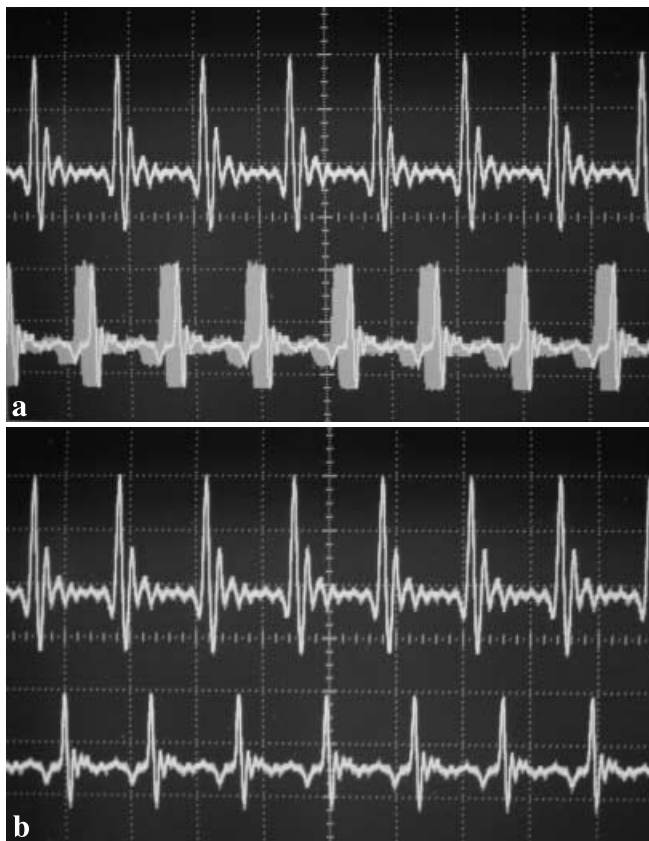


FIGURE 2 The pulse traces of Ti:sapphire (top) and Cr:forsterite (bottom) lasers at the modes of free running (**a**) and synchronization (**b**). The oscilloscope was triggered by the Ti:sapphire laser and set at 10 ns/div. Both repetition rates have been pre-set at the same values. In (**a**) the pulse trains of the Cr:forsterite laser shows the slip of the trace due to the environmental perturbations before success in synchronization. The traces in (**b**) show the pulse locking when synchronization occurs

were locked together when both repetition rates tended to be the same. The repetition rate of the Cr:forsterite laser jumped to the same value as that of the Ti:sapphire laser and then the oscilloscope showed the stable trace as shown in Fig. 2b. Even if we continuously changed the repetition rate of the Ti:sapphire laser by tuning the PZT, the pulse locking still remained, until further driving the PZT collapsed the lock; then the pulse-train trace of the Cr:forsterite laser displayed slip again. This phenomenon reflected the typical synchronization between the Ti:sapphire and Cr:forsterite lasers.

Figure 3 shows the behaviors of the repetition rates of Ti:sapphire (squares) and Cr:forsterite (circles) lasers when the PZT is extended (in Fig. 3a, the cavity length is decreased) and shortened (Fig. 3b) respectively. The horizontal scales are shifts of the end mirror M8 driven by the PZT; the repetition rates are plotted on the vertical coordinate axis. At the beginning both lasers worked at the different round-trip frequencies independently; adjusting the displacement of M8 via the PZT will change the repetition rate of the Ti:sapphire laser. When the repetition rate of the Ti:sapphire laser is close enough to that of the Cr:forsterite laser, the Cr:forsterite laser will be captured by the Ti:sapphire laser and then forced to follow the repetition rate determined by the cavity length of the Ti:sapphire laser. It reveals a master–slave behavior within the regime of synchronization, until out of the tolerance region of

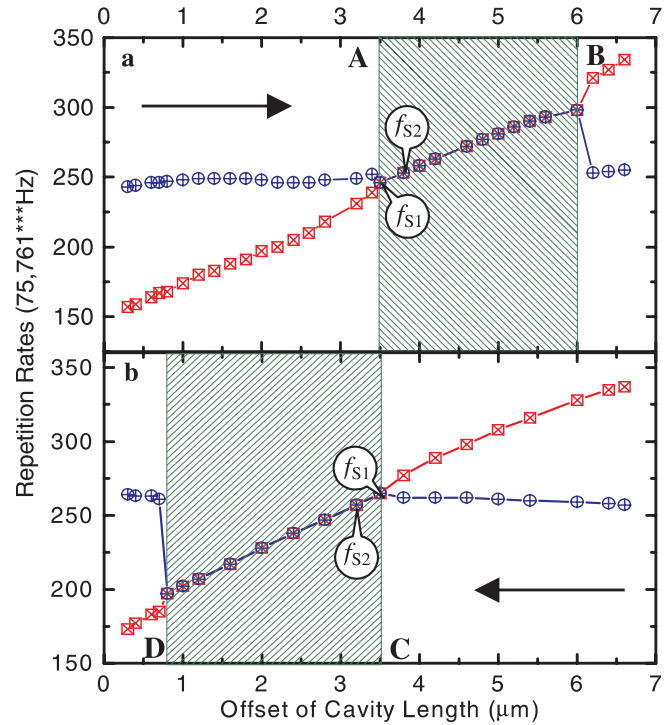


FIGURE 3 The repetition rates of the Ti:sapphire (normal cross squares) and Cr:forsterite (slope cross circles) lasers versus the offset of cavity length by shortening (**a**) and lengthening (**b**) the cavity length of the Ti:sapphire laser. The synchronization occurs in the range (shade) from A (C) to B (D). f_{S1} is the locked repetition rate at the critical positions of starting synchronization, f_{S2} is that at the next positions. To easily scale the ordinate we subtracted 75.761000 Hz from the exact repetition rate

cavity-length mismatch. Then the Cr:forsterite laser returned to its initial repetition rate and was independent of the further shift of the PZT. In general, this feature was explained as the higher power and shorter pulse duration of the Ti:sapphire laser. Since the Ti:sapphire laser induces a stronger nonlinear effect on the Cr:forsterite laser than the Cr:forsterite laser on the Ti:sapphire laser, this results in the Cr:forsterite laser being pulled to match the repetition rate of the Ti:sapphire laser. In fact, although the Cr:forsterite laser causes a weaker nonlinear effect, it still should affect the feature of the Ti:sapphire laser. We present further experimental results and an explanation in Sect. 3.2.

With the optimized coupling of two laser pulses inside the Ti:sapphire crystal and the suitable pulse durations, we observed that the synchronization occurred when the difference in the repetition rates was close to about 15 Hz (around the starting positions A and C). Further, a long tolerance of cavity-length mismatch over 2.5 μm was demonstrated. The difference in repetition rates was over 60 Hz out of the synchronized regime (around the end positions B and D) by continuously tuning the cavity length via the PZT. In general, driving the PZT in the reverse direction showed similar behaviors except for a backward shift of the synchronized regime. Although we measured both synchronized regimes partly overlapped in the initial experiment, our recent work showed the reversed synchronization normally occurred around the starting position (A) of the first synchronized regime. When driving the PZT oppositely before the end position B (or D), we found that the synchronization almost covered both regimes, until

the mirror M8 shifted around the end position D (or B) in the reversed synchronized regime, corresponding to a total tolerance of about $5\text{ }\mu\text{m}$. The long-term synchronized operation maintained over many hours was also obtained by shifting M8 in the middle region of the synchronized regimes.

3.2 Wavelength towing and tuning

Under the synchronized mode, we observed that both laser wavelengths were shifted relative to each other in opposite directions as the end mirror M8 was driven via the PZT [13]. Figure 4 shows the measured results when we scanned the offset of cavity length over the synchronized regimes. Compared to the measurement of repetition rates, a bigger error existed in estimating the central wavelength because of the resolution of spectrometers for broadband spectra. However, the measured data still well revealed the unique feature of wavelength towing in the synchronized regime [14]. Different to the result in the pure two-color femtosecond Ti:sapphire lasers [15], our experiment showed that both wavelengths were affected by the coupling process. In fact, this feature can be explained with the XPM mechanism.

For our discussion, we denote the repetition frequencies of free-running Ti:sapphire and Cr:forsterite lasers as f_{Ti} and f_{Ci} , where $i = 1, 2$ correspond to the notation in Fig. 3. When we shorten the cavity length by moving the end mirror M8 to the critical position A for synchronization (Fig. 4a),

an occasional overlap between two laser pulses in the Ti:sapphire crystal will start the synchronization. After the next round trip, the Ti:sapphire laser pulse will arrive at the crystal behind the pulse of the Cr:forsterite laser because of its slightly lower repetition rate f_{Ti} than f_{Ci} . Then, the nonlinear coupling will occur at the leading and trailing Ti:sapphire and Cr:forsterite laser pulses respectively. In this case the former should be blue-shifted to wavelength λ_{Ti1} and the latter should be red-shifted to λ_{Ci1} . Considered the negative group dispersion inside laser cavities, the repetition rate f_{Ti1} will increase and f_{Ci1} will decrease, resulting in them evolving to the same value f_{S1} ($f_{Ti1} < f_{S1} < f_{Ci1}$) and then being locked together. With the further shortening of its cavity length, the Ti:sapphire laser has a potential to be operated at a bigger repetition rate f_{Ti2} , so that its pulse is going to be ahead of the Cr:forsterite laser pulse. In this situation the opposite wavelengths shift (λ_{Ti2} and λ_{Ci2}) compared to the coupling process at the critical position A, resulting in both lasers once again evolving to a new common repetition rate f_{S2} . When continuously tuning the cavity length, not only the repetition rates, but also the wavelengths, showed similar behaviors and shifted reasonably, until they left the end position B of the synchronized regime where the XPM effect can not compensate the difference from the free-running one any more. Above the critical point, both lasers operated independently again and operated at the free-running wavelengths. Vice versa, by lengthening the cavity length, the synchronized lasers showed the opposite shift in wavelengths with a similar mechanism (Fig. 4b).

The behaviors of both repetition rates observed in Fig. 3 are also consistent with the above explanation of the XPM mechanism. Compared to the normal free-running mode, we clearly found that the repetition rate of the Ti:sapphire laser was varied at an increasing slope as the displacement of M8 was close to the synchronizing border A (or C). The reason is that the increasing nonlinear effect gradually plays a significant role for the repetition rate of the Ti:sapphire laser besides the cavity length changing during this process. With the increasing nonlinear effect, the repetition rate of the Cr:forsterite laser was also shifted at the same time. When the cavity length was tuned at the critical position A (or C), the nonlinear coupling effects between the two lasers were capable of evolving their repetition rates (f_{Ti1} and f_{Ci1}) to the same one (f_{S1}) and then they locked the two repetition rates together. Within the synchronized regime, both laser pulses cross in the opposite parts as the cavity-length tuning, so that the locked repetition rate varied at a smaller slope than that in the free-running mode, until they arrive at the end border B (or D). Once further tuning the cavity length has collapsed the synchronization, we can see the sudden recovery of both repetition rates to the values in the free-running mode. In view of the above analysis, we consider the contribution of the Ti:sapphire laser was not so strictly dominant in the synchronization, in spite of its master-like behavior on the repetition rate. In the synchronized operation, the values of the locked repetition frequency and the laser wavelengths should be balanced with both lasers. Not only the power and pulse width of each laser, but also the intra-cavity dispersion of the lasers, should affect the values.

By changing the insertion of two prisms, we could tune the corresponding laser wavelengths independently. Figure 5

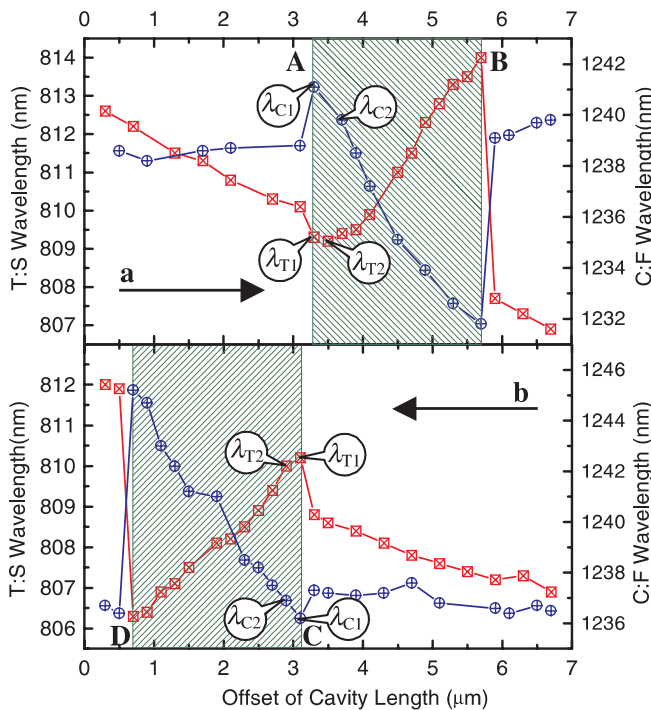


FIGURE 4 The wavelengths of the Ti:sapphire (normal cross squares) and Cr:forsterite (slope cross circles) lasers versus the offset of cavity length by shortening (a) and lengthening (b) the cavity length of the Ti:sapphire laser. Because of the increasing nonlinear coupling effect, the wavelengths of both lasers were shifted to λ_{Ti1} and λ_{Ci1} respectively at the critical positions A and C for synchronization. Further changing the cavity length will reverse shift the two wavelengths to λ_{Ti2} and λ_{Ci2} respectively for pulse locking. The XPM effect vanished from the synchronized regime and led to both lasers freely operating at the original wavelengths

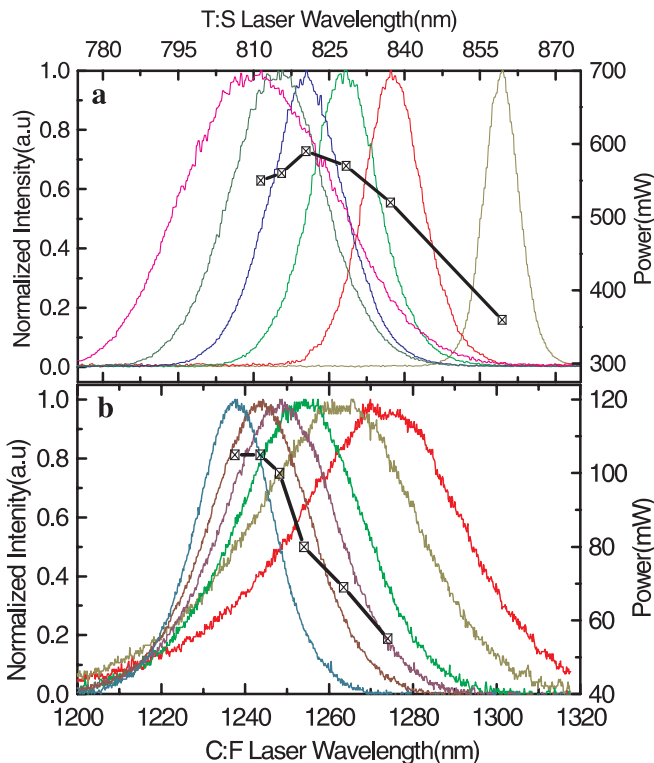


FIGURE 5 The tuning characteristics for synchronized operation of the Ti:sapphire (**a**) and Cr:forsterite (**b**) lasers. Both output powers versus their wavelengths were plotted as the *cross square lines*. The normalized spectra for both lasers showed the characteristic of bandwidth versus wavelengths

shows the tunable ranges of both laser branches with synchronizing mode, which were limited by the lower laser power in the longer-wavelength side and bandwidths of the mirrors (whose center wavelengths are 850 nm and 1300 nm) in the shorter-wavelength side, respectively. For the Ti:sapphire laser, the maximum output power was 590 mW around the central wavelength of 820 nm and that for the Cr:forsterite laser was 105 mW around 1250 nm. We measured that the pulse widths of both lasers are inversely proportional to their bandwidths. Although the shortest pulses appeared at the central wavelengths around 810 nm and 1280 nm respectively, synchronizing lasers under those situations showed the shorter tolerance of cavity-length mismatch.

3.3 Measurement of cross correlation

To measure the cross correlation, we aligned the synchronized lasers operated with the best stability and a long tolerance of cavity-length mismatch. A home-made cross correlator was used to measure the correlation trace between the Ti:sapphire and Cr:forsterite lasers (Fig. 6). After passing through a variable delay line with the PZT-controlled roof reflector, the Ti:sapphire laser beam was overlapped with the Cr:forsterite laser beam on the metal beam splitter (B.S.). The co-linear beams of both lasers were focused in the nonlinear crystal BBO to generate the sum-frequency signal (SFG). After the collimating with the second lens, a grating was used to separate the SFG and two SHG signals generated by the Ti:sapphire and Cr:forsterite lasers respectively. This setting enables us to catch easily the cross signal with the eyes. By

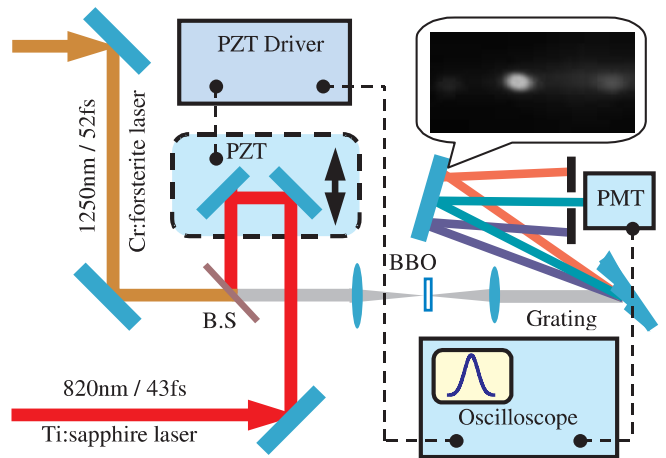


FIGURE 6 Schematic of the configuration for measurement of the cross-correlation traces. B.S.: metal beam splitter. The inset picture shows the beam patterns dispersed with the grating. The green one in the middle is the SFG between the two lasers. The blue and red ones are the SHG of the Ti:sapphire and Cr:forsterite lasers respectively

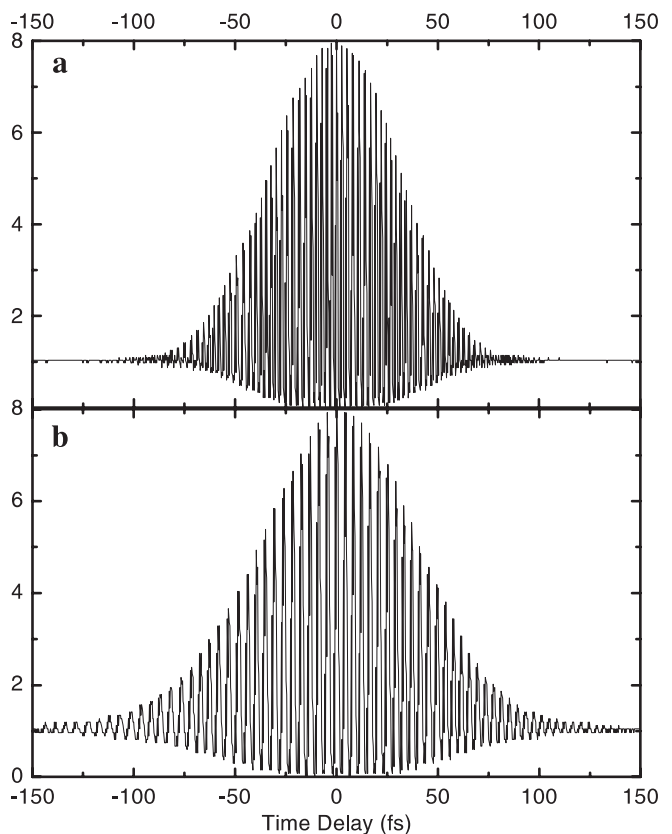


FIGURE 7 Fringe-resolved interferometric autocorrelation traces of the synchronized Ti:sapphire (**a**) and Cr:forsterite (**b**) lasers. The pulse durations were 43 ± 2 fs and 52 ± 1 fs with the assumption of a sech^2 shape, corresponding to the spectra centered around 820 nm and 1250 nm respectively

blocking the two SHG signals with a pinhole, we can accurately record the cross-correlation trace with a PMT and an oscilloscope.

Before the cross-correlation measurement between the Ti:sapphire and Cr:forsterite lasers, we first measured their pulse durations at the BBO crystal with the same configuration. Figure 7 shows the typical interferometric autocorrela-

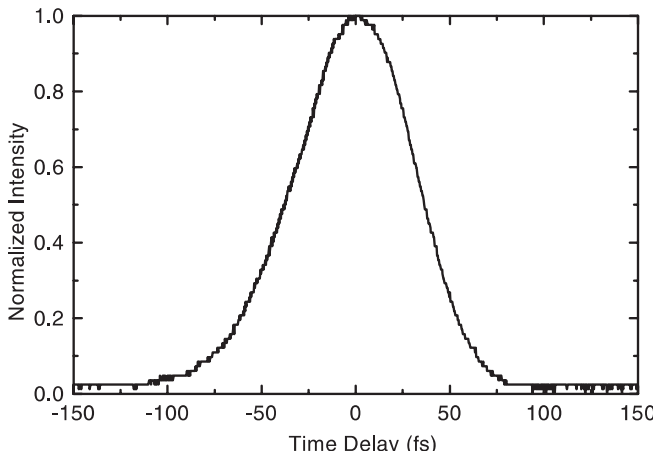


FIGURE 8 The cross-correlation trace between the Ti:sapphire and Cr:forsterite lasers. The measured width (FWHM) is 74 ± 2 fs within the experimental accuracy

tion traces. With careful calibration, we deduced both pulse widths of 43 ± 2 fs and 52 ± 1 fs with the assumption of a sech^2 shape, corresponding to the spectra centered at around 820 nm and 1250 nm respectively. Different to the autocorrelation, the cross-correlation measurement had some difficulty because of the delay matching of the two lasers (i.e. distance matching from the Ti:sapphire crystal to the beam splitter). Setting the distances as close as possible, we observed two alternate SFG signals at the central wavelength of around 495 nm by scanning the delay line via the PZT, which correspond to the forward and backward synchronized regimes started by shortening and lengthening the cavity length. We also found that the forward and backward synchronized regimes have a similar allowable range of cavity-length mismatch. Adjusting the length from the Ti:sapphire crystal to the output coupler T1 (or T2) enables us to observe the two types of SFG signal at the same delay range. By sweeping the delay line, we measured the typical cross-correlation trace as shown in Fig. 8. Using the same calibration of delay-time scale as the case of fringe-resolved autocorrelation, we deduced the width (FWHM) of the cross-correlation trace of 74 ± 2 fs within the experimental accuracy. Based on the pulse durations of the Ti:sapphire and Cr:forsterite lasers, we also calculated the theoretical value of 74 ± 2 fs with a sech^2 fit. The surprising coincidence between the two values infers that the two-color laser is synchronized with a timing jitter of only a few femtoseconds.

4 Conclusions

In summary, we successfully realized the stable synchronization between two independent femtosecond Ti:sapphire and Cr:forsterite lasers by crossing them inside the Ti:sapphire crystal. A long tolerance of cavity-length mismatch of $5 \mu\text{m}$ and a long-term synchronized operation over

many hours were demonstrated. For the first time, our experiment demonstrated the unique towing effects in both repetition rates and wavelengths between the two lasers. Using a simple picture with the nonlinear coupling effect, we satisfactorily explained behaviors of the synchronizing process and gave a basis for detailed analysis in the future. Sliding prisms inside the cavities also enables us to tune the wavelengths of the two lasers independently under the synchronizing mode. Tuning the two central wavelengths around 820 nm and 1250 nm, we measured that the pulse durations were 43 ± 2 fs and 52 ± 1 fs respectively within the experimental accuracy. The calculated width (FWHM) of the cross-correlation trace coincides exactly with the measured value of 74 ± 2 fs, inferred that the two-color laser is synchronized with a timing jitter of only a few femtoseconds. The novel two-color femtosecond laser will not only supply an ideal tool for ultra-fast spectroscopy and frequency metrology, but also enable us to open a way to synchronize any different femtosecond KLM lasers.

ACKNOWLEDGEMENTS We gratefully acknowledge Zhigang Zhang for his early work on the Cr:forsterite laser. The authors also thank Masayuki Kakehata for the helpful discussion and appreciate the assistance of Hideyuki Takada, Kazuya Takasago and Shinji Ito. This research was conducted partially under the management of the Femtosecond Technology Research Association, which is supported by the New Energy and Industrial Technology Development Organization. Z. Wei also acknowledges partial support by the National Science Foundation of China under Grant No. 69878032.

REFERENCES

- 1 C. Chudoba, J.G. Fujimoto, E.P. Ippen, H.A. Haus, U. Morgner, F.X. Kärtner, V. Scheuer, G. Angelow, T. Tschudi: Opt. Lett. **26**, 292 (2001)
- 2 R. Ell, U. Morgner, F.X. Kärtner, J.G. Fujimoto, E.P. Ippen, V. Scheuer, G. Angelow, T. Tschudi, M.J. Lederer, A. Boiko, B. Luther-Davies: Opt. Lett. **26**, 373 (2001)
- 3 L.-S. Ma, R.K. Shelton, H.C. Kapteyn, M.M. Murnane, J. Ye: Phys. Rev. A **64**, 021802(R) (2001)
- 4 D.E. Spence, W.E. Sleat, J.M. Evans, W. Sibbett, J.D. Kafka: Opt. Commun. **101**, 286 (1993)
- 5 S.A. Crooker, F.D. Betz, J. Levy, D.D. Awschalom: Rev. Sci. Instrum. **67**, 2068 (1996)
- 6 M.R.X. de Barros, P.C. Becker: Opt. Lett. **18**, 631 (1993)
- 7 D.R. Dykaar, S.B. Darack: Opt. Lett. **18**, 634 (1993).
- 8 J.M. Evans, D.E. Spence, D. Burns, W. Sibbett: Opt. Lett. **18**, 1074 (1993)
- 9 Z. Zhang, T. Yagi: Opt. Lett. **18**, 2126 (1993)
- 10 A. Leitenstorfer, C. Fürst, A. Laubereau: Opt. Lett. **20**, 916 (1995)
- 11 W. Shuicai, Z. Changjun, H. Junfang, Y. Hongru, X. Dong, H. Xun: Appl. Phys. B **68**, 211 (1999)
- 12 Z. Zhang, K. Torizuka, T. Itatani, K. Kobayashi, T. Sugaya, T. Nakagawa, H. Takahashi: Opt. Lett. **23**, 1465 (1998)
- 13 Z. Wei, Y. Kobayashi, Z. Zhang, K. Torizuka: Opt. Lett. **26**, 1806 (2001)
- 14 S.J. White, J.-M. Hopkins, M. Mazilu, A. Miller, W.H. Knox: Tech. Dig. CLEO 2000, CThB5, p. 395
- 15 C. Fürst, A. Leitenstorfer, A. Laubereau: IEEE J. Sel. Top. Quantum Electron. **2**, 473 (1996)

Coherent short wavelength radiation via picosecond Nd:glass lasers

H. KURODA,¹ T. OZAKI,¹ A. ISHIZAWA,¹ T. KANAI,¹ K. YAMAMOTO,¹ R. LI² AND J. ZHANG³

¹Institute for Solid State Physics, University of Tokyo, 5-1-5 Kashiwanoha, Kashiwa, Chiba 277-8581, Japan

²Shanghai Institute of Optics and Fine Mechanics, P.O. Box 800-211, Shanghai 201800, P. R. China

³Institute of Physics, Chinese Academy of Sciences, P.O. Box 603, Beijing 100080, China

(RECEIVED 2 May 2001; ACCEPTED 11 October 2001)

Abstract

The generation of coherent soft X rays is studied using a terawatt picosecond Nd:glass laser system. Two different methods are investigated as candidates for efficient generation of such radiation, namely, longitudinally pumped transient collisional excitation nickel-like molybdenum X-ray laser, and high-harmonic generation from solid–vacuum interfaces. In the course of experiments on longitudinally pumped X-ray lasers, unexpected jetlike structures are observed in the visible emission of the molybdenum plasma, extending over a length of several millimeters. An interesting characteristic of this phenomena is that clear jets are observed only for longitudinal pump intensities between 5×10^{14} and 7×10^{14} W/cm². The effects of a finite scale length density gradient on surface harmonics is also investigated. The efficiency of harmonic generation from near-solid density plasma is found to increase by a factor of 2 to 3 when using prepulses. The scale length of the preplasma is simulated using a one-dimensional hydrodynamic code, and the increase in efficiency is verified to be in accordance with particle-in-cell simulation results.

Keywords: Harmonic generation; Plasma jet; Preplasma; X-ray lasers

1. INTRODUCTION

Scientists have strived to generate coherent sources of X rays using various methods, with high motivation for application in such areas as lithography, spectroscopy, and biological imaging. As a result, saturated nickel-like ion X-ray lasers with wavelengths between 13.9 and 20.3 nm have been generated using pump energies as small as 7 J (Dunn *et al.*, 2000), and capillary discharge technology has succeeded in developing high repetition rate extreme-ultraviolet lasers at 46.9 nm (Rocca *et al.*, 1994). Relatively large amplification of water-window X-ray lasers have been observed using huge fusion devices, and various works are now underway to reduce the energy requirement of such lasers for increased accessibility. There are, however, still many hurdles to clear before the X-ray laser technology matures enough for application research to flourish. One of the most important factors is a higher repetition-rate operation, which should be accompanied by shorter wavelengths and higher efficiency.

We are presently attempting to demonstrate a high-repetition rate coherent X-ray source by adopting two different methods. The first is longitudinal pumping of transient collisional-excitation X-ray lasers, where the high-intensity picosecond-duration main pulse pumps the preformed plasma from a longitudinal direction, rather than the transverse pumping used in conventional schemes. As a result of the smaller gain volume and the higher small-signal gain coefficient achieved in such pumping configurations, the total pump energy required for saturation is greatly reduced, and is about 250 mJ for the 18.9-nm nickel-like molybdenum laser. Another promising method for highly efficient generation of coherent soft X rays is harmonic generation from a solid–vacuum interface. Simulations (Gibbon, 1996) have shown that the conversion efficiency to the higher-order harmonics is a constantly increasing function of the pump laser intensity. Experiments using large Nd:glass lasers have demonstrated conversion efficiencies greater than 10^{-6} for harmonics up to the 68th order at 15.5 nm (Norreys *et al.*, 1996).

In this paper, we present results of our experimental investigations on the above two novel schemes of coherent soft X-ray generation. We will describe several interesting characteristics of the picosecond laser–plasma interaction

Address correspondence and reprint requests to the following present address: Tsuneyuki Ozaki, Ultrafast Optical Physics Group, Physical Science Laboratory, NTT Basic Research Laboratories, 3-1 Morinosato Wakamiya, Atsugi, Kanagawa 243-0198, Japan. E-mail: ozaki@will.brl.ntt.co.jp

revealed in these investigations. We will first give in Section 2 a short description of the high-peak-power picosecond laser system used in the present work. We will then present in Section 3 investigations of the interaction of a high-intensity picosecond laser pulse pumping a preformed plasma from a longitudinal direction. An unusually long jetlike emission from the plasma is observed, which extends over a length of 10 mm. A distinctive characteristic of the present phenomena is that it is only observed under longitudinal pump intensities between 5×10^{14} and 7×10^{14} W/cm². In Section 4, we investigate the effects of density gradients at the surface–vacuum interface on the conversion efficiency of surface harmonics. The optimum ratio and time interval between the intensity of the main pulse and prepulse is experimentally clarified. Simulations are performed, which show that the density gradients of the preformed plasma which results in the highest efficiencies are in accordance with predictions based on particle-in-cell simulation results of Lichters *et al.* (Lichters & Meyer-ter-Vehn, 1997).

2. LASER

In this work, we use the picosecond terawatt chirped pulse amplification laser system at the Institute for Solid State Physics of the University of Tokyo (Itatani *et al.*, 1996). A

schematic diagram of the layout of the system is shown in Figure 1. The master oscillator is a laser-diode-pumped mode-locked Nd:YLF laser (Lightwave model 131), which produces a stable train of 10-ps pulses at a wavelength of 1053 nm. These pulses are coupled into a 110-m-long, polarization-preserving single-mode fiber. With a combination of self-phase modulation and group-velocity-dispersion effects, the spectrum of the laser pulse is broadened and chirped. The high pointing stability and intensity stability of the laser-diode-pumped oscillator assures the stable operation of the whole system, which is especially important for a single-shot device. The chirped pulses are then sent to a folded two-pass stretcher equipped with one gold-coated holographic grating (Jobin-Yvon, 1740 l/mm). The temporal duration of the resulting pulse is stretched to 600 ps. A hard aperture is placed within the stretcher to limit the spectral bandwidth to 3 nm, which is necessary to keep the intensity of the pedestal low. The hard aperture is also used to match the central wavelength of the laser pulse to that of the gain bandwidth of the Nd:phosphate glass amplifier, at 1054 nm. The seed is then preamplified by a Ti:sapphire regenerative amplifier, which is pumped by the second harmonic of a Q-switched Nd:YAG laser. The typical output energy from the regenerative amplifier is 1 mJ, which is then sent through a four-pass 25-mm aperture flashlamp-pumped Nd:phosphate glass rod amplifier. For the longitudinally

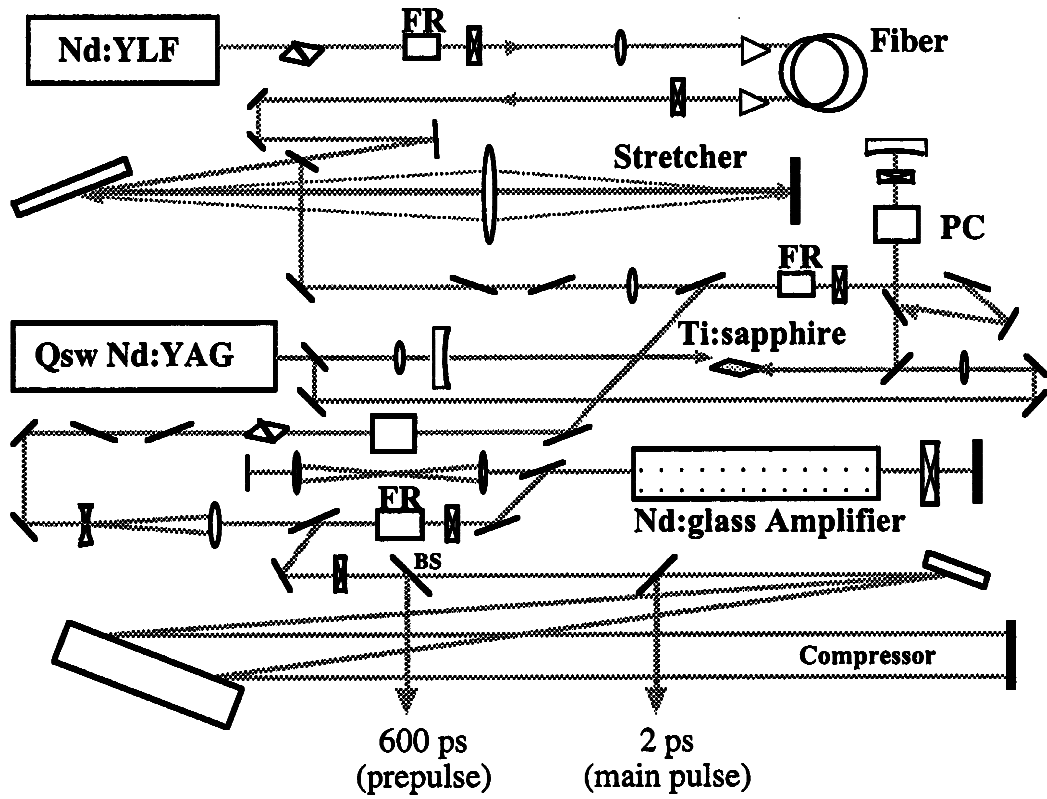


Fig. 1. Schematic diagram of the multiterawatt picosecond Nd:glass laser system.

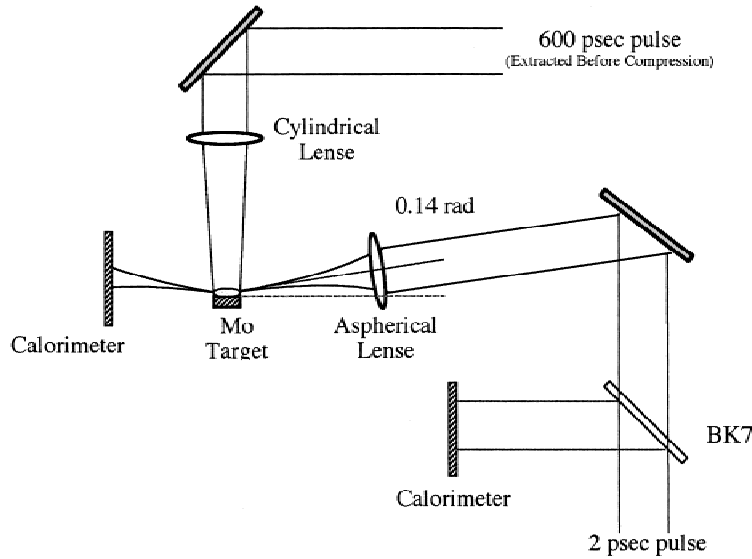


Fig. 2. Schematic diagram of the experimental setup in the vicinity of the target.

pumped X-ray laser experiments, the beam is then divided into two beams using a beam splitter. The reflected beam is used as a prepulse to produce the preformed plasma, while the transmitted beam is sent to a parallel grating pair compressor and compressed to a temporal duration of 2 ps. For surface harmonics experiments, compressed pulses are split into two beams to produce a picosecond prepulse. Large aperture Faraday isolators and a Pockel's cell is placed between the regenerative amplifier and the Nd:phosphate glass amplifier to increase the contrast ratio in the main pulse, and also to prevent amplified beams from returning to the vulnerable Ti:sapphire crystal and single-mode fiber. The contrast ratio between the pedestal to the main pulse is on the order of 10^{-6} , which is achieved mainly by spectral windowing. The maximum possible energy of the output from this system is 2 J, but it is usually operated at subjoule levels to prevent damage to the optics.

3. LONGITUDINALLY PUMPED TCE X-RAY LASERS

Figure 2 is a schematic diagram of our setup near the target vacuum chamber. The 600-ps prepulse is line-focused onto a 2-mm-long slab molybdenum target using a pair of cylindrical lenses. The 2-ps, p-polarized longitudinal beam is incident onto the preplasma at a grazing incidence angle of 0.14 rad. This angle is selected to maximize the propagation length of the picosecond laser through the preplasma, based on ray trace simulations. An $f/32$ aspherical lens is used to focus the longitudinal beam to a spot size of $140 \mu\text{m}$ at the entrance position of the preformed molybdenum plasma. Charge coupling devices (CCD) and PIN photodiodes observe the visible emission from the plasma, from a direction vertical to both the 2-ps beam and the 600-ps beam. These detectors are used to obtain the image and temporal

profile of visible emission from the laser-produced plasma. A 300-mm aperture calorimeter is also used to monitor the energy of the laser pulse after interaction with the molybdenum target or preformed plasma.

The transverse intensity profile of the longitudinal beam observed using a CCD camera after interaction with the preplasma is shown in Figure 3. Figure 3a is the picture observed for a simultaneous irradiation of both the prepulse and the main pulse. The peak intensity of the longitudinal and transverse beams are $8.0 \times 10^{14} \text{ W/cm}^2$ and $1.9 \times 10^{11} \text{ W/cm}^2$, respectively, and the peak-to-peak time delay between the main pulse and prepulse is 3.1 ns. The ordinate in

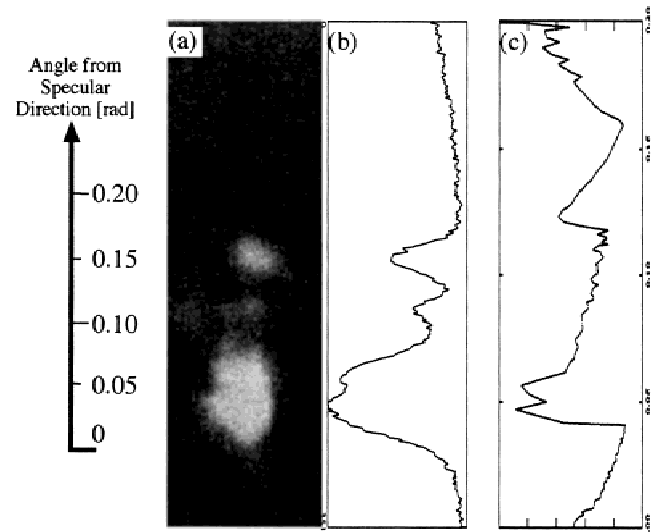


Fig. 3. (a) Transverse intensity profile of the transmitted longitudinal laser through preplasma. The intensity profile (b) is compared with simulation results (c).

Figure 3 corresponds to a direction vertical to the target surface, and the origin corresponds to the specular direction of the reflected longitudinal beam. We find that when the longitudinal beam travels through the preplasma produced by the transverse 600-ps laser, the beam profile on the negative angle side disappears, and instead a scattered pattern is observed at angles between 0.10 and 0.16 rad from the specular direction. The intensity of the transmitted beam is also considerably reduced compared with those observed without the prepulse.

Numerical simulations are performed to model the experimental observation, using a one-dimensional hydrodynamic code HYADES (Larsen & Lane, 1994) and a paraxial approximation ray tracing code. Outputs from the hydrodynamics code such as electron density, temperature, and average ionization are fed into the ray tracing code, which includes absorption of the incident laser based on the inverse bremsstrahlung effect. The experimental conditions such as pump intensity, temporal duration, and incidence angle are used as the input to the codes, without any artificial manipulations. Using the various outputs from these codes, we then calculate the angular intensity profile of the transmitted beam and compare the results with our experimental observations. In Figure 3c, we show the results of this simulation, and the experimentally observed profile is shown in Figure 3b. Although there are some differences in the position of the beamlets, the overall profile is excellently reproduced. When we look into the details of the simulation results, we find that the absence of the beam on the negative side of the specular direction is mainly due to defocusing of the beam, while the bright beamlets are the result of focusing of the beams after traveling through the preplasma.

Next we observed the visible emission from the plasma using a CCD camera. We show in Figure 4a the picture that was taken with an interference band-pass filter centered at a wavelength of 527 nm. The longitudinal beam enters from the left, and the transverse beam from the top, and the approximate position of the 2-mm-long Mo target is drawn in the figure. The peak intensity of the longitudinal beam in this case is $6.4 \times 10^{14} \text{ W/cm}^2$. Interestingly enough, several jetlike emissions are observed, which exist over a length of

several millimeters. Additional filters were added to decrease the fluence to the CCD, but the jetlike emission is still observed, as is shown in Figure 4b. When we irradiate the target with the 600-ps transverse pump only, no such jetlike emission is observed, even if the filters are reduced.

Next, with the shield left on, we observed the temporal profile of the plasma emission using a fast PIN photodiode. Scattered pump laser was eliminated by using a heat-absorbing filter. As a result, the emission is found to last for about 1 μs , which is typical for visible emissions from a laser-produced plasma. From spectroscopic observations we find that the jetlike emission consists mainly of line emission from singly ionized and neutral Mo, and continuum emissions are relatively weak. Another interesting aspect of the present phenomena is that the jetlike emission is clearly observable only for a longitudinal pump intensity range between 5×10^{14} and $7 \times 10^{14} \text{ W/cm}^2$. The actual cause for such jets is presently under investigation. However, this phenomenon may have some common mechanisms involved with a recently observed generation of massive plasma blocks moving toward the incident laser beam (Vogel & Kochan, 2001).

4. HARMONICS FROM A SOLID–VACUUM INTERFACE

Recent developments in generating ultrahigh peak power lasers (Perry & Mourou, 1994) have made possible a new range of experiments on laser–matter interactions. One of the most interesting phenomena is high-order harmonic generation from a solid surface. This method has attracted much attention because of the possibility of generating coherent X rays with wavelengths up to the water window at conversion efficiencies higher than those attainable with gas targets. Several experiments (Carman *et al.*, 1981a, 1981b; Kohlweyer *et al.*, 1995; von der Linde *et al.*, 1995, 1996; Norreys *et al.*, 1996; Zepf *et al.*, 1998; Földes *et al.*, 1999, 2000; Ishizawa *et al.*, 1999, 2000, 2001; Ganeev *et al.*, 2001) and theoretical results (Bezzerides *et al.*, 1982; Wilks *et al.*, 1993; Gibbon, 1996; Lichters & Meyer-ter-Vehn 1997) have been reported. Recently, the PIC simulation by Lichters *et al.* (1997) predicts that varying the density scale length L , which is produced when a high-intensity laser pulse irradiates the solid target, influences the harmonic emission. In an experiment, Zepf *et al.* (1998) showed that the harmonic efficiency depends strongly on the density scale length L/λ , where λ is the wavelength of the incident laser. Almost all previous experiments on harmonic generation from solid surfaces have been performed using a single pump pulse. In this work, we demonstrate a higher efficiency for harmonic generation by controlling the density scale length using double pulses. Harmonics of higher order are observed, and detailed model calculations are carried out using simulations.

The experiment was performed using the previously described chirped pulse amplification (CPA) Nd:glass laser system (Itatani *et al.*, 1996) for the driving laser. The 1054-nm

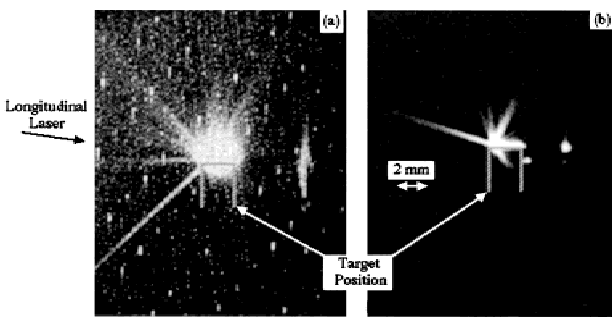


Fig. 4. Plasma emission in the visible wavelength observed with (a) a 527-nm band-pass filter, and (b) with additional neutral density filters.

wavelength laser pulse is point focused onto an Al-deposited target within a vacuum chamber by using a 100-mm focal length achromatic lens. The incidence angle of the laser is 75°, the polarization of the driving laser is p-polarized, and harmonics generated from the plasma surface in the specular direction are spectrally dispersed by a monochromator and detected using a fast rise time photomultiplier. To modify the plasma scale length, we carried out experiments in which a 2.2-ps prepulse irradiates the solid target 0–20 ps prior to the arrival of the main Nd:glass laser pulse with the same pulse duration. Figure 5 shows the harmonic intensities of the third harmonics, when the prepulse intensity is (a) 0.04 and (b) 0.004 times that of the main pulse. We also show in the figure error bars corresponding to the standard deviation of the shot-to-shot variation in the harmonic intensity. Our present observations are limited up to the fifth harmonic. Although third harmonic radiation can also be observed when a single pulse is used (corresponding to the

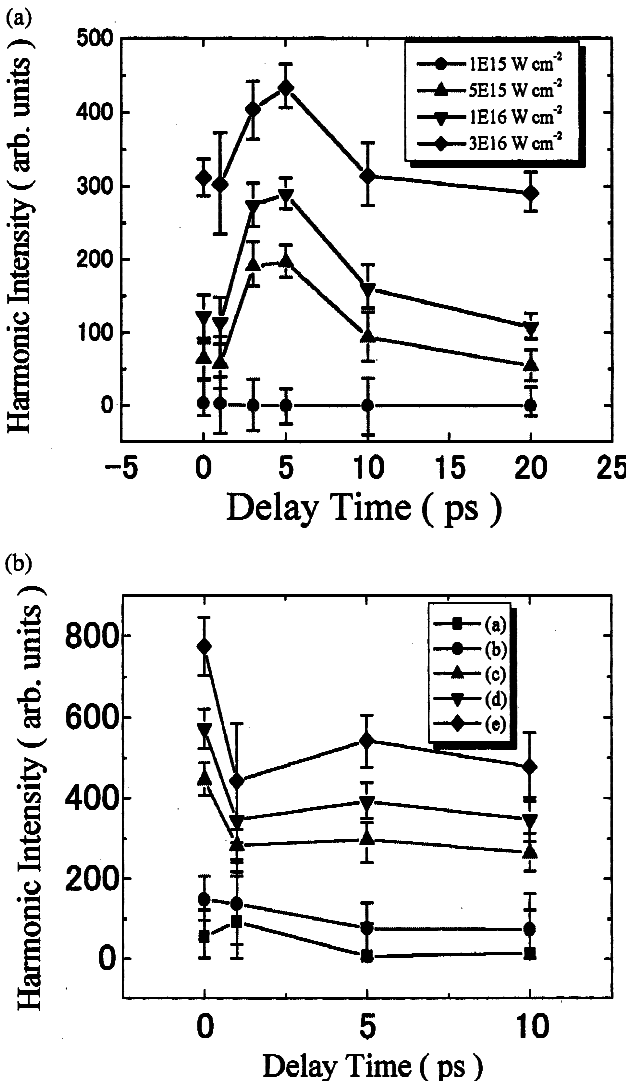


Fig. 5. The harmonic intensities of the third harmonics, when the prepulse intensity is (a) 0.04 and (b) 0.004 times that of the main pulse.

data for 0 delay time), ~5-ps time difference results in an increase in the harmonic signal by a factor of 2–3, which then decreases after 10 ps when the prepulse intensity is 0.04 times that of the main pulse. The results of the fourth and fifth harmonics are similar. The results for the fourth harmonics are of greatest importance because the even harmonics cannot be generated in a bulk of a preplasma, produced by amplified spontaneous emission or the pedestal. It is assumed that the divergence of a harmonic generated by irradiating double pulses is similar or larger than those generated by irradiating a single pulse, because the critical electron density surface will be more distorted for the former condition. Therefore, there is a possibility that the harmonic generation using the double pulses is more effective compared with that by single pulse irradiation.

On the other hand, the harmonic intensity for a single pulse (0 delay time) and double pulse irradiation is found to be smaller when the prepulse intensity is 0.004 times that of the main pulse. We can attribute this difference to the difference in the density scale length L/λ , produced when the laser pulse irradiates the solid target.

Figure 6 shows the density scale length L/λ as a function of the time difference between the main pulse and the prepulse, obtained from calculation using a 1D hydrodynamic code HYADES (Rubenchik *et al.*, 1998). When a high-intensity laser pulse is irradiated onto the solid target, the ponderomotive force acts on the target. As a result, density profiles initially resemble the step-shelf profiles (Estabrook & Kruer, 1978). We assume an upper shelf density n_0 of $27.5625 \times n_c$ in order to compare our result with the PIC simulation result of Lichters and Meyer-ter-Vehn (1997), where n_c is the critical density. We also assume that the plasma density increases linearly over a length from vacuum to the upper-shelf density. The gray zone in Figure 6 shows the optimum condition for the density scale length L/λ obtained from the PIC simulation result of Lichters *et al.* (1997). These calculation results show that harmonics are generated at a higher efficiency when the prepulse intensity is 0.04 times that of the main pulse, the time difference is ~5 ps, and the main pulse intensity is between $I\lambda^2 = 5 \times 10^{15}$ and $1 \times 10^{16} \text{ W} \cdot \text{cm}^{-2} \cdot \mu\text{m}^2$. This calculation result is in good agreement with our experiment results. As a result, it is found that the conversion efficiency of the harmonics does not strictly follow the $I\lambda^2$ scaling law, but rather depends strongly on the density scale length L/λ . A favorable density scale length L/λ depends on a trade-off between harmonics generated as a result of the strong light amplitude driving the free electron at the critical surface and the effect of resonance absorption. In the future, we plan to investigate the optimum double pulse irradiation condition combining both experiment and simulation.

5. CONCLUSION

Investigations have been performed on the generation of coherent short wavelength radiation using picosecond

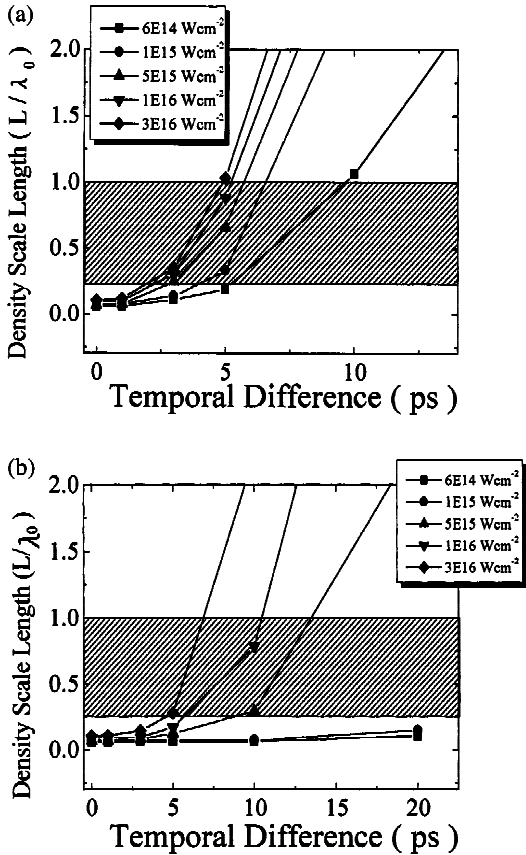


Fig. 6. The density scale length L/λ as a function of the time difference between the main pulse and the prepulse when the prepulse intensity is (a) 0.04 and (b) 0.004 times that of the main pulse. The gray zone shows the optimum condition for the density scale length L/λ from the PIC simulation result by Lichters and Meyer-ter-Vehn (1997).

Nd:glass lasers, and several new and interesting phenomena have been observed. Long jetlike structures in the visible emission have been unexpectedly observed, as a result of the interaction of a high-intensity laser interacting with a solid molybdenum target at an extremely oblique angle. The efficiency of harmonic generation from a solid–vacuum interface has been shown to increase by a factor of two to three, by using a low intensity prepulse to modify the density scale length. Investigations are presently underway to clarify the physics underlying these novel findings.

REFERENCES

- BEZZERIDES, B., JONES, R.D. & FORSLUND, D.W. (1982). Plasma mechanism for ultraviolet harmonic radiation due to intense CO₂ light. *Phys. Rev. Lett.* **49**, 202–205.
- CARMAN, R.L., FORSLUND, D.W. & KINDEL, J.M. (1981a). Visible harmonic emission as a way of measuring profile steepening. *Phys. Rev. Lett.* **46**, 29–32.
- CARMAN, R.L., RHODES, C.K. & BENJAMIN, R.F. (1981b). Observation of harmonics in the visible and ultraviolet created in CO₂-laser-produced plasmas. *Phys. Rev. A* **24**, 2649–2663.
- DUNN, J., LI, Y., OSTERHELD, A.L., NILSEN, J., HUNTER, J.R. & SHLYAPTSEV, V.N. (2000). Gain saturation regime for laser-driven tabletop, transient Ni-like ion X-ray lasers. *Phys. Rev. Lett.* **84**, 4834–4837.
- ESTABROOK, K. & KRUER, W.L. (1978). Properties of resonantly heated electron distributions. *Phys. Rev. Lett.* **40**, 42–45.
- FÖLDES, I.B., BAKOS, J.S., BAKONYI, Z., NAGY, T. & SZATMÁRI, S. (1999). Harmonic generation in plasmas of different density gradients. *Phys. Lett. A* **258**, 312–316.
- FÖLDES, I.B., BAKOS, J.S., GÁL, K., JUHÁSZ, Z., KEDVES, M.Á., KOCSIS, G., SZATMÁRI, S. & VERES, G. (2000). Properties of high harmonics generated by ultrashort UV laser pulses on solid surfaces. *Laser Physics* **10**, 264–269.
- GANEV, R.A., CHAKERE, J.A., RAGHURAMAIAH, M., SHARMA, A.K., NAIK, P.A. & GUPTA, P.D. (2001). Experimental study of harmonic generation from solid surfaces irradiated by multipicosecond laser pulses. *Phys. Rev. E* **63**, 026402/1–6.
- GIBBON, P. (1996). Harmonic generation by femtosecond laser-solid interaction: A coherent “water-window” light source? *Phys. Rev. Lett.* **76**, 50–53.
- ISHIZAWA, A., INABA, K., KANAI, T., OZAKI, T. & KURODA, H. (1999). High-order harmonic generation from a solid surface plasma by using a picosecond laser. *IEEE J. Quantum Electronics* **35**, 60–65.
- ISHIZAWA, A., KANAI, T., OZAKI, T. & KURODA, H. (2000). The spatial distribution of high-order harmonics from solid surface plasmas. *IEEE J. Quantum Electronics* **36**, 665–668.
- ISHIZAWA, A., KANAI, T., OZAKI, T. & KURODA, H. (2001). Enhancement of high-order harmonic generation efficiency from solid surface plasma by controlling the electron density gradient of a picosecond laser produced plasmas. *IEEE J. Quantum Electronics* **37**, 384–389.
- ITATANI, J., KANAI, T., OZAKI, T. & KURODA, H. (1996). Nd:glass and Ti:sapphire hybrid short pulse laser system. *Prog. Cryst. Growth Charact. Mater.* **33**, 281–284.
- KOHLWEYER, S., TSAKIRIS, G.D., WAHLSTRÖM, C.G., TILLMAN, C. & MERCER, I. (1995). Harmonic generation from solid–vacuum interface irradiated at high laser intensities. *Opt Commun.* **117**, 431–438.
- LARSEN, J.T. & LANE, S.M. (1994). HYADES—A plasma hydrodynamics code for dense plasma studies. *J. Quant. Spectrosc. Radiat. Transf.* **51**, 179–186.
- LICHTERS, R. & MEYER-TER-VEHN, J. (1997). High laser harmonics from plasma surface: Intensity and angular dependence, cutoffs and resonance layers at density ramps. *Inst. Phys. Conf. Ser.* **154**, 221.
- NORREYS, P.A., ZEPF, M., MOUSTAIZIS, S., FEWS, A.P., ZHANG, J., LEE, P., BAKAREZOS, M., DANSON, C.N., DYSON, A., GIBBON, P., LOUKAKOS, P., NEELY, D., WALSH, F.N., WARK, J.S. & DANGOR, A.E. (1996). Efficient extreme UV harmonics generated from picosecond laser pulse interactions with solid targets. *Phys. Rev. Lett.* **76**, 1832–1835.
- ROCCA, J.J., SHLYAPTSEV, V., TOMASEL, F.G., COTÁZAR, O.D., HARTSHORN, D. & CHILLA, J.L.A. (1994). Demonstration of a discharge pumped table-top soft X-ray laser. *Phys. Rev. Lett.* **73**, 2192–2195.
- RUBENCHIK, A.M., FEIT, M.D., PERRY, M.D. & LARSEN, J.T. (1998). Numerical simulation of ultra-short laser pulse energy deposition and bulk transport for material processing. *Appl. Surf. Sci.* **129**, 193–198.
- VOGEL, N.I. & KOCHAN, N. (2001). Experimental investigation of stochastic pulsation and formation of light bullets with mega-

- gauss magnetic fields by an intense laser pulse propagating in a preionized plasma. *Phys. Rev. Lett.* **86**, 232–235.
- VON DER LINDE, D., ENGER, T., JENKE, G., AGOSTINI, P., GRILLON, G., NIBBERING, E., CHAMBARET, J.-P., MYSYROWICZ, A. & ANTONETTI, A. (1996). Generation of ultrashort XUV pulses by harmonic generation from solid surfaces. *SPIE* **2770**, 98–105.
- VON DER LINDE, D., ENGER, T., JENKE, G., AGOSTINI, P., GRILLON, G., NIBBERING, E., MYSYROWICZ, A. & ANTONETTI, A. (1995). Generation of high-order harmonics from solid surfaces by intense femtosecond laser pulses. *Phys. Rev. A* **52**, R25–27.
- WILKS, S.C., KRUER, W.L. & MORI, W.B. (1993). Odd harmonic generation of ultra-intense laser pulses reflected from an over-dense plasma. *IEEE Trans. Plasma Sci.* **21**, 120–124.
- ZEPF, M., TSAKIRIS, G.D., PRETZLER, G., WATTS, I., CHAMBERS, D.M., NORREYS, P.A., ANDIEL, U., DANGOR, A.E., EIDMANN, K., GAHN, C., MACHACEK, A., WARK, J.S. & WITTE, K. (1998). Role of the plasma scale length in the harmonic generation from solid targets. *Phys. Rev. E* **58**, R5253–5256.

Measurement of energetic electrons from atomic clusters irradiated by intense femtosecond laser pulses

L. M. Chen,^{a)} J. J. Park, K. H. Hong, and I. W. Choi

Department of Physics and Coherent X-ray Research Center, Korea Advanced Institute of Science and Technology, Taejon 305-701, Korea

J. L. Kim

Korea Atomic Energy Research Institute, Taejon 305-600, Korea

J. Zhang

Laboratory of Optical Physics, Institute of Physics, Beijing 603, China

C. H. Nam^{b)}

Department of Physics and Coherent X-ray Research Center, Korea Advanced Institute of Science and Technology, Taejon 305-701, Korea

(Received 5 February 2002; accepted 16 May 2002)

Spectra of energetic electrons in the 100 keV range were measured from the interaction of intense femtosecond laser pulses with clusters of xenon or argon. The interaction of 28 fs pulses with cluster targets revealed quite different results with respect to applied laser intensity. At the laser intensity of $1 \times 10^{16} \text{ W/cm}^2$, the absorption by xenon clusters was about 25%; however, at the laser intensity of $1 \times 10^{17} \text{ W/cm}^2$, the laser energy absorption drastically increased to 78%, and the efficient coupling between the laser pulse and cluster target produced electrons with energy as high as 500 keV. The estimated hot electron temperatures ranged from about 30 to 90 keV depending on atoms and backing pressures. © 2002 American Institute of Physics. [DOI: 10.1063/1.1492804]

I. INTRODUCTION

Recent development of ultrashort high-power laser technologies^{1,2} has opened a new regime of laser–matter interactions in a very intense laser field. Using ultrashort high-power lasers, it is now possible to study matter under extreme conditions, such as the fast ignition scheme for inertial confinement fusion,³ high harmonic generation,^{4,5} ultrashort x-ray production,⁶ and laser accelerators.⁷ Interaction between intense ultrashort laser pulses and atomic clusters has also been studied intensively in recent years. High local density within a cluster, coupled with low average density, creates unique conditions for efficient transfer of laser energy to a medium in a debris-free condition. Cluster targets can absorb efficiently incident laser energy before significant expansion occurs⁸ and are very effective in producing strong x-ray radiation,⁹ high-energy electrons¹⁰ and ions.¹¹ In addition, fusion reactions have been demonstrated in laser–cluster interactions.¹²

In contrast to investigations on x-rays^{9,13} and high-energy ions¹¹ produced by the intense irradiation of clusters, the electron measurement from laser–cluster interactions has not received much attention. The interaction of an intense laser pulse with clusters can efficiently couple laser energy to electrons, comparable to the interaction of intense laser pulses with solid targets. Rapid heating of electrons in a cluster target prior to significant expansion of generated

plasma yields an electron energy distribution that exhibits two distinctive peaks.¹⁰ Thermal electrons are the result of collisional heating early in the pulse, and hot electrons, on the other hand, result from a resonance absorption due to resonant coupling of a laser field with electron plasma waves at the critical density layer, where the electron plasma frequency equals the laser frequency. The resonance absorption then can generate energetic electrons through wave breaking. Shao *et al.*¹⁰ reported a hot electron generation, up to 3 keV, with an applied laser intensity of $1 \times 10^{16} \text{ W/cm}^2$ and a pulse duration of 150 fs. Their measured electron energy was limited to several keV to avoid an electric shortage in a time-of-flight drift tube; therefore, more experimental results are needed for proper understanding of intense laser–cluster interactions, such as at higher laser intensity with various kinds of atoms and cluster parameters as well as a measurement range of much higher electron energy, especially at shorter laser pulse duration.

In this paper we report electron energy spectra with energy higher than 10 keV, obtained from the interaction of intense femtosecond pulses with argon or xenon clusters. Hot electrons were measured using a magnetic electron spectrometer, and, at a laser intensity of $1 \times 10^{17} \text{ W/cm}^2$, observed electron energy was as high as 500 keV. Results from the absorption measurement of laser energy by clusters and extreme ultraviolet (XUV) spectra, obtained while scanning laser pulse duration, showed the achievement of efficient coupling of intense laser pulses, even with the pulse duration as short as 28 fs.

^{a)}Electronic mail: lmchen18@yahoo.com

^{b)}Electronic mail: chnam@mail.kaist.ac.kr

II. EXPERIMENTAL SETUP

Experiments were carried out with a chirped-pulse amplification Ti:Sapphire laser operating at a wavelength of 820 nm and a repetition rate of 10 Hz. The laser delivered pulses of 30 mJ energy in 28 fs pulses. The Ti:sapphire oscillator was operated in a long cavity mode to facilitate good pulse selection in a Pockels cell so as to minimize the amplification of any leakage femtosecond pulses. The ratio between a femtosecond prepulse to a main pulse, less than 10^{-5} , was measured with a frequency-resolved optical-gating (FROG) system. A linearly polarized laser beam was focused with a 45 cm focal length spherical mirror, yielding a peak intensity of $1 \times 10^{17} \text{ W/cm}^2$ at 28 fs. We were able to vary the laser pulse length up to 2 ps by changing the distance between gratings in a pulse compressor.

Atomic clusters were produced with a pulsed sonic gas jet with a nozzle diameter of 0.2 mm. With sufficiently high backing pressure, clusters were produced in the gas jet flow due to the adiabatic cooling of the expanding gas into vacuum.¹⁴ The jet was operated with a backing pressure up to 20 bars. For large rare gas clusters, the mean cluster size (number of atoms per cluster) is reasonably well predicted by the expression^{14,15} $\langle N \rangle = 33(\Gamma^*/1000)^{2.35}$ (for $\Gamma^* > 1000$), where Γ^* is the dimensionless “Hagena parameter” given by $\Gamma^* = k[d/\tan(\alpha)]^{0.85} p_0 T_0^{-2.29}$. Here $k = 1650$ for Ar and $k = 5500$ for Xe, and d and α are the nozzle diameter (μm) and the expansion angle, and p_0 and T_0 are the backing pressure (mbar) and pre-expansion gas temperature (K), respectively. In experiments reported here, average cluster radii were 88 Å for Xe at a backing pressure of 18 bars, 32 Å for Ar at 20 bars and 12 Å for Ar at 6 bars, deduced from Rayleigh scattering measurements along with the Hagena formula.^{13,15}

The main diagnostic of hot electron measurements was a 45°-focusing magnetic spectrometer, fitted with a permanent magnetic field of 650 Gauss, with a LiF thermoluminescent dosimeter (TLD) as a detector. Recent development of ultra-sensitive LiF TLD made thin TLDs feasible for hot electron detection.¹⁶ The energy range of this instrument was between 7 keV to 1 MeV, and its energy resolution was better than 5%. The entrance hole of the electron spectrometer was aligned transversely to the laser propagation direction. The collection angle of the spectrometer was about 5×10^{-3} sr. The background level of TLD used was less than 5 μGy when it was pre-heated to 240 °C. When a TLD wrapped with 18 μm thick Al foil was put in the spectrometer at the position corresponding to 40 keV, the dose on the TLD dramatically dropped to several μGy from several mGy in the case of a bare TLD. This confirmed hot electrons mainly caused the dose on TLDs. In addition, by placing an array of TLDs inside a hemispherical surface, the angular distribution of hot electron emission was measured.

Time-integrated XUV emission was measured using a space-resolving, flat-field XUV spectrometer.¹⁷ The spectrograph utilized a varied line-spacing concave grating with 1200 grooves/mm in combination with gold-coated toroidal mirror, and a backside-illuminated x-ray charge-coupled device (CCD) as a detector. The spectral resolution was ap-

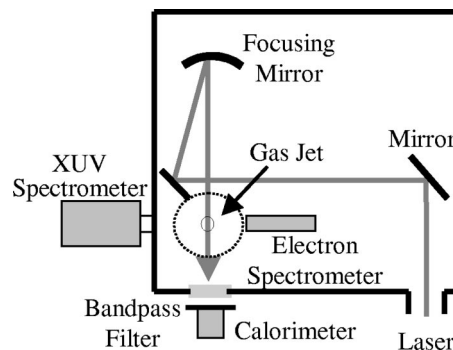


FIG. 1. Experimental setup used for laser–cluster interactions.

proximately 0.2 Å near 200 Å. The spectrograph was positioned to view the target perpendicularly to the laser propagation direction. For the measurement of laser energy absorption, a large calorimeter was used in combination with an interference filter that transmits only the laser wavelength. The experimental arrangement is shown in Fig. 1.

III. EXPERIMENTAL RESULTS

For the measurement of an electron spectrum ranging from 10 keV to 1 MeV, 15–20 pieces of circular TLDs of 5 mm in diameter were installed inside the electron spectrometer. A dose of exposed TLDs was measured with a TLD reader system (Teledyne 310). The inset in Fig. 2 shows the TLD heating process in time and typical glow curves recorded with a photomultiplier tube (PMT) during the heating process. The glow curve for an experimental TLD piece (solid curve in the inset of Fig. 2), placed at the electron energy of 100 keV in the electron spectrometer, shows an experimental signal level, as compared to the background level measured with an unexposed piece (dashed glow curve). We see that the glow signal of the TLD taken out from the spectrometer was about 100 times higher than the unexposed piece.

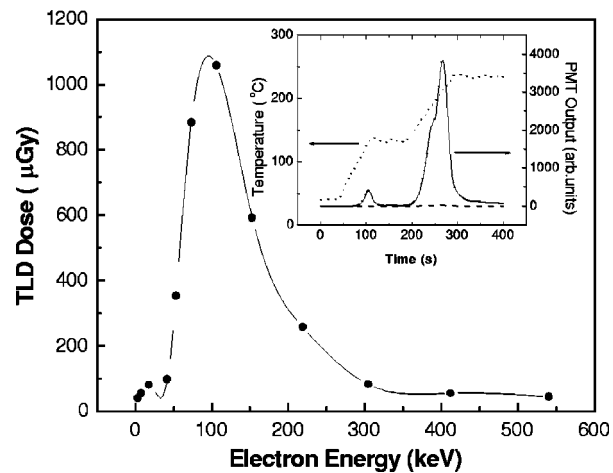


FIG. 2. Hot electron spectrum from Xe, measured using a magnetic electron spectrometer. Applied laser intensity was $1 \times 10^{17} \text{ W/cm}^2$, and backing pressure of Xe was 18 bars. The inset shows the TLD heating process in time (dotted line) and typical glow curves of a TLD piece placed at 100 keV electron energy (solid line) and an unexposed TLD (dashed line).

The electron spectrum from xenon of 18 bars irradiated with a laser intensity of $1 \times 10^{17} \text{ W/cm}^2$ is shown in Fig. 2. All results presented here were obtained with laser beams focused at 0.5 mm above the nozzle. The TLD dose was calibrated for energy response and dose response.¹⁶ Figure 2 reveals that (1) hot electrons with energy in the 100 keV range were generated, (2) the maximum energy of hot electrons was as high as 500 keV, and (3) the electron spectrum is peaked around 100 keV. The peaked electron spectrum indicates that a charge separation potential was developed due to space charges that held low-energy electrons in the clusters.

Angular dependence of the hot electron emission in the plane that contains the laser propagation axis and laser polarization was measured. An array of TLD pieces wrapped with 18 μm thick Al foil was placed around a hemispherical surface. Since xenon ions with energy below 10 MeV, scattered laser light, most XUV emissions, and electrons with energy below 50 keV cannot pass through the Al foil, this arrangement can be used to detect hot electrons with energy higher than 50 keV. The result showed that hot electron emission was nearly isotropic.

In order to verify that detected hot electrons originated from laser-irradiated clusters, additional experiments were carried out. A prepulse containing 7% of laser energy was delivered to the target at 80 ps before the main pulse. This prepulse is still intense enough to make clusters start to expand. Most clusters will be completely disassembled by the time the main pulse arrives, according to an expansion time scale for a cluster-plasma,¹⁸ especially in the central part of focused spot. Under these laser conditions, the observed electron spectrum was quite different from that in Fig. 2. Compared to the electron spectrum in Fig. 2, the TLD dose in the case with the prepulse dramatically decreased to less than 1% and no peaked structure was observed. This finding confirmed that the hot electrons in Fig. 2 came from a cluster-plasma. The experiment was repeated with a circularly polarized laser; however, hot electrons were not detected in this case, either. Thus, the observed results showed that the production of hot electrons originated from the resonance absorption of linearly polarized laser pulses by clusters.

For the investigation of the dependence of hot electron spectrum on cluster size, we used argon as well as xenon with different backing pressures. Figure 3 shows the electron spectra from argon and xenon irradiated with 28 fs laser pulses of an intensity $1 \times 10^{17} \text{ W/cm}^2$. We found that larger clusters generated more hot electrons, especially in the tail. For small clusters such as Ar at 6 bars, the maximum electron energy did not reach 200 keV, but for Ar at 20 bars the maximum electron energy increased to higher than 500 keV. For larger clusters such as Xe at 18 bars, the number of hot electrons at the energy of 500 keV is several times larger than that of Ar at 20 bars. The energy at which the electron distribution peaks shows similar tendency. For Ar at 6 bars, the peak electron energy is about 50 keV; it is 70 keV for Ar at 20 bars and 100 keV for Xe at 20 bars. Consequently, the results showed that the interaction with larger clusters pro-

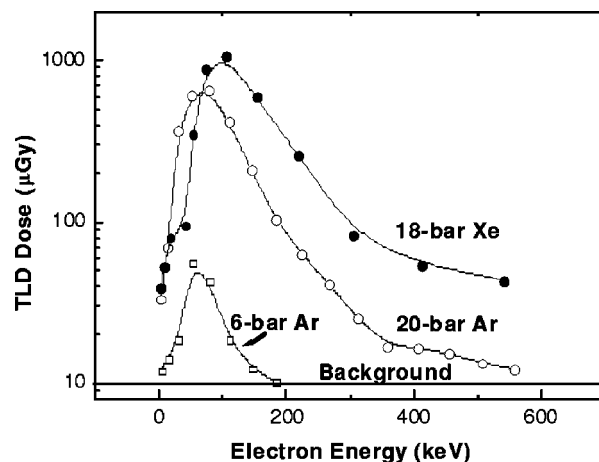


FIG. 3. Electron spectra from laser-irradiated clusters made from Xe gas at 18 bars (solid circle), Ar gas at 20 bars (open circle), and Ar gas at 6 bars (open square). The duration and applied laser intensity were 28 fs and $1 \times 10^{17} \text{ W/cm}^2$, respectively.

duced more energetic electrons and increased space charge potential.

A similar trend has been found for hot electron temperature measured by fitting with a Maxwellian distribution with particular temperature. The hot electron temperature obtained in this way was about 70 keV for Ar 20 bars, and 28 keV for Ar 6 bars, as shown in Fig. 4. For the case of Xe at 18 bars, the hot electron temperature was about 90 keV. If we use the temperature scaling law^{19,20} for hot electrons from solid-target plasmas due to resonance absorption: $T_h(\text{keV}) \approx 7 \times 10^{-5} (I\lambda^2)^{1/3}$, where laser intensity I is in units of W/cm^2 and wavelength λ is in units of μm , the hot electron temperature is about 30 keV, comparable to the measured hot electron temperature for argon 6 bars and lower than those of Ar 20 bars and Xe 18 bars. The hot electron temperature estimated from the Maxwellian fitting increased with cluster size for given laser intensity. This may be understood by considering the difference in the duration of resonance ab-

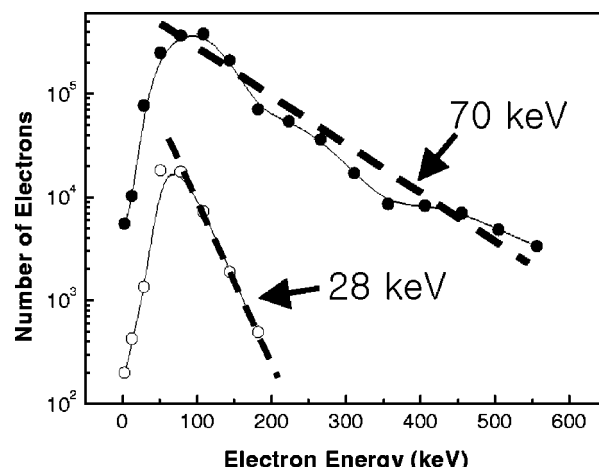


FIG. 4. Hot electron temperature obtained by fitting with a Maxwellian distribution: Ar gas at 20 bars (solid line) and at 6 bars (dashed line). Dashed lines show Maxwellian fitting. The duration and applied laser intensity were 28 fs and $1 \times 10^{17} \text{ W/cm}^2$, respectively.

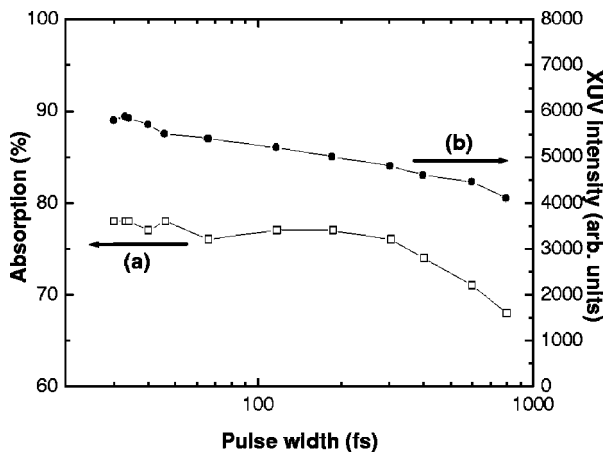


FIG. 5. Laser absorption (a) and XUV intensity of Xe^{7+} $4d-6p$ transition at 108 Å (b) for Xe clusters at 18 bars, given as a function of laser pulse duration. The pulse duration and applied laser intensity were 28 fs and $1 \times 10^{17} \text{ W/cm}^2$, respectively, and the pulse duration was scanned while maintaining the incident laser energy of 30 mJ.

sorption and in the electric field strength of space charge potential for various cluster sizes. A larger cluster can contain generated electrons more effectively, preventing a Coulomb explosion of cluster plasma and making the cluster evolve through hydrodynamic expansion.²¹ The larger cluster can sustain its electron density above the critical density longer than a small cluster so that the resonance absorption can occur for longer period, which results in hot electron production with higher temperature.

The dependence of laser absorption and XUV line intensity on laser pulse duration has been measured. Figure 5(a) shows the laser absorption by Xe clusters at 18 bars as a function of laser pulse duration. The incident laser energy of 30 mJ was kept the same while scanning the pulse duration by changing the grating separation in the pulse compressor. The laser intensity at the shortest pulse duration of 28 fs was $1 \times 10^{17} \text{ W/cm}^2$. The maximum absorption for Xe clusters reached as high as 78% and slowly decreased for longer pulse duration. A similar tendency was observed in the XUV line intensity (Xe^{7+} $4d-6p$ at 108 Å), as shown in Fig. 5(b). These results mean that a strong absorption occurred through efficient coupling even in the case of 28 fs pulses. The laser energy absorption and XUV line emission for Ar at 20 bars showed a similar tendency, with a slightly more rapid decrease than that of Xe.

When the laser energy decreased to 3 mJ, the behavior of XUV intensity to the pulse duration was much different from the 30 mJ case shown in Fig. 5. The laser intensity was $1 \times 10^{16} \text{ W/cm}^2$ at 28 fs, and the pulse duration was scanned while maintaining the incident energy. For the case of Xe at 18 bars, Fig. 6 shows that with the increase of pulse duration the XUV intensity increased at first, then reached maximum at the pulse duration of 500 fs, forming a plateau until 2 ps long pulses, and finally decreased with further increase of the pulse duration. The laser absorption measurement showed a similar plateau structure and the absorption of laser energy for the case of 28 fs pulse was only about 25%. Figure 6 also shows that large clusters formed at 18 bars radiate much

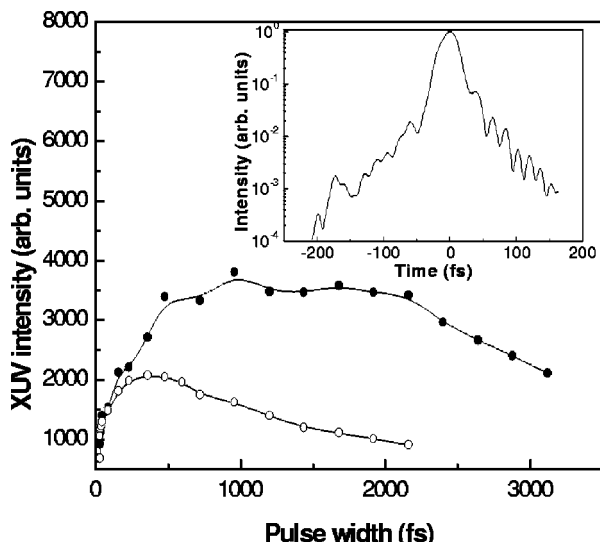


FIG. 6. Dependence of XUV intensity of Xe^{7+} $4d-6p$ transition at 108 Å on laser pulse duration for Xe clusters at 18 bars (solid circle) and at 6.5 bars (open circle) irradiated with 3 mJ laser pulses, corresponding to an intensity of $1 \times 10^{16} \text{ W/cm}^2$ at 28 fs. The pulse duration was scanned while maintaining the incident laser energy. Inset shows the intensity profile of a 28 fs laser pulse measured using a FROG system.

more strongly than small clusters formed at 6.5 bars. Another difference for the two curves was found in the plateau structure; the clusters at 18 bars maintained its high XUV intensity up to the pulse duration of 2 ps, but the small clusters at 6.5 bars did not show the plateau structure. The plateau structure of the XUV intensity over the pulse duration resulted from the long containment of a cluster plasma with high electron density, above the critical density, providing a suitable condition for resonance absorption. The results in Fig. 6 show that the interaction with larger clusters sustained the resonance condition for longer period of time than smaller clusters. This supports the hydrodynamic expansion model by Milchberg *et al.*²¹ that presented the resonance absorption in a critical density layer, instead of three times the critical density as seen in the uniform density model.²² Since the assumption of uniform density plasma required in the latter model is too idealistic, it is hardly satisfied in real cluster plasmas.²³

The difference in cluster expansion dynamics between the 30 and 3 mJ energy cases is attributed to a plasma density evolution during a laser pulse. The inset in Fig. 6 shows the temporal profile of a 28 fs laser pulse measured using a FROG system.²⁴ When the laser energy and intensity are 30 mJ and $1 \times 10^{17} \text{ W/cm}^2$, respectively, the rising edge with an intensity of about 10^{13} W/cm^2 starts at 200 fs before the peak. At this intensity the cluster can be heated and ionized. This pre-heating procedure in the leading edge of the laser pulse makes the cluster expand while heated, providing a proper condition for resonance absorption before the laser peak arrives. So the majority of the laser energy can be resonantly coupled to the pre-heated clusters, maximizing absorption and XUV emission even at the pulse duration of 28 fs. On the other hand, if the laser peak intensity is decreased by a factor of 10, the pre-heating will be shorter with much

smaller absorbed energy, not enough to reach a condition for resonance absorption. In this case, the process of pre-heating will be insufficient, and the peak of the laser pulse will interact with comparably high local density cluster. Significant resonance absorption will not occur at the pulse duration of 28 fs; however, by increasing the pulse duration over several hundred femtoseconds, the laser pulse can make clusters expand toward the resonance condition during the laser pulse. As a result, the XUV intensity was enhanced with a long pulse in the 3 mJ case, as confirmed by our experimental results.

IV. CONCLUSION

The interaction of intense femtosecond laser pulses with cluster targets of xenon and argon produced energetic electrons. At a low energy irradiation, the interaction was not efficient at the pulse duration of 28 fs (intensity of $1 \times 10^{16} \text{ W/cm}^2$) but grew stronger as the pulse duration was increased to several hundred femtoseconds while keeping applied laser energy the same. At the laser intensity of $1 \times 10^{17} \text{ W/cm}^2$, the coupling of laser and cluster plasmas was efficient even with 28 fs laser pulses, and the strong interaction produced energetic electrons of energy as high as 500 keV, which is a significant enhancement of hot electron energy in cluster plasmas over the previous result.¹⁰ The estimated hot electron temperatures ranged from about 30 to 90 keV depending on atoms and backing pressures.

ACKNOWLEDGMENT

This research was supported by the Ministry of Science and Technology of Korea through the Creative Research Initiative Program.

¹M. D. Perry and G. Mourou, *Science* **264**, 917 (1994).

²D. Strickland and G. Mourou, *Opt. Commun.* **56**, 219 (1985).

³M. Tabak, J. Hammer, M. E. Glinsky, W. L. Kruer, W. C. Wilks, and R. J. Mason, *Phys. Plasmas* **1**, 1626 (1994).

⁴P. A. Norreys, M. Zepf, S. Moustaijis, A. P. Fews, J. Zhang, P. Lee, M.

Bakarezos, C. N. Danson, A. Dyson, P. Gibbon, P. Loukakos, D. Neely, F. N. Walsh, J. S. Wark, and A. E. Dangor, *Phys. Rev. Lett.* **76**, 1832 (1996).

⁵D. G. Lee, J. H. Kim, K. H. Hong, and C. H. Nam, *Phys. Rev. Lett.* **87**, 243902 (2001).

⁶J. D. Kmetec, C. L. Gordon, J. J. Macklin, B. E. Lemoff, G. S. Brown, and S. E. Harris, *Phys. Rev. Lett.* **68**, 1527 (1992).

⁷A. Modena, Z. Najmudin, A. E. Dangor, C. E. Clayton, K. A. Marsh, C. Joshi, V. Malka, C. B. Darow, C. Danson, D. Neely, and F. N. Walsh, *Nature (London)* **377**, 606 (1995); C. I. Moore, A. Ting, K. Krushelnick, E. Esarcy, R. F. Hubbard, B. Hafizi, H. R. Burris, C. Manka, and P. Sprangle, *Phys. Rev. Lett.* **79**, 3909 (1997).

⁸T. Ditmire, R. A. Smith, J. W. G. Tisch, and M. H. R. Hutchinson, *Phys. Rev. Lett.* **78**, 3121 (1997).

⁹A. Mcpherson, B. D. Thompson, A. B. Borisov, K. Boyer, and C. K. Rhodes, *Nature (London)* **370**, 631 (1994).

¹⁰Y. L. Shao, T. Ditmire, J. W. G. Tisch, E. Springate, J. P. Marangos, and M. H. R. Hutchinson, *Phys. Rev. Lett.* **77**, 3343 (1997).

¹¹T. Ditmire, J. W. G. Tisch, E. Springate, M. B. Mason, N. Hay, R. A. Smith, J. Marangos, and M. H. R. Hutchinson, *Nature (London)* **386**, 54 (1997).

¹²J. Zweiback, R. A. Smith, T. E. Cowan, G. Hays, K. B. Wharton, V. P. Yanovsky, and T. Ditmire, *Phys. Rev. Lett.* **84**, 2634 (2000).

¹³T. Mocek, C. M. Kim, H. J. Shin, D. G. Lee, Y. H. Cha, K. H. Hong, and C. H. Nam, *Appl. Phys. Lett.* **76**, 1819 (2000); *Phys. Rev. E* **62**, 4461 (2000).

¹⁴O. F. Hagena and W. Obert, *J. Chem. Phys.* **56**, 1793 (1972).

¹⁵E. Parra, I. Alexeev, J. Fan, K. Y. Kim, S. J. McNaught, and H. M. Milchberg, *Phys. Rev. E* **62**, R5931 (2000).

¹⁶L. M. Chen, J. Zhang, H. Teng, Q. L. Dong, Z. L. Chen, T. J. Liang, L. Z. Zhao, and Z. Y. Wei, *Phys. Rev. E* **63**, 036403 (2001); L. M. Chen, J. Zhang, Q. L. Dong, H. Teng, T. J. Liang, L. Z. Zhao, and Z. Y. Wei, *Phys. Plasmas* **8**, 2925 (2001).

¹⁷I. W. Choi, J. U. Lee, and C. H. Nam, *Appl. Opt.* **36**, 1457 (1997).

¹⁸J. Zweiback, T. Ditmire, and M. D. Perry, *Phys. Rev. A* **59**, R3166 (1999); *Opt. Express* **6**, 236 (2000).

¹⁹W. L. Kruer, *The Physics of Laser Plasma Interactions* (Addison-Wesley, New York, 1988).

²⁰N. H. Burnett and G. D. Enright, *Can. J. Chem.* **64**, 920 (1986).

²¹H. M. Milchberg, S. J. McNaught, and E. Parra, *Phys. Rev. E* **64**, 056402 (2001).

²²T. Ditmire, E. Springate, J. W. G. Tisch, Y. L. Shao, M. B. Mason, H. Hay, J. P. Marangos, and M. H. R. Hutchinson, *Phys. Rev. A* **57**, 369 (1998).

²³The condition of uniform density plasma may be found when clusters are mainly field-ionized by uniform laser field, such as an early ionization phase of clusters with a size much smaller than the laser wavelength.

²⁴K. H. Hong, Y. H. Cha, and C. H. Nam, *J. Korean Phys. Soc.* **33**, 315 (1998).

Transient characteristics of a neon-like x-ray laser at 19.6 nm

Xin Lu, Ying-jun Li, and Jie Zhang^{a)}

*Laboratory of Optical Physics, Institute of Physics, Chinese Academy of Sciences,
Beijing 100080, People's Republic of China*

(Received 4 December 2001; accepted 3 January 2002)

A transient Ne-like x-ray laser at 19.6 nm ($J=0\rightarrow 1$, $3p\rightarrow 3s$) is numerically investigated using a hydrodynamic code for a 100 μm thick Ge planar target irradiated by a nanosecond prepulse followed by a subpicosecond or a picosecond main optical laser pulse. Simulations are performed for different main pulse lengths of 50 fs, 500 fs, 5 ps, and 50 ps but with fixed pulse energy. For a drive pulse even as short as 500 fs, the x-ray laser gain still shows quasisteady state behaviors. A real transient nature can only be seen when the x-ray laser is driven by a laser pulse with a duration as short as tens of femtoseconds. © 2002 American Institute of Physics. [DOI: 10.1063/1.1458029]

I. INTRODUCTION

Since the first demonstration of soft x-ray lasers in 1985,¹ quasisteady state (QSS) collisional x-ray lasers have been investigated intensively.^{2–9} By comparison, the transient collisional excitation (TCE) was proposed as an alternative scheme to significantly save drive energy.^{10–14} In the QSS excitation scheme, electrons at the lower level decay into the ground state due to the strong dipole radiation while the upper level is populated through the monopole collisional excitation. This results in a population inversion between the upper and lower energy levels. In recent years, the QSS is usually reached by using a low intensity prepulse followed by a high intensity main pulse.^{2–9} Saturated output has been demonstrated at many wavelengths from several tens of nm to 5.8 nm,^{5–8} and the pump energy has been reduced to less than 100 joules for x-ray lasers with wavelengths of >10 nm. Recently, the QSS x-ray lasers also made a great progress of improving the efficiency. Saturated output has been reached for Ne-like Fe (25.5 nm), Ni-like Ag (14.0 nm), and Ni-like Pd (14.7 nm) using only 30 J laser energy in the main laser pulse.⁹

According to the theory of Afanasiev, the population inversion in the TCE scheme appears to be due to the different transient pump rates of the energy levels.¹⁰ The analytical approach for TCE was performed in an ideal model: the electron temperature has a sudden jump to high value during a very short time and then becomes constant. The ionization process can be ignored. During the pump time, the theoretical estimate of transient gain can be higher than 100 cm^{-1} .¹¹ In experiments the hydrodynamic conditions of the TCE scheme can be realized by using a low intensity long prepulse to produce a preplasma with rich population of Ni-like or Ne-like ions in the ground state. After the prepulse, a high intensity short main pulse is used to make a jump of electron temperature. In the last five years, the CPA (Chirped Pulse Amplification) laser technology has made the high intensity picosecond and femtosecond pulse lasers available at

university laboratories. This situation has created a great possibility to realize TCE x-ray lasers at small laser laboratories, thus making the wide application of x-ray lasers possible. More than 100 cm^{-1} local gain for the Ne-like Ge x-ray laser at 19.6 nm was predicted using 1 ns prepulse at $5 \times 10^{12} \text{ W/cm}^2$ and 2 ps main pulse at 10^{15} W/cm^2 .¹¹ The first experiments were performed by using a nanosecond prepulse and a picosecond main pulse.^{12–16} The pump energy for a saturated laser output has been reduced to 10 J.¹⁶ Nilsen analyzed the population kinetics for a transient Ne-like Ti x-ray laser at wavelengths of 32.6 and 30.1 nm. The results show that over picosecond scales, the gain of the Ne-like Ti laser has a quasisteady state nature with regard to the equilibrium of the excited-state population.¹⁷ A similarity model for the hydrodynamic characteristics of Ni-like TCE x-ray lasers was also developed,¹⁸ which can be very useful to optimize the drive pulse parameters.

Analytical analysis shows,¹⁰ that the transient excitation time of a fixed ionization stage decreases with the increase of nuclear charge. Thus in the Ne-like Ge plasma, the transient collisional pumping should have a shorter time scale than Ne-like Ti ions. In this paper, we model the Ne-like Ge x-ray laser at 19.6 nm numerically to investigate plasma conditions and the gain characteristics in QSS and TCE regimes, respectively. The simulations were performed for main pump pulses with fixed energy but various pulse durations from 50 fs to 50 ps. The transient nature of x-ray laser pumping can be reflected from the ionization balance in the plasma. Comparison of gain characteristics and the plasma state for different drive pulses shows that real transient nature of the Ne-like Ge x-ray laser at 19.6 nm can be generated by laser pulses with tens of femtosecond duration.

II. PLASMA MODELING

Simulations were carried out for 100 μm thick germanium slab targets irradiated by a 1 ns prepulse and a picosecond main pulse at 1.06 μm wavelength. Both pulses have a Gaussian profile in time. The 1D Lagrangian hydrodynamic code MED103 was used to simulate the time evolution of laser-plasma interactions and to calculate the gain

^{a)}Author to whom correspondence should be addressed. Electronic mail: jzhang@aphy.iphy.ac.cn

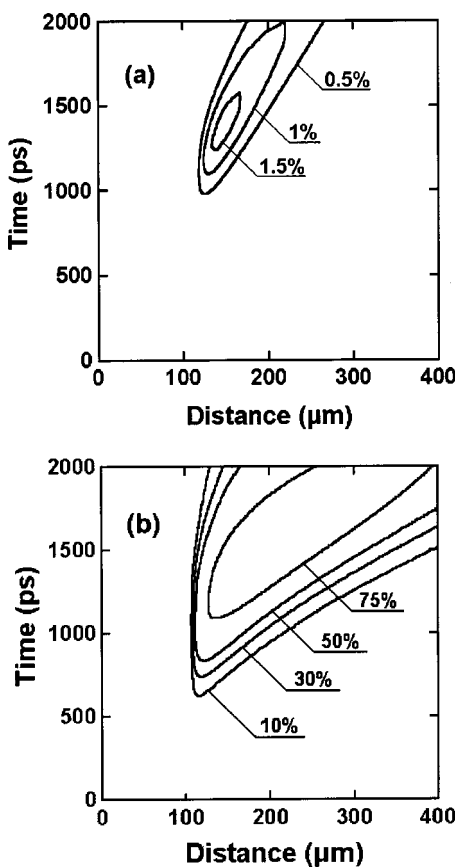


FIG. 1. The fraction of the ground state Ne-like ions versus space and time in the plasmas generated by 1 ns long prepulses with a peak intensity of $1 \times 10^{12} \text{ W/cm}^2$ (a) and $5 \times 10^{12} \text{ W/cm}^2$ (b). The initial position of target surface is located at $100 \mu\text{m}$.

coefficients. The MED103 code has been well tested and widely used for the investigation of x-ray lasers, laser-plasma interactions and laser fusion.^{19–21}

It is well known that the preplasma for TCE should have a rich population of ground state ions. In order to obtain an optimum peak intensity of prepulse, the simulations have been performed for a 1 ns prepulse with different peak intensities of $1 \times 10^{12} \text{ W/cm}^2$, and $5 \times 10^{12} \text{ W/cm}^2$. Figure 1 shows the spatio-temporal profile of Ne-like ions fraction in plasmas produced by such prepulses. The peak intensity of prepulses exists at 1 ns in the figures. It is apparent that the $1 \times 10^{12} \text{ W/cm}^2$ intensity prepulse is not high enough to ionize the preplasma to a Ne-like state. The prepulse with a peak intensity of $5 \times 10^{12} \text{ W/cm}^2$ is enough to generate a rich Ne-like ionization population in the preplasma for a TCE x-ray laser.

In order to see the difference between TCE and QSS excitation we did calculations with different main pulse duration but a fixed energy. The main pulse durations used in the simulations are 50 ps, 5 ps, 500 fs, and 50 fs. The peak intensities of the main pulse are 10^{14} W/cm^2 , 10^{15} W/cm^2 , 10^{16} W/cm^2 , and 10^{17} W/cm^2 . All simulations performed with a 1 ns prepulse at $5 \times 10^{12} \text{ W/cm}^2$. The peak to peak time delay between the prepulse and main pulse was set to be 0.5 ns. The main pulse reaches its peak intensity at 1500 ps on the time scale used in Figs. 2–4. For a high pump inten-

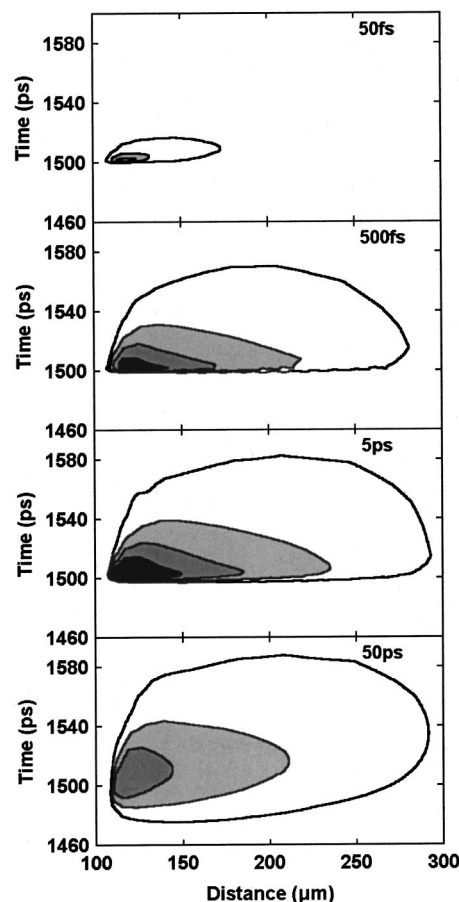


FIG. 2. Gain contours versus space and time for four values of the drive pulse durations 50 fs, 500 fs, 5 ps, and 50 ps. The gain in plot reduces from 80 cm^{-1} (black) to 20 cm^{-1} (white) by step of 20 cm^{-1} .

sity 10^{16} W/cm^2 and 10^{17} W/cm^2 , the effect of high field ionization on the gain region has been considered and the correction to the absorption of laser radiation by inverse bremsstrahlung is included. By analyzing the spatial characteristics of the results, we found that the high field ionization can affect the state of the plasma, but weakly affect the gain region. The high field ionization mainly has effects on the characteristics of local regions close to the critical density.

III. RESULTS AND DISCUSSIONS

Figure 2 shows the spatio-temporal behaviors of gain contours for four different drive pulse durations of 50 fs, 500 fs, 5 ps, and 50 ps. The spatial and temporal evolution of electron temperature is presented in Fig. 3. Figure 4 shows the fraction of ground state F-like ions in plasma. This reflects the ionization balance. The main characteristics of the x-ray laser are summarized in Table I.

It is apparent that the characteristics of the x-ray laser driven by a 50 ps main pulse are a typical QSS case. The high gain of 83 cm^{-1} is due to the high density of Ne-like ions in plasma. In case of 5 ps drive pulse, the electron temperature increases rapidly from $\sim 200 \text{ eV}$ to 2.2 keV near the critical density, and from 400 eV to $\sim 1.5 \text{ keV}$ in the

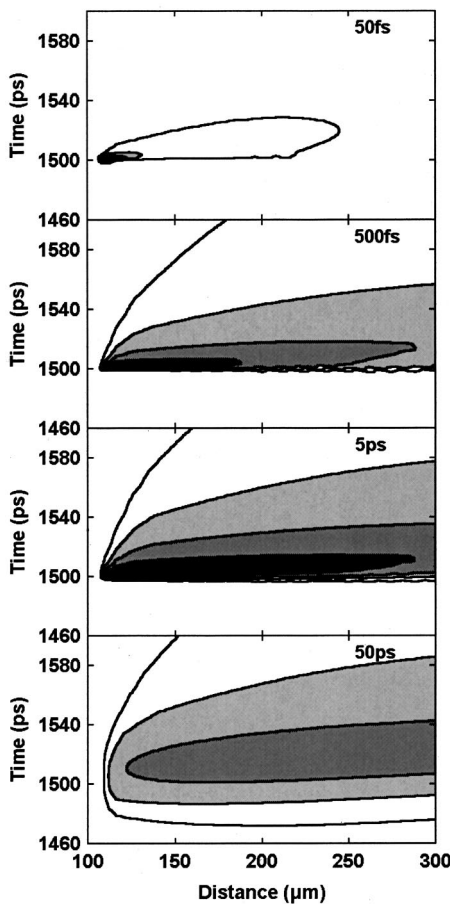


FIG. 3. Contours of electron temperature versus space and time of the four values of the drive pulse durations 50 fs, 500 fs, 5 ps, and 50 ps. The electron temperature in plot reduces from 1500 eV (black) to 600 eV (white) by step of 300 eV.

corona region of $n_e < n_c$ when the main pulse comes. During the main pulse pumping the ion temperature is almost unchanged, 15% ions are over-ionized to F-like state. The 500 fs pulse driven x-ray laser has a similar situation with the case driven by a 5 ps pump pulse. Detailed investigation shows that from 500 fs to 50 ps pulse duration, the maximum gain coefficients slowly decrease from about 100 cm^{-1} to 83 cm^{-1} . We should note that the peak gain coefficients and electron temperature for 500 fs–5 ps drive pulse are located near the critical density and have narrow spatial width. In the corona region where the laser energy is mainly deposited, the spatial gain extent, and electron temperature of plasmas are similar for 500 fs, 5 ps, and 50 ps drive pulse durations. So we believe that for Ne-like Ge x-ray lasers, the so-called “TCE” scheme, which uses picoseconds pump pulses, has no difference from traditional QSS excitation in the framework. The high gain of short pulse driven x-ray laser is only due to the relative high electron temperature.

For the shortest drive pulse of 50 fs, the maximum gain is 91 cm^{-1} and comes 1.2 ps later after the drive pulse. The peak electron temperature near the critical density can be greater than 6 keV. But this electron temperature is not suitable for collisional x-ray lasers. In the corona region, the gain and electron temperature are much lower than those driven by the other excitation schemes with longer drive

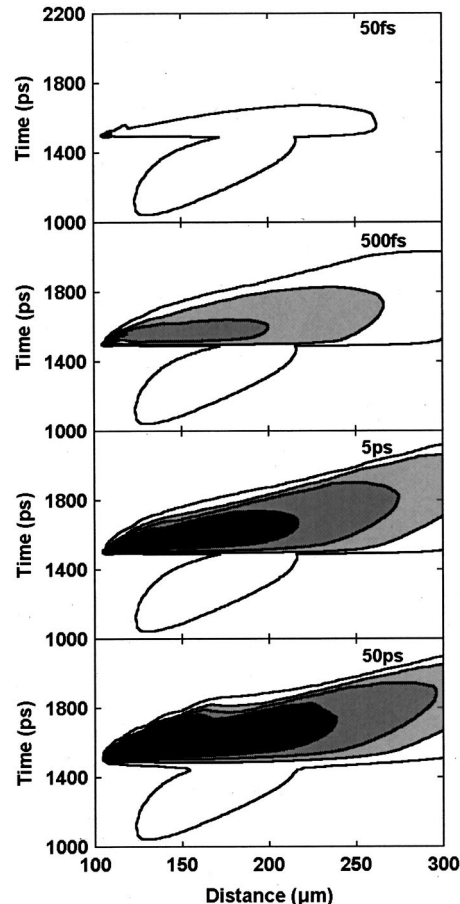


FIG. 4. Contours of the fraction of ground state F-like ions versus space and time for four values of the drive pulse durations 50 fs, 500 fs, 5 ps, and 50 ps. The contours from black to white represent fractions greater than 15%, 10%, 5%, and 1%.

pulses, such as 500 fs, 5 ps, and 50 ps durations. This is because the efficiency of absorption by the inverse bremsstrahlung for ultrashort laser pulses is much lower than for long pulses. From Fig. 4 we can see that for 50 fs laser pulse pumping, there is no overionization.

The ionization balance is the most important criterion to determine QSS and TCE x-ray lasers. The pure TCE does not allow any change of ionization balance during pumping, but actually this condition cannot be realized. The simulation results show that only a 50 fs drive pulse can basically avoid the overionization in the plasma. Thus it can be seen that the Ne-like Ge x-ray laser at 19.6 nm pumped by a pulse as short as 50 fs is the real transient collisional excitation.

TABLE I. Simulated gain and plasma conditions.

Intensity of main pulse (W/cm^2)	Duration of main pulse (ps)	Maximum local gain (cm^{-1})	Maximum T_e (eV)	Fraction of overionized ions (%)
10^{17}	0.05	91	~ 6000	~ 2
10^{16}	0.5	108	~ 3000	~ 5
10^{15}	5	118	~ 2200	~ 10
10^{14}	50	83	~ 1300	15–20

IV. CONCLUSIONS

In conclusion, we have investigated the Ne-like Ge x-ray laser at 19.6 nm numerically using a one-dimensional hydrodynamic code MED103 for a 100 μm thick Ge planar target irradiated by a nanosecond prepulse followed by a short drive pulse with different durations but a fixed energy. The comparison of ionization balance created by different drive pulse shows that in the dynamic range from 500 fs to 50 ps, the transient collisional excitation does not exist. The real transient x-ray laser of Ne-like GE at 19.6 nm wavelength can only be generated by a short laser pulse with tens of femtosecond duration.

ACKNOWLEDGMENTS

This work was supported by the National Nature Science Foundation of China under Grants Nos. 19974074, 60108007, and 19825110, National High Technology High Power Lasers Program.

- ¹D. L. Matthews, P. L. Hagelstein, M. D. Rosen, M. J. Eckart, N. M. Ceglio, A. U. Hazi, H. Medecki, B. J. MacGowan, J. E. Trebes, B. L. Whitten, E. M. Campbell, C. W. Hatcher, A. M. Hawryluk, R. L. Kauffman, L. D. Pleasance, G. Rambach, J. H. Scofield, G. Stone, and T. A. Weaver, Phys. Rev. Lett. **54**, 110 (1985).
- ²J. Nilsen, B. J. MacGowan, L. B. Da Silva, and J. C. Moreno, Phys. Rev. A **48**, 4682 (1993).
- ³J. C. Moreno, J. Nilsen, and L. B. Da Silva, Opt. Commun. **110**, 585 (1994).
- ⁴E. E. Fill, Y. L. Li, D. Schlägl, J. Steingruber, and J. Nilsen, Opt. Lett. **20**, 374 (1995).
- ⁵J. Zhang, P. J. Warwick, E. Wolfrum, M. H. Key, C. Danson, A. Demir, S. Healy, D. H. Kalantar, H. S. Kim, C. L. S. Lewis, J. Lin, A. G. MacPhee, D. Neely, J. Nilsen, G. J. Pert, R. Smith, G. J. Tallents, and J. S. Wark, Phys. Rev. A **54**, R4653 (1996).
- ⁶J. Zhang, A. G. MacPhee, J. Nilsen, J. Lin, T. W. Barbee, Jr., C. Danson, M. H. Key, C. L. S. Lewis, D. Neely, R. M. N. O'Rourke, G. J. Pert, R. Smith, G. J. Tallents, J. S. Wark, and E. Wolfrum, Phys. Rev. Lett. **78**, 3856 (1997).
- ⁷J. Zhang, A. G. MacPhee, J. Lin, E. Wolfrum, R. Smith, C. Danson, M. H. Key, C. L. S. Lewis, D. Neely, J. Nilsen, G. J. Pert, G. J. Tallents, and J. S. Wark, Science **276**, 1097 (1997).
- ⁸R. Smith, G. J. Tallents, J. Zhang, G. Eker, S. McCabe, G. J. Pert, and E. Wolfrum, Phys. Rev. A **59**, R47 (1999).
- ⁹F. Löwenthal, R. Tommasini, and J. E. Balmer, Opt. Commun. **154**, 325 (1998); J. E. Balmer, R. Tommasini, and F. Löwenthal, IEEE J. Sel. Top. Quantum Electron. **5**, 1435 (1999).
- ¹⁰Yu. V. Afanasiev and V. N. Shlyaptsev, Sov. J. Quantum Electron. **19**, 1606 (1989).
- ¹¹S. B. Healy, K. A. Janulewicz, J. A. Plowes, and G. J. Pert, Opt. Commun. **132**, 442 (1996).
- ¹²P. V. Nickles, V. N. Shlyaptsev, M. Kalachnikov, M. Schnürer, I. Will, and W. Sandner, Phys. Rev. Lett. **78**, 2748 (1997).
- ¹³P. J. Warwick, C. L. S. Lewis, M. P. Kalachnikov, P. V. Nickles, M. Schnürer, A. Behjat, A. Demir, G. J. Tallents, D. Neely, E. Wolfrum, J. Zhang, and G. J. Pert, J. Opt. Soc. Am. B **15**, 1808 (1998).
- ¹⁴J. Dunn, A. L. Osterheld, R. Shepherd, W. E. White, V. N. Shlyaptsev, and R. E. Stewart, Phys. Rev. Lett. **80**, 2825 (1998); J. Dunn, J. Nilsen, A. L. Osterheld, Y. Li, and V. N. Shlyaptsev, Opt. Lett. **24**, 101 (1999).
- ¹⁵M. P. Kalachnikov, P. V. Nickles, M. Schnürer, W. Sandner, V. N. Shlyaptsev, C. Danson, D. Neely, E. Wolfrum, J. Zhang, A. Behjat, A. Demir, G. J. Tallents, P. J. Warwick, and C. L. S. Lewis, Phys. Rev. A **57**, 4778 (1998).
- ¹⁶Y. L. Li, J. Dunn, J. Nilsen, T. W. Barbee, Jr., A. L. Osterheld, and V. N. Shlyaptsev, J. Opt. Soc. Am. B **17**, 1098 (2000).
- ¹⁷J. Nilsen, Y. L. Li, and J. Dunn, J. Opt. Soc. Am. B **17**, 1084 (2000).
- ¹⁸Y. J. Li and J. Zhang, Phys. Rev. E **63**, 036410 (2001).
- ¹⁹J. Zhang, M. H. Key, S. J. Rose, and G. J. Tallents, Phys. Rev. A **49**, 4024 (1994).
- ²⁰P. K. Patel, J. S. Wark, D. J. Heading, A. Djaoui, S. J. Rose, O. Renner, and A. Hauer, J. Quant. Spectrosc. Radiat. Transf. **57**, 683 (1997).
- ²¹J. P. Christiansen, D. E. T. F. Ashby, and K. V. Roberts, Comput. Phys. Commun. **7**, 271 (1974).

Forward dynamics of water-plasmas produced by femtosecond laser pulses

Y. T. Li, J. Zhang,^{a)} X. Lu, H. Teng, Y. J. Li, X. Y. Peng, Z. Jin, and L. Z. Zhao
Laboratory of Optical Physics, Institute of Physics, Chinese Academy of Sciences, Beijing 100080, People's Republic of China

(Received 20 March 2002; accepted 17 June 2002)

The evolution of the forward density front of water-plasmas generated by ultrashort laser pulses on an air–water interface is investigated with optical diagnostics. The density front is found to move with supersonic speed at the beginning, as predicted by a hydrodynamics simulation. This plasma-expansion process is followed by a fluid mechanical process. The expansion rate gradually reduces to the acoustic speed in water. © 2002 American Institute of Physics.

[DOI: 10.1063/1.1499951]

I. INTRODUCTON

Earlier work on laser-produced liquid plasmas concentrated mainly on laser-induced breakdowns from focusing long laser pulses (ns or sub-ns) inside a liquid.^{1–3} More recently, there has been much theoretical and experimental research on laser-produced bubbles in liquids. Many interesting phenomena, such as light emission from a single collapsing cavitation bubble, or single cavitation bubble luminescence, have been found.^{4–6} However, many practical laser applications, such as laser surgery, etc.,⁷ involve the interaction of a laser beam with an air–liquid interface.

In this paper we investigate water-plasmas produced by focusing a femtosecond laser pulse on the surface of water. A higher laser intensity is used in our experiments than those used in the earlier works. Water is transparent for laser probing, and it is soft for plasma expansion. Most experimental techniques used in the study of laser plasmas are not applicable in a liquid environment because most plasma particles and x-ray photons, which carry much information about the plasma, cannot escape from the ambient liquid and the container wall, and thus cannot be monitored by the usual passive diagnostics. It is therefore convenient to study the forward (in the laser propagation direction) dynamical processes with direct optical diagnostics in a laser-water experiment. Here, we present some observations on the evolution of the forward dynamics of water plasmas with an optical shadowgraphy technique. Our results are useful in elucidating how laser bubbles are formed, how they evolve, and how they might affect ambient soft tissues.

II. EXPERIMENTAL SETUP

The experiment was carried out using the ultrashort pulse laser facility at the Institute of Physics of the Chinese Academy of Sciences. A Ti:sapphire laser system outputs 5 mJ in 150 fs pulses at 800 nm. The laser beam was focused by a lens with a focal length of 20 mm onto distilled water

surface with an average intensity of $1 \times 10^{16} \text{ W/cm}^2$. The incident angle was 15°. The forward evolution of the water plasma was monitored with an optical shadowgraphy technique. A small portion of the laser beam split from the main (interaction) beam was used after being frequency-doubled to 400 nm as a probe. The plasma was imaged by a microscope on a 16 bit, 512×12 pixel charge-coupled device (CCD) camera. An assembly of neutral and interference filters with a narrow bandwidth singled out the 400 nm probe beam from the background emission. Varying the delay of the probe beam with respect to the main beam on successive shots permitted mapping of the evolution of the density structure of the forward plasma as a function of time. The pixel size of the CCD camera is 25 μm, which gives a pixel-size limited spatial resolution of about 4 μm. The time resolution was determined by the duration of the probe beam of about 150 fs. Other diagnostics included hot electron measurements with LiF (Mg, Cu, P) thermoluminescence dosimeter (TLDs), and hard x-ray measurements with a γ-ray spectrometer with NaI as detector.^{8,9} Intense hard x-ray photons and electron emission were also observed in the water-plasma generated by the main laser beam. These results will be presented elsewhere.

III. EXPERIMENTAL RESULTS AND SIMULATION

To understand the process of forward evolution of the water-plasma, we used a one-dimensional two-temperature hydrodynamics code (MED103)^{10,11} to simulate the behavior of the water-plasma generated by 150 fs, 5 mJ laser pulses. Figures 1(a) and (b) show snapshots of the spatial profiles of the mass density ρ , pressure p , cell velocity v , electron temperature T_e and ion temperature T_i at the time of the laser peak and at 5 ps after the peak, respectively. The water surface was located at 1000 μm; the laser pulse was incident from the right. The undisturbed water density was 1 g/cm³. When the laser pulse reached its maximum energy, a 60 Mbar peak pressure was produced in water. The flow cells of the water surface expanded outwards. However, the inner cells moved into the water in an opposite direction (negative velocity). This led to a rise of the mass density in water. A

^{a)}Author to whom correspondence should be addressed. Electronic mail: jzhang@aphy.iphy.ac.cn

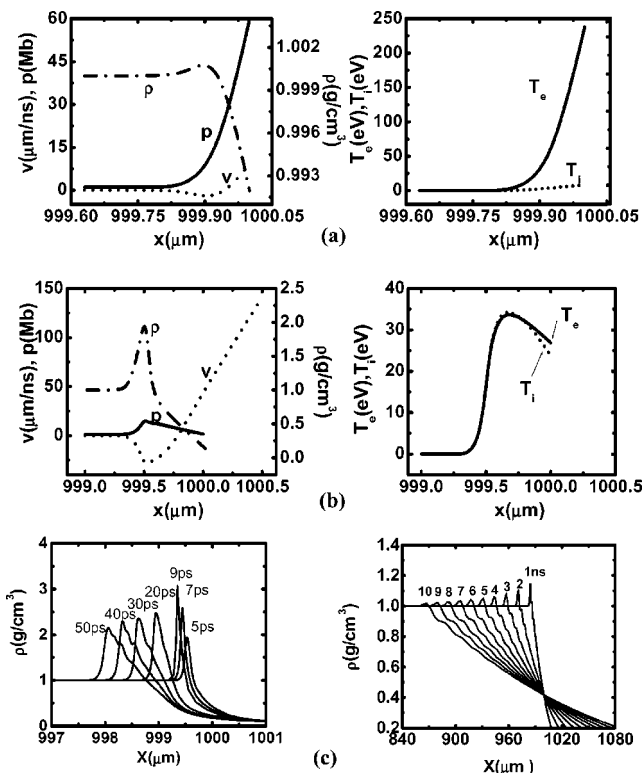


FIG. 1. Snapshots of spatial profiles of the mass density ρ , pressure p , cell velocity v , electron temperature T_e and ion temperature T_i at the time of the laser peak (a) and at 5 ps after the laser peak (b); (c) shows the forward evolution of mass density during 5–50 ps and 1–10 ns. Water surface locates at 1000 μm ; laser is incident from the right.

density cavitation was formed simultaneously. The maximum electron temperature was 240 eV, about 25 times higher than the ion temperature. The ions and electrons could not reach collisional balance in such a short time scale because the corresponding relaxation time is much larger than the laser duration. After the laser pulse is dissipated, the pressure and electron temperature started to decrease. However, the velocities of the flow cells continued to increase, and a higher density compression was produced. The mass compression ratio reached 2 times higher than that in the undisturbed water at 5 ps after the laser peak, as shown in Fig. 1(b). The variation of the density, or refraction index, in water can be measured directly by optical diagnostics such as interferometry, shadowgraphy, etc. Note that at 5 ps the ion and electron temperatures are almost the same. This shows that the electron-ion relaxation time is only a few picoseconds in water. Figure 1(c) presents two graphs that show the forward evolution of mass density during 5–50 ps and 1–10 ns, respectively. The mass density rises to the maximum, three times of the undisturbed water, at 9 ps. Then it decreases to the undisturbed density gradually as propagating into water.

Figure 2(a) shows typical shadowgrams of the forward expansion of the water-plasma produced by different laser energy at the same delay time of 22.2 ns with respect to the main laser beam. The main interaction beam is incident from the top. The probe beam passes through the plasma region parallel to the water surface. The laser energy was adjusted

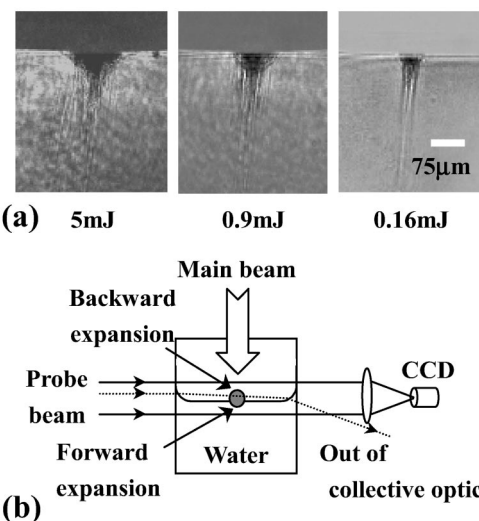


FIG. 2. (a) Shadowgrams of the density front in water at 22.2 ns of the delay time with different laser energies; (b) a schematic drawing of the probe beam and the plasma expansion. Laser is incident from the top. Only forward expansion is recorded on CCD because the optical rays above water surface are deflected out of the collective optical component by the water near the glass flask wall (see the dash line).

by neutral filters with different attenuation factors calibrated in advance. The plasma plume expanding into air (backward expanding) is invisible because the water near the glass flask wall deflects (like a prism) the probe beam out of the optical components. The forward expanding plasma (into the water) can be seen because it is at the bottom of the concave water surface. This is illustrated in Fig. 2(b). From these shadowgrams we can see that a density cavitation is formed by the pressure of plasma expansion. As expected, the size of the cavitation is smaller for lower laser energy. When the laser energy was attenuated by a factor of 1000, no plasma shadow could be seen on the CCD camera. Possible candidates responsible for the filaments shown in Fig. 2(a) include charged particles, clusters formed by laser vaporizing and sputtering, and the laser beam entering into water. Ion effects are negligible because the energy of the ions generated at an irradiance of $1 \times 10^{16} \text{ W/cm}^2$ is not high enough to penetrate several hundred microns of water. Some small clusters injecting into the water are seen by the naked eye during the interaction. We use a digital video recorder to record these clusters. The video images show that neutral water clusters are exploded out from the focal spot. But they need more time to penetrate such a long distance. High-energy electrons and laser beam leaked into water can propagate a long distance in water. However, the same directions of those filaments as the incident laser propagation imply that the laser leaked into water plays a main role in the formation of the filaments.

In Fig. 2(a) cylindrical cumulative shock wave is evident near the laser axis in water. We believe that the shock wave is caused by the self-focusing of leaked laser in water. When the leaked laser pulse enters the water, a hot, elongated filament is formed around the laser axis because the laser power is higher than the self-focusing threshold ($\approx 2 \text{ MW}$ for wa-

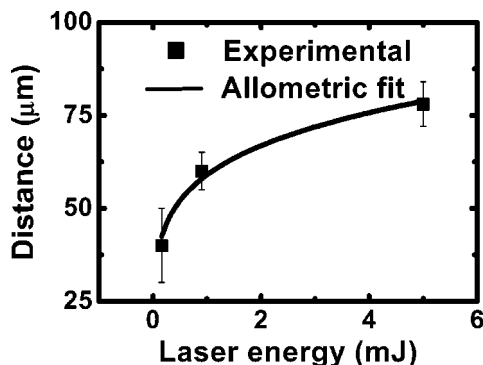


FIG. 3. Distance of the density front from water surface as a function of the laser pulse energy at 22.2 ns of delay time. The experimental data are fitted by an allometric function.

ter). A shock wave is produced as a result of the high pressure exerted by the filamentlike plasma. But the propagating trajectory of the shock wave cannot be distinguished from the density perturbation induced by side leaked laser around the laser axis in some shots. Therefore no quantitative information is obtained about the shock wave.

Figure 3 displays the expansion depth of the density front into water versus the laser energy at a 22.2 ns delay time. The data from five measurements were averaged. The error bars correspond to the shot-shot fluctuations. The experimental data were fitted by an allometric function: distance (mm) = $a \times \text{laser energy (mJ)}^b$, where a and b are the fitting parameters. Although the two parameters are different for different delay times, the parameter b falls within the range 0.2–0.27. A cube root dependence of cavitation radius on the pulse energy was obtained in the studies of nanosecond and picosecond laser breakdown in water.¹² Our results imply that shorter laser pulses are preferable in reducing the side effects in surgical applications.¹³

The temporal series of shadowgrams of the expansion taken from 27 ps to 22.2 ns after the main laser beam are shown in Fig. 4. The displacement of the density front from the water surface as a function of the delay time are shown in

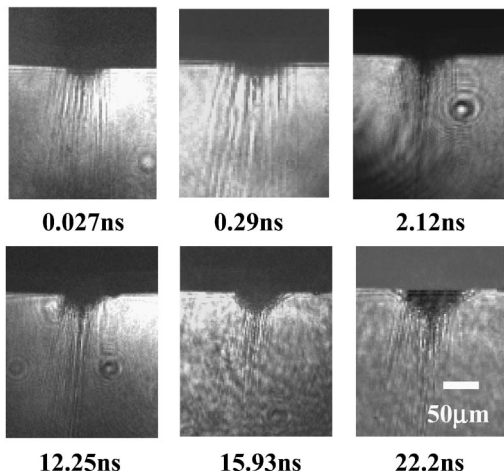


FIG. 4. Time series of shadowgrams showing the evolution of density front with the delay time in water for 5 mJ of laser energy.

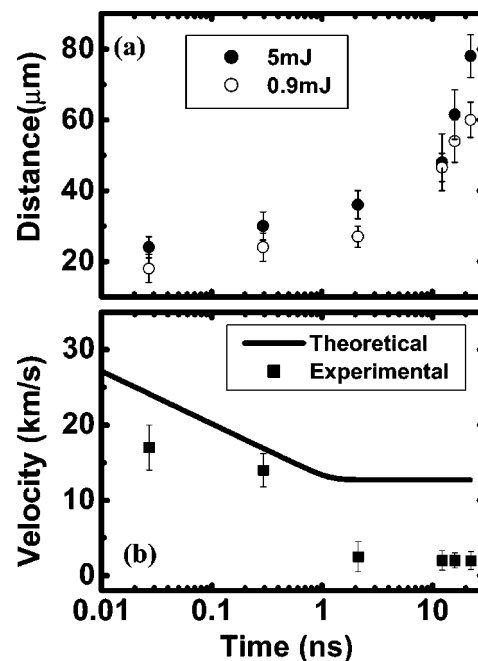


FIG. 5. (a) Measured dependence of distance of the density front from the water surface on the delay time for 5 mJ and 0.9 mJ laser energies. (b) Measured velocity of the density front for 5 mJ laser as a function of time obtained by differentiating the experimental data in (a); the line shows the theoretical velocity obtained by hydrodynamic simulation.

Fig. 5(a) for both 5 and 0.9 mJ laser energies. Two processes of density expansion can be clearly identified: a quickly decelerating process and a near uniform expansion process. This is more apparent in Fig. 5(b), which shows the measured velocity of the density front as a function of time for the case of 5 mJ laser energy by differentiating the experimental data in Fig. 5(a). We find that these two processes correspond to an initial plasma expansion followed by a pure fluid mechanical process, respectively. During the plasma expansion, the high pressure produced by the expansion expels the water in the focal spot. The pressure is transient because of the short duration of the laser pulse. Due to electron recombination and heat conduction, the plasma cools down quickly. This leads to a quickly slowing-down of the velocity of the density front. After the plasma cools down completely, typically on a nanosecond time scale, the movement of the density front is dominated by pure fluid mechanics and the velocity decays gradually to the acoustic speed in water. The line shows the theoretical velocity obtained from our simulation. We see that the theoretical velocity of the density front agrees with our measurements to within a factor of 2 during the plasma stage. However, great discrepancy exists in the later stage. In the code the equations of state used assume the ions is a nondegenerate perfect gas and the electrons behave as an either nondegenerate or partially or fully degenerate perfect gas. The code does not take into account the practical equation of state of water and the dissipation processes, so that it is valid mainly for the early stages when plasma processes dominate. This leads to the discrepancy in the pure fluid process. So one should be careful to estimate the forward expansion for the later stage using a hydrodynamic code.

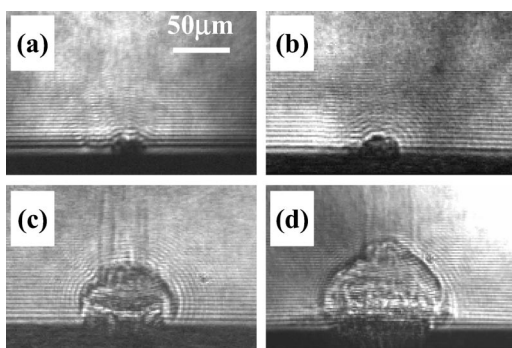


FIG. 6. Time series of shadowgrams showing the evolution of the backward plasma expansion above water surface at 1 ns (a), 2.5 ns (b), 5 ns (c) and 10 ns (d), respectively, for a 5 mJ of laser energy.

The evolution of the backward expansion of the plasma into air is illustrated in Fig. 6. In order to observe the backward expansion, the water surface was adjusted to be convex, so the forward expansion cannot be seen in those images. Compared with the forward movement of the density front, the expansion into air is faster than that into water.

IV. CONCLUSIONS

In summary, the forward density evolution of water plasmas produced by femtosecond laser pulses on an air–liquid interface has been investigated by optical shadowgraphy and numerical simulation. The density front first moves with a supersonic speed but it slows down quickly as the plasma cools down. The expansion speed gradually reduces to the acoustic speed as the fluid dynamic effects become dominate.

ACKNOWLEDGMENTS

This work was supported by the NNSFC (under Project Nos. 19825110, 19974074, 10075075, 10105014, 10176034, the National High-Tech ICF program, the K. C. Wang Education Foundation (Hong Kong) and the NKBRSPF (under Grant No. G199990-75200).

- ¹J. Noack and A. Vogel, *Appl. Opt.* **37**, 4092 (1998).
- ²F. Docchio, P. Regondi, M. R. C. Capon, and J. Mellerio, *Appl. Opt.* **27**, 3661 (1988).
- ³A. G. Doukas, A. D. Zweig, J. K. Frisoli, R. Birngruber, and T. F. Deutsch, *Appl. Phys. B: Photophys. Laser Chem.* **53**, 237 (1991).
- ⁴C. D. Ohl, O. Lindau, and W. Lauterborn, *Phys. Rev. Lett.* **80**, 393 (1998).
- ⁵O. Baghdassarian, B. Tabbert, and G. A. Williams, *Phys. Rev. Lett.* **83**, 2437 (1999).
- ⁶O. Baghdassarian, H. C. Chu, B. Tabbert, and G. A. Williams, *Phys. Rev. Lett.* **86**, 4934 (2001).
- ⁷A. Vogel, S. Busch, and U. Parlitz, *J. Acoust. Soc. Am.* **100**, 148 (1996).
- ⁸P. Zhang, J. T. He, D. B. Chen, Z. H. Li, Y. Zhang, J. G. Bian, L. Wang, Z. L. Li, B. H. Feng, X. L. Zhang, D. X. Zhang, X. W. Tang, and J. Zhang, *Phys. Rev. E* **57**, R3746 (1998).
- ⁹L. M. Chen, J. Zhang, H. Teng, Q. L. Dong, Z. L. Chen, T. J. Liang, L. Z. Zhao, and Z. Y. Wei, *Phys. Rev. E* **63**, 046403 (2001).
- ¹⁰J. P. Christiansen, D. E. T. F. Ashby, and K. V. Roberts, *Comput. Phys. Commun.* **7**, 271 (1974).
- ¹¹J. Zhang, M. H. Key, S. J. Rose, and G. J. Tallents, *Phys. Rev. A* **49**, 4024 (1994).
- ¹²B. Zyss, J. G. Fujimoto, and T. F. Deutsch, *Appl. Phys. B: Photophys. Laser Chem.* **48**, 139 (1989).
- ¹³J. Noack, D. X. Hammer, G. D. Noojin, B. A. Rockwell, and A. Vogel, *J. Appl. Phys.* **83**, 7488 (1998).

Generation of high-amplitude plasma waves for particle acceleration by cross-modulated laser wake fields

Z.-M. Sheng^{a)}

*Laboratory of Optical Physics, Institute of Physics, Chinese Academy of Science, Beijing 100080, China
and Institute of Laser Engineering, Osaka University, 2-6 Yamada-oka, Suita,
Osaka 565-0871, Japan*

K. Mima, Y. Sentoku, and K. Nishihara

Institute of Laser Engineering, Osaka University, 2-6 Yamada-oka, Suita, Osaka 565-0871, Japan

J. Zhang

Laboratory of Optical Physics, Institute of Physics, Chinese Academy of Science, Beijing 100080, China

(Received 2 January 2002; accepted 18 April 2002)

A scheme is proposed to amplify the wake field of an ultrashort laser pulse by a second laser pulse co-propagating behind with a duration of a few plasma wavelengths or longer for particle acceleration. It is found that, due to the cross-phase modulation by the wake field, the second laser pulse is modulated quickly and split into a multipulse train, where the durations of subpulses are around a plasma oscillation period. This pulse train amplifies the wake field in turn to a high level until wave breaking. With this scheme, a large-amplitude plasma wave can be generated with laser pulses only at moderate intensities. For example, the effective acceleration field for trapped electrons injected from wave-breaking exceeds 100 GeV/m for incident laser pulses at intensity $3.4 \times 10^{17} \text{ W/cm}^2$ in plasma at one percent of the critical density, as demonstrated by particle-in-cell simulations. © 2002 American Institute of Physics. [DOI: 10.1063/1.1485771]

I. INTRODUCTION

Since the plasma-based particle accelerators including the laser beat-wave accelerator and the standard wake-field accelerators were suggested two decades ago,¹ some innovations have been proposed, which allow the plasma-based accelerators to work in different parameter regimes and different geometry configurations.^{2–7} In the proposed self-modulated laser wake-field accelerator (SM–LWFA),^{2–4} the plasma wave is generated through a resonant self-modulation process of a relatively long pulse of a few plasma oscillation periods, which is usually coupled with Raman forward scattering (RFS). For the plasma wave to grow up to a high level for efficient acceleration, a time scale of a few tens times that for RFS growth $\sim (\omega_0/\omega_p^2) \gamma_0^2/a_0$ is necessary, where ω_0 is the laser frequency, ω_p is the plasma frequency, a_0 is the normalized laser amplitude, and $\gamma_0 \sim (1+a_0^2/2)^{1/2}$. In this case, the corresponding spatial extension is usually larger than the Rayleigh length in tenuous plasma. Therefore a guiding channel for the laser pulse is necessary. On the other hand, since the plasma wave generated through the self-modulation and RFS processes grows from noise in the plasma, it is not controllable. In order to remove this uncertainty, ways of seeding self-modulation of the laser pulse such as Raman seeding and plasmon seeding have been suggested.⁸ There is also another proposal to generate high amplitude plasma waves by use of two slightly detuned counter-propagating laser pulses, an ultrashort timing pulse

and a long pump pulse.⁷ This can be understood as a kind of Raman seeding. With the plasma wave excited in a controlled way, one may be able to inject electrons right at the acceleration phase of the high amplitude plasma wave, such as in the scheme of the laser injected laser accelerator (LILAC).⁵ In this scheme, electrons are injected by use of another ultrashort intense laser pulse intersecting with the high-amplitude plasma wave. It is supposed to be able to obtain energetic electron beams with low energy spread.

In this paper, we introduce a new scheme to generate a high amplitude wake field up to the wave-breaking amplitude by use of two laser pulses with only modest intensities. The first pulse is an ultrashort laser pulse shorter than a plasma oscillation period, which produces a seed wake field. The second pulse is a relatively long pulse, such as a few plasma oscillation periods. During the propagation process, the second pulse is cross-phase modulated (XPM) by the density gradient of the seed wake field,⁹ and is split up into a multipulse train,^{10,11} where each subpulse has duration around a plasma oscillation period. This pulse train then in turn amplifies the seed wake field up to a high level in a way as discussed in a number of papers.⁶ This process develops in a time scale shorter than that for the SM–LWFA, and there is no necessity for any particular timing between the two pulses. This scheme, named for short as XM–LWFA in the following, is demonstrated by use of particle-in-cell (PIC) simulations. We mention that when the second pulse is initially shorter than a plasma wavelength, it can be significantly compressed by the wake field of the first pulse

^{a)}Electronic mail: zmsheng@aphy.iphy.ac.cn

through XPM if the amplitude of the wake-field exceeds some threshold value.^{10,11}

II. ONE-DIMENSIONAL PIC SIMULATIONS

For laser pulses propagating in a homogeneously tenuous plasma, the one-dimensional envelope evolution of the pulses and the excited wake field can be described by^{3,9–12}

$$\left(2i\frac{\partial}{\partial\tau}+\epsilon^2\frac{\partial^2}{\partial\xi^2}\right)a=\left(\frac{n}{\gamma}-1\right)a, \quad (1)$$

$$\frac{\partial^2\phi}{\partial\xi^2}=n-1, \quad (2)$$

$$n=\beta^2\gamma/(1+\phi-\gamma\gamma_\beta^{-2}), \quad (3)$$

if we assume that the two pulses involved in the present XM–LWFA scheme are at the same frequency and propagate at a group velocity equal to the phase velocity of the plasma wake field. Here a is the slowly varying vector potential of the laser pulse normalized by mc^2/e , ϕ is the scalar potential normalized by mc^2/e , n is the electron density normalized by the unperturbed density n_0 , $\gamma=\gamma_\beta^2[1+\phi-\beta\sqrt{(1+\phi)^2-\gamma_\beta^{-2}(1+|a|^2/2)}]$ is the relativistic factor, $\epsilon=\omega_p/\omega_0=(n_0/n_c)^{1/2}$ with $\omega_p=(4\pi n_0 e^2/m)^{1/2}$ is the unperturbed plasma frequency and ω_0 the laser frequency, $n_c=m\omega_0^2/4\pi e^2$ is the critical density, $\tau=t\omega_p^2/\omega_0$, $\xi=k_p(x-\beta ct)$ with $k_p=\omega_p/c$ and $\beta=v_p/c$ are the phase velocity of a background plasma wave, and $\gamma_\beta=(1-\beta^2)^{-1/2}$. From Eq. (1), one finds immediately that the time scale for XPM is $\sim(\delta n/n_0)\omega_0/\omega_p^2$ in the present scheme, where δn is the electron density perturbation driven by the first ultrashort pulse. In comparison, the modulation of a laser pulse in the SM–LWFA grows from noise, i.e., $\delta n/n_0\sim 0$. Therefore a longer time scale or a larger plasma dimension is necessary to produce a high-amplitude plasma wave.

In the following studies, instead of solving the coupled equations (1)–(3), we conduct PIC simulations to study the XM–LWFA with codes developed in the way described in Ref. 13. Since the high-amplitude wake-field generation through XPM is essentially a one-dimensional (1D) effect, we start with 1D PIC simulations. In our simulations, the longitudinal pulse profile of the first pulse is $|a_1|^2=a_{01}^2\sin^4(\pi t/\tau_1)$, where $0\leq t\leq\tau_1$; here a_1 is the vector potential of the laser field normalized by mc^2/e , time t and τ_1 is normalized by laser cycle $2\pi/\omega_0$. The second pulse is launched after a delay of a few plasma oscillation periods. It has a similar profile with the first pulse in its leading and trailing edges together with a homogeneous part in between, i.e.,

$$|a_2|^2=\begin{cases} a_{02}^2\sin^4(\pi t/\tau_2), & 0\leq t<\tau_2/2, \\ a_{02}^2, & \tau_2/2\leq t<\tau_h+\tau_2/2, \\ a_{02}^2\sin^4[\pi(t-\tau_h)/\tau_2], & \tau_h+\tau_2/2\leq t\leq\tau_h+\tau_2. \end{cases} \quad (4)$$

Here we assume that the second pulse is at the same frequency with the first pulse, a_2 is normalized by mc^2/e , and τ_2 and τ_h are normalized by $2\pi/\omega_0$. The simulation box is 1600λ along the laser propagation direction (x direction),

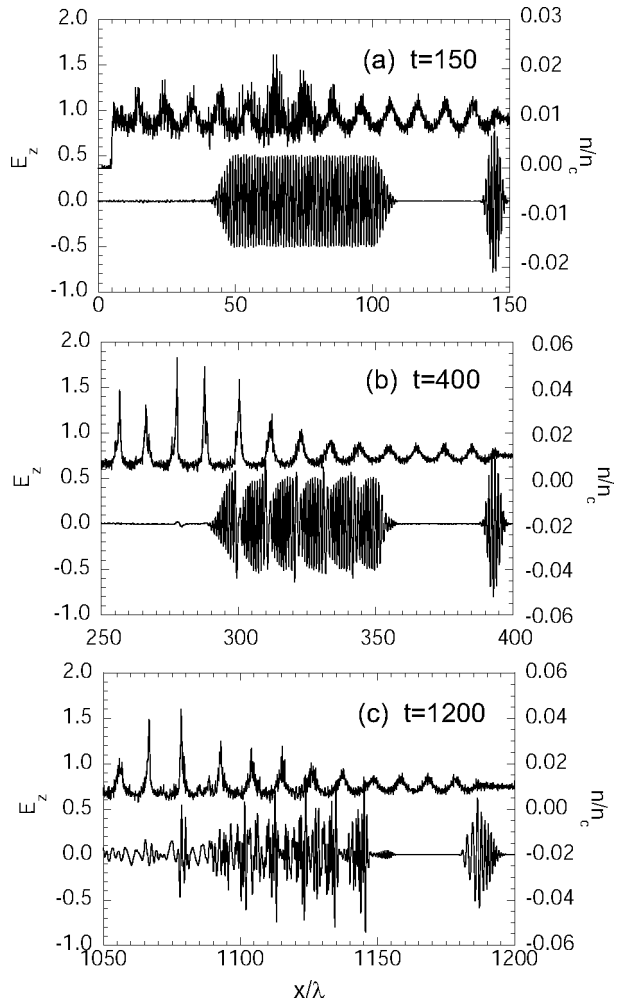


FIG. 1. Snapshots of laser pulses (lower solid line) and electron density (upper solid line) at time $t=150$ (a), 400 (b), and 1200 (c) laser cycles. The initial plasma density is $n/n_c=0.01$ and the pulses are with $a_{01}=0.8$, $a_{02}=0.5$, $\tau_1=10$, $\tau_2=20$, and $\tau_h=50$.

where λ is the laser wavelength in vacuum. Initially, the plasma is homogeneous, locating in the middle of the simulation box. There are vacuum regions of 10λ located at each side of the boundaries in the simulation box. Typically we use 10 particles per cell each for electrons and ions initially and 10 cells in a laser wavelength.

Figure 1 illustrates the evolution of the laser pulses and the electron density when $a_{01}=0.8$, $a_{02}=0.5$, $\tau_1=10$, $\tau_2=20$, $\tau_h=50$, and the electron density $n_0=0.01n_c$ initially. The delay of the second pulse, not an important factor in the present scheme, is taken to be 30 laser cycles in this example. From Figs. 1(a)–1(c), one sees how the second pulse is modulated by the wake field generated by the first pulse. Because the density perturbation associated with the wake field of the first pulse is at a finite amplitude, the modulation of the second pulse grows quickly. In a short time of a few hundreds of laser cycles $\sim(\delta n/n_0)\omega_0/\omega_p^2$ as estimated before, it splits into a multipulse train. Meanwhile, the density perturbation/plasma wave is amplified by the modulated pulse up to a high level until the wave-breaking sets in. Accompanying the plasma wave amplification, one notes that the energy loss of the second laser pulse goes on very fast.

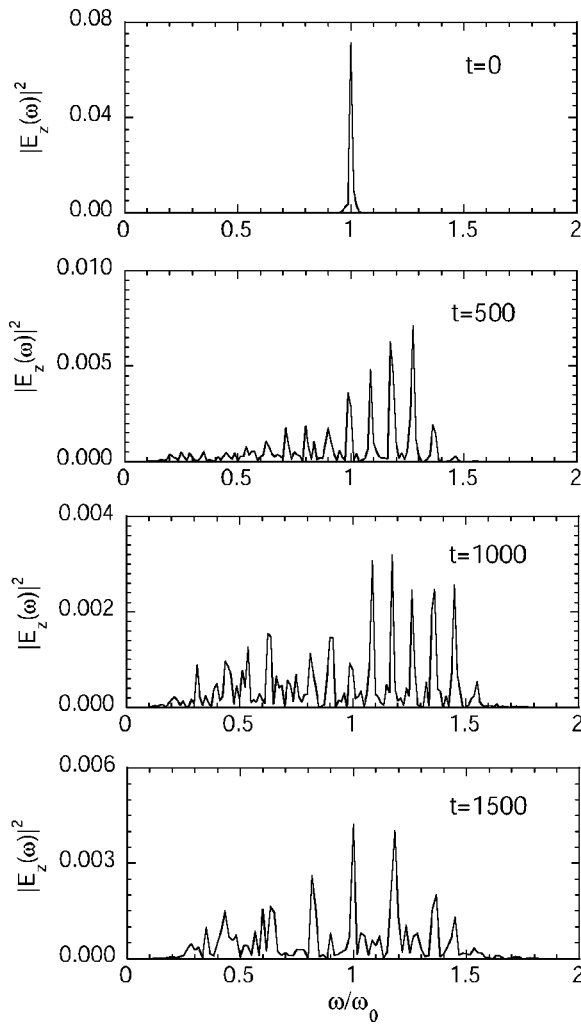


FIG. 2. Frequency spectra of the second pulse at different times in plasma. The laser pulses and plasma parameters are the same as in Fig. 1.

For example, over 80% of the initial energy are lost to plasma after propagating through a distance of about 1200 laser wavelengths. We find that this process depends quite weakly on the rising time at the leading edge of the second pulse $\tau_2/2$ provided it is longer than a plasma oscillation period. Figure 2 shows snapshots of the corresponding frequency spectra of the second pulse, indicating that the pulse is strongly modulated by the wake field of the first pulse at the plasma frequency, accompanied by spectrum-broadening and frequency-shifting/positive pulse chirping. The frequency shift is caused by the electron density gradient comoving with the laser pulse.⁹ It has been pointed out that pulse chirping can lead to a significant change of the growth of Raman forward scattering (RFS), plasma wave excitation, and hot electron generation.¹⁴ In particular, a positively chirped pulse increases the growth of RFS and hot electron production as a result of group-velocity dispersion of light waves in plasmas. Thus the positive pulse chirping generated naturally through XPM in our scheme is favorable for plasma wave excitation and particle acceleration.

As a comparison, we show the pulse evolution and plasma wave excitation only with the second pulse in Figs. 3(a) and 3(b). Without initial plasmon seeding, the self-

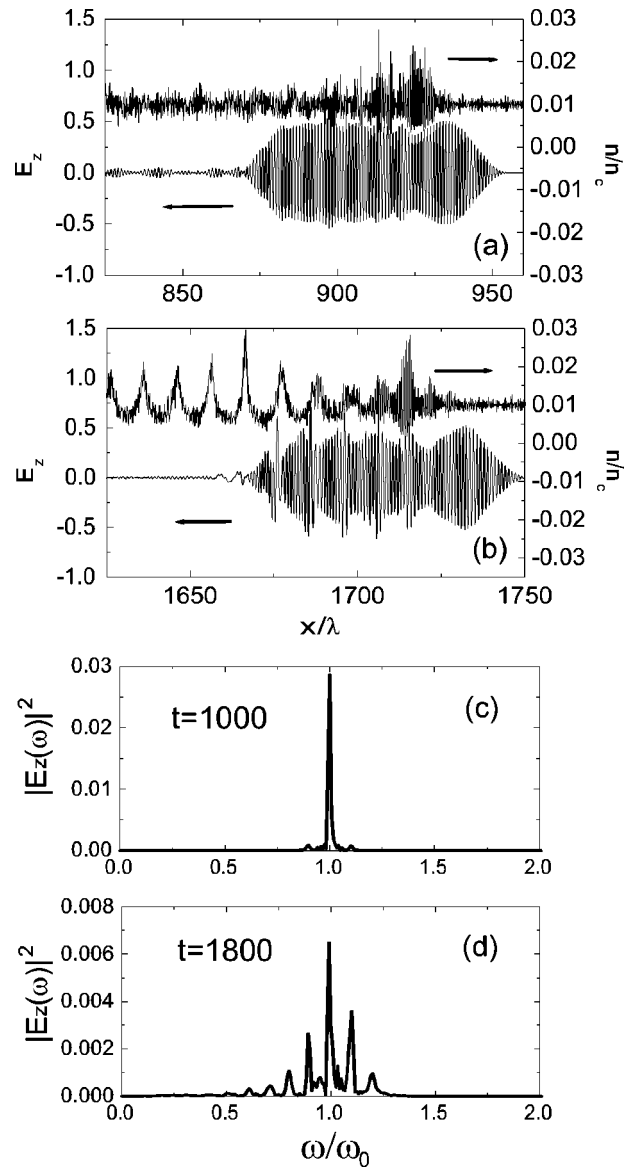


FIG. 3. Snapshots of a laser pulse (nether solid line) and electron density (upper solid line) at time $t = 1000$ (a) and 1800 (b) without an initial seeding wake field. The initial plasma density is $n/n_c = 0.01$ and the laser pulse is with $a_{02} = 0.5$, $\tau_2 = 40$, and $\tau_h = 50$. Frames (c) and (d) show the frequency spectra of the laser pulse around $t = 1000$ and 1800 laser cycles, respectively.

modulation of the laser pulse develops slowly. Also it depends strongly on the rising time at the leading edge of the pulse $\tau_2/2$, a contrast to the XPM shown before which depends only weakly on the rising time of the pulse. In this example, we have taken the rising time to be twice the plasma oscillation periods. Strong modulation and high amplitude plasma wave generation begin to be observed after propagation over 1500 laser wavelengths; Wave breaking and particle acceleration are observed for laser propagation over 1700 laser wavelengths as shown in Fig. 3(b), as well as in Fig. 5(a) plotting the maximum energy of electrons as a function of time observed in the simulations. It is also obvious that the energy loss of the laser pulse to plasma wave goes on slowly in this case. One finds that over 70% of initial energy is remained in the pulse after propagation over 1700

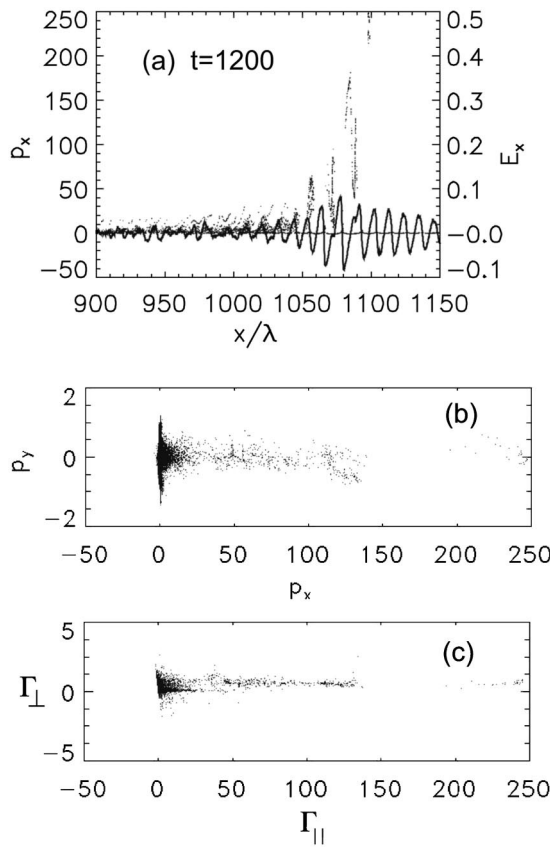


FIG. 4. (a) Electron distributions in phase space (p_x, x) (dots) and corresponding longitudinal electric field (solid line) at time $t = 1200$ laser cycles; (b) electron distributions in momentum space at the same time; (c) energy gain from the longitudinal field versus that from the transverse fields after interactions for $t = 1200$ laser cycles. The laser and plasma parameters are given in Fig. 1.

laser wavelengths. Figures 3(c) and 3(d) shows the pulse frequency spectra corresponding to Figs. 3(a) and 3(b). This example demonstrates that a seeding wake field is essential to build up a high amplitude plasma wave in a controlled way, in a relatively shorter time scale or in a smaller plasma dimension.

Figure 4(a) shows a snapshot of the electron distributions in longitudinal phase space inside the simulation box at $t = 1200$ laser cycles found for the same parameters as in Fig. 1 with the presence of the seeding pulse. It is found that energetic electrons mainly locate at the region occupied by the second pulse, where the plasma wave has high amplitudes. These energetic electrons result from the plasma wave breaking, which enables the electron injection into acceleration phases to occur. One notes that there is not any electron acceleration by the wake field of the first pulse in front of the second pulse, since there is no electron injection there. Figure 4(b) displays electron distributions in phase space (p_x, p_y). It is obvious that energetic electrons predominantly move in the longitudinal direction. Since energetic electrons co-move with the second pulse, it is interesting to know whether the electrons gain energy dominantly from the plasma wave or from the laser fields of the second pulse, both of which could accelerate electrons in the longitudinal direction. From the equation of motions, one finds that¹⁵

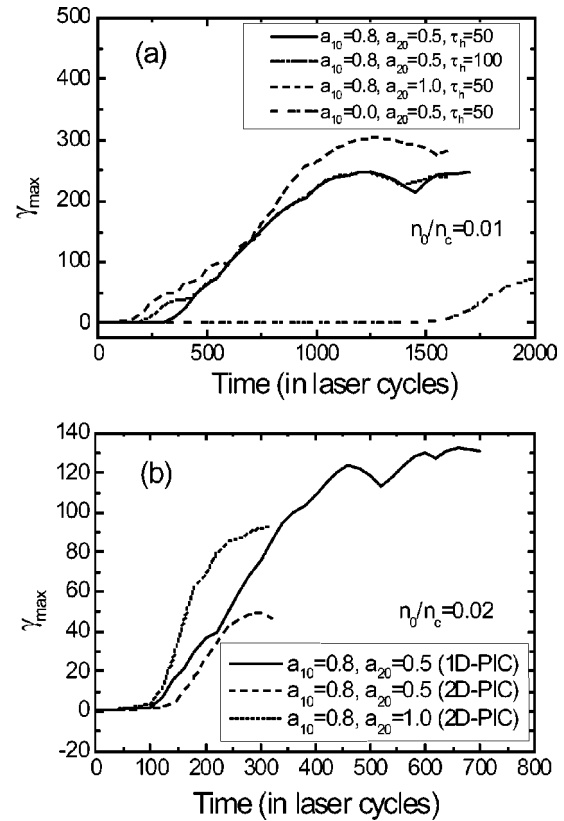


FIG. 5. Maximum electron energy as a function of time for a variety of laser and plasma parameters as observed in the PIC simulations. (a) shows the results obtained from 1D PIC simulations for $n_0/n_c = 0.01$; here $\tau_1 = 10$ laser cycles for the first pulse, $\tau_2 = 20$ and $\tau_h = 50$ or 100 for the second pulse. (b) shows the results obtained both from 1D and 2D PIC simulations for $n_0/n_c = 0.02$; here $\tau_1 = 7$ laser cycles for the first pulse, $\tau_2 = 20$ and $\tau_h = 50$ for the second pulse.

$$d\gamma/dt = -(v_x E_x + v_{\perp} E_{\perp}) = d\Gamma_{||}/dt + d\Gamma_{\perp}/dt, \quad (5)$$

where $\Gamma_{||} = -\int_0^t v_x E_x dt'$ represents energy gain from the plasma wave and $\Gamma_{\perp} = -\int_0^t v_{\perp} E_{\perp} dt'$ represents that directly from the second laser pulse. From Fig. 4(c), it is obvious that energetic electrons are accelerated dominantly by the longitudinal field or the plasma wave in this case.

We have performed a series of simulations by changing the laser pulse and plasma parameters. Figure 5 displays the maximum energy of electrons as a function of time as observed in simulations. In plasma at one percent of the critical density, some electrons are accelerated to energy over 100 MeV in about 1000λ by a laser pulse only at moderate intensities, for example, $3.4 \times 10^{17} \text{ W/cm}^2$ in a simulation (for $a_{02}=0.5$). The corresponding average acceleration field exceeds 100 GeV/m. For the same laser parameters, this field is even larger in plasma with higher densities [see Fig. 5(b)] and electrons are accelerated more quickly, even though the saturated energy is smaller in this case. Partially, this is because the time needed to modulate the second pulse is inversely proportional to plasma densities. The plasma wave is amplified more quickly to wave-breaking amplitude in the high-density case. After certain time, the maximum electron energy is found to become saturated. The higher the plasma density, the lower the maximum electron energy. The maxi-

mum electron energy depends both on the electron density and the amplitude of the plasma wave. This can be explained as following. If assuming the plasma wave potential is $\phi(\xi)$, where $\xi=x-\beta t$ and β is the phase velocity of the plasma wave, it is easy to show that the Hamiltonian $H=(1+p_x^2)^{1/2}-\beta p_x-\phi(\xi)$ is a constant of motion. For an electron to be trapped at the boundary of acceleration phase, it is necessary that $p_x=\beta\gamma_\beta$, where $\gamma_\beta=(1-\beta^2)^{-1/2}$. The maximum energy of electrons is found when electrons move to a region with maximum scalar potential ϕ_{\max} . As a result, one finds^{1,5} $\gamma_{\max}=\gamma_\beta^2[\phi_{\max}+1/\gamma_\beta+\beta(\phi_{\max}^2+2\phi_{\max}/\gamma_\beta)^{1/2}]$. In cold plasmas, it is well known¹⁶ that the electric field can be expressed as $eE/m\omega_p c=\sqrt{2}[(1-v_0^2)^{-1/2}-(1-v^2)^{-1/2}]^{1/2}$, and the potential $\phi=(1-\beta v)/(1-v^2)^{1/2}+\text{const}$, where v_0 and v are, respectively, the maximum velocity and velocity of electrons in the plasma wave. Thus the maximum potential change, corresponding to a change of velocity in the range $[-v_0, v_0]$, is given by $\phi_{\max}=2\beta v_0/(1-v_0^2)^{1/2}$. Close to the wave-breaking limit, the resulting maximum energy is around $\sim 4\beta^2\gamma_\beta^3\sim 4(n_c/n_0)^{3/2}$, if the phase velocity of the plasma wave can be approximated with the group velocity of the laser pulse, i.e., $\beta=(1-\omega_p^2/\omega_0^2)^{1/2}$. This scaling shows explicitly that the maximum energy increases with decreasing plasma density, consistent with our simulations. On the other hand, this estimation is much larger than the saturated energy level observed in the simulation. This can be attributed to the fact that these electrons with maximum energy observed in the simulation are located just behind the leading front of the second pulse, where the amplitude of the plasma wave is still far below the wave-breaking limit. In passing, one notes that if there is no seeding pulse, particle acceleration appears very late as shown in Fig. 5(a).

III. TWO-DIMENSIONAL PIC SIMULATIONS

In real experiments, two-dimensional (2D) effects always have strong impact on electron acceleration in various schemes.^{17,18} Concerning the present scheme, since a laser pulse is always transversely inhomogeneous in practice, the amplitude of the wake field generated by the first pulse is also transversely inhomogeneous. As a result, its phase modulation on the second pulse also becomes inhomogeneous (here we assume that the wake field generated by the first pulse is at a low amplitude so that one can neglect the relativistic effect¹⁹ which tends to produce a horseshoe structure in electron density when the amplitude of the wake field is high enough). Therefore, for the same transverse profiles, one expects that the inhomogeneity of the cross-modulated laser wake field is larger than the normal laser wake field. On the other hand, when the amplitude of the wake field is amplified to a certain level, transverse wave breaking occurs.²⁰ The transverse wave breaking develops at a lower amplitude than that for longitudinal wave breaking in 1D geometry. As a result, for the same maximum laser intensities and pulse durations, one expects that the electron acceleration through the present scheme in 2D simulations can only achieve a

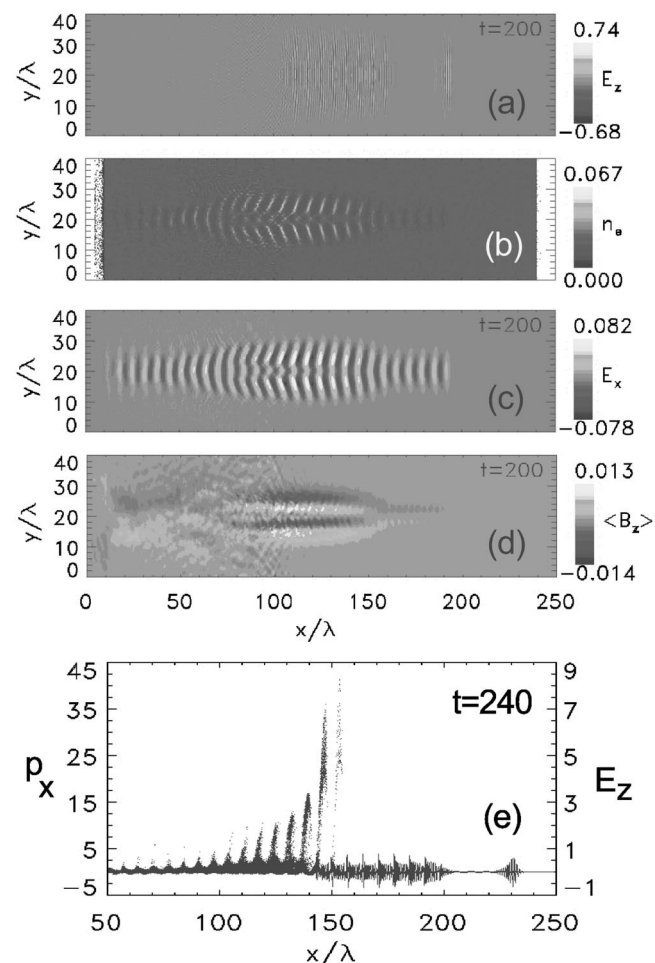


FIG. 6. Snapshots of 2D PIC simulation for initial plasma density $n_0/n_c=0.02025$, and pulse profiles with $a_{01}=0.8$, $a_{02}=0.5$, $\tau_1=7$, $\tau_2=20$, $\tau_0=50$, and beam diameter of 14λ for both pulses. (a) The transverse field; (b) the electron density; (c) the longitudinal electric field; (d) the quasistatic magnetic field; (e) the electron distribution in the longitudinal phase space (dots) and the laser field distribution on the axis (solid line).

lower level than that observed in 1D simulations. To confirm this, we have conducted 2D PIC simulation, taking the transverse profiles of both pulses to be Gaussian.

To reduce the time and spatial scale for the benefit of saving computer memory and computational time, we have used relative large plasma density of $0.02n_c$. The simulation box is $250\lambda \times 40\lambda$, with nine particles per cell each for electrons and ions and 10 cells in a laser wavelength. Figure 6(a) shows a snapshot of the laser fields at $t=200$ laser cycles, obtained for laser pulses with s -polarized incidence (i.e., its electric field component is perpendicular to the incident plane). As is obvious, it is strongly modulated at the period of a plasma wavelength. Figures 6(b)–6(d) show, respectively, the electron density, longitudinal field and the quasi-static magnetic field associated with the excited plasma wave at $t=200$. Transverse wave breaking has set in at this time. As a result, bunches of electron beams separated in transverse space are generated. This is most obvious from the generated quasi-static magnetic field. Figure 6(e) shows that accelerated electrons are located in the region occupied by the second pulse and co-move with it. This is similar to what

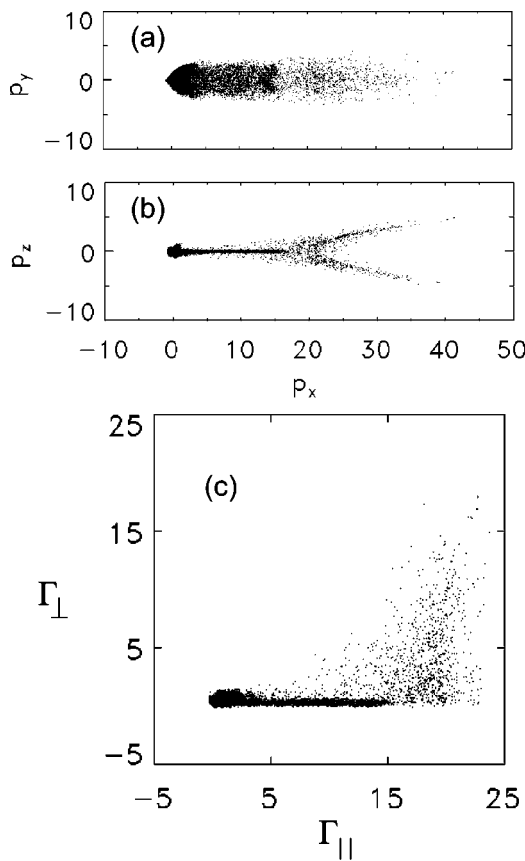


FIG. 7. (a) Electron distributions in phase space (p_x, p_y) at time $t=240$; (b) electron distributions in phase space (p_x, p_z) at the same time; (c) energy gain from the longitudinal field versus that from the transverse fields at the same time. The parameters for the laser pulses and plasma are the same as for Fig. 6.

is observed in the 1D case. Owing to the 2D structure mentioned above, the maximum energy of electrons observed in 2D simulations is smaller than in 1D simulations for the same laser pulse and plasma parameters, as shown in Fig. 4(b).

Figures 7(a) and 7(b) show the electron distributions in momentum space, illustrating that the accelerated electrons move dominantly in the laser propagation direction, which is similar to the 1D simulations. As in 1D simulations, one can calculate the electron energy gains from the longitudinal and transverse fields separately in 2D simulations, even though the meaning of the transverse and longitudinal fields is not strict in 2D geometry and they are somewhat mixed due to the finite transverse size of laser beams. Figure 7(c) shows that electrons with modest energy obtain their energy dominantly from the longitudinal field, while the most energetic electrons gain energy both from the excited plasma wave and the laser field of the second laser pulse. The latter is different from the 1D simulations shown above.

IV. SUMMARY

By use of PIC simulations, we have demonstrated that high-amplitude plasma waves can be generated efficiently with two laser pulses co-propagating in plasma at moderate intensities through XM-LWFA. In this scheme, the first

pulse is an ultrashort pulse to generate a seed wake field and the second pulse is relatively long such as a few plasma oscillation periods to amplify the seed wake field through a cross-phase modulation process. As compared to the normal SM-LWFA scheme, the present scheme allows for high-amplitude plasma-wave generation within relatively small plasma dimensions, with moderate light intensities, as well as in a controlled way. Also it releases the necessity of using ultrashort-intense laser pulses in the standard LWFA scheme and provides an easy way to realize the multiple-pulse scheme for high-amplitude plasma-wave generation.⁶ Our simulations have shown that it is a very efficient way of transferring laser energy to plasma waves for particle acceleration. Plasma wave-breaking, electron acceleration, and energy saturation are observed both in 1D and 2D PIC simulations with laser pulses at moderate intensities. It is found that 2D effects tend to reduce the energy saturation level in comparison with 1D simulations owing to the set-in of transverse wave breaking. Since there is no necessity for any particular timing between the two pulses used in this scheme, it may be realized relatively easily in experiments.

ACKNOWLEDGMENTS

Z.M.S. wishes to thank Professor T. Yamanaka for his support during his research stay at the ILE, Osaka University, Dr. T. Zh. Esirkepov for helpful discussions with the PIC code development, and the Comp-group staffs at ILE for their computation support.

This work was supported in part by the Bai-Ren-Ji-Hua Program of the Chinese Academy of Science and the National Natural Science Foundation of China (Grant No. 10105014).

¹M. N. Rosenbluth and C. S. Liu, Phys. Rev. Lett. **29**, 701 (1972); T. Tajima and J. M. Dawson, *ibid.* **43**, 267 (1979); L. M. Gorbunov and V. I. Kirsanov, Sov. Phys. JETP **66**, 290 (1987); for a review, see E. Esarey, P. Sprangle, J. Krall, and A. Ting, IEEE Trans. Plasma Sci. **PS-24**, 252 (1996).

²E. Esarey, J. Krall, and P. Sprangle, Phys. Rev. Lett. **72**, 2887 (1994); N. E. Andreev, V. I. Kirsanov, and L. M. Gorbunov, Phys. Plasmas **2**, 2573 (1995); W. B. Mori, C. D. Decker, D. E. Hinkel, and T. Katsouleas, Phys. Rev. Lett. **72**, 1482 (1994); R. J. Kingham and A. R. Bell, *ibid.* **79**, 4810 (1997).

³P. Sprangle, E. Esarey, J. Krall, and G. Joyce, Phys. Rev. Lett. **69**, 2200 (1992); T. M. Antonsen and P. Mora, *ibid.* **69**, 2204 (1992).

⁴A. Ting, C. I. Moore, K. Krushelnick, C. Manka, E. Esarey, P. Sprangle, R. Hubbard, A. R. Burris, R. Fischer, and M. Baine, Phys. Plasmas **4**, 1889 (1997).

⁵D. Umstadter, J. K. Kim, and E. Dodd, Phys. Rev. Lett. **76**, 2073 (1996); E. Esarey, R. F. Hubbard, W. P. Leemans, A. Ting, and P. Sprangle, *ibid.* **79**, 2682 (1997); J. K. Kim, E. Dodd, and D. Umstadter, "Simulation of ultrashort electron pulses generated from laser-injection wake-field plasma waves," Phys. Rev. E (submitted).

⁶D. Umstatter, E. Esarey, and J. Kim, Phys. Rev. Lett. **72**, 1224 (1994); V. I. Berezhiani and I. G. Murusidze, Phys. Scr. **45**, 87 (1992); S. Dalla and M. Lontano, Phys. Rev. E **49**, R1819 (1994); G. Bonnaud, D. Teychenne, and J.-L. Bobin, *ibid.* **50**, R36 (1994).

⁷G. Shvets, N. J. Fisch, A. Pukhov, and J. Meyer-ter-Vehn, Phys. Rev. E **60**, 2218 (1999).

⁸D. L. Fisher and T. Tajima, Phys. Rev. E **53**, 1844 (1996).

⁹E. Esarey, A. Ting, and P. Sprangle, Phys. Rev. A **42**, 3526 (1990).

¹⁰Z.-M. Sheng, Y. Sentoku, K. Mima, and K. Nishihara, Phys. Rev. E **62**, 7258 (2000).

¹¹Z.-M. Sheng, J. X. Ma, Z. Z. Xu, and W. Yu, J. Opt. Soc. Am. B **10**, 122 (1993); Phys. Lett. A **176**, 333 (1993).

- ¹²Z. M. Sheng, J. Meyer-ter-Vehn, and A. Pukhov, Phys. Plasmas **5**, 3764 (1998).
- ¹³T. Zh. Esirkepov, Comput. Phys. Commun. **135**, 144 (2001); J. Villaseñor and O. Buneman, *ibid.* **69**, 306 (1992).
- ¹⁴E. S. Dodd and D. Umstadter, Phys. Plasmas **8**, 3531 (2001); T.-W. Yau, C.-J. Hsu, H.-H. Chu, Y.-H. Chen, C.-H. Lee, J. Wang, and S.-Y. Chen, *ibid.* **9**, 391 (2002).
- ¹⁵C. Gahn, G. D. Tsakiris, A. Pukhov, J. Meyer-ter-Vehn, G. Pretzler, P. Thirolf, D. Habs, and K. J. Witte, Phys. Rev. Lett. **83**, 4772 (1999); A. Pukhov, Z.-M. Sheng, and J. Meyer-ter-Vehn, Phys. Plasmas **6**, 2847 (1999).
- ¹⁶A. I. Akhiezer and R. V. Polovin, Sov. Phys. JETP **3**, 696 (1956); Z. M. Sheng and J. Meyer-ter-Vehn, Phys. Plasmas **4**, 493 (1997).
- ¹⁷D. W. Forslund, J. M. Kindel, W. B. Mori, C. Joshi, and J. M. Dawson, Phys. Rev. Lett. **54**, 558 (1985).
- ¹⁸K.-C. Tzeng, W. B. Mori, and T. Katsouleas, Phys. Rev. Lett. **79**, 5258 (1997).
- ¹⁹S. V. Bulanov, F. Pegoraro, and A. M. Pukhov, Phys. Rev. Lett. **74**, 710 (1995).
- ²⁰S. V. Bulanov, F. Pegoraro, A. M. Pukhov, and A. S. Sakharov, Phys. Rev. Lett. **78**, 4205 (1997).

Simulation study of conversion of laser energy into x rays in laser plasmas

W. Wang, Q. L. Dong, and J. Zhang^{a)}

Laboratory of Optical Physics, Institute of Physics, Chinese Academy of Sciences, Beijing 100080,
People's Republic of China

(Received 12 March 2002; accepted 7 June 2002)

A simulation study of the conversion process of laser energy into x rays from a gold foil target irradiated by a 1 ns laser pulse with 10^{14} W/cm^2 intensity at $0.35 \mu\text{m}$ wavelength is presented. The thickness of the foil is optimized to achieve high conversion efficiency on its rear side. The optimized foil can provide unique plasmas with a low spatial gradient of temperature and density.

© 2002 American Institute of Physics. [DOI: 10.1063/1.1497973]

I. INTRODUCTION

With the rapid increase of laser intensities, it has become possible to simulate some astrophysical processes by controlling the conditions of laser-produced plasmas.^{1–3} Most of the astrophysical plasmas are in local thermodynamic equilibrium (LTE) conditions. X rays converted from laser energy in laser–plasma interaction can be used to irradiate on the target in order to generate a LTE plasma which is ideal for simulating astrophysical processes.

The conversion of intense laser pulses into incoherent x-ray radiation during the heating of high Z material has been a subject of experimental and theoretical research since the 1970's.^{4–10} The effects of various parameters, such as intensity, wavelength, and pulse duration of the incident laser pulse on the x-ray conversion, have been studied in detail.^{11–15} In this paper, we present a detailed simulation study of the effect of target thickness on the conversion of laser energy into soft x rays by using the one-dimensional (1-D) radiation hydrodynamic code MULTI,¹⁶ which assumes planar geometry symmetry. The laser-produced plasma is mainly divided into an optically thin conversion zone and an optically thick re-emission zone. This can be distinguished by consideration of the characteristics of both temperature and density in these two zones. Optimized thickness of the gold foil as a converter target is obtained. Taking the converter target as an intense x-ray source, we can get a unique plasma with a low spatial gradient of temperature and density. This is important for simulation of astrophysical process in laboratories.

II. NUMERICAL SIMULATIONS

Our numerical simulations are based on the 1-D radiation hydrodynamic code MULTI. It is a fully implicit code that solves Lagrangian hydrodynamics together with multigroup radiation diffusion. It describes radiation diffusion coupled with hydrodynamic motion and includes laser deposition by the inverse bremsstrahlung absorption with a dump at the critical density with a flux-limited electron heat conduction, tabulated equations of state, and nonlocal thermodynamic

equilibrium atomic physics, which is of importance in expanding laser-heated plasmas. Basic equations for planar geometry of the target are as follows:¹¹

$$\frac{\partial v}{\partial t} - \frac{\partial u}{\partial m} = 0, \quad (1)$$

$$\frac{\partial u}{\partial t} + \frac{\partial p}{\partial m} = 0, \quad (2)$$

$$\frac{\partial e}{\partial t} + p \frac{\partial v}{\partial t} = - \frac{\partial S_L}{\partial m} - \frac{\partial S_e}{\partial m} - \sum_k \frac{\partial S_k}{\partial m}, \quad (3)$$

$$\frac{\partial S_k}{\partial m} = q_k - c \kappa_{P,k} U_k, \quad (4)$$

$$c g_k^2 \frac{\partial U_k}{\partial m} = - \kappa_{R,k} S_k, \quad (5)$$

where m is Lagrangian mass coordinates, v is specific volume ($v = 1/\rho$, ρ = mass density), p and u are pressure and velocity respectively, and e is specific internal energy. The term $\partial S_L / \partial m$ represents the energy (per mass and time) deposited by the laser; $\partial S_e / \partial m$ term represents the energy conduction through electron heat flux (per unit mass and time) and $\partial S_k / \partial m$ represents the radiation flux transport (per unit mass, over different energy groups). q_k is the heat flux and U_k the radiation energy density. $\kappa_{P,k}$ and $\kappa_{R,k}$ are the Planck and Rosseland opacities, respectively. The code allows for two separate temperatures, namely electron temperature T_e and radiation temperature T_{rad} . When the radiation field is under an equilibrium condition, the radiation temperature can be derived from the radiation energy density U :¹⁷

$$T_{\text{rad}} = \left(\frac{U}{\sigma} \right)^{0.25}, \quad (6)$$

where $\sigma = 137 \text{ erg/cm}^3/\text{eV}^4$.

It is worthy of note that there are some limitations for a one-dimension simulation code, which may be the reason for some discrepancies in comparing the experiment results with the numerical simulations, because the planar target experiments may be affected by the lateral and plasma expansion when the laser spot size is very small. Mead *et al.*¹⁸ have carefully compared the one- and two-dimensional models to

^{a)}Author to whom all correspondence should be sent. Electronic mail: jzhang@aphy.iphy.ac.cn

evaluate the effects of the lateral thermal transport and divergence of the hydrodynamic blow-off, and treated two-dimensional effects with a 1-D code for a divergent geometry. This lateral effect has been also eliminated in the uniform irradiation of a spherical target with multiple laser beams¹⁹ in the experiment. Nevertheless, many of the calculations have shown that it is simple and justified to use the 1-D model for a general understanding of the conversion processes of laser energy into x rays in the plasmas.

In our simulation study, we consider the case as follows: a gold foil (solid density 19.3 g/cm³) is irradiated by 1 ns laser pulse with an intensity of 10¹⁴ W/cm² at 0.35 μm wavelength. The temporal pulse shape is a sine square $S_{L0}[\sin(\pi t/2\tau)^2]$ and the electron flux heat limiter is taken as 0.08. For the radiation transport, we define 20 nonequally spaced frequency groups at photon energies ($h\nu \leq 5$ keV), taking into account the spectral characteristics of the gold ions.

A steady-state approximate to describe the absorption and emission coefficient of x rays is used in our calculation, which can make the emission and absorption of x-ray radiation to be defined by the local value of the temperature and density if the hydrodynamic time scale of density and temperature variation is larger than the electron ionization time. Otherwise rate equations for the atomic processes have to be solved simultaneously with the hydrodynamic equations. The tables of the state equation and Rosseland and Planck mean opacities from the SESAME equation of state and opacity library¹⁶ are required as input data by this code, which is of greater advantage in saving computing time than being calculated directly through rate equation. The effects of the nonlocal thermodynamic equilibrium atomic physics in the expanding heated high Z plasmas have been found to be important in determining the characteristics of the plasmas and emission.^{8,20,21} Non-LTE parameters that were calculated independently using atomic physics modeling (SNOP)²² are used for the plasma corona region in our simulation.

III. RESULTS AND DISCUSSION

A. The different zones of laser-produced plasmas

When a high power laser pulse irradiates on a solid target with high Z, an expanding hot plasma is quickly formed on the front surface of the target. The deposited laser energy is transported into the cold material by a number of mechanisms, such as the electron heat conduction and radiation diffusion, etc. To gain further understanding and physical insights of the interaction processes of the laser with high Z material, the plasmas are divided into the conversion zone, the re-emission zone, the shock wave zone, and the undisturbed solid owing to the large density difference.

The simulation study of the variations of both electron temperature and density versus the Lagrangian mass coordinate at different times is performed using the MULTI code. The laser pulse comes from the right-hand side. Its parameters are: intensity of 10¹⁴ W/cm², pulse duration of 1 ns, wavelength of 0.35 μm. The gold foil is massive and its thickness is 1.0 μm. Three regions with different character-

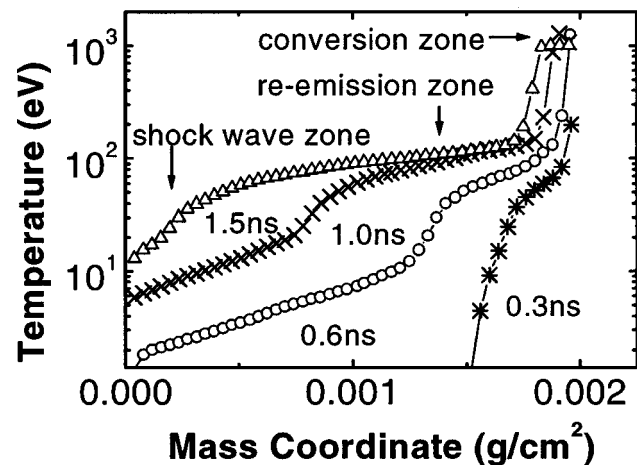


FIG. 1. Electron temperature vs mass coordinate at different times. The laser comes from the right. The laser parameters are intensity 10¹⁴ W/cm², wavelength 0.35 μm, and full width at half maximum of laser pulse 1 ns. The gold foil thickness is 1.0 μm. The electron heat flux limiter is 0.08 and the computation mesh number is 50 cells.

istics are clearly visible in Figs. 1 and 2. The incident laser is mainly absorbed and converted into x rays in the conversion zone.

The conversion zone has the highest temperature (~1 keV) and the lowest density (<0.1 g/cc) of all zones. The electron heat conduction is the important transport mechanism in this region. It is optically thin for emitted thermal x rays, and thus radiates equally toward the front as well as the rear of the target, and is in the non-LTE condition.

The radiation emission toward the rear is absorbed in the re-emission zone. Its characteristics are determined by radiation heat conduction, i.e., by the diffusion of the radiation toward the rear, so we often call this zone the radiation heat wave zone, whereas the electron transport is negligible in this zone. The temperature in the re-emission zone is relatively low (~100 eV), and the density (0.1–1 g/cc) is much higher than that in the conversion zone. The re-emission zone is under LTE condition and is optically thick for its own thermal radiation and emits blackbody radiation through

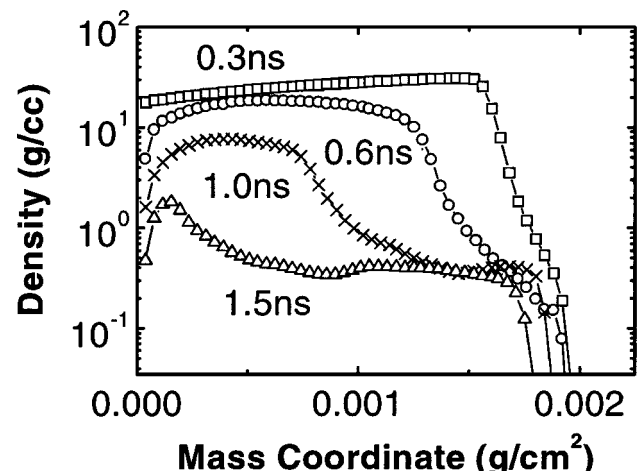


FIG. 2. Density vs mass coordinate at different times for the same conditions as in Fig. 1. The laser comes from the right.

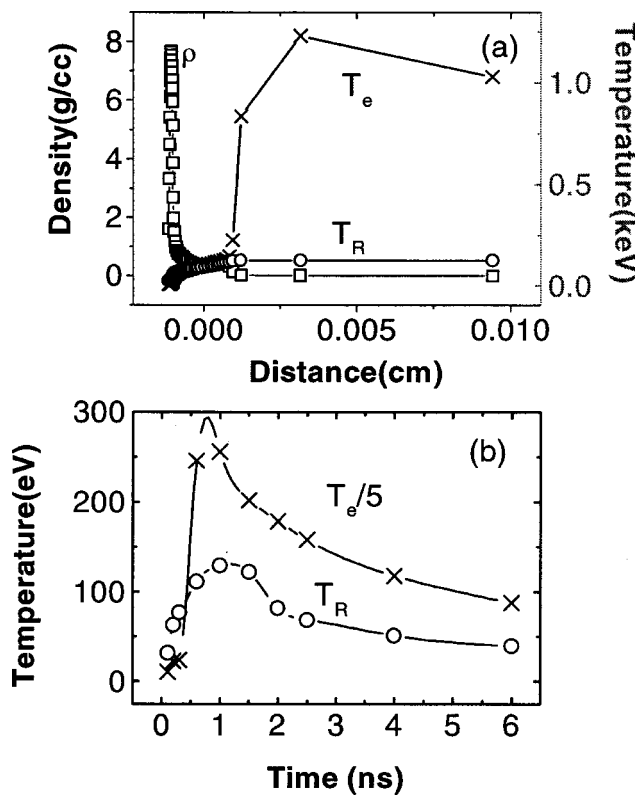


FIG. 3. (a) Both the radiation temperature and the electron temperature, and density vs the spatial coordinate at laser peak time (1 ns). (b) Spatial maximum of the electron temperature and radiation temperature vs time. The conditions are as in Fig. 1. The laser comes from the right.

conversion layer into the vacuum. In the shock wave region that takes up the recoil momentum of the expanding material, the energy transfer is very small and can be neglected because of the high density (>1 g/cc). It is therefore not of direct relevance to the conversion problems.

Of importance for the emission of radiation are the first two zones. In the simulation study of the x-ray emission, we use the CE (corona equilibrium) model in the low density conversion zone and the LTE model in the higher density re-emission zone in order to be similar to the experimental conditions, especially in the case of a high Z target irradiated by an intense laser. There are some differences between the two limits clarified by Eidmann *et al.*¹⁰ In the limiting case of corona equilibrium, the specific emission coefficient is approximately proportional to the density, which is the reason why the temperature in the corona region is very high, because the materials at low densities are not effectively cooled by the loss of energy in the form of thermal radiation as they expand. However, the specific emission is independent of the density in LTE case, thus a fluid element will continue to radiate at the same rate as it expands into vacuum. This may cause the temperature to be much lower in LTE than in CE conditions.

To distinguish the conversion zone from the re-emission zone, the profiles of the radiation temperature versus the space and time are obtained. The characteristics of the radiation temperature in those zones are analyzed (the conditions are as in Fig. 1). Figure 3(a) is the spatial distributions of the

radiation temperature, the electron temperature, and density versus spatial coordinate at peak power time ($t=1$ ns). It shows that the radiation temperature is constant in the optically thin conversion layer. However, it begins to decrease in the optically thick re-emission region that is influenced by absorption of x rays, and reaches the lowest values in the shock wave zone. Based on these characteristics, it is easy to distinguish these three zones. In Fig. 3(b), we simulate the temporal behavior of the electron temperature and the radiation temperature. We note that the rise time of both the electron temperature and the radiation temperature is quite close to that of the incident laser pulse, whereas the fall time is longer, since the plasma continues to radiate its internal energy as it cools. The dominating cooling processes are radiation cooling and hydrodynamic expansion. The highest radiation temperature can reach to about ~ 128 eV at the laser peak time (1 ns) in this case.

B. Optimization of the foil thickness as a converter

It is of great interest to study the converter target as an intense x-ray source for various applications, such as in indirect driven inertial confinement fusion, x-ray laser studies, astrophysics and material properties, etc. The essential features of a converter are that it should be thick enough to absorb most of the incident laser energy to produce more x-ray emission, but be thin enough for efficient x-ray radiation transport to the rear side of the target. Optimization of the thickness of a converter target has to take into account these two aspects.

We assume the conversion fraction is α_c in the conversion zone, which is equally radiated in the two directions. When x rays propagate toward the rear, they are absorbed and some fraction $0 \leq \gamma \leq 1$ of the absorbed x rays is re-emitted in the re-emission region. The x-ray conversion fraction has been expressed by $\eta_F = (1 + \gamma)\alpha_c/2$ at the front side of the target and $\eta_R = (1 - \gamma)\alpha_c/2$ at the rear side under the steady-state approximation conditions by Nishimura *et al.*¹⁹ When the thickness of the foil is so thin that it only consists of the conversion layer, the nearly symmetrical x-ray conversion fractions of $\alpha_c/2$ from each side of the target can be obtained. Under these conditions, the re-emission coefficient γ can approach zero.

Figure 4(a) is the calculation of the conversion efficiency of x rays (the ratio of the x-ray radiation flux to absorbed laser flux) from the laser pulse interacting with the gold foil with different thickness. The simulation study shows that the rear emission trends to be nearly equal to the front emission if the gold foil is very thin. With thicker gold foil, the front emission increases whereas the rear-side emission significantly decreases.

The laser light is efficiently absorbed at the position close to or below its critical density by strong inverse bremsstrahlung collision absorption which heats the plasma electrons, leading to a temperature of several kiloelectron volts. The deposited laser energy is transported into the cold material by the electron heat conduction and radiation diffusion, etc., converted by electron-ion collisions into excitation that leads to x-ray emission, and converted hydrodynamically

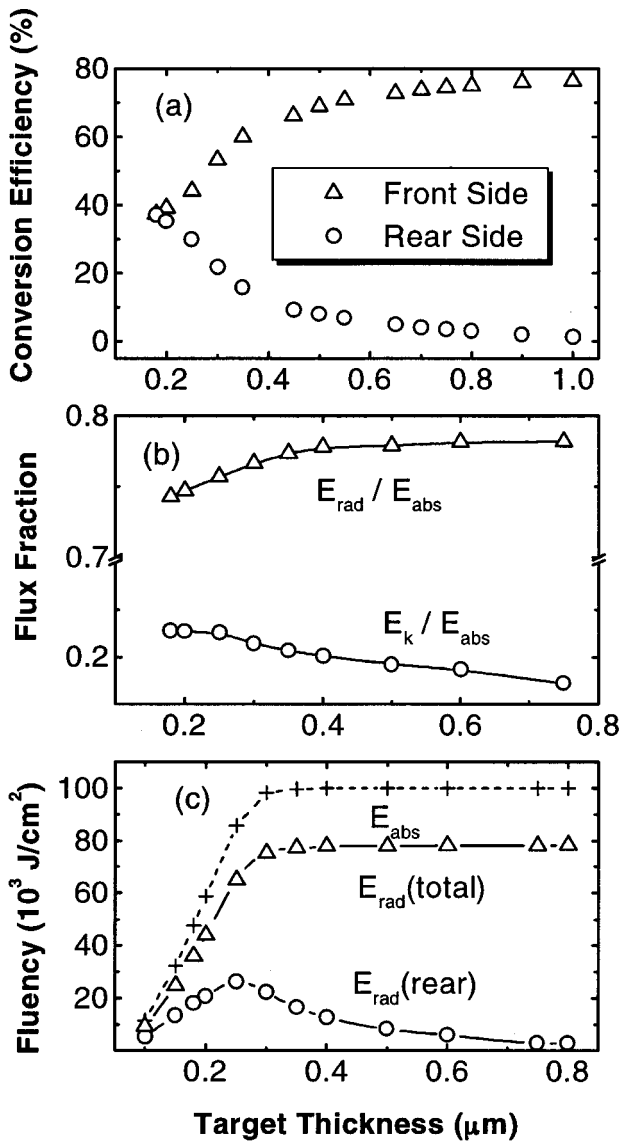


FIG. 4. (a) Conversion efficiency both on the front side and the rear side vs target thickness. (b) The variation profile of the fraction of the total x-ray radiation flux (front+ rear) and the kinetic flux normalized to the absorbed laser flux, respectively, vs the foil thickness. (c) The effect of the target thickness on the absorbed laser flux and the x-ray radiation flux of the total and of the rear side, respectively. The laser parameters are as in Fig. 1.

into convection ion kinetic energy. Figure 4(b) is the variation profile of the fraction of the total x-ray radiation flux (front+ rear) and the kinetic flux normalized to the absorbed laser flux, respectively, versus the foil thickness. From the simulation results, we can see that the conversion fraction of the absorbed laser energy into the kinetic increases with the decrease of the foil thickness and there are more kinetic energies into outward coronal motion at the expense of heating of the foil and the resultant x radiation, which would ultimately lead to a decrease in x-ray conversion efficiency, especially at a sufficiently thin foil. For the thicker target, the fraction of both the kinetic energy and the x-ray radiation energy would trend to be constant.

Figure 4(c) is the simulation results of the effect of the target thickness on the absorbed laser flux and the x-ray radiation flux of the total and of the rear side, respectively. It

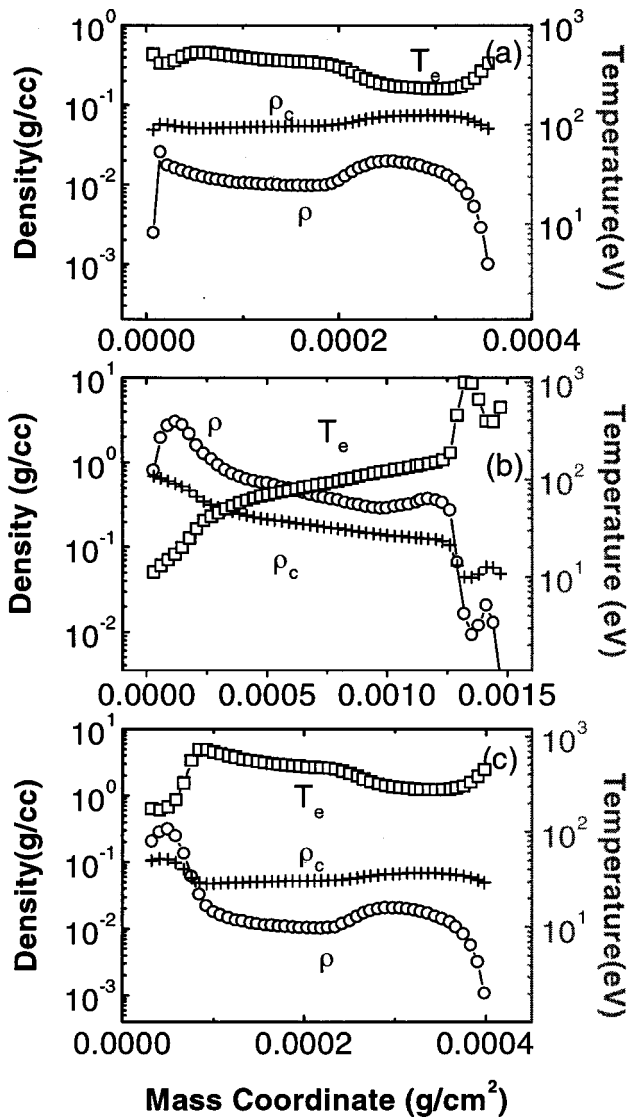


FIG. 5. Optimizing of the target thickness as a converter target. Density and temperature vs mass coordinate in (a) thin target with 0.18 μm , (b) massive target with 0.75 μm , and (c) medium target with 0.25 μm . The laser parameters are as in Fig. 1. The laser comes from the right.

shows that both the absorbed laser flux and the total x-ray radiation flux increase with foil thickness, more rapidly for sufficiently thin foil than the thick foil, and trend to be constant over about 0.25 μm . However, the x-ray radiation flux at the rear surface increases in quite small thickness and reaches to the maximum at about 0.25 μm thickness and then begins to decrease with increasing of the foil thickness, thus it is dependent on both the laser deposition energy and the x-ray conversion efficiency of the rear side.

Figures 5(a), 5(b), and 5(c) are, respectively, the simulation results of the spatial variation of both density and electron temperature at the laser peak time (1 ns) with three different thickness (0.18, 0.25, and 0.75 μm) gold foils irradiated by the laser pulse.

When the foil is quite thin [see Fig. 5(a) (0.18 μm)], we can see that the foil rapidly expands at the beginning of the laser pulse and the density becomes very low (< 0.1 g/cc), lower than the critical density ρ_c ($\rho_c = n_c m_i z_i$ here m_i and z_i

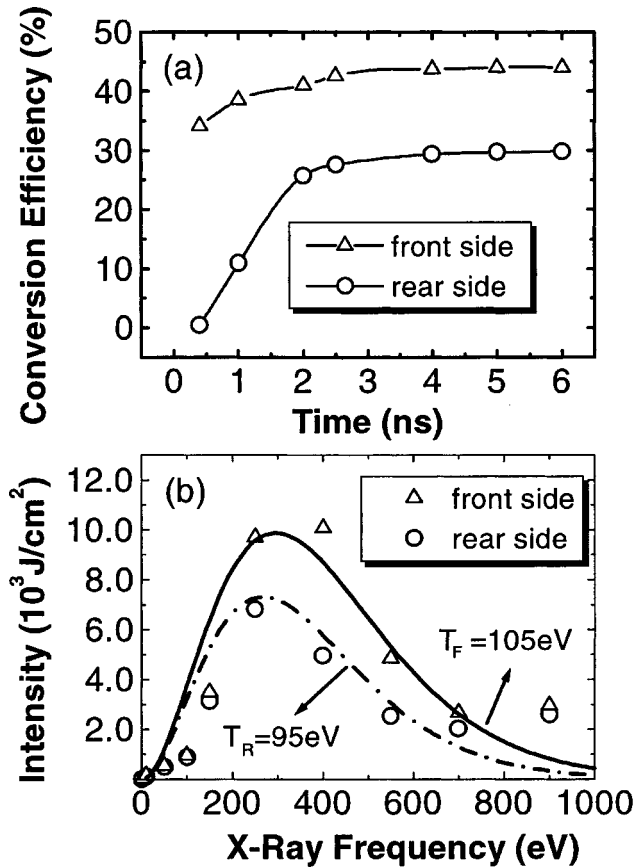


FIG. 6. (a) The profile of the conversion efficiency vs time. (b) Subkiloelectron volt x-ray spectrum distribution both from the front and the rear vs the frequency (<1 keV) out of 20 groups. The solid line is the Planckian spectrum compared with the x-ray spectrum on the front side, and the dash dot line is the Planckian spectrum compared with the x-ray spectrum on the rear side. The laser parameters are as in Fig. 1 with $0.25\ \mu\text{m}$ gold foil.

are the ion mass and charge number, respectively, and n_c is the electron number density given by the condition that the plasmas frequency equals the laser frequency ν_L , $n_c = \pi \nu_L m_e / e^2$, and there is no critical density interface to be formed in this case and the plasma is almost transparent for the incident laser light. Although the x-ray conversion efficiency at the rear side is high (41%), the x-ray radiation flux of the rear is very low because only a small portion of the incident laser flux is absorbed (32%); most of laser flux is transmitted through the foil.²³

Figure 5(b) ($0.75\ \mu\text{m}$) is for a massive target, and it shows that the radiation heat wave does not reach the rear side of the target. The density in the shock wave region near the rear side is close to or even higher than the solid density (≥ 1 g/cc). In this case, the gold foil is thick enough to absorb not only all of the laser energy but also the radiation generated in the conversion zone, which results in the conversion efficiency at rear side being very small (< 2.96%).

Figure 5(c) ($0.25\ \mu\text{m}$) is in the condition that the thickness of the foil is in the medium range, where the plasma only consists of the conversion layer and a part of the radiation heat wave (RHW) zone. We can see that in this case the foil is thick enough for the existence of a narrow RHW zone in the target, which can result in the matter density being

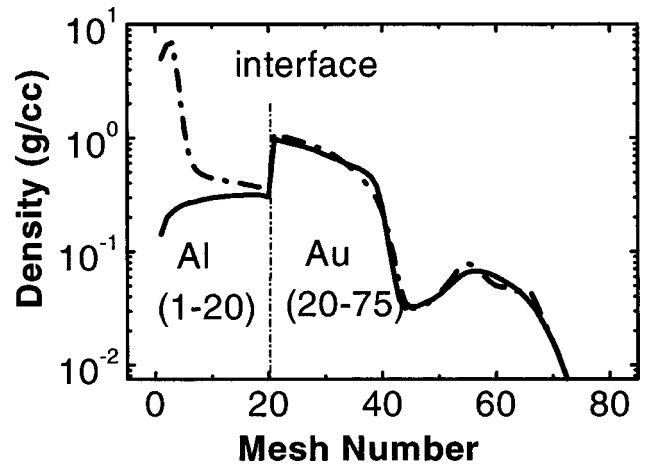


FIG. 7. Density vs mesh number for a composite target of the sample and the converter with different thicknesses. The solid line and dash dot line are, respectively, for the sample aluminum foil thickness of 2.0 and $3.0\ \mu\text{m}$ with the corresponding gold converter thickness of $0.25\ \mu\text{m}$. The mesh number is defined for the sample (1–20) and the converter (20–75). The laser parameters are as in Fig. 1. The laser comes from the right.

high enough (0.1 – 1 g/cc) to absorb most of the laser energy to produce more x-ray radiation; and the foil is thin enough to ensure the conversion efficiency of the rear side is high.

By optimizing the thickness of the gold foil, the thickness of the converter target can be obtained, which is about $0.25\ \mu\text{m}$ in our condition, corresponding to a laser absorption coefficient of 0.86, and the x-ray conversion efficiency at the rear is 30.6%.

In addition, we obtain subkiloelectron volt x-ray conversion efficiency at different times and the spectral output on the front surface as well as the rear surface of the target by using this code. Figure 6(a) is the profile of the soft x-ray conversion efficiency versus time. It can be seen that the conversion efficiency increases rapidly in the initial stage of the laser pulse and tends to be saturated after the laser turns off. Figure 6(b) compares the time-integrated subkiloelectron volt x-ray energy spectrum toward the front and the rear of the converter foil, whose spectrum maximum is about 250

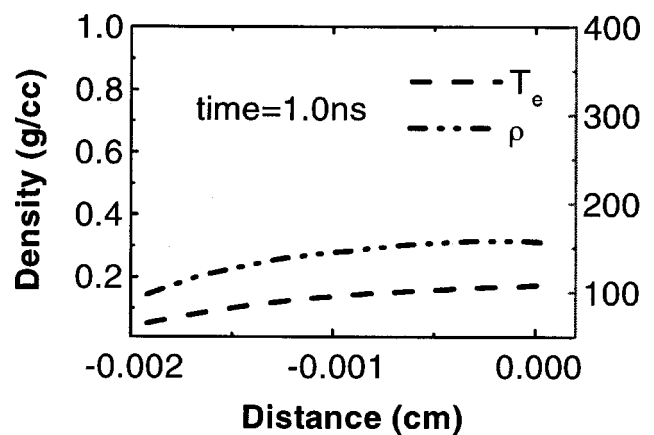


FIG. 8. The distribution profile of the density and the temperature vs space coordinate in an aluminum sample with $2.0\ \mu\text{m}$ radiation heated by a gold converter target with $0.25\ \mu\text{m}$ is presented. The laser conditions are as in Fig. 1. The laser comes from the right.

eV, with the Planckian spectral distributions. It shows that the x-ray spectra approach the spectral distribution of the blackbody radiation. The radiation temperature at $h\nu = 250$ eV estimated from the blackbody radiation is about 105 eV at the front side and 95 eV at the rear.

C. Radiation heating by a converter

The converter target as an intense, approximately Planckian x-ray source may be used for production of a uniform plasma with low gradient of temperature and density, which is of importance for the testing of theoretical calculations of opacities, radiation transfer, and dense plasma effects in laboratory astrophysics.

The simulation study of the plasma conditions of a target heated by x rays from a converter target is performed. The composite target consists of an aluminum foil sample and a gold foil converter. The profiles of the electron temperature and the matter density versus mesh number are shown in Fig. 7. The aluminum foil thickness is 2.0 and 3.0 μm , respectively, with a 0.25- μm -thick gold foil target. The total mesh number is defined to be 75 (1–20 meshes refer to the aluminum foil, 20–75 meshes refer to the gold foil), the laser parameters are a wavelength of 0.35 μm , intensity of 10^{14} W/cm^2 and 1 ns of pulse duration. The results show that the shock compression begins to turn up and leads to the production of the large density gradient in the sample foil if the thickness of the sample foil is not thin enough. According to our calculation, the maximum thickness of aluminum foil should be less than 2.4 μm in order to obtain a uniform plasma when the converter thickness is 0.25 μm .

Figure 8 shows the distribution of the temperature and density of plasma generated in the aluminum foil with 2.0 μm thickness heated by the x rays from a gold converter target with 0.25 μm thickness, and it is clearly seen that the spatial gradient of the temperature and density of the plasma is very low (the variation range is about 0.2–0.3 g/cc for the matter density and is 65–110 eV for the electron temperature). This is required in simulating astrophysical processes in laboratories.

IV. SUMMARY AND CONCLUSIONS

We have carried out a detailed simulation study of the conversion of laser energy into x rays from an Au foil target of different thicknesses irradiated by a laser pulse with 10^{14} W/cm^2 intensity at 0.35 μm wavelength in 1 ns pulses using a one-dimensional Lagrangian code MULTI. The simulation study of the characteristics of the radiation temperature in the plasma is performed. The results show that the radiation temperature is constant in the optical thin conversion layer, but it decreases in the optical thick radiation heat

wave (RHW) zone. Based on these characteristics, it is easy to distinguish the conversion layer from the RHW region. The effects of the target thickness on the conversion efficiency are investigated. Optimized thickness of the target as a converter is obtained. The x-ray spectral profiles are obtained and the results show that the x-ray spectral distribution is similar to the Planckian distribution. Taking the gold converter target as an intense x-ray source, we can obtain a LTE plasma with a low spatial gradient of temperature and density.

ACKNOWLEDGMENTS

This work was jointly supported by the NNSFC (under Grant Nos. 19825110, 10005014 and 60078008), National Hi-tech ICF program, and the NKBRSF (under Grant No. G19999075206).

- ¹S. G. Glendinning, J. Colvin, S. Haan *et al.*, Phys. Plasmas **7**, 2033 (2000).
- ²J. S. Wark, S. J. Rose, P. K. Patel, A. Djaoui, O. Renner, A. Hauer *et al.*, Phys. Plasmas **4**, 2004 (1997).
- ³B. A. Remington, S. G. Glendinning, K. Estabrook *et al.*, AIP Conf. Proc. **426**, 551 (1998).
- ⁴R. L. Kauffman, D. W. Phillion, and R. C. Spitzer, Appl. Opt. **32**, 6897 (1993).
- ⁵P. Alaterre, C. Chenaïs-Popovics, P. Audebert, J. P. Geindre, and J. C. Gauthier, Phys. Rev. A **32**, 324 (1985).
- ⁶K. Eidmann and T. Kishimoto, Appl. Phys. Lett. **49**, 377 (1986).
- ⁷H. N. Kornblum, R. L. Kauffman, and J. A. Smith, Rev. Sci. Instrum. **57**, 2179 (1986).
- ⁸P. D. Goldstone, S. R. Goldman, W. C. Mead *et al.*, Phys. Rev. Lett. **59**, 56 (1987).
- ⁹I. B. Földes, K. Eidmann, G. Veres, J. S. Bakos, and K. Witte, Phys. Rev. E **64**, 016410 (2001).
- ¹⁰R. Sigel, K. Eidmann, F. Lavarenne, and R. F. Schmalz, Phys. Fluids B **2**, 199 (1990).
- ¹¹K. Eidmann, R. F. Schmalz, and R. Sigel, Phys. Fluids B **2**, 208 (1990).
- ¹²P. Alaterre, H. Pepin, R. Fabbri, and B. Faral, Phys. Rev. A **34**, 4184 (1986).
- ¹³W. C. Mead, E. M. Campbell, K. Estabrook *et al.*, Phys. Fluids **26**, 2316 (1983).
- ¹⁴H. Nishimura, F. Matsuoka, M. Yagi, K. Yamada, S. Nakai, G. H. McCall, and C. Yamanaka, Phys. Fluids **26**, 1688 (1983).
- ¹⁵M. D. Rosen, D. W. Phillion, and V. C. Rupert, Phys. Fluids **22**, 2020 (1979).
- ¹⁶R. Ramis, R. Schmalz, and J. Meyer-ter-Vehn, Comput. Phys. Commun. **49**, 475 (1988).
- ¹⁷R. F. Schmalz, J. Meyer-ter-Vehn, and R. Ramis, Phys. Rev. A **34**, 2177 (1986).
- ¹⁸W. C. Mead, E. K. Stoner, R. L. Kauffman, H. N. Kornblum, and B. F. Lansinski, Phys. Rev. A **38**, 5275 (1988).
- ¹⁹H. Nishimura, Y. Kato, H. Takabe *et al.*, Phys. Rev. A **44**, 8323 (1991).
- ²⁰T. Mochizuki, T. Yabe, K. Okada, N. Ikeda, S. Kigel, S. Kiyokawa, and C. Yamanaka, Phys. Rev. A **33**, 525 (1986).
- ²¹W. C. Mead, S. V. Coggeshall, S. R. Goldman *et al.*, *Laser Interaction and Related Plasma Phenomena* (Plenum, New York, 1986), Vol. 7, p. 723.
- ²²K. Eidmann, EUR11930 EN, Inertial Confinement Fusion, edited by A. Caruso and E. Sindoni, Verenna, 6–16 September 1988.
- ²³P. Celliers and K. Eidmann, Phys. Rev. A **41**, 3270 (1990).

Emission of a hot electron jet from intense femtosecond-laser-cluster interactions

L. M. Chen,¹ J. J. Park,¹ K.-H. Hong,¹ J. L. Kim,² J. Zhang,³ and C. H. Nam¹

¹*Department of Physics and Coherent X-Ray Research Center, Korea Advanced Institute of Science and Technology, Taejon 305-701, Korea*

²*Korea Atomic Energy Research Institute, Taejon 305-600, Korea*

³*Laboratory of Optical Physics, Institute of Physics, Chinese Academy of Sciences, Beijing 100080, China*

(Received 28 March 2002; published 28 August 2002)

A directional hot electron jet with energy higher than 100 keV was generated along the laser propagation direction from Ar clusters irradiated with a laser pulse of duration 28 fs and intensity $1 \times 10^{17} \text{ W/cm}^2$. The hot electron jet was detected only with linearly polarized laser pulses, not with circularly polarized pulses. Channel betatron resonance is believed to be the main accelerating mechanism for this directional hot electron jet.

DOI: 10.1103/PhysRevE.66.025402

PACS number(s): 52.38.-r, 36.40.Vz, 33.80.Rv, 36.40.Gk

Hot electrons generated by intense laser pulses incident on rare gas targets have attracted much attention because of their relevance to advanced concept accelerators and radiation sources [1]. Recent development of ultrashort high-power lasers using the chirped pulse amplification technique has achieved laser intensity well above 10^{18} W/cm^2 , intense enough to drive ionized electrons to relativistic velocity. The ponderomotive force of intense laser field can result in relativistic self-focusing of the propagating laser beam and directional electron acceleration [1,2]. A high-energy electron beam can be generated mainly through two mechanisms. One is the laser wake-field acceleration (LWFA) [2], in which the ponderomotive force of a driving laser drives plasma waves quasiresonantly. This mechanism is considered dominant at low gas density and high laser intensity. The second acceleration mechanism is a direct laser acceleration (DLA) at the channel betatron resonance (CBR) [3], observed when transverse oscillation of electrons at betatron frequency matches the laser frequency. The DLA can be stimulated at comparatively lower intensity than LWFA, but at relatively high gas density [4].

The interaction of intense ultrashort laser pulses with van der Waals-bonded atomic clusters creates unique conditions for laser-matter interactions. The high local density within a cluster, coupled with low average-density gas, provides an effective coupling of the intense laser pulse with the interacting medium. It has been observed that cluster targets could absorb incident laser energy efficiently [5]. Efficient coupling of intense ultrashort laser pulses with cluster targets can generate high-temperature plasma with highly charged ions, and local electron density during the laser-pulse duration can be quite high since the plasma expansion is minimal. These interaction conditions can provide quite different environments, compared to those of gas targets, producing strong extreme ultraviolet (XUV) emission [6], along with high-energy electrons [7] and ions [8], or fusion neutrons [9]. In this Rapid Communication, we report on the observation of a hot electron jet emitted from atomic clusters irradiated with a femtosecond laser pulse at modest intensity ($1 \times 10^{17} \text{ W/cm}^2$). The polarization dependence of the hot electron jet emission indicates that the hot electron jet is generated through the DLA at CBR.

The experiments on the generation of hot electron jet were carried out with a chirped pulse amplification Ti:Sapphire laser operating at 820 nm at a repetition rate of 10 Hz. The laser delivered 28-fs, 30-mJ pulses. The Ti:Sapphire oscillator was operated in a long cavity mode (45 MHz) to minimize any leakage femtosecond prepulses. The linearly polarized laser beam was focused with a spherical mirror of 45-cm focal length, yielding a peak intensity of about $1 \times 10^{17} \text{ W/cm}^2$. A quarter-wave plate was used when a circularly polarized light was needed. Atomic Ar clusters were produced with a pulsed gas jet with a nozzle diameter of 0.2 mm. With sufficiently high backing pressure, clusters are formed in the gas jet flow due to the adiabatic cooling of a gas expanding into vacuum [10]. The jet was operated at a backing pressure up to 22 bars, and the gas jet could be cooled by passing the gas line through a liquid nitrogen reservoir that also cooled the nozzle tip [6].

The diagnostic used for the measurement of hot electron spectra was a 45° focusing magnetic spectrometer, placed in a permanent magnetic field of $B=650 \text{ G}$. An array of LiF thermoluminescent dosimeter (TLD) pieces (model GR-200F) was used as detectors. Recent development of ultra-sensitive LiF TLD provided thin TLD for hot electron detection [11]. The energy range of this instrument is from 7 keV to 1 MeV. Its energy resolution was better than 5%. The background of these TLDs that were heat-treated at 240 °C was less than $10 \mu\text{Gy}$ (1 Gy = the radiation dose of one joule of energy absorbed per kilogram of matter). For the measurement of the forward direction, we also piled up a stack of TLD pieces wrapped with 18-μm Al foil to detect hot electrons, which provided an electron spectrum after deconvolution. With an array of TLDs attached inside a hemisphere, the angular distribution of hot electron emission was measured. The electron energy reaching the TLDs was controlled by the thickness of Al foil wrapped around the TLD film. Soft x-ray emission was measured using a space-resolving, flat field XUV spectrometer [12]. We also used a calorimeter to measure a laser absorption rate in laser-cluster interactions and a visible charge coupled device to measure a plasma length.

Hot electron spectra were measured in the transverse and forward directions at a laser intensity of $1 \times 10^{17} \text{ W/cm}^2$ and Ar backing pressure of 20 bars. The gas jet was cooled down to a temperature of -70°C using a cooling reservoir [6]. Figure 1 shows that the hot electron energy in the transverse

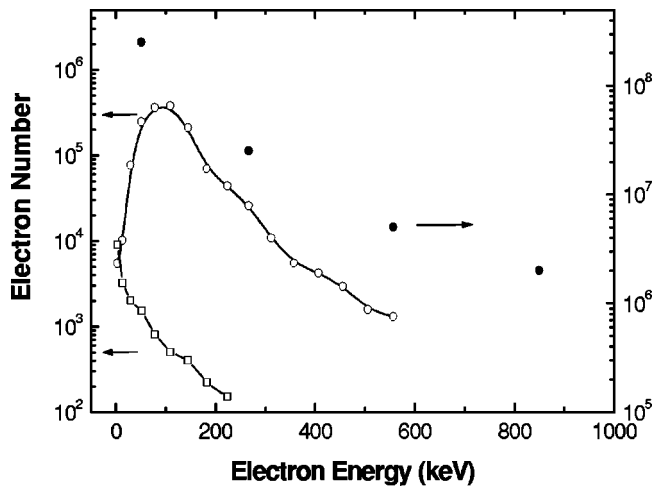
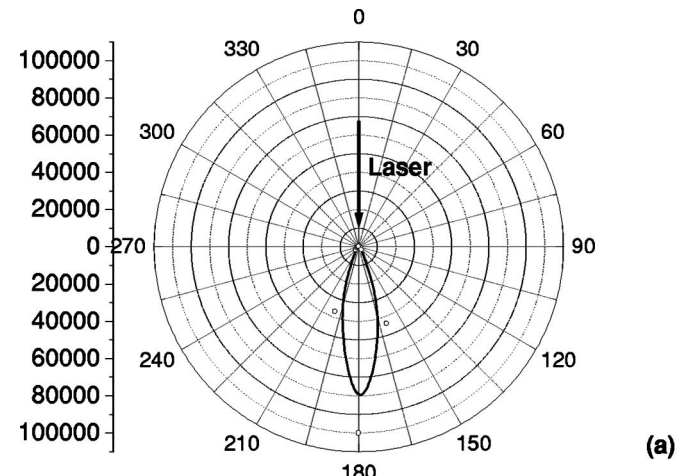


FIG. 1. Hot electron spectra, measured along the transverse direction (open circle) and longitudinal direction (solid circle), from Ar clusters irradiated with a laser pulse of duration 28 fs and intensity $1 \times 10^{17} \text{ W/cm}^2$. The electron spectrum (open square) taken with a femtosecond prepulse at 80 ps before the main pulse is also shown.

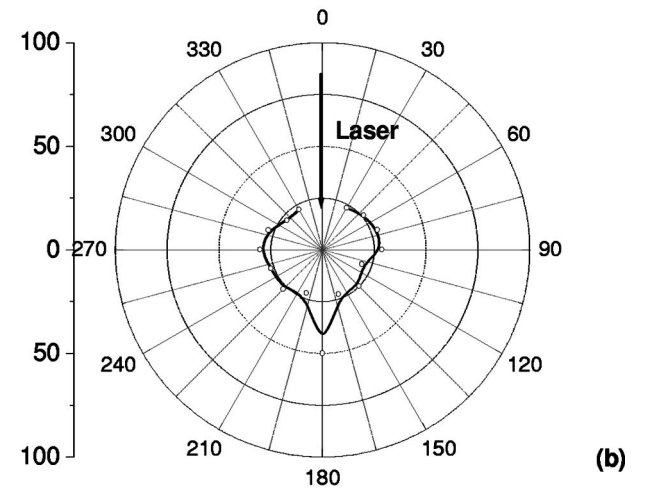
direction reached over 500 keV and that in the forward direction it extended much further. The number of electrons in the forward direction was larger by three orders of magnitude than that in the transverse direction when compared at the same solid angle of $4 \times 10^{-4} \text{ sr}$. Another important feature was a large difference in electron temperature. In the forward direction, hot electron temperature, fitted with a Maxwellian distribution, was as high as 250 keV; however, in the transverse direction, it was only 60 keV. Consequently, it clearly shows that electrons were strongly accelerated along the laser propagation direction.

Hot electrons would not be observed if clusters were disassembled before the arrival of a laser pulse. For verifying the hot electron generation through the interaction of intense laser pulse with clusters, a prepulse was introduced before the main pulse. A part (7%) of the laser pulse was split as the prepulse and injected 80 ps before the main pulse. This prepulse was still strong ($> 10^{15} \text{ W/cm}^2$) enough to heat and expand the clusters. Most clusters should be completely disassembled when the main pulse arrived 80 ps after the prepulse, according to the expansion time scale for clusters [13], especially at the central part of the focal spot. With the prepulse, the observed electron energy spectrum was quite different from the prepulse-free case. As shown in Fig. 1, the number of hot electrons and also the hot electron energy decreased dramatically. Thus, the observed hot electrons in the prepulse-free case were generated from irradiated clusters.

Using hemispherically installed detectors, the angular distribution of hot electron generation was measured to identify the directionality of hot electron generation. An array of TLD detectors wrapped with 18- μm -thick Al foil was placed on the inner side of a hemisphere. This Al foil could block energetic ions, scattered laser light, the majority of soft x rays, and electrons with energy below 50 keV. Thus, this system was suitable for the angular detection of energetic electrons.



(a)



(b)

FIG. 2. Angular distribution of hot electrons at the horizontal plane with energy over 50 keV. (a) Linearly polarized laser pulse with a duration of 28 fs and an intensity of $1 \times 10^{17} \text{ W/cm}^2$ was interacting with Ar clusters and (b) circularly polarized laser pulse with the same duration and intensity was incident on clusters.

Hot electron angular distribution, shown in Fig. 2(a), was obtained with the same experimental conditions as in Fig. 1. At this temperature and Ar backing pressure, an average cluster radius of about 40 Å was estimated from a Rayleigh scattering measurement [14]. The angular detection of hot electrons showed a sharply directional hot electron jet emission along the laser propagation direction. The angular divergence of the hot electron jet was less than 30° at FWHM for electrons with energy above 50 keV. The highest TLD dose was nearly several tens of mGy, which is about 1000 times higher than that in the transverse emission. When a circularly polarized laser pulse was incident on the cluster, noticeable hot electron jet emission was not detected on TLDs placed inside the hemisphere, as shown in Fig. 2(b), and also in the electron spectrometer, which means that the hot electron jet emission occurred only from the interaction of a linearly polarized laser pulse with atomic clusters.

It is of great importance to determine the emission mecha-

nism of the hot electron jet at our experimental conditions. Inverse bremsstrahlung cannot generate high-energy electrons at this modest laser intensity [15]. The result obtained with circularly polarized laser pulses also verifies this assertion. It is not possible for these electrons to come from photoelectrons generated through high-order above-threshold ionization (ATI) process because the ponderomotive energy (average kinetic energy of sinusoidally oscillating free electrons) is less than 6 keV at this intensity [16]. These photoelectrons cannot pass through the 18- μm Al foil and also the direction of the electron emission from ATI is along the laser polarization [17]. Only two kinds of mechanisms can produce hot electrons along the laser propagation direction—LWFA and CBR. With laser intensities well above 10^{18} W/cm^2 , LWFA can produce energetic electrons along the laser propagation direction [1,2]. With ion inertia providing an electrostatic restoring force, an intense laser field can drive a large amplitude electron plasma wave, converting the laser energy into a longitudinal electrostatic laser wake field. Propagating at nearly the speed of light, the electron plasma wave can accelerate electrons along the laser propagation direction. The laser intensity to stimulate the LWFA is much higher than the laser intensity used in our experiments. The observation that the emission of a hot electron jet was absent in the cases of the prepulse and of the circularly polarized pulse rules out the possibility of LWFA because the hot electron emission cannot be greatly affected by a prepulse or by laser polarization in the case of LWFA [2]. In addition, strong electron plasma waves for LWFA can be achieved when the laser-pulse duration is of the order of $1/\omega_p$, where ω_p is the plasma frequency. In particular, the electron density required for the quasiresonant condition to be established is given by $3 \times 10^{-9} \tau^{-2}$ [1], where the pulse duration τ is given in seconds and the density in cm^{-3} . For a 30-fs laser pulse, the optimum density will be $3 \times 10^{18} \text{ cm}^{-3}$ (similar to the case with prepulse), which is much less than the experimental conditions without prepulse ($\sim 5 \times 10^{19} \text{ cm}^{-3}$). This means that LWFA should be weak in this high-density domain. On the other hand, even if LWFA is weakly stimulated, the overoptimum density will generate a backward electric field and accelerate electrons backward, as shown in Ref. [4]. Therefore, LWFA cannot be the mechanism to generate the hot electron jet at our experimental conditions, i.e., linearly polarized laser-cluster interactions.

CBR, on the other hand, may occur in the interaction of high-local-density cluster with a laser at modest intensity. Relativistic self-channeling can occur when a laser power significantly exceeds the critical power for self-focusing, $P_{th} \approx 17(n_e/n_c)\text{GW}$ [18], where n_c and n_e are the critical density ($= 1.7 \times 10^{21} \text{ cm}^{-3}$ at 820 nm) and electron density, respectively. Pukhov *et al.* [3] showed in their simulation results that strong self-generated electric and magnetic fields could confine energetic electrons in the relativistic channel. Energetic electrons in the fields can make oscillations at the betatron frequency $\omega_\beta \approx \omega_p/(2\gamma)^{1/2}$ while drifting along the channel, in which γ is the relativistic factor. When ω_β coincides with the laser frequency seen by relativistically moving electrons, CBR occurs and results in energy transfer from laser light to electrons. The energy gain in the transverse

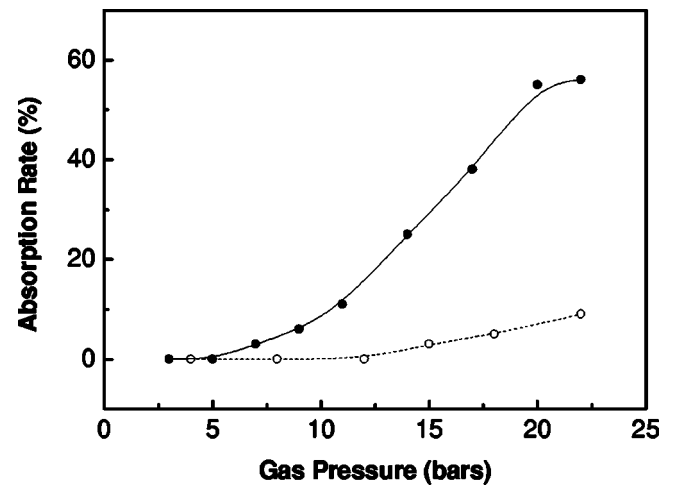


FIG. 3. Laser absorption as a function of the backing pressure of Ar in the case of a laser pulse without a prepulse (solid circle) and with a prepulse of 80 ps in advance (open circle). The laser intensity was $1 \times 10^{17} \text{ W/cm}^2$.

motion is then converted into an energy gain in the longitudinal direction via the $v \times B$ drift by a self-generated azimuthal magnetic field, which was generated by the current of accelerated electrons via ponderomotive expulsion of background plasma electrons from the channel [3].

The hot electron spectrum in the transverse direction in Fig. 1 shows that electrons with energy above 100 keV were generated. These energetic electrons could come from resonance absorption at the critical density layer [19,20], resulting from resonantly driven electrons in expanding clusters by the incident laser pulse. The electron spectrum in the case with a prepulse (7% splitting of the main femtosecond pulse) in Fig. 1 shows that hot electron number was dramatically reduced and electron energy dropped monotonically. Since the prepulse destroyed clusters, electron density could not reach the critical density needed for resonance absorption. These results indicate that the hot electrons in the case without prepulse were generated in the laser-cluster interaction through the resonance absorption process. This was also supported by an energy absorption measurement. Figure 3 shows the laser absorption by Ar targets with respect to different backing pressure. The absorption of laser light was more than 50% at a backing pressure of 20 bars. But in the case with prepulse, the interaction became much weaker and the absorption was less than 10%. Thus, the experimental results show that the efficient coupling of laser and cluster generates energetic electrons through resonance absorption. The energy of the electrons can be enhanced further through CBR under appropriate conditions.

For the stimulation of CBR the laser power must exceed the critical power for laser self-channeling, which depends on electron density. The gas density at our experiment was $6 \times 10^{18} \text{ cm}^{-3}$. At the applied laser intensity of $1 \times 10^{17} \text{ W/cm}^2$, strong emission from Ar^{8+} ions were observed [14], providing an average electron density close to $5 \times 10^{19} \text{ cm}^{-3}$. With this electron density, the laser power used, 1.1 TW, exceeds the self-focusing threshold of $P_{th} \approx 0.6 \text{ TW}$. Because the local electron density in a cluster

during the laser pulse can be much higher, a small-scale density modulation along the direction of the laser electric field can serve as an initial perturbation for the growth of ponderomotive filaments [21]. In this way, laser self-focusing can be enhanced much more efficiently. However, detailed theoretical investigations on this kind of conditions have not been performed until now; it will be a challenging task that is required to develop for clear understanding of intense femtosecond laser interaction with clusters. On the other hand, in the case with a prepulse most clusters are destroyed before the arrival of the main pulse; so, the electron density cannot be as high as that without prepulse. The threshold laser power for self-channeling will increase in this case. Thus in the case with prepulse CBR could not occur, consistent with the observation of no jet emission.

One method to verify the CBR stimulation may be to detect the formation of a plasma channeling [4]. We obtained visible images of plasma to show the formation of a plasma channel. The visible images of plasmas generated by laser pulses with and without prepulse are shown in Figs. 4(a) and 4(b), respectively. The gas temperature was cooled up to -70°C . The plasma length obtained with a prepulse was about $500\ \mu\text{m}$ [Fig. 4(a)], and this length did not change significantly at different gas temperatures. In the case without prepulse, the plasma length increased by more than a factor of 2, reaching $1400\ \mu\text{m}$ [Fig. 4(b)], and the plasma volume and brightness were increased with cooling. Because the self-channeling critical power dropped to below the applied laser power, the plasma channel was formed and much more laser energy is trapped in the channel. This will contribute to higher energy absorption. The electrons trapped in the channel start to continuously gain energy by catching the



FIG. 4. Visible images of plasma observed when Ar clusters were irradiated with (a) a laser pulse with a prepulse at 80 ps in advance, and (b) without prepulse. The experimental conditions were the same as in Fig. 2.

laser pulse at the right phase and form a directional electron jet along the laser propagation direction.

In conclusion, we observed the emission of a directional hot electron jet when intense femtosecond laser pulses with duration of 28 fs and intensity of $1 \times 10^{17}\ \text{W/cm}^2$ interacted with Ar clusters. Experimental results from the polarization dependence, prepulse effect, and channel formation indicate that the hot electron jet emission came from CBR when the intense femtosecond laser pulse efficiently coupled with clusters. There can be attractive applications using this result. The laser intensity for an electron accelerator can be decreased through clustering of a high-pressure gas. This will result in a new method to generate an electron beam at moderate laser intensity, especially when a high atomic number medium, such as argon, is used.

This research was supported by the Ministry of Science and Technology of Korea through the Creative Research Initiative Program. L.M.C. would like to thank Z.-M. Sheng and H. Lin for useful discussions.

-
- [1] T. Tajima and J.M. Dawson, Phys. Rev. Lett. **43**, 267 (1979).
 - [2] A. Modena *et al.*, Nature (London) **377**, 606 (1995); R. Wagner *et al.*, Phys. Rev. Lett. **78**, 3125 (1997); D. Gordon *et al.*, *ibid.* **80**, 2133 (1998).
 - [3] A. Pukhov *et al.*, Phys. Plasmas **6**, 2847 (1999).
 - [4] C. Gahn *et al.*, Phys. Rev. Lett. **83**, 4772 (1999).
 - [5] T. Ditmire *et al.*, Phys. Rev. Lett. **78**, 3121 (1997).
 - [6] T. Mocek *et al.*, Phys. Rev. E **62**, 4461 (2000).
 - [7] Y.L. Shao *et al.*, Phys. Rev. Lett. **77**, 3343 (1997).
 - [8] T. Ditmire *et al.*, Nature (London) **386**, 54 (1997).
 - [9] J. Zweiback *et al.*, Phys. Rev. Lett. **84**, 2634 (2000).
 - [10] O.F. Hagen and W. Obert, J. Chem. Phys. **56**, 1793 (1972).
 - [11] L.M. Chen *et al.*, Phys. Rev. E **63**, 036403 (2001).
 - [12] I.W. Choi *et al.*, Appl. Opt. **36**, 1457 (1997).
 - [13] J. Zweiback *et al.*, Phys. Rev. A **59**, R3166 (1999).
 - [14] T. Mocek *et al.*, Appl. Phys. Lett. **76**, 1819 (2000).
 - [15] D.F. Price *et al.*, Phys. Rev. Lett. **75**, 252 (1995).
 - [16] B. Walker *et al.*, Phys. Rev. Lett. **73**, 1227 (1994).
 - [17] C.I. Moore *et al.*, Phys. Plasmas **8**, 2481 (2001).
 - [18] C. Max *et al.*, Phys. Rev. Lett. **33**, 209 (1974); P. Monot *et al.*, *ibid.* **74**, 2953 (1995); M. Borghesi *et al.*, *ibid.* **78**, 879 (1997).
 - [19] H.M. Milchberg *et al.*, Phys. Rev. E **64**, 056402 (2001).
 - [20] L.M. Chen *et al.*, Phys. Plasmas **9**, 3539 (2002).
 - [21] W.L. Kruer, *The Physics of Laser Plasma Interactions* (Addison-Wesley, New York, 1988).

Self-focusing and merging of two copropagating laser beams in underdense plasma

Quan-Li Dong, Zheng-Ming Sheng, and Jie Zhang

Laboratory of Optical Physics, Institute of Physics, Chinese Academy of Science, Beijing 100080, China

(Received 28 March 2002; published 7 August 2002)

The propagation of two laser beams copropagating in underdense plasma has been studied numerically by solving their coupled envelope equations. It shows that two beams can merge each other, or split into three beams, or propagate with unstable trajectories, depending upon their power and initial beam separation. During the merging process, strong emission of radiation is observed. It also shows that the density cavitation channels due to the transverse ponderomotive force of the beams tend to trap them inside and prevent them from merging each other.

DOI: 10.1103/PhysRevE.66.027402

PACS number(s): 52.35.Mw, 52.38.Hb, 42.65.Jx

Optical spatial solitons have been attracting continued interest since 1960's [1]. A variety of nonlinear optical materials, including Kerr media, photorefractive materials, quadratic nonlinear material, saturable nonlinear media, and plasmas, etc., can support the self-focusing/self-trapping of light beams. In some particular case, it appears as optical spatial solitons, provided that the diffraction of light beams is exactly balanced by the nonlinear focusing effect. Recently, there has been much interest in the interaction between such kind of spatial solitons as well as two or more light beams, which are launched into these nonlinear media in directions either parallel to each other or at some crossing angles. Compared with the interaction of one-dimensional temporal solitons in optical fibers, the interaction between two optical spatial solitons exhibits distinctive features such as mutual attraction/beam fusion [2–4], repulsion, beam fission [5,6], and beam spiraling [7,8], etc. This mutual interaction occurs intensively around the critical power or above for self-focusing/self-trapping, which ranges from a few microwatt (μW) only in photorefractive materials biased with some external dc field [9] up to terawatt (TW) or above in plasmas [10,11].

Energy transfer between interacting laser beams in plasma directly addresses fundamental aspect of laser plasma interaction and is also relevant to laser-driven inertial confined fusion [12,13]. In plasma, usually the nonlinear coupling between the interacting beams comes from the relativistic mass correction and the plasma density modification owing to the ponderomotive push on electrons [11], if one neglects beam coupling through stimulated Brillouin and Raman scattering and ion-acoustic wave [12,13]. For examples, in the geometry of counterpropagating laser beams, Shvets and Pukhov has proposed the electromagnetically induced guiding owing to the formation of a high-amplitude density grating produced by the interference of the two beams [14]; for two spatially separated intense laser beams copropagating in underdense plasma, Ren *et al.* have observed the mutual beam attraction and beam spiraling in recent three-dimensional particle-in-cell simulations [8]. These features have been attributed mainly due to the relativistic effect. At weakly relativistic light intensities $I\lambda^2 \ll 10^{18} \text{ W/cm}^2 \mu\text{m}^2$ (here I is the laser intensity and λ the laser wavelength), the corresponding envelope equation of laser beams can be reduced to that in Kerr-type materials. However, when $I\lambda^2$

$\geq 10^{18} \text{ W/cm}^2 \mu\text{m}^2$, each beam will produce significant density depression along their propagation axes due to the transverse ponderomotive force of laser beams [11], which cannot be neglected. The effect of this density modification on the mutual interaction of spatially separated beams has not yet been explored explicitly in earlier studies. This nonlinearity is found only in plasmas and is very important when the laser power exceeds the relativistic self-focusing threshold about $17(\omega/\omega_p)^2 \text{ GW}$ [11], where ω and ω_p are the laser frequency and electron plasma frequency, respectively.

In this paper, we present numerical simulation studies on the interaction between two light beams launched into underdense plasma in the direction parallel to each other. We solve a set of coupled envelope equations numerically with both the relativistic nonlinearity and the ponderomotive-force effect taken into account. We demonstrate that under some circumstances, two beams can merge each other, split into three beams, or remain to be trapped in the density channel. Hosing propagation owing to the mutual interaction is observed.

In the slowly varying envelope approximation, the coupled evolution equations for two laser beams copropagating in underdense plasma can be written as [11,15]

$$2i \frac{\partial a_1}{\partial \tau} + \nabla_{\perp}^2 a_1 + (1 - n/\gamma) a_1 = 0, \quad (1)$$

$$2i \frac{\partial a_2}{\partial \tau} + \nabla_{\perp}^2 a_2 + (1 - n/\gamma) a_2 = 0, \quad (2)$$

which describe the beam propagation in a comoving frame $\xi = x - (k_0 c^2 / \omega_0) t$. Here a_1 and a_2 are the slowly varying vector potentials of the two beams normalized by mc^2/e , respectively, the relativistic factor $\gamma = (1 + |a_1 + a_2|^2)^{1/2}$, the density $n = \text{Max}(0, 1 + \nabla_{\perp}^2 \gamma)$ addressing the ponderomotive expulsion of electron density from the high intensity regions, which is normalized by the unperturbed plasma density n_0 . Also here $\tau = \omega_p^2 t / \omega_0$, with ω_0 the frequency of laser beams and $\omega_p = (4\pi n_0 e^2 / m)^{1/2}$ the plasma frequency, $\nabla_{\perp}^2 = \partial^2 / \partial y^2 + \partial^2 / \partial z^2$ with transverse coordinate y and z normalized by c/ω_p . We assume that the two beams are parallel polarized. The coupled Eqs. (1) and (2) can describe the mutual interaction of two beams through the nonlinear effects including

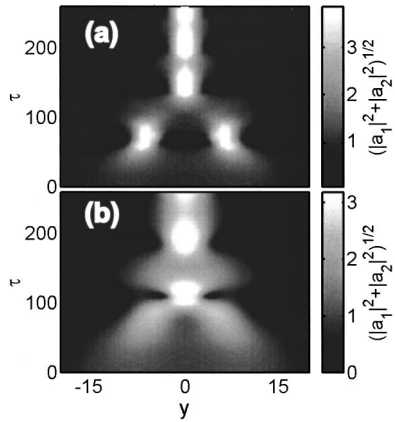


FIG. 1. Evolution of the absolute amplitude of two beams $(|a_1|^2 + |a_2|^2)^{1/2}$ with initial parameters $a_{01} = a_{02} = 0.6$, $\rho_{01} = \rho_{02} = 8$, $y_{01} = 10$, and $y_{02} = -10$. (a) Taking into account the electron-density modification due to the ponderomotive force; (b) neglecting the electron-density modification.

the relativistic nonlinearity and the density modification by the transverse ponderomotive force. However, certain kinetic effects, such as electron acceleration, attraction of electron filaments, and corresponding quasistatic magnetic generation, etc. [16,17], have been neglected. These are known to contribute to the merger of light filaments. Usually, these effects are significant in plasma with moderate densities, but relatively weak in tenuous plasma [18,19]. Thus the results described following should apply preferably in tenuous plasma such as $n_0/n_c < 0.01$, where n_c is the critical density of incident laser beams. In addition, since we have neglected the longitudinal profiles of laser beams, our results should apply to the case when the durations of the laser beams are much longer than a plasma oscillation period.

Equations (1) and (2) have been solved with the algorithm of the alternating-directing implicit method [15]. A rectangular simulation box is used in the y - z plane. In the simulations, the input beams are launched along the x direction; the transverse beam profiles are in Gaussian with $a_1 = a_{01} \exp\{-[(y - y_{01})^2 + z^2]/2\rho_{01}^2\}$ and $a_2 = a_{02} \exp\{-[(y - y_{02})^2 + z^2]/2\rho_{02}^2\}$. With these, the normalized threshold power for relativistic self-focusing for individual beams is reached when $a_{01}^2 \rho_{01}^2 \geq 16$ and $a_{02}^2 \rho_{02}^2 \geq 16$. One notes that it is important to study the beam interaction in rectangular geometry rather than in slab geometry, so that one could compare the simulation results with real experiments; in slab geometry, there is not any power threshold for self-focusing [21].

Our simulations show that the interaction of two beams displays a variety of interesting features such as attraction, fusion, fission, and beam hosing. Some of them are similar to those found in earlier studies in nonlinear optical materials, while some of them are distinctive owing to the nonlinearity related to the transverse ponderomotive force of light beams in plasma. Figure 1(a) illustrates the evolution of the two beams when $a_{01} = a_{02} = 0.6$, $\rho_{01} = \rho_{02} = 8$, $y_{01} = 10$, and $y_{02} = -10$. The two beams start to self-focus individually in the earlier stage. Meanwhile, they appear to attract each other. Around $\tau = 70$, they are focused to the minimum spot size and then begin to defocus. After $\tau = 100$, the two beams be-

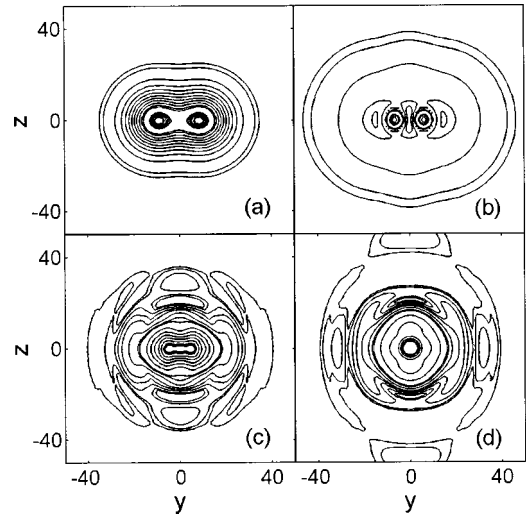


FIG. 2. Snapshots of the transverse section of the beam profile at $\tau = 0$ (a), 70 (b), 110 (c), and 170 (d). The initial parameters are the same as in Fig. 1, taking into account the electron-density modification.

gin to merge into a single beam very quickly, which remains self-focused as a single beam afterwards. Figure 1(b) shows the evolution of the two beams for the same parameters as in Fig. 1(a), except for ignoring the density depression caused by the transverse ponderomotive force, i.e., let $n = 1$ instead of $n = \text{Max}(0, 1 + \nabla_\perp \gamma)$. In this case, the two beams merge into a single beam more quickly than that in Fig. 1(a). One notes that the final beam-spot size is smaller in Fig. 1(a) than in Fig. 1(b), demonstrating that the ponderomotive force helps to trap the light beam. One also notes that, during merging process, there exists strong emission of radiation in both cases. This emission appears to be much stronger than that when there is only one laser beam self-focusing in plasma [22]. This is more obvious in Fig. 2 showing snapshots of the transverse section of the incident beams at different times. One observes that, after merging into a single beam, its transverse section is nearly isotropic in y - z plane in the central region. This suggests that a rounded beam is more stable than other shaped beams in this case.

Figure 3 shows the beam evolution at a higher laser intensity and a higher beam power when $a_{01} = a_{02} = 1$, $\rho_{01} = \rho_{02} = 8$, $y_{01} = 10$, and $y_{02} = -10$. In this case, electron-density modification is much stronger than that for Fig. 1(a). During the earlier stage, mutual attraction of beams is found while the two beams are undergoing self-focusing individually. Afterwards, the beam intensities around the beam center regions increase significantly. As a result, the electron-density depression gets deeper around the individual beam axes until electron-density cavitation occurs. These density cavities trap the two beams, preventing them from merging into a single beam. The centroids of the two beams are shifted, respectively, from their original positions due to their mutual attraction. Strong emission of radiation is found before the trapping process. However, after the beams are fully trapped in their density cavities, there is almost no new emission of radiation from the trapped beams as shown in Fig. 3(a). Figure 3(b) shows snapshots of electron-density distri-

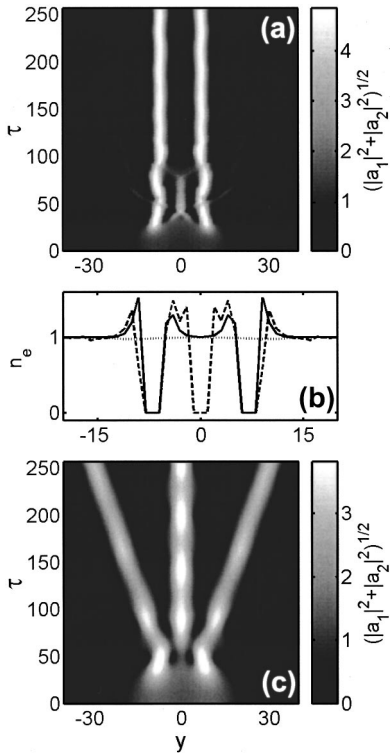


FIG. 3. Evolution of the absolute amplitude of two beams ($|a_1|^2 + |a_2|^2$) $^{1/2}$ with initial parameters $a_{01} = a_{02} = 1$, $\rho_{01} = \rho_{02} = 8$, $y_{01} = 10$, and $y_{02} = -10$. (a) Taking into account the electron-density modification due to the ponderomotive force; (b) electron-density profiles cut at $z = 0$ at $\tau = 0$ (dotted line), 50 (dashed line), and 150 (solid line); (c) beam evolution when ignoring the electron-density modification.

butions along y axis cut at $z = 0$. If one excludes the electron-density modification by the ponderomotive force, the beam evolution is illustrated in Fig. 3(c). It differs from Fig. 1(b) for the case at lower incident power as well as from Fig. 3(a)—the two beams neither merge into a single beam nor remain individual self-focusing. In the earlier stage, the two beams attract each other as usual. At certain time around $\tau = 60$, rather than merging into a single beam, the two beams split into three beams; one beam at the center propagates along the original incident direction of the two beams, while the other two beams propagate obliquely. This appears to be a more stable state than merging into a single beam. This suggests that the density depression caused by the ponderomotive force plays role in intense multibeam interaction in plasma. Figure 4 shows snapshots of the transverse section of the incident beams when the ponderomotive force is taken into account, corresponding to Fig. 3(a). Strong emission of radiation is found around $\tau = 90$ in Fig. 4(c).

If one increases the initial distance between the centroids of the two beams, it is expected that their mutual interaction becomes weaker and the two beams would remain as individual. Figure 5 shows the evolution of the two beams for $a_{01} = a_{02} = 1$, $\rho_{01} = \rho_{02} = 8$, $y_{01} = 12$, and $y_{02} = -12$, i.e., with larger displacement than that for Fig. 3. In earlier stage, the mutual attraction is still found while the two beams are undergoing self-focusing individually. Afterwards, however,

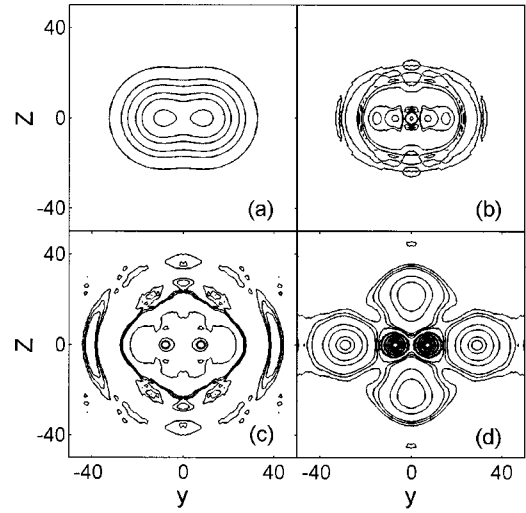


FIG. 4. Snapshots of the transverse section of the beam profile at $\tau = 0$ (a), 50 (b), 90 (c), and 190 (d). The initial parameters are the same as in Fig. 3 taking into account the electron-density modification.

rather than propagating straight forward in the density channels, the two beams change their propagation directions continually, i.e., the trajectories of both beams becomes unstable. This hosinglike instability is caused by both the

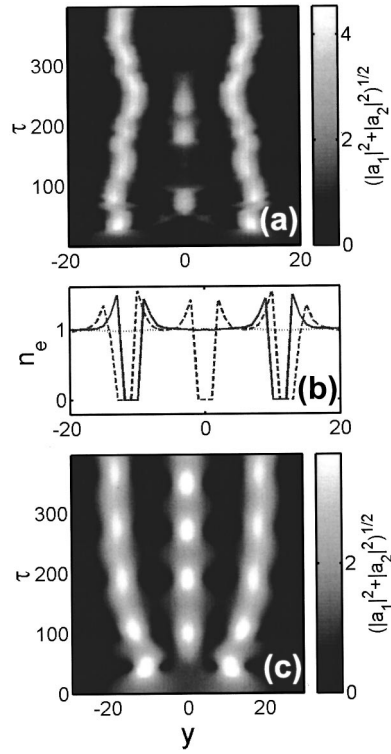


FIG. 5. Evolution of the absolute amplitude of two beams ($|a_1|^2 + |a_2|^2$) $^{1/2}$ with initial parameters $a_{01} = a_{02} = 1$, $\rho_{01} = \rho_{02} = 8$, $y_{01} = 12$, and $y_{02} = -12$. (a) Taking into account the electron-density modification due to the ponderomotive force; (b) electron-density profiles cut at $z = 0$ at $\tau = 0$ (dotted line), 70 (dashed line), and 300 (solid line); (c) beam evolution when ignoring the electron-density modification.

mutual attraction and density cavitation that prevents two beams from merging into a single one. As a result, it has a different physical origin from the normal hosing instability when a laser propagating in underdense plasma [20], which is caused by upward or downward tilting of the local wave fronts due to the transverse phase velocity difference across the wave front. This kind of instability cannot be observed for a single laser beam propagating in plasma in our simulations working in a comoving frame. As in earlier examples, we have simulated the beam envelope evolution for the same parameters, except for excluding the ponderomotive force. In this case, similar to the case for Fig. 3(c), one finds that two beams split into three beams after a self-focusing stage at the beginning. In these three beams, one propagates straight forward along the initial direction of incident beams, while the other two propagate at some angles from the initial propagation axis. Later on, they bend toward the central beam owing to mutual attraction.

In conclusion, the interaction of two copropagating light beams in underdense plasma has been studied numerically. Beam fusion/mergence, fission, and hosing during the propagation are observed. It shows that the relativistic nonlinearity can lead to beam fusion and fission, while the electron-density cavitation due to the transverse ponderomotive force of light beams tends to prevent the beam from merging into a single beam for laser beams at high intensities. The mutual interaction may also cause hosing propagation of beams. Strong emission of radiation is found during beam fusion process.

This work has been supported in part by the National Natural Science Foundation of China (Grant Nos. 10105014, 19825110, 10075075), the Bai-Ren-Ji-Hua Program of the Chinese Academy of Science, and the National High-Tech ICF program.

-
- [1] G.I. Stegeman and M. Segev, *Science* **286**, 1518 (1999); G.I. Stegeman, D.N. Christodoulides, and M. Segev, *IEEE J. Sel. Top. Quantum Electron.* **6**, 1419 (2000).
 - [2] D. Anderson and M. Lisak, *Phys. Rev. A* **32**, 2270 (1985).
 - [3] W. Krolikowski *et al.*, *Opt. Lett.* **23**, 97 (1998).
 - [4] V. Tikhonenko, J. Christou, and B. Luther-Davies, *Phys. Rev. Lett.* **76**, 2698 (1996).
 - [5] W. Krolikowski and S.A. Holmstrom, *Opt. Lett.* **22**, 369 (1997).
 - [6] L. Torner, J.P. Torres, and C.R. Menyuk, *Opt. Lett.* **21**, 462 (1996); Y. Baek *et al.*, *ibid.* **22**, 1550 (1997).
 - [7] M.-F. Shih, M. Segev, and G. Salamo, *Phys. Rev. Lett.* **78**, 2551 (1997); A.V. Buryak *et al.*, *ibid.* **82**, 81 (1999); M.R. Belic, A. Stepken, and F. Kaiser, *ibid.* **82**, 544 (1999).
 - [8] C. Ren *et al.*, *Phys. Rev. Lett.* **85**, 2124 (2000).
 - [9] M. Segev *et al.*, *Phys. Rev. Lett.* **73**, 3211 (1994); Z.-M. Sheng *et al.*, *J. Opt. Soc. Am. B* **13**, 854 (1996).
 - [10] P. Sprangle, C.M. Tang, and E. Esarey, *IEEE Trans. Plasma Sci.* **PS-5**, 145 (1983).
 - [11] G.Z. Sun *et al.*, *Phys. Fluids* **30**, 526 (1987); A. Borisov *et al.*, *Phys. Rev. A* **45**, 5830 (1992); Z.M. Sheng and J. Meyer-ter-Vehn, *Phys. Rev. E* **54**, 1833 (1996).
 - [12] C.J. McKinstry *et al.*, *Phys. Plasmas* **3**, 2686 (1996); **5**, 1142 (1998).
 - [13] W.L. Kruer *et al.*, *Phys. Plasmas* **3**, 382 (1996); V.V. Eliseev *et al.*, *ibid.* **3**, 2215 (1996); H.A. Rose and S. Ghosal, *ibid.* **5**, 1461 (1998); C. Labaune *et al.*, *ibid.* **6**, 2048 (1999); K.B. Wharton *et al.*, *ibid.* **6**, 2144 (1999).
 - [14] G. Shvets and A. Pukhov, *Phys. Rev. E* **59**, 1033 (1999).
 - [15] Z.-M. Sheng *et al.*, *Phys. Rev. E* **64**, 066409 (2001); W. H. Press, S. A. Teukolsky, W. T. Vetterling, and B. P. Flannery, *Numerical Recipes in Fortran* (Cambridge University Press, New York, 1992), p. 861.
 - [16] A. Pukhov and J. Meyer-ter-Vehn, *Phys. Rev. Lett.* **76**, 3975 (1996).
 - [17] Y. Sentoku *et al.*, *Phys. Rev. E* **65**, 046408 (2002).
 - [18] J.C. Adam *et al.*, *Phys. Rev. Lett.* **78**, 4765 (1997).
 - [19] G. Malka *et al.*, *Phys. Rev. Lett.* **79**, 2053 (1997).
 - [20] P. Sprangle, J. Krall, and E. Esarey, *Phys. Rev. Lett.* **73**, 3544 (1994); G. Shvets and J.S. Wurtele, *ibid.* **73**, 3540 (1994); B.J. Duda *et al.*, *ibid.* **83**, 1978 (1999); C. Ren and W.B. Mori, *Phys. Plasmas* **8**, 3118 (2001).
 - [21] K.C. Tzeng and W.B. Mori, *Phys. Rev. Lett.* **81**, 104 (1998).
 - [22] F. Vidal and T.W. Johnston, *Phys. Rev. Lett.* **77**, 1282 (1996).

Effects of delay time on transient Ni-like x-ray lasers

Y. J. Li,^{1,2} X. Lu,¹ and J. Zhang^{1,*}

¹Laboratory of Optical Physics, Institute of Physics, Chinese Academy of Sciences, Beijing 100080, People's Republic of China

²Department of Physics, China University of Mining and Technology, Beijing 100083, People's Republic of China

(Received 3 June 2002; published 30 October 2002)

In transient collisional excitation scheme, a long (nanosecond) prepulse is used to perform and ionize plasmas. After a delay time, a short (sub- or picosecond) intense laser pulse is used to rapidly heat the plasma. This results in transient x-ray lasers with high gain. Effects of delay time on transient collisional excitation *nickel-like* x-ray lasers are investigated analytically using a simple model. The calculations show that the longer delay time can greatly relax the density gradient. This is very critical for the propagation of x-ray lasers. However, a too long delay will reduce the electron temperature of the plasma before the arrival of the short pulse. Increasing the intensity of the long pulse or extending the pulse duration can keep the temperature required to maintain a high percentage of Ni-like ions while the delay time is longer. Similarly, increasing the intensity of the short pulse or extending the duration can also raise the electron temperature, resulting in higher gain coefficient. Our results indicate that extending the pulse duration is more efficient than that of increasing the intensity.

DOI: 10.1103/PhysRevE.66.046501

PACS number(s): 52.59.Ye, 42.55.Vc

I. INTRODUCTION

Since high gain transient collisional excitation (TCE) scheme was first demonstrated in 1997 with only a few Joule pump energy [1], great attention was attracted [2–5]. The result of neonlike titanium TCE x-ray laser was reproduced by Dunn in 1998 and extended to nickel-like palladium, and nickel-like molybdenum with a gain coefficient of up to 35 cm^{-1} [2,6–8]. Kalachnikov in 1998 also demonstrated the saturation output of neonlike titanium TCE x-ray laser with only 5-J pump energy [9]. Nilsen modeled the neonlike titanium transient x-ray laser [10] and calculated the hydrodynamic evolution of the plasma under the experimental conditions using LASNEX and XRASER code [4]. In calculations, effects of the delay time between the long pulse and the following short pulse was investigated theoretically for the first time.

A suitable delay time between the long pulse and the short pulse is beneficial for relaxing the plasma density gradient, and thus is very critical for the propagation of x-ray lasers [11].

One of the main objectives to enhance the efficiency of x-ray lasers is to develop a “table-top” x-ray laser for applications [12,13,9]. In the “traditional” quasi-steady state scheme, the prepulse is only to create a preplasma. The delay is used to make a longer scale length. The main pulse is then not only required to heat plasma to reach the electron temperature required by population inversion, but also needed to ionize the plasma to a correct ionization state of Ni-like (or Ne-like). By comparison, the prepluses and main pulses serve different functions in the TCE scheme. The long (pre) pulse is not only required to create a preplasma, but also needed to prepare an optimized preplasma with a rich Ni-like (or Ne-like) ionization stage. Then the short (main) pulse

heats the plasma rapidly to reach required conditions with high electron temperature while keeping the ion temperature low. This is beneficial for forming a high gain transient population inversion. For the TCE scheme, a longer delay can make a longer scale length. But a too long delay will also reduce the temperature in the plasma [14]. Thus, if we would like to use the delay to relax the plasma density gradient, the delay and the pulse duration between the long pulse and the short pulse should be optimized.

In this paper, we investigate the effects of the delay time on hydrodynamics of transient Ni-like Pd x-ray lasers using the formulas of Ref. [14]. In order to understand the optimization conditions of plasmas, we calculate the electron temperature, scale length, electron density for different delay time. The results show that extending the pulse duration is more efficient than that of increasing the intensity to generate transient x-ray lasers with high gain.

II. ANALYTIC FORMULAS FOR TCE NI-LIKE X-RAY LASERS

According to the formula of Ref. [14], useful scaling laws for plasma variables are used to describe the hydrodynamic process of TCE Ni-like x-ray lasers. The convenient units listed in Table I are employed, which scale the variable with underline in the whole derivation, to simplify the calculation.

TABLE I. Normalized values for scaled variables.

Physical variable	Symbol	Normalized value
Time	t	1 ns
Laser intensity	I	$10^{14} \text{ W cm}^{-2}$
Laser wavelength	λ	$1.053 \mu\text{m}$
Ablation mass	m	$10^{-4} \text{ g cm}^{-2}$
Ion charge	Z	65
Atomic mass	A	240
Coulomb logarithm	Λ	5

*Correspondence should be addressed to J. Zhang; Email address: jzhang@aphy.iphy.ac.cn.

The processes of laser pulses interacting with plasmas are divided into four distinct periods. They are $t \leq t_{1L}$, $t_{1L} \leq t \leq t_m$, $t_m \leq t \leq t_{2L}$, and $t_{2L} \leq t$, respectively, where $t_{1L} = \Delta t_{1L}$ is the long pulse duration, Δt_m is the delay time, $t_m = \Delta t_{1L} + \Delta t_m$ is the time when the short pulse arrives, Δt_{2L} is the short pulse duration, $t_{2L} = t_m + \Delta t_{2L}$ is the turning off time of the short pulse.

A. During the time of $t \leq t_{1L}$

The long pulse creates an optimized preplasma. The analytic solutions after the influence of the initial conditions are

$$T = 3.90 \text{ keV } I^{5/9} A^{2/9} \Lambda^{2/9} \lambda^{2/3} t^{2/9}, \quad (1a)$$

$$L = 2.87 \times 10^{-2} \text{ cm } I^{10/27} A^{-2/27} \lambda^{4/9} \Lambda^{4/27} t^{31/27}, \quad (1b)$$

$$n_0 = 20.82 \times 10^{20} \text{ cm}^{-3} I^{11/54} A^{4/27} \lambda^{-5/9} \Lambda^{-2/54} t^{-14/27}, \quad (1c)$$

where I is the laser intensity, λ is the laser wavelength, Λ is the Coulomb logarithm, A is the atomic mass. T is the electron temperature, L is the scale length, n_0 is the maximum value of the electron density.

B. During the time of $t_{1L} \leq t \leq t_m$

After the time t_{1L} , the long laser pulse is turned off and the plasma continues to expand adiabatically. The exact analytical solutions can be obtained for this period using the condition before t_{1L} ,

$$T = T_{1L} t_{1L}^{2/3} t^{-2/3}, \quad (2a)$$

$$L = L_{1L} t_{1L}^{-5/9} t^{5/9}, \quad (2b)$$

$$n_o = n_{1L} t_{1L}^{7/9} t^{-7/9}, \quad (2c)$$

where T_{1L} , L_{1L} , and n_{1L} are the electron temperature, scale length, and electron density at t_{1L} .

C. During the time of $t_m \leq t \leq t_{2L}$

At time t_m , when the short pulse has switched on, the solutions can be obtained by considering the initial conditions before t_m :

$$T = 23.12 \text{ keV } I_2 m^{-1} A Z^{-1} t \left(1 - t_m^{5/3} t^{-5/3} + \frac{T_m t_m^{2/3}}{T_2} t^{-5/3} \right), \quad (3a)$$

$$L = 5.16 \times 10^{-2} \text{ cm } I_2^{1/2} m^{-1/2} t^{3/2} \times \left(1 - t_m^{5/3} t^{-5/3} + \frac{L_m^2}{L_2^{2/3} t_m^{4/3}} t^{-5/3} \right)^{1/2}, \quad (3b)$$

$$n_0 = 3.16 \times 10^{20} \text{ cm}^{-3} I_2^{-1/2} m^{3/2} A^{-1} Z t^{-3/2} \times \left(1 - t_m^{-5/3} t^{-5/3} + \frac{n_2^2 t_m^{1/6}}{n_m^2} t^{-5/3} \right)^{-1/2}, \quad (3c)$$

where T_m is the electron temperature at t_m , $T_2 = 23.12 \text{ keV } I_2 m^{-1} A Z^{-1}$. L_m is the scale length at t_m , $L_2 = 5.16 \times 10^{-2} \text{ cm } I_2^{1/2} m^{-1/2}$. n_m is the electron density at t_m , $n_2 = 3.16 \times 10^{20} \text{ cm}^{-3} I_2^{-1/2} m^{3/2} A^{-1} Z$.

D. During the time of $t_{2L} \leq t$

After the time t_{2L} , the short laser pulse is turned off and the plasma continues to expand adiabatically. The analytical solutions can be obtained for this period using the condition before t_{2L} :

$$T = 23.12 \text{ keV } I_2 m^{-1} A Z^{-1} t_{2L}^{5/3} t^{-2/3} \times \left(1 - t_m^{5/3} t_{2L}^{-5/3} + \frac{T_m t_m^{2/3} t_{2L}^{-5/3}}{T_2} \right), \quad (4a)$$

$$L = L_2 t_{2L}^{5/6} t^{2/3} \left(1 - t_m^{5/3} t_{2L}^{-5/3} + \frac{L_m^2}{L_2^2} t_m^{2/3} t_{2L}^{-5/3} \right)^{1/2}, \quad (4b)$$

$$n_0 = n_2 t_{2L}^{-5/6} t^{-2/3} \left(1 - t_m^{-5/3} t_{2L}^{-5/3} + \frac{n_2^2 t_{2L}^{-5/3}}{n_m^2 t_m^{2/3}} \right)^{-1/2}. \quad (4c)$$

III. RESULTS AND DISCUSSION

In order to understand the effects of the delay time on hydrodynamics of the transient collisional x-ray laser under different conditions, we calculate the hydrodynamics of the transient collisional Ni-like Pd x-ray laser for different intensity and duration for the long pulse and the short pulse, respectively. First, we discuss why the transient x-ray laser is *sensitive* to the delay time. Second, we investigate the effects of the delay time by changing the intensity and the duration for long pulse. Finally, we discuss how to effectively enhance the electron temperature in the preplasma before the short pulse comes.

A. The effects of sensitivity of x-ray laser gain to the delay time

Experimental results and numerical simulations have shown that the x-ray laser output is quite sensitive to the delay time between the long- and the short-pulse drive lasers [15,4]. In order to understand the dependence of the x-ray laser on the delay time, we calculate hydrodynamics of the transient collisional Ni-like Pd x-ray laser with three different values of delay time of 1.1, 1.9, and 2.6 ns. The conditions in the calculations are as almost the same as in Ref. [2], except the intensity of the long pulse of $I_1 = 3.0 \times 10^{12} \text{ W/cm}^2$.

The calculations show that the densities are 5.79×10^{20} , 4.41×10^{20} , and $3.68 \times 10^{20} \text{ cm}^{-3}$ for the three different delay times, respectively, as shown in Fig. 1(a). The difference among the three densities will not much affect the gain of the x-ray lasers. In the calculations, 152.7 μm is the longest scale length for the 2.6 ns delay time, as shown in Fig. 1(b). For this delay time, the electron temperature is 160.9 eV, as shown in Fig. 1(c). This results in an average ionization of

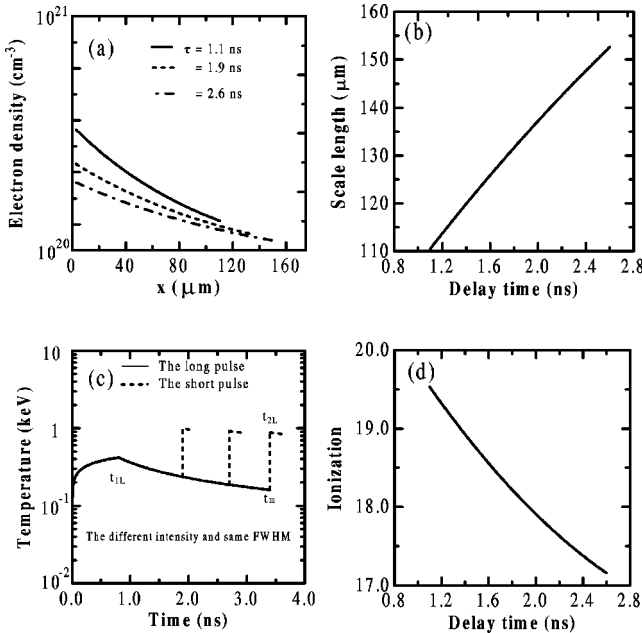


FIG. 1. (a) Electron density versus x with deferent delay, (b) temperature versus delay, (c) temperature history, (d) ionization versus delay. The conditions are $I_1 = 0.7 \times 10^{12} \text{ W/cm}^2$, $t_{1L} = 0.8 \text{ ns}$, $\lambda = 1.053 \mu\text{m}$, $I_2 = 5.2 \times 10^{14} \text{ W/cm}^2$, $t_{2L} = 1.1 \text{ ps}$, the delay time τ is from 1.1 to 2.6 ns.

only 17.16, as shown in Fig. 1(d). This is lower than the requirement for rich Ni-like Pd ionization population. For the 1.9 ns of the delay time, the scale length is 134.3 μm , which is middle among the three scale lengths. But the temperature is 187.6 eV, corresponding to an ionization of about 18.06. This is almost the Ni-like Pd ionization population. For the 1.1 ns of the delay time, the scale length is 110.5 μm , which is the shortest one. The temperature is 237.1 eV, corresponding to an ionization of about 19.5. This is obviously overionized. In nanosecond process, the ionization is sensitively dependent on the temperature. The temperature depends sensitively on the delay time, as seen in the Fig. 1(c). Thus the different delay time cause ionization difference sensitively. From the comparison between the sensitivity of the ionization to delay time and the x-ray laser output to delay time, it is clear that the sensitivity of the x-ray laser output to the delay time is finally due to the different ionization population. The scale length also depends sensitively on the delay time. However, This will not sensitively affect the gain of the x-ray lasers.

We know that the main function of the long pulse is to prepare a preplasma with a rich Ni-like (or Ne-like) ionization population and a low ion temperature before the arrival of the short pulse. And the main function of the delay time is to relax the density gradient, that is critical for the x-ray laser propagation [14]. Of course, a longer delay time can make the scale length longer. However, a rich Ni-like (or Ne-like) ionization population is the most important condition. Thus in the design of the x-ray laser experiment, we not only need to optimize the scale length, but also need to optimize the ionization, which is more important than the scale length.

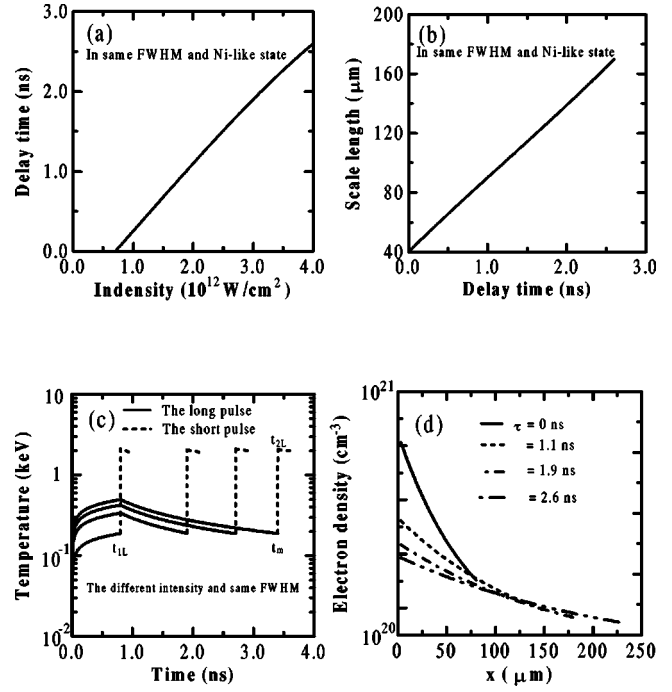


FIG. 2. (a) Delay time versus long-pulse intensity, (b) scale length vs delay time, (c) temperature history, (d) electron density vs x with deferent delay for the same long-pulse duration and Ni-like ionization. The conditions are I_1 from 0.7×10^{12} to $4 \times 10^{12} \text{ W/cm}^2$, $\lambda = 1.053 \mu\text{m}$, $t_{1L} = 0.8 \text{ ns}$, $I_2 = 5.2 \times 10^{14} \text{ W/cm}^2$, $t_{2L} = 1.1 \text{ ps}$, the delay time τ is from 0 to 2.6 ns.

B. The efficiency of the long pulse heat under the delay time

From the calculations above, we know that a delay time will decrease the Ni-like (or Ne-like) ionization population while it relaxes the density gradient. Thus we have to increase the temperature so that the average ionization is kept in the Ni-like (or Ne-like) ionization state before the arrival of the short pulse. There are two ways to increase the temperature. The first one is to enhance the intensity of the long pulse. The another one is to extend the duration of the longer pulse. Here what we want to know is which one is more efficient.

We calculate the change of the intensity, scale length, density, and temperature while extending the delay time from 0 to 2.6 ns and keeping the duration to be a constant of 0.8 ns. The results show that the intensity has to be increased from 0.7×10^{12} to $4.0 \times 10^{12} \text{ W/cm}^2$ so that the most Pd ions are kept in Ni-like ionization stage, as shown in Fig. 2(a). The scale lengths are prolonged from 40 to 169.8 μm with the extension of the delay, as shown in Fig. 2(b). And the electron density range is from 3.90×10^{20} to $8.44 \times 10^{20} \text{ cm}^{-3}$, as shown in Fig. 2(d). However, the highest temperature during the short pulse laser is dropped from 1.84 keV to 800 eV with the extension of the delay, as shown in Fig. 2(c).

As a comparison with the case of changing the pulse intensity, we calculate the same parameters' change by extending the delay time from 0 to 1.0 ns and keep the intensity as a constant of $0.7 \times 10^{12} \text{ W/cm}^2$. The results show that the durations are increased from 0.8 to 2.4 ns with the extension of the delay time while keeping the Pd ions as Ni-like ions,

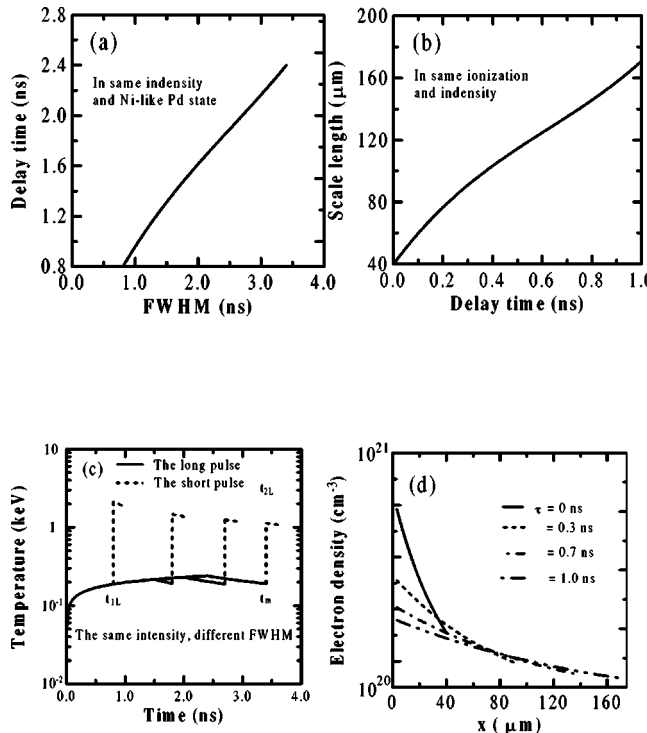


FIG. 3. (a) Delay time versus full width at half maximum (long-pulse duration), (b) scale length versus delay time, (c) temperature history, (d) electron density vs x for deferent delay for the same intensity and Ni-like ionization. The conditions are $I_1 = 0.7 \times 10^{12} \text{ W/cm}^2$, the long-pulse duration t_{1L} are from 0.8 to 2.4 ns, $\lambda = 1.053 \mu\text{m}$, $I_2 = 5.2 \times 10^{14} \text{ W/cm}^2$, $t_{2L} = 1.1 \text{ ps}$, the delay time τ is from 0 to 1.0 ns.

as shown in Fig. 3(a). The scale lengths are prolonged from 40 to 170.8 μm with the extension of the delay, as shown in Fig. 3(b). And the highest temperature is only dropped from 1.84 to 1.1 keV during the short pulse with the extension of the delay time, as shown in Fig. 3(c). The electron density range is from 3.64×10^{20} to $8.44 \times 10^{20} \text{ cm}^{-3}$, which is almost the same as the case above, as shown in Fig. 3(d).

From the comparison, we know that the prolonged ranges of the scale lengths and density ranges are almost the same for both cases. However, the intensity is increased from 0.7×10^{12} to $4.0 \times 10^{12} \text{ W/cm}^2$ when the duration is a constant of 0.8 ns, and the duration is only increased from 0.8 to 2.4 ns when the intensity is a constant of $0.7 \times 10^{12} \text{ W/cm}^2$. While keeping the Pd ionization stage in Ni-like, the efficiency of the heating pulse for prolonging the long-pulse duration while keeping the constant intensity is greater than that for increasing the intensity while keeping the constant duration. It is significant because prolonging the pulse duration is much easier than increasing the pulse intensity in the x-ray laser experiment.

C. The influence of the delay time on the short-pulse conditions

For the TCE scheme, the change of the ionization state and ablation mass can be neglected during the short pulse [14]. To help understand the influence of the delay time, we

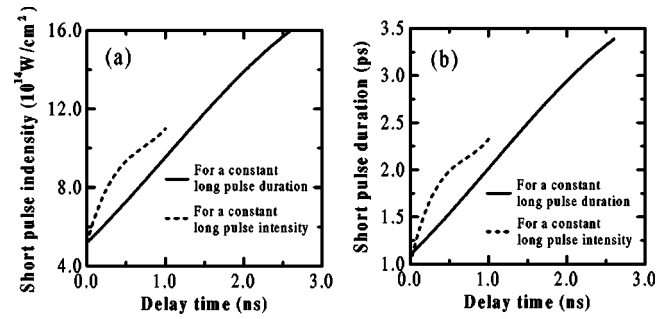


FIG. 4. (a) The short-pulse intensity versus delay time for a constant long-pulse duration, the ionization is Ni-like and the electron temperature is optimized temperature of 1.84 keV during the short pulse. The conditions are I_1 from 0.7×10^{12} to $4 \times 10^{12} \text{ W/cm}^2$, $\lambda = 1.053 \mu\text{m}$, $t_{1L} = 0.8 \text{ ns}$, I_2 are from 5.2×10^{14} to $1.6 \times 10^{15} \text{ W/cm}^2$ or t_{2L} are from 1.1 to 3.4 ps, the delay time τ is from 0 to 2.6 ns. (b) The short-pulse duration versus delay for a constant long-pulse intensity, the ionization is Ni-like and the electron temperature is optimized temperature of 1.84 keV during the short-pulse. The conditions are $I_1 = 0.7 \times 10^{12} \text{ W/cm}^2$, $\lambda = 1.053 \mu\text{m}$, t_{1L} are from 0.8 ns to 2.4 ns, I_2 are from 5.2×10^{14} to $1.2 \times 10^{15} \text{ W/cm}^2$ or t_{2L} are from 1.1 ps to 2.3 ps, the delay time τ is from 0 to 1.0 ns.

calculate only the temperature changed with different delay time, which is very important for the gain, and find out the optimized intensity or duration of the short pulse while keeping the electron temperature as 1.84 keV and the Pd ions as Ni-like.

The temperature during the short pulse goes down with the extension of the delay time from Fig. 1(c) and Fig. 2(c). It is not beneficial for the output of the x-ray laser because the gain coefficient is proportional to the electron temperature and inversely proportional to the square root of the ion temperature. The ways to enhance the temperature are also to increase the intensity or the duration of the short pulse.

We first calculate the case of changing short-pulse intensity while keeping the pulses duration the same for different long-pulse intensity or duration and delay time. The calculations show that the short-pulse intensity needs to increase from 5.2×10^{14} to $1.6 \times 10^{15} \text{ W/cm}^2$ with the delay extension from 0 to 2.6 ns for a constant long-pulse duration, as shown as the solid line in Fig. 4(a). And the intensity only needs to increase from 5.2×10^{14} to $1.2 \times 10^{15} \text{ W/cm}^2$ with the delay extension from 0 to 1.0 ns for a constant long-pulse intensity, as shown as the dashed line in Fig. 4(a). The efficiency for keeping the long-pulse intensity constant is greater than that for keeping the long-pulse duration constant.

Then we calculate the case of changing short-pulse duration while keeping the pulses intensity the same for different long-pulse intensity or duration and delay. The calculations show that the short-pulse durations need to increase from 1.1 to 3.4 ps with the delay extension from 0 to 2.6 ns for a constant long-pulse duration, as shown as the solid line in Fig. 4(b). And the duration only need to increase from 1.1 to 2.3 ps with the delay extension from 0 to 1.0 ns for a constant long-pulse intensity, as shown as the dashed line in Fig. 4(b). The efficiency for keeping the long-pulse intensity con-

stant is also greater than that for keeping the long-pulse duration constant.

From the calculations above, the conclusion we get here is that increasing the duration of the short laser pulse will be more beneficial to enhance the temperature than that of increasing the intensity. However, it should be noted that the duration for the short pulse could also not be too long because of the requirements of TEC limit.

IV. CONCLUSIONS

We investigate analytically the effects of delay time on nickel-like Pd TCE x-ray lasers using an analytical model. The calculations show that a longer delay time can greatly relax the density gradient. This is very critical for the propagation of x-ray lasers. However, a too long delay will reduce the electron temperature before the arrival of the short pulse.

Increasing the long-pulse intensity or extending the pulse duration can keep the temperature required, and therefore high percentage of Ni-like Pd ions. Extending the long-pulse duration is more efficient than that of increasing the intensity. Similarly, increasing the short-pulse intensity or extending the duration can also raise the temperature that is important for enhancing gain coefficient because it is proportional to the electron temperature and inversely proportional to the square root of the ion temperature. As a result, extending the short-pulse duration is also more efficient than that of increasing the intensity.

ACKNOWLEDGMENTS

This work was supported by the National Nature Science Foundation of China under Grant Nos. 19974074, 60108007, 19825110, and the National High Technology ICF program.

-
- [1] P.V. Nickles *et al.*, Phys. Rev. Lett. **78**, 2748 (1997).
 - [2] J. Dunn *et al.*, Phys. Rev. Lett. **80**, 2825 (1998).
 - [3] J. Dunn *et al.*, Phys. Rev. Lett. **84**, 4834 (2000).
 - [4] J. Nilsen, Y. Li, and J. Dunn, J. Opt. Soc. Am. B **17**, 1084 (2000).
 - [5] Lu Xin, Li Ying-Jun, and Zhang Jie, Chin. Phys. Lett. **18**, 1353 (2001).
 - [6] J. Dunn, J. Nilsen, A.L. Osterheld, Y.L. Li, and V.N. Shlyaptsev, Opt. Lett. **24**, 101 (1999).
 - [7] Y.L. Li, J. Nilsen, J. Dunn, A.L. Osterheld, A. Ryabtsev, and S. Churilov, Phys. Rev. A **58**, R2668 (1998).
 - [8] J. Nilsen, J. Dunn, A.L. Osterheld, and Y.L. Li, Phys. Rev. A **60**, R2677 (1999).
 - [9] M.P. Kalachnikov *et al.*, Phys. Rev. A **57**, 4778 (1998).
 - [10] J. Nilsen, Phys. Rev. A **55**, 3271 (1997).
 - [11] J. Zhang *et al.*, Phys. Rev. A **53**, 3640 (1996).
 - [12] J. Zhang *et al.*, Science **276**, 1097 (1997).
 - [13] F.G. Tomasel, J.J. Rocca, V.N. Shlyaptsev, and C.D. Macchietto, Phys. Rev. A **55**, 1437 (1997).
 - [14] Y.J. Li and J. Zhang, Phys. Rev. E **63**, 036410 (2001).
 - [15] A.L. Osterheld *et al.*, *X-ray Lasers 1998*, edited by Y. Kato, H. Takuma, and H. Daido, IOP Conf. Proc. No. 159 (Institute of Physics, Bristol, UK, 1999), pp. 353–362.

Characteristics of self-guided laser plasma channels generated by femtosecond laser pulses in air

Hui Yang, Jie Zhang,* Yingjun Li, Jun Zhang, Yutong Li, Zhenglin Chen, Hao Teng, Zhiyi Wei, and Zhengming Sheng
Laboratory of Optical Physics, Institute of Physics, Chinese Academy of Sciences, Beijing 100080, China

(Received 30 August 2001; revised manuscript received 21 March 2002; published 29 July 2002)

With ultrashort laser pulses (25 fs) and low energy ($E=15$ mJ), we observe laser plasma channels with a length over 5 m in air. The diameter of the plasma channel is measured to be $120\ \mu\text{m}$. The average electron density in the channel is inferred to be about $10^{18}\ \text{W/cm}^3$ with an interferometric method. At the same time, the temporal evolution of the electron density in the plasma channel is investigated. The resistivity in the plasma channel is measured to be less than $1\Omega\ \text{cm}$. It is suggested that the lifetime of the plasma channel can be greatly prolonged by launching another long laser pulse along the plasma channel.

DOI: 10.1103/PhysRevE.66.016406

PACS number(s): 52.35.Mw, 52.40.Db

I. INTRODUCTION

There is a great interest in understanding the propagation process of femtosecond laser pulses through air [1–9]. In 1996, Braun *et al.* [1] observed self-focusing into filaments in air with infrared laser pulses. The filaments can persist over several tens of meters. The mechanism for femtosecond laser pulses propagating over long distance in air is the balance between the Kerr self-focusing due to the nonlinear effects in air and defocusing due to the tunneling ionization and diffraction of the laser beam [6].

In this paper, we present our investigations on characteristics of plasma channels in air generated by femtosecond laser pulses. With an interferometric method, the initial average electron density in the channel is measured to be about $10^{18}\ \text{cm}^{-3}$. The resistivity of the channel is found to be less than $1\Omega\ \text{cm}$. A plasma channel with a length longer than 5 m is observed and the channel diameter is measured to be about $120\ \mu\text{m}$.

II. EXPERIMENTAL SETUP

In our experiments, femtosecond laser pulses were slightly focused with a positive lens ($f=40\ \text{cm}, 2\ \text{m}, 4\ \text{m}$) in air. At the same time, with an interferometric method as shown in Fig. 1, the electron density in the plasma channel was measured. The laser system is a home-made Ti:sapphire laser system, that can provide up to 45 mJ energy, in 25 fs pulses, at a central wavelength of 800 nm. The laser beam was focused in air and formed a plasma channel. A small portion of the laser beam was frequency doubled by a BBO crystal to serve as a probing laser beam. The delay between the main laser beam and the probing laser beam could be adjusted. After transmitting through the plasma channel, the probing beam was focused through a Wollaston prism and a polarizer. Finally the interferometric fringes were recorded by a charge-coupled device (CCD) camera. At the same time, we measured the length and diameter of the plasma channel with a CCD camera (512×512 pixels) with a pixel size of $24\ \mu\text{m}$.

III. RESULTS AND ANALYSIS

A typical image of the plasma channel is shown in Fig. 2, where a lens with $f=2\ \text{m}$ was used to slightly focus the laser beam. Generally the length of the channel varied with the focus length of the lens. The length of the channel was about 30 cm when using a lens of $f=1.5\ \text{m}$. It became longer than 50 cm as shown in Fig. 2(a), when a lens of $f=2\ \text{m}$ was used. Furthermore, when a lens with $f=4\ \text{m}$ was used, a good conductive plasma channel with a length greater than 5 m was observed. From Fig. 2(b), we can find that the laser intensity distribution in the channel is close to a Gaussian and the Gaussian-fitting diameter of the filament is about $120\ \mu\text{m}$. The Rayleigh length of the laser beam is about 14 mm for this diameter. We then know that the laser beam can propagate over hundred Rayleigh lengths. This result is in good agreement with our calculations [6].

An analysis shows that the electron distribution initially created by the laser pulse can be very quickly smoothed by recombination and collisional processes. To measure the electron density in the channel, we used an interferometric method as shown in Fig. 1 [12]. Because the laser intensity in the channel is only about $10^{14}\ \text{W/cm}^2$, the static magnetic field can be omitted. The refractive index in air therefore can be expressed as

$$N^2 = 1 - \omega_p^2/\omega_L^2, \quad (1)$$

where N is the refractive index of the plasma channel, ω_p is the plasma frequency, and ω_L is the laser frequency. When the probing beam traverses the plasmas channel, the phase-shifted probing beam can be written as

$$\Delta\Phi = \int (k_p - k_0) dl = \int (N - 1) \omega / c dl, \quad (2)$$

where $k_0 = \omega/c$ is the wave number. $N^2 = 1 - \omega_p^2/\omega_c^2 = 1 - n_e/n_c$, $n_c = \omega^2 m \epsilon_0 / e^2$ is the critical density. If the plasma density is small enough, we then have $n_e/n_c(\omega_p^2/\omega_c^2) \ll 1$. This condition is satisfied in our experiment. So the phase shift of the interference fringe is

$$\Delta\Phi = \frac{\omega}{c} \int \left[\left(1 - \frac{n_e}{n_c} \right)^{1/2} - 1 \right] dl \approx \frac{\omega}{2c n_c} \int n_e dl. \quad (3)$$

*Author to whom correspondence should be addressed. Email address: jzhang@aphy.iphy.ac.cn

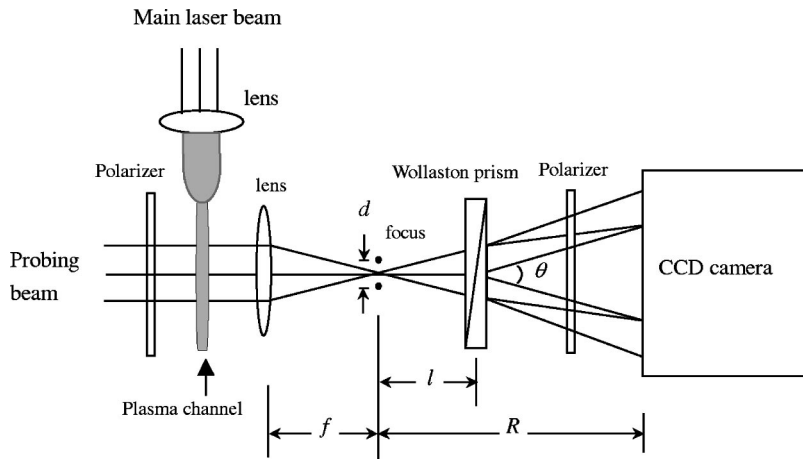


FIG. 1. Schematic of the experimental setup.

Assuming that the shift number is D , and $\Delta\Phi = 2\pi D$, then we have

$$\int n_e dl = 2Dn_c\lambda. \quad (4)$$

In this experiment, we are interested in the average electron density, so the expression (4) can be rewritten as

$$\overline{n_e}d = 2Dn_c\lambda, \quad (5)$$

where d is the diameter of the plasma channel. In the experiment, when the delay between the main laser and the probing beam is about 600 ps, the shift of the interference fringes was measured as shown in Figs. 3(a) and 3(b). The average shift number can be measured to be $\bar{D} = 1/8$. We can then obtain

$$\overline{n_e} = 2.7 \times 10^{18} \text{ cm}^{-3}. \quad (6)$$

The temporal history of the electron density was measured by the interferometric method as shown in Fig. 4. The

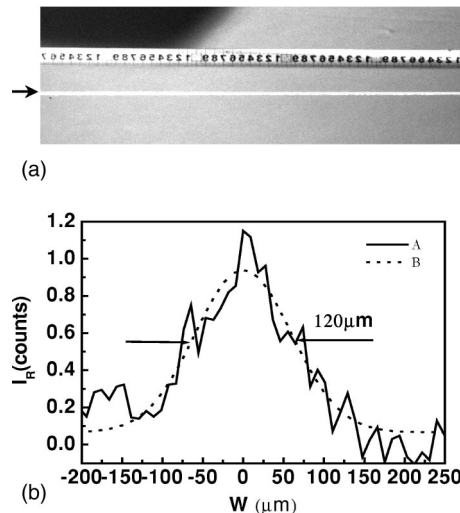


FIG. 2. (a) The image of a part of the plasma channel formed by a femtosecond laser beam with an $f=2$ m lens. (b) The relative intensity (I_R) distribution in the channel fitted by a Gaussian function (dotted curve).

solid curve is the measured result and the dotted line is the fitting curve by the following expression:

$$n_e = 6.18 \times 10^{18} \exp^{-t/0.684}. \quad (7)$$

We can estimate the lifetime of the plasma channel from this result. After the plasma channel is formed, dynamics of the channel will follow the equation of continuity as follows [10,11]:

$$\frac{\partial n_e}{\partial t} + \frac{\partial Vn_e}{\partial z} = \alpha n_e - \eta n_e - \beta_{ep} n_e n_{pn}. \quad (8)$$

$$\frac{\partial n_p}{\partial t} + \frac{\partial Vn_p}{\partial z} = \alpha n_e - \beta_{ep} n_e n_{pn} - \beta_{np} n_n n_p, \quad (9)$$

$$\frac{\partial n_n}{\partial t} + \frac{\partial Vn_n}{\partial z} = \eta n_e - \beta_{np} n_n n_{pn}. \quad (10)$$

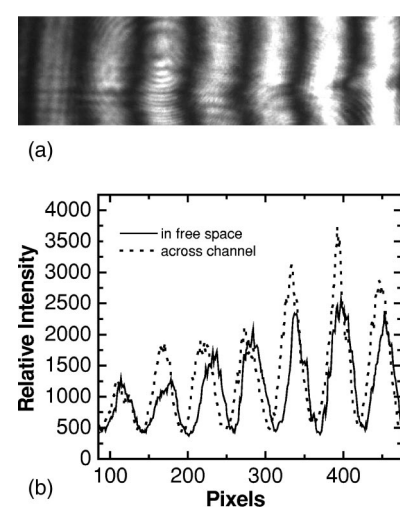


FIG. 3. (a) The image of the interferometric fringes by a CCD camera. (b) The average shift in every interferometric fringe. The dotted curve represents the probing beam traversed the plasma channel, and the solid curve represents the probing beam in free space.

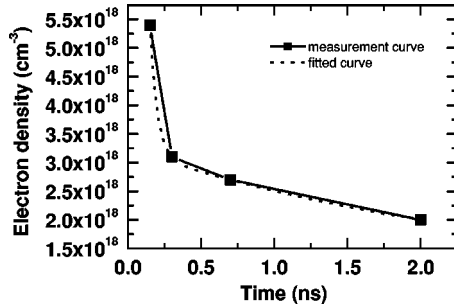


FIG. 4. The decay of the electron density in the plasma channel versus time.

where n_e , n_p , n_n are electron density, positive ions, and negative ions in air, respectively, as reported in Refs. [7,8], and α , η , β_{ep} , β_{np} are the collisional ionization rate, the attachment rate, the electron-ion recombination coefficient, and the ion-ion recombination coefficient, respectively. Assuming that the plasma density in the channel is uniform in space and neglecting the collisional ionization rate, we take $\eta = 2.5 \times 10^7 \text{ s}^{-1}$ for the attachment rate of electrons to oxygen, $\beta_{ep} = 2.2 \times 10^{-13} \text{ m}^3/\text{s}$ for the electron-ion recombination, and $\beta_{np} = 2.2 \times 10^{-13} \text{ m}^3/\text{s}$ for ion-ion recombination. Taking the following initial conditions,

$$n_e(t=0) = n_p(t=0) = 10^{18} \text{ cm}^{-3}, \quad n_n(t=0) = 0,$$

we can then obtain temporal evolution of the electron density in the channel as shown by curve *a* in Fig. 5, and find that the electron density decays three orders within 30 ns from curve *a*. In Fig. 5, the dashed curve *c* is an exponential decay fitting. So from curve *a* and *c* in Fig. 5, we can find that in the initial period, the electron density follows an exponential decay as we measured shown in Fig. 4. But at the longer time, the decay of the electron will deviate from the exponential decay. In many applications such as triggered lightning, plasma channels with longer lifetime are required. Usually, the plasma lifetime is constrained by the strong attachment of electrons to oxygen molecules to form negative ions O^- and O_2^- in air [11]. In order to maintain a high electron density in plasma channel, another long laser pulse is launched along the plasma channel, with an intensity I_2 to detach electrons from O^- and O_2^- . So we add another term $\gamma_l n_n$ in Eqs. (8)–(10), where γ_l is the detachment coefficient. For simplicity we can set the detachment rate η to be equal to the attachment rate, and the required intensity $I_2 = 6.8 \times 10^5 \text{ W/cm}^2$ was given by Ref. [11]. Then we can calculate the electron density in the plasma channel again, and find that the lifetime of the plasma is greatly prolonged, as shown by curve *b* in Fig. 5. The decay time for three orders is now greatly extended in the order of μs . This is an efficient way to extend the lifetime of plasma channel.

We measured the conductivity of the plasma channel using a similar method as described in Ref. [5]. Because the

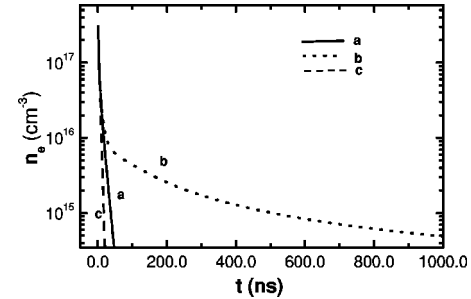


FIG. 5. The temporal dependence of the electron density in the channel. The solid curve *a* represents the free decay of the electron density in the channel, the dotted curve *b* represents the temporal evolution of the electron density in the plasma channels with a long-pulse laser after an femtosecond laser pulse. The dashed curve *c* represents the exponential decay fitting.

collisional frequency of electrons is about $1/\nu = 1.1 \text{ ps}$ in air, this is much shorter than the characteristic time for the evolution of an electron plasma. So we can treat it with a steady limit, which is Ohm's law. In our experiment, the parallel copper plates were separated by 6.5 cm. The electrical signals were recorded by a digital oscilloscope with a 500 MHz bandwidth (Tekex Corporation). A $8 \text{ k}\Omega$ resistance was used to limit the current and the signal voltage was obtained from a 50Ω resistance by an oscilloscope. The signal voltage is shown in Fig. 4, when the applied voltage is 1500 V. The peak signal voltage across a 50Ω resistance was 1580 mV. Following Ohm's law, we have

$$\eta = 0.76 \Omega \text{ cm}. \quad (11)$$

Because the connection between the plasma channel and the copper electrodes was not perfect, so the measured value is only the upper limit of the resistivity of the channel.

IV. CONCLUSIONS

Plasma channels over 5 m were observed when a femtosecond laser pulse propagated in air. The plasma lifetime can be greatly prolonged by launching another long laser pulse along the plasma channel. The size of the plasma channel was measured to be about $120 \mu\text{m}$. Furthermore, the electron density in the plasma channel was measured to be about $n_e = 2.7 \times 10^{18} \text{ cm}^{-3}$ with an interferometric method and the resistivity of the plasma channel was less than $1\Omega \text{ cm}$, respectively. These experimental results are in good agreement with our theoretical analysis.

ACKNOWLEDGMENTS

We are thankful for the helpful discussion with Professor J. X. Ma. This work was supported by the National Natural Science Foundation of China (Nos. 19825110, 1000405, and 1997074) and National Key Basic Research Special Foundation (Grant No. G1990075200).

- [1] A. Braun, G. Korn, X. Liu, D. Du, J. Squier, and G. Mourou, Opt. Lett. **20**, 73 (1995).
- [2] E. T. J. Nibbering, P. E. Curley, G. Grillon, B. S. Prade, M. A. Franco, F. Salin, and A. Mysyrowicz, Opt. Lett. **21**, 62 (1996).
- [3] A. Brodeur, C. Y. Chien, A. Ilkov, S. L. Chin, O. G. Kosareva, and V. P. Kandidov, Opt. Lett. **22**, 304 (1997).
- [4] L. Wöste *et al.*, Laser Optoelektron. **5**, 29 (1997).
- [5] S. Tzortzakis, M. A. Franco, Y.-B. Andr, A. Chiron, B. Lamouroux, B. S. Prade, and A. Mysyrowicz, Phys. Rev. E **60**, R3505 (1999).
- [6] H. Yang, J. Zhang, W. Yu, Y. J. Li, and Z. Y. Wei, Phys. Rev. E **65**, 016406 (2002).
- [7] S. Tzortzakis, B. Prade, M. Franco, and A. Mysyrowicz, Opt. Commun. **181**, 123 (2000).
- [8] B. L. Fontaine, F. Vidal, D. Comtois, C. Y. Chien, A. Desparois, T. W. Johnston, J. C. Kieffer, H. P. Mercure, H. Pépin, and F. A. M. Rizk, IEEE Trans. Plasma Sci. **27**, 688 (1999).
- [9] H. Yang, J. Zhang, J. X. Ma, and W. Yu, High Power Laser Particle Beams **5**, 537 (2000), in Chinese.
- [10] L. B. Loeb, *Basic Processes of Gaseous Electronics* (University of California Press, Berkeley, 1960), p. 618.
- [11] X. M. Zhao, J. C. Diel, C. Y. Wang, and J. M. Elizondo, IEEE J. Quantum Electron. **31**, 599 (1995).
- [12] Y. T. Li *et al.*, Sci. China, Ser. A Math., Phys., Astron. **43**, 1249 (2000).

Efficient Chirped-Pulse Multi-Pass Preamplifier

H. TENG, J. F. XIA, Z. Y. WEI and J. ZHANG*

Laboratory of Optical Physics, Institute of Physics, Chinese Academy of Sciences, Beijing 100080, China

(Received 10 April 2001)

A multi-pass preamplifier with two pairs of spherical mirrors has been developed, and an extraction efficiency as high as 23 % has been obtained. This corresponds to a gain of 4×10^6 . To our best knowledge, this is the highest efficiency achieved for multi-pass preamplifiers.

I. INTRODUCTION

In recent years, the great progress on chirped-pulse amplification (CPA) Ti:sapphire lasers has led to a rapid increase in peak power and to wide applications of ultra-short pulse lasers, such as high field physics, fast ignition laser fusion, ultrafast X-ray generation, relativistic plasma physics, etc. A peak power of 1.5 PW has been achieved with a CPA technique in a glass laser system [1]. Shaping the spectrum in a special regenerative preamplifier has also been used to compress amplified pulses to sub-20fs [2].

A typical CPA laser system consists of a femtosecond (fs) laser oscillator, a pulse stretcher, a preamplifier, a main amplifier, and a compressor. Firstly, a train of seeding fs pulses is generated by a mode-locking laser oscillator. For amplification of seeding pulses with nJ energy to a higher level without nonlinear effects and damage, a stretcher is used to extend the seeding pulse to hundreds of picosecond (ps). After synchronization with the pump laser pulse, the stretched pulses are injected into a preamplifier for gain amplification and for further power amplification with the main amplifier. Finally, the amplified pulses are compressed to the duration of seeding pulses by a negative dispersion system, which normally consists of a pair of gratings to cancel the positive dispersion from the stretcher and the optical components in the amplification process. During this process, the preamplifier plays an important role in generating chirped pulses with enough energy and bandwidth.

There are two types of preamplifiers, regenerative [3] and multi-pass [4]. In general, a regenerative amplifier is composed of a cavity and a pulse picker, just like an oscillator. The regenerative amplifier supports good beam quality and high efficiency. However, its stability strongly depends on the design and alignment of the cavity as well as the pump energy. Moreover, the laser operation in the resonator results in strong gain-narrowing

and material dispersion. Both of these effects will lead to non-idealy compressed pulses. As for the multi-pass amplifier, the gain-narrowing effect and material dispersion can be minimized and in principle shorter compressed pulses can be obtained. Because of these benefits, multi-pass amplifiers are now widely used as preamplifiers [5]. However, with this design, the only shortcoming is the efficiency is normally lower than the efficiency of a regenerative preamplifier. In this paper, we report a novel multi-pass amplifier, which can not only compensate the gain-narrowing effects, but also obtain an efficiency as high as 23 %. To our best knowledge, not only is this the highest efficiency achieved for multi-pass pre-amplifiers, but it is also close to the best result for a generative preamplifier [6].

II. EXPERIMENTAL RESULTS

Figure 1 is the experimental configuration constructed at the Institute of Physics, Chinese Academy of Sciences. It consists of a homemade 13 fs self-mode-locked Ti:sapphire oscillator, an Öffner stretcher, two-stage amplifiers and a grating compressor. The final output is peak power of 1.4 TW in 25-fs pulses [7]. The detailed

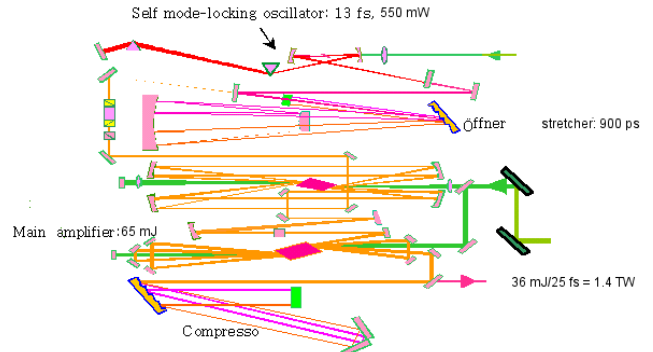


Fig. 1. Schematic of a TW laser system.

*E-mail: jzhang@aphy.iphy.ac.cn

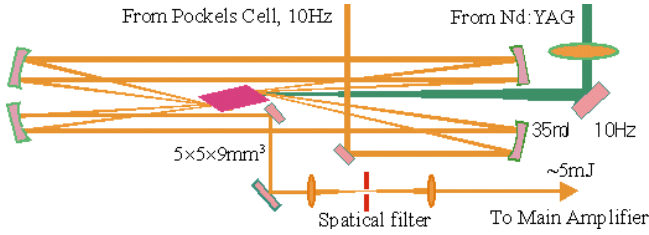


Fig. 2. An 8-pass preamplifier.

optical scheme for the preamplifier is shown in Fig. 2. Two pairs of spherical mirrors with curvature radii of 1039 mm and 931 mm, respectively, are aligned in a confocal configuration. A $5 \times 5 \times 9\text{-mm}^3$ Brewster-angle cut Ti:sapphire crystal is located at the common focal point. All mirrors are 30 mm in diameter and coated with a high reflectivity dielectric film for the wavelength range between 700 and 900 nm at normal incidence. Compared with the previous design with a smaller aperture of 25.4 mm, the new mirrors with bigger apertures make it much easier to align and to support 10- to 12-pass amplification.

The amplification principle can be illustrated with the propagation of chirped pulses in this unstable cavity. Because of the asymmetric design of the curvature radii at a 1:1.1 ratio, the amplified laser beam will vertically move to the optical axis after each pass. This will lead to well-separated laser beams on the spherical mirrors; these beams can be picked up from the system. More precisely, the distance between the beam spots on the mirrors will be decreased by a factor of 1 : 1.1². Figure 3 shows the beam-spot distribution on the mirror during amplification, where 4 spots represent 8-pass amplification.

In addition, the areas of the laser beams on the spherical mirrors are decreased by a factor of 1.1². On each amplification pass, the focal spot size on the crystal will be enlarged by a factor of 1.1². Therefore, the energy

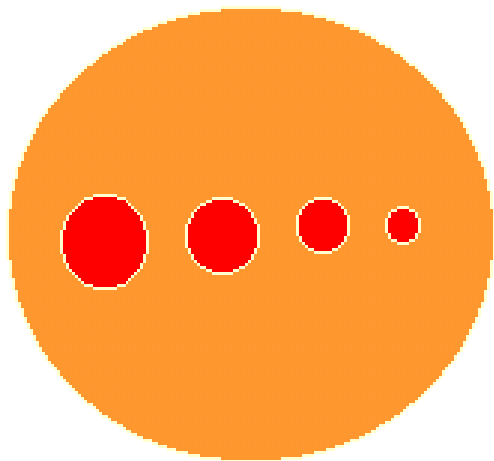


Fig. 3. Beam patterns on the reflective mirror.

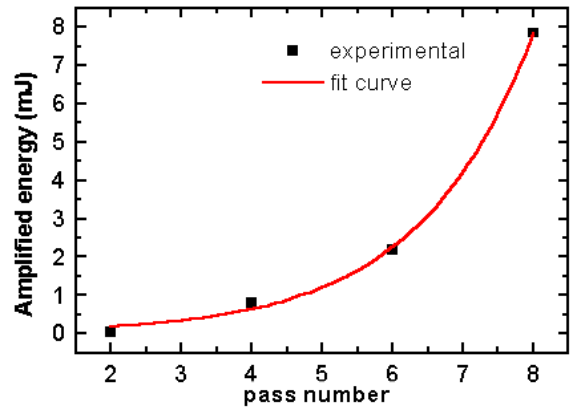


Fig. 4. Evolution of the amplified energy in an 8-pass preamplifier.

density in the gain medium will be equalized and will not reach gain saturation. This promises higher energy without gain narrowing. In order to study the dependence of the amplified energy on the number of passes, we set a small rectangle mirror in a movable stage. By transversally moving the stage, we could easily control the pass and pick out the last amplified laser pulse from the system for measurement.

After stretching and pulse picking with the Pockels cell, the energy in the seeding pulses for amplification is decreased to about 2nJ. A Ti:sapphire crystal is single-sided pumped with a 35-mJ, 532-nm Nd:YAG laser at a 10-Hz repetition rate (S-P company). For good overlap with the chirped pulse, a lens with a 700-mm focal length is used to focus the pump laser and to keep the focus spot behind the gain medium to prevent optical damage. The typical pump spot size on the crystal is about 1.5 mm. Figure 4 shows the evolution of the amplified energy in a 8-pass preamplifier. The amplified energy grows exponentially. Stable amplified pulses with an output energy as high as 5 mJ are obtained under this pump energy. Our theoretical calculation shows that the focal spot size on the crystal for the last pass (8th pass) is about 950 μm , corresponding to an energy density of about 0.7 J/cm^2 . This is close to the saturation fluence for a Ti:sapphire crystal. However, the peak power density is still below the threshold for nonlinear effects. It is the special design with an increased focal spot size on the crystal at each amplification pass that minimizes the saturation effect and the nonlinear effect, although the amplified energy is increased on successive passes. This assures an increase in the amplified energy without serious gain narrowing and nonlinear effects. With further careful alignment, an output energy as high as 8 mJ without ASE(Amplified Spontaneous Emission) from the preamplifier was obtained. This corresponds to a gain of 4×10^6 and an efficiency of 23 %. This is an obviously improved result compared with the reports for normal multi-pass and even for some regenerative amplifiers. The energy stability is better than 3 %, and the

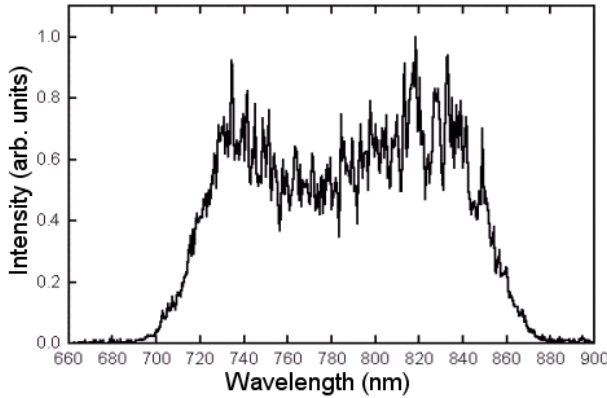


Fig. 5. Spectrum of the seeding pulse before a preamplifier.

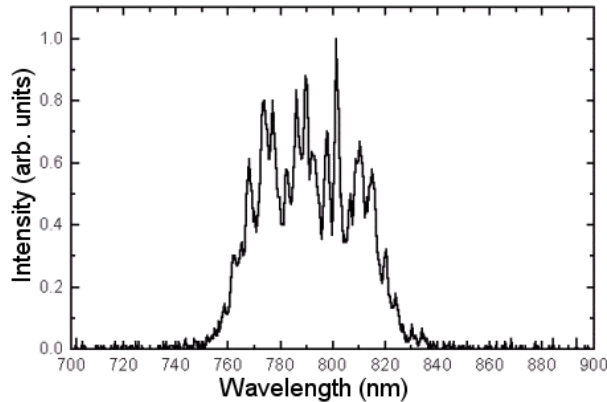


Fig. 6. Spectrum of a compressed pulse.

beam structure is a uniform TEM_{00} .

Figure 5 and 6 show the spectrum of the seeding pulse before the preamplifier and the spectrum of the compressed pulse after the final compressor, respectively.

This demonstrates our multi-pass amplifiers can maintain high bandwidths and support short pulses.

III. CONCLUSION

In conclusion, we have developed an asymmetric confocal reflective multi-pass preamplifier with 4 mirrors. A gain and efficiency as high as 4×10^6 and 23 % have been achieved respectively. This well assures energy amplification in main amplifier to 65 mJ under a 255 mJ pump. With an acceptable gain-narrowing in this design, 25-fs compressed pulses are obtained. This corresponds to a 1.4-TW peak power.

ACKNOWLEDGMENTS

This work was jointly supported by the National Natural Science Foundation of China (grant no. 19825110&10075075) and the National High-Tech Inertial Confinement Fusion program.

REFERENCES

- [1] M. D. Perry, D. Pennington, B. C. Stuart, *et al.*, Opt. Lett. **24**, 160 (1999).
- [2] K. Yamakawa, M. Aoyama, *et al.*, Opt. Lett. **23**, 1468 (1998).
- [3] F. Salin, J. Squier, *et al.*, Opt. Lett. **16**, 1964 (1991).
- [4] J. Zhou, C. P. Huang, M. M. Murnane, *et al.*, Opt. Lett. **20**, 64 (1995).
- [5] G. Cheriaux, P. Rousseau, F. Salin, *et al.*, Opt. Lett. **21**, 414 (1996).
- [6] S. Takeuchi, and T. Kobayashi, Opt. Comm. **109**, 518 (1994).
- [7] Z. Wei, J. Zhang, J. Xia, *et al.*, Science in China **43**, 1083 (2000).

Studies of Interactions of Femtosecond Laser Pulses with Foil Targets

J. ZHANG*, Y. T. LI, L. M. CHEN, H. TENG, Q. L. DONG and Z. Y. WEI

Laboratory of Optical Physics, Institute of Physics, Chinese Academy of Sciences, Beijing 100080 P. R. China

(Received 10 April 2001)

The emission of hot electrons is measured in the interaction of femtosecond laser pulses with foil targets at a moderate laser intensity. A collimated jet of backward hot electrons is observed in the target's normal direction whereas forward hot electrons are found to be deflected to the laser propagation direction. The low energy electrons spread into a much wider cone angle due to the collisional effects in the plasma and the target material. These results are supported by 3D Monte Carlo simulations. The temperature dependence of the hot electrons and laser absorption measurements imply the resonance absorption is partly responsible for the generation of hot electrons.

I. INTRODUCTION

The rapid development of short-pulse ultra-intense lasers provides a powerful tool to study relativistic laser-plasma interactions and to explore new approaches to ignite inertial confinement fusion (ICF). The fast ignitor concept proposed by Tabak *et al.* is a very promising way to achieve this goal [1]. One of the major physical issues to implement fast ignition is the generation and the propagation of energetic hot electrons in a high-density plasma. The laser energy conversion efficiency to hot electrons, the electron direction, and the effective temperature are main issues of studies. Recently, energetic hot electrons escaping from plasmas were studied experimentally and theoretically [2-7]. Hot electrons with energies up to 100 MeV were observed in laser-solid interactions at an intensity as high as $3 \times 10^{20} \text{ W/cm}^2$ [8]. Malka *et al.* measured relativistic electrons produced by a relativistic intensity laser pulse interacting with solid targets [9]. The results were attributed to a $J \times B$ acceleration mechanism [10]. The forward moving relativistic electrons propagating along the laser pulse beam were studied in the plasma channel of picosecond laser pulses [11,12].

Collimated electron beams in vacuum and dense plasmas have been observed by several research groups. Tatarakis *et al.* found a plasma at the rear surface of thin foils. The plasma was believed to have been formed by a collimated electron beam [13]. A more direct experiment was carried out using a transparent glass target coated with an aluminum layer, in which an ionization track induced by a beam of MeV electrons was clearly observed [14,15]. Norreys *et al.* observed a highly directional g-

ray beam with energies above 10 MeV nearly opposite to the target normal direction by using the photo-neutron reaction in copper, which indicated the generation of a directional relativistic electron beam [16]. These experimental results imply that the transport of hot electrons can be collimated by self-generated magnetic fields. The generation of hot electron jets and the pinching effects of magnetic fields were reproduced in particle-in-cell (PIC) simulations [17,18].

Many mechanisms can produce hot electrons. In the interaction of an intense laser pulse with a sharp solid-vacuum interface, the ponderomotive potential model and the Brunel absorption model [19] play important roles. Other mechanisms, such as wake fields [20], parametric instabilities [21,22], B-loop mechanisms [23], and propagating waves [24], are effective when a large-scale preplasma is formed before the arrival of the main laser beam.

The directional emission of hot electrons is not a phenomenon unique to relativistic laser intensities. In this paper, we report the observation of an electron jet produced at a moderate laser intensity. The angular distribution of the backward and the forward hot electrons, the electron energy spectrum, the generation mechanism, and the transport of hot electrons into cold target material were investigated in ultrashort-pulse, laser-foil target experiments.

II. EXPERIMENTAL SETUP

The experiments were carried out at the ultrashort pulse laser facility at the Institute of Physics, Chinese Academy of Sciences. The Ti:sapphire laser system has a 5-mJ output energy in 150 fs at 796 nm. The p-polarized

*E-mail: jzhang@aphy.iphy.ac.cn

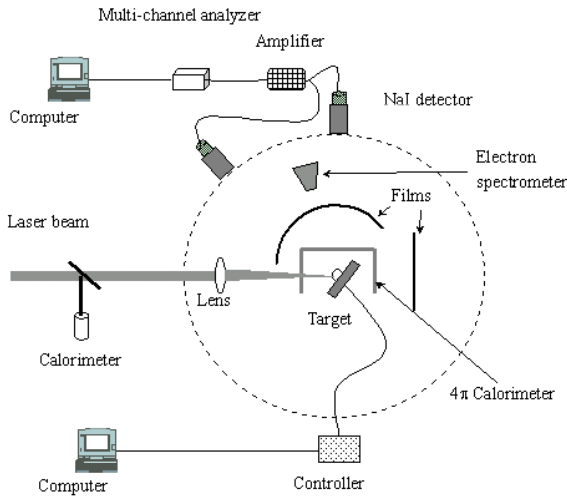


Fig. 1. Schematic of experimental setup. A 4π calorimeter was used to measure the energy absorption. The laser energy was monitored by using the calorimeter outside the target chamber. The energy distribution and the spatial distribution of hot electrons ejected from the plasma were detected by an electron spectrometer and by radiochromic films surrounding the plasma, respectively. A NaI system was used to monitor the intensity of hard x-ray emission, which monitored the focal condition.

laser beam was focused by an $f/5$ lens onto solid targets with an average intensity of $5 \times 10^{15} \text{ W/cm}^2$. The target was moved 0.5 mm per second so that the laser pulses interacted with a fresh target surface for every shot. For some shots, a pre-pulse with 8 % of the energy of the main laser pulse was applied to create a pre-plasma with which the main laser pulse interacted after a 50-ps delay time.

Figure 1 shows the experimental layout. In the first laser, thick- foil, target experiments, the laser beam was incident onto a $100\text{-}\mu\text{m}$ -thick aluminum foil at 45° to the target normal. A 6-channel electron spectrometer with 380-G permanent magnets was set in the normal direction to measure the electron energy distribution in the range of 7 – 500 keV [25]. LiF was used as the detector. Radiochromic film with an aluminum filter surrounding the focal spot recorded the backward electrons escaping from the plasma at the frontside of the target. A 4π calorimeter measured the laser energy absorption. A 2-mm-thick cylinder made of quartz and placed inside the calorimeter blocked the charged particle and X-ray emission. In order to study the forward hot electrons, more relevant to the ‘fast ignition’ concept, the laser, thin-foil, target experiments were performed, too. Forward energetic hot electrons along the laser propagation direction, after they penetrated the thin foil target, were recorded by using a radiochromic film at the backside of the target. Five- μm -thick foil targets were employed in these experiments. The incident measurement showed a higher coupling efficiency at a 30° incidence. The NaI

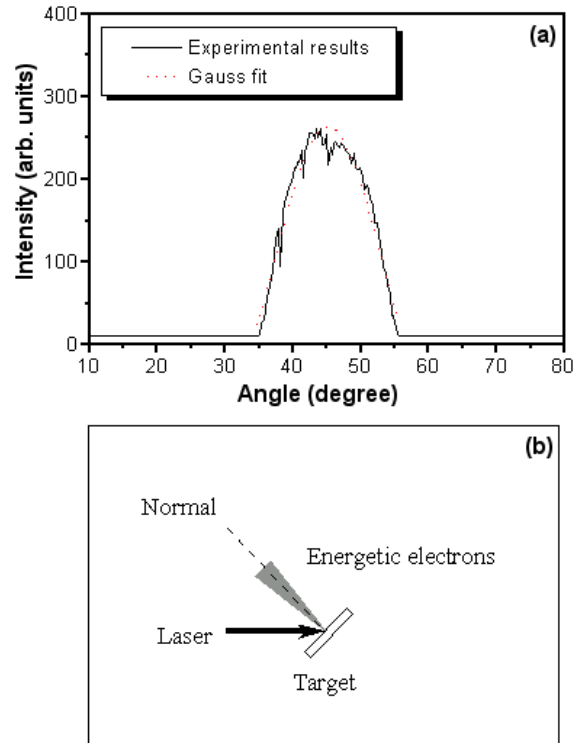


Fig. 2. (a) The angular distribution of backward hot electrons with energies over 50 keV in the incident plane. The electrons were generated by p-polarized light at 45° incidence with a pre-pulse 50 ps before the main beam. The laser intensity was $5 \times 10^{15} \text{ W/cm}^2$. The peak was located at the normal direction (45°). (b) A sketch of the backward energetic electron emission in front of the target.

detector system shown in Fig. 1 was used to measure the hard X-ray emission [26].

III. EXPERIMENTAL RESULTS AND DISCUSSION

1. Thick Foil Experiments

1. Angular distribution of backward hot electrons

An aluminum filter assembly was used in front of the radiochromic film to determine the desirable electron energy range. The radiochromic film recorded the electrons, ions, and hard X-ray photons passing through the filter assembly. However, the film sensitivity to charged particles is higher than it is to photons. Previous ion measurements using CR-39 detectors showed that the maximum proton energy produced under similar conditions was less than 500 keV [27], corresponding to a penetration depth about $4 \mu\text{m}$ in aluminum material. Therefore, the ion contribution to the film exposure is negligible because the thickness of aluminum filter used was

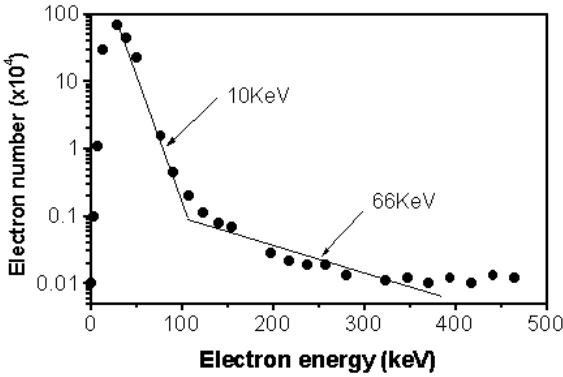


Fig. 3. Typical normal-direction energy spectrum of backward hot electrons produced in laser, thick-foil target interactions. The foil was irradiated by p-polarized laser at 45° incidence with a pre-pulse separated from the main beam by 50 ps. The laser intensity was $5 \times 10^{15} \text{ W/cm}^2$. Two hot electron temperatures are obtained from exponential fits to the experimental data.

greater than $8 \mu\text{m}$ at least. To check the effects of hard X-rays on the film exposure, we performed a verification experiment. Two permanent magnets were employed to deflect electrons with energies less than 500 keV. This would remove most of the electrons escaping from the plasma (see Fig. 3). Comparison of the D value of the film with and without an external magnetic field showed that the contribution of hard X-rays was two orders of magnitude lower than that of electrons. This result assured us that the exposure of the film was mainly caused by electrons.

Figure 2 shows the angular distribution in the incident plane of backward hot electrons with energies greater than 50 keV. The electrons were generated by a p-polarized laser beam at 45° incidence with a pre-pulse 50 ps in front of the main pulse. The solid line in Fig. 2(a) is a microdensitometer trace of the angular distribution of hot electrons produced in a $100 \mu\text{m}$ -thick aluminum foil. The dotted line is a Gaussian fit. Each data point here represents an average of 30 shots. Zero degrees on the x-axis corresponds to the backward direction of laser pulse. We can see that the backward electrons escaping from plasma in a direction normal to the target were well collimated.

The observed electron jet is very similar to the theoretical results obtained by Ruhl *et al.* [17] and Sentoku *et al.* [18] using PIC and Vlasov simulations. They found that electron jets were generated in the interaction of a p-polarized laser beam incident at 30° and 45° on a fully ionized target with an underdense pre-plasma corona. Self-generated magnetic fields occurred simultaneously and collimated the energetic electrons. The scaling law for the angle of the ejected electrons determined by lateral canonical momentum conservation in boost frame

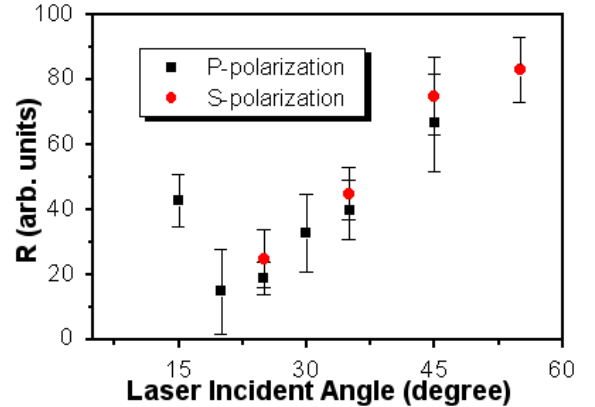


Fig. 4. Angular dependence of the measured reflectance for a p-polarized beam (square) and a s-polarized beam (circle) with a pre-pulse 50 ps before the main beam. Each point is the average of several shots with the statistical errors shown as error bars.

coordinates was proposed as

$$\theta' = \tan^{-1} \left[\frac{\sqrt{1 + \alpha \lambda^2 / 10^{18}} - 1}{\sqrt{\alpha \lambda^2 / 10^{18}}} \tan \theta \right], \quad (1)$$

where θ' is the angle of electron emission relative to the target normal. θ is the laser incident angle. λ^2 is the laser intensity in $\text{W cm}^{-2} \mu\text{m}^2$. α is estimated to $2.8 \text{ W}^{-1}\text{cm}^2 \mu\text{m}^{-2}$ for non-relativistic intensities by using PIC and Vlasov simulations, which relates the mean longitudinal momentum to the laser intensity. Under our experimental conditions, this formula yields an electron emission angle of $\sim 3^\circ$ to the normal direction. This value is very close to our result of 2.5° .

2. Electron energy spectrum

A typical hot-electron energy spectrum measured in the normal direction is shown in Fig. 3. The laser pulses irradiated the aluminum foil at 45° . Eight percent prepulses were introduced so as to arrive at the target surface 50 ps earlier than the main pulse. It is apparent that two groups of hot electrons were generated in the interaction. The experimental data were fitted using a Boltzmann distribution, and the effective temperatures were 10 keV and 66 keV. The lower temperature is consistent with conventional resonant absorption scaling [21], $T_h = 6 \times 10^{-5} [I \lambda^2 (\text{Wcm}^{-2} \mu\text{m}^2)]^{0.33} \text{ keV}$, which gives 9 keV for an intensity of $5 \times 10^{15} \text{ W/cm}^2$. The 66-keV hot temperature is higher than the value given by ponderomotive potential energy scaling [10]. However, the scaling proposed by Beg *et al.* [28], $T_h = 100 [I \lambda^2 (\text{Wcm}^{-2} \mu\text{m}^2)]^{1/3} \text{ keV}$, gives a hot temperature of 32 keV, which is not very different from our experimental value.

3. Energy absorption measurement

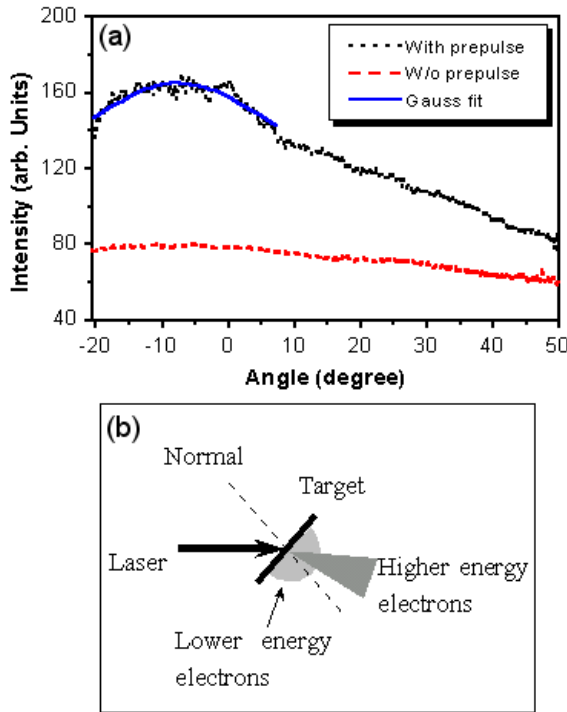


Fig. 5. (a) Angular distribution of forward hot electrons with energies greater than 30 keV and measured at the back-side of a 5 μm thick foil target. The dotted line and the dashed line are for the cases with and without the pre-pulse, respectively. A peak at -8° with a 24° FWHM is superposed on a very broad continuous distribution for the case with a pre-pulse. No such peak is seen for the distribution without a pre-pulse. (b) Sketch of the electron emission at the back-side of the target for the case with a pre-pulse. Low energy electrons spread into a wide angle as a continuum of higher energy electrons.

Hot electron generation is closely related to laser-plasma coupling processes. We carried out an absorption experiment to confirm the dominant energy absorption mechanism. Initially, we used two separated calorimeters with 20-mm-diameter apertures to measure the scattered laser light. The spatial distribution of scattered light was obtained by setting the calorimeters at different positions. It was found that nearly all of the light was reflected into a small solid angle in the specular direction when the laser beam was incident obliquely without a pre-pulse. This implies that short pulses interact with a very thin skin layer of less than a laser wavelength. However, the light was scattered into a wide solid angle when a prepulse was introduced. Therefore, in the later experiments, the separated calorimeters were replaced by a 4π spherical calorimeter. The 4π spherical calorimeter collected all the scattered light, except the backreflected light. This part is only a few percent and is thus negligible.

The results of absorption measurements conducted with a 100- μm -thick aluminum foil target for both p-

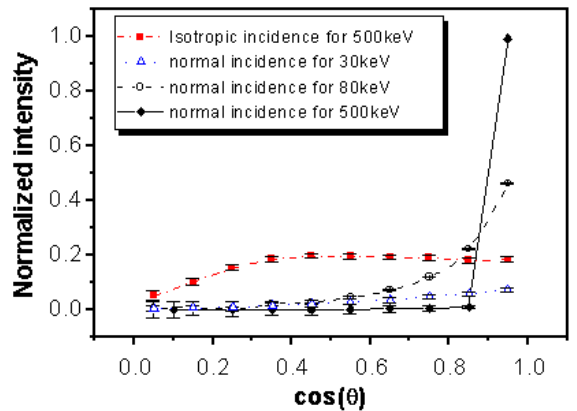


Fig. 6. Theoretical angular distribution of hot electrons recorded behind a 5 μm -thick aluminum foil, as obtained by using a 3D Monte Carlo code. The circle is for an isotropic electron source (shown $\times 5$). θ is the angle relative to the direction normal to the surface of aluminum foil. For collimated electron beams perpendicular to the foil, the divergent angles are wider for lower energy electrons.

polarized and s-polarized laser beams are shown in Fig. 4. A pre-pulse 50 ps in front of the main pulse was introduced. The absolute absorption coefficient could not be obtained because the calorimeter was not calibrated. We can see that the absorption is both angle and polarization dependent. This is one of the main characteristics of resonance absorption. The maximum absorption for p-polarized laser pulse was at a 20° angle of incidence. This corresponded to a plasma scale length $L/2\lambda$. These results may imply that resonance absorption plays an important role in laser plasma coupling. Other processes, such as vacuum heating [19,20], may also be responsible for the generation of energetic hot electrons.

2. Thin Foil Experiments

Hot electrons produced in laser-plasma interactions were ejected from the focal spot. Some of them escaped into vacuum from the plasma region after overcoming the charge separation potential. We have presented their angular distribution in Part A, Section 1. On the other hand, the hot electrons in the forward direction will be transported into the overdense plasma region and the cold target region. Hot electrons with higher energies even run through the foil target. In fast ignition studies, a bunch of directional energetic electrons is required.

We measured the angular distribution of forward electrons by using radiochromic films with an aluminum filter set at the backside of the foil target. Figure 5 shows that angular distribution of the forward hot electrons with energies greater than 30 keV. The target was a 5- μm -thick aluminum foil. The incident laser intensity was $5 \times 10^{15} \text{ W/cm}^2$. The incident angle was 30° , and the

laser beam was p-polarized in these experiments. The dotted line and the dashed line in Fig. 5(a) denote the results obtained with an 8 % pre-pulse 50 ps in front of the main pulse and without a pre-pulse, respectively. Zero degree on the x-axis corresponds to the direction of laser propagation. A negative angle represents an angle measured clockwise from the direction of laser propagation. Although the angular distribution didn't cover the entire solid angle of the backside of the target, we can see immediately that a) the angular distribution without pre-pulses is isotropic b) the electron flux with pre-pulses is stronger than that without pre-pulses; c) the distribution with pre-pulses consists of two components, a very broad distribution, which can be regarded as a continuous background and a peak, superposed on a continuous background. When the distribution is fitted with a Gaussian distribution (shown as a solid line), the FWHM of the peak is 24, and the maximum occurs at -8°. Compared with the backward electrons, which emit in the normal direction, the forward electrons are deflected close to the direction of laser propagation.

The forward hot electrons recorded on the radiochromic films have to pass through two regions: the plasma region and the cold target region. The physical processes are different for these two regions. In the plasma region, the main effects on hot electron transport are due to the self-generated electric and magnetic fields apart from collisional effects. On the other hand, in the cold target region, the collisions of hot electrons with target ions as well as with bound and free electrons, leads to a change of direction and energy loss. We employ a 3D Monte Carlo code to calculate the transport of the energetic electron beam inside an aluminum foil. The foil thickness is chosen to be 5 mm, the same as the foil target used in the experiments. An electron source is put at the front surface of the foil. The electron number and energy are recorded behind the foil. In the first modeling, electrons with energies of 500 keV, 80 keV, and 30 keV were perpendicularly poured into the foil. In the second modeling, an electron source with an energy of 500 keV was set to be isotropic. We divided the 2p space behind the foil into many small annular zones. The differential solid angle for each zone is $2\pi d(\cos \theta)$. Figure 6 shows the angular distribution of electrons passing through the foil. For normal incidence in the first model, almost all of the 500-keV electrons fall into the 0 annular zone. That is to say, these electrons remain well collimated. However, the angular divergence increases decreasing electron energy. For 80-keV electrons as an example, only 46 % of the electrons fall into the 26 cone angle and are shown as the open circles in Fig. 6. For the isotropic input in the second model, the distribution remains isotropic within the range of 0–70. The number of electrons falling into a range greater than 70 decreases because of longer paths in the target. Here, we are not interested in the electrons that are very far away from the direction of laser propagation.

The emission direction of hot electrons is different for

different acceleration mechanisms. Resonance absorption produces electrons in the direction of the electron density gradient, which was partially observed for the backward electrons in our experiments. The ponderomotive potential and the wake field mechanism generate hot electrons along the direction of laser propagation. However, they become important only for significantly higher laser intensities. No such longitudinal acceleration scheme was present for our intensity of $5 \times 10^{15} \text{ W/cm}^2$. The collision effect and angular scattering, both in the plasma region and the cold target region, are the main reasons for the angular divergence of hot electrons, but these effects cannot explain the deflection of the hot electron peak toward the direction of laser propagation. It is well known that intense electric fields and magnetic fields exist in laser-plasma interactions. These fields play important roles in plasma behaviors, including electron transport into solid targets. Davies *et al.* considered the transport of hot electrons by using a relativistic Fokker-Planck equation. They proposed that the growth rate of the magnetic field could be written approximately as [30]

$$\frac{\partial B}{\partial t} \sim 8 \times 10^{-9} \frac{\eta f_a I}{d\lambda} T \text{ ps}^{-1}, \quad (2)$$

where η is the resistivity in $\Omega \cdot m$, f_a is the absorption fraction, I is the laser intensity in W/cm^2 , d is the focal spot diameter in ns, λ is the laser wavelength in ns, and B is the self-generated magnetic field in T. The magnetic field will reach a large magnitude very rapidly. The role of the electric field is to reduce the kinetic energy of hot electrons. The magnetic fields can collimate and deflect the hot electrons. This may be a reasonable explanation for the experimental deflection of the energetic electron beam toward the direction of laser propagation.

Our hard X-ray measurements showed that the pre-pulses could enhance the hot electron number and temperature dramatically [26]. The hot temperature deduced from the hard X-ray spectrum was about 10 keV for the case without prepulse. When a pre-pulse was used, the hard X-ray spectrum presented double Maxwellian distributions. A group of electrons was accelerated to a much higher energy close to the temperature measured using the electron spectrometer (Fig. 3). Therefore, the angular distribution of forward electrons without pre-pulses (dashed line in Fig. 5) was scattered seriously due to their lower energy, which results in the less number recorded and in poor directionality.

Based on the angular distribution of backward hot electrons in thick foil interactions, the electron energy spectrum, the hard X-ray measurement, and the theoretical calculation of electron transport in aluminum material, the angular distribution of forward hot electrons may be explained as follows: When the forward hot electrons produced in the laser interactions pass through the plasma region, they are deflected by the self-generated magnetic field and tend to propagate along the laser axis. Collisional effects in the plasma region and in the cold

material region lead to energy loss and broaden the angular distribution. Multiple scattering of hot electrons with higher energies is not very effective, so they remain directional. However, hot electrons with lower energies can be steered significantly due to serious scattering. Therefore, they present as a continuum-like background.

We can see from the above analysis that the electrons suffer serious scattering and are sensitive to the electromagnetic fields during transport in a dense plasma and a cold target material. More recently, a collimated proton beam with up to 55 MeV of energy was observed in petawatt laser plasma interactions [31]. It is not easy to deflect protons by collisions and electromagnetic fields due to their large mass. Thus, the trajectory of protons approximates a straight line in a dense plasma. Furthermore, the efficiency of energy transfer of protons to nuclear fuel is much higher than that of hot electrons, so protons may become competitive candidates for the energy carrier in fast ignitor concept studies.

IV. CONCLUSION

The angular distributions and the energy spectrum of hot electrons produced in interactions of femtosecond laser pulses with aluminum plasmas were investigated at a moderate intensity. A collimated jet of hot electrons was observed in a direction normal to surface. The ejected angle agreed with angular scaling from canonical momentum conservation. However, the forward energetic electron beam passing through the foil target was deflected close to the laser propagation direction, which might be due to self-generated magnetic fields. The lower energy electrons diffused into a much wider cone angle due to the collisional effect in the plasma and the target material. This process was supported by 3D Monte Carlo simulations. The hot temperature obtained from the electron spectrum and the absorption measurement implies that resonance absorption may be partially responsible for the generation of hot electrons.

ACKNOWLEDGMENTS

This work was jointly supported by the National Natural Science Foundation (grant nos. 19825110, 10075075,

and 100005014), the National High-Tech Inertial Confinement Fusion program, and the Pre-Research Founds of CAEP.

REFERENCES

- [1] M. Tabak, *et al.*, Phys. Plasmas **1**, 1626 (1994).
- [2] K. B. Wharton, *et al.*, Phys. Rev. Lett. **81**, 822 (1998).
- [3] M. H. Key, *et al.*, Phys. Plasmas **5**, 1966 (1998).
- [4] S. Bastiani, *et al.*, Phys. Rev. E **56**, 7179 (1997).
- [5] J. Fuchs, *et al.*, Phys. Plasmas **6**, 2569 (1999).
- [6] Th. Schlegel *et al.*, Phys. Rev. E **60**, 2209 (1999).
- [7] U. Teubner, *et al.*, Phys. Rev. E **54**, 4167 (1996).
- [8] M. Roch, T. E. Cowan, A. W. Hunt, *et al.*, *Inertial Fusion Sciences and Applications 99*, Edited by Christine Labaune, William J. Hogan, Kazuo A. Tanaka (Elsevier, Paris, 2000).
- [9] G. Malka and J. L. Miquel, Phys. Rev. Lett. **77**, 75 (1996).
- [10] S. C. Wilks, W. L. Cruger, M. Tabak and A. Loudon, Phys. Rev. Lett. **69**, 1383 (1992).
- [11] A. J. Mackinnon, *et al.*, Phys. Plasmas **6**, 2185 (1999).
- [12] M. Borghesi, A. J. Mackinnon, R. Gaillard, *et al.*, Phys. Rev. Lett. **80**, 5137 (1998).
- [13] M. Tatarakis, *et al.*, Phys. Rev. Lett. **81**, 999 (1998).
- [14] M. Borghesi, *et al.*, Phys. Rev. Lett. **83**, 4309 (1998).
- [15] L. Gremillet, *et al.*, Phys. Rev. Lett. **83**, 5015 (1996).
- [16] P. A. Norreys *et al.*, Phys. Plasmas **6**, 2150 (1999).
- [17] H. Ruhl, *et al.*, Phys. Rev. Lett. **82**, 743 (1999).
- [18] Y. Sentoku, *et al.*, Phys. of Plasmas **6**, 2855 (1999).
- [19] F. Brunel, Phys. Rev. Lett. **59**, 52 (1987).
- [20] D. Gordon, *et al.*, Phys. Rev. Lett. **80**, 2133 (1998).
- [21] W. L. Kruer, *The physics of laser plasma interactions* (Addison-Wesley publishing company, Redwood City, California, 1988).
- [22] Erik Lefebvre, *et al.*, Phys. Rev. E **55**, 1011 (1997)
- [23] A. Pukhov, *et al.*, Phys. Plasmas **5**, 1880 (1998)
- [24] Q. L. Dong, J. Zhang, Phys. Plasmas **8**, 1025 (2001).
- [25] L. M. Chen, J. Zhang, *et al.*, Phys. Rev. E **63**, 036403 (2001).
- [26] P. Zhang, *et al.*, Phys. Rev. E **57**, R3746 (1998)
- [27] Y. T. Li, J. Zhang, *et al.*, Science in China A **44**, 98 (2001).
- [28] F. N. Beg, *et al.*, Phys. Plasmas **4**, 447 (1997)
- [29] P. Gibbon and A. R. Bell, Phys. Rev. Lett. **68**, 1535 (1992).
- [30] J. R. Davies, A. R. Bell, M. G. Haines and S. M. Guerin, Phys. Rev. E **56**, 7193 (1997).
- [31] M. D. Perry, Science & Technology Review **25** (2000).

Hot electron generation via vacuum heating process in femtosecond laser–solid interactions

L. M. Chen, J. Zhang,^{a)} Q. L. Dong, H. Teng, T. J. Liang, L. Z. Zhao, and Z. Y. Wei
Laboratory of Optical Physics, Institute of Physics, Chinese Academy of Sciences, Beijing 100080, People's Republic of China

(Received 16 August 2000; accepted 9 March 2001)

Hot electron generation by the vacuum heating process has been studied in the interaction of 150 fs, 5 mJ, 800 nm *P*-polarized laser pulses with solid targets. The measurements have suggested that the “vacuum heating” is the main heating process for the hot electrons with high energies. The energy of the vacuum-heated hot electrons has been found to be higher than the prediction from the scaling law of resonance absorption. Particle-in-cell simulations have confirmed that the hot electrons are mainly generated by the vacuum heating process under certain experimental conditions. © 2001 American Institute of Physics. [DOI: 10.1063/1.1371956]

I. INTRODUCTION

Rapid developments in intense ultrashort laser technology,¹ have opened a new regime of laser–matter interaction, in which intense laser pulses deposit their energy into solid targets faster than the hydrodynamic expansion of the target surface.² Thus, using table-top ultrashort pulse lasers, it is now possible to study laser–matter interaction under extreme conditions in relation to the fast ignition scheme for inertial confinement fusion (ICF),³ harmonic generation,^{4,5} ultrashort x-ray generation⁶ and laser-cluster Coulomb explosions,⁷ etc.

Hot electrons in laser-plasmas can be generated by different absorption or acceleration mechanisms under different experimental conditions.^{8–11} Previous measurements⁸ of the absorption of laser pulses by solid targets showed that at low laser intensities inverse Bremsstrahlung (IB) is the main absorption mechanism, which depends on the electrical conductivity associated with electron mean-free-path comparable to the interatomic spacing. The measurements showed three distinct regions as a function of laser intensity. At low intensities $I < 10^{13} \text{ W/cm}^2$, the absorption was quite high. For an intensity in the range of $10^{13} \text{ W/cm}^2 < I < 10^{14} \text{ W/cm}^2$, the absorption decreased as the laser intensity increased. The absorption then increased with laser intensity for an intensity $> 3 \times 10^{14} \text{ W/cm}^2$. These measurements are broadly consistent with collisional absorption theory. Another experiment⁹ showed that at high intensities of $3 \times 10^{15} \text{ W/cm}^2$, the absorption was at a low level of 10% and practically independent of the target material. This behavior was attributed to the high reflection from an over-dense plasma layer caused by the rapid ionization of a thin front layer of the target. Brunel¹⁰ proposed over ten years ago that moderately intense *P*-polarized laser pulses incident obliquely on an atomically abrupt metal surface could be strongly absorbed by pulling electrons into vacuum during an optical cycle, then returning them to the surface with approximately the quiver velocity.

This is the so-called vacuum heating process. Later simulations¹¹ by Paul Gibbon predicted that, with a slight surface expansion of scale lengths, the laser optical field would pull more electrons into the vacuum and the laser energy would be more strongly absorbed, as long as the scale length $L = (\partial \ln n_e / \partial z)^{-1}$ does not significantly exceed the electron quiver amplitude $x_{\text{osc}} = eE/m\omega^2$.

Recently, hot electron generation was studied at moderate intensities.^{12,13} Both hot electron spectra and x-ray spectra from the Bremsstrahlung radiation, when hot electrons undergo de-acceleration in solid targets, showed that, when smooth solid targets were irradiated obliquely by *P*-polarized laser pulses, a group of hot electrons can be resonantly heated to a quasi-Maxwellian temperature characterized by the scaling: $T_h \propto (I\lambda^2)^{1/3}$,¹⁴ while another group of hot electrons with higher energies can be produced by nonlinear resonant absorption if there is a thin layer of corona preplasma in front of the target surface. Typically electrons produced by the IB absorption process are known as thermal electrons and have energies less than keV at modest laser intensities.⁹ The electrons generated by resonance absorption and the other nonlinear resonant absorption are called hot electrons, that have much higher kinetic energies.

In this paper, we report a study on hot electron generation from aluminum solid targets irradiated by intense ultrashort laser pulses. The measurements of the laser absorption suggested that the vacuum heating (VH) was responsible for the generation of the hot electrons with high energies. Particle-in-cell (PIC) simulations also showed that the electron spectrum generated by the vacuum heating process is consistent with the experimental results.

II. EXPERIMENTAL SETUP

The experiments were carried out at the Laboratory of Optical Physics of the Institute of Physics with a Ti:Sapphire chirped pulse amplification (CPA) laser system operating at around 800 nm at a repetition rate of 10 Hz. The laser delivered 5 mJ energy in 150 fs pulses and produced a peak irradiance of $8 \times 10^{15} \text{ W/cm}^2$ at the focus. The contrast ratio of

^{a)}Author to whom correspondence should be addressed. Electronic mail: jzhang@aphy.iphy.ac.cn

the laser pulses was measured to be $\sim 10^{-5}$ at 2 ps before the peak and 10^{-6} at 1 ns, by third-order autocorrelation techniques. The target material used was 100 μm thick pure Al on glass plates. The roughness of the surface was less than 1 μm . The target mount was controlled by step-motors in xyz dimension to ensure the laser pulses interacted with a fresh target surface for each shot.

The main diagnostic of the hot electrons was a magnetic spectrometer, fitted with a permanent magnetic field of $B = 380$ Gauss. An array of LiF thermoluminescent dosimeters (TLDs) was used as detectors. Recent development of ultra-sensitive LiF TLD material provides the possibility of using a thin TLD for hot electron detection.¹⁵ The energy range this instrument covered was from 7 to 500 keV. The collection angle of the spectrometer was on the order of 1×10^{-3} Steradian. Its energy resolution was better than 2%. Because the TLDs are insensitive to visible light, it was not necessary to use aluminum foils in front of the TLDs. The background of these TLDs was less than 1.2 μGy when they were heated to 240 °C. When we placed a piece of 20 μm Al foil on the surface of the TLD, which was located in the position of the spectrometer, corresponding to an energy of 20 keV, the dose on the TLDs would drop dramatically from several tens of mGy to several μGy . This verified that the dose on the TLDs was mainly caused by hot electrons.

Two calibrated γ -ray spectrometers were also used to study the x-ray Bremsstrahlung radiation from the laser-plasma.¹³ The γ -ray spectrometer consisted of a NaI detector, an electronic gated shutter, a photomultiplier, an amplifier and a multichannel energy analyzer. A 20 mm diameter hole in a 50 mm thick Pb block was used to collimate the x-ray radiation and to shield the detector. The detector response was calibrated using a 511 keV and a 1.274 MeV γ -ray ^{22}Na source and a 665 keV ^{137}Cs source.

The plasma absorption was measured by a calorimeter. Slightly focusing (with an f/10 lens) of the reflected beam ensured that the whole beam was collected by the calorimeter. An 800 nm filter was placed at the entrance of the calorimeter ensured only the reflected and scattered laser energy could be measured.

III. ABSORPTION MEASUREMENTS

All of the experimental results presented here were obtained for laser pulses incident on the target at an angle of 45° with respect to the normal of Al targets.

The measurement of reflectivity (solid dots) from the target is shown in Fig. 1 for different focused laser intensities on the target. The scattered light out of the collecting optics was found to be negligible. When the focused laser intensity was $5 \times 10^{12} \text{ W/cm}^2$, no hard x-ray photons could be detected. The measured reflectivity was found to be as high as 80%. This is consistent with the previous measurements,⁸ in which the IB absorption was believed to take a major role. As the laser intensity was increased from $I > 3 \times 10^{13} \text{ W/cm}^2$, x-ray photons began to be detectable and the x-ray flux and photon energy increased with the laser intensity. In the meantime, the measured reflectivity decreased for higher laser intensities. This implies that there were other

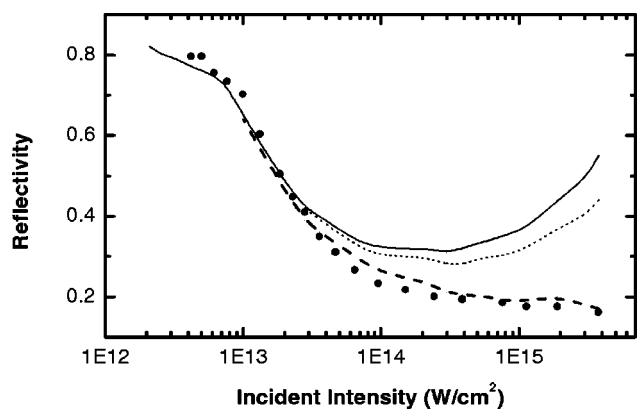


FIG. 1. The laser reflectivity (solid circle) vs laser intensity on Al target for P -polarized 45° irradiation. The solid line is from calculation of IB absorption with Fresnel–Drude formulas. The dotted line is the IB absorption plus the VH absorption with $\eta=6$ (without plasma expansion). The dashed line is the IB absorption plus the VH absorption with $\eta=20$ (with slight plasma expansion).

absorption mechanisms starting to play a role, which generated the hot electrons. Compared with the calculated results using the Fresnel–Drude formula with Perrot and Dharmawardana's conductivity model⁸ (shown in Fig. 1, by the solid line), we can see that our measurements also began to deviate from the previous measurements⁸ and the calculation from $I > 3 \times 10^{13} \text{ W/cm}^2$. Increasingly more energy was absorbed through other mechanisms for higher laser intensities. At an intensity of $4 \times 10^{15} \text{ W/cm}^2$, the total absorption was as high as more than 80%, in which nearly 40% extra laser energy was absorbed through other mechanisms.

Unlike the calculation from the Fresnel–Drude formula or the previous experimental results,⁸ in which IB was the main absorption mechanism, it can be seen that the extra absorption, therefore the total absorption, increased with the laser intensity. This behavior is consistent with Grimes measurements¹⁶ using femtosecond time-resolved reflectivity.

We can now investigate the possible mechanisms for the extra absorption in the measurements. The laser pulse duration was 150 fs and the pedestal was not enough to generate significant plasma expansion before the peak of the laser pulse.¹⁷ The plasma scale-length was measured to be below 0.01λ using a shadowgraphy technique. The electron quiver amplitude under the experimental laser intensity was $X_{\text{osc}}/\lambda \sim 0.02$. Therefore, the plasma scale length was satisfied with the requirements of the VH heating process.

There are other competing linear absorption mechanisms, such as anomalous skin effect (ASE),¹⁸ sheath inverse Bremsstrahlung (SIB),¹⁹ sheath transit absorption (STA),²⁰ and resonance absorption (RA)¹⁴ in the laser–plasma interactions. If we choose an intensity of $I = 10^{15} \text{ W/cm}^2$, for example, the peak electron temperature of $kT_e \sim 100 \text{ eV}$, this would result in a collision frequency $\nu \sim 5 \times 10^{15} \text{ s}^{-1}$. The skin depth in our experiment is $l_s \sim 10\nu_{\text{th}}/\nu$.²¹ This is much thicker than the required collisionless transit of the skin depth ($l_s \sim 100 \text{ \AA} \ll \nu_{\text{th}}/\nu$) for efficient ASE, SIB, and STA absorption processes. Therefore, the ASE, SIB, and STA processes contribute very little to the absorption under our

experimental conditions. On the other hand, the RA absorption involves a slow, many-cycle building up of a resonant plasma wave, which eventually breaks, and an electric field at the critical surface. For the steep plasma gradients in our experiments, the building up time might be too short for RA to efficiently enhance the critical surface field. Paul Gibbon's simulation¹¹ showed that the VH dominates over the resonance absorption for scale lengths of $L/\lambda < 0.1$. According to his simulations, the absorbed energy goes into two kinds of hot electrons. A bi-Maxwellian distribution will be formed by the electrons heated, within the laser penetration depth, by the RA absorption process, and the VH heated electrons with much higher energies, escaped from the high-density boundary.

In principle, the VH absorption can be distinguished from other competing linear mechanisms by its intrinsic intensity dependence $f_{\text{VH}} \sim \sqrt{I\lambda^2}$ and its unique incident angle and polarization dependence. From Fig. 1, we can find that the extra energy absorption is mainly due to the VH process because of the intensity dependence, as described by Brunel equation. The fractional VH absorption is

$$f_{\text{VH}} = (\eta/2\pi)(v_{\text{osc}}^3/v_L^2 c \cos \theta), \quad (1)$$

where $v_L = eE_L/m\omega$ is the electron velocity in the incident laser field (E_L is the incident laser electric field) and v_{osc} is the quiver velocity due to the total electric field of incident and reflected fields $E_0 = \xi E_L \sin \theta$. Here $\eta = 1.75(1 + 2v_{\text{th}}/v_{\text{osc}})$ is an empirical scaling value determined by the density gradient.¹⁰ In order to compare the fractional VH absorption and the measurements in Fig. 1, the fractional absorption from IB should be considered. The solid line in Fig. 1 is the calculation from the IB collisional theory. It is apparent that the absorption in our experiments was mainly the IB absorption for laser intensities of $I < 3 \times 10^{13} \text{ W/cm}^2$, while some other absorption mechanisms played roles for higher laser intensities $I > 3 \times 10^{13} \text{ W/cm}^2$. If we assume there was no hydrodynamic expansion in the interaction ($\eta = 6$), the total energy absorption (VH+IB) would be much lower than the experimental data (as the dotted line shows in Fig. 1). This implies that the ideal abrupt density gradient without any plasma expansion does not fit for our experimental situation. If we assume that there is a slight plasma expansion so that we can assume $\eta = 20$, just as Grimes did,¹⁶ in the empirical scaling value, the total energy absorption curve (the dashed line in Fig. 1) will be very close to the experiment data. This change is more realistic for experiments because a slight plasma expansion will build at the pedestal of the laser pulse anyway. As a result, we found the extra absorption is nearly 40% at the intensity $4 \times 10^{15} \text{ W/cm}^2$. This calculation based on Brunel's VH intensity dependence $f_{\text{VH}} \propto \sqrt{I\lambda^2}$. However, if we choose Grimes' intensity dependence $f_{\text{VH}} \propto (I\lambda^2)^{0.64}$,¹⁶ the extra absorption would be nearly 55%, beyond the difference between experimental data and IB value under the intensity of $4 \times 10^{15} \text{ W/cm}^2$. Therefore, we found that Brunel's VH laser intensity dependence is more reliable.

From this comparison, we can find: (1) The VH is the main absorption mechanism apart from the IB absorption in our experiments, especially at high intensities, because the

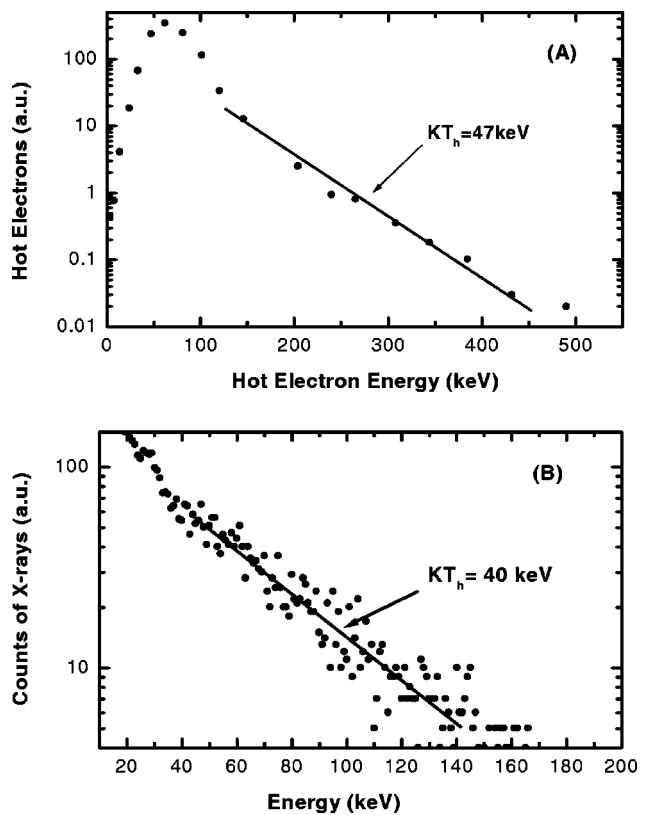


FIG. 2. (A) The energy spectrum of hot electrons emission and (B) the Bremsstrahlung hard x-ray radiation from the Al target. The solid lines in two figures are the Maxwellian distribution fit for the temperature.

VH absorption is proportional to the square root of laser intensity. (2) The measured absorption is somewhat larger than Brunel's idealized case. This supports the assumption of enhancement of VH absorption for a slightly expanded plasma¹¹ because the laser field can penetrate further into the surface and can pull more electrons into the VH orbits. As a result, electrons will have a longer mean-free-path in the plasma to gain higher energies. Paul Gibbon predicted a 60% VH absorption²² for an expanded plasma at an intensity of $4 \times 10^{15} \text{ W/cm}^2$. This is more or less similar to our experiment data.

The optimum incident angle for maximum absorption was found to be about 45° in our experiment. By contrast, the optimal incident angle for the RA absorption is generally in the range of 20° – 30° . This is additional evidence to showing that the VH absorption is the main mechanism to account for the extra absorption in our experiments.

IV. HOT ELECTRON MEASUREMENTS

The out-going electron energy spectrum [Fig. 2(A)] generated by the interaction at an intensity of $5 \times 10^{15} \text{ W/cm}^2$ was measured directly using the electron magnetic spectrometer placed in the normal direction of the solid target. The spectrum exhibits bi-Maxwellian distribution. The lower hot electron temperature was independent of target materials and was generated by RA mechanism with the scaling law: $T_H(\text{keV}) \approx 6 \times 10^{-5} (I\lambda^2)^{0.33}$.¹⁴ At the laser intensity of $5 \times 10^{15} \text{ W/cm}^2$, it is about 8 keV. This group of electrons is

called bulk plasma electrons by Paul Gibbon in Refs. 11 and 22. Another group of hot electrons with higher temperature about 47 keV at the intensity of $5 \times 10^{15} \text{ W/cm}^2$, was generated by the VH process. This bi-Maxwellian hot electron distribution is similar to Paul Gibbon's simulation with mobile-ions.²² This strongly suggests that the vacuum heating is the main absorption mechanism to heat hot electrons in our experiments. That means at the contrast ratio of 10^5 , the VH mechanism is really stimulated and it is the main hot electron heating mechanism.

The hard x-ray spectrum is generally dominated by Bremsstrahlung radiation, which is produced by high energy hot electrons colliding with atom nuclei. The shape and intensity of the Bremsstrahlung radiation is the principle diagnostic for the injecting hot electron flux and temperature^{13,23} because the Bremsstrahlung hard x-ray spectrum has the same Maxwellian distribution as colliding electrons. In our experiments, the hard x-ray Bremsstrahlung radiation from injecting electrons was measured by the NaI γ -ray spectrometer. The hard x-ray spectrum also shows a bi-Maxwellian distribution and the hot electron temperature was nearly the same as that measured by the electron spectrometer, shown in Fig. 2(B). The temperature deduced from the hard x-ray spectrum is slightly lower than that from electron spectrum. The reason why the energy of the injecting hot electrons was less than that of out-going electrons might be because the injecting electrons experience deceleration when reentering the solid targets.

V. PIC SIMULATIONS

Simulations using a $1\frac{1}{2}$ -dimensional (i.e., x, v_x, v_y, v_z) fully electromagnetic particle in cell (LPIC++) code have been performed, where an electromagnetic wave is launched obliquely from the left-hand side onto an overdense plasma located on the right-hand side with $n_e/n_c=20$, $T_e=200 \text{ eV}$.²¹ Based on the simulation results of Paul Gibbon,²² we chose the ratio of thermal electron temperature to ions as $T_e/T_i=3-5$, and mass ratio $m_i/Zm_e=1836$, original plasma scale length $L=0.004$. A square-sine profile of incident laser pulse was used. Typically 150×2680 electrons and ions and 2680 cells were used. We consider the initial situation in which the ions are mobile and electrons are pulled out into vacuum by the component of the electrical field normal to the target.

Figure 3 shows the electron phase space at $t=12.574$ and $t=13.170$ optical cycles (i.e., electron phase normalized by 2π), respectively. Here we chose $a=0.06$, corresponding an laser intensity of $5 \times 10^{15} \text{ W/cm}^2$. We can see another group of electrons accelerated by the laser field appearing at $t=13.170$ after a half of optical cycle, in comparison with the case at $t=12.574$. We also notice most of the electrons heated before cannot return to the target surface in one laser cycle. This implies that these electrons are not quivering in the laser field and a huge electrostatic field (charge separation potential) will be produced by them. It is known that only those electrons ionized in $\omega t=0^\circ-80^\circ$ can return to ions.²⁴ This suggests that a group of electrons will be pulled out at each optical cycle and an array of electron "trains"

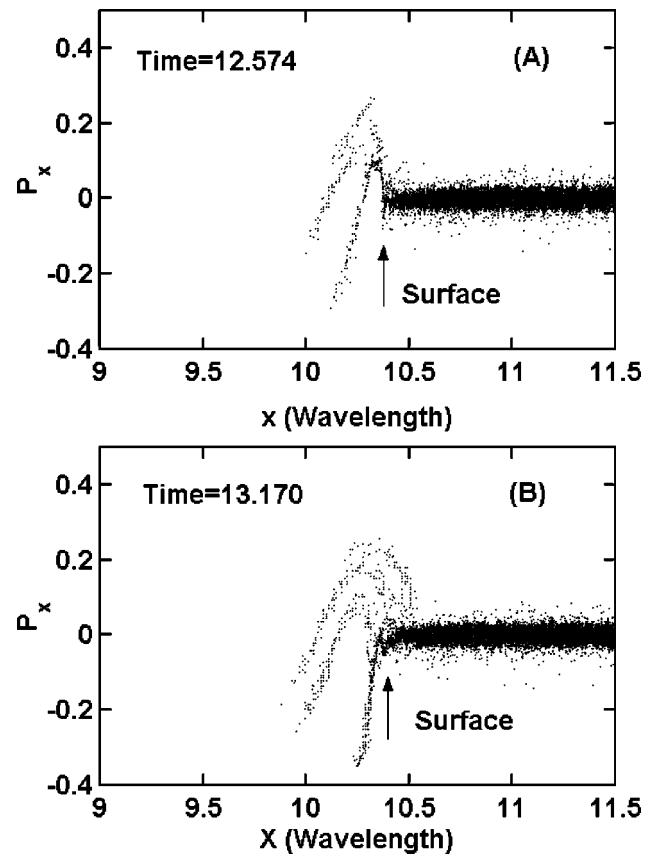


FIG. 3. Simulated electron phase space P_x vs X at $t=12.574$ and 13.170 optical cycle (i.e., electron phase normalized by 2π). $a=0.06$, $L/\lambda=0.004$. The target boundary is at $X=10.3$. P_x is normalized by $m_e c$. X is normalized by laser wavelength λ .

will be generated in the normal direction of the target surface,²⁵ forming an electron jet emission in the integrating angular distribution.²⁶ On the other hand, some of the heated electrons will come back to the target surface, due to the strong charge separation potential, to heat the target plasmas after several optical cycles. This is the accurate picture of the VH.²⁷

Figure 4 is the spectrum of electrons heated by laser field

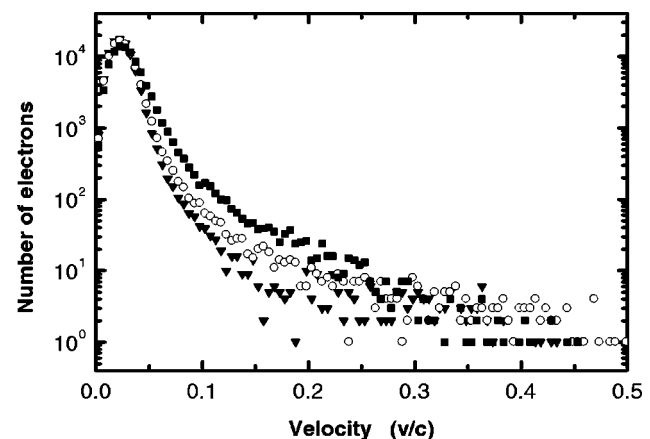


FIG. 4. Simulated spectrum of electrons heated by the laser pulse at $t=15$ (solid downtriangle \blacktriangledown), 30 (open circle \circ), and 70 (solid square \blacksquare) optical cycles, respectively.

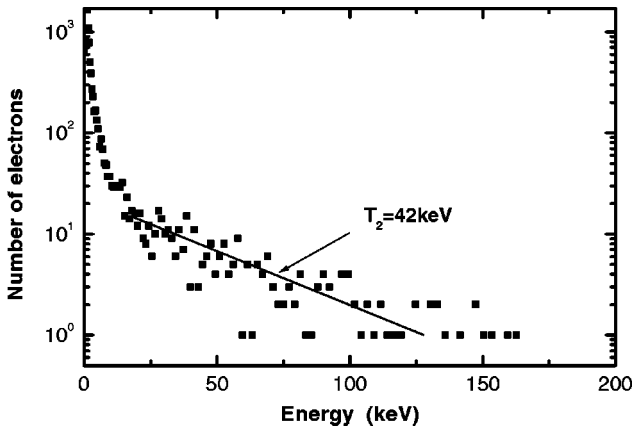


FIG. 5. The time-integrated hot electron spectrum after 75 optical cycles from the PIC simulations.

at different optical cycles. It is apparent that the number of heated electrons increases with interacting time. This demonstrates that the VH is stimulated and heats a group of electrons in each optical cycle. Here we can also see that more electrons with higher energies are generated at the rising edge of the pulse at the curve of $t=30$. This means the laser field accelerates the electrons greatly in the rising edge of laser pulse.

Figure 5 is the time-integrated hot electron energy spectrum after 75 optical cycles, when it is at the end of laser pulse. This is a typical bi-Maxwellian energy distribution. The higher energy hot electron temperature is about 42 keV for $L=0.004\lambda$, $a=0.06$. This agrees well with experimental measurement. In order to check the dependence of temperature on scale-length, the scale-length was changed from 0.001 to 0.07 in the simulations. We found the temperature only slightly changed. The reason is that in this region of scale length, the electrons were accelerated by VH with the total electric field (incident electric field plus reflected electrical field), which is similar for those two scale-lengths, the enhancement of critical surface ($\omega=\omega_p$) field, which is very sensitive to the scale length, is negligible.

VI. CONCLUSIONS

In summary, we have studied the energy absorption, the hot electron generation in the interaction of P -polarized femtosecond laser pulses with Aluminum solid targets. The measurements have suggested that Vacuum Heating is the main heating mechanism for the hot electrons with high energies. The PIC simulations have shown that the hot electrons are pulled out from the target on every optical cycle, forming an electron train-structure in the normal direction of the target. These simulations are consistent with the conclusion that the hot electrons are mainly generated by the vacuum heating process under our experimental conditions.

ACKNOWLEDGMENTS

The authors would like to thank Professor Wei Yu for his valuable discussions.

This work was jointly supported by the National Natural

Science Foundation of China (Grant Nos. 19825110, 10005014 and 10075075) and the National Hi-tech ICF Program.

- ¹M. D. Perry and G. Mourou, *Science* **264**, 917 (1994).
- ²R. M. More, Z. Zinamon, K. H. Warren, R. Falcone, and M. Murnane, *J. Phys. (Paris)*, Colloq. **61**, C7-43 (1988).
- ³M. Tabak, J. Hammer, M. E. Glinsky, W. L. Kruer, W. C. Wilks, and R. J. Mason, *Phys. Plasmas* **1**, 1626 (1994).
- ⁴A. Modena, Z. Najmudin, A. E. Dangor *et al.*, *Nature (London)* **377**, 606 (1995).
- ⁵P. A. Norreys, M. Zepf, S. Moustakidis, A. P. Fews, J. Zhang, P. Lee, M. Bakarezos, C. N. Danson, A. Dyson, P. Gibbon, P. Loukakos, D. Neely, F. N. Walsh, J. S. Wark, and A. E. Dangor, *Phys. Rev. Lett.* **76**, 1832 (1996).
- ⁶J. D. Kmetec, C. L. Gordon, J. J. Macklin, B. E. Lemoff, G. S. Brown, and S. E. Harris, *Phys. Rev. Lett.* **68**, 1527 (1992).
- ⁷T. Ditmire, J. W. G. Tisch, E. Springate, M. B. Mason, N. Hay, R. A. Smith, J. Marangos, and M. H. R. Hutchinson, *Nature (London)* **386**, 54 (1997); T. D. Donnelly, T. Ditmire, K. Neuman, M. D. Perry, and R. W. Falcone, *Phys. Rev. Lett.* **76**, 2472 (1996).
- ⁸H. M. Milchberg, R. R. Freeman, S. C. Davey, and R. M. More, *Phys. Rev. Lett.* **61**, 2364 (1988); F. Perrot and M. W. C. Dharma-wardana, *Phys. Rev. A* **36**, 238 (1987); A. Ng, P. Cellier, A. Forsman, R. M. More, T. T. Lee, F. Perrot, M. W. C. Dharma-wardana, and G. A. Rinker, *Phys. Rev. Lett.* **72**, 3351 (1994).
- ⁹D. F. Price, R. M. More, R. S. Walling, G. Guethlein, R. L. Shepherd, R. E. Stewart, and W. E. White, *Phys. Rev. Lett.* **75**, 252 (1995).
- ¹⁰F. Brunel, *Phys. Rev. Lett.* **59**, 52 (1987); *Phys. Fluids* **31**, 2714 (1998).
- ¹¹P. Gibbon and A. R. Bell, *Phys. Rev. Lett.* **68**, 1535 (1992); **73**, 664 (1994).
- ¹²S. Bastiani, A. Rousse, J. P. Geindre, P. Audebert, C. Quoir, G. Hamoniaux, A. Antonetti, and J.-C. Gauthier, *Phys. Rev. E* **56**, 7179 (1997); S. Bastiani, P. Audebert, J. P. Geindre, Th. Schlegel, C. Guoix, G. Hamoniaux, G. Grillon, and A. Antonetti, *ibid.* **60**, 3439 (1999).
- ¹³P. Zhang, J. T. He, D. B. Chen, Z. H. Li, Y. Zhang, J. G. Bian, L. Wang, Z. L. Li, B. H. Feng, X. L. Zhang, D. X. Zhang, X. W. Tang, and J. Zhang, *Phys. Rev. E* **57**, R3746 (1998).
- ¹⁴W. L. Kruer, *The Physics of Laser Plasma Interactions* (Addison-Wesley, New York, 1988); S. J. Gitomen, R. D. Jones, F. Begay, A. W. Ehler, J. F. Kephart, and R. Kristal, *Phys. Fluids* **29**, 2679 (1986); D. W. Forslund, J. M. Kindel, and K. Lee, *Phys. Rev. Lett.* **39**, 284 (1977).
- ¹⁵L. M. Chen, J. Zhang, H. Teng, Q. L. Dong, Z. L. Chen, T. J. Liang, L. Z. Zhao, and Z. Y. Wei, *Phys. Rev. E* **63**, 036403 (2001).
- ¹⁶M. K. Grimes, A. R. Rundquist, Y. S. Lee, and M. C. Downer, *Phys. Rev. Lett.* **82**, 4010 (1999).
- ¹⁷Y. Zhang, J. Zhang, S. H. Pan, and Y. X. Nie, *Opt. Commun.* **126**, 85 (1996).
- ¹⁸E. S. Weibel, *Phys. Fluids* **10**, 741 (1967); A. A. Andreev, K. Yu. Platonov, and J.-C. Gauthier, *Phys. Rev. E* **58**, 2424 (1998).
- ¹⁹P. J. Catto and R. M. More, *Phys. Fluids* **20**, 704 (1977); T.-Y. B. Yang, W. L. Kruer, R. M. More, and A. B. Langdon, *Phys. Plasmas* **2**, 3146 (1995).
- ²⁰T.-Y. B. Yang, W. L. Kruer, A. B. Langdon, and T. W. Johnston, *Phys. Plasmas* **3**, 2702 (1996).
- ²¹W. Rozmus, V. T. Tikhonchuk, and R. Cauble, *Phys. Plasmas* **3**, 360 (1996).
- ²²P. Gibbon, *Phys. Rev. Lett.* **73**, 664 (1994).
- ²³M. N. Rousenbluth and R. Z. Sagdeev, *Physics of Laser Plasmas* (North-Holland, Amsterdam, 1991); F. N. Beg, A. R. Bell, A. E. Dangor, C. N. Danson, A. P. Fews, M. E. Glinsky, B. A. Hammel, P. Lee, P. A. Norreys, and M. Tatarakis, *Phys. Plasmas* **4**, 447 (1997).
- ²⁴L. M. Chen, W. Yu, J. Zhang, Z. Y. Chen, and W. M. Jiang, *Sci. China A* **43**, 1202 (2000).
- ²⁵Y. Sentoku, H. Ruhl, K. Mima, R. Kodama, K. A. Tanaka, and Y. Kishimoto, *Phys. Plasmas* **6**, 2855 (1999); R. Kodama, K. A. Tanaka, Y. Sentoku, T. Matsushita, H. Fujita, Y. Kitagawa, Y. Kato, T. Yamanaka, and K. Mima, *Phys. Rev. Lett.* **84**, 674 (2000).
- ²⁶Y. T. Li, J. Zhang, L. M. Chen, J. F. Xia, H. Teng, L. Z. Zhao, J. Q. Lin, Y. J. Li, Z. Y. Wei, L. Wang, and W. M. Jiang, *Sci. China A* **44**, 98 (2000).
- ²⁷L. H. Cao, W. W. Chang, and Z. W. Yue, *Phys. Plasmas* **5**, 499 (1998).

Electron acceleration by static and oscillating electric fields produced in the interaction between femtosecond laser pulses and solid targets

Q. L. Dong and J. Zhang^{a)}

*Laboratory of Optical Physics, Institute of Physics, Chinese Academy of Sciences,
Beijing 100080, People's Republic of China*

(Received 15 August 2000; accepted 14 December 2000)

The interaction of modest, femtosecond (fs) laser pulses with solid targets is studied with particle-in-cell (PIC) simulations. A bi-temperature distribution of hot electrons is found. The first hot electron temperature can be attributed to the resonance absorption of the laser field, whereas the second hot electron temperature is identified to be due to the combined acceleration by the static electric field in front of the target and by the laser induced oscillating electric field in the thin plasma layer between the vacuum and the target. © 2001 American Institute of Physics.

[DOI: 10.1063/1.1348036]

I. INTRODUCTION

Hot electrons can be produced in ultrashort pulse laser-plasma interaction through different processes, such as resonance absorption,¹ vacuum heating,² parametric instabilities,³ ponderomotive $\mathbf{V} \times \mathbf{B}$ acceleration,⁴ and wake-field acceleration.⁵ Umstadter and Modena demonstrated the dependence of the production of relativistic electrons on laser intensity and plasma density in their investigation on parametric instability of underdense plasmas.^{6,7} If the plasma density distribution is inhomogeneous with a large enough scale length $L = (\partial \ln n_e / \partial x)^{-1}$, the resonance absorption will take place⁸ where the scaling for hot electron temperature $T_H \sim 6 \times 10^{-5} (I\lambda)^{0.33}$ was derived and generally is consistent with experiments.^{9–11} A plasma wave can be driven by the laser electric component parallel to the density gradient. When the wave breaks, hot electrons can be produced.⁹ The process of interaction between femtosecond (fs) laser pulses and plasmas with a step-like density profile (solid targets) was investigated by several groups through experiments,¹² particle-in-cell (PIC) simulations¹³ and analytical theories.¹⁴ The main absorption mechanism was attributed to the vacuum heating (VH).^{12,13} However, some physics problems in this interaction process, such as electron acceleration are still unclear, in particular, there are very few studies on the interaction of intermediately intense, femtosecond laser pulses with solid targets. In this paper, we present our investigation of the plasma heating process and electron acceleration in the interaction between intermediately intense fs laser pulses and solid targets.

II. PIC SIMULATIONS AND LABORATORY EXPERIMENTS

To investigate the interaction process between fs laser pulses and solid targets, we use a 1D3V fully relativistic PIC code Lpic++ (Ref. 15) which solves Maxwellian equations

for the fields and the motion equations for macroparticles simultaneously. The simulation box has a length of 20.5λ along the x direction. A region of 7λ in the middle of the box is occupied by a plasma whose electron density rises exponentially from $10^{-5} n_c$ at the point of 10λ to $20n_c$ with a scale length L of 0.04λ , where n_c is the critical density for laser pulses with a wavelength of λ . A p -polarized laser pulse is launched from the left boundary of the box with an incident angle of 45° from the normal of the target. The normalized strength of the laser field is taken as 0.06 (normalized through $a_0 = eE_{L0}/m\omega_0c$, where E_{L0} and ω_0 are the amplitude and the frequency of the laser field; c is the light velocity in the vacuum; e and m are charge and mass of electrons, respectively). 56 periods of the laser field is taken as the pulse duration. These parameters correspond to an intensity of $5 \times 10^{15} \text{ W } \mu\text{m}^2/\text{cm}^2$ in 150 fs pulses used in our laboratory experiments. In the simulation, initial electron temperature is assumed to be 100 eV, and ions are mobile.

Figure 1(a) gives the energy distribution of hot electrons with momentum directing into targets at a time of the 35th laser period in the PIC simulation. The hot electron distribution has a bi-temperature structure. The first hot electron temperature is about 6 keV, which is consistent with the scaling of the resonance absorption mechanism for $a_0 = 0.06$. The second hot electron temperature is 43 keV. This is similar to the main characteristic of our experimental data [Fig. 1(b)]. Obviously, this high temperature can not simply be attributed to the resonance absorption. There are some mechanisms for hot electron production in underdense plasmas in front of the target, as suggested by Ref. 10. One of these mechanisms is Raman scattering. The growth threshold of the Raman scattering process is determined by the criteria $(v_{osc}/c)^2 > 2/k_0L$, where $v_{osc} = eE_{L0}/m\omega_0$ is the quiver velocity of electrons in the laser field; and k_0 is the wave number of the laser field. In our simulation, however, $(v_{osc}/c)^2$ is only as small as 0.0036, much smaller than $2/k_0L = 50$, suggesting that Raman scattering cannot take place in our experiments. So it is necessary to find new acceleration mecha-

^{a)}Author to whom correspondence should be addressed. Electronic mail: jzhang@aphy.iphy.ac.cn

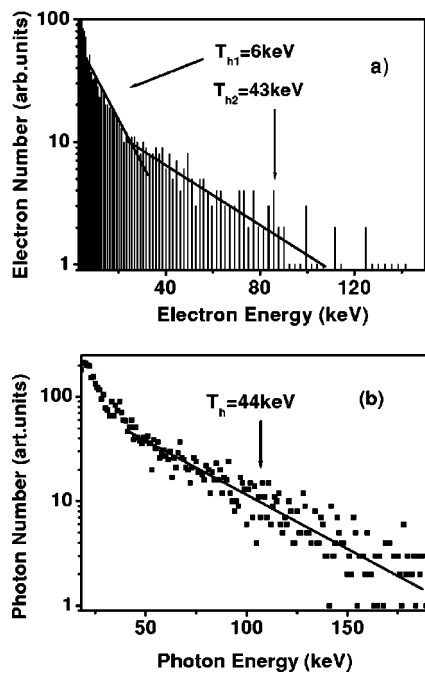


FIG. 1. (a) Electron energy distribution at the 35th laser period from the PIC simulation. (b) X-ray spectrum measured behind the back of the Al target in experiments.

nism to explain the production of the high energy electrons under the experimental conditions.

In the laboratory, it is usual to use bremsstrahlung x-ray emission as plasma diagnostics.^{16–18} Simple estimates and experiments with monoenergetic electron beams show that x-ray emission by an electron propagating through solid targets can be expressed as $j_{\text{sol}}(E, h\nu) \propto (E - h\nu)$, where E is the kinetic energy of electrons and $h\nu$ is the energy of radiated photons.¹⁸ With the assumption of electron distribution, one can deduce the effective electron temperature from the x-ray spectrum in experiments.^{18–20} In our experiments, the x-ray radiation up to a few hundreds keV is measured using a calibrated x-ray spectrometer set behind the targets. Figure 1(b) gives the measured x-ray spectra, achieved after deconvolution the detector response and the transmission effects of filters and solid targets. We put together in Fig. 1 the electron energy spectrum from the PIC simulation and the x-ray spectrum from laboratory experiments. The two/three-dimensional effects and the complication of production, transmission and detection of x rays make it very difficult to compare directly the results from PIC simulation and laboratory experiments. But two common characteristics of the two results are worth pointing out here. First, the simulated electron spectrum and the measured x-ray spectrum both show a bi-temperature structure. The maximum energy of hot electrons extends to a few hundred of keV with the second temperature of tens of keV. Secondly, PIC simulations and experimental results both show the fact that there are hot electrons penetrating into solid targets, which indicates an accelerating electric field pointing out of targets.

Figure 2(a) shows the snapshot of the electron phase space. Three characteristics of the electron distribution at the phase space should be noted. First, some electrons are accel-

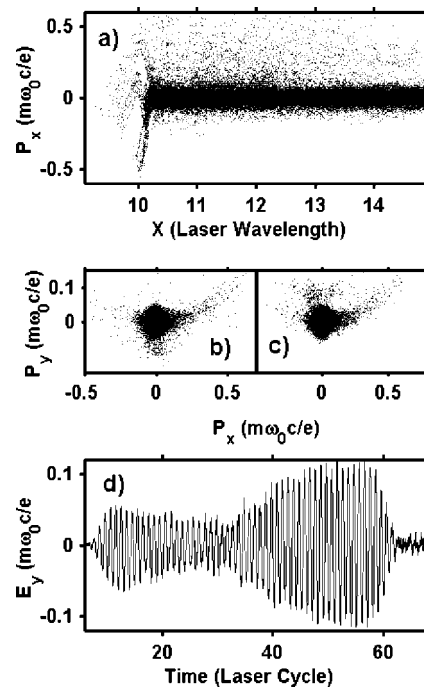


FIG. 2. (a) Electron longitudinal momentum P_x vs x in the 28th laser period. (b), (c) Electron transverse momentum P_y vs longitudinal momentum P_x at time 42.560th and 42.957th laser period. (d) Transverse part E_y of the electric component of the laser electromagnetic field.

erated up to $0.5c$ in both directions in and out of the target. Obviously, this cannot be achieved only through direct laser field acceleration, since the laser amplitude is only 0.06. Secondly, inside the plasma, electrons with velocities larger than $0.2c$ are directed into the plasma, and only out of the target are there some electrons with negative velocities up to $0.5c$. This implies that hot electrons with negative velocities are accelerated in a thin layer of the plasma at the interface between the target and the vacuum, whereas, those with higher positive velocities are mainly accelerated in the vacuum, since they are injected into the plasma from the vacuum, as clearly shown in the snapshot. Thirdly, as shown by other snapshots of electron phase space in different laser periods, electrons are pulled out of targets and ejected into the vacuum every cycle by the laser electric component. Many of them stay out of the targets, building up an electron cloud.²¹

Those electrons staying out of the target are driven by the laser electric component and oscillate with the same frequency as the laser field. Figures 2(b) and 2(c) show the transverse momentum P_y vs the longitudinal momentum P_x of electrons at different times. It is apparent from the figures that there are a great number of electrons with oscillating transverse momentum, whereas the longitudinal momentum of these electrons is almost zero. P_y 's amplitude reaches $0.12(m\omega_0 c/e)$. This can be explained by taking into account the enhanced laser field in Fig. 2(d), which shows the E_y part of the laser fields in front of the target. At the time of the 30th laser period, the amplitude of the laser field increases by a factor of 2. We note that in Figs. 2(b) and 2(c), electron distribution at the larger positive longitudinal momentum

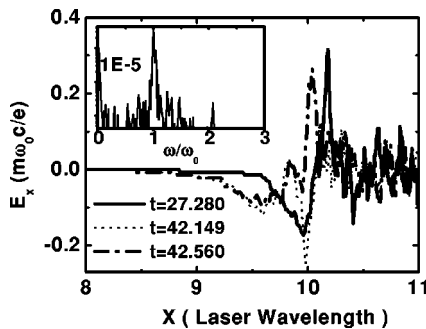


FIG. 3. Laser induced E_x vs x at different time. Inset: Spectrum of E_x measured at 1 wavelength before the target for all the interaction time.

does not change with time. This is because those electrons with such high momentum are inside the target where the laser field cannot penetrate and therefore has no effects on electrons. This situation is also implied by Fig. 2(a).

III. ELECTRON ACCELERATION

In order to understand the acceleration mechanism of hot electrons, we diagnose the laser-induced longitudinal electric field at different times in Fig. 3. As we can see, all of the induced E_x curves show that there always is a negative static charge separation potential in front of the target. This electrostatic field forms when the electrons are pulled out and ions remain in the target due to the ion heavy mass. Experiments using an inductance-capacitance-resistance (LCR) circuit to deduce the positive target potential demonstrate the existence of the electrostatic field.²² According to the results of PIC simulation, the electrostatic field has an average strength of 0.1 (normalized through $eE_x/m\omega_0 c$), corresponding to an accelerating field of about 10^{11} V/m. Inside the target, however, the longitudinal electric field E_x oscillates as shown by the two curves for the first and second half of the 42nd laser period. Especially in the layer of the plasma between vacuum and target, E_x can even reach a value as high as 0.4. The inset is the E_x spectrum diagnosed at the 9λ position. The zero frequency component is strong evidence of the quasisteady potential during the interaction process. The second harmonic with a small blue shift is from the laser light scattered by the oscillation of electrons inside the target discussed above. Other frequency components may be produced by Thomson scattering or by some other mechanisms. But they do not play any important roles, since from Fig. 2(d), it can be seen that E_y does not show these frequencies, apparently.

Electrons with large positive velocities are accelerated by the quasistatic electric field in the vacuum and injected into the target. In the vacuum, the electron motion equation is $mdv/dt = -e(E_s(x) + E_L(t,x))$, $E_s(x)$ and $E_L(t,x)$ are the electrostatic field and the oscillating longitudinal component of the laser electric field, respectively. The laser magnetic component effect is omitted for simplicity, although after acceleration due to the static potential in front of the target, the magnetic effect is comparable to the laser electric component. In the equation, $E_s(x)$ can be obtained by read-

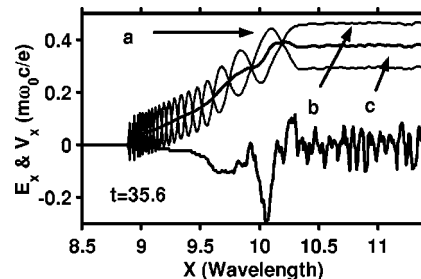


FIG. 4. Electron velocity vs x , showing electrons accelerated by the induced E_x . The effects of the Laser electric component E_L is also shown: Curve a and b with $E_L(\Phi_1)$ and $E_L(\Phi_2)$, respectively; Curve c without the E_L function.

ing the data of the PIC simulation results. Since the induced E_x always exists and changes little with time, we select an intermediate E_s strength. $E_L(t,x) = 2(1-\eta)E_{L0} \cos(\omega_0 t + k_0 x + \Phi)$ when $x \leq 10.3\lambda$ or $E_L(t,x) = 0$ when $x > 10.3\lambda$ with a rough approximation. Here, $\eta = 40\%$ is the absorption coefficient according to laboratory experiments and PIC simulations; Φ is the initial phase of the laser pulse when it begins to interact with an electron. Figure 4 gives the integration results, with and without the laser field having different initial phase Φ_1 and Φ_2 . We can see that the induced $E_s(x)$ by itself can accelerate electrons to about $0.4c$.

The oscillating part of the laser-induced longitudinal electric field E_x in the plasma layer between the vacuum and the target plays an important role in producing hot electrons penetrating into or escaping away from targets. When this part of E_x is negative and the laser has a proper initial phase, electrons returning from the vacuum can be accelerated subsequently up to $0.5c$, whose temperature can be deduced from the x-ray spectrum obtained in the laboratory experiment. If this part of E_x is positive, electrons accelerated in the vacuum will be decelerated to a lower velocity. On the other hand, the positive E_x in the plasma layer will pull electrons out of the target, as shown in Fig. 2(a). The two groups of hot electrons with opposite directions, which are produced by different parts of the laser-induced longitudinal electric field, constitute the second temperature of the energy distribution of electrons injected into or ejected out from targets, respectively. Moreover, from Fig. 2(a), we can exclude the plasma wave action in producing hot electrons because of the very small density scale length and the fact that many energetic electrons with positive velocities are injected into the target by the electrostatic potential. The possibility of electron acceleration by the ponderomotive force of laser beam can also be excluded due to the small laser strength used in the simulation.

In order to understand the effects of initial conditions on the production of hot electrons, we did some simulations with different density scale lengths and laser intensities. We find that the production of the electrostatic field is not unique in the interaction between fs laser pulse and plasmas with a step-like density profile. When the electron excursion length in the laser field is larger than the density scale length, electrons can be ejected out of its original region, causing a charge separation potential. Even in plasmas with a larger

scale length, electrons can still be separated from ions through plasma wave breaking toward the vacuum.¹¹

IV. CONCLUSION

In summary, through PIC simulations, the electron acceleration by the static and oscillating electric fields is studied, which produce the bi-temperature structure of the hot electron distribution. The first hot electron temperature is due to the resonance absorption. Those electrons are the main part of the accelerated electrons in the interaction process. The second hot electron temperature is due to the combined acceleration by the static electric field in front of the target and the oscillating electric field in the thin layer plasma between vacuum and target surface, which accelerate electrons to higher energies.

ACKNOWLEDGMENTS

This work is jointly supported by the National Natural Science Foundation (Grant Nos. 19825110, 10005014 and 100F50F5) and the National Hi-Tech ICF program of China.

- ¹D. W. Forslund, J. M. Kindel, K. Lee, L. Lindman, and R. L. Morse, Phys. Rev. A **11**, 679 (1975).
- ²F. Brunel, Phys. Rev. Lett. **59**, 52 (1987); Phys. Fluids **31**, 2714 (1988).
- ³N. A. Ebrahim, H. A. Baldis, C. Joshi, and R. Benesch, Phys. Rev. Lett. **45**, 1179 (1980); C. Joshi, T. Tajima, J. M. Dawson, H. A. Baldis, and N. A. Ebrahim, *ibid.* **47**, 1285 (1981).
- ⁴G. Malka, J. Fuchs, F. Amiranoff *et al.*, Phys. Rev. Lett. **79**, 2053 (1997); S. B. Liu, J. Zhang, and W. Yu, Phys. Rev. E **60**, 3279 (1999).
- ⁵T. Tajima and J. M. Dawson, Phys. Rev. Lett. **43**, 267 (1979); P. Sprangle, E. Esarey, A. Ting, and G. Joyce, Appl. Phys. Lett. **53**, 2146 (1988); E. Esarey, P. Sprangle, J. Krall, and A. Ting, IEEE Trans. Plasma Sci. **24**, 252 (1996).
- ⁶D. Umstadter, S.-Y. Chen, A. Marksimchuk, G. Mourou, and R. Wagner, Science **273**, 472 (1996).
- ⁷A. Modena, Z. Najmudin, A. E. Dangor, C. E. Clayton, K. A. Marsh, C. Joshi, V. Malka, C. B. Darrow, C. Danson, D. Neely, and F. N. Walsh, Nature (London) **377**, 606 (1995).
- ⁸W. L. Kruer and K. Estabrooks, Phys. Fluids **20**, 1688 (1977).
- ⁹J. P. Freidberg, R. W. Mitchell, R. L. Morse, and L. I. Rudinski, Phys. Rev. Lett. **28**, 795 (1972); S. V. Bulanov, N. M. Naumova, and F. Pegoraro, Phys. Plasmas **1**, 745 (1994).
- ¹⁰P. Gibbon, Phys. Rev. Lett. **73**, 664 (1994).
- ¹¹R. Fedosejevs, R. Ottmann, R. Sigel, G. Kühnle, S. Szatmari, and F. P. Schäfer, Phys. Rev. Lett. **64**, 1250 (1990); H. M. Milchberg and R. R. Freeman, J. Opt. Soc. Am. B **6**, 1351 (1989).
- ¹²D. F. Price, R. M. More, R. S. Walling, G. Guethlein, R. L. Shepherd, R. E. Stewart, and W. E. White, Phys. Rev. Lett. **75**, 252 (1995); M. K. Grimes, A. R. Rundquist, Y.-S. Lee, and M. C. Downer, *ibid.* **82**, 4010 (1999).
- ¹³P. Gibbon and A. R. Bell, Phys. Rev. Lett. **68**, 1535 (1992).
- ¹⁴S. Kato, B. Bhattacharyya, A. Nishiguchi, and K. Mima, Phys. Fluids B **5**, 564 (1993); W. Rozmus, V. T. Tikhonchuk, and R. Cauble, Phys. Plasmas **3**, 360 (1996).
- ¹⁵R. Lichters, J. Meyer-ter-Vehn, and A. Pukhov, Phys. Plasmas **3**, 3425 (1996).
- ¹⁶T. W. Phillips, M. D. Cable, T. E. Cowan, S. P. Hatchett, E. A. Henry, M. H. Key, M. D. Perry, T. C. Sangster, and M. A. Stoyer, Rev. Sci. Instrum. **70**, 1213 (1999).
- ¹⁷S. P. Hatchett, C. G. Brown, T. E. Cowan *et al.*, Phys. Plasmas **7**, 2076 (2000).
- ¹⁸S. Hokin, Rev. Sci. Instrum. **63**, 5041 (1992).
- ¹⁹K. A. Brueckner, Nucl. Fusion **17**, 1257 (1977); M. Lamoureux, P. Waller, P. Charles, and N. B. Avdonina, Phys. Rev. E **62**, 4091 (2000).
- ²⁰P. Zhang, J. T. He, D. B. Chen, Z. H. Li, Y. Zhang, J. G. Bian, L. Wang, Z. L. Li, B. H. Feng, X. L. Zhang *et al.*, Phys. Rev. E **57**, R3746 (1998).
- ²¹W. Yu, M. Y. Yu, Z. M. Sheng, and J. Zhang, Phys. Rev. E **58**, 2456 (1998).
- ²²L. Z. Zhao, L. M. Chen, P. Zhang, T. J. Liang, L. Wang, and J. Zhang, "Studies on escaping electrons in ultrashort pulse laser interaction with solid targets," Nature (submitted).

Self-modulation of an intense laser beam in near-critical homogeneous plasma

Hai Lin^{a)}

CCAST (World Laboratory), P.O. Box 2735, Beijing 100080, China

and Graduate School, China Academy of Engineering Physics, P.O. Box 2101, Beijing 100080, China

Li-Ming Chen

Southwest Institute of Nuclear Physics and Chemistry, China Academy of Engineering Physics, P.O. Box 919, Mianyang 621900, China

Jie Zhang

Laboratory of Optical Physics, Institute of Physics, Chinese Academy of Science, P.O. Box 603, Beijing 100080, China

Ping Zhang and Wen-Bing Fan

CCAST (World Laboratory), P.O. Box 2735, Beijing 100080, China

and Graduate School, China Academy of Engineering Physics, P.O. Box 2101, Beijing 100080, China

(Received 25 May 2000; accepted 2 January 2001)

An investigation of longitudinal intensity modulation of a relativistic laser beam in near-critical homogeneous plasma ($n_e > \frac{1}{4}n_{cr}$) is performed in this paper. On the basis of a nonlinear Schrödinger equation of electromagnetic vector potential, a model equation of the intensity profile is derived via the variational approach from Action and Lagrangian. Longitudinally uniform and longitudinally modulated pulse structures are viewed as different solutions of this model equation. For these two different types of pulse structure, their relative stability under different structure parameters is numerically studied. Numerical results indicate that this relative stability depends closely on the transverse structures of the laser pulse. © 2001 American Institute of Physics.

[DOI: 10.1063/1.1351550]

I. INTRODUCTION

The interaction of high-power lasers (\geq TW level) with plasma has been an active research area because of the great progress in the development of compact terawatt lasers.¹ In this intensity level, the quiver velocity of electrons is close to light speed. In addition to the well-known relativistic correction of electron mass, there is another important nonlinear effect: ponderomotive cavitation, which refers to electrons being expelled from the high laser intensity region, is not negligible. In some theoretical works which contain both of these two nonlinear effects,² the laser pulse (relative to the observer in the pulse frame) is described by a nonlinear Schrödinger equation (NLSE) of the vector potential. A similar NLSE has been used in nonlinear optics in the weak field limit where the cavitation effect is absent.³ In the framework of the NLSE, self-focusing and the filamentary transverse profile of the laser beam are thoroughly studied.²

Compared with the transverse profile, the longitudinal profile of the laser beam, which is related to the generation of the longitudinal wakefield, is more pertinent to a laser-driven plasma acceleration application.⁴ As a promising mechanism of wakefield generation, which can operate at higher laser intensity and plasma density, self-modulation has been thor-

oughly studied on the basis of a coupled two-fluid model.⁵ In those theories, self-modulation is taken as the dynamic fluctuation of the laser intensity profile which arises from density oscillation within a pulse driven by the finite rising edge of the pulse. Moreover, those investigations are addressed to laser-plasma interaction in the weak field regime where the dimensionless field amplitude A is far less than 1 and ponderomotive cavitation is not taken into account. In the strong field regime $A \sim 1$, some theories in the framework of the NLSE (Ref. 2) show that the laser will become self-focusing in the transverse direction as its power becomes sufficiently high. The generation of a nonlinear wakefield under a high-intensity beam has been studied in a one-dimensional (1D) fluid model.⁶ However, the effect of the self-focusing transverse structure on self-modulation is less explored. In the weak field regime, the effects of pulse transverse inhomogeneity on self-modulation have been studied on the basis of a coupled two-fluid model.⁵ On the other hand, we know, from Poisson's equation, that a large-amplitude wakefield demands a sufficient amount of electrons in the interaction region to undertake oscillation. Whereas ponderomotive cavitation causes electron density to decrease in the interaction region, this seems unfavorable to generation of a wakefield. Hence, the effect of transverse focusing on self-modulation is deserving of study.

Here, as in discussions of the self-focusing transverse profile,² we intend to study self-modulation in the framework

^{a)}Mailing address: Graduate School, China Academy of Engineering Physics, P.O. Box 2101, Beijing 100080, China; electronic mail: Hai_Lin72@hotmail.com

of the NLSE. Unlike previous theories,⁵ we focus our study on the pulse body, regardless of its head and tail edge, and study whether there exist other modulation mechanisms in addition to that due to the pulse head. For the self-focusing pulse body, if its intensity profile is longitudinally invariant, the resulting transverse quiver energy of a single electron in a section perpendicular to the propagation axis, as well as the number of electrons having this quiver energy quantum, is also longitudinally invariant. Nevertheless, for other possible longitudinally variant profiles, for example, the self-modulated profile, the transverse quiver energy is not so simple. In the high-intensity section, the quiver energy of a single electron is high but the number of electrons having this quiver energy is low, since more electrons are expelled away from the high-intensity region. Whereas in the low-intensity section, the contrary case presents itself. By comparing the respective total quiver energy of electrons, we can know the relative stability among those possible intensity profiles. In this paper, we will study, after taking into account the transverse self-focusing effect, the self-modulation of the intense laser pulse via the analysis on the stability of the longitudinal intensity profiles. Moreover, we confine our study to plasma with a density larger than a quarter of the critical density in order to avoid modulation due to forward Raman scattering.⁷ Theoretically, the investigations of self-modulation in the parameter regime with high laser intensity ($A \sim 1$) and high plasma density ($n_e \leq 0.25n_{cr}$) have been less reported. There are two reasons for us to focus our investigation on this density regime. The first arises from the fact that the stimulated Raman scattering cannot occur in this regime and, hence, cannot produce the modulation of the laser pulse. In order to understand the behavior of a high-power laser pulse in this regime, it is necessary to study the possibility of self-modulation due to other mechanisms in addition to Raman scattering. The other reason is that, for some applications, such as laser inertial confinement, the laser pulse interacts with a target of varying density from an overdense regime to an extremely tenuous regime, the interaction in the intermediate regime is also important to influence the effect of the pressurization of the laser pulse on the overdense target core. Furthermore, self-modulation has been regarded as an effective mechanism to excite a large-amplitude plasma wave to accelerate electrons to high energy. Thus, the effect of a laser pulse on a target will increase if the self-modulation can occur in the intermediate regime, in addition to the regime of density below the quarter critical density, because the acceleration length is not confined to the regime of the density below the quarter critical regime.

This paper is arranged as follows. The theoretical model is given in Sec. II. The numerical results of the model equations are discussed in Sec. III. A brief summary is presented in Sec. IV.

II. THEORY

A. Model equation

In general, the laser-plasma interaction is described by a set of fluid equations of vector potential A scalar potential ϕ , electronic density, and flowing speed.² By casting those

equations to the pulse frame, which moves in laser phase speed, i.e., $A = a \exp(ikz - i\omega t)$, where the normalization of a , $|a|^2$, represents the laser intensity and equals that of A , $|A|^2$, a nonlinear Schrödinger equation is readily attained:²

$$i\partial_t a = -\frac{1}{2\omega} * \left(c^2 \nabla_\perp^2 a + \frac{c^2}{4} \partial_{\xi\xi} a - \partial_{tt} a \right) - \frac{1}{4} \frac{ikc^2}{\omega} \partial_\xi a + \frac{1}{2\omega} V(a) a, \quad (1)$$

$$V = \frac{\omega_{p,0}^2}{\gamma} - \omega^2 + \frac{1}{4} k^2 c^2 + \left[\frac{c^2 \nabla_\perp^2 \gamma - \partial_{tt} \gamma + \frac{c^2}{4} (\partial_{z_0 z_0} \gamma + 2\partial_{z_0} \partial_\xi \gamma + \partial_\xi \gamma)}{\gamma} \right],$$

and the corresponding Hamiltonian, which depends on the independent variables, I (intensity profile) and θ (phase profile), is

$$H = \frac{1}{2\omega} \int \left\{ \frac{k\partial_\xi \theta}{2} I c^2 + (\nabla_\perp \theta)^2 I c^2 + \frac{1}{4} (\partial_\xi \theta)^2 I c^2 + \frac{k^2 c^2}{4} I + 2\omega_{p,0}^2 \sqrt{1+I} - \omega^2 I + \frac{(\nabla_\perp I)^2}{4I(1+I)} c^2 + \frac{1}{4} \frac{(\partial_\xi I)^2}{4I(1+I)} c^2 \right\} d\tau, \quad (2)$$

where $\xi = z - ct$ is the intrapulse longitudinal coordinate and $d\tau = dx dy d\xi$ is the pulse volume. $I = |a|^2$ and $\xi = 0$ are defined at the pulse center and the pulse extends from $\xi = -l$ to $\xi = l$ in the longitudinal direction. Here, ∇_\perp denotes the transverse gradient relative to the transverse coordinate and has its form in plan geometry $e_\perp \nabla_\perp = e_x \nabla_x + e_y \nabla_y$.

The steady-state structure equation, attained from $\delta L^s / \delta I = 0$ [see Lagrangian L^s in Eq. (A21) in the Appendix], is

$$[S(\mu) + \omega^2]/c^2 = \left(-\frac{2}{4} \frac{\nabla_\perp^2 I}{I+I^2} + \frac{1}{4} (\nabla_\perp I)^2 \frac{2I+1}{(I+I^2)^2} \right) + \frac{1}{4} \left(-\frac{2}{4} \frac{\partial_\xi^2 I}{I+I^2} + \frac{1}{4} (\partial_\xi I)^2 \frac{2I+1}{(I+I^2)^2} \right) + \frac{\omega_{p,0}^2}{c^2} \frac{1}{\sqrt{1+I}}, \quad (3)$$

where $S(\mu) = 2\omega\mu + \mu^2$ is defined in the Appendix [Eq. (A21)] and μ is the frequency associated with a and reflects the frequency shift due to the spatially varying laser amplitude. The boundary conditions are

$$\begin{aligned} I(|r|=\infty) &= 0; \quad \nabla_{\perp} I|_{|r|=\infty} = 0, \\ I(|\xi|=\pm\infty) &= 0; \quad \partial_{\xi} I|_{|\xi|=\pm\infty} = 0. \end{aligned} \quad (4)$$

For a long-duration pulse, we use the ξ -independent solution to describe the intensity profile in its body. Equation (3) is reduced to

$$\begin{aligned} [S(\mu) + \omega^2]/c^2 &= \left(-\frac{2}{4} \frac{\nabla_{\perp}^2 I}{I + I^2} + \frac{1}{4} (\nabla_{\perp} I)^2 \frac{2I+1}{(I+I^2)^2} \right) \\ &\quad + \frac{\omega_{p,0}^2}{c^2} \frac{1}{\sqrt{1+I}}. \end{aligned} \quad (5)$$

This equation is actually equivalent to

$$\frac{\partial \mathcal{L}}{\partial I} - \nabla_{\perp} \left(\frac{\partial \mathcal{L}}{\partial (\nabla_{\perp} I)} \right) = 0, \quad (6)$$

where \mathcal{L} is the Lagrangian density, which is defined in the Appendix. Via a Legendre transform, we define a functional Q , which depends on the independent variables I and θ ,

$$Q = \mathcal{L} - \frac{\partial \mathcal{L}}{\partial (\nabla_{\perp} I)} (\nabla_{\perp} I). \quad (7)$$

For Q , there is

$$\nabla_{\perp} Q = \left[\frac{\partial \mathcal{L}}{\partial I} - \nabla_{\perp} \left(\frac{\partial \mathcal{L}}{\partial (\nabla_{\perp} I)} \right) \right] \nabla_{\perp} I. \quad (8)$$

For any solution of Eq. (5), the values of functional Q at this solution are r independent, $\nabla_{\perp} Q = 0$. Note that Q is not equivalent to Hamiltonian density $h = [\partial \mathcal{L}/\partial(\partial_t a)](\partial_t a) - \mathcal{L}$. Thus, there is $Q = Q(r=\infty)$, i.e.,

$$\begin{aligned} S(\mu)I_{\mu} + \omega^2 I_{\mu} + \frac{(\nabla_{\perp} I_{\mu})^2}{4I_{\mu}(1+I_{\mu})} c^2 - 2\omega_{p,0}^2 \sqrt{1+I_{\mu}} \\ = -2\omega_{p,0}^2 + U, \\ U = \lim_{|r| \rightarrow \infty} \frac{(\nabla_{\perp} I)^2}{I} = \lim_{|r| \rightarrow \infty} (\nabla_{\perp} a)^2. \end{aligned} \quad (9)$$

Here, the boundary conditions include $a(r \rightarrow \infty)$ and $\nabla a(r \rightarrow \infty)$. $a(r \rightarrow \infty) = 0$ is essential, since it has been adopted in

the derivation of the Lagrangian and model equations. As for another boundary condition $\nabla a(r \rightarrow \infty)$, its nonzero but finite value will not influence the Lagrangian and model equations derived in its zero value. For finite nonzero $\nabla a(r \rightarrow \infty)$, the boundary conditions of $I: I(r \rightarrow \infty)$ and $\nabla I(r \rightarrow \infty) = 2a\nabla a$, are both zero due to the zero value of a at $r \rightarrow \infty$. Because $U \neq 0 (\infty > |\nabla a(r \rightarrow \infty)| > 0)$ can also lead to the same boundary condition of I with $U = 0$, it should not be ignored in discussing the solubility of Eq. (9).

Since the spatial variance of a is related to magnetic-field amplitude, $\nabla a(r \rightarrow \infty) \neq 0$ implies a nonzero magnetic-field amplitude at $r \rightarrow \infty$. Actually, this extension of $\nabla a(r \rightarrow \infty)$ to its nonzero value situation is useful to consider the effect of the pulse transverse surface where electrons outside the pulse can influence the laser field distribution via their collective current. The magnetic field of this outside current provides the boundary condition to the laser field. Because we do not limit the pulse distribution in the transverse direction, it seems that electrons outside the pulse, which are taken as extending to $r \rightarrow \infty$, do not exist. Hence, their effects are expressed in the form of the surface boundary condition on the laser field. From another viewpoint, if we discuss, at first, the finite transverse distribution of the laser pulse and take R as the transverse boundary, now the outside electrons refer to those locating at $r > R$, they can provide various boundary conditions at $r = R$ to the laser pulse according to their state. $\nabla a(r = R) \neq 0$ represents a possible boundary condition determined by the outside electrons. As we study the special case with $R = \infty$, the effect of the outside electrons now is expressed as the surface boundary condition at $R = \infty$.

Using a transform $y^2 = \sqrt{1+I} - 1$, we obtain

$$I = y^4 + 2y^2, \quad \nabla_{\perp} I = 4(y^3 + y)\nabla_{\perp} y. \quad (10)$$

Equation (9) becomes an elementary form

$$\nabla_{\perp} y^2 = \pm y^2 \sqrt{(2\omega_{p,0}^2 - 2\tilde{S} - \tilde{S}y^2)(y^2 + 2)}, \quad (11)$$

where $\tilde{S} = S + \omega^2 = (\mu + \omega)^2 > 0$. This equation has the solutions in slab geometry

$$y^2 = \begin{cases} \frac{4(\omega_{p,0}^2 - \tilde{S})}{\omega_{p,0}^2 \sin[2\sqrt{\tilde{S} - \omega_{p,0}^2}(x_{\perp} + lt)] - \omega_{p,0}^2 + 2\tilde{S}} < 0, & \text{if } \omega_{p,0}^2 - \tilde{S} < 0, \\ \frac{2\sqrt{4(\omega_{p,0}^2 - \tilde{S})} \exp(-\sqrt{4[(\omega_{p,0}^2 - \tilde{S})(x_{\perp} + lt)]})}{\left[\exp[-\sqrt{4(\omega_{p,0}^2 - \tilde{S})(x_{\perp} + lt)}] - \frac{2\omega_{p,0}^2 - 4\tilde{S}}{2\sqrt{4(\omega_{p,0}^2 - \tilde{S})}} \right]^2 + \tilde{S}} > 0, & \text{if } \omega_{p,0}^2 - \tilde{S} > 0, \end{cases} \quad (12)$$

where x_{\perp} is the transverse coordinate in slab geometry and lt is an integral constant. For $\omega_{p,0}^2 - \tilde{S} < 0$, $y^2 < 0$ solution should be discarded. For $\omega_{p,0}^2 - \tilde{S} > 0$, I has an analytic form which exhibits a focusing feature and monotonically approaches zero at $r = \infty$. As lt meets

$$lt = -\frac{1}{4\sqrt{\omega_{p,0}^2 - \tilde{S}}} \ln \frac{\omega_{p,0}^2}{4(\omega_{p,0}^2 - \tilde{S})}, \quad (13)$$

y^2 at $\omega_{p,0}^2 - \tilde{S} > 0$ has a symmetric dependence on x_{\perp}

$$y^2 = 4 \left(1 - \frac{\tilde{s}}{\omega_{p,0}^2} \right) \frac{1}{\left[ch(2\sqrt{\omega_{p,0}^2 - \tilde{s}}x_\perp) - \frac{\omega_{p,0}^2 - 2\tilde{s}}{\omega_{p,0}^2} \right]}, \quad (14)$$

and thus the resulting transverse intensity profile I also depends on x_\perp symmetrically.

For $U \neq 0$, there is

$$\begin{aligned} \nabla_\perp y^2 &= \pm \sqrt{(-Uy^2 + 2\omega_{p,0}^2 y^4 - 2\tilde{s}y^4 - \tilde{s}y^6)(y^2 + 2)} \\ &= \pm \sqrt{ay^8 + by^6 + cy^4 + dy^2}. \end{aligned} \quad (15)$$

Even though we can use a translation: $\tilde{y}^2 = y^2 + t$ to transform the right-hand side of this equation to same form as that in Eq. (11), the nature of the new equation of \tilde{y}^2 is complicated. Here, constant t is only introduced for the convenience of solving the equation and is not time variable, and it is determined as follows: the coefficients of the linear term of \tilde{y}^2 , \tilde{y}^{2^1} , and that of the zero-order term, \tilde{y}^{2^0} , are zero and the right-hand side of Eq. (15) has the general form: $\tilde{a}(t)\tilde{y}^{2^1} + \tilde{b}(t)\tilde{y}^{2^2} + \tilde{c}(t,U)\tilde{y}^{2^0}$, thus the equation of \tilde{y}^2 can be solved in the same way as y^2 in the $U=0$ scenario. We note that \tilde{a} , \tilde{b} , \tilde{c} are t dependent due to the transform, and especially \tilde{c} is also U dependent. Hence, t should meet

$$\begin{aligned} at^4 + bt^3 + ct^2 + dt &= 0, \\ 4at^3 + 3bt^2 + 2ct + d &= 0, \end{aligned} \quad (16)$$

i.e., t meets

$$3at^2 + 2bt + c = 0, \quad (17)$$

and $d = 2U$ has the relation with the solution of this equation

$$d = -at^3 - bt^2 - ct. \quad (18)$$

Clearly, only for some special value of U can these two equations be simultaneously satisfied. Hence, for $U \neq 0$, we directly seek a numerical solution of Eq. (15).

For given μ , I with different lt satisfy Eq. (9) under the respective origin transverse boundary condition: $\nabla_\perp I|_{x_\perp=0} = 0$. Hence, the origin of the transverse boundary condition is necessary to specify the solutions of Eqs. (5) and (3). Similarly, the origin boundary conditions, both transverse and longitudinal, have the same importance to specify the solutions of Eq. (3). For a long-duration pulse, the longitudinal homogeneous solution of Eq. (3) meeting $\partial_\xi I|_{\xi=0} = 0$ describes its body. We will discuss, in the following paragraph, the structure stability of a longitudinally homogeneous structure relative to other longitudinally modulated ones which satisfy $\partial_\xi I|_{\xi=0} \neq 0$.

B. Stability of the longitudinal homogeneous structure relative to a longitudinal modulated one

Although our aim is at the longitudinal structure, the transverse structure of the pulse, especially for a self-focusing beam, should not be ignored. In principle, we can solve the longitudinally modulated structures from Eq. (3) by choosing the relevant origin conditions, both the transverse and longitudinal ones. However, such an exact three-dimensional (3D) structure calculation is a cumbersome

computational task. Hence, we develop an approximate method, saving computer time. In this approximation, the longitudinally homogeneous structure is taken as a background for various modulated structures growing from it.

Because we treat two different profile types, the longitudinally uniform structure and the longitudinally modulated one, as two different solutions of the model equation, it is natural for us to study, when $a_0 = \sqrt{I_0}e^{-i\mu_0 t}$ meets propagation Eq. (1), the condition $a_g = \sqrt{I_0 + I_g}e^{-i(\mu_0 + \mu_g)t}$, which that ensures a_g is also satisfying the propagation equation. The essence of our approximation is the invariance of variational equation $\delta L^s / \delta I = 0$:

$$\left. \frac{\delta L^s}{\delta I} \right|_{I=I_0+I_g} = 0 = \left. \frac{\delta L^s}{\delta I} \right|_{I=I_0}, \quad (19)$$

where $I = I_0 g$ and I_0 is the even function of x_\perp while g is the odd function. Here, the transverse coordinate we used is $-\infty < x_\perp < \infty$. Actually, this invariance means the condition $I_0 + I_g$ if $I_0 + I_g$ is also, like I_0 , the solution of Eq. (3). For the two different possible forms of the laser field, a_g and a_0 , we can analysis their relative stability from the variation of L^s :

$$\text{Re } L^s(a_g) = \text{Re } L^s(a_0) + \int dS * I_0 d\tau + dH^s, \quad (20)$$

$$\text{Im } L^s(a_g) = \text{Im } L^s(a_0) + \int c^2 \frac{k}{\omega^2} \partial_\xi I_g d\tau, \quad (21)$$

$$dS = S(\mu_0 + \mu_g) - S(\mu_0), \quad (22)$$

$$dH^s = H^s(I_0 + I_g) - H^s(I_0) = \int \{G_1 I_g^2 + G_2 (\nabla I_g)^2\} d\tau, \quad (23)$$

where $a_g = \sqrt{I_0 + I_g}e^{-i(\mu_0 + \mu_g)t}$, $a_0 = \sqrt{I_0}e^{-i\mu_0 t}$, μ_g is the space-independent frequency shift caused by I_g , and $d\tau$ is the volume unit of the region occupied by the laser field. Here, the variation of L^s comes from the variation of the intensity profile I_g and that of frequency μ_g . We discuss the two possible field forms, having slight variations of the intensity profile and frequency, hence, only low-order terms of I_g , μ_g are kept in $L^s(a_g) - L^s(a_0)$. As for background a_0 , its amplitude I_0 and frequency μ_0 satisfy Eqs. (3) and (4). The coefficients in the integral kernel of dH^s are

$$G_1 = -\frac{\omega_{p,0}^2}{2} (1 + I_0)^{-3/2} + c^2 \frac{\nabla^2 I_0}{2} \left(\frac{1}{I_0^2} - \frac{1}{(1 + I_0)^2} \right), \quad (24)$$

$$G_2 = c^2 \frac{1}{2} \left(\frac{1}{I_0} - \frac{1}{1 + I_0} \right). \quad (25)$$

Note that the higher-order terms have been neglected because I_g is small, and the odd-order terms are absent, since their spatial integrals are zero. For $I_g = I_0 g$ with transverse homogeneous g , there is

$$\partial_\xi I_g = I_0 \partial_\xi g + \partial_\xi I_0 * g; \quad \nabla_\perp I_g = \frac{\nabla_\perp I_0}{I_0} I_g, \quad (26)$$

and we substitute it into dH^s to achieve

$$dH^s = \int \left\{ \left[G_1 + G_2 \left(\frac{\nabla_{\perp} I_0}{I_0} \right)^2 \right] I_g^2 + G_2 (\partial_{\xi} I_g)^2 \right\} d\tau. \quad (27)$$

Since I_0 and μ_0 are related via Eq. (3), we consider backgrounds at different μ_0 , i.e., different frequency shifts relative to laser frequency ω in vacuum. We choose two types of focusing I_0 as the background. One, at the $U=0$ scenario in which the amplitude of the magnetic field at the transverse boundary of the laser field is zero or no collective charge current outside the laser pulse exists to effect the the laser field distribution, has the form $I_0 = y^4 + 2y^2$ with y^2 expressed as formula (14) at the $\mu_0 = -\frac{1}{2}\omega$ case. In this $\mu_0 = -\frac{1}{2}\omega$ case, the frequency of the laser field is shifted from ω due to the transverse intensity profile of the laser field. Since the intensity profile can cause the frequency shift, various different frequency shifts have their respective transverse profiles. Whether there exists an intensity profile corresponding to the zero-frequency shift case $\mu_0 = 0$ depends on the solubility of Eq. (3) at $\mu_0 = 0$. Because ω^2 is larger than $\omega_{p,e}^2$, one can find, from Eq. (3), that, unless intensity I can be negative, the intensity profile at $\mu_0 = 0$ is not a transverse uniform one with zero spatial gradient. The other, in the $U \neq 0$ scenario, is the numerical solution of Eq. (5) when the origin boundary condition is $\nabla I|_{x_{\perp}=0} = 0$ and μ_0 is chosen as zero. The effect of the difference between various backgrounds I_0 on g will be studied via a numerical experiment in the following paragraph.

The invariance of the variational equation, or Eq. (18), yields

$$0 = \frac{\delta dL^s}{\delta I_0} + \frac{\delta dL^s}{\delta I_g}. \quad (28)$$

It should be stressed that $\delta dL^s/\delta I_0$ is the even function, while $\delta dL^s/\delta I_g$ is the odd one. Thus, Eq. (28) has a solution only when

$$\frac{\delta dL^s}{\delta I_0} = 0, \quad \frac{\delta dL^s}{\delta I_g} = 0. \quad (29)$$

The first equality in this equation gives the relation between μ_g and I_g :

$$dS(\mu_0, \mu_g) = \frac{dH^s}{\int I_0 d\tau}, \quad (30)$$

and the second one reads

$$\int \left\{ G_2 \partial_{\xi}^2 I_g + \partial_{\xi} G_2 \partial_{\xi} I_g - \left[G_1 + G_2 \left(\frac{\nabla_{\perp} I_0}{I_0} \right)^2 \right] I_g \right\} dx_{\perp} = 0, \quad (31)$$

i.e., this is an equation of $g = I_g/I_0$:

$$T_2 \partial_{\xi}^2 g + T_1 \partial_{\xi} g + T_0 g = 0, \quad (32)$$

where three coefficients are dependent on the background profile I_0 ,

$$T_2 = \int [G_2 I_0] dx_{\perp},$$

$$T_1 = \int [2G_2 \partial_{\xi} I_0 + I_0 \partial_{\xi} G_2] dx_{\perp}, \quad (33)$$

$$T_0 = \int \left\{ G_2 \partial_{\xi\xi} I_0 + \partial_{\xi} G_2 \partial_{\xi} I_0 - \left[G_1 + G_2 I_0 \left(\frac{\nabla_{\perp} I_0}{I_0} \right)^2 \right] \right\} dx_{\perp}.$$

Obviously, $g(\xi) = 0$ is a trivial solution of Eq. (32) and meets the origin condition $\partial_{\xi} g = 0$, correspondingly, we obtain $dH^s|_{g(\xi)=0} = 0$. The nature of other nontrivial solutions depends on (T_2, T_1, T_0) , which are determined by background I_0 . For longitudinally homogeneous I_0 with $\partial_{\xi} I_0 = 0$, the three coefficients read

$$T_0 = \int \left[G_1 I_0 + G_2 \frac{(\nabla_{\perp} I_0)^2}{I_0} \right] dx_{\perp}, \quad (34)$$

$$T_1 = 0, \quad T_2 = \int G_2 I_0 dx_{\perp} > 0,$$

and the resulting analytic solutions are

$$g = \begin{cases} sh(\sqrt{|T_{20}|} \xi), & \text{if } T_{20} = T_0/T_2 < 0 \\ \sin(\sqrt{|T_{20}|} \xi), & \text{if } T_{20} = T_0/T_2 > 0 \end{cases}. \quad (35)$$

Hence, modulated structures can only exist for longitudinal homogeneous I_0 with $T_{20} > 0$ (i.e., $T_0 > 0$). From the expressions of T_0 and dH^s , we know that $T_0 > 0$ implies $G_1 + G_2[(\nabla_{\perp} I_0)^2/I_0^2]$, as well as dH^s , can possibly be negative. Since G_2 is always positive [see Eq. (25)], only G_1 , which depends on plasma density N_i and intensity gradient ∇I_0 , can lead to negative dH^s . Once nontrivial solutions of g with negative dH^s exist, the I_0 background is unstable, since other steady-state structures $I = I_0(1+g)$ have lower H^s than I_0 does.

C. Dynamic modulation

So far, we have studied the static modulation of the steady-state longitudinal uniform backgrounds. For those backgrounds, as shown in the Appendix, their phase θ meets $\partial_{\xi} \theta = -k$, $\nabla_{\perp} \theta = 0 = \partial_t \theta = \partial_{tt} \theta$ and, hence, the intensity profiles are time-independent $\partial_t I = 0$. Correspondingly, we can undertake a discussion on the basis of H expressed as Eq. (2), where $\partial_t I$ -dependent terms in the real part of the action, Re Ac [see Eq. (A19) in the Appendix], are absent. Now, we discuss the case of $\partial_{\xi} \theta = -k + q$, ($q \neq 0$) and $\nabla_{\perp} \theta = 0 = \partial_t \theta = \partial_{tt} \theta$. Nonzero phase gradient q implies the shift in the fundamental wave vector $-k$ as a result of the interaction. Using the continuity equation of a [see Eq. (A10) in the Appendix], we rewrite the $\partial_t I$ -dependent terms in Re Ac as

$$\frac{(\partial_t I)^2}{4I(1+I)} = c^2 \frac{q^2 c^2}{(\omega + \mu)^2} \frac{(\partial_{\xi} I)^2}{4I(1+I)}, \quad (36)$$

and substitute it into H and H^s ,

$$\tilde{H} = H - \int \left[c^2 \frac{q^2 c^2}{(\omega + \mu)^2} \frac{(\partial_\xi I)^2}{4I(1+I)} \right] d\tau, \quad (37)$$

$$\tilde{H}^s = H^s + \int \left[\frac{q^2 c^2}{4} I - c^2 \frac{q^2 c^2}{(\omega + \mu)^2} \frac{(\partial_\xi I)^2}{4I(1+I)} \right] d\tau. \quad (38)$$

For $q \neq 0$, the intensity profile can still possibly be time-independent $\partial_\xi I = 0$ if its longitudinal gradient $\partial_\xi I = 0$. Those $q \neq 0$ steady states have not been included in our previous discussion. Now, we study them in the parallel approaches adopted previously with some slight changes: H^s is now replaced by \tilde{H}^s , and the model equation becomes

$$\begin{aligned} \frac{[S(\mu) + \omega^2]}{c^2} = & \frac{q^2 c^2}{4} + \left(-\frac{2}{4} \frac{\nabla_\perp^2 I}{I+I^2} + \frac{1}{4} (\nabla_\perp I)^2 \frac{2I+1}{(I+I^2)^2} \right) \\ & + \frac{1}{4} \left(1 - \frac{q^2 c^2}{(\omega + \mu)^2} \right) \left(-\frac{2}{4} \frac{\partial_\xi^2 I}{I+I^2} \right. \\ & \left. + \frac{1}{4} (\partial_\xi I)^2 \frac{2I+1}{(I+I^2)^2} \right) + \frac{\omega_{p,0}^2}{c^2} \frac{1}{\sqrt{1+I}}. \end{aligned} \quad (39)$$

Obviously, \tilde{H}^s and the model equation return to H^s and Eq. (3) as $q = 0$.

Comparing H^s with \tilde{H}^s , we find that they have different dependence on the $\partial_\xi I$ -dependent terms and the I -dependent ones. This difference leads to the resulting coefficient of $d\tilde{H}^s$: $\tilde{G}_2 = \{1 - [q^2 c^2 / (\omega + \mu)^2]\} G_2 / = G_2$, while $\tilde{G}_1 = G_1 d\tilde{H}^s$ now reads

$$d\tilde{H}^s = \int \left\{ \left[G_1 + \tilde{G}_2 \left(\frac{\nabla_\perp I_0}{I_0} \right)^2 \right] I_g^2 + \tilde{G}_2 (\partial_\xi I_g)^2 \right\} d\tau. \quad (40)$$

Furthermore, the variation of \tilde{G}_2 will cause \tilde{T}_2 and of \tilde{T}_{02} . Hence, for the $q \neq 0$ steady-state background, the existence and the stability of the modulated structures should be carefully considered. For $q \neq 0$, the continuity equation implies that once the structures become modulated ($\partial_\xi I \neq 0$), the modulation is not time independent. Hence, we term the modulation in this case a dynamic one.

III. NUMERICAL RESULTS AND DISCUSSION

In the following numerical calculation, we put field the vector potential a in units of Compton potential e^2/m^2c^2 , the length in units of the laser wavelength in microns λ , and the ion density N_i in units of the critical density $m_{0,e}\omega^2/4\pi e^2$. The laser frequency is taken as 1. In particular, our calculation is toward the strong field limit $I = |a|^2 > 1$.

We solve Eq. (5) to obtain a longitudinally uniform focusing background I_0 in the $U \neq 0$ scenario. We seek the solution of the form $I = \sum_{i=0}^{\infty} \beta_i x_\perp^{2i}$ and coefficients β_i are calculated one by one. The calculation results show that the absolute value of those β_i decrease with rising i and their signs change alternatively. These ensure the convergence of the solution at $|x_\perp| = \infty$. Moreover, the calculated coefficients show $|\beta_{i+1}/\beta_i|$ to be almost constant. Thus, for simplicity, we fit I to a general form $a/(1 + |b|x_\perp^2)$. Some typical results with the above features are plotted in Fig. 1. Then, we

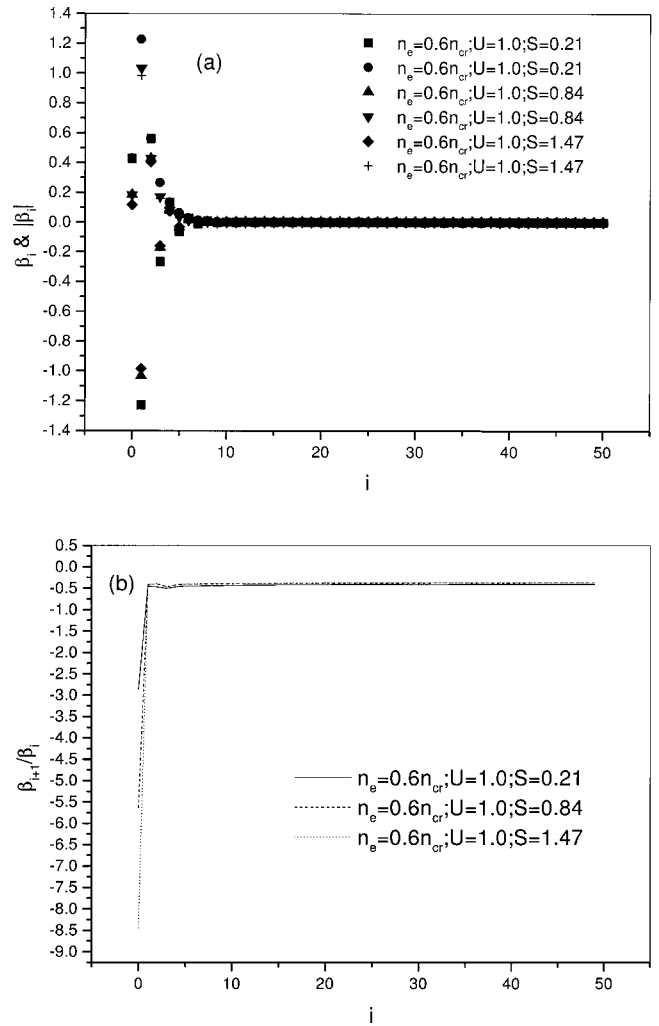


FIG. 1. (a) β_i at $U \neq 0$. (b) Corresponding β_{i+1}/β_i .

calculate Eq. (32) with two different backgrounds: I_0 at $U \neq 0$ and I_0 at $U = 0$. Here, ion density N_i is from $\frac{1}{4}\omega^2$ to ω^2 and μ_0 is chosen as $-\frac{1}{2}\omega$ and 0 for $U = 0$ and $U \neq 0$, respectively. $T_{20} = T_0/T_2$ [see Eq. (33)] at the different values of ion density N_i are given in Fig. 2. For the parameter regime we used, T_{20} in both these two scenarios are negative and, hence, the resulting $g(\xi)$ are not sinusoidal. This result reveals the nature of the background, which has a close relation to the static longitudinal modulation. For the focusing background, it is unfavorable for growing the static modulated distortion, since even though t_0 is positive near the axis region, negative t_0 in other regions makes the integral $T_0 = \int t_0 dx_\perp$ negative, where t_0 is the integral kernel in the definition of T_0 [see Eq. (33)]. Hence, the variation of the two controllable parameters: plasma density N_i and laser power $P = \int I dx_\perp$, and that of boundary condition U , do not influence the result that the static modulation is depressed.

Contrarily, for the transverse homogeneous structure $I = I(x_\perp = 0)(|x_\perp| < P/I_0)$, its $G_1 = -(\omega_{p,0}^2/2)[1 + I(x_\perp = 0)]^{-3/2} < 0$, $G_2 = 0$ and relevant $T_0 = -\int G_1 I dx_\perp > 0$, thus its T_{20} is positive and the resulting sinusoidal modulations exist. The stability of those sinusoidal modulations depends on whether their dH^s are lower than that of the longitudinally

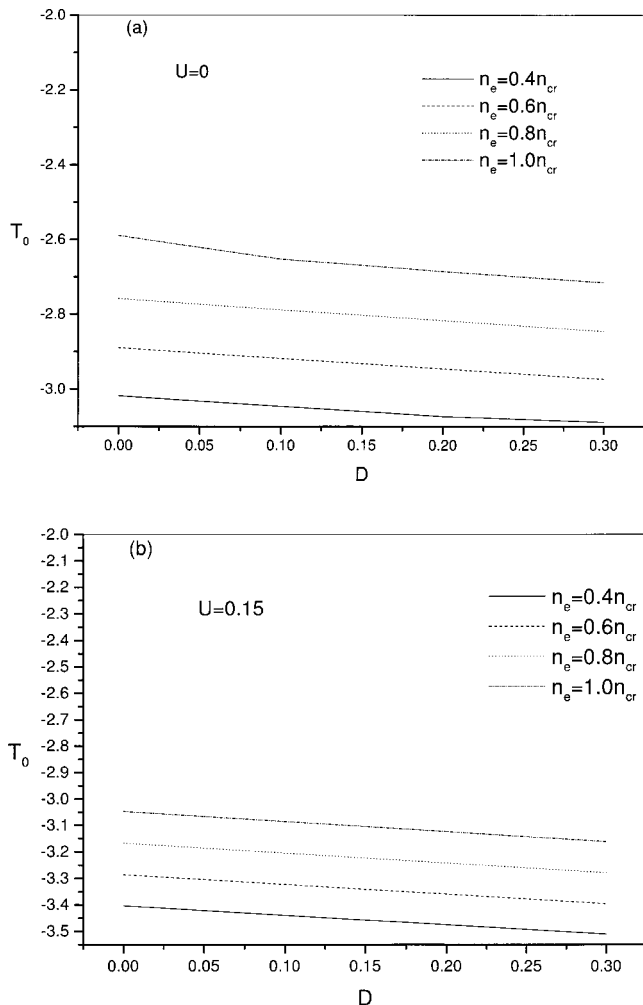


FIG. 2. T_0 vs D at various parameters, where $D = \bar{s} - (q^2 c^2 / 4)$. (a) and (b) correspond to different boundary condition U , respectively.

uniform background structure ($dH^s = 0$). Due to $G_1 < 0$, it is possible that dH^s is negative for some g . In other words, longitudinally static modulation can occur in the nonfocusing beam within the near-critical plasma with density $0.25 < N_i < 1$.

Then, we solve Eq. (39) to seek the $q \neq 0$ longitudinally uniform focusing background and follow a parallel procedure to discuss the dynamic modulation. Relevant T_{20} for different parameters are plotted in Fig. 3(a). Comparing these results with previous results, we find that $q \neq 0$ causes the essential change. For any possible field form, we introduce a quantity $D = (\mu + \omega)^2 - (q^2 c^2 / 4)$, which depends on the phase of the field form and specifies the corresponding intensity profile. We know, from previous theory, that the intensity profiles depend on the space gradient and time gradient of the phase, q and μ . Therefore, with the D parameter varying, the intensity profile changes correspondingly. In some special parameter regime [$D = \bar{s} - (q^2 c^2 / 4) \sim 0$], as shown in Fig. 3(a), T_{20} is positive and suggests the existence of dynamic modulation. The reason for positive T_{20} is that T_2 can become negative at high q . Then, the Hamiltonian values for those negative T_{20} are calculated to determine the stability of the modulation. The calculation results, which are

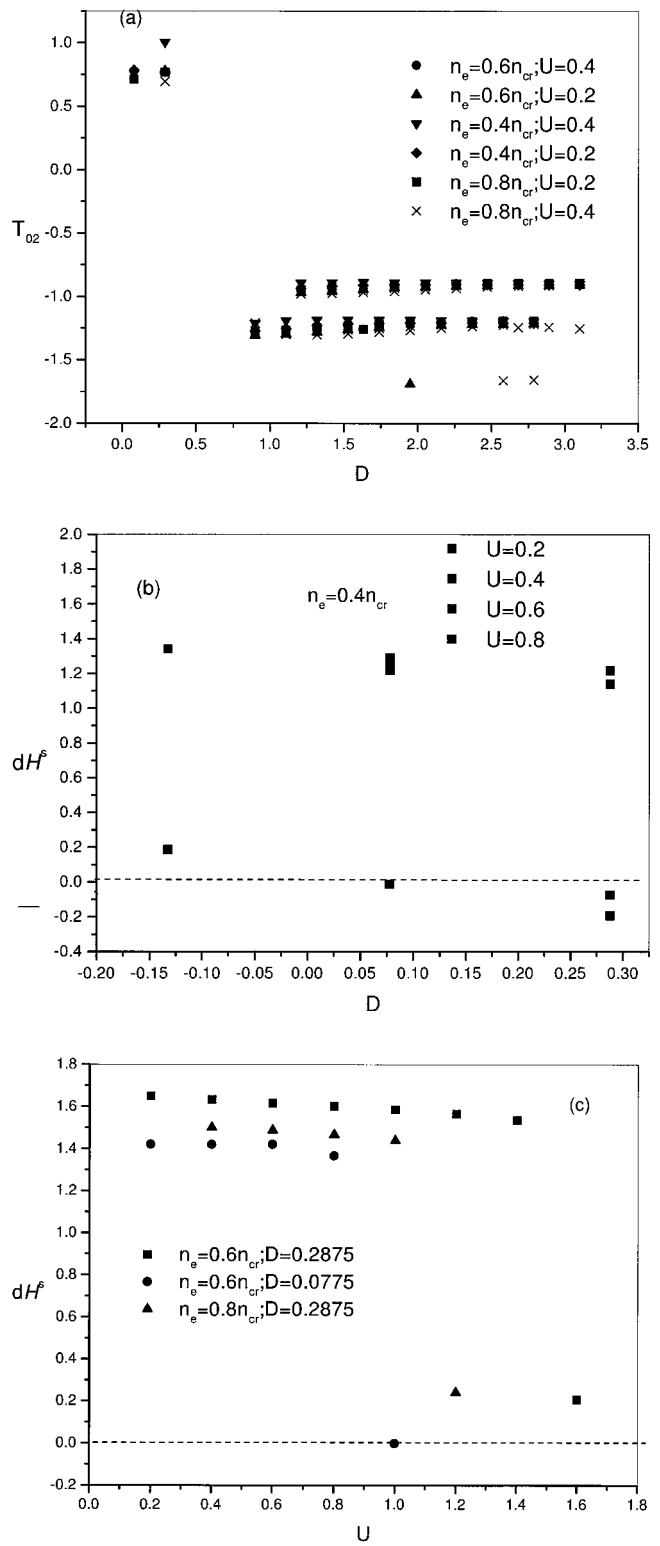


FIG. 3. (a) T_{20} vs D at $q \neq 0$. (b) dH^s vs D at $q \neq 0$. (c) dH^s vs U at $q \neq 0$.

plotted in Figs. 3(b) and 3(c), show that, in some narrow parameter regimes which are represented by dots under the horizontal line, profiles with dynamic modulation are more stable than background I_0 . Hence, for some steady-state longitudinally uniform profiles, whether they are stable relative to the longitudinal modulation is determined by their space-

gradient of field phase q , and other parameters: plasma density N_i , frequency-shift μ_0 , and boundary condition U , have less effect on their stability.

IV. SUMMARY

So far, we have presented a theoretical investigation on the self-modulation of the intense laser beam in the near-critical plasma, in which the self-modulation is understood from the viewpoint of the structure stability. In contrast with some published works on this issue, for example, Ref. 5, which start from a set of fluid equations and are focused in the weak field limit $|a| \ll 1$ and tenuous plasma with $N_i \leq 0.25$, we construct our theory on the basis of a nonlinear Schrödinger equation of laser vector potential a and focus our investigation on the strong field limit $a \geq 1$ and the near-critical plasma with $0.25 \leq N_i \leq 1$. Especially, we take the transverse structure into account and regard the longitudinally homogeneous self-focusing structure as a reference, then we further study its stability relative to the longitudinally modulated structures by comparing their Hamiltonian values. In some published works,⁵ the effect of the transverse profile on the evolution of the longitudinal modulation is numerically studied in the weak field limit and tenuous plasma. In these works,⁵ the self-modulation, however, arises from the modulation in the refractive index due to the plasma wave, which is induced by the rising edge of the pulse and propagates in the following pulse body. Here, we consider this effect in view of the structure stability of the pulse body. Furthermore, we confine our consideration to the strong field limit and near-critical plasma.

Our calculations indicate that the details of the reference structures have a close relation to the existence of the modulated structure. Here, the details refer to four parameters: plasma density N_i , boundary condition U , frequency-shift μ_0 and the space gradient of field phase q . For the parameter regime we used, there exist no longitudinally static-modulated solutions of the steady-state structure equation and, hence, the occurrence of longitudinally static modulation is excluded, while dynamic modulation can exist and be more stable than some backgrounds in some parameter regimes. The result reveals that, among these four parameters, q or the longitudinal gradient of the phase of the background vector potential, has the closest relation to the structure stability of the background profiles.

In short, we have discussed, in the strong field limit, the occurrence of spontaneous modulation due to the structure stability of the pulse. This mechanism can be taken as a complement to the pulse-head mechanism to increase our knowledge of self-modulation.

In addition, we note the recent published work by Duda *et al.*⁸ dealing with the hosing instability of a laser beam in tenuous plasma. Despite the difference in our respective investigation subjects, the kernel part of the theory in this paper has some similarities with that in the work of Duda *et al.* These two works both adopt a variational principle method to deal with the intensity instability and derive a set of motion equations describing the intensity fluctuation around some reference intensity profiles. The intensity fluctuations

are discussed in the framework of these motion equations, which depend on the nature of the reference intensity profile. The most marked difference between these two works is that in this paper, the reference intensity profiles are numerically solved from the structure equation, whereas in the work by Duda *et al.*, they are not obtained numerically. Since the derived motion equations of the intensity fluctuations are greatly dependent on the nature of the reference intensity profile, in order to make the discussion of the intensity fluctuation more believable, it is necessary to obtain the reference profile from the structure equation.

ACKNOWLEDGMENTS

We thank Dr. Cheng Tai Wang for constructive discussions.

This work is supported by the National Natural Science Foundation of China.

APPENDIX

We view a pulse as a moving 3D region occupied by radiation. For laboratory longitudinal-coordinate z , there is a pulse center longitudinal-coordinate z_0 and an intrapulse longitudinal-coordinate ξ meeting, $z = z_0 + \xi$; ($-l < \xi < l$) and $\partial_{zz} = \frac{1}{4}[\partial_{\xi\xi} + 2\partial_{\xi z_0} + 2\partial_{z_0 z_0}]$, where $2l$ is the longitudinal length of the pulse and is less than the plasma thickness.

Wave equations of the vector potential of radiation field A_\perp and scalar potential ϕ are written as

$$\left[\nabla_\perp^2 + \frac{1}{4}(\partial_{\xi\xi} + 2\partial_{\xi z_0} + \partial_{z_0 z_0}) - \frac{1}{c^2}\partial_{tt} \right] A_\perp = -\frac{4\pi}{c} j_\perp, \quad (A1)$$

$$\left[\nabla_\perp^2 + \frac{1}{4}(\partial_{\xi\xi} + 2\partial_{\xi z_0} + \partial_{z_0 z_0}) - \frac{1}{c^2}\partial_{tt} \right] \phi = -4\pi\rho, \quad (A2)$$

where $j = eN_i v_i - en_e v_e \sim -en_e v_e$ and $\rho = eN_i - en_e$. From the motion equation of electron

$$d_t p_e = -e \left(-\nabla \phi - \frac{1}{c} \partial_t A + \frac{v_e}{c} \times \nabla \times A \right), \quad (A3)$$

where $p_e = \gamma m_{e,0} v_e$ and $\gamma = \sqrt{1 + (p_\perp/m_{e,0}c)^2}/\sqrt{1 - (v_z/c)^2}$ is the relativistic factor, v_z is the speed of the longitudinal quasistatic electronic current and $A = A_\perp$ represents the vector potential of the laser field. One can find that as

$$-e\phi + m_{e,0}c^2\gamma = \text{const}, \quad \nabla \cdot v_z = 0, \quad (A4)$$

there is

$$p_\perp = eA_\perp, \quad p_z = \gamma m_{e,0} v_z, \quad d_t v_z = 0, \quad (A5)$$

and time-averaged γ [over $(2\omega_0)^{-1}$] meets

$$\gamma = \gamma_\perp \gamma_z = \sqrt{1 + \left(\frac{e|A_\perp|}{m_{e,0}c^2} \right)^2} / \sqrt{1 - (v_z/c)^2}. \quad (A6)$$

For convenience, we choose the energy constant as zero. Thus, the effect of the longitudinal quasistatic current is represented by $\gamma_z = [\sqrt{1 - (v_z/c)^2}]^{-1}$. For an ultraintense laser pulse with dimensionless vector potential $e|A_\perp|/m_{e,0}c^2 \sim 1$ or $e|A_\perp|/m_{e,0}c^2 > 1$, the perturbation expanding of the elec-

tronic momentum about the vector potential^{4,6} is improper and, therefore, we choose a cut: let $p = eA$. Similarly, the linear-dependent part of electrostatic potential ϕ on A is also zero. Thus, for the second-order perturbation $(\delta v_2, \delta n_2)$, there are

$$\begin{aligned} \partial_t \delta v_2 &= \frac{|e|}{m} \nabla (\delta \phi_2 + \phi_L), \\ \partial_t \delta n_2 + n_0 \nabla^* \delta v_2 &= 0, \\ \nabla^2 \delta \phi_2 &= 4\pi |e| \delta n_2, \end{aligned} \quad (\text{A7})$$

$\phi_L \sim$ quiver energy.

Obviously, as $\delta \phi_2 = -\phi_L$ holds everywhere, there are $\delta v_2 = 0$ and temporal-independent $\delta n_2, \delta \phi_2$ meeting those equations if ϕ_L is temporal independent. For a pulse head with $\partial_\xi \phi_L \neq 0$, the local electrostatic potential yields the relevant charge separation force $\partial_\xi \phi = \partial_\xi \delta \phi_2$ to cancel this laser pressure. We, therefore, term the equilibrium $(p, \delta n_e) = (eA, \nabla^2 \phi_L)$ as a first-order response of the plasma, and any derivation from this equilibrium as higher order.

We cast our model to the pulse frame by expressing vector potential A_\perp as the product of a rapid temporarily oscillating $\exp i(kz_0 - \omega t)$ and a temporarily slowly varying a :

$$A_\perp = e^\perp [a(x, y, \xi; t) \exp i(k^* z_0 - \omega t) + cc], \quad (\text{A8})$$

$$k = \frac{\omega}{c} \sqrt{1 - \omega_{p,0}^2/\omega^2},$$

where $\omega_{p,0}^2 = 4\pi e^2 N_0 / m_{e,0}$ and ω is the laser frequency in vacuum, $N_0 = N_e = N_i$ is the electronic or ionic mean density, and $m_{e,0}$ is the rest mass of electrons. The vector potential in this form yields a Z_0 -independent field distribution $|A|^2$, like the results of a paraxial approximation in which the field amplitude is weakly dependent on the longitudinal coordinate. Here, we have hypothesized that, when electromagnetic energy is conserved, the global moving of the pulse in the homogeneous plasma does not lead to a change of its structure. Hence, $|A|$ does not explicitly depend on pulse center coordinate Z_0 , i.e., $\partial_{Z_0} |A| = 0$. Slowly varying vector potential a meets

$$\begin{aligned} i \partial_t a &= -\frac{1}{2\omega} * \left(c^2 \nabla_\perp^2 a + \frac{c^2}{4} \partial_{\xi\xi} a - \partial_{tt} a \right) \\ &\quad - \frac{1}{4} \frac{ikc^2}{\omega} \partial_\xi a + \frac{1}{2\omega} V(a) a, \\ V &= \frac{\omega_{p,0}^2}{\gamma} - \omega^2 + \frac{1}{4} k^2 c^2 \\ &\quad + \left[\frac{c^2 \nabla_\perp^2 \gamma - \partial_{tt} \gamma + \frac{c^2}{4} (\partial_{z_0 z_0} \gamma + 2\partial_{z_0} \partial_\xi \gamma + \partial_\xi \gamma)}{\gamma} \right]. \end{aligned} \quad (\text{A9})$$

Moreover, there is the continuity equation of $I = |a|^2$:

$$\begin{aligned} \partial_t I &= \frac{1}{\omega - \partial_t \theta} \left[\left(\partial_{tt} \theta - c^2 \nabla_\perp^2 \theta - \frac{c^2}{4} \partial_{\xi\xi} \theta \right) I - c^2 \nabla_\perp \theta \nabla_\perp I \right. \\ &\quad \left. - \frac{c^2}{4} \partial_\xi \theta \partial_\xi I - \frac{kc^2}{4} \partial_\xi I \right], \end{aligned} \quad (\text{A10})$$

where $I = |a|^2 > 0$, θ is the phase of a . I and θ are both real. Considering $W(I, \nabla I, \nabla^2 I, \partial_t I, \partial_{tt} I)$, which meets

$$Va = \frac{\delta W}{\delta a^*} = \frac{\delta W}{\delta I} a, \quad (\text{A11})$$

this equality leads to

$$\begin{aligned} V &= \frac{\partial W}{\partial I} - \nabla_\perp \frac{\partial W}{\partial \nabla_\perp I} + \nabla_\perp^2 \frac{\partial W}{\partial \nabla_\perp^2 I} - \partial_\xi \frac{\partial W}{\partial \partial_{xi} I} + \partial_{\xi\xi} \frac{\partial W}{\partial \partial_{\xi\xi} I} \\ &\quad - \partial_t \frac{\partial W}{\partial \partial_t I} + \partial_{tt} \frac{\partial W}{\partial \partial_{tt} I}. \end{aligned} \quad (\text{A12})$$

We compare V in this form with its previous form

$$\begin{aligned} V &= \frac{\omega_{p,0}^2}{(1+I)^{1/2}} - \omega^2 + \frac{1}{4} k^2 c^2 + c^2 \frac{\nabla_\perp^2 I}{2(1+I)} \\ &\quad - c^2 \frac{(\nabla_\perp I)^2}{4(1+I)^2} + \frac{c^2}{4} \left(\frac{\partial_\xi^2 I}{2(1+I)} - \frac{(\partial_\xi I)^2}{4(1+I)^2} \right) \\ &\quad - \left(\frac{\partial_{tt} I}{2(1+I)} - \frac{(\partial_t I)^2}{4(1+I)^2} \right), \end{aligned} \quad (\text{A13})$$

where the ∂_{z_0} γ -dependent term has been dropped due to the approximation $\partial_{z_0} I \sim 0$. From the comparison, we know W must have the following form:

$$\begin{aligned} W(V) &= F(I) + M(I) * [c^2 (\nabla_\perp I)^2 + c^2 \frac{1}{4} (\partial_\xi I)^2 - (\partial_t I)^2] \\ &\quad + G(I) * [c^2 \nabla_\perp^2 I + c^2 \frac{1}{4} \partial_\xi^2 I - \partial_{tt} I]. \end{aligned} \quad (\text{A14})$$

Otherwise, if $M = M(I, \nabla I)$, there will exist a term like $\nabla^2 I \nabla I$, which is not included in V . Thus, there are

$$\begin{aligned} \frac{\partial F}{\partial I} &= \frac{\omega_{p,0}^2}{(1+I)^{1/2}} - \omega^2 + \frac{k^2 c^2}{4}, \\ \frac{\partial G}{\partial I} - M &= \frac{1}{4(1+I)}, \\ \frac{\partial^2 G}{\partial I^2} - \frac{\partial M}{\partial I} &= \frac{-1}{4(1+I)^2}, \end{aligned} \quad (\text{A15})$$

and

$$\begin{aligned} F &= \omega_{p,0}^2 * 2\sqrt{1+I} - \omega^2 * I + \frac{k^2 c^2}{4} * I, \\ \frac{\partial G}{\partial I} - M &= \frac{1}{4(1+I)}, \\ \frac{\partial G}{\partial I} &= \lambda \frac{1}{4(1+I)}, \quad M = (\lambda - 1) \frac{1}{4(1+I)}. \end{aligned} \quad (\text{A16})$$

It is easy to find

$$W = 2\omega_{p,0}^2(1+I)^{1/2} - \omega^2 I + \frac{k^2 c^2}{4} I$$

$$- \frac{c^2 (\nabla_\perp I)^2 + \frac{c^2}{4} (\partial_\xi I)^2 - (\partial_t I)^2}{4(1+I)}$$

$$+ \lambda * \left\{ c^2 \nabla_\perp \left[\frac{1}{4} \ln(1+I) \nabla_\perp I \right] \right.$$

$$\left. + \frac{c^2}{4} \partial_\xi \left[\frac{1}{4} \ln(1+I) \partial_\xi I \right] + \partial_t \left[\frac{1}{4} \ln(1+I) \partial_t I \right] \right\}, \quad (A17)$$

where λ is constant. Since I is zero at the pulse boundary, there is

$$\int W d\tau = \int \left[2\omega_{p,0}^2(1+I)^{1/2} - \omega^2 I + \frac{k^2 c^2}{4} I \right.$$

$$\left. - \frac{c^2 (\nabla_\perp I)^2 + (c^2/4) (\partial_\xi I)^2 - (\partial_t I)^2}{4(1+I)} \right] d\tau. \quad (A18)$$

Now, we write out Action and Hamiltonian, where Re Ac and Im Ac represent the real and imaginary parts of Action, respectively,

$$\text{Action} = \int \left\{ a^* i \partial_t a + i c^2 \frac{k}{4\omega} a^* \partial_\xi a + \frac{1}{2\omega} * \left[\partial_t a^* \partial_t a \right. \right.$$

$$\left. \left. - c^2 \nabla_\perp a^* \nabla_\perp a - \frac{c^2}{4} \partial_\xi a^* \partial_\xi a \right] - \frac{1}{2\omega} W \right\} d\tau dt$$

$$= \text{Im Ac} + \text{Re Ac}, \quad (A19)$$

$$\text{Im Ac} = \int \left[i \frac{1}{2} \partial_t I + i c^2 \frac{k}{8\omega} \partial_\xi I \right] d\tau dt,$$

$$\text{Re Ac} = \int \left\{ \int \left[I \left(\frac{1}{2\omega} (\partial_t \theta)^2 - \partial_t \theta \right) \right. \right.$$

$$\left. \left. + \frac{1}{2\omega} \frac{(\partial_t I)^2}{4I(1+I)} \right] d\tau - H \right\} dt,$$

$$H = \frac{1}{2\omega} \int \left\{ \frac{k \partial_\xi \theta}{2} I c^2 + (\nabla_\perp \theta)^2 I c^2 + \frac{1}{4} (\partial_\xi \theta)^2 I c^2 \right.$$

$$+ \frac{k^2 c^2}{4} I + 2\omega_{p,0}^2 \sqrt{1+I} - \omega^2 I + \frac{(\nabla_\perp I)^2}{4I(1+I)} c^2$$

$$\left. + \frac{1}{4} \frac{(\partial_\xi I)^2}{4I(1+I)} c^2 \right\} d\tau.$$

It should be noted that the Hamiltonian does not contain terms explicitly dependent on $\partial_t I$.

Since the first-order response of the plasma is related to the steady structure ($\partial_t I = 0$), we confine our investigation to the steady structure. As θ meets

$$\nabla_\perp \theta = 0, \quad \partial_\xi \theta = -k, \quad (A20)$$

$$\partial_t \theta = -\mu, \quad \partial_{tt} \theta = 0,$$

where μ is time independent, the continuity equation indicates $\partial_t I = 0$. There is

$$\text{Action} \rightarrow \text{Act}^s = \int L^s dt,$$

$$\text{Im } L^s = \int c^2 \frac{k}{2\omega} \partial_\xi I d\tau = 0,$$

$$\text{Re } L^s = \frac{1}{2\omega} \int S(\mu) * I d\tau - H^s, \quad (A21)$$

$$S(\mu) = 2\omega\mu + \mu^2,$$

$$H^s = \frac{1}{2\omega} \int \left[2\omega_{p,0}^2 \sqrt{1+I} - \omega^2 I + \frac{(\nabla_\perp I)^2}{4I(1+I)} c^2 \right.$$

$$\left. + \frac{1}{4} \frac{(\partial_\xi I)^2}{4I(1+I)} c^2 \right] d\tau,$$

where the upper-index s denotes the steady state. Since we are interested in an ultraintense laser beam with dimensionless intensity $I > 1$, we do not intend to make some simplification in the model Hamiltonian, and the resulting equation as a weak-relativistic limit case where the relativistic factor γ is expanded to the low order of I .

The variation principle $\delta \text{Act}^s / \delta I = 0$ yields the steady structure equation

$$[S(\mu) + \omega^2]/c^2 = \left(-\frac{2}{4} \frac{\nabla_\perp^2 I}{I+I^2} + \frac{1}{4} (\nabla_\perp I)^2 \frac{2I+1}{(I+I^2)^2} \right)$$

$$+ \frac{1}{4} \left(-\frac{2}{4} \frac{\partial_\xi^2 I}{I+I^2} + \frac{1}{4} (\partial_\xi I)^2 \frac{2I+1}{(I+I^2)^2} \right)$$

$$+ \frac{\omega_{p,0}^2}{c^2} \frac{1}{\sqrt{1+I}}, \quad (A22)$$

μ can be taken as the frequency shift associated with the structure. In addition, there are $|r| = \sqrt{x^2 + y^2} \rightarrow \infty$ and $\xi = \pm\infty$ boundary conditions

$$I(|r|=\infty) = 0, \quad \nabla_\perp I|_{|r|=\infty} = 0, \quad (A23)$$

$$I(|\xi|=\pm\infty) = 0, \quad \partial_\xi I|_{|\xi|=\pm\infty} = 0,$$

and the positivity requirement on solution $I > 0$. Furthermore, as the total photon number $M = \int I d\tau = \int P(\xi) d\xi$ is given, where $P(\xi)$ is the laser flux or power through the transverse section located at ξ , H^s is determined by the solution of Eq. (A22).

¹D. Strickland and G. Mourou, Opt. Commun. **56**, 219 (1985); G. Mourou and D. Umstadter, Phys. Fluids B **4**, 2315 (1992); M. D. Perry and G. Mourou, Science **64**, 917 (1994); P. Sprangle, E. Esarey, and A. Ting, Phys. Rev. Lett. **64**, 2011 (1990); Phys. Rev. A **41**, 4463 (1990); A. Ting, E. Esarey, and P. Sprangle, Phys. Fluids B **2**, 1390 (1990).

²G. Z. Sun, E. Ott, Y. C. Lee, and P. Guzdar, Phys. Fluids **30**, 526 (1987); T. Kurki-Suonio, P. J. Morrison, and T. Tajima, Phys. Rev. A **40**, 3230 (1989); A. B. Borisov, A. V. Borovskiy, O. B. Shiryaev, V. V. Korobkin, A. M. Prokhorov, J. C. Solem, T. S. Luk, K. Boyer, and C. K. Rhodes, *ibid.* **45**, 5830 (1992); X. L. Chen and R. N. Sudan, Phys. Fluids B **5**, 1336 (1993); X. L. Chen and R. N. Sudan, Phys. Rev. Lett. **70**, 2082 (1993); G. Schmidt and W. Horton, Comments Plasma Phys. Control. Fusion **9**, 85 (1985).

³F. Vidal and T. W. Johnston, Phys. Rev. Lett. **77**, 1282 (1996).

- ⁴T. Tajima and J. M. Dawson, Phys. Rev. Lett. **43**, 263 (1979); V. N. Tsytovich, U. DeAngelis, and R. Bingham, Comments Plasma Phys. Control. Fusion **12**, 249 (1989); E. Esarey and P. Sprangle, IEEE Trans. Plasma Sci. **24**, 252 (1996); E. Esarey, A. Ting, P. Sprangle, and G. Joyce, Comments Plasma Phys. Control. Fusion **12**, 191 (1989); E. Esarey, J. Krall, and P. Sprangle, Phys. Rev. Lett. **72**, 2887 (1994).
- ⁵P. Sprangle, E. Esarey, J. Krall, and G. Joyce, Phys. Rev. Lett. **69**, 2200 (1992); T. M. Antonsen and P. Mora, *ibid.* **69**, 2204 (1992); E. Esarey, P. Sprangle, J. Krall, A. Ting, and G. Joyce, Phys. Fluids B **5**, 2690 (1993).
- ⁶P. Sprangle, E. Esarey, and A. Ting, Phys. Rev. Lett. **64**, 2011 (1990); Phys. Rev. A **41**, 4463 (1990); A. Ting, E. Esarey, and P. Sprangle, Phys. Fluids B **2**, 1390 (1990).
- ⁷W. B. Mori, C. D. Decker, D. E. Hinkel, and T. Katsouleas, Phys. Rev. Lett. **72**, 1482 (1994); S. C. Wilks, W. L. Kruer, E. A. Williams, P. Amendt, and D. E. Eder, Phys. Plasmas **2**, 274 (1995); C. D. Decker, W. B. Mori, T. Katsouleas, and D. E. Hinkel, *ibid.* **3**, 1360 (1996).
- ⁸B. J. Duda, R. G. Hemker, K. C. Tzeng, and W. B. Mori, Phys. Rev. Lett. **83**, 1978 (1999); B. J. Duda and W. B. Mori, Phys. Rev. E **61**, 1925 (2000).

Experimental study of a subpicosecond pulse laser interacting with metallic and dielectric targets

L. M. Chen,^{1,2} J. Zhang,^{1,*} H. Teng,¹ Q. L. Dong,¹ Z. L. Chen,¹ T. J. Liang,¹ L. Z. Zhao,¹ and Z. Y. Wei¹

¹Laboratory of Optical Physics, Institute of Physics, Chinese Academy of Sciences, Beijing 100080, China

²Laboratory for Laser Fusion, Institute of Nuclear Physics and Chemistry, Mianyang 621900, China

(Received 14 August 2000; published 27 February 2001)

We have studied laser absorption, hot electron emission, and the energy spectrum of hot electrons produced during the interaction of a 150 fs, 5 mJ, 800 nm *p*-polarized laser pulse at $8 \times 10^{15} \text{ W/cm}^2$ with metallic and dielectric target materials. Because dielectric targets are much less conductive, the charge separation potential in dielectric targets is higher than that of metallic targets. This leads to a smaller laser absorption, fewer emitted electrons, and a lower hot electron temperature in dielectric than in metallic targets.

DOI: 10.1103/PhysRevE.63.036403

PACS number(s): 52.50.Jm, 52.40.-w, 52.25.Os, 52.38.-r

I. INTRODUCTION

The recent availability of intense ultrashort subpicosecond laser pulses [1] has enabled investigation of a new regime of laser-matter interaction in which intense laser pulses are deposited into a solid target faster than the target surface can hydrodynamically expand [2]. Thus, using high power laser systems of table-top size, it is now possible to study interaction physics under extreme conditions in relation to the fast ignition scheme for inertial confinement fusion [3], harmonic generation [4,5], and ultrashort x-ray generation [6], etc.

Previous measurements [7] of absorption of high contrast laser pulses have shown that at low laser intensities inverse bremsstrahlung (IB) is the main absorption mechanism and it is dependent on the electrical conductivity associated with an electron mean free path comparable to the interatomic spacing. However, at high intensities exceeding $3 \times 10^{15} \text{ W/cm}^2$, the absorption reaches “resistivity saturation” at a low level of 10% and becomes essentially independent of the target material. This behavior was attributed to the generation of a highly reflecting overdense plasma layer caused by rapid ionization of a thin front layer of the target. It seems that the plasma properties should be independent of the target material. However, Saemann and Eidmann [8] reported that the total x-ray emission from Al targets is much higher than that from glass targets with x-ray photons in the range of 1–20 keV. This implies that there are still many material dependent aspects in intense-laser–matter interactions. In particular, for laser pulses incident obliquely on targets, Brunel [9] and Gibbon and Bell [10] proposed that *p*-polarized laser pulses could be strongly absorbed by pulling electrons into vacuum during an optical cycle and then returning them to the surface with approximately the quiver velocity. This is called the “vacuum heating” (VH) mechanism [9].

In this paper, we report a systematic study of the laser absorption and hot electron emission from aluminum and glass targets (with a similar average *Z*) irradiated by intense ultrashort laser pulses with sufficiently high contrast such that the surface expansion is no greater than the peak amplitude of electron quiver motion during the interaction. We

found that the total number of hot electrons with energies over 7 keV from aluminum targets was considerably more than that from glass targets. The charge separation potential we measured was greater than the prediction of Yang *et al.* [11,12], and in metallic targets this potential was found to be lower than that of dielectric targets because the free electrons partly “neutralize” the potential.

II. EXPERIMENTAL SETUP

The experiments were carried out at the Laboratory of Optical Physics of the Institute of Physics with a Ti:sapphire chirped pulse amplification (CPA) laser system operating at around 800 nm at a repetition rate of 10 Hz. The laser delivered 5 mJ energy in 150 fs pulses and produced a peak intensity on the target of $8 \times 10^{15} \text{ W/cm}^2$ at a laser focus of 20 μm diameter. The contrast ratio was approximately 10^{-5} at 1 ps before the peak of the pulse. The targets we used were 2 mm thick Al and glass plate targets. The roughness of the surface was less than 1 μm . The mount was controlled by microstep motors in the *xyz* dimensions to ensure that the laser interacted with fresh target surface at each shot.

The main diagnostic of fast electrons was a magnetic spectrometer, fitted with a permanent magnetic field of $B = 380 \text{ G}$. An array of LiF thermoluminescent dosimeter (TLDs) detectors was used behind the spectrometer to detect hot electrons. The recent development of ultrasensitive LiF TLDs provides the possibility of using thin TLDs for hot electron detection [13]. The energy range of this instrument covered from 7 to 500 keV. The collection angle of the spectrometer was on the order of $1 \times 10^{-3} \text{ sr}$. Its energy resolution was better than 2%. Because the TLDs are insensitive to visible light, it was not necessary to use aluminum foils in front of the TLDs. The background of these TLDs was less than 1.2 μGy when they were heated to 240 °C.

The metallic target potential used to diagnose the total number of electrons emitted in each shot was measured directly by a fast oscilloscope (Tektronix TDS 520A) [14,15]. The leakage of the frequency doubled output of a *Q*-switched Nd:YAG (yttrium aluminum garnet) laser that pumped the CPA laser system was used to trigger the oscilloscope so as to ensure the synchronization of the detection signal with the femtosecond laser pulse. The target was connected by a very short wire to a sealed electric connector on one end flange of

*Author to whom correspondence should be addressed. Email address: jzhang@aphy.iphy.ac.cn

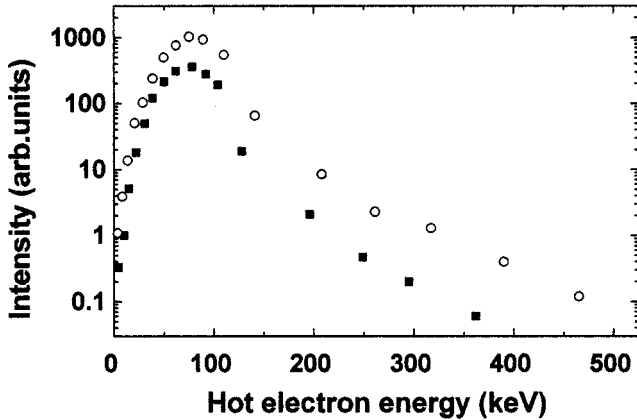


FIG. 1. The hot electron spectrum from Al (open circles) and glass (solid squares) targets irradiated by *p*-polarized femtosecond laser pulses at $8 \times 10^{15} \text{ W/cm}^2$.

the cylindrical vacuum chamber. Then the signal from the target was fed via a coaxial cable to the input of the oscilloscope. The input impedance of the oscilloscope of 50Ω was matched to that of the connected cable in order to avoid reflection of signals. A Faraday cup 17 cm away from the target without a bias voltage in the direction normal to the target was also used to collect electrons emitted from the plasma.

The plasma absorption was measured by calorimeters. Slight focusing (with an $f/10$ lens) of the reflected beam ensured that all the scattering signals were collected by the calorimeters. An interference filter at a central wavelength of 800 nm was placed at the window of the calorimeter to ensure that only the reflected laser signal could be detected.

III. RESULTS AND DISCUSSION

All the experimental results presented here were obtained for laser pulses incident on targets at an angle of 45° with respect to the target normal without any prepulse.

The energy spectrum of the outgoing electrons was measured with the electron magnetic spectrometer shown in Fig. 1. The spectrum of ingoing electrons was measured indirectly by a NaI γ -ray spectrometer [16]. The hot electron spectrum resembles a bi-Maxwellian distribution. The low hot electron temperature is independent of target material and is generated by a resonance absorption mechanism with the scaling law $T_H \text{ (keV)} \approx 6 \times 10^{-5} (I\lambda^2)^{0.33}$ [17]. The high hot electron temperature is generated by the vacuum heating process [18,19]. This bi-Maxwellian hot electron distribution was also predicted by the simulation of Gibbon and Bell [10].

For the high hot electron temperature, the two diagnostics gave similar values. We can thus deduce that those outgoing and ingoing electrons are heated by the same mechanism [19]. The Al and glass targets were measured and the high hot electron temperature obtained for each: 62 keV for Al and 44 keV for glass targets. The number of hot electrons ($E_k > 10 \text{ keV}$) measured in this way for Al is almost four times greater than for SiO_2 targets.

The energy spectrum we measured is from the emission

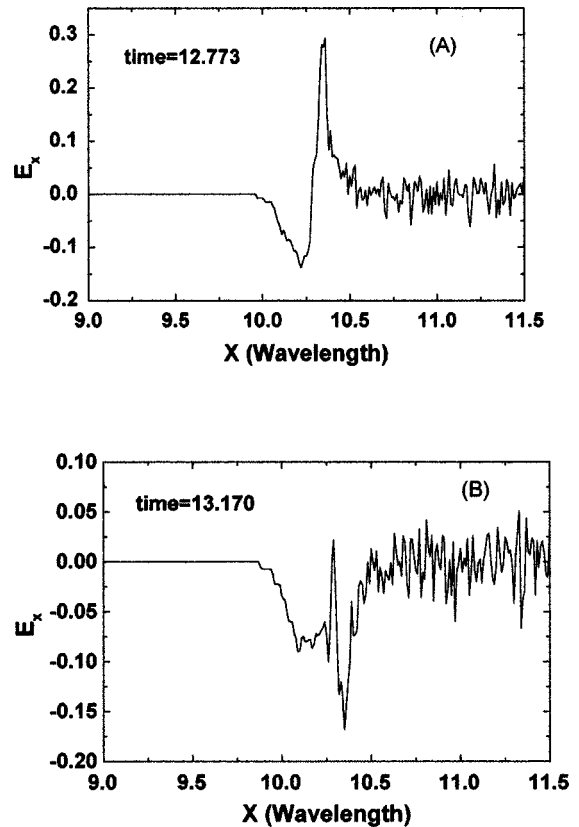


FIG. 2. The amplitude of the oscillating longitudinal electric field in Al targets at $t = 12.773$ and 13.179 optical cycles of the laser field. The solid surface is at $X = 10.3$ (> 10.3 is into the target). The electric field at the target boundary changes its polarity periodically. The electric field here is in normalized units of $m\omega_0 c/e$.

of hot electrons with energies greater than the charge separation potential (CSP) generated by less mobile ions. Those electrons with energies less than the CSP would be pulled back to the surface by the CSP. Figure 2 shows the normalized amplitude (in units of $m\omega_0 c/e$) of the oscillating electric field in the direction normal to the solid surface. Here m is the mass of an electron, ω_0 is the laser frequency, c is the speed of light and e is the charge of an electron. The $+x$ direction in Fig. 2 is in toward the target. The simulations used a one-dimensional 1D fully electromagnetic LPIC++ code, where an electromagnetic wave is launched obliquely from the left-hand side into an overdense plasma located on the right-hand side. $n_e/n_c = 20$, $T_e = 100 \text{ eV}$, $T_e/T_i = 3-5$, and the mass ratio $m_i/Zm_e = 1836$. A Gaussian profile for the incident laser pulse was assumed in the simulation. Typically 150×2680 electrons and ions and 2680 cells were used. We consider an initial situation in which the ions are mobile and electrons are pulled out into vacuum by the component of electrical field normal to the target. The simulations show that an “electron cloud” always exists in front of the target, forming a strong negative electric field. This means a charge separation potential is generated and many hot electrons will be pushed back to the target surface.

The CSP we measured is greater than the prediction of

Bastiani *et al.* [20], calculated from the sheath-transit absorption (STA) of Yang *et al.* [11]. The sheath electric field is

$$E(x,t) = -\frac{m v_e^2}{e \lambda_D} \frac{2}{\sqrt{2} \exp(0.5) - (x/\lambda_D)} + \frac{2 c k_y}{\omega} \times B_0 \cos(\omega t + \phi). \quad (1)$$

The first term on the right-hand side of Eq. (1) is the sheath electrical field associated with the electrostatic potential to be determined by the self-consistent Poisson equation. If calculated with Eq. (1), the sheath potential under our experimental conditions is not more than 5 keV. That is much less than what we measured.

From our experimental conditions, we can calculate the CSP like this: the total electron number emitted from the target was measured to be about 6.5×10^9 for each shot [15]. The focal spot diameter was about 20 μm . The average distance between maximum positive and negative field is about 0.2λ (see Fig. 2), that is, 0.16 μm . Thus we can see that the electrons and less mobile ions form a “capacitor” of capacitance $7 \times 10^{-15} \text{ F}$. So the potential on this “capacitor” is about 60 kV. This is more or less the same as we measured with the electron spectrometer.

The energy spectrum of hot electrons in Fig. 1 was measured at the same laser intensity with Al and glass targets. The peak position for the two target materials is almost the same but the maximum dose from Al targets is about four times that from glass targets, so there must be some effect decreasing the CSP in metallic targets relative to dielectric targets. One possible cause might be the great difference of electrical conductivity between metallic and dielectric targets. That is, when electrons are emitted from the focal spot of the target and generate the charge separation potential, this potential will be decreased immediately by free electrons in the metallic target, but the dielectric target has no free electrons to “neutralize” this potential due to its zero electrical conductivity.

This phenomenon can be observed also through measurement of the average hot electron energy and the total emitted electron number. The total number of escaping electrons from metallic targets can be measured exactly through the target potential [15] and is 6.5×10^9 at an intensity of $8 \times 10^{15} \text{ W/cm}^2$. But the dielectric targets cannot be measured by this method. Other ways have to be found to solve this problem. A feasible way is to place a metallic probe (or metallic collector) in the direction normal to the target near the target surface. It can collect the emitted electrons. The first negative peak of the single diagram measured by the oscilloscope suggested that this was produced by escaping electrons. The value for the Al targets was about 1.6 V and 0.38 V for the glass targets. This showed that the total number of escaping electrons from Al targets is four times that from glass targets. The average energy of the emitted hot electrons was measured with a Faraday cup triggered by the target potential or the probe near the target surface. The distance from the focal spot to the Faraday cup was about 17 cm. In our experiment, the flight time from the target surface to the Faraday cup was about 1.5 ns for the Al target. This

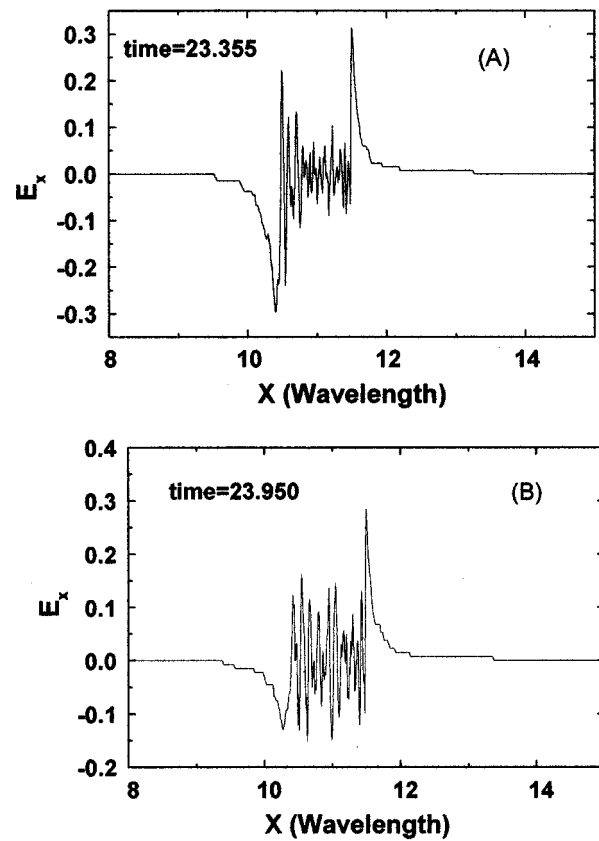


FIG. 3. The amplitude of the oscillating longitudinal electric field in glass targets at $t=23.355$ and 23.950 optical cycles. The solid surface is at $X=10.3$ (>10.3 is into the target).

means the average hot electron energy was about 50 keV. The flight time was about 1.3 ns for glass targets. The average hot electron energy of glass is slightly greater than that of Al targets.

According to the capacitor model, the CSP is proportional to the emitted electron number. But the CSP's we measured in Al and glass targets were almost the same. As the CSP builds up in Al targets at the focal spot, electrons around the focal spot are attracted to neutralize this potential instantly and cause decrease of the CSP. So, from Fig. 2, we cannot find a permanent positive electric field in the solid surface. But in dielectric targets (as shown in Fig. 3) the electrons near the focal spot are fixed. They cannot neutralize the less mobile ions, so this CSP keeps the same value.

Another difference between Al and glass targets associated with electrical conductivity is the laser absorption. With calorimeters, we measured the laser energy absorption in Al and glass targets shown in Fig. 4. The level of light scattered from the collecting optics was found to be negligible [7]. When the incident laser was focused on Al targets at 10^{13} W/cm^2 , the reflection coefficient was about 80%, showing that the energy absorption for IB is near 20%. For the laser focused on Al targets at $8 \times 10^{15} \text{ W/cm}^2$, the reflectivity dropped to 20%.

But this phenomenon did not occur for the glass targets. As the laser intensity increased, the reflection coefficient dropped to a minimum at the intensity of 10^{13} W/cm^2 and

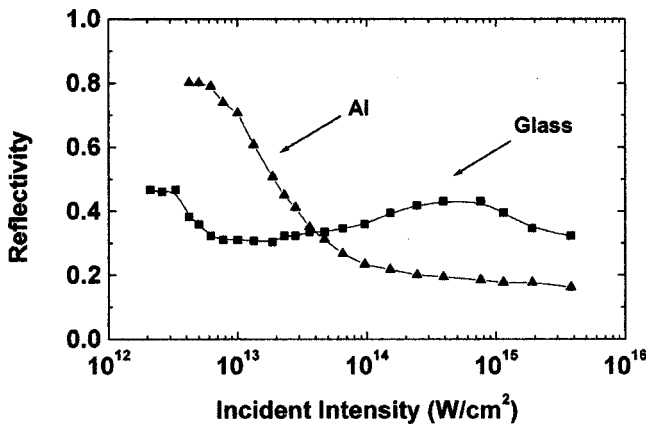


FIG. 4. The laser energy reflectivity vs laser intensity at 45° incidence on Al and glass targets.

then kept increasing up to 10^{15} W/cm^2 . Compared with dielectric targets, metallic targets are easy to ionize and have many more electrons to form the plasma wave which contributes to the laser energy absorption. In other words, the laser can pump electrons from metallic targets continuously because of the metal's great electrical conductivity and those electrons can get more energy from the laser pulses. So the absorption coefficient in metallic targets is greater than that in dielectric targets. This process was shown clearly in Figs. 2 and 3. In metallic targets, the strong oscillating electric field will pull electrons out from inner target layers during the positive half period and push them out of the target surface in the negative half period. Electrons can be heated continuously in this way. But in dielectric targets a strong

positive electric field is always exhibited behind the solid surface. This field reenforces the CSP and prevents electrons from accelerating. Of course, this phenomenon can also be explained numerically by the Fresnel equations in the Drude model, where the complex index of refraction [$n^2 = 1 + i4\pi\sigma(\nu)/\omega$] is related to the dc resistivity of the target material ($\rho_{dc} = \nu m_e/N_e e^2$).

IV. CONCLUSION

In summary, we have studied the energy absorption, hot electron emission, and hot electron energy spectrum produced during the interaction of a *p*-polarized laser pulse at $8 \times 10^{15} \text{ W/cm}^2$ with metallic and dielectric target materials. The charge separation potential we measured was greater than the prediction of Yang *et al.* using the STA mechanism because the main heating process is the VH mechanism under our experimental conditions. In metallic targets the charge separation potential is lower than that of dielectric targets because free electrons continuously "neutralize" this potential. The laser absorption in metallic targets is higher than that in dielectric targets. The total number of electrons emitted from metallic targets is more than that from dielectric targets and the hot electron temperature in metallic targets is higher than that of dielectric targets.

ACKNOWLEDGMENTS

The authors would like to thank Professor Wei Yu for valuable discussions. This work was jointly supported by the National Natural Science Foundation of China under Grant Nos. 19825110 and 10075075 and the National Hi-Tech ICF Program.

-
- [1] M. D. Perry and G. Mourou, *Science* **264**, 917 (1994).
 - [2] R. M. More *et al.*, *J. Phys. (Paris), Colloq.* **61**, C7-43 (1988).
 - [3] M. Tabak, J. Hammer, M. E. Glinsky, W. L. Kruer, W. C. Wilks, and R. J. Mason, *Phys. Plasmas* **1**, 1626 (1994).
 - [4] A. Modena *et al.*, *Nature (London)* **377**, 606 (1995).
 - [5] P. A. Norreys, M. Zepf, S. Moustakidis, A. P. Fews, J. Zhang, P. Lee, M. Bakarezos, C. N. Danson, A. Dyson, P. Gibbon, P. Loukakos, D. Neely, F. N. Walsh, J. S. Wark, and A. E. Dangor, *Phys. Rev. Lett.* **76**, 1832 (1996).
 - [6] J. D. Kmetec, C. L. Gordon, J. J. Macklin, B. E. Lemoff, G. S. Brown, and S. E. Harris, *Phys. Rev. Lett.* **68**, 1527 (1992).
 - [7] D. F. Price, R. M. More, R. S. Walling, G. Guethlein, R. L. Shepherd, R. E. Stewart, and W. E. White, *Phys. Rev. Lett.* **75**, 252 (1995).
 - [8] A. Saemann and K. Eidmann, *Appl. Phys. Lett.* **73**, 1334 (1998).
 - [9] F. Brunel, *Phys. Rev. Lett.* **59**, 52 (1987); *Phys. Fluids* **31**, 2714 (1998).
 - [10] P. Gibbon and A. R. Bell, *Phys. Rev. Lett.* **68**, 1535 (1992); **73**, 664 (1994).
 - [11] P. J. Catto and R. M. More, *Phys. Fluids* **20**, 704 (1977); T.-Y. Brian Yang, William L. Kruer, Richard M. More, and A. Bruce Langdon, *Phys. Plasmas* **2**, 3146 (1995).
 - [12] T.-Y. Brian Yang, W. L. Kruer, A. B. Langdon, and T. W. Johnston, *Phys. Plasmas* **3**, 2702 (1996).
 - [13] P. Bilski *et al.*, *Radiat. Prot. Dosim.* **66**, 101 (1996).
 - [14] V. V. Ivanov, A. K. Knyazev, N. E. Korneev, A. A. Matsveiko, Yu. A. Mikhailov, V. P. Osetrov, A. I. Popov, G. V. Skizkov, and A. N. Starodub, *Zh. Eksp. Teor. Fiz.* **109**, 1257 (1996) [JETP **82**, 677 (1996)].
 - [15] L. Z. Zhao *et al.* (unpublished).
 - [16] P. Zhang, J. T. He, D. B. Chen, Z. H. Li, Y. Zhang, J. G. Bian, L. Wang, Z. L. Li, B. H. Feng, X. L. Zhang, D. X. Zhang, X. W. Tang, and J. Zhang, *Phys. Rev. E* **57**, 3746 (1997).
 - [17] W. L. Kruer, *The Physics of Laser Plasma Interactions* (Addison-Wesley, New York, 1988); S. J. Gitomen *et al.*, *Phys. Fluids* **29**, 2679 (1986); D. W. Forslund, J. M. Kindel, and K. Lee, *Phys. Rev. Lett.* **39**, 284 (1977).
 - [18] M. K. Grimes, A. R. Rundquist, Y. S. Lee, and M. C. Downer, *Phys. Rev. Lett.* **82**, 4010 (1999).
 - [19] L. M. Chen, J. Zhang, Q. L. Dong, H. Teng, T. J. Liang, L. Z. Zhao, and Z. Y. Wei (published).
 - [20] S. Bastiani, A. Rousse, J. P. Geindre, P. Audebert, C. Quoilx, G. Hamoniaux, A. Antonetti, and J.-C. Gauthier, *Phys. Rev. E* **56**, 7179 (1997).

Absorption of femtosecond laser pulses in interaction with solid targets

Q. L. Dong, J. Zhang,* and H. Teng

Laboratory of Optical Physics, Institute of Physics, Chinese Academy of Sciences, Beijing 100080, China

(Received 4 April 2001; published 24 July 2001)

We have studied the effects of the plasma density scale length on the absorption mechanism of the femtosecond (fs) laser pulses interacting with solid targets. Experiments and particle-in-cell (PIC) simulations demonstrate that the vacuum heating is the main absorption in the plasma in the interaction of fs laser pulses with solid targets when no prepulses are applied. The energy spectrum of hot electrons ejected out of or injected into the plasma show a bitemperature distribution. While the first temperature of the two groups of hot electrons can be attributed to the “pull-and-push” exertion of the laser field, the second temperature refers to the electrons accelerated by the static part (in front of the target) and the oscillating part (in the plasma layer) of the laser-induced electric field, respectively. PIC simulations also show that with an appropriate density scale length, the femtosecond laser energy can be absorbed locally through different mechanisms.

DOI: 10.1103/PhysRevE.64.026411

PACS number(s): 52.38.-r, 52.50.Jm, 52.65.Rr

I. INTRODUCTION

The research of the femtosecond laser-plasma interaction is of importance because of many potential applications, such as the fast ignition scheme of inertial confinement fusion [1], plasma-based particle accelerator [2], and coherent x/γ ray sources [3], etc. The laser-produced plasmas also provide a test bed for the high temperature, high-density plasmas relative to some astrophysical phenomena [4]. Those topics are strongly dependent on the laser energy absorption in plasmas [5–12]. However, with long laser pulses, the plasma evolution during the duration of the laser pulse makes the physical process in the laser-plasma interaction very complex. The recent availability of the intense ultrashort lasers with chirped pulse amplification (CPA) [13] has enabled the investigation of different physics mechanisms by significantly reducing the hydrodynamic effects of plasmas during the interaction. In this paper, we report our study on the absorption mechanism in the interaction between femtosecond laser pulses and plasmas with various density scale lengths. In Sec. II, the vacuum heating (VH) mechanism is demonstrated to be responsible for the absorption through particle-in-cell (PIC) simulations and laboratory experiments for an abrupt density profile in the interaction between femtosecond laser pulses and solid targets. We will show that the laser-induced longitudinal electric field perpendicular to the target surface plays an important role in the electron acceleration and the laser absorption. In Sec. III, the effects of the density scale length on the absorption mechanism are investigated using PIC simulation. The laser energy can be absorbed locally if an appropriate density scale length is used.

II. ABSORPTION AT THE PLASMA SURFACE

The absorption mechanism for ultrashort laser pulses irradiating on solid targets or a plasma with a very steep electron

density profile was studied by several authors [5–7,9,10]. At normal incidence for intermediate intensities, the dominant absorption mechanism includes the normal skin effect ($eE_0/m\omega_0^2 \ll v_{th}/v \ll l_s$), the anomalous skin effect ($v_{th}/v \gg eE_0/m\omega_0^2 \gg l_s$) [9], and the sheath inverse bremsstrahlung absorption SIB ($eE_0/m\omega_0^2 \ll l_s \ll v_{th}/v$) [10], etc. Here e , m , and v_{th} are the charge, mass, and thermal velocity of electrons. E_0 and ω_0 is the electric field amplitude and the cycle frequency of the laser field, respectively. v is the collision ratio between electrons and ions in the skin layer of the plasma with a thickness of l_s . However, the interaction process between a p -polarized laser pulse and a plasma with steep density profile differs much in that the electric field of the laser, which has component perpendicular to the target surface, can directly pull electrons out of and send them into the plasma. If the excursion length of electrons in the laser field during one cycle, i.e., $r_0 = eE_0/m\omega_0^2$, exceeds the density scale length of the plasma $L = (\partial \ln n_e / \partial x)^{-1}$, those electrons will then deposit their quivering energy into the over-dense plasma where the laser field can not penetrate into. Such an absorption process is called VH and was first predicted by Brunel [5], and then studied further by Gibbon [6] and Kato [7]. This topic is still worthy of further investigation because some physical processes are still unclear to us, for example, the electron acceleration mechanism under such conditions. Furthermore, there are few experiments devoted to the investigation of this absorption mechanism of ultrashort laser pulses directly interacting with solid targets due to the difficulties to measure the electron density scale length. But such problem is solved perfectly by the technique of frequency domain interferometry to give 0.01λ resolution or better [14].

In this section, we first give out some characteristics of VH obtained through PIC simulations, then by combining experiments and PIC simulations, we demonstrate the vacuum heating mechanism of the ultrashort laser pulse on solid target surface.

A. Vacuum heating in PIC simulations

We used a 1D3V relativistic electromagnetic PIC code LPIC++ [15] to simulate fs laser pulses interacting with a

*Author to whom correspondence should be addressed. Electronic address: jzhang@aphy.iphy.ac.cn

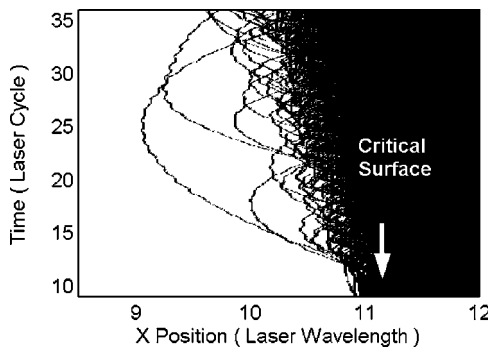
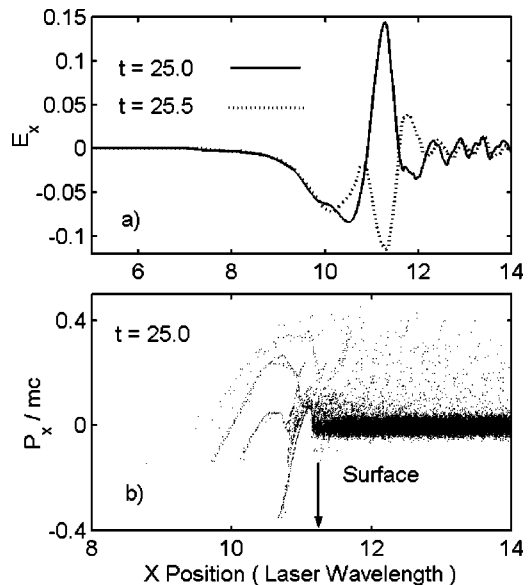


FIG. 1. Electron orbits in the space-time coordinate.

solid target. In order to understand the detailed process of laser absorption, most PIC variables are initialized based on the conditions of the experiments conducted at our laboratory for better comparison of PIC simulations with laboratory experiments. The simulation box has a length of 20.5λ along the x direction. A region of 5.5λ in the middle of the box is occupied by the plasma with an electron density rising exponentially from $0.01n_c$ at the point of 10λ to $35n_c$ with a scale length L of 0.04λ . Here, n_c is the critical density for the laser pulses with a wavelength of λ . The initial electron temperature was set to be 100 eV and ions are mobile [16]. A p -polarized fs laser pulse was launched from the left boundary at an incidence angle of 45° between the laser propagation and x direction. It has a duration of 56 periods and a relativistic intensity of 0.06, corresponding to the conditions of our experiments of laser wavelength, duration, and intensity of $0.8 \mu\text{m}$, 150 fs and $5 \times 10^{15} \text{ W } \mu\text{m}^2 \text{ cm}^{-2}$, respectively.

For the intensity and time scale studied here, the produced plasma has little time to expand and the electrons' quiver amplitude r_0 and the density scale length L satisfy the condition of $r_0/L > 1$. This suggests that the classical resonance absorption is weak, because as a collective action, plasma oscillation needs the particles "keeping in order" for a time long enough so that its amplitude grows in a space interval at the critical density position where the plasma frequency equals to the driver frequency [8]. However under the conditions we consider here, the electrons are pulled out of targets in the first half of the laser cycle. Some of them are sent back again in the same cycle, while others stay out of the target until several laser cycles later. Figure 1 shows the electron orbits in the space-time coordinates. The fact that these electrons have the parabolic orbits suggests that there is a force pointing to the target. In order to understand this phenomenon, we diagnose the laser-induced electric field through the simulation box, and obtain the snapshot of its component E_x perpendicular to the target surface, which is shown in Fig. 2(a). It can be seen clearly that a negative electric field locate in front of the target. The spectrum of E_x shows a zero component indicating that the negative electric field exists in the laser-plasma interaction process. It is the negative electric field that results in the electron parabolic orbits. Obviously, the negative electric field is induced by the charge separation as some electrons are pulled out and staying out of the plasma, constituting an electron cloud in front

FIG. 2. Laser-induced longitudinal E_x (a) and the electron phase space (b) in the 25th laser cycle.

of the target, while ions stay at their original position due to their great mass ratio to electrons. This electron cloud plays an important role in the absorption of the laser energy as we can see later.

In the skin layer of the plasma, the longitudinal electric field E_x oscillates with the frequency equal to ω_0 . Its maximum value here can reach 0.4 (normalized through $eE_x/m\omega_0$) with a spatial width of half of the laser wavelength along the x direction. The negative static electric field in front of the target and the oscillating part of E_x play the dominant role in accelerating electrons out of or into the plasma. In Fig. 3, we give out the simulated energy spectrum of hot electrons going out of the plasmas as well as an experimental one measured using a magnetic spectrometer set in front of the target in the normal direction. Both spectra show a bitemperature structure. The two equivalent temperatures are determined from the quasiexponential slope. The first temperature T_{h1} refers to electrons being heated by the laser's "pull-and-push" exertion. However, the second temperature T_{h2} is much higher than T_{h1} and cannot be simply attributed to such a process. In fact, this group of the outgoing hot electrons is accelerated by the oscillating part of the longitudinal electric field E_x . Such electrons can overcome the static field in front of the target and be detected by the magnetic spectrometer. On the other hand, the static part of the electric field will accelerate those electrons staying out to higher energies. This can be seen as those with positive momentum up to 0.4 inside the plasma as shown in Fig. 2(b). Such energetic electrons will be decelerated in the overdense plasmas, emitting x rays from which, after deconvolution of the detector response and the transmission effects of solid targets, the temperature of hot electrons penetrating into the overdense plasma can be deduced [17]. Experiments conducted here show that the x-ray spectra also has a similar bitemperature structure with the second one referring to

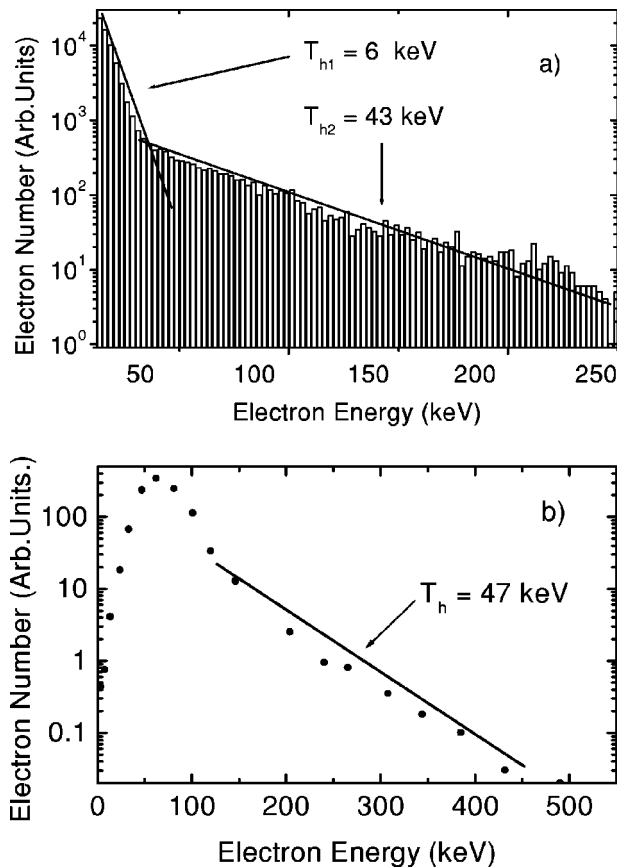


FIG. 3. The electron energy spectrum obtained from the PIC simulation (a) and the laboratory experiments (b).

those electrons accelerated by the static field as mentioned above.

An important aspect of the physics studied here is the detailed behavior of the laser energy absorption. By monitoring the reflected laser flux at the left boundary, we get the detailed behavior of absorption during the laser-plasma interaction. In our simulations, there are two main absorption peaks during the laser-plasma interaction process. The absorption behaviors should be understood by taking into account the electron cloud in front of the targets. We get the evolution of the electron density and the laser-induced electric field in front of the targets. This is shown in Fig. 4. Once the laser begins to interact with the plasma at about tenth period, the two diagnostic variables increase gradually, and at later time corresponding to the two main absorption peaks, there are two minima (electron density) or maxima (electric field), respectively. This shows us a picture of the interaction process. Once the laser pulse reaches the plasma target, electrons are pulled out and accumulate in front of the target and a negative electrostatic field builds up as shown by Fig. 2(a). This process continues until the dc field reaches a minimum value which is about two times the longitudinal part of the laser electric component, say, $E_x = 2E_0 \sin(\pi/4)$. Then many electrons will be sent back into the plasma in groups by the charge separation potential. Since these electrons are quivering with the laser electric component, the returning electron bunch can result in great absorption of laser energy nonadi-

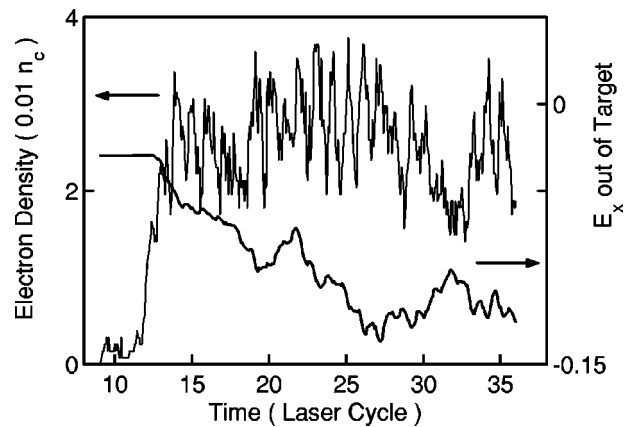


FIG. 4. The temporal evolution of the electron density and the static electric field in front of the target.

batically. The total absorption due to the VH process can reach 46% as deduced from the ratio of the incident and reflected energy.

To ensure that our simulation with $L = 0.04\lambda$ is not a special case, we did several simulations with the same set of parameters described but with different L , which varies between 0.01λ and 0.1λ . We wish that this should reduce the density scale length difference between our simulations and the laboratory experiments. It was found that as long as L is controlled within a certain range ($L < 0.1\lambda$), the physics mechanism to produce hot electrons is independent of plasma density scale length. The main results obtained from the simulations for L between 0.01λ and 0.1λ are also the same as the case with $L = 0.04\lambda$. These simulations confirm that during the interaction between fs laser and solid targets, the vacuum heating is the main absorption mechanism.

B. The vacuum heating in experiments

The experiments were conducted at the Laboratory of Optical Physics of the Institute of Physics with a Ti:sapphire chirped pulse amplification (CPA) laser system operating at around 800 nm at a repetition rate of 10 Hz. The laser delivered 5 mJ energy in 150 fs with a peak-to-pedestal contrast ratio of 10^5 at 1 ps. The p -polarized laser pulse (with a polarization ratio of 95%) was focused at an incidence angle of 45° on an Al target. The target was moved in the direction parallel to the target surface to ensure that the laser pulse interacts directly with a fresh surface at each shot. By moving the target perpendicularly to the target surface, we get the focused intensities varying in the range between 5×10^{12} and $5 \times 10^{15} \text{ W } \mu\text{m}^2/\text{cm}^2$ at the best focus. The absorption of the laser beam was determined by measuring the scattered and specularly reflected lights with a group of calorimeters. The electron density scale length is monitored by the interferometry in frequency domain.

Figure 5 gives the determined absorption (hollow-circle line) in experiments. As a comparison, we also plotted the measured absorption by the inverse bremsstrahlung (IB) process in the plasma (solid line) given by Price [18]. The great discrepancy between the two groups of data is not surprising. In order to investigate the process during the interaction, we

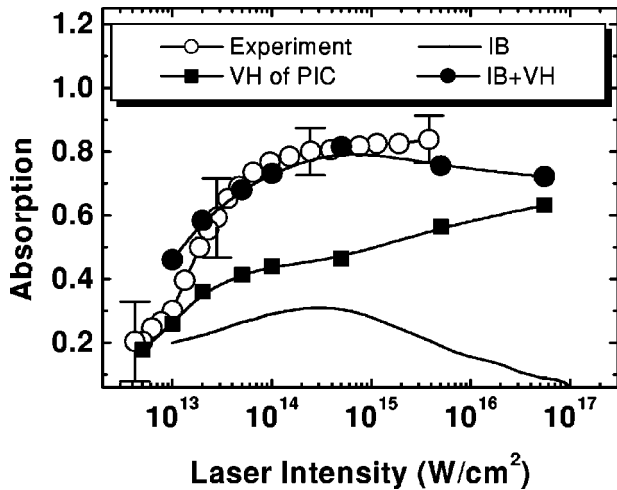


FIG. 5. Absorption ratio versus laser intensities. Our experimental value: hollow-circle line; The IB absorption [18], solid line; the VH absorption, solid-square line; the sum of VH and IB, solid-circle line. In PIC simulations, the L are applied as the following: $L=0.01\sim 0.02\lambda$ when $I<10^{14}$ W/cm 2 ; $L=0.04\pm 0.01\lambda$ for I between 10^{14} and 5×10^{15} W/cm 2 ; $L=0.07\pm 0.01\lambda$ when $I>5\times 10^{15}$ W/cm 2 .

did some PIC simulations using the electron scale length measured by the technique of the frequency domain interferometry and the temperature deduced by supposing isothermal expansion of plasma in the experiments [19]. The values of L applied are: $L=0.01\sim 0.02\lambda$ when $I<10^{14}$ W/cm 2 ; $L=0.04\pm 0.01\lambda$ for I between 10^{14} and 5×10^{15} W/cm 2 ; $L=0.07\pm 0.01\lambda$ when $I>5\times 10^{15}$ W/cm 2 . The PIC simulations show that the absorption ratio from PIC simulations at a fixed intensity is more sensitive to the density scale length L at low intensities than at high intensities. The collision between electrons and electrons/ions is not included in the PIC code. The simulation results show that, under those conditions, the vacuum heating dominates the absorption of laser pulses. After we added the experimental data of IB absorption to the values from PIC simulations and compared the sum (solid-circle line) with our experimental results, we found a good agreement. This implies that the vacuum heating does exist in the experiments at the intermediate intensities. We noticed the discrepancy at the low and high intensity end. The reasons are different and can be explained as follows. At lower intensities, the laser intensity is just over the ionization threshold. The ionization process and the intraatomic absorption play important roles in the interaction. The behavior of such plasma can not be simulated by the PIC method. At higher intensities, an overdense plasma is formed. However, because the plasma surface is disturbed by the electric component dragging electrons out of and pushing them back into the plasma, it cannot be regarded as a plasma mirror as in the experiments conducted by Price [18]. Given the IB absorption is increased due to the plasma surface disturbance, we believe that the sum of the absorption due to VH and IB will give a better agreement with our experiments at the higher intensity.

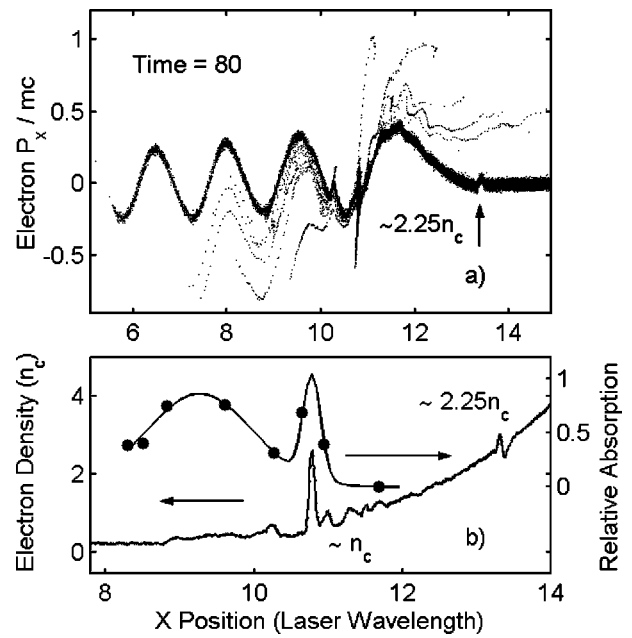


FIG. 6. The electron distribution in its phase space (a). (b) The disturbed electron density profile (solid line) and the relative absorption (solid-circle line). The parameters for the simulation are $L=2\lambda$ and $a_0=0.2$.

III. VOLUME HEATING OF PLASMAS

For plasmas with a larger density scale length, the absorbing region shifts from overdense plasma towards critical density with the corresponding change in the absorption mechanism, for example, change to resonance absorption (RA) when $L<1\lambda$. However, recent PIC simulations [20] and laboratory experiments by Zhang *et al.* [21] demonstrated more than one absorption peak for different scale lengths. This indicates that during the interaction between fs laser pulses and plasmas with a larger scale length $L>1\lambda$, other absorption mechanisms will play roles apart from the IB and RA. In this section, we investigate the absorption of ultrashort laser pulses by plasmas with various scale lengths. We focus on the parametric instabilities taking place in the underdense plasma.

Figure 6(a) gives the electron distribution in the phase space with the initial condition: $a_0=0.2$, $L=2\lambda$. The regular Langmuir wave breaks in the region at the critical density, causing density profile disturbance as shown by solid line in Fig. 6(b). Corresponding to the wave break, the laser pulse deposits its energy irreversibly to hot electrons in this region, limited by half of the Langmuir wavelength [solid-circle line in Fig. 6(b)]. The absorption process in this region can be considered as RA. We also find another wide absorption peak crossing the region between $0.25n_c$ and $0.5n_c$. This absorption peak should be attributed to the two-plasmon decay instability (TPD) in that the $\frac{1}{2}\omega_0$ and $\frac{3}{2}\omega_0$ components appear in the electromagnetic fields with the conversion efficiency about 1% as shown in its time integrated spectra. Indeed, with parameters mentioned above, the predicted TPD threshold in inhomogeneous plasmas is satisfied, i.e., $k_0Lv_0^2/v_{th}^2\sim 4>3$. Here, $v_0=eE_0/m\omega_0$ is the electron quiver velocity

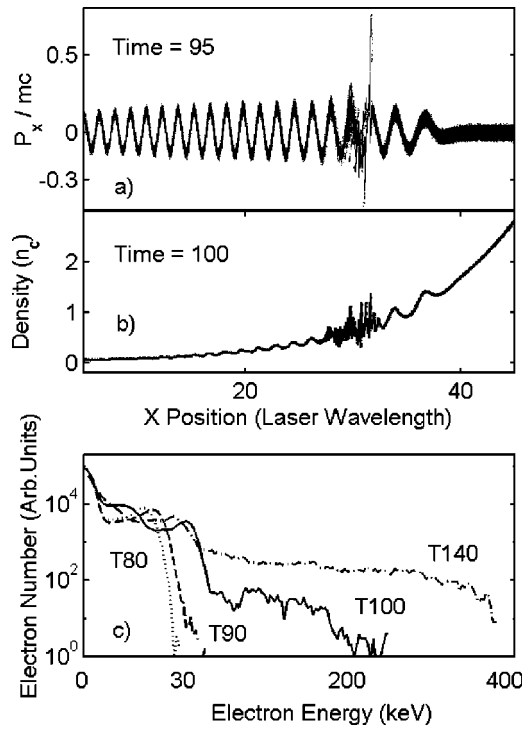


FIG. 7. The electron phase space (a), the disturbed electron density profile (b), and the temporal evolution of the electron energy distribution (c). The parameters for the simulation are $L = 25\lambda$ and $a_0 = 0.2$.

in the laser field; k_0 is the laser wave number. Also, there is a disturbance at the position of $2.25n_c$ in the snapshot of the phase space [Fig. 6(a)] and on the density profile [Fig. 6(b)]. Such disturbance is caused by the $\frac{3}{2}\omega_0$ part of the electromagnetic field, which is generally considered to be the secondary signature of TPD.

It is a well known problem that the primary unstable Langmuir wave from TPD is required to propagate a distance to match with photons of frequency ω_0 to produce the $\frac{3}{2}\omega_0$ light. The disturbance of density profile at $\frac{9}{4}n_c$ also indicates the existence of the Langmuir wave propagating towards the higher density with increasing wavelength. This case is much clearer when L increases as shown in Fig. 7(a). Such Langmuir waves will be reflected at the corresponding critical surface, causing irregular density profile in a wide range from $0.5n_c$ to $0.8n_c$ which can be seen from Fig. 7(b).

The TPD parametric instability provides anomalous absorption mechanism by which laser energy is converted to that of hot electrons. Figure 7(c) gives out the temporal evolution of the electron energy spectrum, showing the sudden acceleration of electrons through wave break, producing a non-Maxwellian distribution of electrons. Such an acceleration process is quite different from that in the VH process where the hot electron energy increases gradually with time. The energetic component of the electron distribution may transport into the overdense plasma during the laser pulse. They can be used to ignite the precompressed fuel in the fast ignition scheme of the inertial confinement fusion [1]. The non-Maxwellian distribution of electrons also has a pronounced effect on the physical process in the overdense re-

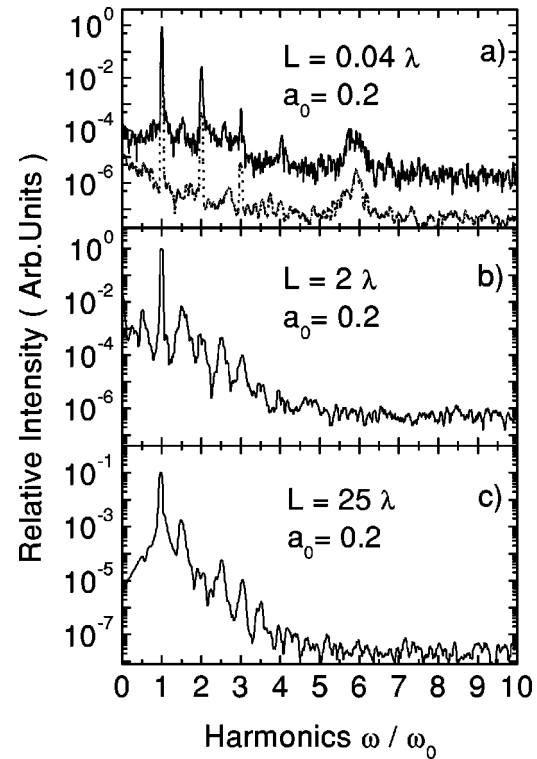


FIG. 8. The time-integrated spectra for different parameters as shown in the graphs.

gion of plasmas. For example, the ratio of some special satellite lines in the x-ray spectroscopy from the overdense plasma can be greatly enhanced [22,23]. However, the transportation of such energetic electrons may be inhibited by the self-generated magnetic field or by the local electrostatic field produced by the charge separation due to the finite conductivity of plasmas [24]. High absorption can still be achieved by the heat flow parallel to the target surface [25]. It needs at least two-dimensional PIC simulations to investigate the detail of the laser absorption at higher intensities at which the inclusion of the target deformation in consideration is necessary.

The time-integrated spectra of the reflected laser pulse are shown in Fig. 8 for three different density scale length. With a steep electron density profile, the integral harmonics of the reflected laser pulse dominate the whole spectrum as shown in Fig. 8(a). Such spectra is caused by electrons, which are pulled out of and then sent back into plasmas inducing disturbance at the plasma surface [15,26]. In the simulation with a smoother profile, the obtained spectrum is dominated by the harmonics of $\frac{1}{2}\omega_0$ [Figs. 8(b) and 8(c)], which is the consequence of TPD as demonstrated above. However, with much larger scale length $L = 25\lambda$, the plasma wave and the laser pulse propagate a long distance together so that the $\frac{1}{2}\omega_0$ component is significantly reduced compared to that with $L = 2\lambda$. There is also a line emission of the plasma as shown in Fig. 8(a). Such line emission is one feature of the Langmuir wave in the plasma stimulated here by the injected electrons originating from the plasma surface as shown in Fig. 1 and Fig. 2(b). A time-integrated spectra from another simulation with the same parameters but fixed ions is given as a dotted

line in Fig. 8(a) for a comparison. With ions mobile, the broadening of the harmonic lines is obvious, indicating that when studying the spectra from the plasma, it is necessary to include the ion motion especially when the laser pulse is long or very intense.

IV. CONCLUSION

In summary, we have reported our investigation of the absorption of fs laser pulses interacting with solid targets. Our experiments and PIC simulations indicate that without prepulses, the vacuum heating and the IB mechanism play the dominant role in the laser's absorption. Experiments show that the two groups of electrons ejected out of and/or injected into the plasma both have a bitemperature distribution. According to the PIC simulation, the first temperature of the ejected and injected electrons refers to electrons heated by the laser pulse's "pull-and-push" exertion. However, the second temperatures of such electrons are induced by different parts of the longitudinal electric field. The second temperature of hot electrons penetrating into the over-dense plasma refers to those staying out of the target and

being accelerated by the static electric field. On the other hand, the second temperature of out-going hot electrons refers to those accelerated by the oscillating part of the longitudinal electric field in the skin layer. We also studied the interaction between fs laser pulses and preformed plasmas with various density scale lengths L . The PIC simulations show that fs laser pulses, interacting with plasmas with an intermediate L , can be absorbed locally along the density profile. The main absorption mechanism in this case is considered to be parametric instabilities apart from RA and IB. The time-integrated spectra of the reflected pulse are also given, confirming these absorption mechanisms discussed above.

ACKNOWLEDGMENTS

This work was jointly supported by the National Natural Science Foundation (NNSF) of China under Grants Nos. 19825110 and 10075075 and the National High-Tech ICF program and the National Key Basic Research Special Foundation (NKBRSF) under Grant No. G1999075200.

-
- [1] M. Tabak *et al.*, Phys. Plasmas **1**, 1626 (1994).
 - [2] A. Modena *et al.*, Nature (London) **377**, 606 (1995), and references therein; C. L. Moore *et al.*, Phys. Rev. Lett. **79**, 3909 (1997); A. J. Mackinnon *et al.*, *ibid.* **86**, 1769 (2001).
 - [3] M. M. Murnane *et al.*, Science **251**, 531 (1991); J. D. Kmetec *et al.*, Phys. Rev. Lett. **68**, 1527 (1992); U. Teubner *et al.*, Phys. Rev. E **54**, 4167 (1996); M. H. Key *et al.*, Phys. Plasmas **5**, 1966 (1998); P. A. Norreys *et al.*, *ibid.* **6**, 2150 (1999).
 - [4] B. A. Remington *et al.*, Science **284**, 1488 (1999); J. S. Wark *et al.*, Phys. Plasmas **4**, 2004 (1997).
 - [5] F. Brunel, Phys. Rev. Lett. **59**, 52 (1987); Phys. Fluids **31**, 2714 (1988).
 - [6] P. Gibbon and A. R. Bell, Phys. Rev. Lett. **68**, 1535 (1992); P. Gibbon, *ibid.* **73**, 664 (1994).
 - [7] S. Kato *et al.*, Phys. Fluids B **5**, 564 (1993).
 - [8] D. W. Forslund *et al.*, Phys. Rev. A **11**, 679 (1975).
 - [9] E. S. Weibel, Phys. Fluids **10**, 741 (1967); A. A. Andreev, K. Yu. Platonov, and J.-C. Gauthier, Phys. Rev. E **58**, 2424 (1998).
 - [10] P. J. Catto *et al.*, Phys. Fluids **20**, 704 (1977); T. Y. Brian Yang *et al.*, Phys. Plasmas **2**, 3146 (1995).
 - [11] T.-Y. Brian Yang *et al.*, Phys. Plasmas **3**, 2702 (1996).
 - [12] D. A. Russell *et al.*, Phys. Rev. Lett. **86**, 428 (2001).
 - [13] M. D. Perry *et al.*, Science **264**, 917 (1994).
 - [14] E. Tokunaga *et al.*, Opt. Lett. **17**, 1131 (1992); P. Blanc *et al.*, J. Opt. Soc. Am. B **13**, 118 (1996).
 - [15] R. Lichters *et al.*, Phys. Plasmas **3**, 3425 (1996).
 - [16] H. M. Milchberg and R. R. Freeman, Phys. Fluids B **2**, 1395 (1990); W. Rozmus *et al.*, Phys. Plasmas **3**, 360 (1996).
 - [17] S. Hokin, Rev. Sci. Instrum. **63**, 5041 (1992); T. W. Phillips *et al.*, *ibid.* **70**, 1213 (1999); S. P. Hatchett *et al.*, Phys. Plasmas **7**, 2076 (2000). P. Zhang *et al.*, Phys. Rev. E **57**, R3746 (1998); L. M. Chen *et al.*, *ibid.* **63**, 036403 (2001).
 - [18] D. F. Price *et al.*, Phys. Rev. Lett. **75**, 252 (1995).
 - [19] W. L. Kruer, *The Physics of Laser Plasma Interaction* (Addison-Wesley, New York, 1988).
 - [20] E. Lefebvre and G. Bonnaud, Phys. Rev. E **55**, 1011 (1997).
 - [21] J. Zhang *et al.*, Phys. Rev. Lett. (to be published).
 - [22] A. Simon *et al.*, Phys. Fluids **26**, 3107 (1983).
 - [23] J. P. Matte *et al.*, Phys. Rev. Lett. **72**, 1208 (1994).
 - [24] T. Feurer *et al.*, Phys. Rev. E **56**, 4608 (1997).
 - [25] H. Ruhl *et al.*, Phys. Rev. Lett. **82**, 2095 (1999).
 - [26] P. Gibbon, Phys. Rev. Lett. **76**, 50 (1996).

Hydrodynamic characteristics of transient Ni-like x-ray lasers

Y. J. Li and J. Zhang*

Laboratory of Optical Physics, Institute of Physics, Chinese Academy of Science, Beijing 100080, People's Republic of China

(Received 7 August 2000; revised manuscript received 23 October 2000; published 27 February 2001)

A simple similarity model is presented to study the hydrodynamics of transient collisional excitation nickel-like x-ray lasers. Scaling laws for the temperature, scale length, and electron density are obtained by analytic derivation. The hydrodynamic characteristics of transient Ni-like Pd x-ray lasers are investigated using this model. The calculations agree well with Dunn's experimental results.

DOI: 10.1103/PhysRevE.63.036410

PACS number(s): 52.59.Ye, 42.55.Vc

I. INTRODUCTION

Two main objectives on developing x-ray lasers are to deliver a coherent, monochromatic, saturated output at successively shorter wavelengths toward, the "water window" and to provide a "table-top" x-ray laser for applications [1–3]. "Traditional" collisionally pumped Ni-like x-ray lasers are believed to be more promising to provide the saturated output in the spectral band near the "water window" [4,5]. However, the efficiency of the "traditional" collisional excitation schemes is still far below the requirements for the "table-top" operation mode.

Recently, a novel transient collisional excitation (TCE) scheme has been demonstrated by Nickles *et al.* for the Ne-like Ti 3p-3s ($J=0\rightarrow 1$) transition at 32.6 nm, where a high gain of 19 cm^{-1} is measured with only a few Joule pump energy [6,7]. More recent results have been reported by Dunn *et al.* [8], where a gain coefficient of 35 cm^{-1} and a gain-length product of 12.5 were measured on the 4d-4p ($J=0\rightarrow 1$) transition for the Ni-like Pd laser at 14.7 nm using only 5 J pump energy. This new scheme greatly enhances the efficiency of collisional excitation schemes by increasing the gain coefficient and shows us a way towards "table-top" x-ray lasers [9].

To date, the design and analysis of TCE x-ray lasers relies heavily on complicated one- or two-dimensional numerical simulations of hydrodynamics and atomic kinetics [10]. In this paper, we present a simple model for the TCE Ni-like x-ray lasers and make a detailed analysis using a set of self-similar, coupled ordinary differential equations. The purpose of our work is to understand the hydrodynamic characteristic of the transient collisional x-ray lasers and to provide a simple tool for experimentalists to quickly scan and optimize parameters to design experiments.

II. SIMILARITY EQUATIONS AND EQUATION OF STATE

The "standard" TCE x-ray lasers are pumped [8] by a combination of irradiation of nanosecond and picosecond laser pulses. The nanosecond laser pulse is used to create an optimized preplasma with Ni-like (or Ne-like) ionization

stage and longer scale length. Then, the picosecond pulse heats plasma rapidly to reach required conditions with high electron temperature while keeping a low ion temperature. This is beneficial to produce high gain because the gain coefficient is proportional to the electron temperature and inversely proportional to the square root of the ion temperature.

It is well known that the region of interest for x-ray laser gain is the corona region of $n_e < n_c$ and there is an isothermal expansion region during the pulse. The velocity distributions of electrons and ions reach their own Maxwellian equilibrium in this region, respectively. Because the mass of the ions is much heavier than that of the electrons, we assume that the ions are a background of the electrons and plasma is an ideal gas. Thus single-fluid, ideal hydrodynamic equations are adopted in the work,

$$\frac{\partial \rho}{\partial t} + \frac{\partial \rho v}{\partial x} = 0, \quad (1)$$

$$\rho \left(\frac{\partial v}{\partial t} + v \frac{\partial v}{\partial x} \right) = - \frac{\partial p}{\partial x}, \quad (2)$$

$$\frac{\partial}{\partial t} \left[\rho \left(\varepsilon + \frac{v^2}{2} \right) \right] = - \frac{\partial}{\partial x} \left[\rho v \left(\varepsilon + \frac{v^2}{2} \right) + \rho H \right] + \rho H, \quad (3)$$

where x is the spatial coordinate measured perpendicular to the slab surface; t is time; ρ , v , p , and T are the mass density, velocity, pressure, and temperature, respectively; ε is the internal energy per unit mass; and H is the net heating rate per unit mass. The equation of state and the laser heat deposition will be discussed below.

To obtain the similarity equations, we assume that the expansion of the plasma is homogeneous and satisfies the rarefaction wave solution varied with time:

$$v = C_s + x/t, \quad (4)$$

where C_s is the transient isothermal sound speed ($C_s = \sqrt{TZ/M_i} = T^{1/2}Z^{1/2}/M_i^{1/2}$). The momentum equation [Eq. (2)] separates in space and time with these assumptions. The solution of the spatial part (at constant time) gives an exponential attenuation density profile, which is normalized with the continuity equation,

$$\rho = m/L \exp(-x/L), \quad (5)$$

*Author to whom correspondence should be addressed. Email address: JZhang@aphy.iphy.ac.cn

where m is the mass ablated by the laser pulse from the slab target and L is the scale length of the plasma. With the equation of the mass ablation rate derived by De Groot *et al.* [11], which is valid for the ablation process of the thick slab target irradiated by a ns laser pulse, we derive the relations between the ablation mass and the intensity of the drive laser and the target element with the assumption of a homogeneous process of the ablation:

$$m = m_0 t^{2/3}, \quad (6)$$

where

$$m_0 = 2.55 \times 10^{-13} l^{2/3} [A/(Z+1)]^{7/6} / (Z \ln \Lambda)^{1/3}, \quad (7)$$

where the unit of m is g/cm^2 , the unit of t is ns, the unit of I is W/cm^2 , A is the atomic number of the element, Z is the average charge of ion, and $\ln \Lambda$ is the natural Coulomb logarithm. With the assumption of the homogeneous expansion, the momentum and energy equations can be simplified to

$$LC_s \left(\frac{l}{2} \frac{d \ln T}{dt} + 1 \right) = \frac{pt}{\rho}, \quad (8)$$

$$C_v \frac{dT}{dt} = H - \frac{p}{\rho t}, \quad (9)$$

where C_v ($\equiv d\varepsilon/dT$) is the specific heat per unit mass.

The laser heating rate changes with τ_{ib} , i.e., $H \approx I\tau_{\text{ib}}/m$, when $\tau_{\text{ib}} < 1$, while the laser heating rate is a constant, i.e., $H \approx I/m$, when $\tau_{\text{ib}} > 1$, where τ_{ib} is the inverse bremsstrahlung optical depth through the plasma:

$$\tau_{\text{ib}} = \int \kappa_{\text{ib}} dx. \quad (10)$$

The opacity κ_{ib} is determined by the following equation [12]:

$$\kappa_{\text{ib}} = \left(\frac{2}{\pi} \right)^{1/2} \frac{4}{3} \left(\frac{Z n_e^2 e^6 \lambda^2 \ln \Lambda}{c^3 (m_c T)^{3/2} (1 - n_c^2/n_c^2)^{1/2}} \right), \quad (11)$$

where λ is the laser wavelength, n_e is the electron density, n_c is the critical density ($\approx 1.1 \times 10^{21}/\lambda^2 \text{ cm}^{-3}$), T is the electron temperature in energy unit, m_e is the electron mass, and c is the light velocity.

In the corona region of $n_e \leq n_c$, electron temperature is higher than a few tens eV, and the corona model for the average charge of ion may be adopted [13]:

$$Z \approx \frac{2}{3} [AT_e(\text{eV})]^{1/3}. \quad (12)$$

The formulas we use for the EOS are

$$p = ZT\rho/M, \quad \text{and} \quad C_v = \frac{3}{2} Z/M_i \quad (13)$$

where M_i is the ion mass.

TABLE I. Normalized values for scaled variables.

Physical variable	Symbol	Normalized value
Time	t	1 ns
Laser intensity	I	10^{14} W m^{-2}
Laser wavelength	λ	$1.053 \mu\text{m}$
Ablation mass	m	$10^{-4} \text{ g cm}^{-2}$
Ion charge	Z	65
Atomic mass	A	240
Coulomb logarithm	Λ	5

III. ANALYTIC SOLUTIONS OF THE SIMILARITY EQUATIONS

Useful scaling laws for plasma variables have been derived from analytic solutions for flat-top laser pulses by using a similarity model of the Ni-like scheme. We employed convenient units listed in Table I [14] and scaled the variable with underlines in the whole derivation in order to simplify the calculation. Two distinct periods for the long pulse ($0 < t \leq t_{1L}$ and $t_{1L} \leq t \leq t_m$, where $t_{1L} = \Delta t_{1L}$ is the long pulse duration and t_m is the delay between the long pulse and the short pulse) and two distinct periods for the short pulse ($t_m \leq t \leq t_{2L}$ and $t \geq t_{2L}$, where $t_{2L} = t_m + \Delta t_{2L}$ and Δt_{2L} is the short pulse duration) are adopted in order to clearly show the physics process in the calculation.

A. Analytic solutions for the long laser pulse

The purpose for the long laser pulse is to produce a long scale length plasma with optimized initial conditions; the heating and ionization processes take place for the whole pulse duration. The laser energy is mainly deposited near the critical density.

1. During the time of $t \leq t_{1L}$

During the time of $t \leq t_{1L}$, an expression for the optical depth is obtained by integrating Eq. (10) over the density profile since the heating and ionization processes take place in the region where the electron density is close to the critical density [13]. That is,

$$\tau_{\text{ib}} = 5.757 \sqrt{\pi} \times 10^{-3} \underline{m}^2 \underline{A}^2 \underline{Z}^3 \underline{\Lambda} \underline{\lambda}^2 \underline{T}^{3/2} L, \quad (14)$$

where $\underline{\Lambda}$ is taken as a constant in the corona. Solving Eqs. (8) and (9) with Eqs. (6), (12), and (13), the analytic solutions satisfying the similarity equations, after the influence of the initial conditions disappeared, i.e., taking $\tau_{\text{ib}} < 1$, are

$$T = 3.902 \text{ keV} \underline{I}^{5/9} \underline{A}^{2/9} \underline{\Lambda}^{2/9} \underline{t}^{2/9}. \quad (15a)$$

Because t is close to t_{1L} , the temperature is kept nearly constant due to a balance of laser heating with expansion cooling, see Fig. 1,

$$L = 2.87 \times 10^{-2} \text{ cm} \underline{I}^{10/27} \underline{A}^{-2/27} \underline{\lambda}^{4/9} \underline{\Lambda}^{4/27} \underline{t}^{31/27}, \quad (15b)$$

$$n_0 = 20.82 \times 10^{20} \text{ cm}^{-3} \underline{I}^{11/54} \underline{A}^{4/27} \underline{\lambda}^{-5/9} \underline{\Lambda}^{-2/54} \underline{t}^{-14/27}, \quad (15c)$$

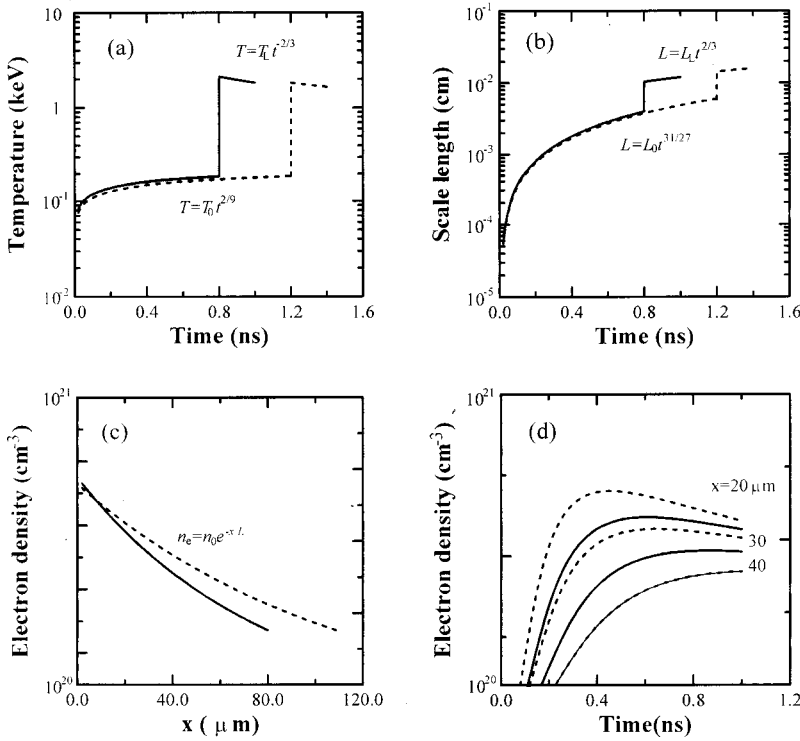


FIG. 1. (a) Temporal history for electron temperature, (b) scale length history, (c) electron density vs x at the center of the pulse, and (d) electron density history at different x for different long pulse duration of a flat-top pulse with the same short pulse conditions. The solid line is the solutions for $I_1=0.7\times 10^{12}$ W/cm², $\lambda=1.053$ μm, $\Delta t_{1L}=0.8$ ns, $I_2=5.2\times 10^{14}$ W/cm², and $\Delta t_{2L}=1.1$ ps. The dashed line is the solutions for $I_1=0.6\times 10^{12}$ W/cm², $\lambda=1.053$ μm, $\Delta t_{1L}=1.2$ ns, $I_2=5.2\times 10^{14}$ W/cm², and $\Delta t_{2L}=1.1$ ps.

where n_0 is the maximum value of n_e . Using Eq. (5), we can determine the electron density for position x and time t with Eq. (15c).

2. During the time of $t_{1L} \leq t \leq t_m$

After the time t_{1L} , the long laser pulse is turned off and the plasma continues to expand adiabatically. The exact analytical solutions can be obtained for this period using the condition before t_{1L} :

$$T=T_{1L}t_{1L}^{2/3}t^{-2/3}, \quad (16a)$$

$$L=L_{1L}t_{1L}^{-5/9}t^{5/9}, \quad (16b)$$

$$n_o=n_{1L}t_{1L}^{7/9}t^{-7/9}, \quad (16c)$$

where T_{1L} , L_{1L} , and n_{1L} are the electron temperature, scale length, and electron density at t_{1L} .

B. Analytic solutions for the short laser pulse

For the case of a “standard” transient collisional x-ray laser, the second pulse is so short that we can believe the following. First, we can assume that $m=m_0t_{1L}^{2/3}$ is a constant after the time t_{1L} and the heating rate is constant after the time t_m ($H=I/m$) with $\tau_{ib}>1$ because the preplasma is not transparent for the second pulse since the transparent temperature is proportional to the three-fourth power of the intensity. Second, there is not enough time to change the state of ion charge. This means Z can be taken as a constant. The formula we use for the EOS here is Eq. (13).

1. During the time of $t_m \leq t \leq t_{2L}$

At time t_m , when the second short laser pulse has started, the solutions can be obtained by considering the initial conditions before t_m :

$$T=23.123 \text{ keV } I_2 m^{-1} A Z^{-1} \underline{t} \left(1 - t_m^{5/3} t^{-5/3} + \frac{T_m t_m^{2/3}}{T_2} t^{-5/3} \right), \quad (17a)$$

where T_m is the electron temperature at t_m , $T_2=23.123 \text{ keV } I_2 m^{-1} A Z^{-1}$,

$$L=5.164 \times 10^{-2} \text{ cm } I_2^{1/2} m^{-1/2} \underline{t}^{3/2} \times \left(1 - t_m^{5/3} t^{-5/3} + \frac{L_m^2}{L_2^2 t_m^{4/3}} t^{-5/3} \right)^{1/2}, \quad (17b)$$

where L_m is the scale length at t_m , $L_2=5.164 \times 10^{-2} \text{ cm } I_2^{1/2} m^{-1/2}$,

$$n_0=3.157 \times 10^{20} \text{ cm}^{-3} I_2^{-1/2} m^{3/2} A^{-1} Z \underline{t}^{-3/2} \times \left(1 - t_m^{-5/3} t^{-5/3} + \frac{n_2^2 \tau_m^{1/6}}{n_m^2} t^{-5/3} \right)^{-1/2}, \quad (17c)$$

where n_m is the electron density at t_m , $n_2=3.157 \times 10^{20} \text{ cm}^{-3} I_2^{-1/2} m^{3/2} A^{-1} Z$.

2. During the time of $t_{2L} \leq t$

After the time t_{2L} , the second short laser pulse is turned off and the plasma continues to expand adiabatically. The analytical solutions can be obtained for this period using the condition before t_{2L} :

$$T = 23.123 \text{ keV} I_2 m^{-1} A Z^{-1} t_{2L}^{5/3} t^{-2/3} \times \left(1 - t_m^{5/3} t_{2L}^{-5/3} + \frac{T_m t_{nl}^{2/3} t_{2L}^{-5/3}}{T_2} \right), \quad (18a)$$

$$L = L_2 t_{2L}^{5/6} t^{2/3} \left(1 - t_m^{5/3} t_{2L}^{-5/3} + \frac{L_m^2}{L_2^2} t_m^{2/3} t_{2L}^{-5/3} \right)^{1/2}, \quad (18b)$$

$$n_0 = n_2 t_{2L}^{-5/6} t^{-2/3} \left(1 - t_m^{-5/3} t_{2L}^{-5/3} + \frac{n_2^2 t_{2L}^{-5/3}}{n_m^2 t_m^{2/3}} \right)^{-1/2}. \quad (18c)$$

IV. RESULTS AND DISCUSSION

It is well known that the laser energy is mainly deposited in the corona region of $n_e \leq n_c$. The model is more valid for heavy elements than for light elements [13]. This comes from the corona model of the average state of charge. In order to justify the model, we calculate the hydrodynamics of the transient collisional Ni-like Pd x-ray laser under the same experimental conditions as Ref. [8] and compare the results between our model calculation and the experiment.

The first goal for the long laser pulse is to produce more Ni-like ions. A longer constant temperature period is, of course, beneficial for the production of a sort of ions from Eq. (12). The electron temperature during the isothermal period is the two-ninth power of the time from Eq. (15a). This makes the temperature almost a constant at the later time during the long pulse. Thus, the longer the pulse duration is, the closer to a constant temperature for the later time the temperature is, as shown in Fig. 1(a). Simultaneously, the longer pulse duration can also make a longer scale length, as shown in Fig. 1(b). This is beneficial for the propagation of an x-ray laser pulse.

The second goal is to enhance efficiency. The law of enhancing efficiency is certainly to use the lower intensity to reach the electron temperature required by ionization for the long pulse. It will be highly efficient when the long pulse not only ionizes the plasma to the Ni-like ions, but also achieves thermodynamic equilibrium between electrons and ions. Thus, we define the ratio of time of the long pulse duration to the equilibrium time as a standard of approximation. The time of the thermodynamic equilibrium is

$$t_{ei} = \left(\frac{4\pi\varepsilon_0}{e^2} \right)^2 \frac{3m_i m_e^{-1/2} (T_e)^{3/2}}{8\sqrt{2\pi} Z^2 n_i (\log_{10} \Lambda)}. \quad (19)$$

Equation (19) can also be used to judge whether the short pulse duration is short enough to ignore the ionization change. We can neglect the change of Z if the ratio between the short pulse duration and the equilibrium time is smaller than 10^{-4} .

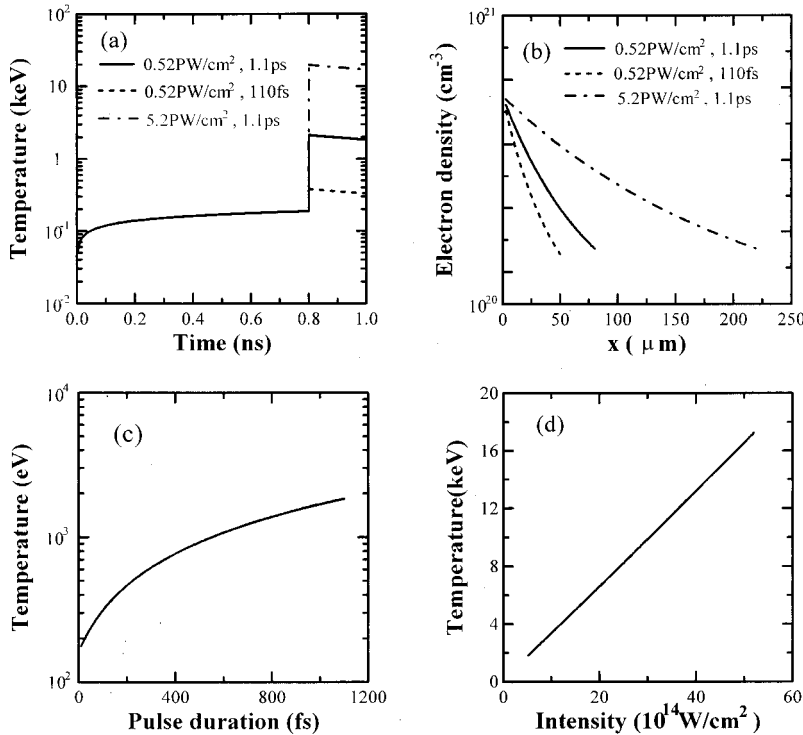
We calculated the Ni-like Pd ions for the long pulse under the same conditions of Dunn's experiment ($I_1 = 0.7 \times 10^{12} \text{ W/cm}^2$, $\lambda = 1.053 \mu\text{m}$, $t_{1L} = 0.8 \text{ ns}$, slab target). The calculated results show that the maximum electron temperature during the long pulse is 188 eV, which can ionize the Pd to an average state of charge $Z = 18.1$, as shown by the solid line in Fig. 1(a). The scale length is about 40 μm , as the

solid line shows in Fig. 1(b). The electron density is $7.52 \times 10^{20} \text{ cm}^{-3}$, as shown by the solid line in Fig. 1(c). However, the equilibrium time is about 1.4 ns. The t_{1L}/t_{ei} is about 0.57. For comparison, we also calculated the electron temperature and the average state of charge with the conditions of $I_1 = 0.6 \times 10^{12} \text{ W/cm}^2$, $\lambda = 1.053 \mu\text{m}$, $t_{1L} = 1.2 \text{ ns}$, slab target and the same short pulse. The results are $T_e = 188.8 \text{ eV}$, $Z = 18.1$, $L = 60 \mu\text{m}$, $n_e = 7.28 \times 10^{20} \text{ cm}^{-3}$, shown by the dashed line in Fig. 1. The equilibrium time is about 1.8 ns. The t_{1L}/t_{ei} is about 0.67. For the short laser pulse, the temperature is 1.84 keV under Dunn's condition and 2.07 keV in the second case. The equilibrium time is about 55.5 and 66.2 ns, respectively. The radio t_{2L}/t_{ei} is about 1.98×10^{-5} and 1.66×10^{-5} , respectively. It is clear that the pulse duration for the long pulses is shorter than the equilibrium time for both cases. However, it is more efficient for the second case than Dunn's case and the scale length is longer than Dunn's. The conclusion we get here is that the lower intensity and longer duration of the long laser pulse will be more beneficial to enhance the efficiency. The electron density history at different positions for the two cases is shown in Fig. 1(d).

In contrast with the period during the long pulse, the first important thing for the period during the short pulse is that T_e cannot be lower than ΔE_u [8], where ΔE_u is the upper laser level excitation energy. The reason for the requirement of $T_e > \Delta E_u$ is that we want to achieve the optimum gain. Here $\Delta E_u = 450.3 \text{ eV}$. The calculation results show that the electron temperature during the short pulse is 1.84 keV under the same conditions of Dunn's experiment ($I_2 = 5.2 \times 10^{14} \text{ W/cm}^2$, $\lambda = 1.053 \mu\text{m}$, $t_{2L} = 1.1 \text{ ps}$, slab target). This is about four times as large as $\Delta E_u = 450.3 \text{ eV}$, and the plasma can be heated rapidly, as shown by the solid line in Fig. 1(a). The second important thing for the period during the short pulse is to use a pump pulse with a duration so long that it can heat the electron temperature up rapidly while keeping the ion temperature as low as possible. This will be advantageous to enhance the gain coefficient because it is proportional to the electron temperature and inversely proportional to the square root of the ion temperature.

In order to show the hydrodynamic characteristic of the plasma for the short pulse, we investigated the relations of electron temperature, scale length, and electron density with different pulse duration and intensity. The result shows that the electron temperature increases rapidly from 330 eV to 1.84 keV with an increase of pulse duration from 110 fs to 1.1 ps, as shown in Figs. 2(a) and 2(c). At the same time, the scale length increases from 50 to 80 μm with the increase of pulse duration, too, which makes the density gradient more relaxed for the longer pulse than the shorter one, as shown in Fig. 2(b). The electron density is $7.5 \times 10^{20} \text{ cm}^{-3}$. It is clear that a shorter pulse is not beneficial for the production of an x-ray laser under the same intensity.

For the same pulse duration, the electron temperature increases rapidly from 1.84 to 16.7 keV with an increase of intensity from 5.2×10^{14} to $52 \times 10^{14} \text{ W/cm}^2$, as shown in Figs. 2(a) and 2(d). This is much more beneficial to enhance the gain coefficient. The scale length increases from 80 to 217 μm , as shown in Fig. 2(b). This is also much more



beneficial to enhance the total output of x-ray lasers. The results show that the higher the intensity is, the more advantageous it is for the production of the transient population inversion under the same laser duration.

By comparison, we also calculated the case in which there is a delay time between the long and short pulses. The 1-ns delay time is used and other conditions are identical to Dunn's case. The results are shown in Fig. 3. The electron

FIG. 2. (a) Temporal history for electron temperature, (b) electron density vs x at the center of the pulse, (c) electron temperature vs the pulse duration while the intensity of the short pulse is being held constant ($5.2 \times 10^{14} \text{ W/cm}^2$), and (d) electron temperature vs the intensity while the pulse duration is being held constant (1.1 ps). The conditions are $I_1 = 0.7 \times 10^{12} \text{ W/cm}^2$, $\lambda = 1.053 \mu\text{m}$, $\Delta t_{1L} = 0.8 \text{ ns}$, $\Delta t_{2L} = 1.1 \text{ ps}$, and $\Delta t_{2L} = 110 \text{ fs}$, respectively, with the same intensity $I_2 = 5.2 \times 10^{14} \text{ W/cm}^2$ or $I_2 = 5.2 \times 10^{14} \text{ W/cm}^2$ and $I_2 = 52 \times 10^{14} \text{ W/cm}^2$, respectively, with the same short pulse duration $\Delta t_{2L} = 1.1 \text{ ps}$.

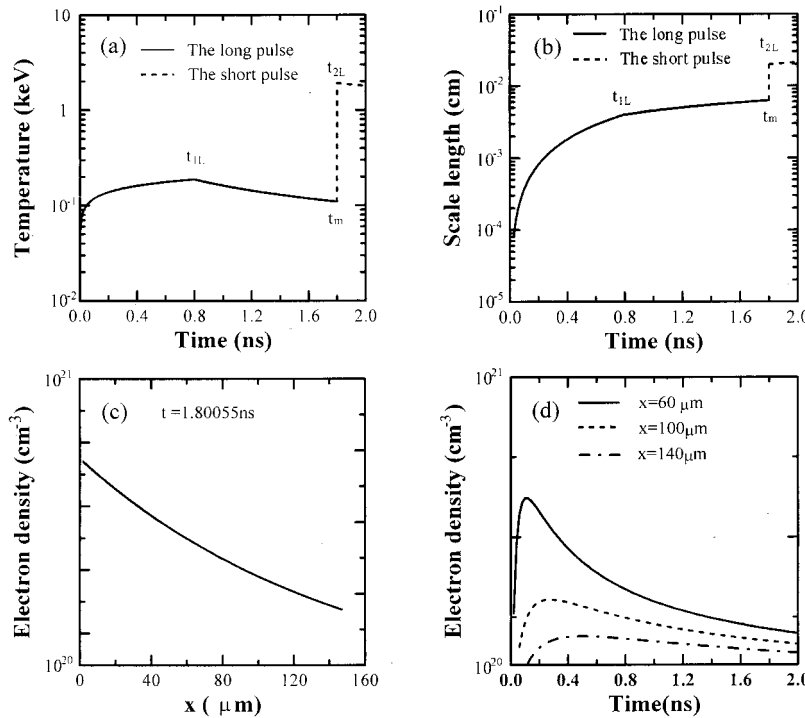


FIG. 3. (a) Temporal history for electron temperature, (b) scaling length history, (c) electron density vs x at the center of the pulse, and (d) electron density history for different x from the similarity equations. The conditions are $I_1 = 0.7 \times 10^{12} \text{ W/cm}^2$, $\lambda = 1.053 \mu\text{m}$, $\Delta t_{1L} = 0.8 \text{ ns}$, $I_2 = 5.2 \times 10^{14} \text{ W/cm}^2$, $\Delta t_{2L} = 1.1 \text{ ps}$, and the delay time $t_m = 1 \text{ ns}$.

shown in Fig. 3(c). The electron density is about $7.1 \times 10^{20} \text{ cm}^{-3}$. It shows that delay time is not beneficial to enhance the efficiency for the long pulse. However, it can enhance the efficiency for the short pulse, and more importantly it can sufficiently relax the electron density. This can certainly be beneficial for the propagation of an x-ray laser pulse. From this calculation, a conclusion might be possible. An optimum delay time might exist if the propagation of x-ray-laser pulses is considered. This would involve ray-tracing calculation.

V. CONCLUSIONS

In conclusion, we have developed a similarity model for transient x-ray lasers. The calculation results are in agree-

ment with Dunn's experimental results. The results show that a longer long laser pulse can provide higher efficiency, the production of Ni-like ions, and the relaxation of the density gradient, and the high intensity and moderate pulse duration for the short laser pulse are beneficial to enhance both the gain coefficient and scale length. The model is useful for an approximate, quick parameter scan for experimental design and analysis.

ACKNOWLEDGMENTS

This work was supported by the National Nature Science Foundation of China under Grant Nos. 19974074 and 19825110, National High Technology High Power Lasers Program.

-
- [1] J. Zhang *et al.*, *Science* **276**, 1097 (1997).
 - [2] F. G. Tomasel, J. J. Rocca, V. N. Shlyaptsev, and C. D. MacCietto, *Phys. Rev. A* **55**, 1437 (1996).
 - [3] M. P. Kalachnikov *et al.*, *Phys. Rev. A* **57**, 4778 (1998).
 - [4] Y. Li, G. Pretzler, P. Lu, E. E. Fill, and J. Nilson, *Phys. Plasmas* **4**, 479 (1997).
 - [5] A. Prag, A. Glinz, J. E. Balmer, Y. Li, and E. Fill, *Appl. Phys. B: Lasers Opt.* **63**, 113 (1996).
 - [6] P. V. Nickles *et al.*, *Phys. Rev. Lett.* **78**, 2748 (1997).
 - [7] P. J. Warwick *et al.*, *J. Opt. Soc. Am. B* **15**, 1808 (1998).
 - [8] J. Dunn *et al.*, *Phys. Rev. Lett.* **80**, 2825 (1998).
 - [9] J. Dunn *et al.*, *Phys. Rev. Lett.* **84**, 4834 (2000).
 - [10] J. Nilsen, Y. Li, and J. Dunn, *J. Opt. Soc. Am. B* **17**, 1084 (2000).
 - [11] J. S. De Groot *et al.*, *Phys. Fluids B* **4**, 701 (1992).
 - [12] T. W. Johnston and W. M. Dawson, *Phys. Fluids* **16**, 722 (1973).
 - [13] D. Colombant and G. T. Tonon, *J. Appl. Phys.* **44**, 3524 (1973).
 - [14] R. A. London and M. D. Rosen, *Phys. Fluids* **29**, 3813 (1986).

Hot electrons in the interaction of femtosecond laser pulses with foil targets at a moderate laser intensity

Y. T. Li,^{1,2} J. Zhang,^{1,*} L. M. Chen,^{1,2} Y. F. Mu,² T. J. Liang,³ Z. Y. Wei,¹ Q. L. Dong,¹ Z. L. Chen,¹ H. Teng,¹ S. T. Chun-Yu,² W. M. Jiang,² Z. J. Zheng,² and X. W. Tang³

¹Laboratory of Optical Physics, Institute of Physics, Chinese Academy of Sciences, Beijing 100080, Peoples Republic of China

²National Key Laboratory for Laser Fusion, Institute of Nuclear Physics and Chemistry, China Academy of Engineering Physics, Mianyang 621900, Peoples Republic of China

³Institute of High Energy Physics, Chinese Academy of Sciences, Beijing 100039, People's Republic of China

(Received 6 December 2000; revised manuscript received 9 April 2001; published 26 September 2001)

Characteristics of hot electrons produced in the interaction of femtosecond laser pulses with foil targets were investigated at a moderate laser intensity. Both outgoing and ingoing hot electrons from the femtosecond laser plasma were studied. A collimated jet of outgoing hot electrons was observed in the target normal direction. An ingoing energetic hot-electron beam was found in the laser propagation direction, while the low-energy ingoing electrons spread into wider cone angle due to the collisional effects in the plasma and target material. These observations were supported by three-dimensional Monte Carlo simulations. The hot-electron temperature obtained from electron spectra and absorption experiments implies that resonance absorption is partially responsible for the generation of hot electrons.

DOI: 10.1103/PhysRevE.64.046407

PACS number(s): 52.25.Os, 52.38.-r

I. INTRODUCTION

The rapid development of short pulse ultraintense lasers provides powerful tools to study relativistic laser-plasma interactions and explore approaches to ignition of inertial confinement fusion. For example, the fast ignition concept proposed by M. Tabak *et al.* is one of the most promising ways [1]. One of the major physics issues to implement fast ignition is the generation and propagation of energetic hot electrons in high-density plasmas. Recently, the energetic hot electrons outgoing from plasmas were studied experimentally and theoretically [2–7]. Hot-electron energies up to 100 MeV were observed in laser-solid interactions at an intensity of 3×10^{20} W/cm² using petawatt laser system at LLNL [8]. G. Malka and J. L. Miquel also studied relativistic electrons produced by interaction of relativistically intense laser pulses with solid targets [9]. The high energy of hot electrons was attributed to $\mathbf{J} \times \mathbf{B}$ acceleration mechanism [10]. On the other hand, hot electrons ingoing along the laser propagation direction, which is directly related with fast ignition, were also studied in detail [11,12]. M. Tatarakis *et al.* observed a plasma at the back surface of a thin foil. This was believed to be formed by a collimated electron beam passing through the foil [13]. A more direct experiment was carried out using a transparent glass target coated with an aluminum layer. An ionization track induced by a beam of energetic hot electrons was clearly observed through the target [14,15]. P. A. Norreys *et al.* observed a highly directional γ -ray beam with energies above 10 MeV in the direction nearly opposite to the target normal direction. This indicated the generation of a directional relativistic electron beam [16]. These experimental results imply that the hot-electrons could be collimated by self-generated magnetic fields. The generation of hot-

electron jet and the pinching of magnetic fields were reproduced by particle-in-cell (PIC) simulations [17,18].

Many mechanisms can produce hot electrons. In the interaction of intense laser pulses with sharp solid-vacuum interface, the ponderomotive potential model and Brunel absorption model [19] play important roles. Other mechanisms such as wake fields [20], parametric instabilities [21,22], B-loop mechanism [23], and propagating wave [24] are effective when a large-scale preplasma is formed before the arrival of the main laser beam.

In this paper, we show that the well-collimated emission of hot electrons is not only generated at relativistic laser intensities, but also at a moderate laser intensity. The angular distribution of the outgoing and ingoing hot electrons, the electron energy spectrum, the generation mechanism, and the transport of hot electrons into cold target material are investigated in interaction of femtosecond laser pulses with foil targets.

II. EXPERIMENTAL SETUP

The experiments were carried out with a Ti:Sapphire laser system at the Institute of Physics, Chinese Academy of Sciences. The laser has a 5 mJ output energy in 150 fs pulses at 796 nm. A *p*-polarized laser beam was focused by an *f/5* lens onto foil targets with an average intensity of 5×10^{15} W/cm². The target was moved 0.5 mm per second so that the laser pulses interacted with a fresh target surface for every shot. For some shots, a prepulse with 8% energy of the main laser pulse was applied to create a preplasma with which the main laser pulse interacted after a 50-ps delay time.

Figure 1 shows the experimental layout. In the first part of the experiments, the laser beam was focused onto a 100- μm -thick aluminum foil at 45° to the target normal. A six-channel electron spectrometer with 380 G permanent magnets was set in the normal direction to measure the electron energy distribution in the range of 7–500 keV [25]. LiF detectors were used. Radiochromic films with aluminum fil-

*Author to whom correspondence should be addressed. Email address: jzhang@aphy.iphy.ac.cn

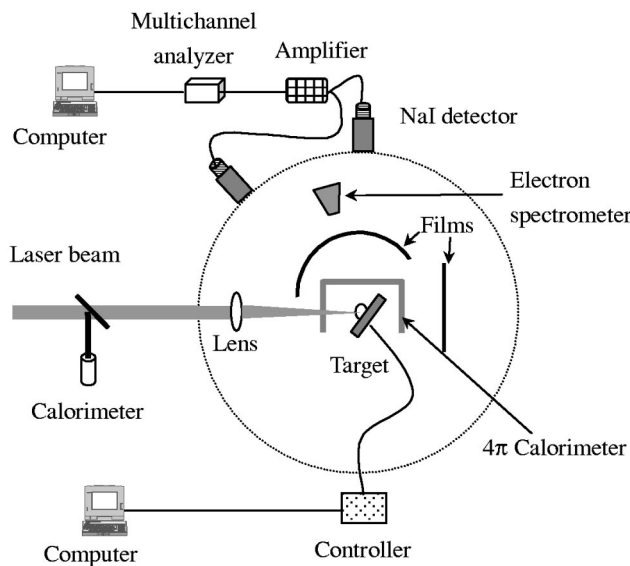


FIG. 1. Schematic of experimental setup. A 4π calorimeter was used to measure the energy absorption. The laser energy was monitored by the calorimeter outside the target chamber. The energy distribution and the spatial distribution of hot electrons ejected from the plasma were detected by an electron spectrometer and radiochromic films surrounding the plasma, respectively. The NaI system was used to monitor the intensity of x-ray emission, which provided information on focal quality.

ters, surrounding the plasma generated by the laser beam, recorded the outgoing hot electrons escaping from the plasma at the front side of the target. A 4π calorimeter measured the laser energy absorption. A 2-mm-thick quartz cylinder inside the calorimeter blocked charged particles and x-ray emission. In order to study the ingoing hot electrons, in the second part of experiments, 5- μm thin foil targets were used. The ingoing energetic hot electrons along the laser propagation direction, after passing through the thin foil, were recorded by a radiochromic film at the backside of the target. The incident angle was chosen to be 30° , because the energy absorption measurement showed a higher coupling efficiency at 30° incidence angle. The NaI detective system shown in Fig. 1 was used to measure the x-ray emission [26]. This system has become our routine diagnostic not only to

study the hard x-ray emission, but also to monitor the focal condition.

III. RESULTS AND DISCUSSION

A. Thick foil experiments

1. Angular distribution of backward hot electrons

We used an aluminum filter assembly in front of the radiochromic film to select the desirable electron energy range. The radiochromic film recorded the electrons, ions, and x-rays passing through the filter assembly. However, the sensitivity of the film to charged particles is higher than that to photons. Previous ion measurements using CR-39 showed that the maximum proton energy produced under the same conditions was less than 500 keV [27], whose penetration depth was about 4 μm in aluminum material. Therefore the ion contribution to the film exposure is negligible because the thickness of the aluminum filter used in our experiments was at least larger than 8 μm . To check the effects of x-rays on the film exposure, a calibration experiment was performed. Two permanent magnets were employed to remove the electrons with energies less than 500 keV (see Fig. 3). Comparison of the exposure value of the film for the conditions with and without external magnetic field showed that the contribution of x rays was two-orders magnitude lower than that of hot electrons. This comparison ensured us that the exposure of the film was mainly caused by hot electrons.

Figure 2 shows the angular distribution of outgoing hot electrons with energies greater than 50 keV in the incident plane. The electrons were generated by p -polarized laser irradiation at a 45° incidence angle with a prepulse 50 ps before the main beam. The solid line in Fig. 2(a) is a microdensitometer trace of angular distribution of hot electrons produced from a 100- μm -thick aluminum foil. The dotted line is a Gaussian fit. Each data point here represents an average of 30 shots. 0° on the x axis corresponds to the backward direction of the laser beam. We can see that the outgoing electrons escaped from the plasma in the target normal direction were well collimated.

The collimated electron jets observed here are very similar to the theoretical prediction obtained by H. Ruhl *et al.* [17] and Y. Sentoku *et al.* [18] using PIC and Vlasov simu-

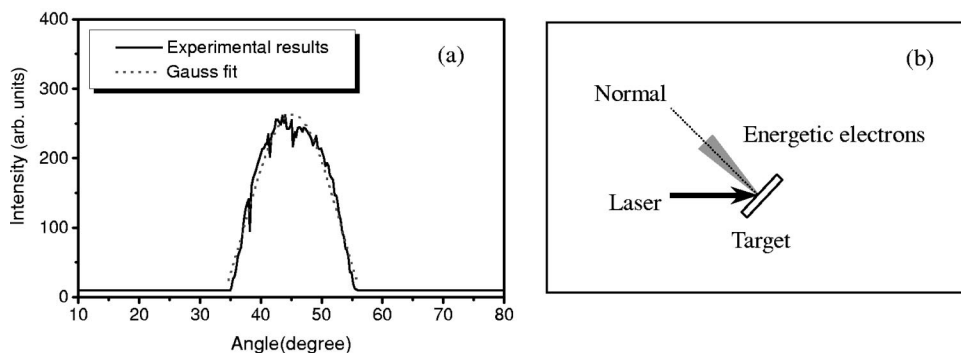


FIG. 2. (a) The angular distribution of outgoing hot electrons with energies over 50 keV in the incident plane. The electrons were generated by p -polarized irradiation at 45° incidence with a prepulse 50 ps before the main beam. The laser intensity was $5 \times 10^{15} \text{ W/cm}^2$. The peak located at the normal direction (45°). (b) Sketch of the outgoing energetic electron emission in front of the target.

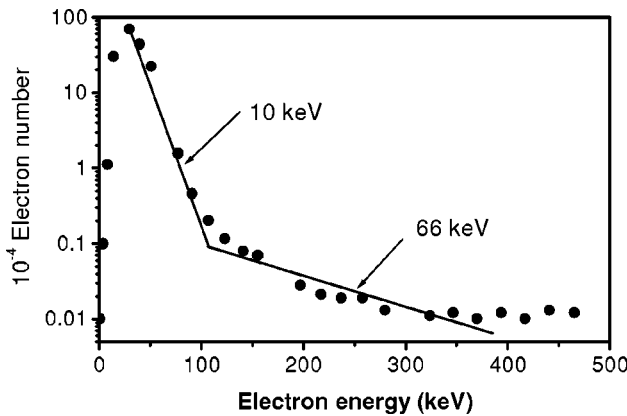


FIG. 3. Typical energy spectrum of outgoing hot electrons measured in the normal direction produced in the laser-thick foil target experiments. The foil was irradiated by *p*-polarized laser at 45° incidence with a prepulse of 50 ps separation time with the main beam. The laser intensity was $5 \times 10^{15} \text{ W/cm}^2$. The two hot-electron temperatures were obtained from exponential fit to the experimental data.

lations. They found electron jets in the interaction of *p*-polarized laser irradiation incident at 30° and 45° on a fully ionized target with an underdense preplasma corona. The self-generated magnetic fields occurred simultaneously and collimated the energetic hot electrons. A scaling law of the outgoing angle of the hot electrons determined by lateral canonical momentum conservation in boost frame coordinates was proposed as

$$\theta' = \tan^{-1} \left[\frac{\sqrt{1 + \alpha I \lambda^2 / 10^{18}} - 1}{\sqrt{\alpha I \lambda^2 / 10^{18}}} \tan \theta \right], \quad (1)$$

where θ' is the electron emission angle to the target normal, θ is the laser incident angle, $I \lambda^2$ is the laser intensity in $\text{W cm}^{-2} \mu\text{m}^2$, and α relates the mean longitudinal momentum to the laser intensity. Two simulations were made by H. Ruhl using PIC and Vlasov simulations for nonrelativistic intensities and for relativistic intensities, respectively. Substituting the simulation parameters used by the authors into Eq. (12) in Ref. [17], one can obtain $\alpha = 2.8 \times 10^{-18} \text{ W}^{-1} \text{ cm}^2 \mu\text{m}^{-2}$ for the case of a nonrelativistic intensity, and $\alpha = 1.25 \text{ W}^{-1} \times 10^{-18} \text{ cm}^2 \mu\text{m}^{-2}$ for the case of a relativistic intensity. We adopt $\alpha = 2.8 \times 10^{-18} \text{ W}^{-1} \text{ cm}^2 \mu\text{m}^{-2}$ here for our case. From Eq. (1), one can get an electron emission angle of $\sim 3^\circ$ to the normal direction under our experimental conditions. This value is very close to our result.

2. Electron energy spectrum

A typical hot-electron energy spectrum measured in the normal direction is shown in Fig. 3. The laser irradiated an aluminum foil at 45° incidence angle. The 8% prepulse arrived target surface 50 ps earlier than the main pulse. It is obvious that two groups of hot electrons were generated in the interaction. Fitted with the experimental data with Boltzmann distribution, the effective temperatures are 10 and 66

keV, respectively. The lower temperature is consistent with the conventional resonant absorption scaling [21], $T_h = 6 \times 10^{-5} [I \lambda^2 (\text{Wcm}^{-2} \mu\text{m}^2)]^{0.33}$ keV, which gives 9 keV for the intensity $5 \times 10^{15} \text{ W/cm}^2$. The 66-keV hot temperature is higher than the value given by ponderomotive potential energy scaling [10]. The scaling proposed by Beg *et al.* [28], $T_h = 100 [I \lambda^2 / 10^{17} (\text{W cm}^{-2} \mu\text{m}^2)]^{1/3}$ keV, gives a hot temperature of 32 keV. This temperature value is different from our experimental value. However, taking the differences in the experimental conditions and the temperature measurement techniques into account, the two values are comparable. (K_α x-ray spectra and bremsstrahlung spectra measurement techniques were adopted by Beg *et al.* The self-generated magnetic fields may affect the K_{alpha} measurement technique [29]. Purely collisional interpretations of fast electron transport in K_α emission experiments will underestimate the number and energy of fast electrons [30].)

3. Energy absorption measurement

Hot-electron generation is closely related to laser-plasma coupling processes. We carried out an energy absorption experiment to confirm the dominant energy absorption mechanism. Initially we used two separate calorimeters with 20 mm diameter aperture to measure the scattered laser lights. The spatial distribution of scattered light was obtained by setting the calorimeters at different positions. We found that nearly all of the light was reflected into a small solid angle in the specular direction when laser beam was incident obliquely without prepulses. This implies that short pulses interact with a very thin skin layer less than a laser wavelength. However, the light was scattered into a wide solid angle when a prepulse was introduced. Therefore, the separated calorimeter was replaced by a 4π calorimeter in the later experiments. The 4π calorimeter collected all the scattered light except the back-reflected light, which is only a few percent and thus negligible.

The absorption measurements conducted with 100 μm -thick aluminum foil target for both *p*-polarized and *s*-polarized laser beams are shown in Fig. 4. A prepulse 50 ps before the main beam was introduced. The absolute absorption coefficient could not be obtained because the calorimeter was not calibrated. We can see the reflectivity dependence on incident angle for both *p*- and *s*-polarized irradiation. Similar results have been observed in absorption experiments with picosecond laser-plasma interactions [31,32]. The maximum absorption for a *p*-polarized laser is at a 20° incidence angle. This corresponds to a plasma scale length of $L \sim 2\lambda$. These results indicate that the resonance absorption plays an important role in the laser-plasma coupling process. Other processes such as vacuum heating [19,33], etc., may also be responsible for the generation of hot electrons with higher energy.

B. Thin foil experiments

Outgoing hot electrons produced in laser-plasma interactions were ejected from the plasma after overcoming the charge separation potential. On the other hand, the in-going hot electrons in the forward direction will be transported into

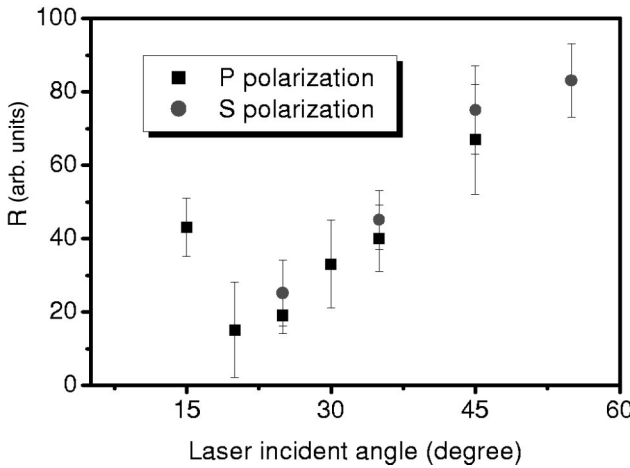


FIG. 4. Angular dependence of the measured reflectance for *p*-polarized beam (square) and *s*-polarized beam (circle) with a prepulse 50 ps before the main beam. Each point is the average of several shots with the statistical error shown as error bar.

the overdense plasma region and cold target region. Hot electrons with higher energies can even pass through the foil target.

We measured the angular distribution of ingoing electrons using radiochromic films with aluminum filter set at the back side of the foil target. Figure 5 shows the angular distributions of the in-going hot electrons with energies greater than 30 keV. The targets were 5- μm -thick aluminum foils. The incident laser intensity was $5 \times 10^{15} \text{ W/cm}^2$. The incident angle was 30° and the light was *p* polarized in these experiments. The dotted line and the dashed line in Fig. 5(a) denote the results obtained with an 8% prepulse 50 ps before the main pulse and without prepulses, respectively. The 0° on *x* axis corresponds to the laser propagation direction. Negative angle represents the angle clockwise from the laser propagation direction. From Fig. 5, we can see immediately that, (a) the angular distribution of hot electrons for the case without preplasmas is isotropic; (b) the hot-electron flux for the case with preplasmas is stronger than that without preplasmas; (c) the distribution of hot electrons for the case with preplasmas consists of two components. One is a very broad distribution,

which can be regarded as a uniform background. A peak distribution at -8° is superposed on the uniform background. Fitted with a Gaussian distribution (shown as solid line), the full width at half maximum (FWHM) of the peak is 24°, and the maximum emission is at -8° . Compared with the outgoing hot electrons, which emit in the normal direction, the ingoing electrons are in the direction close to the laser propagating direction.

The ingoing hot electrons recorded by Radiochromic films have to pass two regions: the plasma region and the cold target region. The physics processes are different for these two regions. In the plasma region, the main effects on hot-electron transport come from the self-generated electric and magnetic fields apart from collisional effects. On the other hand, in the cold target region, the collisions of hot electrons with target ions, bound and free electrons will lead to the direction change and energy loss. We employed a three dimensional (3D) Monte Carlo code to calculate the transport of the energetic electron beam inside an aluminum foil. The foil thickness was chosen to be 5 μm , the same as the foil target used in experiments. An electron source was set to be in the front surface of the foil. The electron number and energy were recorded behind the foil. In the first simulation, electrons with energies of 500, 80, and 30 keV were perpendicularly injected into the foil, respectively. In the second simulation, the electron source with energy of 500 keV was set to be isotropic. We divide the 2π space behind the foil into many smaller annular zones. The differential solid angle for each zone is $2\pi d(\cos\theta)$. Figure 6 shows the angular distribution of electrons passing through the foil. In the Monte Carlo simulations, both the electron energy spectra and spatial distributions were calculated. However, we are more interested in the angular distribution here, so the data shown in Fig. 6, which represents the angular distributions of electrons, were obtained by integrating the whole electron spectra in each annular zone. For the normal incidence in the first simulation, almost all of the 500 keV electrons fall into the 0° annular zone. That is to say, these electrons remain well collimated. However, the angular divergence increases with the reduction of electron energy. Taking 80 keV electrons for example, only 46% of electrons fall into the 26°

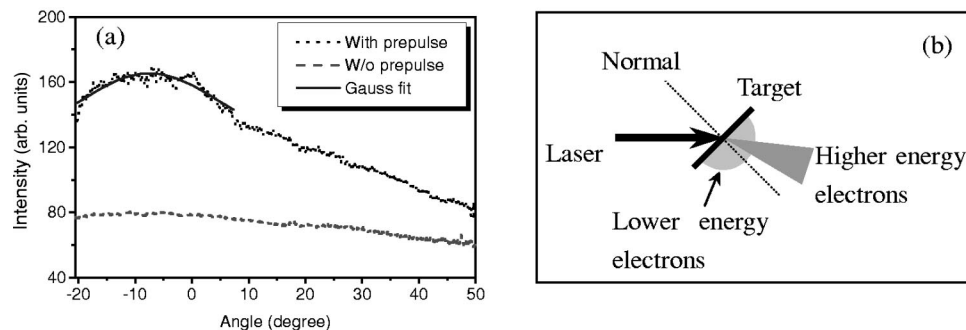


FIG. 5. (a) Angular distribution of ingoing hot electrons with energies greater than 30 keV, measured at the backside of a 5 μm -thick foil target. The dotted line and dashed line are for the case with and without prepulse, respectively. A peak at -8° with 24° FWHM is superposed on a very broad uniform distribution for the case with prepulses. No such peak for the distribution without prepulses. (b) Sketch of the hot-electron emission at the backside of the target for the case with prepulses. Low-energy electrons spread into wide angle as a uniform background of the higher-energy electrons.

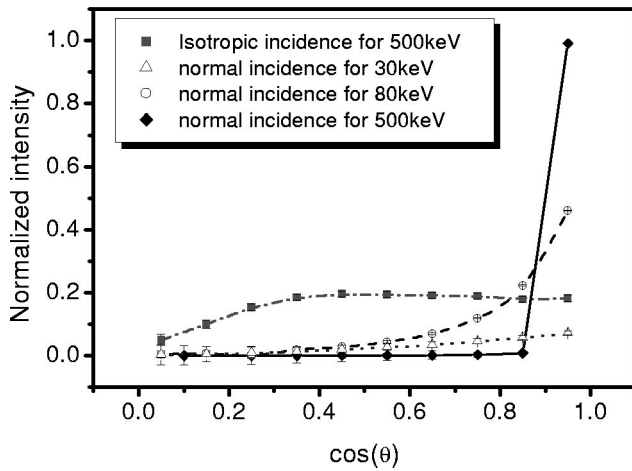


FIG. 6. The theoretical angular distribution of hot electrons recorded behind a 5- μm -thick aluminum foil obtained by 3D Monte Carlo code. The circle is for an isotropic electron source (shown $\times 5$). θ is the angle relative to the normal direction of aluminum foil. For the collimated electron beams perpendicular to the foil, the divergence angles are wider for the lower-energy electrons.

cone angle, shown as the open circles in Fig. 6. For the isotropic input in the second simulation, the distribution remained isotropic within the range of angle $0^\circ \sim 70^\circ$. The number of electrons falling into the range greater than 70° decreases because of their longer path in the target.

The emission direction of hot electrons is different for different acceleration mechanisms. The resonance absorption produces electrons in the direction of electron density gradient, which is observed for the outgoing electrons in our experiments. Ponderomotive potential and wake field mechanisms generate hot electrons along the laser propagation direction. However, they are significant only for higher-laser intensities. No such longitudinal acceleration scheme present for our intensity of $5 \times 10^{15} \text{ W/cm}^2$. Both of the collisional effects and the angular scattering processes in the plasma region and the cold target region are the main reasons for the angular divergence of hot electrons. But these effects cannot explain the collimation of the hot electrons in the laser propagation direction. It is well known that the intense electric fields and magnetic fields exist in laser-plasma interactions. These fields may play important roles in electron transport process into solid targets. J. R. Davies *et al.* considered the transport of hot electrons using a relativistic Fokker-Planck equation. The proposed growth rate of the magnetic field can be written approximately [30] as

$$\frac{\partial B}{\partial t} \sim 3 \times 10^{-2} \frac{\eta f_a}{d} \left(\frac{I}{\lambda} \right)^{2/3} \text{ T ps}^{-1}, \quad (2)$$

where η is the resistivity in $\Omega \cdot \text{m}$, f_a is the absorption fraction, I is the laser intensity in W/cm^2 , d is the focal spot diameter in micro, λ is the laser wavelength in micro, B is the self-generated magnetic field in T. The magnetic field increases to a large magnitude very rapidly. The role of the electric field is to reduce the kinetic energy of hot electrons. On the one hand, the self-generated magnetic fields can col-

limate the electrons, on the other hand the propagation direction of electron beam can be changed or deflected if the fields are nonsymmetrical distributed. The direction of hot electrons is easily changed by any minor nonsymmetry of magnetic fields due to their light mass. Our previous optical diagnostic experiments using laser probing showed a non-symmetrical plasma expansion [34]. The deflection of protons due to self-generated magnetic fields was also observed. E. Clark, etc., observed a ring structure of protons, and the ring center deviated about 10° from the target normal in the ultraintense laser-solid interactions [35,36]. The authors believed that the protons were deflected by magnetic fields. Another experiment to study the effects of plasma density scale length on the direction of hot electrons showed that two electron beams were produced, and depending on the structure of the magnetic fields, the two electron beams could change their direction or coalesce together while traversing such fields [37]. These analyses suggest that the hot electrons propagating through the solid target might be bent by the magnetic fields in the interaction region and the overdense region.

The x-ray measurements showed that the prepulses could enhance the emission and energy of hot electrons dramatically [26]. The hot-electron temperature deduced from the x-ray spectrum was about 10 keV for the case without prepulses. When a prepulse was used, the x-ray spectrum presented a double Maxwellian distribution. A group of electrons was accelerated to a much higher energy (66 keV) measured by the electron spectrometer (Fig. 3)

Based on experimental results and theoretical calculation, the angular distribution of in-going hot electrons may be explained as follows. When the in-going hot electrons produced in the laser interactions pass through the plasma region, they are deflected by the self-generated magnetic fields and tend to propagate in the laser propagation direction. The collisional effects in plasma region and in cold material region lead to the energy loss and broaden its angular distribution. The multiple scattering is not very effective for the hot electrons with higher energies, so they remain well directional. However, the hot electrons with lower energies can be steered significantly due to the serious scattering, therefore, they present as a uniform background.

We can see from the above analyses that the ingoing electrons suffer serious scattering and are sensitive to the electromagnetic fields during transport in dense plasma and cold target material. More recently, a collimated proton beam with up to 55 MeV energy was observed in petawatt laser plasma interactions [38]. It is not easy to deflect protons by collisions and electromagnetic fields due to their large mass. Thus, the trajectory of protons approximates a straight line in dense plasma. Furthermore, the efficiency of the energy transfer of protons to nuclear fuel is much higher than that of hot electrons. So protons may become one of competitive candidates as energy carrier in the fast ignitor concept studies.

IV. CONCLUSION

The angular distributions, energy spectrum of hot electrons produced in the interaction of femtosecond laser pulses

with the aluminum plasmas are investigated at a moderate intensity. A collimated jet of hot electrons is observed in the target normal direction. The emission angle of the hot electrons is in agreement with the angular scaling from the canonical momentum conservation. However, the in-going energetic electron beam passing through the foil target is observed to be in the laser propagation direction. This may be the result of the self-generated magnetic fields. The low-energy electrons, which spread into a wider cone angle due to the collisional effect in plasma and target material, present as continuous background. This process is supported by 3D

Monte Carlo simulations. The hot temperatures obtained from the electron spectrum and absorption measurement suggest that resonance absorption might be partially responsible for the generation of hot electrons.

ACKNOWLEDGMENTS

This work was supported by the National Natural Foundation of China under Grant Nos. 19825110, 10005014, and 10075075, the National High-Tech ICF program, and the NKBRSP under Grant No. G19999075200.

-
- [1] M. Tabak *et al.*, Phys. Plasmas **1**, 1626 (1994).
 - [2] K.B. Wharton *et al.*, Phys. Rev. Lett. **81**, 822 (1998).
 - [3] M.H. Key *et al.*, Phys. Plasmas **5**, 1966 (1998).
 - [4] S. Bastiani *et al.*, Phys. Rev. E **56**, 7179 (1997).
 - [5] J. Fuchs *et al.*, Phys. Plasmas **6**, 2569 (1999).
 - [6] Th. Schlegel *et al.*, Phys. Rev. E **60**, 2209 (1999).
 - [7] U. Teubner *et al.*, Phys. Rev. E **54**, 4167 (1996).
 - [8] M. Roch *et al.*, in *Inertial Fusion Sciences and Applications* 99, edited by Christine Labaune, William J. Hogan, and Kazuo A. Tanaka (Elsevier, Paris, 2000).
 - [9] G. Malka and J.L. Miquel, Phys. Rev. Lett. **77**, 75 (1996).
 - [10] S.C. Wilks, W.L. Cruer, M. Tabak, A. Loudon, Phys. Rev. Lett. **69**, 1383 (1992).
 - [11] A.J. Mackinnon *et al.*, Phys. Plasmas **6**, 2185 (1999).
 - [12] M. Borghesi *et al.*, Phys. Rev. Lett. **80**, 5137 (1998).
 - [13] M. Tatarakis *et al.*, Phys. Rev. Lett. **81**, 999 (1998).
 - [14] M. Borghesi *et al.*, Phys. Rev. Lett. **83**, 4309 (1999).
 - [15] L. Gremillet *et al.*, Phys. Rev. Lett. **83**, 5015 (1999).
 - [16] P.A. Norreys *et al.*, Phys. Plasmas **6**, 2150 (1999).
 - [17] H. Ruhl *et al.*, Phys. Rev. Lett. **82**, 743746 (1999).
 - [18] Y. Sentoku *et al.*, Phys. Plasmas **6**, 2855 (1999).
 - [19] F. Brunel, Phys. Rev. Lett. **59**, 52 (1987).
 - [20] D. Gordon *et al.*, Phys. Rev. Lett. **80**, 2133 (1998).
 - [21] W. L. Cruer, *The physics of Laser Plasma Interactions* (Addison-Wesley, Redwood City, CA, 1988).
 - [22] E. Lefebvre *et al.*, Phys. Rev. E **55**, 1011 (1997).
 - [23] A. Pukhov *et al.*, Phys. Plasmas **5**, 1880 (1998).
 - [24] W. Yu *et al.*, Phys. Rev. Lett. **85**, 570 (2000).
 - [25] L.M. Chen *et al.*, Sci. China, Ser. A: Math., Phys., Astron. **43**, 1294 (2000).
 - [26] P. Zhang *et al.*, Phys. Rev. E **57**, R3746 (1998).
 - [27] L.M. Chen *et al.*, Phys. Rev. E **63**, 036403 (2001).
 - [28] F.N. Beg *et al.*, Phys. Plasmas **4**, 447 (1997).
 - [29] A.R. Bell *et al.*, Phys. Rev. E **58**, 2471 (1998).
 - [30] J.R. Davies *et al.*, Phys. Rev. E **56**, 7193 (1997).
 - [31] A.G.M. Maaswinkel, K. Eidmann, and R. Sigel, Phys. Rev. Lett. **42**, 1625 (1979).
 - [32] K.R. Manes *et al.*, Phys. Rev. Lett. **39**, 281 (1977).
 - [33] P. Gibbon and A.R. Bell, Phys. Rev. Lett. **68**, 1535 (1992).
 - [34] Li Yutong *et al.*, Sci. China, Ser. A: Math., Phys., Astron. **44**, 98 (2001).
 - [35] E.L. Clark *et al.*, Phys. Rev. Lett. **85**, 1654 (2000).
 - [36] E.L. Clark *et al.*, Phys. Rev. Lett. **84**, 670 (2000).
 - [37] M.I.K. Santala *et al.*, Phys. Rev. Lett. **84**, 1459 (2000).
 - [38] M.D. Perry, *Science Technology*, LLNL Report No. 25 (2000).

Long plasma channels generated by femtosecond laser pulses

H. Yang,¹* J. Zhang,^{1,*} W. Yu,² Y. J. Li,¹ and Z. Y. Wei¹

¹Laboratory of Optical Physics, Institute of Physics, Chinese Academy of Sciences, Beijing 100080, China

²Shanghai Institute of Optics and Fine Mechanics, Chinese Academy of Sciences, Shanghai 230026, China

(Received 16 November 2000; revised manuscript received 4 June 2001; published 17 December 2001)

Generation of a long plasma channel by femtosecond laser pulses is investigated. The results show that the balance between the nonlinear self-focusing of the laser beam and plasma defocusing forms a long plasma channel, which guides the laser beam to propagate a long distance in air. This phenomenon can be used to trigger lightning.

DOI: 10.1103/PhysRevE.65.016406

PACS number(s): 52.38.-r

I. INTRODUCTION

Propagation of intense short laser pulses over a long distance in gases and plasmas has been studied at different laboratories [1–4]. The propagation of intense laser pulses is important in a wide range of applications, such as guiding a very long electrical discharge for triggering lightning. Natural lightning is very harmful to humankind, and causes huge financial losses. For example, the power industry loses a few billion dollars every year because of lightning strikes. One possible way of protecting dedicated facilities from lightning strikes is to divert the lightning to a safe place.

The control of lightning was envisioned by Benjamin Franklin when he conducted his legendary experiments in 1752. A modern method for triggering lightning is to fire small rockets trailing ground wires toward thunder clouds. However, its success rate is only about 60%. Moreover, it cannot be launched on a semicontinuous basis. Laser-triggered lightning was proposed by Ball in 1974 [5], but it was not successful due to the limitation of the laser technology at that time. Japanese researchers in Osaka reported experiments of successful triggered lightning using 2-kJ CO₂ laser pulses [6]. As a result of the progress in chirped pulse amplification (CPA) technology, we can now obtain intense ultrashort laser pulses from table-top laser systems. The laser intensity can reach the order of 10¹⁹ W cm⁻². This provides a promising way to generate a long plasma channel to trigger lightning.

The formation of the long plasma channels is attributed to the balance of self-focusing and defocusing of the laser beam, due to the intensity-dependent nonlinear index of air and the axial plasma filaments created by tunneling ionization of air, respectively. Braun *et al.* [7] observed that ultrashort laser pulses can be self-channeled into a filament with an intensity of 7 × 10¹³ W cm⁻² and propagate through a distance greater than 20 m. The average electron density in the channel was found to be around 10¹⁷ cm⁻³. The long filaments provide a channel with enhanced conductivity that could initiate and guide lightning. In this paper, we use a one-dimensional (1D) propagation code to simulate this pro-

cess and obtain results in agreement with experimental measurements.

II. PRINCIPLE OF FORMING A LONG PLASMA CHANNEL

The formation of a long plasma channel in air is of key importance for laser-triggered lightning. In vacuum, the propagation distance of a Gaussian laser beam is confined to the Rayleigh length $Z_R = kr_0^2/2$, where r_0 is the laser spot size at focus and k is the wave number. Generally, high laser intensities require tight focusing, which in turn results in very short propagation distance (e.g., when $r_0 = 80 \mu\text{m}$ and $\lambda = 0.8 \mu\text{m}$, the Rayleigh length is only $Z_R = 25 \text{ mm}$). However, we shall show that it is possible for a laser beam to propagate over a greatly extended distance (many Rayleigh lengths) in air. We find that the laser propagation in the air is strongly affected by the nonlinear self-focusing and ionization-induced defocusing effects. The balance between these two effects can guide the propagation of laser pulses and create a long plasma channel.

The wave equation for laser propagation in a medium can be written as [8–10]

$$\nabla^2 E - \frac{1}{c^2} \frac{\partial^2}{\partial t^2} E = k^2(1 - \eta^2)E, \quad (1)$$

with the refractive index

$$\eta = 1 + \eta_2 I - n_e / 2n_c. \quad (2)$$

For air at 1 atm we have $\eta_0 = 1$ and the nonlinear index $\eta_2 = 5 \times 10^{-19} \text{ cm}^2 \text{ W}^{-1}$, $I = (c/8\pi)|E|^2$ is the laser intensity, n_e is the density of free electrons, and $n_c = m_e \omega^2 / 4\pi e^2$ is the plasma critical density. The second term in Eq. (2) describes the optic-field-induced nonlinear self-focusing in gas, which can be attributed to the fact that the central part of the beam, having higher intensities, experiences a larger refractive index than the beam edge. The third term describes ionization-induced defocusing, since there are more free electrons in the central part of the beam.

Let us consider a Gaussian laser beam focused upon the opening of a gas chamber with a field strength E_0 and a minimum spot size r_0 . Assuming the wave amplitude varies slowly compared to the laser wavelength, the laser beam remains approximately Gaussian during its propagation in the gas. It can be expressed as

*Author to whom correspondence should be addressed. Email address: jzhang@aphy.iphy.ac.cn

$$|E(r,y)| = E_0(r_0/r_s) \exp(-r^2/2r_s^2), \quad (3)$$

where we neglect the energy loss during propagation in Eq. (3), $r_s(z)$ is the spot size at which the field strength reduces to e^{-1} of its peak value at the propagation axis, and r_0 is the laser beam waist at $z=0$. The variation of the spot size in the propagation direction is given by

$$d^2r_s/dz^2 = (\partial\eta/\partial r)_{r_s} + 4/k^2 r_s^3, \quad (4)$$

where η is a function of $|E|$ and

$$\partial\eta/\partial r = (\partial\eta/\partial|E|)(\partial|E|/\partial r) = -(2r/r_s^2)(|E|\partial\eta/\partial|E|).$$

We have assumed that around the spot size the factor of $(|E|\partial\eta/\partial|E|)$ is slowly varying with r .

When laser intensity is $I \geq 10^{14} \text{ W cm}^{-2}$, tunnel ionization dominates the ionization process [11–17]. According to the tunneling model, the ionization rate is given by

$$dn_e(t)/dt = w(t)(N_0 - n_e), \quad (5)$$

where $n_e(t)$ is the time-dependent electron density, N_0 is the initial neutral gas density, and $w(t)$ is given by

$$w(|E|) = 4\Omega \left(\frac{E_i}{E_h} \right)^{5/2} \frac{E_a}{|E|} \exp \left[-\frac{2}{3} \left(\frac{E_i}{E_h} \right)^{3/2} \frac{E_a}{|E|} \right], \quad (6)$$

where E_i and E_h are the ionization potential of the gas under consideration and of hydrogen, respectively, $\Omega = me^2/h^3 = 4.16 \times 10^{16} \text{ s}^{-1}$ is the atomic frequency, and $E_a = m^2 e^5 / h^4 = 5.1 \times 10^9 \text{ V cm}^{-1}$ is the field strength at the Bohr radius. For simplicity, considering a flat-top laser pulse beam in the time domain, the density of ionized electrons can be expressed as

$$n_e = N_0 [1 - \exp(-w(|E|\tau))], \quad (7)$$

where τ is the duration of laser pulses. From the above equations we get

$$\frac{d^2R}{dZ^2} = \left(1 - \alpha \frac{P}{P_N} \right) R^{-3} + \frac{(DR-1)}{\exp(DR+FDR/\exp(DR))}, \quad (8)$$

where $\alpha = 4/e$, $R = r_s/r_0$, $Z = z/z_R$, $A = E_i/E_h$, $B = E_a/E_0$, $C = N_0 \Omega \tau k^2 r_0^2 A^{5/2} B e^{1/2} / n_c$, $D = 2A^{3/2} B \exp(0.5)/3$, $F = 6\Omega A \tau$, P is the laser power, and $P_N = 2\pi/k^2 \eta_2$ is the critical power for nonlinear self-focusing.

We have now obtained the equation describing the variation of spot size R with respect to propagation distance Z . The first term on the right-hand side of the equation is responsible for the nonlinear self-focusing and the second term for the plasma defocusing. A proper balance between the two effects could be used to guide the laser propagation over a long distance.

III. CALCULATION RESULTS

We have assumed that the incident laser beam is focused upon the opening of a gas chamber. If there is no gas inside

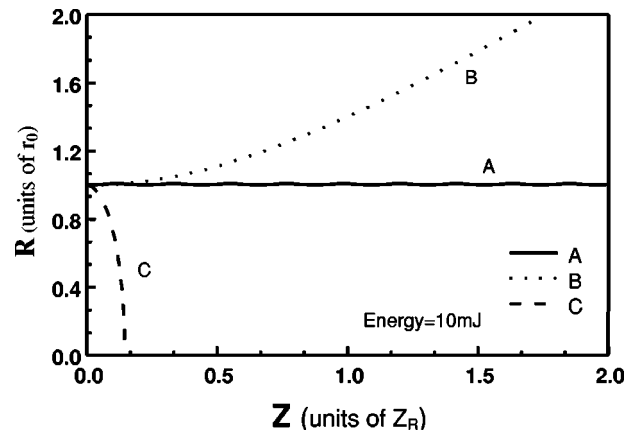


FIG. 1. Variation of the laser-beam radius with the propagation distance Z . The dashed curve (C) is self-focusing without ionization; the solid curve (A) represents propagation of a laser pulse in air; the dotted curve (B) is free propagation in vacuum ($r_0 = 180 \mu\text{m}$, $\tau = 150 \text{ fs}$).

the chamber, the laser beam will diffract with its spot size increasing monotonically with Z , as shown in Fig. 1 by the dotted curve (B). If there is gas inside but without any ionization processes, the propagation of the laser beam in the atomic gas is governed by

$$d^2R/dZ^2 = (1 - \alpha P/P_N) R^{-3}. \quad (9)$$

Its solution can be written as

$$R^2 = 1 + (1 - \alpha P/P_N) Z^2, \quad (10)$$

where we have assumed that $R = 1$ and $Z = 0$. When the laser power is $P > P_N/\alpha$, the laser beam will be self-focused with a spot size decreasing monotonically during propagation, as shown by the dashed curve (C) in Fig. 1. According to Eq. (10), when $Z = (\alpha P/P_N - 1) Z_R$, the spot size R reduces to zero and a singularity in field strength occurs. In reality, this will not happen since the enhancement in field strength will inevitably lead to ionization. The solid curve (A) in Fig. 1, calculated from Eq. (8) with $r_0 = 180$ (we can get this with a lens), pulse energy $E = 10 \text{ mJ}$ ($P = 67 \text{ GW}$), $\tau = 150 \text{ fs}$, and a laser wavelength of 800 nm, shows the real situation for the propagation of an intense laser beam in ionizing gases. The variation of the beam radius R with the propagation distance Z is presented. It shows that the beam radius remains almost constant (about 180 μm), and the slight oscillation reflects the competition between self-focusing and defocusing. When the laser beam is focused to a certain extent, the tunneling ionization rate increases. The ionized electrons make the beam defocused. Because of defocusing, the ionization rate will decrease. The nonlinear effect in gases will then make the beam focused again. We find the laser intensity inside the channel to be about $10^{14} \text{ W cm}^{-2}$ in Fig. 2 (curve A), close to the threshold of the tunnel ionization of air. This result agrees with the measurements in Ref. [7], in which the laser intensity in the channel was measured to be $7 \times 10^{13} \text{ W cm}^{-2}$. Curves B and C in Fig. 2 correspond to the laser intensity of Fig. 1 (curves B and C). From Eq. (8), we

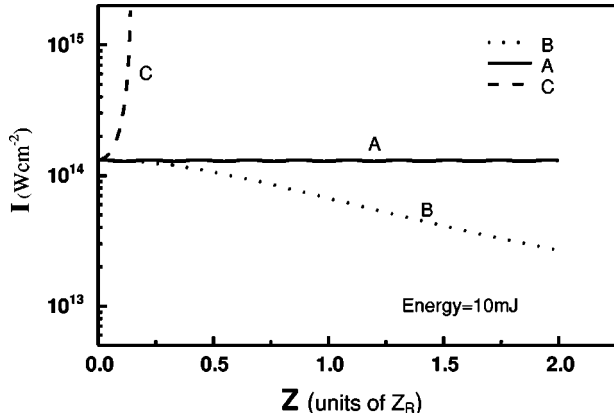


FIG. 2. The laser intensity in the channel versus the propagation distance ($r_0 = 180 \mu\text{m}$, $\tau = 150 \text{ fs}$).

simulate variation of the laser beam radius with the input laser pulse energy (power). The results are shown in Fig. 3. The behavior of the laser propagation is sensitive to the input laser energy (power). Only the laser energy (power) in the range shown by curves *B*, *C*, *D*, and *E* in Fig. 3 can lead to an oscillated propagation of the laser beam to a very large distance (many Rayleigh lengths). A channel length larger than 20 m was observed in the experiment in Ref. [7]. In order to show the characteristics of the channel more clearly, we only draw a short range covering two Rayleigh lengths in Figs. 1–3. Characters of the plasma channels formed are different because of a variation of the laser power. From curves *B*, *C*, *D*, and *E* in Fig. 3, there must exist an energy (power) which can cause the laser-beam radius to keep a constant (such as curve *C*). The oscillation amplitude of the laser-beam radius becomes very large when the laser power departs from this power. So the small disturbance would cause the laser beam to spread and the laser beam could not propagate a very long distance. Furthermore, this would generate a discontinued distribution of electrons in the channel (as shown in Fig. 5 and Fig. 6). For a too high or too low laser power, the laser beam would spread as curves *A* and *F* in Fig. 3.

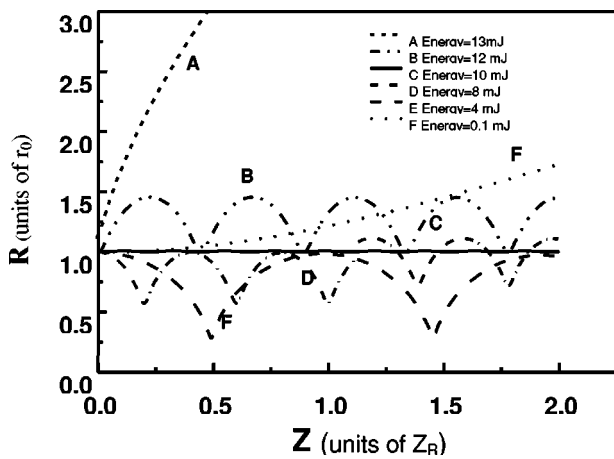


FIG. 3. The laser-beam propagation for different initial energy ($r_0 = 180 \mu\text{m}$, $\tau = 150 \text{ fs}$).

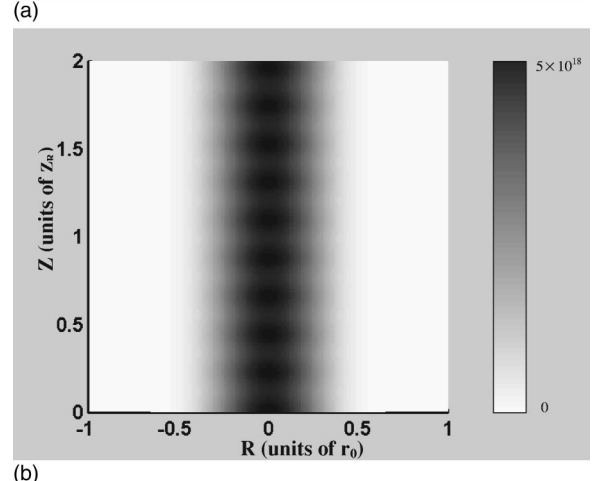
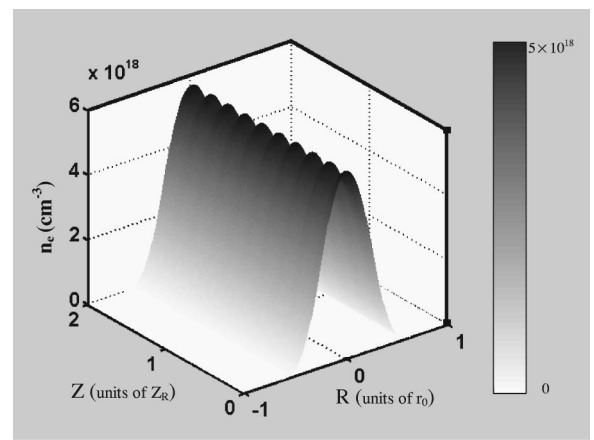


FIG. 4. Spatial distribution of the electron density in the plasma channel. (a) represents the distribution of the electrons in the channel. (b) is the contour curve of the electron density (the pulse energy $E = 10 \text{ mJ}$, $r_0 = 180 \mu\text{m}$, and $\tau = 150 \text{ fs}$).

The density of ionized electrons in the channel also oscillates along Z as shown in Fig. 4(a) and Fig. 4(b) corresponding to Fig. 1 (curve *A*). The electron density is semicontinuous and the maximum density at the center of the plasma

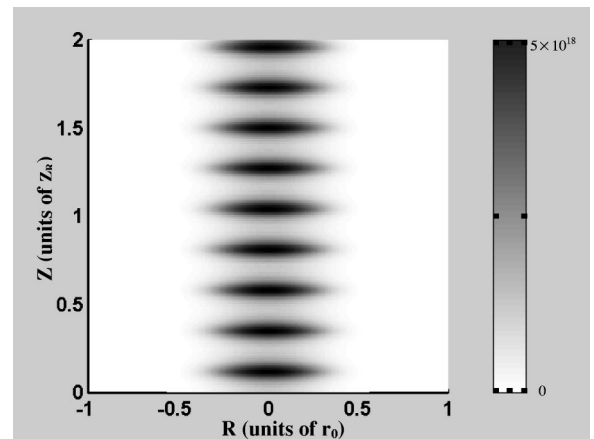


FIG. 5. The contour curve of the electron density in the plasma channel with the pulse energy $E = 12 \text{ mJ}$ ($r_0 = 180 \mu\text{m}$, and $\tau = 150 \text{ fs}$).

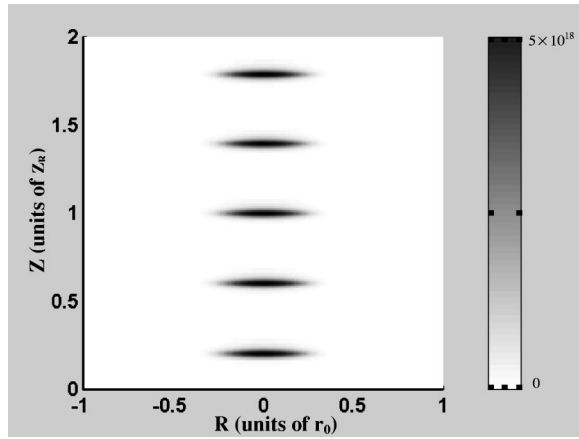


FIG. 6. The contour curve of the electron density in the plasma channel with the pulse energy $E=4$ mJ ($r_0=180$ μm , and $\tau=150$ fs).

channel can reach 10^{18} cm^{-3} , while the average electron density is about 10^{17} cm^{-3} . An average electron density of about 6×10^{16} cm^{-3} was measured by Braun *et al.* [7] in the laser channel. We find that the radius of the ionized channel in Fig. 4 is about 40–50 μm and is a quarter radius of the initial laser beam. In the calculation, we find that the plasma channel can be discontinued like beads when the laser power largely departs from the optimum energy (power). For example, if the laser pulse energy $E=12$ mJ or $E=4$ mJ, the plasma channel would be discontinued as shown in Fig. 5 and Fig. 6.

In the above calculations, we did not consider the loss of the laser energy in the propagation, because usually this energy loss is very small. In the propagation process, the main energy loss is due to the ionization. Assuming the plasma channel is in a column configuration and taking the average laser intensity to be $I=10^{14}$ W/cm^2 , the energy loss is

$$E_{\text{loss}}=1.6 \times 10^{-19} \bar{n}_e \pi d_0^2 L U_i / 4. \quad (11)$$

If we take the ionized channel $L=1$ m, $d=80$ μm (the ionized channel diameter is about a quarter of the laser beam diameter from Fig. 4), and assume $\bar{n}_e=6 \times 10^{16}/\text{cm}^3$ (in Ref. [7]), the ionization energy is $U_i=15.5$ eV, and the energy loss is

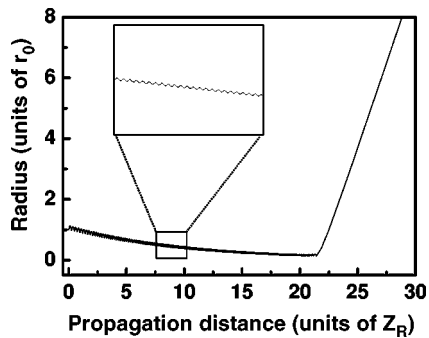


FIG. 7. The propagation of a laser beam taking into account the loss of the laser energy. The inset shows details of a portion of the magnified plasma channel.

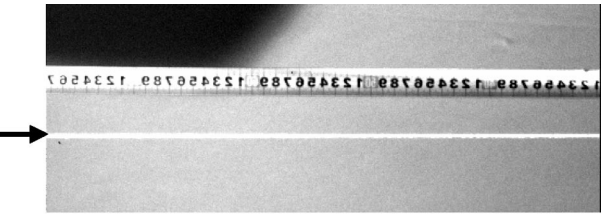


FIG. 8. One portion of the laser plasma channel taken by a CCD camera.

$$E_{\text{loss}}=0.74 \text{ mJ.}$$

We find that the energy loss is relatively small compared with the total input energy. The electron density in the channel is almost uniform with our stimulation in Fig. 4. We believe the laser energy decays approximately linearly and the laser energy with propagation distance becomes

$$\varepsilon(z)=\varepsilon(0)(1-\beta z), \quad (12)$$

where β is the laser energy decay coefficient per Rayleigh length and $\varepsilon(0)$ is the initial laser energy. Following the above evaluation of the energy depletion and Eq. (12), we can get $\beta=0.094$ per Rayleigh length. Because β is very small, the $\varepsilon(z)$ can be written as

$$\varepsilon(z) \approx \varepsilon(0) \exp(-\beta z).$$

Therefore, the amplitude of Eq. (3) has to be multiplied by $\exp(-\beta z/2)$. We can get new simulation results of laser propagation from Eq. (8) shown in Fig. 7. From it we find that the radius of the channel begins to decrease and finally collapse. This appearance is caused by a decay of the energy. The laser beam has to keep the balance of the focusing and defocusing by decreasing the radius. At last, this balance becomes unstable when the depletion of laser energy becomes large enough. Smaller laser radius and depletion of energy would lead to the collapse of the laser beam. In the stimulation process, we let $\beta=0.094$, $\tau=150$ fs, and $\varepsilon(0)=10$ mJ. From Fig. 7, we know that the laser beam can propagate longer than 20 Rayleigh lengths and collapse (for a laser beam of $r_0=180$ μm , the corresponding Rayleigh length is $Z_R=12.7$ cm). In order to show this more clearly, we magnify a small part of the channel as the inset in Fig. 7. The inset gives details for about five Rayleigh lengths in the process of the beam propagation. From it we can observe the oscillation of the beam, as in Fig. 1. Furthermore, in our experimental measurements, we observed a plasma channel longer than 5 m as shown in Fig. 8 (laser parameter $E=15$ mJ, $\tau=25$ fs). Because of the limited imaging range of the CCD camera, only a part of the laser channel can be taken in Fig. 8 (about 50 cm). Moreover, the resistivity of the channel was measured to be smaller than $0.5 \Omega \text{ cm}$. Such a long and conductive channel provides a good testbed for the investigation of triggered lightning.

IV. CONCLUSION

A short-pulse laser beam with a Gaussian profile can propagate over a long distance in air due to the balance be-

tween focusing and defocusing of the laser beam. The variation of the beam radius with propagation distance is studied. There exists an optimum energy (power) which can lead the laser beam to propagate a very long distance. It is found that the profile of the electron density in the channel is oscillating and the peak electron density is about 10^{18} cm^{-3} cm in the channel.

ACKNOWLEDGMENTS

We acknowledge helpful discussions with L. M. Chen, Q. L. Dong, and T. Z. Lu. This work was supported by the National Natural Science Foundation of China (Grant Nos. 19825110 and 10004015) and NKBRSPF (Grant No. G1999075200).

-
- [1] B. La Fontaine, F. Vidal, Z. Jiang, C.Y. Chien, D. Comtois, A. Desparois, T.W. Johnston, J.-C. Kieffer, and H. Pepin, Phys. Plasmas **6**, 1615 (1999).
 - [2] X.M. Zhao, J.-C. Diels, C.Y. Wang, and J.M. Elizondo, IEEE J. Quantum Electron. **31**, 599 (1995).
 - [3] S. Tzortzakis *et al.*, Phys. Rev. E **60**, R3505 (1999).
 - [4] B.M. Penetrante and J.N. Bardsley, Phys. Rev. A **43**, 3100 (1991).
 - [5] L.M. Ball, Appl. Opt. **13**, 2292 (1974).
 - [6] T. Yamanaka, Asian Science Seminar on High-power Laser Matter Interaction, Osaka, Japan, 1999.
 - [7] A. Braun, G. Korn, X. Liu, D. Du, J. Squier, and G. Mourou, Opt. Lett. **20**, 73 (1995).
 - [8] Y.R. Shen, *The Principles of Nonlinear Optics* (Academic, New York, 1993).
 - [9] R. Fedosejevs, X.F. Wang, and G.D. Tsakiris, Phys. Rev. E **56**, 4615 (1997).
 - [10] E. Esarey *et al.*, IEEE J. Quantum Electron. **33**, 1879 (1997).
 - [11] S. Augst, D. Dmeyerhofer, D. Strickland, and S.L. Chin, J. Opt. Soc. Am. B **8**, 858 (1991).
 - [12] M. Mlejnek, E.M. Wright, and J.V. Moloney, Phys. Rev. E **58**, 4903 (1998).
 - [13] B. La Fontaine *et al.*, IEEE Trans. Plasma Sci. **27**, 688 (1999).
 - [14] W.P. Leemans, C.E. Clayton, W.B. Mori, K.A. Marsh, P.K. Kaw, A. Dyson, C. Joshi, and J.M. Wallace, Phys. Rev. A **46**, 1091 (1992).
 - [15] P. Sprangle, E. Esarey, and A. Ting, Phys. Rev. A **41**, 4463 (1990).
 - [16] R. Bharuthram, J. Parashar, and V.K. Tripathi, Phys. Plasmas **6**, 1611 (1999).
 - [17] B. Corkum, N.H. Burnett, and F. Brunel, Phys. Rev. Lett. **62**, 1259 (1989).